

OTIC FILE COPY

AD-A217 606

AGARD-CP-470

AGARD-CP-470

AGARD

ADVISORY GROUP FOR AEROSPACE RESEARCH & DEVELOPMENT

7 RUE ANCELLE 92200 NEUILLY SUR SEINE FRANCE

AGARD CONFERENCE PROCEEDINGS No.470

Flight in Adverse Environmental Conditions

DISTRIBUTION STATEMENT A

Approved for public release
Distribution Unlimited

DTIC
ELECTE
JAN 05 1990
S DCS D

NORTH ATLANTIC TREATY ORGANIZATION



DISTRIBUTION AND AVAILABILITY
ON BACK COVER

90 01 05 028

AGARD-CP-470

**NORTH ATLANTIC TREATY ORGANIZATION
ADVISORY GROUP FOR AEROSPACE RESEARCH AND DEVELOPMENT
(ORGANISATION DU TRAITE DE L'ATLANTIQUE NORD)**

**AGARD Conference Proceedings No.470
FLIGHT IN ADVERSE ENVIRONMENTAL CONDITIONS**

**Copies of papers presented at the Flight Mechanics Panel Symposium held at
Gol, Norway from 8 to 11 May 1989.**

THE MISSION OF AGARD

According to its Charter, the mission of AGARD is to bring together the leading personalities of the NATO nations in the fields of science and technology relating to aerospace for the following purposes:

- Recommending effective ways for the member nations to use their research and development capabilities for the common benefit of the NATO community;
- Providing scientific and technical advice and assistance to the Military Committee in the field of aerospace research and development (with particular regard to its military application);
- Continuously stimulating advances in the aerospace sciences relevant to strengthening the common defence posture;
- Improving the co-operation among member nations in aerospace research and development;
- Exchange of scientific and technical information;
- Providing assistance to member nations for the purpose of increasing their scientific and technical potential;
- Rendering scientific and technical assistance, as requested, to other NATO bodies and to member nations in connection with research and development problems in the aerospace field.

The highest authority within AGARD is the National Delegates Board consisting of officially appointed senior representatives from each member nation. The mission of AGARD is carried out through the Panels which are composed of experts appointed by the National Delegates, the Consultant and Exchange Programme and the Aerospace Applications Studies Programme. The results of AGARD work are reported to the member nations and the NATO Authorities through the AGARD series of publications of which this is one.

Participation in AGARD activities is by invitation only and is normally limited to citizens of the NATO nations.

The content of this publication has been reproduced directly from material supplied by AGARD or the authors.

Published September 1989

Copyright © AGARD 1989
All Rights Reserved

ISBN 92-835-0527-1



*Printed by Specialised Printing Services Limited
40 Chigwell Lane, Loughton, Essex IG10 3TZ*

PREFACE

Although AGARD has continued to be active in the various fields of flight in adverse environmental conditions it was considered to be important and timely to review the subject in a wider forum such as a Symposium.

Four aspects of adverse environmental conditions of interest to the flight mechanics specialist were addressed by this Symposium: atmospheric disturbances, reduced visibility, icing, and electromagnetic disturbances. All four of these can seriously affect flight safety, comfort, and operational capability.

The topic was considered to be particularly relevant to the needs of the military community which is putting increased emphasis on the ability of today's and tomorrow's aircraft to fly safely and effectively in the types of adverse conditions dealt with in this symposium.

* * *

Quoique l'AGARD ait continue a jouer un rôle actif dans le domaine du vol dans des conditions hostiles ces dernières années, le Panel le jugeait important et opportun de faire le point de la question dans le cadre plus large que représente un Symposium.

Les quatre aspects des conditions hostiles qui intéressent le spécialiste en mécanique du vol, à savoir, les perturbations atmosphériques, la visibilité réduite, le givrage et les perturbations électromagnétiques, furent examinés lors du Symposium. Chacun de ces quatre éléments peut avoir des répercussions importantes sur la sécurité de vol, le confort du pilote et la capacité opérationnelle de l'aéronef.

Le sujet était particulièrement bien adapté aux besoins de la communauté militaire où il y a un intérêt accru dans la capacité des avions actuels et futurs d'effectuer des vols dans des conditions de sécurité acceptables et de façon efficace, lorsqu'ils sont soumis aux conditions hostiles dont il fut question lors du Symposium.



Accession For:	
NTIS CRA&I	<input checked="" type="checkbox"/>
DTIC TAB	<input type="checkbox"/>
Unannounced	<input type="checkbox"/>
Justification:	
By _____	
Distribution /	
Availability Codes	
Dist	Avail and for Special
A-1	

FLIGHT MECHANICS PANEL OFFICERS

Chairman: Mr R.C.A. Harrah

O.C.N.R.

Code 00JDL

800 N. Quincey Street HCT/1

Arlington

Virginia 22217-5000

USA

Deputy Chairman: ICA J.-M. Due

Commission des Communautés Européennes

DG 12-11

Rue de la Loi, 200

B-1049

Belgium

TECHNICAL PROGRAMME COMMITTEE

Dr B.W. McCormick

Department of Aerospace Engineering

Pennsylvania State University

233 Hammond Building

University Park

PA 16802

USA

Prof. Dr-Ing. G. Schanser

Director of Institute of Guidance & Control

Technical University Braunschweig

Hans Sommer-Str. 66

D-3300 Braunschweig

Federal Republic of Germany

HOST NATION COORDINATOR

Mr H. Fr. Hoiseih

Royal Norwegian Air Force

Material Command

P O Box 10

N-2007 Kjeller

PANEL EXECUTIVE

Mr M.K. Foster

Flight Mechanics Panel

AGARD/NATO

7 rue Ancelle

92200 Neuilly-sur-Seine

France

ACKNOWLEDGEMENT

The Flight Mechanics Panel wishes to express its thanks to the Norwegian National Delegate for the invitation to hold this meeting in Norway, and for the facilities and personnel which made the meeting possible.

Le Panel du Mécanique du Vol tient à remercier le Délégué National de la Norvège auprès de l'AGARD de son invitation à tenir cette réunion en Norvège ainsi que des installations et du personnel mis à sa disposition.

CONTENTS

	Page
PREFACE	iii
PANEL OFFICERS	iv
Keynote Address: SOME MILITARY AVIATION ASPECTS OF FLIGHT IN ADVERSE ENVIRONMENTAL CONDITIONS by H.W.J. Childes	Reference K1*
Keynote Address: THE HUMAN ELEMENT - THE KEY TO SAFE CIVIL OPERATIONS IN ADVERSE WEATHER by J.H. Enders	K2
DESCRIPTION DE LA TURBULENCE ATMOSPHERIQUE par P.-M. Hulin	1
WIND SHEAR MODELS FOR AIRCRAFT HAZARD INVESTIGATIONS by M. Swolinsky	2
ANALYSIS OF SEVERE ATMOSPHERIC DISTURBANCES FROM AIRLINE FLIGHT RECORDS by R.C. Wragg, R.E. Bach, Jr and T.A. Schultz	3
SYSTEMS FOR AIRBORNE WIND AND TURBULENCE MEASUREMENT by P. Vörsmann	4
Paper 5 withdrawn	
THE UNITED STATES AIR FORCE APPROACH TO ALL-WEATHER TESTING by C.D. Tompkins and J.A. Ford	6
INFLUENCE OF WINDSHEAR, DOWNDRAFT AND TURBULENCE ON FLIGHT SAFETY by G. Schänzer	7
CLASSIFICATION OF WIND SHEAR SEVERITY by A.A. Woodfield	8
HOW TO FLY WINDSHEAR USING THE FLY-BY-WIRE CONCEPT by J.-L. Bonafe	9
Paper 10 withdrawn	
A PITCH CONTROL LAW FOR COMPENSATION OF THE PHUGOID MODE INDUCED BY WINDSHEARS by L.M.B.C. Calopos, A.J.N.M. Agular and J.R. C. Azinheira	11
ADVERSE WEATHER OPERATIONS DURING THE CANADIAN ATLANTIC STORMS PROGRAM by J.I. MacPherson and G.A. Isaac	12
CANARD VERSUS AFT-TAIL: RIDE QUALITIES PERFORMANCE AND PILOT COMMAND RESPONSE, by L.V. Cioffi and L. Mangiacasale	13
THE INTERFERENCE OF FLIGHT MECHANICAL CONTROL LAWS WITH THOSE OF LOAD ALLEVIATION AND ITS INFLUENCE ON STRUCTURAL DESIGN by M. Molton and R. Moebert	14
TURBULENCE EFFECTS ON AIRCRAFT FLIGHT DYNAMICS AND CONTROL	15

* Not available at time of printing.

	Reference
ACTIVE CONTROL SYSTEM FOR GUST LOAD ALLEVIATION AND STRUCTURAL DAMPING by H. Böhrert and J. Winter	16
AIRCRAFT RESPONSE AND PILOT BEHAVIOUR DURING A WAKE VORTEX ENCOUNTER PERPENDICULAR TO THE VORTEX AXIS by R. König	17
A STUDY OF THE EFFECTS OF ROTATING FRAME TURBULENCE (RFT) ON HELICOPTER FLIGHT MECHANICS by D. P. Schrage, J. V. R. Prasad and G. H. Gaonkar	18
MEASUREMENTS OF HORIZONTAL VISIBILITY IN THE LOWEST 300m OVER NORTHERN GERMANY by R. Roth and A. H. Siewer	19
IMAGING PROBABILITIES, GEOMETRY AND ERGONOMICS IN LIMITED VISIBILITY HELICOPTER OPERATIONS by R. H. Wright	20
THE ASSESSMENT OF VISIBILITY FROM AUTOMATIC CONTRAST MEASUREMENTS by A. W. Puffett	21
NASA'S PROGRAM ON ICING RESEARCH AND TECHNOLOGY by J. J. Reinmann, R. J. Shaw and R. J. Ranaudo	22
ICE INDUCED AERODYNAMIC PERFORMANCE DEGRADATION OF ROTORCRAFT - AN OVERVIEW by K. D. Korkan and R. K. Britton	23
FLIGHT AND WIND TUNNEL INVESTIGATION OF AERODYNAMIC EFFECTS OF AIRCRAFT GROUND DEICING/ANTI-ICING FLUIDS by L. J. Runyan, T. A. Zierden and E. G. Hill	24
Paper 25 withdrawn	
EFFECTS OF LIGHTNING ON OPERATIONS OF AEROSPACE VEHICLES by B. D. Fisher	26
Paper 27 withdrawn	
AIRCRAFT TESTING IN THE ELECTROMAGNETIC ENVIRONMENT by P. M. Newton	28
PRINCIPALES CARACTERISTIQUES DES FOUROIEMENTS SUR AVIONS par J. L. Boulay	29
DISCUSSION SESSION WITH REPRESENTATIVES OF THE ROYAL NORWEGIAN AIR FORCE	RTD

THE HUMAN ELEMENT - THE KEY TO SAFE CIVIL OPERATIONS IN ADVERSE WEATHER

by

John H. Eiders
President
Flight Safety Foundation
320 Wilson Boulevard
Suite 500
Arlington, Virginia 22201-3306
USA

SUMMARY

This keynote address discusses in general terms the problems of civil flight in adverse weather and uses specific examples to illustrate the nature of technical, procedural and human factors, with a view toward the mitigation of serious events.

GENERAL

A paper given to a technical group is usually expected to contain a great deal of statistical information, data, and other bits of quantitative information on which conclusions can be based. However, I believe that this keynote address might better help set the stage for the excellent technical program that follows by discussing some issues that may be peripheral to the research and development community's focus, but central to the end objective of much of our collective effort...the safe completion of the assigned flight mission. It is my intention to present a very brief view of how safe flight in adverse environmental conditions has often been denied, with some discussion of reasons for that unfortunate consequence.

Even though weather has always been the foe of safe aircraft operations, flight in adverse environmental conditions today has become commonplace. Gusting wind conditions frustrated the first would-be aviators, and the first accident sustained by the Wright Brothers occurred in 1904 when Orville Wright encountered an uncontrollable sharp gust that resulted in a crash, almost killing him. The battle against the environment was thus joined. Ever since, it has been a major objective of the aircraft designer to provide a machine that can sustain the assaults of Mother Nature, and the objective of the operator to avoid, as much as is safely possible, the constraints otherwise imposed by weather.

The overall safety records of air carrier, corporate and private civil aviation continues to improve in terms of individual risk exposure. Schedule reliability of air carriers is taken for granted, despite current congestion delays and frustrations of many passengers. The present-day traveller expects to reach his or her destination without undue problems regardless of weather, because of the good record of completing flights to destination. There is good reason for this confidence. A solid base of technology, coupled with a curiosity about why things go wrong and a determination to correct erroneous designs, procedures and operations, have built air transportation into a safe, highly-efficient and productive mode of travel.

Accident occurrences continue their downward trend. More is known about weather phenomena than ever before. Yet, the major weather phenomena: precipitation, turbulence, ice, fog and lightning, in all their manifestations, continue to figure in the determinations of accident probable causes or as contributing factors.

Civil air carrier operations continue to improve in terms of individual exposure to risk, despite some rather spectacular accidents within the past several years. World-wide, scheduled civil air transport has achieved a safety record of one fatal accident per one million flights. U.S. Carriers' record is about 0.3 fatal accidents per one million flights. The Australasian carriers are operating at a rate of about 0.1 fatal accidents per one million flights [1][2]. Business aircraft operated by professional full-time crews logged seven fatal accidents in world-wide operations last year. General aviation's accident record has improved, and civil helicopter operations, with the exception of emergency medical service flights, have not degraded in safety.

But I don't want to talk about the general trends today. They are indeed what we like to see and give us confidence that in general we are doing things right. However, looking at the individual accidents that do occur tells us something about how we go about our business of civil flights. And it is not a picture to be particularly proud of. Figure 1 shows that for the past 30 years, approximately 60% of all air carrier accidents occur in the descent, approach and landing phases, while 30% occur in the takeoff and climb phases. But this 90% share of accidents occurs within only about 40% of the total flight time. The same general proportions apply to business and general aviation operations. There is a remarkable congruence among many accident studies that indicates that the flight crews have the opportunity to prevent 60-70% of all accidents [3].

Figure 2 shows a breakout of different primary causal factors for hull loss accidents to transport aircraft. Again, business and general aviation aircraft operations show approximately the same proportions. Note that some 70% are attributable to the flight crew, and about 6% are attributable to weather. Buried in that flight crew figure, however, are many weather situations that taxed the flight crew's capabilities and judgment.

THE DECISION TO FLY

The decision to fly is a human act. It should be based on a number of important factors. I say 'should be', for as we will see later in this discussion, sometimes important factors are omitted or overlooked. The factors include:

- o Type of aircraft consistent with the mission
- o Condition of the aircraft
- o Equipment aboard
- o Pilot's experience with aircraft and mission
- o Pilot's physical and mental fitness for duty
- o Environmental conditions along the route
- o Conditions of airports and nav/comm aids available
- o Any unusual conditions expected

The decision to fly is made by the pilot upon accepting the aircraft as airworthy. The hand-over from ground personnel to flight crew is a critical point in the process, for the duty of care that everyone in aviation has, demands that the airplane be presented to the flight crew in condition adequate for safe completion of the flight. The primary responsibility for the safety of the flight shifts from ground to flight crew at that moment, and the pilot, having accepted an airplane he or she believes to be airworthy, must now assess the remaining factors. Is the equipment aboard sufficient and functioning for the expected flight mission? Is the aircraft's performance and structure adequate for the expected flight? Is the pilot in good physical and mental state for the flight? Is the pilot's experience adequate for safe completion of the flight? Are the takeoff weather conditions satisfactory for launching? And, what is the forecast weather enroute and at destination? What navigation and communication aids are available along the flight path? Are there adequate alternate landing sites?

Just as the maintenance organization provides support to the pilot, so does the duty of care extend to ATC and weather personnel. They must make certain that support is given to the operating crew in terms of supplying accurate up-to-date weather information and assessment of changes expected.

The pilot's decision to go considers two major weather questions:

Is the expected weather within the pilot's capability?

The answer to this question lies in the training and experience of the pilot in both weather flying and familiarity with the equipment, how much IMC flying is expected, whether the flight is to be conducted with solo pilot or multiple crew, the quality of the weather information available to the pilot for the flight, and any special detection equipment aboard the airplane, e.g., radar, navigation equipment, cockpit configuration and display, ice probes, etc., and the pilot's proficiency in operating the equipment.

Is the expected weather within the aircraft's capability?

The answer to this question depends on the aircraft's design (performance, structural strength, aerodynamics, powerplant, de- and anti-icing systems, maneuverability and handling qualities, etc.) and the aircraft's condition (airworthiness, MEL, inoperable systems, adequate fuel reserves for the flight, system redundancies, etc.).

Given this general structure, I would like to address some specifics that are illustrated by a random sampling of over 800 accidents involving weather as a factor that civil aviation has experienced over the past decade. The specifics will include:

- Deviation from planned flight,
- Inaccurate weather forecasts,
- Faulty judgment,
- Mismanagement of cockpit resources,
- Deficiencies in basic knowledge/understanding of the airplane, pilot capabilities and the environment,
- Lack of critical information for the crew,
- Failure to communicate critical information to the pilot in a timely fashion
- Lack of adequate operational nav/comm ground facilities

FACING THE MOMENT OF TRUTH--SOME ACCIDENT CASES

The following brief synopses have been culled from world-wide accident data:

Quebec: DHC-6. Loss of directional control on the runway. Freezing drizzle covered the sanded area of the runway surface, but runway condition was still reported as sanded with poor to fair braking action. 0 fatalities to 12 exposed

Kenya: Cessna 310. Visibility poor in holding pattern with rain and thunderstorms. Aircraft struck terrain while maneuvering in the pattern. 2 fatalities to 4 exposed. 2 seriously injured.

New York: Swearingen Metro. Aircraft hit large chunk of ice on runway during landing roll. 0 fatalities to 14 exposed.

Japan: YS-11. Maneuvering below low cloud base, aircraft descended into terrain. 0 fatalities to 23 exposed. 18 serious injuries.

Venezuela: DC-9. ILS into heavy fog. Landed hard, with damage to gear and subsequent fire. 23 fatalities with 50 exposed.

Germany: Cessna 414. Landed in heavy rain. Poor braking. Hydroplaned off end of runway. 0 fatalities to 5 exposed.

Maryland: B707. Aircraft encountered unforecast turbulence 25 minutes before landing. Cabin attendant thrown to ceiling, fell to floor. Serious back injury. 0 fatalities with 191 exposed.

Orkney Islands: Twin Otter. Landed on 1.6t downslope with 28Kt crosswind gusting to 38Kt. Aircraft's left wing rose, aircraft swerved as right wing struck ground and catapulted. 6 fatalities to 12 exposed.

Boston: Cessna 402. In level flight, aircraft passed behind Airbus A300 in descent. Vortex turbulence caused the Cessna to roll inverted. Pilot regained control and landed safely. Both aircraft on instrument flight procedures in IMC being vectored.

Spain: B727. On takeoff run, aircraft collided with DC-9 taxiing onto runway in heavy fog. DC-9 crew could not obtain adequate visual reference for taxiing. 57 fatalities to 93 exposed.

Malaysia: A300. During ILS approach in poor visibility, thunderstorms and heavy rain, aircraft undershot and came to rest 1000 meters before runway threshold. The aircraft was leased and had different cockpit configuration than the main fleet aircraft. Heavy cockpit crew workload as a result distracted crew in low visibility approach. 0 fatalities to 247 exposed.

Australia: Rockwell Commander 685. Pilot reported descending to cruise at 500 feet AGL. The weather was overcast with low cloud covering hills. Wreckage was found on northern slope of east-west ridge. 1 fatality to 1 exposed.

New York: DC-10. Copilot flying ILS approach in tailwind. Aircraft landed 4700 feet beyond threshold, 36Kt above programmed touchdown speed. Aircraft ran off runway into tidal inlet. 0 fatalities to 177 exposed.

Bolivia: F-27. Adverse weather on arrival at San Borja. ATIS/Com/Met/VHF, HF, and VOR/DME radio aids were inoperative. Aircraft overflew airport at 1500 feet. Ten minutes later, equipment operation was restored, and call was received from aircraft before impacting hillside. 23 fatalities to 23 exposed.

Pago Pago: DHC-6. Light to moderate turbulence led crew to fly slightly faster than normal approach. During flare, windshear was encountered, causing decrease in airspeed and excessive rate of descent. Despite adding power, the aircraft sustained a hard landing. 0 fatalities to 20 exposed.

France: Piper Chayenne II. During second IFR approach in thick fog, aircraft diverted 30 degrees from centerline and collided with light post, struck ground and caught fire. 7 fatalities to 7 exposed.

Scotland: SA330 Puma. Helicopter was in cruise at FL40 when #1 engine failed. Some ice had built up on the windscreen wiper blades and substantial rime ice had built up on the icing probe. Second engine failed in descent to FL30. Autorotation commenced and both engines were restarted in time for recover at 200 feet AGL. Engine inlet icing suspected. 0 fatalities to 12 exposed.

Khatmandu: DHC-6. Collision with terrain on climb. Aircraft deviated from track. Suspect bad weather and possible load limited rate of climb. 15 fatalities to 23 exposed.

New Zealand: B737. While descending through 11000 feet in the clear, aircraft encountered brief period of Clear Air Turbulence. Passenger standing in rear foyer was thrown to floor with compression fracture of lumbar vertebra. 0 fatalities to 112 exposed.

Arkansas: B727. Aircraft experienced severe turbulence associated with thunderstorm. Two flight attendants injured. 0 fatalities to 5 exposed.

Ireland: Short 360. Aircraft was established on ILS at 900 feet AGL when periodic and divergent rolling motion developed. Bank angles up to 56° with maximum roll rates of 55°/sec were experienced, along with a maximum rate of descent of 3000 fpm. The descent was arrested in time to make a gentle ground contact 3.5 km short of runway. Airframe ice degraded aircraft stability and control, with turbulence and downdraft contributing. 0 fatalities to 35 exposed. 2 serious injuries.

Denmark: DC-8-63. During VMC approach using ILS guidance, the aircraft was subjected to severe turbulence. At 1000 feet, windshear brought IAS from 150 to 180Kt. On short final, conditions improved and pilot elected to land. Aircraft outboard engine pod contacted ground on touchdown. 0 fatalities to 258 exposed.

Iceland: PA-23 Aztec. Air taxi flight in IFR with icing above 3000 feet in clouds. Wind at cruising altitude of 8000 feet was up to 80Kts. Reaching mountain range, pilot requested minimum altitude and was cleared to 5000 feet. He was seen descending to 4300 feet and then disappeared. A very strong mountain wave, with roll cloud was present. Rate of descent of the air on leeward side was calculated to be up to 5000 fpm. The aircraft altimeter very likely showed 600 feet too high because of wind and temperature deviations. 5 fatalities to 7 exposed. 2 serious injuries.

Sweden: DHC-2 Beaver. On advice of chief pilot, pilot took off from mountain lake. Weather was bad and pilot lost all visual references. Lack of instrument training made him decide to make precautionary landing. Due to whiteout, aircraft collided with ground. 0 fatalities to 1 exposed.

Japan: DC-10. Cruising at FL210, aircraft encountered severe turbulence. Seat belt sign not on. DFDR showed g values varying from +0.29 to +1.97 of 16 seconds duration. 3 serious injuries to 137 exposed.

Japan: MD-80. Severe turbulence was encountered at FL290 in cruise. DFDR records showed g ranging from -1.1 to +1.76 of 2 seconds duration. 2 serious injuries to 104 exposed.

Japan: MD-80. Descending through 8000 feet, aircraft encountered severe turbulence. Seat belt sign on. One passenger in toilet seriously injured. DFDR showed g values of +1.82 to +0.65 of 2 seconds duration. 1 serious injury to 104 exposed.

Japan: DC-9. In cruise at FL255, aircraft encountered severe turbulence. DFDR showed g values from -2.20 to +2.30 with 2-3 seconds' duration. 1 serious injury to 58 aboard.

Argentina: B727. During landing roll, aircraft drifted outside runway 13 which was wet and had quartering gusts from 90-110 degrees at 23Kts gusting to 35Kts. Loss of directional control was followed by nose gear collapsing. 0 fatalities to 114 exposed.

England: B747. On departure, aircraft was struck by lightning. No thunderstorms forecast nor did aircraft radar show any returns. After third strike, aircraft radar failed and autopilot disengaged. Pilot returned for overweight landing which was normal except for no reverse thrust on J2 and J3 engines, and no auto spoilers. Over 100 discrete burn marks were found on the fuselage. Four square feet of paint was discolored. The tip of the right tailplane was damaged and aft section of tip cap was missing. HF radios, two bonding straps at hinge position on right elevator and part of passenger address system also failed. the PDR was unserviceable. 0 fatalities to 243 exposed.

USSR: YAK-40. Approach was flown with tailwind in heavy rain shower. Weather presumed below crew minima. Following a high speed touchdown, a go-around was attempted. The take-off was aborted and aircraft overran the end of the runway, collided with obstacle, broke up and caught fire. 8 fatal to 29 exposed. 12 serious injuries.

USSR: TU-134. Aircraft was cleared for non-standard approach in IMC at night. The crew was not informed that nav aids were turned off and weather had changed. Entering conditions of reduced visibility with no reliable visual contact with approach lights and with landing lights turned off, pilot and copilot continued approach through decision height. The aircraft, which was not in landing attitude, made hard landing beside runway, broke up on impact and caught fire. 20 fatalities to 51 exposed. 30 seriously injured.

DISCUSSION

To the above list can be added some better-known accidents: the wind shear landing accident in Dallas/Fort Worth, the icing take-off accident at Washington National, the icing/gusting wind take-off accident at Denver and the ~~flaps~~ take-off accident at Detroit, where crew concern over possible wind shear conditions contributed to a checklist distraction. I purposely chose the less well-known accidents from the accident reports to show clearly that adverse environmental factors are no respecters of geography, aircraft type or the particular human operator. Many of the pilots involved were highly-skilled and highly-experienced. Though mercifully, many aircraft occupants escaped injury or death, the numbers exposed to risk are high and should be kept in mind as we all perform our tasks with a duty of care.

Though the pilot or crew was often determined to be at fault, the presence of adverse environmental situations was the determining factor in many of these accidents; that is to say, lacking the added complication of low visibility, gusts, wind shear, icing, thunderstorms, etc., the accidents likely would not have happened. What does this mean? Well, for one thing, it means that we have been collectively unable to get basic understanding of the potential hazards represented by adverse environmental factor instilled in crew and management thinking to a high enough level to raise the proper questions in the decision-making process.

The judgments of the pilot or crew thus become the key factors. What influences this judgment? There are many influences and it is impossible to quantitatively rank their importance, for each situation calls for its own hierarchy of priorities. However, included in these influences must be: fundamental knowledge and understanding of weather processes and hazards by both operations and management people, situational awareness on the part of the pilot or crew, peer pressure, schedule pressure, ATC slot assignments,

and cockpit resource management or how well the crew works together to provide adequate checks and balances in the man-machine-environment interface.

Senior management's visible commitment to safe operations has probably the largest potential positive effect on judgment. Such commitment is manifested in tight crew selection procedures, training and organization of the operation so as to operate with the highest practical level of safety, as mandated by most national codes of aeronautical regulations. However, self-discipline and professionalism are also important attributes for the pilot or crew.

A major contribution to crew performance improvement is the modern flight simulator, where realistic weather situations can be experienced with such realism that the training is highly effective. However, private pilots and small operators are often unable to avail themselves of such training though technologies are continually emerging that promise to bring this excellent educational and training tool within the reach of the smaller operator.

The changes taking place today in aviation are dramatic. The accident reports reviewed leave no doubt that the modern airplane is very forgiving of human error. Likewise it is protective of its occupants in all but the most severe accidents. Nevertheless, new demands are being placed on the operation, and new equipment and procedures are being introduced that have subtle requirements for the support system. ECRPS, for example, is technologically sound for the newer twin-engine transport aircraft, but it demands a much more precise forecasting of enroute and destination weather, so that contingencies for safe conclusion of flight may be maintained. Likewise, the hub-and-spoke route structure in the U.S. brought about by deregulation has introduced requirements for more schedule precision to efficiently make the hub transfers of passengers. There is thus a subtle pressure to make schedule, or else throw the entire system out of sync. In Europe, the congested air traffic and airport systems have caused an enormous amount of anxiety about obtaining and maintaining a "slot" in the traffic flow, and a recent item appeared in the U.K.'s CHIRP reports wherein a pilot was reported as having suffered a mild heart attack in the cockpit while awaiting take-off clearance, but elected to continue with the take-off rather than lose the assigned slot!

The nature of delivery of weather services to the operator has also changed, with datalinking via computer and satellite. The measurement, collection and analysis of meteorological data has made great strides, but in some cases it has become more remote from the traditional flight operation. Software design is accomplished in many cases by people who have more software-orientation than operational awareness. Acquaintance with operational needs by weather personnel may not be as focused as in earlier years, but improvements in measurement and forecasting precision likely compensate to some extent. We must, however, maintain our own engineering and scientific situational awareness to ensure that our end product is functionally safe.

As key to this situational awareness you must realize that at the operational end, the rapid expansion in aviation operations has strained the ready supply of pilots and mechanics just as it has the delivery of weather services. Air carrier and corporate operators no longer have the luxury of the military services' screening and training their pilot hires. An increased number of ab initio training schools has been established by airlines and manufacturers. Recruitment of naive civil candidates is now done by civil operators, and variations in selection standards are wider than for military flight candidates. Maintenance training has to compete with many other career fields that are attractive and financially rewarding to young people today.

This has led to an overall lowering of experience level in the maintenance and operational ranks. The larger airlines now recruit personnel from commuters, air taxi, and business aviation operators. They have largely replaced the military as a major source of pilots for the major airlines. Not only are the smaller operators lacking in a uniform standard of strict selection and training practices compared with the military, but the constant turnover in pilot and mechanics staffing condemns these smaller operators to a never-ending low experience level.

The situation just described holds strong implications for the need to technically compensate with research on environmental hazards that will yield more certain information and forecasts so that the criticality of pilot judgments is less dependent on training and seasoning. Likewise, initial and recurrent training of pilots in adverse weather phenomena cannot be underestimated in its importance.

CONCLUSION

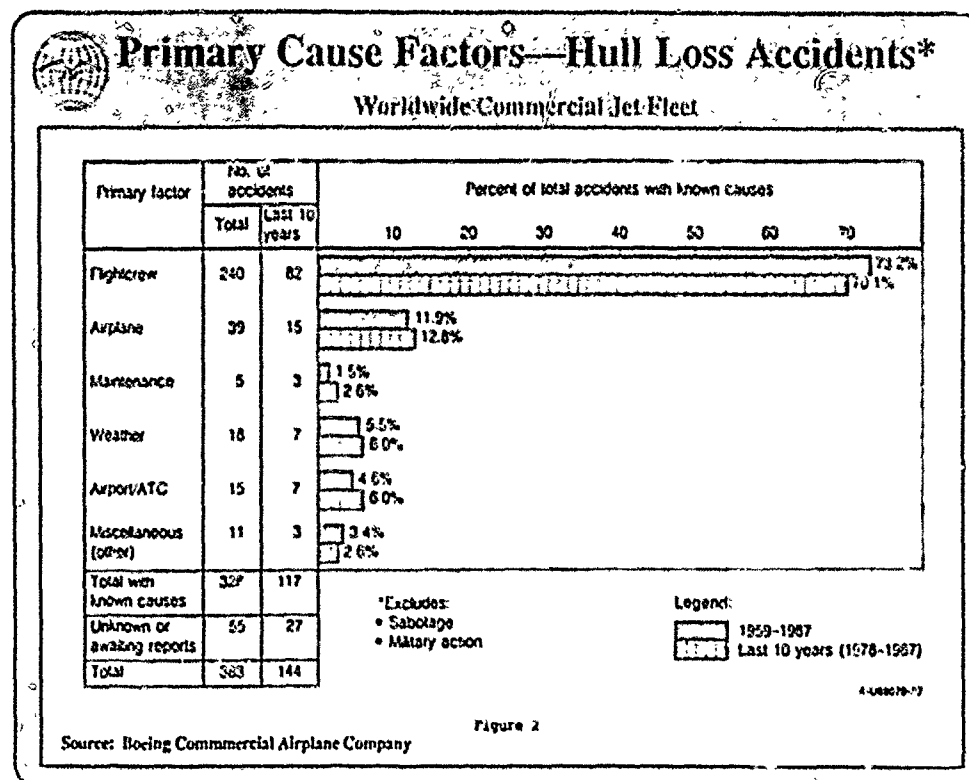
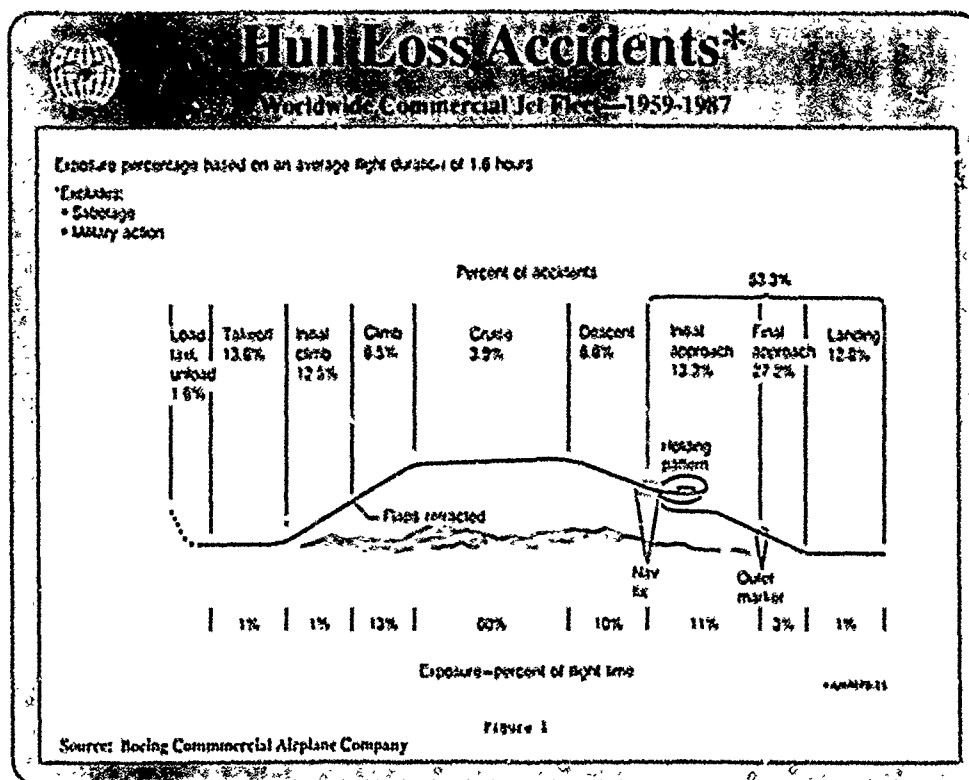
Adverse weather is a given. It is up to the human to deal with it. We must measure it, analyze it, continue to design our machines to withstand its assaults, define safe operating boundaries, and train ourselves to operate within these boundaries. We must do better in providing our pilots with a strong basic education in weather and its potential for risk. Our support system of air traffic control and weather observation, analysis, forecast and warning must be improved to provide the pilot with the information needed to make quick and prudent decisions. Our air transportation system, whether public carrier or private, must recognize the limits imposed by adverse environmental conditions, and thereby avoid subtle transgressions of the pilot decision making process that might encourage undue risk-taking. We must continue our refinement of the forecasting art and science.

Most of the accidents discussed underscore two major deficiencies: Education and Communication.

A breakdown of the process by which the pilot recognizes a deteriorating situation calling for safer alternative action occurs frequently. Initial and recurrent training in weather must be strengthened. Likewise, the failure to provide accurate and up-to-date weather information to the pilot in a timely fashion is demonstrated time and time again in the accident reports. The research activities represented on the agenda at this symposium are absolutely essential to ensuring that these deficiencies are eventually overcome. They should be carried out fully mindful of our duty of care and with the realization that the understanding and knowledge gained will not be useful unless the operational system can exploit it in the interests of safe operation.

REFERENCES

1. J. F. Lederer and J. H. Enders, Flight Safety Foundation, "Aviation Safety--The Global Conditions and Prospects," Flight Safety Foundation, June 1987.
2. R. P. Sears, Boeing Commercial Airplanes, "Prevention Strategies for the Crew-Caused Accident," Second Egyptian Aircraft Accident Investigation and Prevention Annual Seminar, Cairo, February 1989.
3. Boeing Commercial Airplanes, "Statistical Summary of Commercial Jet Aircraft Accidents--Worldwide Operations, 1959-1987," Boeing Commercial Airplanes, Seattle, Washington, November 1988.
4. J. H. Enders, Flight Safety Foundation, "The Decision To Fly," Flight Safety Foundation Accident Prevention Bulletin, December 1988.
5. R. Clarke, "Winter Flying: Sharing Experience," Flight Safety Foundation Accident Prevention Bulletin, October 1988.
6. CAP472, Civil Aviation Authority, "World Accident Record, 1946-Present, with supplements," Civil Aviation Authority, London.
7. G. M. Bruggink, "Reflections on Air Carrier Safety," Flight Safety Foundation Flight Safety Digest, June 1988.
8. DOT/FAA/FM-86/46: R. S. Jensen, Ohio State University Research Foundation, "Aeronautical Decision Making--Cockpit Resource Management," Federal Aviation Administration, January 1989.



DESCRIPTION DE LA TURBULENCE ATMOSPHERIQUE

par Pierre-Marie HUTIN

Office National d'Etudes et de Recherches Aéronautiques (ONERA)
92322 Châtillon-Cedex - France

73rd Symposium AGARD/FMP - GOLF, NORWAY 8-11 Mai 1969

RÉSUMÉ

L'analyse des dépassements de facteur de charge supérieur à 0.5 g sur plus d'un million d'heures de vol a permis de proposer une description de la turbulence atmosphérique cohérente. Une analyse critique des méthodes utilisées pour déduire des facteurs de charge mesurés, les valeurs des niveaux de turbulence rencontrés est faite, et on expose une amélioration possible d'une de ces méthodes. On présente ensuite les résultats obtenus sur la description de la turbulence atmosphérique par traitement des banques de données constituées à partir d'enregistrements recueillis sur les vols d'avions commerciaux de plusieurs compagnies.

INTRODUCTION

Le but de cet article est de faire le point sur les méthodes permettant de passer des valeurs de dépassement de facteurs de charge aux valeurs de niveaux de turbulence atmosphérique. On fera une analyse des différentes méthodes existantes et des conséquences qu'elles peuvent avoir sur les règles de certification.

L'intérêt renouvelé des constructeurs pour la turbulence vient des problèmes rencontrés sur les nouveaux avions :

- Avions civils à grand allongement
- Avions militaires de pénétration à basse altitude et grande vitesse
- Contrôle actif du vol et des charges
- Justification de l'accroissement de durée de vie en fatigue des avions civils existants.

Il faut se rappeler que l'étude de la turbulence atmosphérique se fait de deux façons. D'abord, une mesure par des avions spécialement équipés (gyroscopie, gyromètre, plateforme à inertie) a été faite, et a été longtemps la seule et unique moyen d'obtenir une évolution dans le temps de la turbulence d'où l'on a déduit les valeurs des densités spectrales de puissance et de l'échelle. Cette mesure a donné une base solide pour les méthodes de turbulence continue, mais ne peut être utilisée pour fournir des statistiques du fait du faible nombre d'avions et de vols concernés. D'un autre côté, il faut considérer les avions commerciaux qui parcourent des millions de milles nautiques chaque année et rencontrent de ce fait beaucoup de "pavés" de turbulence au cours de leur vie. Ils sont depuis quelque temps équipés d'enregistreurs qui saisissent les valeurs d'accélération au centre de gravité, de vitesse indiquée, d'altitude, de masse et de nombre de Mach à l'instant de chaque dépassement d'un niveau fixé d'accélération. On trouve de plus des ordinateurs puissants et rapides capables de mémoriser et de traiter des grandes banques de données.

Ainsi l'apparition simultanée des moyens et de la motivation, a poussé les laboratoires et industriels à raffiner leurs analyses (en prenant en compte par exemple l'effet d'isotropie de la turbulence ou l'équilibre des charges quand la turbulence continue est le cas de calcul utilisé pour la justification de la structure). Ceci explique également les nouvelles tentatives exposées ici pour élargir les banques de données et justifier les règles de certification.

Les premières tentatives pour passer des données de variation de facteur de charge aux valeurs de turbulence sont apparues dans la période 1931 à 1949 avec les travaux de RHODE et DONELY prenant en compte un seul degré de liberté pour la réponse de l'avion à une rafale simple et isolée. Entre 1950 et 1956, PRATT et ALI introduisent le coefficient d'atténuation de rafale et la rafale en 1-cos. Ils travaillèrent alors sur quelque 55000 vols. Plus tard (1956-1970), PRESS et HOUBOLT proposent le principe de turbulence continue, qui a conduit à un amendement de la FAR 25, préparé par HOBLIT et aujourd'hui largement accepté. Vinrent ensuite les travaux de HALL et KAYNES, qui introduisent, toujours avec un système à un seul degré de liberté, une répartition non uniforme en envergure de la turbulence.

Très récemment, HOUBOLT a proposé une nouvelle méthode qui prend en compte les deux degrés de liberté rigides de l'avion. Pendant le même temps, l'acquisition de données a été poursuivie et des statistiques de variation de facteur de charge sont disponibles sur plus d'un million d'heures de vol.

Dans une première partie, on envisagera la validité des traitements des données acquises et la signification des valeurs de turbulence déduites des données d'accélération. Ensuite, on décrira sommairement quelques méthodes utilisées (PRATT, HALL et HOUBOLT). Enfin on en tirera quelques conclusions.

NOTATIONS

On utilise ici les mêmes notations que J.C. HOUBOLT dans sa présentation AGARD/SMP à ATHENES en septembre 1986.

a	Pente de la courbe de portance ($C_{Z\alpha}$)
\bar{A}	Coefficient de transfert $\sigma_{\Delta n} = \bar{A} \sigma_w$
A_T	Allongement
c	Corde moyenne
k	Fréquence réduite $k = \frac{\omega c}{2V}$
k_s	Fréquence réduite de l'oscillation d'incidence
K	Coefficient d'atténuation de rafale
L	Echelle de turbulence
N_0	Nombre de passage par zéro d'un paramètre
S	Surface de référence
V	Vitesse avion
W	Poids de l'avion
α	Incidence (par rapport à l'incidence de portance nulle)
Δn	Variation du facteur de charge due à la turbulence
μ	Paramètre de masse
ρ	Masse volumique de l'air
σ_w	Valeur rms de la turbulence

σ_z	$\sigma_z = \frac{\sigma_w}{\pi \left(\frac{z}{L}\right)^{1/3}}$
Φ_w	Densité spectrale de puissance de la vitesse verticale de turbulence
ω	Pulsation
Ω	Fréquence réduite $\Omega = \frac{\omega}{V}$
M	Nombre de Mach

I-PRESENTATION GENERALE

Une description de la turbulence atmosphérique est essentielle pour définir les charges qu'un avion peut rencontrer au cours de sa vie normale. Comme montré dans l'introduction, les statistiques de rafale ne peuvent être obtenues par un très petit nombre d'avions spécialement équipés pour mesurer l'évolution dans le temps de la turbulence. En conséquence, il nous faut relier les valeurs de Δn enregistrées sur les avions commerciaux aux valeurs de turbulence par différentes méthodes. Une dernière remarque : si le calcul de la variation du facteur de charge d'un avion au cours de la traversée d'une rafale de forme donnée est assez simple grâce à des méthodes plus ou moins sophistiquées, il est pratiquement impossible de trouver une valeur de turbulence à partir d'un Δn donné si l'on ignore la forme de la rafale et tous les détails des conditions de vol (par exemple le centrage).

Dans le passé, différentes formules ont été développées pour le calcul des avions à la rafale, elles ont alors été utilisées pour trouver des valeurs d'intensité de rafale à partir des Δn . Depuis son apparition en 1954, le principe du facteur d'atténuation de rafale de PRATT et WALKER a reçu une approbation quasi-générale et a fait partie des règles de certification pour les avions civils et militaires pendant plusieurs années. Le principe de base de la " formule de PRATT " a été de prédire le pic d'accélération dû à une rafale discrète sur un certain avion à partir du pic d'accélération mesuré sur un autre avion traversant une rafale de même forme et de même intensité. Ainsi la valeur de l'intensité de rafale n'est pas vraiment une grandeur physique mais plutôt un coefficient de transfert rafale-charge dépendant des termes de la formule. De ce fait la formule est plus précise si son utilisation est limitée à des avions de caractéristiques voisines.

L'utilisation de formules simples pour traiter les Δn , était nécessaire à l'époque de PRATT, parce que les capacités de calcul étaient limitées; elle est essentielle maintenant car il nous faut travailler sur plus de dix mille événements. Toutes les méthodes décrites ici sont des outils simples et peu coûteux pour la réduction des données. Mais de ce fait elles souffrent des mêmes défauts que la formule de PRATT. En conséquence, il faut garder à l'esprit que la description des statistiques de turbulence à partir des Δn n'est pas une représentation physique de la turbulence, et qu'elle doit être utilisée avec précaution sur des avions qui diffèrent beaucoup de ceux sur lesquels les données ont été acquises.

A ce point, il semble nécessaire de parler des difficultés dues au fait, que, en général, il n'y a pas de moyen de séparer les accélérations dues aux manoeuvres imposées par le pilote, de celles dues à la turbulence. Ceci n'est peut-être pas très important sur les variations de facteur de charge élevées, mais altère certainement les données de faible accélération.

En résumé, on peut dire qu'actuellement la tendance est à l'utilisation de formules simples pour la réduction des données. Ces formules peuvent être utilisées avec succès pour une grande quantité d'avions de différentes masses, formes et vitesses et elles tiennent compte des deux degrés de liberté de corps rigide de l'avion. Ceci est possible car la mécanique du vol des différents avions est pratiquement la même pour des besoins de pilotage.

En tout état de cause, il ne s'agit que de formules approchées qu'il faut utiliser avec beaucoup de précautions pour les besoins de la certification.

II-LES DIFFÉRENTES MÉTHODES

On va maintenant décrire certaines des différentes méthodes disponibles pour réduire les données Dn en valeurs de rafale : la formule de PRATT, la méthode de HALL et la toute nouvelle approche de J.C. HOUBOLT. Toutes sont basées sur l'utilisation du paramètre de masse qui joue un rôle fondamental dans la réponse de l'avion à la turbulence.

$$\mu = \frac{2W}{\rho c q S}$$

II.1 Formule de PRATT

Le point le plus important de la formule de PRATT est, qu'elle introduit le facteur d'atténuation de rafale K dans la formule qui donne le facteur de charge en fonction de la turbulence :

$$(1) \quad \Delta n = \frac{\rho S V}{2W} K U_c$$

PRATT et WALKER (1954) ont fait les hypothèses suivantes :

- L'avion est considéré comme une masse ponctuelle avec le seul degré de liberté de mouvement vertical.
- Le nombre de passage par zéro de l'accélération verticale est le même pour tous les avions.
- La rafale est une simple rampe de longueur donnée jusqu'à ce que le maximum d'accélération soit atteint.
- La rafale est uniforme en envergure.

Avec ces hypothèses, on obtient la "Formule de PRATT" :

$$(2) \quad K = \frac{.88 \mu}{5.3 + \mu}$$

Les valeurs de calcul de vitesse de rafale, dans les règles de certification courantes, sont obtenues, par la formule de PRATT, à partir des statistiques de dépassements d'accélération au centre de gravité mesurés, pour la plus grande part, sur des avions de transport américains avant 1950 et confirmées par des données acquises sur des avions commerciaux en Europe avant 1960.

Plus tard, la formule de PRATT a été améliorée par l'introduction d'une rafale en 1-cos, longue de 25 cordes, et toujours uniforme en envergure.

II-2 méthode de HALL

La méthode de HALL est basée sur une hypothèse de turbulence continue, qui est un procédé stochastique caractérisé par sa densité spectrale de puissance $\Phi_w(k)$ à laquelle la densité spectrale de puissance de la réponse est reliée par la formule :

$$(3) \quad \Phi_{\Delta n}(k) = |T(k)|^2 \Phi_w(k)$$

où T(k) est la fonction de transfert de l'avion. J. HALL donne une formule simple pour T(k) dans le cas où les effets du lagage et de l'envergure finie sur l'accroissement de portance dû à la turbulence sont négligeables :

$$|T(k)|^2 = \left[\rho S \alpha V g / 2W \right]^2 \frac{\xi^2}{p^2 + \xi^2} - \left[\frac{B_1}{\alpha_1^2 (1 + \xi_1^2 \xi^2)} + \frac{B_2}{\alpha_2^2 (1 + \xi_2^2 \xi^2)} \right]$$

avec : $\xi = 2 \pi \cdot L$

$$p = \frac{L}{c \mu}$$

$$\alpha_1 = \frac{.26 + 2/A_1}{1 + .83\pi + .95\pi^2}$$

$$\alpha_2 = \frac{2 + 2/A_1}{1 + .83\pi + .95\pi^2}$$

$$\frac{\beta_1}{\alpha_1^2} = \frac{\alpha_1 + 3\alpha_2}{4(\alpha_1 + \alpha_2)}$$

$$\frac{\beta_2}{\alpha_2^2} = \frac{\alpha_2 + 3\alpha_1}{4(\alpha_1 + \alpha_2)}$$

$$\zeta_1 = \frac{c}{L \alpha_1}$$

$$\zeta_2 = \frac{c}{L \alpha_2}$$

Le facteur d'atténuation de rafale s'écrit alors :

$$(4) \quad K^2 = \int_0^\infty \frac{\xi^2}{\rho^2 + \xi^2} \left[\frac{\beta_1}{\alpha_1^2 (1 + \xi_1^2 \xi^2)} - \frac{\beta_2}{\alpha_2^2 (1 + \xi_2^2 \xi^2)} \right] \frac{\Phi_w(k)}{2\pi L \sigma_w^2} d\xi$$

Le premier terme est donné par l'accroissement de portance instantané dû à la rafale; le second terme peut être relié aux effets stationnaires.

Si le modèle utilisé pour la densité spectrale de puissance de turbulence est celui de VON KARMAN, il faut effectuer une intégration sous forme numérique; par contre si on utilise le modèle de DRYDEN, l'intégration peut être menée jusqu'au bout sous forme littérale et donne ainsi le résultat suivant :

$$(5) \quad K^2 = \left(\frac{\beta_1}{2\alpha_1^2} \right) \frac{2 - \frac{1}{2}(1+p) - \frac{1}{2}h_1 S_1}{(1+p)(1+S_1)(1+pS_1)} + \left(\frac{\beta_2}{2\alpha_2^2} \right) \frac{2 - \frac{1}{2}(1+p) + \frac{1}{2}(1+S_2)}{(1+p)(1+S_2)(1+pS_2)}$$

Cette formule est plus facile à manipuler, mais implique les hypothèses du modèle de DRYDEN qui est moins réaliste. De toute façon c'est un progrès car elle prend en compte les effets d'aérodynamique stationnaire et d'échelle intégrale de turbulence.

Comme on le verra plus loin, cette formule se compare très bien avec des valeurs "exactes" obtenues par l'approche de J.C. HOUBOLT.

11-3 Méthode de HOUBOLT

La plus grande partie de cet article concerne la méthode proposée récemment par J.C. HOUBOLT, qui est très prometteuse car elle tient compte des deux degrés de liberté de corps rigide de l'avion et également de la variation en envergure de la rafale. La densité spectrale de turbulence utilisée est celle de VON KARMAN mais écrite sous la forme suivante :

$$(6) \quad \Phi_w(k) = \sigma_w^2 \left(\frac{2L}{c} \right)^{5/2} \frac{[1 + \frac{1}{2}(1.335 \frac{2Lk}{c})^2]}{[1 + (1.335 \frac{2Lk}{c})^2]^{7/2}}$$

avec (7) $\sigma_w^2 = \frac{\omega^2}{\pi \left(\frac{2L}{c} \right)^{3/2}}$

Par cette formulation tous les spectres se confondent à haute fréquence quelle que soit l'échelle de turbulence (Figure 1).

La prise en compte du degré de liberté de langage a une grande importance sur la réponse de l'avion en accélération. Sur la figure 2 on compare les densités spectrales de puissance d'accélération pour un avion à un seul degré de liberté avec le cas deux degrés de liberté. On peut noter qu'il y a une réponse plus importante à basse fréquence dans le cas du seul mouvement vertical, et que ces réponses dépendent beaucoup de la valeur de L . Au contraire dans le cas où l'on tient compte des mouvements de langage et de pompage, les niveaux de réponse sont plus importants autour de la fréquence d'oscillation d'incidence et moins sensibles à la valeur de L . On peut mettre la réponse en accélération sous la forme suivante :

$$\Delta n = \frac{V}{cg} \frac{K_1}{\mu}$$

où K_1 est le coefficient réduit d'atténuation de rafale associé à α_1 et qui peut s'écrire ainsi :

$$(8) \quad K_1^2 = \int_0^\infty f_0(k) \cdot f_1(k) \cdot f_2(k) \cdot f_3(k) dk$$

Dans cette formulation de K_1 , $f_0(k)$ est la fonction de transfert de l'avion, $f_1(k)$ représente les effets de portance instantanée, $f_2(k)$ prend en compte la variation en envergure de la rafale, et

$$f_3(k) = \frac{\Phi_W(k)}{\sigma_1^2}$$

est la densité spectrale réduite de puissance de turbulence. J.C. HOUBOLT a proposé pour les fonctions $f_1(k)$ et $f_2(k)$ les formulations suivantes :

$$(9) \quad f_1(k) = \frac{1}{1 + 2.32 \gamma k + \gamma^2 k^2}$$

et

$$(10) \quad f_2(k) = \frac{1 + .55 A_r k}{1 + .66 A_r k + .34 A_r^2 k^2}$$

$$\text{ou} \quad \gamma = \frac{1.5}{\beta} \frac{A_r}{3 + A_r \beta} \quad \text{avec} \quad \beta = \sqrt{1 - M^2}$$

Connaissant la fonction de transfert de l'avion, il est possible de calculer la valeur "exacte" de K_1 . Malheureusement, un tel travail n'est pas réalisable quand il s'agit de traiter plus de dix mille données; en conséquence HOUBOLT a cherché une formule approchée très simple qui donnerait une bonne approximation de la valeur "exacte". Une étude a porté sur un certain nombre d'avions différents et a montré qu'une approximation acceptable de la valeur de K_1 pouvait être donnée par :

$$(11) \quad K_1 = .95 \sqrt{\mu}$$

En utilisant l'équation (7) on peut déterminer le coefficient d'atténuation de rafale K :

$$(12) \quad K = \frac{1}{\sqrt{\pi}} \left(\frac{c}{2L} \right)^{1/2} K_1$$

Malheureusement, les résultats obtenus par la méthode de HOUBOLT montrent des écarts pouvant aller jusqu'à 10% avec la valeur "exacte" de K déduite de l'équation (8).

III - RESULTATS ET COMMENTAIRES

III-1 Avant-propos:

On vient de décrire ici trois des méthodes les plus couramment utilisées pour passer des facteurs de charge aux valeurs de rafale. Ces trois méthodes sont basées essentiellement sur l'utilisation du paramètre de masse μ ; la première (formule de PRATT) part d'une description très simple de la rafale, et déduit la valeur de la turbulence de l'accélération verticale de l'avion; la seconde et la troisième reposent sur l'hypothèse de turbulence continue, la méthode de HALL en prenant un seul degré de liberté pour le mouvement de l'avion, la méthode de HOUBOLT en utilisant les deux degrés de liberté de corps rigide pour la mécanique du vol; ces deux approches fournissent des formulations simples et prennent en compte la valeur de l'échelle intégrale de turbulence. On peut alors être étonné par le fait que la turbulence continue et les méthodes de densité spectrale soient utilisées pour obtenir des valeurs d'intensité de rafale isolée à partir des accélérations, par le biais des quantités K et H_0 . Mais ceci est acceptable car, au cours de sa vie, un avion rencontre des rafales de différentes longueurs, la distribution de ces longueurs correspondant à la densité spectrale de puissance de turbulence.

Comparons maintenant les valeurs de K obtenues par les méthodes de PRATT et de HOUBOLT, en fonction du paramètre de masse μ . Les résultats sont donnés sur la Figure 3 pour différentes valeurs de l'échelle de turbulence. On peut constater que, à la fois les valeurs et la forme des courbes sont essentiellement différentes, ce qui semble vouloir dire qu'une de ces formules est fautive.

Prenons maintenant les valeurs de K dites "exactes" données par l'intégrale (8), et comparons-les avec les valeurs obtenues par la formule de HOUBOLT (12). Le Tableau (1) donne cette comparaison portant sur 15 configurations de vol très différentes de BOEING 747, pour une échelle de turbulence de 750 m.

Comme on peut le voir sur ce tableau, on trouve des écarts allant jusqu'à 10% entre les deux valeurs de K , mais dont la moyenne se situe autour de 5%. Ainsi on peut dire que la formule de HOUBOLT donne des résultats acceptables, ce qui montre que la formule de PRATT ne doit plus être considérée comme valable. Cependant des écarts de l'ordre de 5 à 10% peuvent être la cause d'écarts plus grands sur les courbes de dépassement, il faut donc trouver une amélioration simple à cette méthode.

MASSE kg	TAS knts	ALTITUDE ft	MACH	μ	K EXACT	K HOUBOLT	% ERREUR
275300	355	9931	.538	28.60	.540	.507	-6.1
255400	491	33028	.811	55.26	.684	.710	+3.2
317800	373	9902	.578	33.11	.574	.546	-4.9
213700	298	5512	.460	19.13	.454	.415	-8.6
202100	477	28970	.765	37.08	.584	.578	-1.0
207600	474	21036	.748	29.41	.529	.515	-2.6
230400	397	17464	.635	29.05	.538	.512	-5.0
269600	515	32906	.829	58.44	.696	.726	+4.3
244000	530	35133	.850	54.23	.669	.699	+4.5
287500	515	30954	.831	56.03	.689	.717	+4.1
233700	513	36074	.853	53.89	.665	.697	+4.7
222300	205	3843	.313	15.27	.413	.371	-10.2
312800	451	18110	.706	41.50	.621	.612	-1.4
315900	230	3283	.359	21.91	.486	.444	-8.6
236700	458	25722	.733	39.18	.603	.594	-1.5

Tableau (1)

III-2 Méthode de HOUBOLT améliorée:

Le Tableau (1) montre des écarts négatifs pour les petites valeurs de u et des écarts positifs pour les grandes valeurs. Ceci donne une idée sur la façon de modifier la formule (12):

$$(14) K = \frac{1}{17} \left(\frac{c}{2L} \right)^{1/3} K_0 (b + t_1 \mu)$$

où b et h doivent être déterminés par une méthode de moindre carrés appliquée sur les valeurs du Tableau (1). Uniquement pour 15 configurations, il est nécessaire de calculer l'intégrale (8), les milliers d'événements enregistrés ne doivent être traités que par la formule (14), ce qui est très commode à faire. Dans la formule (8), on prendra, comme valeur de $P(k)$ pour le mouvement rigide de l'avion (2 degrés de liberté).

$$P(k) = \frac{k^4 - \left(\frac{1}{\alpha_2} - 2\alpha_3 k_3 \right) k^2}{(k^2 - k_3^2)^2 + 4\alpha_3^2 k_3^2 k^2}$$

où α_2 est le coefficient d'amortissement du mode de tangage de l'avion. Les résultats du lissage par moindre carrés sont présentés sur la figure (4). Ils donnent pour valeurs de b et h :

$$b = 0.846$$

$$h = 0.0035$$

Les valeurs de K pour les 15 configurations présentées ont été recalculées par la formule (14) et les résultats figurent dans le Tableau (2).

MASSE kg	TAS knts	ALTITUDE ft	MACH	μ	K EXACT	K HC	% ERREUR
275300	355	9931	.530	28.60	.540	.535	-1.0
255400	491	33028	.011	55.26	.684	.678	-1.0
317800	373	9902	.578	33.11	.574	.567	-1.2
213700	298	5512	.460	19.13	.454	.451	-0.7
202100	477	28970	.765	37.08	.584	.592	+1.4
207600	474	21036	.748	29.41	.529	.541	+2.3
230400	397	17464	.635	29.05	.538	.538	+0.0
269600	515	32906	.829	58.44	.696	.689	-1.0
244000	530	35133	.850	54.23	.669	.674	+0.7
287500	515	30954	.831	56.03	.689	.685	-0.6
233700	513	36074	.853	53.89	.666	.673	+1.1
222300	205	3843	.313	15.27	.413	.408	-1.2
312800	451	18110	.706	41.50	.621	.617	-0.6
315900	230	3283	.359	21.91	.486	.479	-1.4
236700	458	25722	.733	39.18	.603	.604	+0.2

Tableau (2)

Dans le Tableau (2), K_{HC} représente la valeur de K HOUBOLT modifiée pour la formule (14).

On peut voir immédiatement sur ce tableau que les écarts entre K "exact" et K_{HC} sont maintenant limités à 2%, ce qui est tout à fait acceptable. La même procédure a été appliquée à la flotte de BAC 111 et BOEING 737 de British Airways avec le même succès.

En résumé, il semble que le meilleur moyen pour passer des valeurs de Δn aux valeurs de turbulence, est d'utiliser la méthode HOUBOLT améliorée, en "calibrant" la formule (14) par un calcul exact sur un petit nombre de configurations de vol différentes, et ensuite d'utiliser cette formule pour le traitement des toutes les données.

III-3 Résultats

La plus grande partie des données que l'on peut utiliser provient d'enregistrements effectués par British Airways, pour des variations de facteur de charge supérieur à 0.5 g, et pour lesquels on a enlevé les charges dues aux manœuvres. En 6 années d'enregistrement, sur 8 types d'appareil, British Airways a analysé 1209462 heures de vol, qui se répartissent entre autres comme ceci :

540949 heures sur BOEING 747
177092 heures sur BOEING 737
101484 heures sur BAC 1-11.

Pour tous ces types d'avions, le profil de vol moyen est connu.

La meilleure façon de tester les méthodes précédemment exposées, est de faire des comparaisons des descriptions des turbulences déduites des mesures sur ces différents types d'avions; si une méthode est acceptable, ces descriptions doivent être proches l'une de l'autre.

Les trois méthodes ont été utilisées pour traiter les données: la formule de PRATT, la formule de HALL avec un spectre de DRYDEN et les méthodes de HOUBOLT. La formule de PRATT n'a pas permis d'obtenir une description de la turbulence cohérente à partir des données enregistrées sur les différents types d'avion. Les figures (5), (6), (7), (8) montrent pour chaque tranche d'altitude, le nombre par 1000 milles nautiques de dépassements d'un niveau donné de turbulence. Ces résultats ont été obtenus avec la formule de HOUBOLT, mais les valeurs données par la méthode de HALL sont très proches. Les deux méthodes donnent pratiquement la même description de la turbulence, quelque soit l'avion qui a servi de support à la mesure. Les plus grands écarts arrivent pour les plus basses altitudes, probablement à cause du BAC 1-11 qui, par son utilisation, vole très souvent à une altitude inférieure à 10000 pieds.

En conclusion on peut dire, que la méthode de HOUBOLT fournit, à partir des Δn enregistrés sur un type d'avion, des probabilités de niveaux de turbulence qui, appliqués à un autre type d'appareil, prédisent avec une bonne précision les dépassements de niveau de facteur de charge. Il est ainsi clair que la méthode de réduction de HOUBOLT est un bon outil pour la certification, au moins pour les grandes turbulences associées à des Δn supérieurs à 0.5.

III-4 Discussion

Une autre question est de savoir si la technique de HOUBOLT peut fournir une bonne description de l'atmosphère physique réelle. Il semble que l'on puisse dire que cette description n'est pas trop mauvaise globalement, pour les fortes rafales s'il y a un nombre suffisant de dépassements du niveau de turbulence de référence. Dans de telles conditions, on peut penser que l'effet d'imprécision du aux paramètres inconnus comme :

- fonction de transfert réelle,
- valeur exacte de a (C_{y0}),
- valeur de l'échelle de turbulence,
- fonction de transfert exacte du pilote automatique,

est moyenné.

Cette conclusion n'est valable que pour les vols British Airways, pour lesquels charges de turbulence et charges de manœuvre ont été clairement séparées, de ce fait les résultats montrent des courbes de dépassements symétriques pour des rafales positives ou négatives. Malheureusement cette séparation n'a pu être faite pour la plupart des enregistrements d'autres flottes. Sur les BOEING 747 de British Airways et pour des Δn supérieurs à 0.5 g, 25% des événements correspondent à des manœuvres.

Comme les manœuvres donnant de fortes accélérations sont rares, il est bien clair que ce pourcentage va augmenter pour les faibles facteurs de charge au moins à basse altitude; dans ce cas les courbes de dépassements de rafales positives et négatives ne sont plus symétriques, avec un plus grand nombre de valeurs positives. C'est ce que l'on a observé sur les enregistrements provenant du MLR, également sur BOEING 747, mais où les manœuvres et la turbulence n'ont pas été séparées. Dans la tranche d'altitude 0-5000 pieds, les nombres de dépassements d'accélération positive et négative supérieur à 0.3 g sont respectivement 1452 et 449; ils ont tendance à devenir égaux pour des Δn supérieur à 0.5 g.

IV-CONCLUSION

L'étude présentée ici repose sur l'analyse de plus d'un million d'heures de vols commerciaux de différentes compagnies (British Airways, Air France). Elle a mis en lumière les points suivants :

- La formule de PRATT doit être abandonnée car elle aboutit à des descriptions de l'atmosphère incohérentes, c'est à dire différentes suivant le type d'avion sur lequel les informations ont été collectées.

- La formule de HALL, avec un choix approprié et raisonnable de l'échelle, aboutit à une description cohérente de la turbulence, relativement indépendante des types d'avion considérés.

- La méthode de HOUBOLT, surtout dans sa forme améliorée telle que proposée ici, fournit une bonne description de l'atmosphère, mais elle nécessite un "étalonnage" de la formule qui conduit à des calculs plus importants sur un nombre limité de configurations pour un avion de type donné.

- Pour les fortes turbulences, le nombre moyen de dépassements par mille nautique d'un seuil de référence décroît exponentiellement avec ce seuil.

- Pour les faibles niveaux de turbulence, l'interprétation des mesures est très délicate, car les accélérations dues aux manœuvres représentent un pourcentage important des dépassements enregistrés, et il ne semble pas possible actuellement de séparer les deux cas de manœuvre et de turbulence.

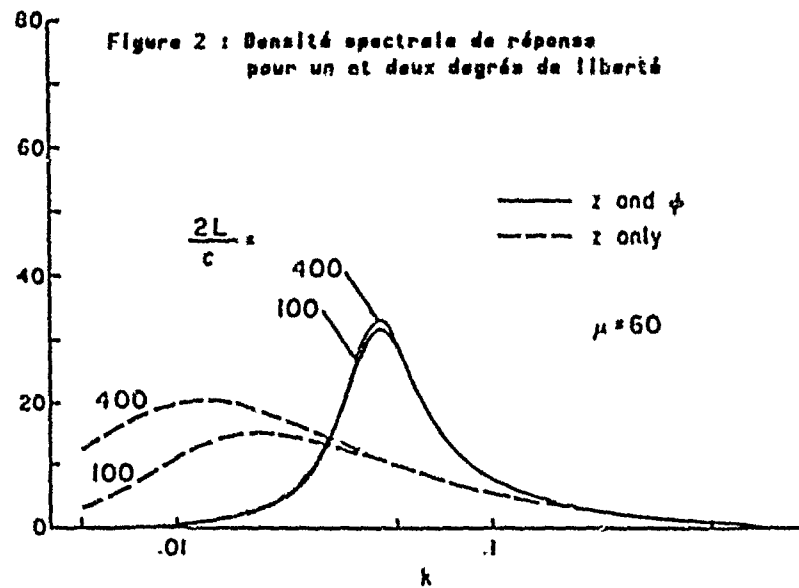
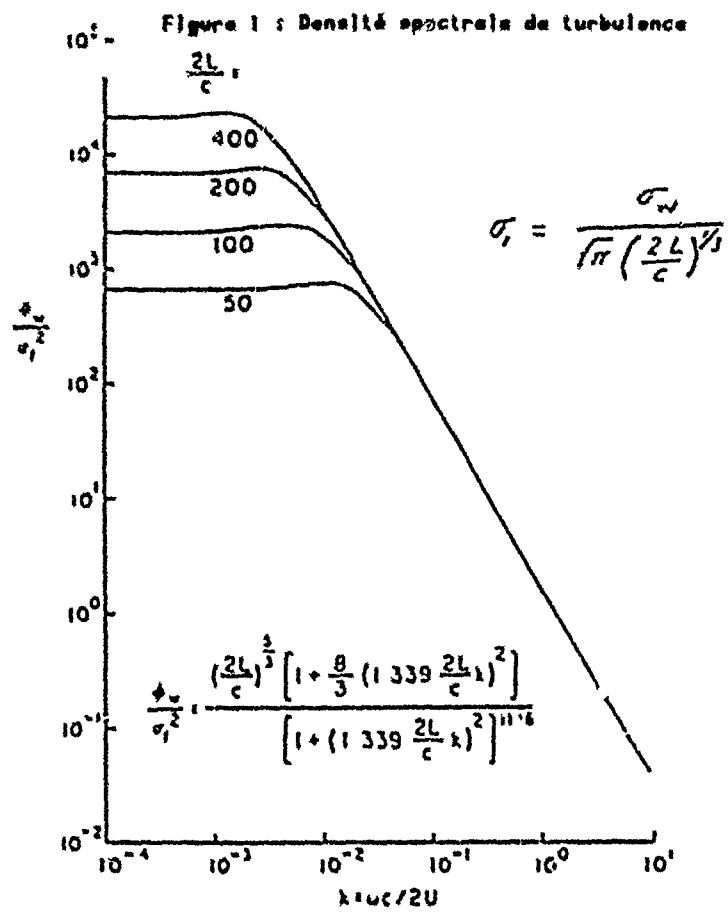
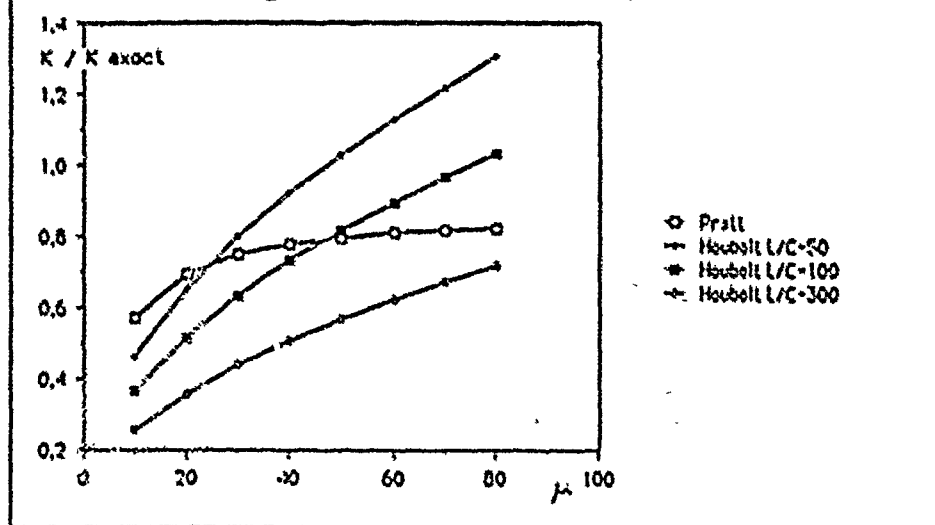
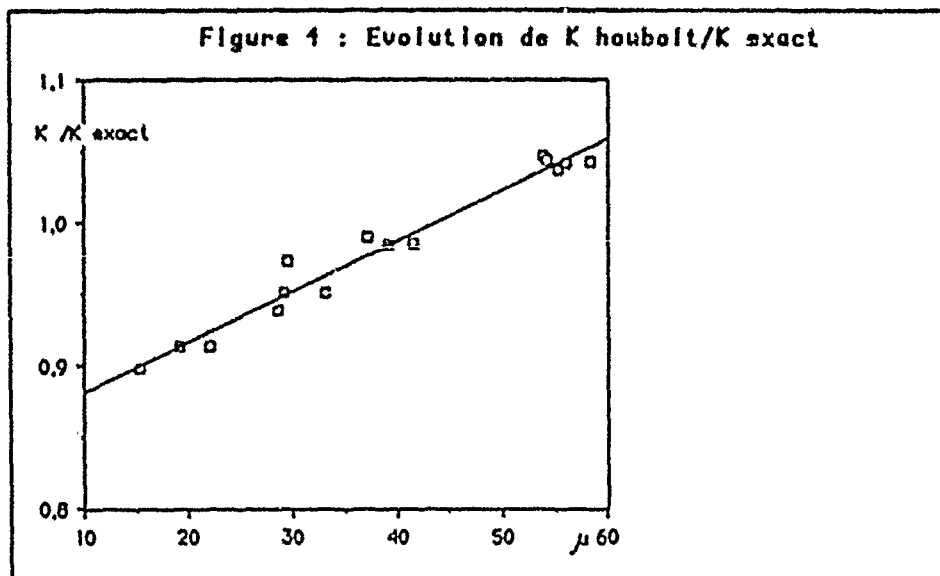
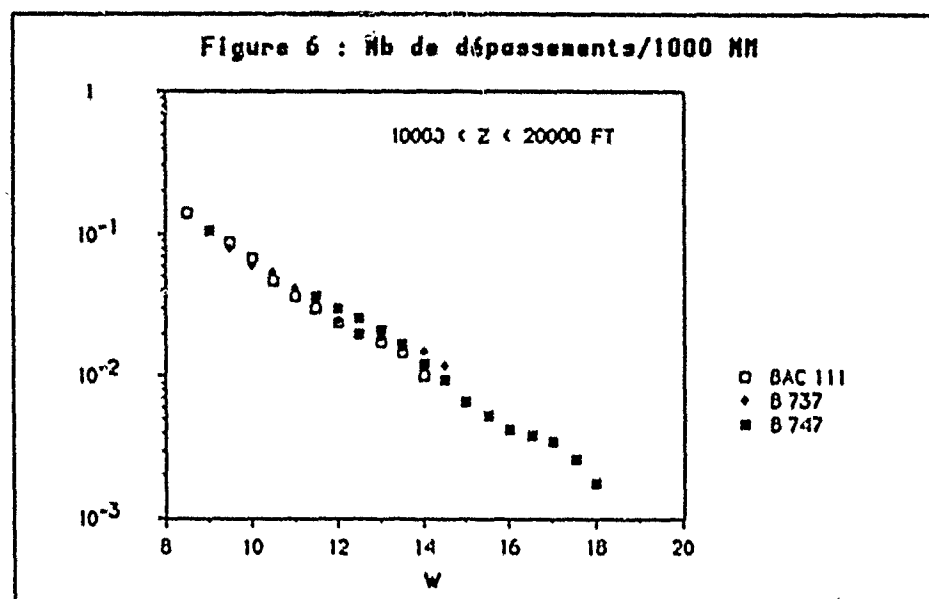
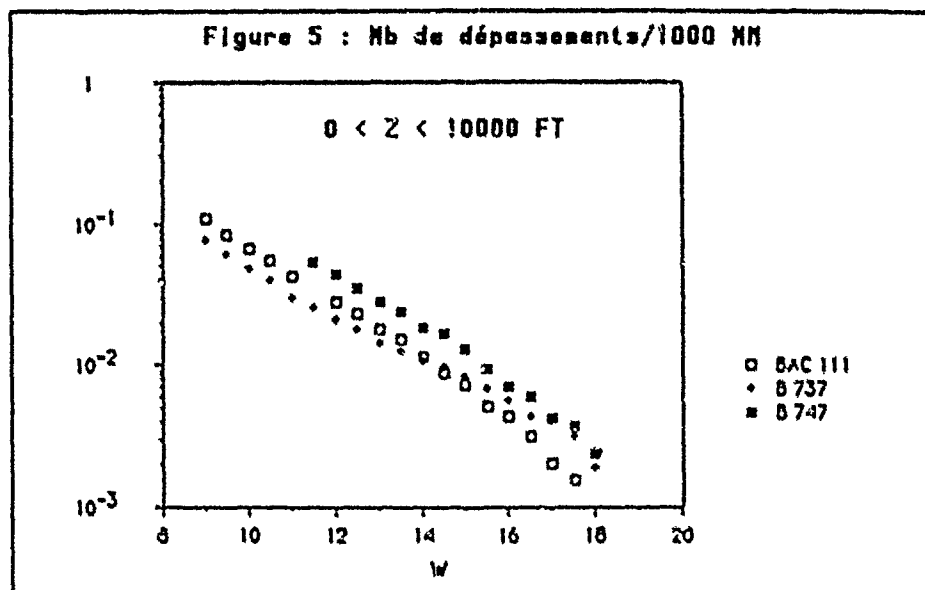
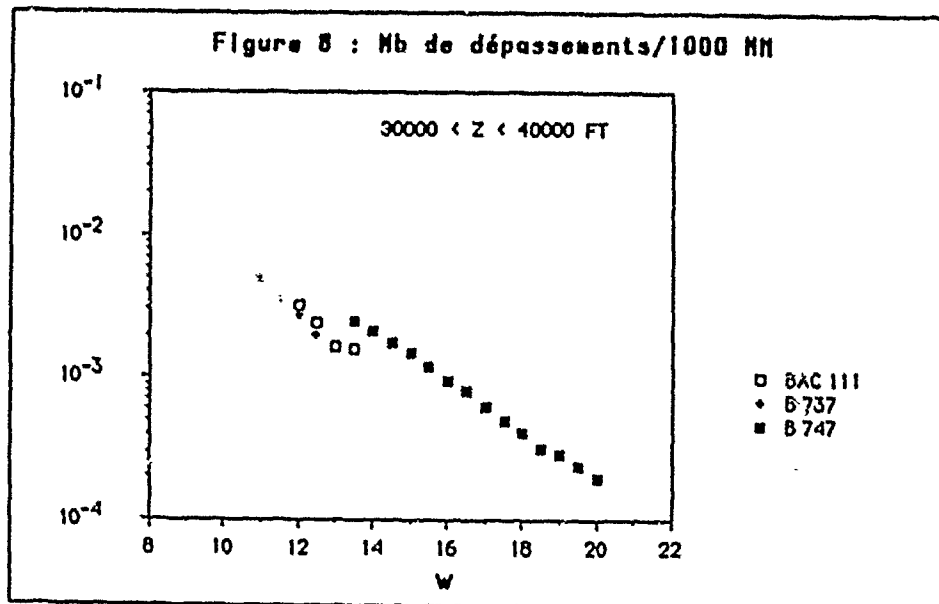
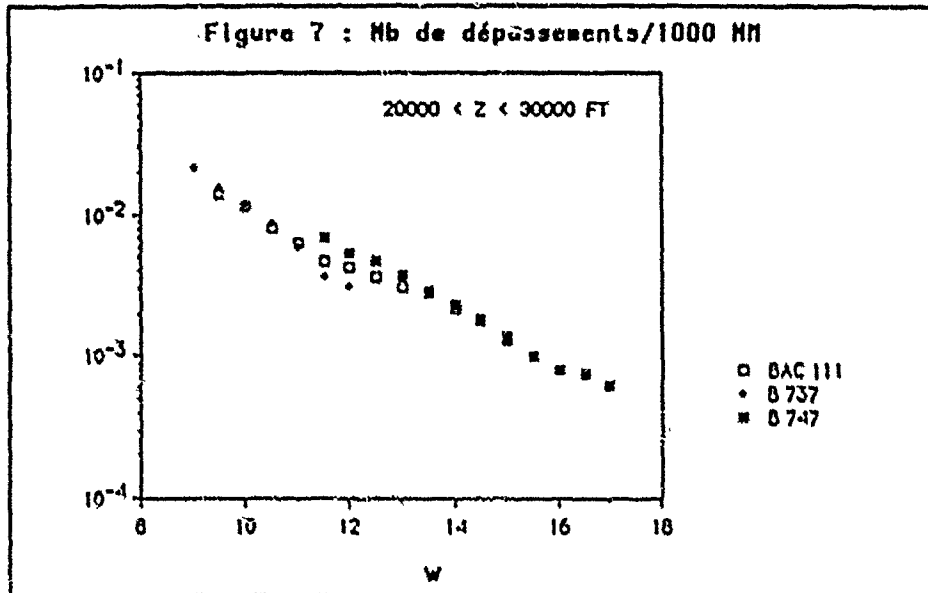


Figure 3 : Evolution de K / K_{exact} Figure 4 : Evolution de $K_{\text{houbolt}} / K_{\text{exact}}$ 





WIND SHEAR MODELS FOR AIRCRAFT HAZARD INVESTIGATION

by

Manfred Swolinsky
Institute of Guidance and Control
Technical University Braunschweig
Hans-Sommer-Str. 66
3300 Braunschweig
FRG

SUMMARY

Wind shear hazard investigations, flight simulation for pilot training as well as design, development and testing of flight control systems require suitable wind models. Basing on flight test data, airline flight data and meteorological tower measurements, engineering models for dangerous wind shear situations have been developed in the frame of different wind shear research projects. Derived from simplified fluid dynamic concepts the engineering models for downburst, frontal wind shear and low level jet meet the requirements for real-time flight simulation. The comparison of the windmodels with measured wind data show good accordance.

For the analyses of simulated landing approaches in wind shear conditions a hazard definition is given by means of aircraft energy height deficit, respectively the required energy supply for landing approach on nominal glide slope and constant air speed.

List of Symbols

E	Energy	χ_W	Wind azimuth
e	Coefficient	γ	Flight path angle
f	Coefficient		
G	Aircraft weight	Ref	Reference
g	Constant of gravitation		
H	Height, altitude		
H _E	Energy height		
ΔH_E	Energy height error		
H ₀	Surface roughness height		
k	Von Karman's constant		
m	Exponent of power law, Mass of aircraft		
u, v, w	Components of flow		
u _{Hg}	Horizontal wind component		
u*	Friction velocity		
V	Airspeed		
V _K	Flight path velocity		
V _W	Wind velocity		
V _{stall}	Stall speed		
w _{Hg}	Vertical wind component		

1. INTRODUCTION

Systematic analyses of wind shear effects on flight safety require the use of simulation techniques and consequently the implementation of suitable wind models. Specifications for these models are on the one hand a sufficient mathematical description of the flow field and on the other hand a simple mathematical structure to work at adequate expense under condition of real time simulation. For the most part of the investigations the aeronautical engineer may concentrate on the design of quasi-stationary fluid dynamic engineering models.

This engineering models substantial differ in design method and model structure from that used in the area of meteorology. Unsteady meteorological wind models described by extensive simulation programmes are generally unsuitable for application in flight simulation because of the mathematical expense and the insufficient horizontal and vertical resolution.

Turbulent windprofiles may be separated into a low frequency trend and turbulent fluctuations of wind speed (Fig.1). In some cases gusts are considered for the description of nonhomogenous disturbances. The definition of mean wind is rather difficult. Using earth fixed sensors, a temporal averaging is performed for each measuring point. But the question for the right averaging interval is difficult to answer. In many cases of meteorological tower measurements a 10 minute time average is usual. In the case of airborne wind measurement the mean wind has to be calculated from the instantaneously sampled profile along the flight path by means of low pass filtering (Fig.1). The choice of the time constant of the filter is the critical point instead of average interval. A suitable criteria is to be found supposing that the separated turbulence has to be stationary with regard to the mean of the turbulent portion.

This paper will concentrate on engineering models only for low frequency mean wind profiles. The aircraft response on wind shear is quite different from the reaction on turbulence. In the case of wind shear the mean wind considerably influences the state of the aircraft energy. Hence, wind shear hazard definition can be expressed by aircraft energy deficit. For landing approach it is possible to formulate hazard definition limits in a rather simple way.

2. WIND SHEAR CHARACTERIZATION AND MODELING

In the planetary boundary layer wind shear can exist under a broad variety of weather conditions. The main influences on usual boundary layer wind profiles are surface roughness and stability of the atmosphere. In addition to the ordinary wind shear situation, found in the planetary boundary layer, there are three basic wind conditions which may restrict flight safety during take-off and landing: downburst and microburst cells in connection to thunderstorm activities, or high cumulus clouds, fast moving cold or warm fronts, and the low level jet.

2.1 BOUNDARY LAYER WIND SHEAR

In general the planetary boundary layer is divided in two different horizontal layers (Fig.2). The surface layer (the so called PRANDTL-Layer) is the lower portion of the atmospheric friction layer. The PRANDTL-Layer extends up to about 50 -100 m above the surface and describes a region of approximately constant shearing-stress and only small change in wind direction. Above this layer there is a region of transition from the disturbed flow near the surface to the frictionless free atmosphere. This height is

considerably variable; it can go up to more than 1000 m. There are a number of models for the mean wind profile valid for the PRANDTL-layer.

The most widely used profile for this layer is PRANDTL's logarithmic wind profile (Fig.3 and eq.1). Its wind speed with respect to height is a function of roughness length and friction velocity, which depends on shear stress and air density.

$$V_H = \frac{U_*}{K} \ln \frac{H}{H_0} \quad (1)$$

As the logarithmic law is valid only for adiabatic atmospheric conditions many other models have been developed for the case of non-adiabatic conditions. Most of them are applications of MONIN-OSUKHOV similarity theory with different universal functions. The well known logarithmic-linear profile is a simple form of this approach. In this case a linear with height varying term is added to PRANDTL's adiabatic profile, depending on stability of the atmosphere (fig.4).

One of the most simple and for flight simulation widely used empirical wind model is described by the power law (Fig.3 and eq.2). The expression V_{Ref} refers to the wind speed at reference altitude H_{Ref} .

$$V_H = V_{H,Ref} \left(\frac{H}{H_{Ref}} \right)^m \quad (2)$$

The exponent m depends on surface roughness and stability of the atmosphere. Many investigations in determining the value of m as a function of these parameters have been carried out (for example Ref.5). Fig.(5) illustrates that the power law gives a good approximation of measured wind profiles up to some hundred meters of height. Furthermore this figure demonstrates that the neglect of wind direction change, as considered for the PRANDTL-layer, is not generally valid for the whole boundary layer. In principle the wind direction is changing clockwise on northern hemisphere from the rotating surface of the earth to the boundary layer. The change of direction is extremely variable, making any quantitative investigations rather difficult.

The first theoretical study of wind veering for laminar flow condition led to the well known EXMAN-spiral. But it gives only a quantitative description of direction change with respect of height. A simple approximation for the turbulent flow type has been published by PRANDTL (Ref.22). This approach seems to be suitable for application in flight simulation. In eq.(3b) the deviation from the wind direction of free atmosphere depends on thickness of the boundary layer H_0 and the difference between direction of geostrophic and surface wind Δx_{H_0} (see Fig.(6)):

$$\tan x_H = \left(1 - \frac{H}{H_0} \right) \tan \Delta x_{H_0} \quad (3b)$$

The determination of the angle Δx_{H_0} , given in eq.(4), is a function of power law exponent m :

$$\tan \Delta x_{H_0} = \sqrt{m(m+2)} \quad (4)$$

In the case of missing information about the direction of geostrophic wind and the height of the boundary layer, a simple derivation of PRANDTL's law eq.(3) can be made for fitting measured wind direction profiles:

$$x_H = x_{H_0} + \arctan \left(\frac{H - H_0}{H_1 - H_0} \right) \tan(x_{H_1} - x_{H_0}) \quad (5)$$

$$x_{H_1} - x_{H_0} = \Delta x_H$$

$\Delta\alpha_H$ is the veering angle between wind direction at height H_0 and H_1 .

Some examples for the comparison between model and measurement are illustrated in Fig.(5).

It must be mentioned that the shape of wind profile can be influenced by meteorological and topographic conditions like inhomogeneity of the atmosphere and terrain, lee-effects of hills, etc., which can not be pointed out in detail in this paper. An illustration for the influence of temperature inversion to wind speed and direction is given in Fig.(7).

2.2 Low Level Jet

The term "low level jet" is used to describe wind phenomena of the lower part of the boundary layer, characterizing jet like wind profiles with a low altitude wind maximum. This kind of wind profiles has been observed in connection with specific local terrains, thermal effects in mountain valley regions, frontal activities, and the nocturnal boundary layer. Usually the nocturnal low level jet is to be found in the time between late afternoon and morning under clear nocturnal sky when a strong radiation temperature inversion develops. Because of the strong stability in the inversion layer friction disappears and the unbalanced Coriolis and pressure gradient forces produce an acceleration of wind speed. Ref.6 describes the evolution of low level jet as a nonstationary process where the vector difference between the actual wind and the geostrophic wind is rotating nearly circular around the geostrophic wind (inertial oscillation, see Fig.(8)).

In the northern part of Germany the low level jet can be found approximately in 10 percent of all nights. Hence, a lot of data has been collected in the last years by means of tower and aircraft measurement (Ref.7, 8, 9). Fig.(9) shows a typical low level jet sample recorded during a wind shear measuring project by means of a LUFTHANSA AIRBUS A 300. A wind maximum of the 1.8-fold value of geostrophic wind speed and the 4.5-fold value of reference speed ($H_{Ref}=10$ m) was observed as well as a change of wind direction of about 90 degrees in a vertical layer of 300 m height. Investigations in the plains of northern Germany, carried out by two 300 m high meteorological towers (Ref.9), show a cycle period of 14,5 hours for the inertial oscillation. During take-off and landing approach the critical zone of wind shear is passed in only one or two minutes. In this case the temporal evolution is not relevant and modeling can concentrate on quasi-stationary engineering models. Velocity profiles like low level jet wind profiles have been observed in fluid dynamic research of free jet and wall jet. As a first low level jet approximation a superposition of a boundary layer profile (for instance the power law) and a plane free jet velocity profile is used (see Fig.10). Measured data and equations for the free jet have been published among others by Ref.10 and 11.

Describing the wind direction with respect to height a proceeding similar to the magnitude of wind speed is used. In comparison to the direction profile of the boundary layer (eq.(5)) the superposition of a suitable function is intended. The principle procedure is illustrated in Fig.(11) and eq.(7).

For a large number of data records a comparison of measured data with modeled low level jet has been carried out. The examples of tower data (Fig.12) and aircraft data (Fig.13) are in good agreement with the model.

Derived from Soviet measurements (Ref.12), worst case profiles for the low level jet have been approximated (see Fig.14) by using model eq.(6) and eq.(7).

2.3 FRONTAL WIND SHEAR

During the passage of fast moving cold or warm fronts considerable wind shears may develop due to changes of wind direction ahead and behind the frontal line. Especially strong fronts with sharp transition zones may affect aircraft operation. Fig.15 illustrates the principle development of meteorological parameters like wind speed, wind direction, temperature, and atmospheric pressure during the passage of a frontal system (cyclone). In the range of the warm front warm air displaces the cold air while sliding upon the cold air situated ahead the front line. The maximal change of wind direction is about 90 degrees. In the following cold front zone cold air is flowing beneath the warm air ahead to the front line. The wind direction changes of about 135 degrees. A wind speed change of about 15 m/s and a vertical wind speed of 4 m/s (updraft) can be observed. In principle similar conditions as described for cold fronts are to be found in gust fronts in connection with a thunderstorm outflow.

A mathematical description of the velocity field in the front line region can be generated by superposition of vortex induced flow velocities. The principle proceeding is shown in Fig.16.

Another approach is based on a fluid dynamic description of streamsurface bifurcations. Local solutions in the vicinity of stream surface bifurcation lines (see eq.8), obtained for the NAVIER-STOKES and continuity equations by Ref.13 can be adapted and modified for the problem of modeling frontal wind shear.

$$\begin{aligned} u &= e x + f H \\ v &= k H \\ w &= e H \end{aligned} \quad (8)$$

The front slope angle θ is determined by the coefficients e and f in eq.9:

$$\tan \theta = -2 e / f \quad (9)$$

An example for a modeled frontal velocity field is shown in Fig.17. The lower part of this figure illustrates magnitude and direction of the wind vector along a 3-glide slope, compared with measured data (Ref.14).

2.4 THUNDERSTORM OUTFLOWS

The thunderstorm, with typical effects like strong downdraft, severe turbulence, flash light, and hail showers, is well known to be dangerous to aviation. A number of fatal and near-fatal accidents in the last 20 years, which have been attributed to thunderstorm wind phenomena, initiated world wide research activities in hazard investigations and downburst modeling. Different basic modeling techniques have been used. One method is the construction of wind components from measured data by interpolation between the grid points (Ref.15). A second way consists of the use of dynamic meteorological models (Ref.1). In general these models are too extensive to be used in real time flight simulations. The third technique for the generation of downburst wind fields is based on relatively simple fluid dynamic approaches. A number of different concepts have been published in the last years (Ref.17, 18, 25). In this paper two other concepts will be discussed:

As the downburst produces a flow like a vertically downward directed jet, which spreads out horizontally as it approaches the ground, the first one uses a steady jet flow toward a stagnation point for the description of the flow field in the center region of the downburst cell. It has to be complemented by zones of vicinity and transition flow. A vertical cross section through the center of the downburst model is shown in Fig.18.

The second concept is based on the superposition of a number of spreaded vortices in combination with the same number of image vortices. This method is characterized by more variability and allows for instance the modeling of a downburst wind field including the mean flow of the gust front. The center of vortices are positioned along a stream line of the downburst cell (2-dimensional model with 24 vortex doublets see Fig.19a). In the case of a 3-dimensional mode, ring vortices have to be used instead of flat vortices (Fig.19b). An optimum program was applied to evaluate the model parameters for the best fitting of measuring data. Using a simple DIGITAL MicroVAX2 computer for the computation of the whole 3-dimensional aircraft model and the ring vortex down burst a combination of maximum 11 doublets of ring vortices could be obtained for real time simulation with a computation frequency of 25 cycles per second.

3. EXAMPLES OF FLIGHT SIMULATION RESULTS

Some flight simulation results with a heavy transport aircraft may demonstrate the experience in using the engineering models "low-level-jet" and "downburst" for aircraft hazard investigations.

3.1 LANDING APPROACH IN A LOW LEVEL JET

For the low-level-jet-investigations the the Khabarovsk tower measurement approximation was applied as "worst case"- wind profile. Fig.20 shows flight path and airspeed profiles during landing approach with fixed controls. The full line curve characterizes trimming and thrust setting 6 km distant from threshold while the dash-dotted line curve results from the thrust setting and trimming at the location of wind speed maximum. This leads to a maximum of flight path deviation. It may be supposed that the flight profile appearing in manual flight under this low-level-jet conditions will be occur in the area between the two flight pathes. This anticipation could be proved in a number of simulated landing approaches with test pilots of the Institute of Flight Guidance. Two examples from this flight simulator investigations are shown in Fig.21a and Fig.21b. In the first case the pilot reduces the thrust to avoid extensive flight path deviation during increasing headwind. Compared with an ideal thrust control law (eq.10), which allows no flight path deviation and airspeed deviation in relation to the nominal values, the pilots throttle activity has a time delay of roughly 17 seconds. This seems to be a typical behaviour for one part of the pilots in appropriate wind situations. An other pilot behaviour is presented in Fig.21b. It is characterized by very low throttle activity (except at the final phase of the approach) and a higher excess of potential energy in the region of the wind speed maximum.

Systematic investigations performed by parameter variation of the low-level-jet-model show, that the height of maximum headwind and the headwind difference between wind maximum value u_m and reference wind speed $u_{H_{Ref}}$ (H_{Ref} is chosen to 10 m) are the most influential parameters for the severity of landing approach in a low level jet flow field. Hazard increases with increasing headwind difference in connection with decreasing height of the headwind maximum. This means for an aircraft moving through the windfield on an inclined flight path a corresponding high value of wind acceleration. The temporal derivation of the headwind component is one of the essential parameters in a thrust control law, formulating the required additional thrust for the acceleration of the aircraft with the wind. Under ideal conditions this measure avoids any deviations from nominal flight path and airspeed. An approximation for the required additional thrust-weight-ratio may derived from the simplified equations of the longitudinal and vertical aircraft motion:

$$\Delta F/G = \dot{u}_{Hg}/g + (\Delta u_{Hg} \gamma + \Delta w_{Hg})/\gamma \quad (10)$$

$$\text{with } \Delta u_{Hg} = u_{Hg} - u_{Hg,Ref} \text{ and } \Delta w_{Hg} = w_{Hg} - w_{Hg,Ref}$$

The required additional thrust essentially depends on wind parameters, considering that the nominal flight path angle has an specified value and the nominal airspeed has almost the same order of magnitude for heavy transport aircraft.

The step from required thrust-weight-ratio to the required energy height adaption to variable wind conditions can be realized by integration of eq.(10) with respect to flight path distance x_k :

$$\Delta H_E = \int_{x_0}^{x_k} \Delta F/G \, dx_k \quad (11)$$

The required energy height may be used for the approximation of the energy height error appearing if no thrust adaption is intended (see Fig.22). Occuring flight path deviations from the commanded ILS-glide slope are producing a potential energy height error

$$\Delta H_{E,pot} = H - H_{Ref}, \quad (12)$$

and airspeed deviations from the commanded speed V_{Ref} lead to a kinetic energy height error

$$\Delta H_{E,kin} = (V^2 - V_{Ref}^2)/(2g). \quad (13)$$

As the airspeed has to be kept constant during landing approach (nominal value about $1.3 V_{stall}$) it is useful to define the kinetic energy with regard to the surrounding air ("aerokinetic energy"). Therefore the airspeed V is used instead the flight path velocity V_k in eq.(13). In order to use the energy height error as a quantitative measure for aircraft hazard, hazard definition limits have to be defined. Ref.21 proposes hazard limits for the kinetic energy expressed by the "stick shaker"-velocity $1.1 V_{stall}$ and for the potential energy by the maximum allowable height deficit related to the obstacle clearance surface of a CAT I -approach (assumed worst glide path minus 30 meters). Comparing the actual kinetic and potential energy height deficit with the hazard limit values a hazard scale is formed. If potential and kinetic energy error limits are not reached simultaneously, shifting between airspeed (kinetic energy) and height (potential energy) is feasible. Otherwise energy height deficit must be compensated by means of thrust setting.

In Fig.23 energy error and hazard definition limits are illustrated for the manual low level jet approach of the example in Fig.21a. About 1.2 km ahead of the runway threshold the hazard limits are almost reached.

3.1.1 TAKEOFF AND LANDING APPROACH IN A DOWNBURST

Hazard investigations for takeoff and landing approach in downburst flow fields have been performed by means of the expanded steady jet flow model as well as the ring vortex superposition model. In general the ring vortex model has a better capability for the approximation of accident conditions and measuring data.

The result for an off line flight simulation of a landing approach is illustrated in Fig.24. The flow conditions in the steady jet model is similar to the conditions of the approach accident in New York on June 24,1975. The flight path with fixed aircraft controls is not very different from that of the accident flight. A landing approach with an automatic flight control system (autopilot/autothrottle) could be performed with very low deviations from nominal flight path and airspeed (this is not valid for a pure autopilot approach). Thus we can assume a delayed and inefficient pilot reaction, implied by insufficient information about the situation.

While an aircraft has reserved energy in landing approach it is flying at its maximum performance capability during takeoff. In addition the downdraft intensity in a downburst in general is increasing with increasing height. Hence, a takeoff into a downburst may be the more dangerous situation. An example for the takeoff and climb situation shows Fig.25, using the vortex ring superposition downburst model (similar Fig.29a). The diagrams illustrate the three wind components in earth fixed coordinates and the flight path in the vertical plane. Takeoff direction is 274 degrees, i.e. the east wind component corresponds with the headwind. After takeoff the pilot begins an normal climb procedure. Drawing near to the downburst core zone a decreasing angle of climb results from the increasing downdraft and decreasing headwind. The loss of height down to 60 Meters leads to touch of the obstacle clearance surface of the airport. In other cases the aircraft had a ground impact. In opposition to the low level jet the wind components were varying with all three coordinates. Thus the aircraft hazard depends not only from the wind characteristics but also from the flight path in relation to the flowfield in combination with other parameters like thrust setting, trim situation, aircraft operation mode and the pilot behaviour.

The aircraft hazard investigations have led on concepts to increase flight safety for takeoff and landing in wind shear conditions (see /19/, /20/, /21/, /24/), like wind shear warning displays, thrust control laws and improved automatic flight control systems.

4. SUMMARY

Simplified fluid dynamic concepts have been used to develop engineering models for wind shear phenomena like downburst, frontal flow and low level jet. The data base used for the modeling task is composed of own flight test data, airline flight data, and tower data, complemented by other informations and experimental results. A number of examples demonstrate the good approximation of measured wind profiles by the developed wind models.

This simple engineering wind models have been an essential base for aircraft hazard investigation by means of flight simulation. The results have led on suitable hazard definitions as well as concepts and systems to improve flight safety in wind shear conditions.

5. References

- | | |
|--|--|
| <p>/1/ Thorpe, A.J.
Miller, H.J.
Moncrieff</p> <p>Dynamic Models of Two-Dimensional Downdraughts.
Quart. J. R. Met. Soc.(1980), 106, 463-484</p> | <p>/2/ Deluge, Y.</p> <p>A Numerical Study of the Nocturnal Atmospheric Boundary Layer.
Quart. J. R. Met. Soc. 100 (1974), 351-364</p> |
|--|--|

- /32/ Fiedler, F.
Die Grenzschicht der Atmosphäre:
Struktureller Aufbau.
In: *Frankf. Z.*, Heft 1, 1974, S. 1-2
- /4/ Monin, A.S.
Obukhov, A. M.
Fundamentale Gesetzmäßigkeit der tur-
bulenten Vermischung in der bodennahen
Schicht der Atmosphäre.
In: *Statistische Theorie der Turbulenz*
Akademie-Verlag, Berlin 1959, S. 199-226
- /5/ Counihan, J.
Adiabatic Atmospheric Boundary Layers
A Review and Analysis of Data from
the Period 1880-1972.
Atmosph. Environment, Vol 9, S. 871-905
Pergamon Press 1975
- /6/ Blockador, A.K.
Boundary Layer wind maxima and their
significance for the growth of nocturnal
inversions. *Bull. Am. Meteorol. Soc.* 33,
283 - 290, 1957
- /7/ Swolinsky, M.
Krauspe, P.
Windbestimmung aus Flugmeßdaten
eines Linienflugzeugs.
Meteorologische Rundschau 37, 72-81,
Juni 1984
- /8/ Krauspe, P.
Swolinsky, M.
Yörsmann, P.
Wind Determination and Wind Shear
Detection from Flight Test and
Airline Flight Data.
International Conference on Aviation
Weather System, American Meteorological
Society, Montreal, Que, May 1981
- /9/ Kottmeyer, C.
Die Vertikalstruktur hochliegender Grenz-
schichtstrahlströme.
Dissertation am Institut für Meteor-
ologie und Klimatologie der Universität
Mannover, 1982
- /10/ Reichardt, K.
Gesetzmäßigkeiten der freien Turbulenz.
VDI-Forschungsheft 414 (1962), 2. Aufl. 1951
- /11/ Schlichting, H.
Grenzschicht-Theorie.
Verlag G. Braun, Karlsruhe 1982.
- /12/ Shelkovenkov, M.S.
Strujnye techeniya na mal'kh vysoikh
(Strahlströme in geringer Höhe).
Meteorologiya i gidrologiya, 1983,
Nr. 11, Moskau, S. 44 - 46
- /13/ Horning, H.
Perry, A.E.
Some Aspects of Three-Dimensional Separation.
Part I : Streamsurface Bifurcations
Z. Flugwiss. Weltraumforsch. 8 (1984), Heft 2
- /14/ Ellis, G.V.
Keenan, M.G.
Development of Wind Shear Models and
Determination of Wind Shear Hazards.
FAA-Report No. FFA-RD-79-113
January 1978,
- /15/ Barr, M.H. et.al.
Wind models for Flight Simulator
Certification of Landing and Approach
Guidance and Control Systems.
FAA-RD-74-206, Dec. 1974

/16/ Krauspe, R.

Beiträge zur Klärung von Flugee-
gen in Windscherungen.
Dissertation, Fakultät für Maschinenbau
und Elektrotechnik der TU Braunschweig,
1983

/17/ Shanglong Zhu
Ethio, B.

Field-Dynamic Model of a Downburst.
UTIAS-Report No. 273, April 1983

/18/ Bray, R.S.

A Method for Three-Dimensional Modelling of
Wind-Shear Environments for Flight Simulator
Applications.
NASA TM 85969, 1985

/19/ Mohn, K.-H.J.

Takeoff and Landing in a Downburst.
Journal of Aircraft, Vol. 24, No. 8, Aug. 1987
Page 552-558

/20/ König, R.
Krauspe, R.
Schönzer, G.

Procedures to Improve Flight Safety in Wind
Shear Conditions.
12th Congress of the International Council of the
Aeronautical Sciences, Oct. 12-17, München, 1980

/21/ König, R.

Erhöhung der Flugsicherheit bei Scherwinden-
flügen durch Modifikation von Schubregelungs-
systemen und bestehender Cockpit-Instrumentierung.
Jahrestagung der DGLR, Stuttgart,
S. - 7. Oktober 1982 Vortrag Nr. B2 - 033
und Wissenschaftliche Berichte 1982, SFB 58
"Flugführung" TU Braunschweig u. DFVLR

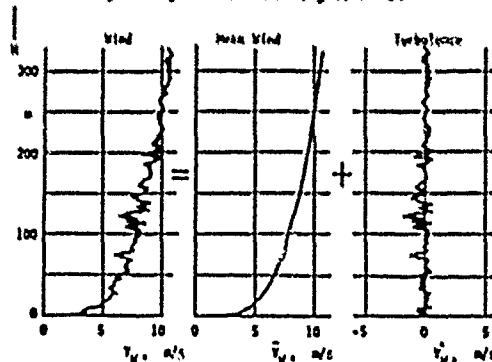


Fig.1 : Separation of Turbulence

/22/ Prandtl, L.

Strömungslehre
Vieweg-Verlag, Braunschweig, 1965

/23/ England, J.
Wibrich, H.

Flugmeteorologie.
Transpress VEB Verlag für Verkehrswesen
Berlin 1990

/24/ Redtzer, A.

A New Control System for Flight in Turbulence
and Wind Shear.
2nd International Symposium on Aviation Safety,
Toulouse, May, 1986

/25/ Woodfield, A.A.
Wood, J.F.

Worldwide Experience of Wind Shear
During 1981-1982
AGARD CP No. 347
Athens, 10.-13. May, 1983

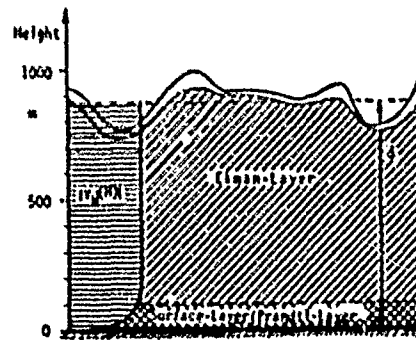


Fig.2: Classification of planetary boundary layer (Ref.3)

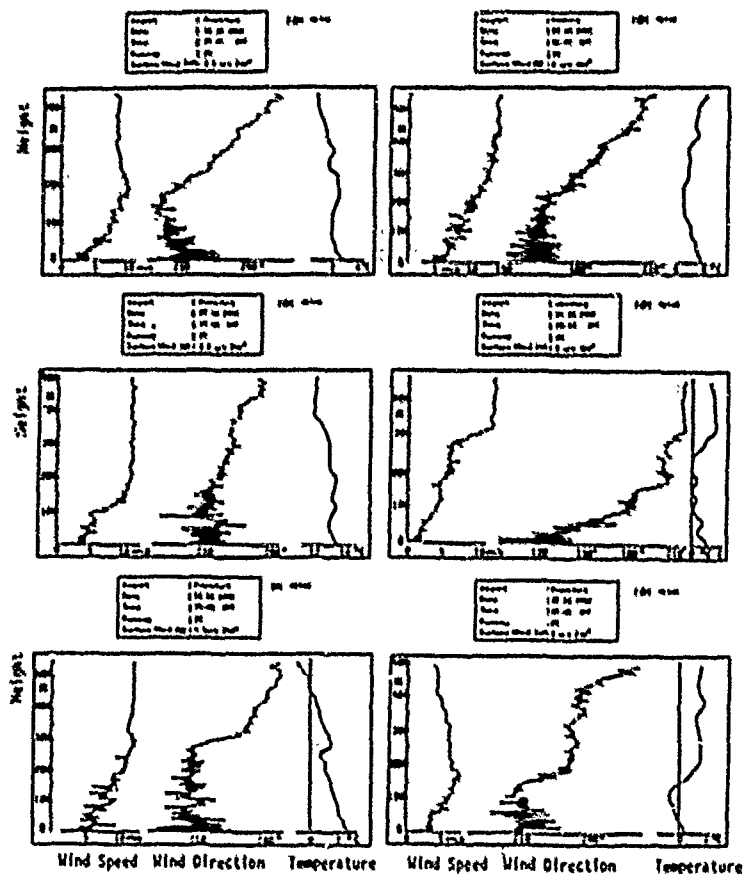


Fig.7: Influence of temperature inversion on wind profile

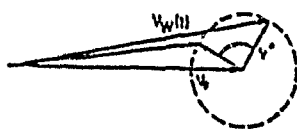


Fig.8: Inertial oscillation supposed by Ref.6

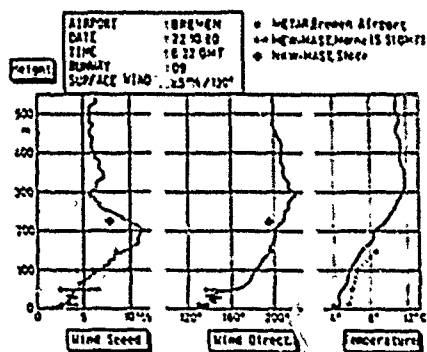


Fig.9: Sample of flight measured low level jet

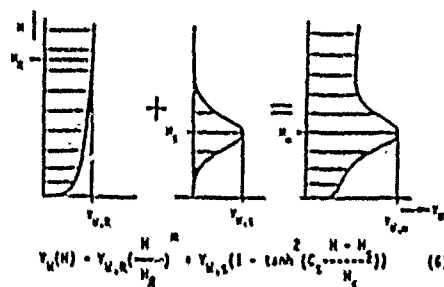


Fig.10: Composition of the low level jet model

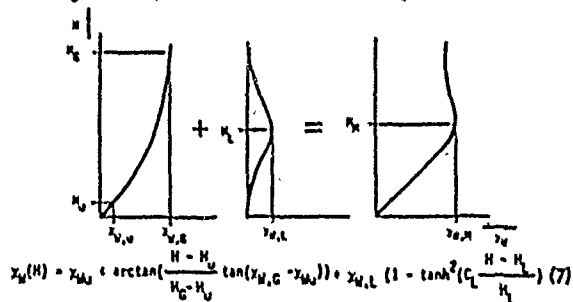


Fig.11: Composition of the wind direction

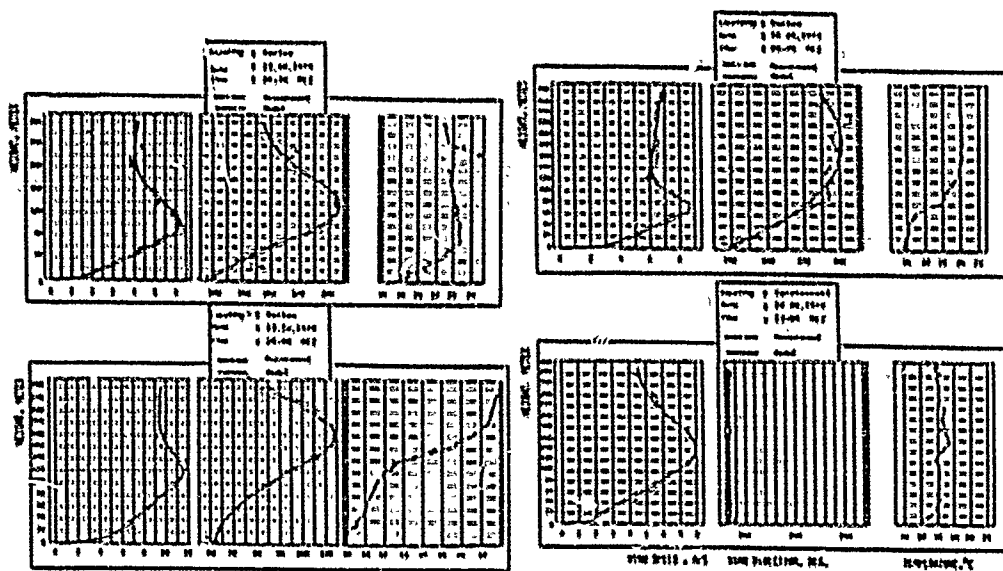


Fig.12: Approximation of tower data

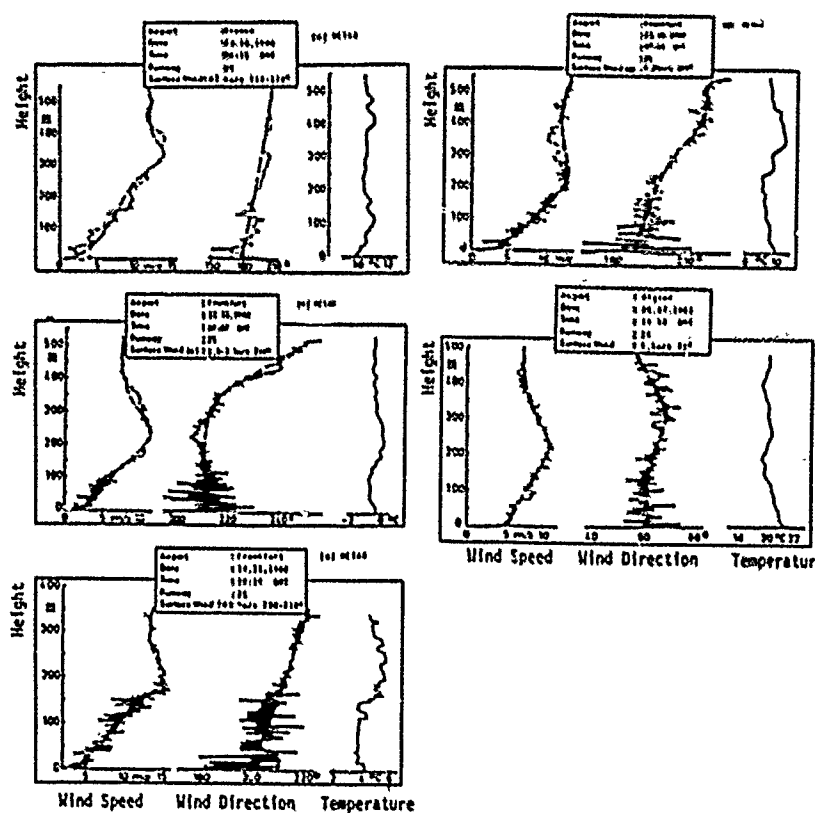


Fig.13: Approximation of flight data

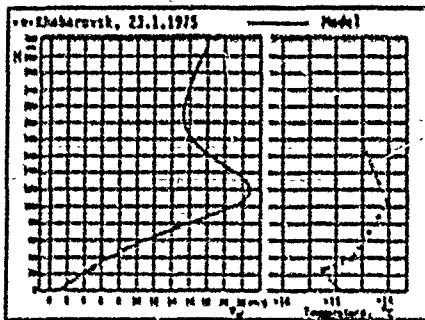


Fig.14: Approximation of worst case profiles

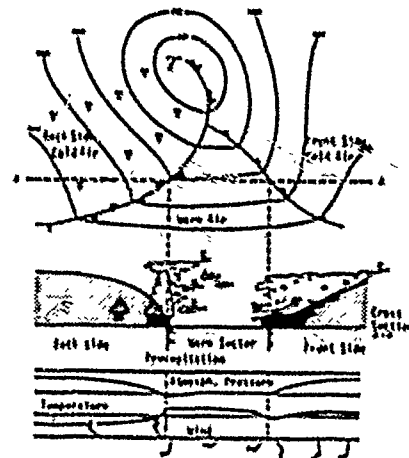


Fig.15: The passage of a frontal system (Ref.23)

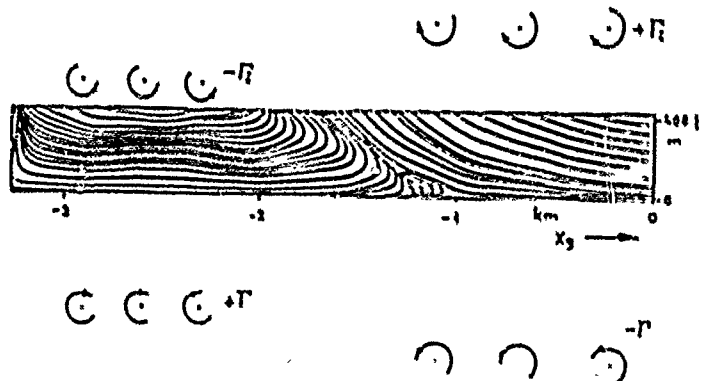


Fig.16: Principle proceeding for the generation of a frontal flow field

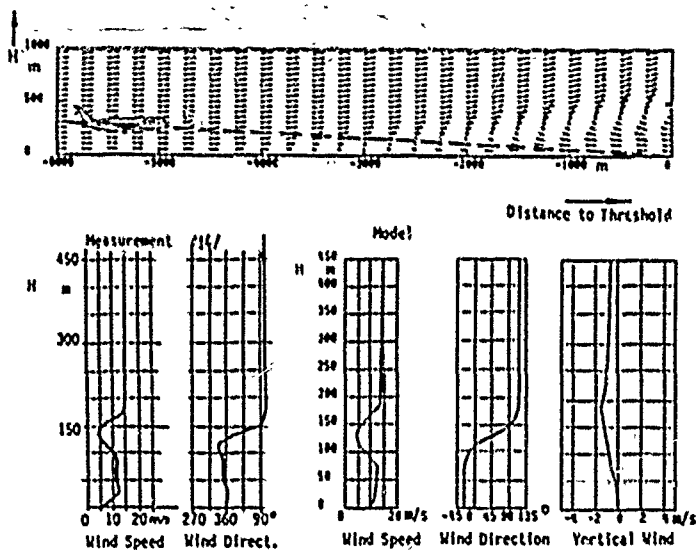


Fig.17: Measured wind speed and front model along a 3°-glide slope

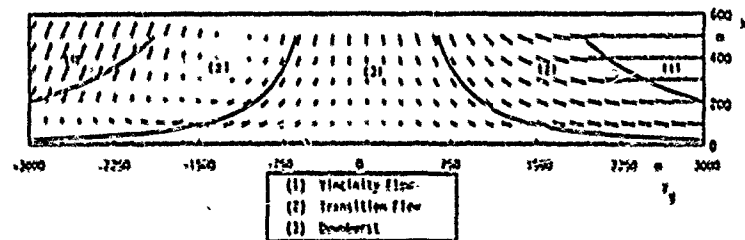


Fig.18: Extended steady jet flow model



Fig.19a: Vortex superposition method

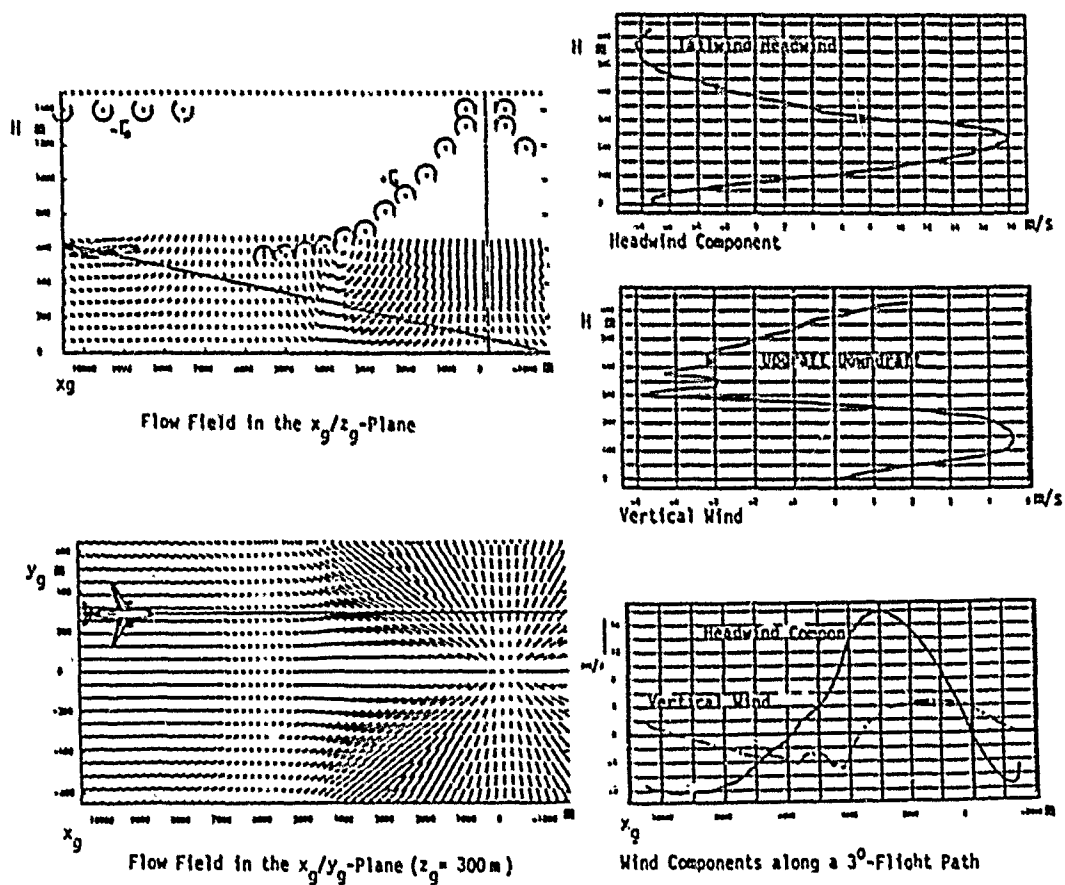


Fig.19b: 3-dimensional vortex superposition model

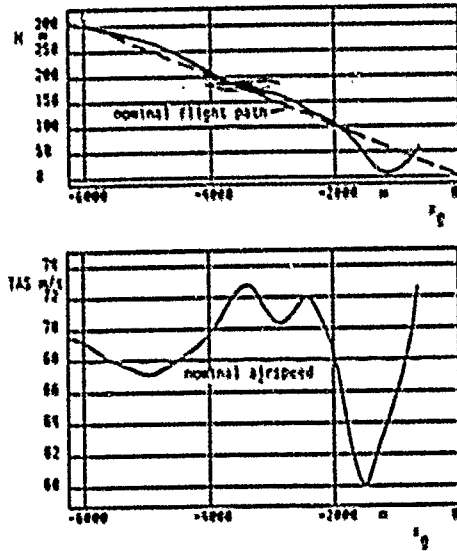


Fig.21a: Simulation results of a manual approach in a low level jet (pilot A)

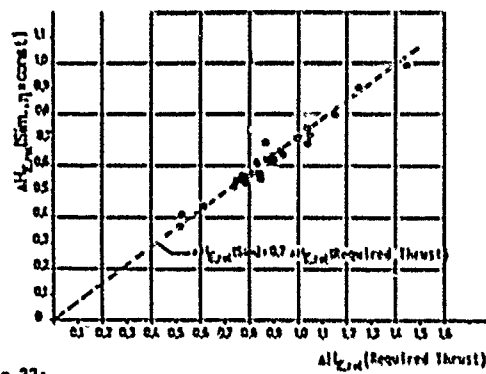


Fig.22: Relation between the relative energy error and relative required energy

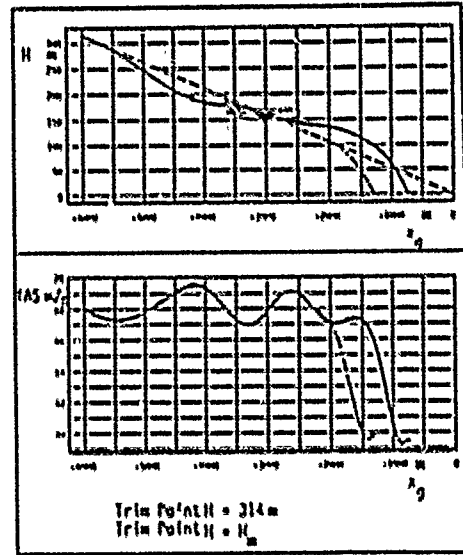


Fig.20: Flight path and velocity profile during approach in low level jet conditions (controls fixed)

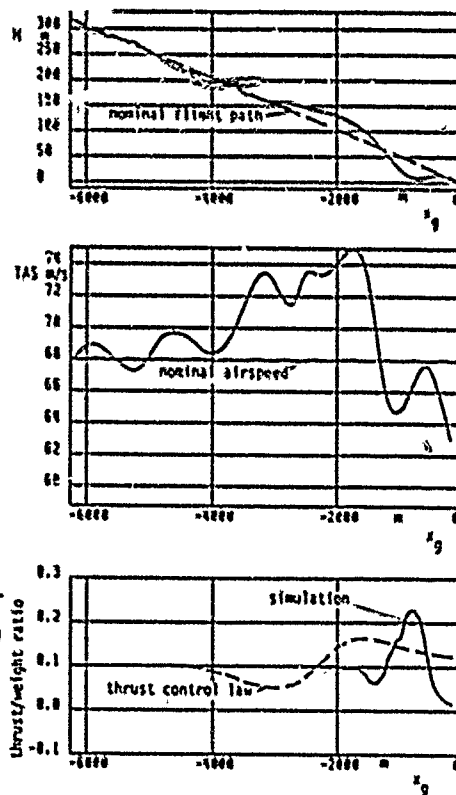


Fig.21b: Simulation results of a manual approach in a low level jet (pilot B)

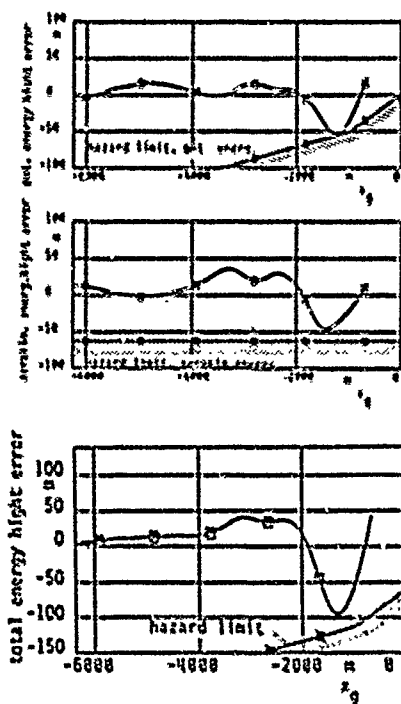


Fig.23: Energy errors in relation to hazard definition limits for example Fig.21a

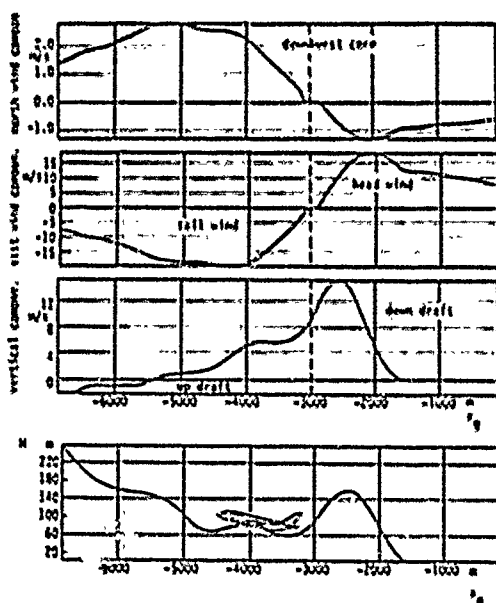


Fig.25: Takeoff in a downburst flow field

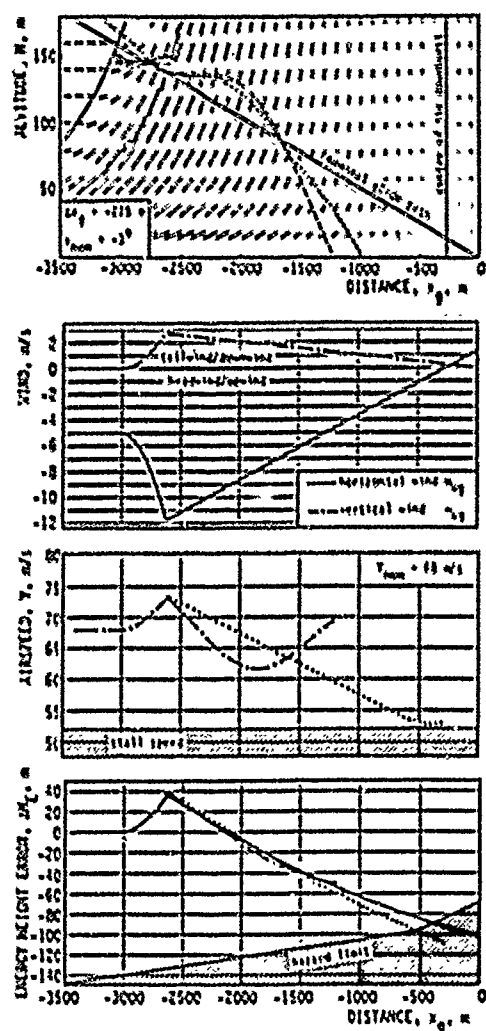


Fig.24: Landing approach in a downburst flow field (Ref 19)

— calculation by eqatlon (11)
 --- fixed aircraft controls
 autopilot
 - - - - - reconstructed accident flight path

ANALYSIS OF SEVERE ATMOSPHERIC DISTURBANCES FROM AIRLINE FLIGHT RECORDS

R. C. Wingrove, R. E. Bach, Jr., and T. A. Schultz
NASA Ames Research Center
Moffett Field, CA 94035

SUMMARY

Advanced methods have been developed to determine time-varying winds and turbulence from digital flight-data recorders carried aboard modern airliners. Analysis of several cases involving severe clear-air turbulence encounters at cruise altitudes has shown that the aircraft encountered vortex arrays generated by destabilized wind-shear layers above mountains or thunderstorms. A model has been developed to identify the strength, size, and spacing of vortex arrays. This model is used to study the effects of severe wind hazards on operational safety for different types of aircraft. The study demonstrates that small remotely piloted vehicles and executive aircraft exhibit more violent behavior than do large airliners during encounters with high-altitude vortices. Analysis of digital flight data from the accident at Dallas/Ft. Worth in 1985 indicates that the aircraft encountered a microburst with rapidly changing winds embedded in a strong outflow near the ground. A multiple-vortex-ring model has been developed to represent the microburst wind pattern. This model can be used in flight simulators to better understand the control problems in severe microburst encounters.

1. INTRODUCTION

Flight encounters with severe atmospheric disturbances are a continuing problem that must be better understood to improve safety. One way to investigate the nature and cause of severe disturbances is through the analysis of airline flight records. In the past, analysis was hindered by insufficient data. Recent encounters have involved modern airliners equipped with multichannel, digital flight-data recorders (DFDRs). These digital records, along with air traffic control (ATC) radar position records, provide a means of determining and analyzing the turbulent wind environment (Ref. 1).

In conjunction with the National Transportation Safety Board (NTSB), researchers from Ames Research Center have analyzed a series of disturbance encounters, listed in Table I, involving airliners equipped with DFDRs. The severe atmospheric disturbances to be considered in this report include high-altitude turbulence and low-level microbursts.

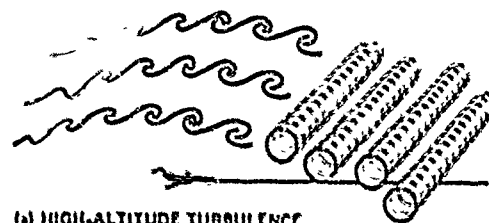
TABLE I - DIGITAL FLIGHT RECORDS FROM AIRLINE ENCOUNTERS WITH SEVERE ATMOSPHERIC DISTURBANCES.

DATE	AIRCRAFT	LOCATION	DURATION	DISTURBANCE
6/75	L1011	JFK, NY	Go-around	Microburst
11/75	DC10	Calgary, Canada	33,000'	Clear air turbulence
4/81	DC10	Hannibal, MO	37,000'	Clear air turbulence
7/82	DC10	Morton, WY	39,000'	Clear air turbulence
10/83	DC10	Near Bermuda	37,000'	Convective turbulence
11/83	L1011	Offshore SC	37,000'	Clear air turbulence
1/85	B747	Over Greenland	33,000'	Clear air turbulence
2/85	B747	Over Greenland	33,000'	Clear air turbulence
2/85	B747SP	Offshore CA	41,000'	Wind shear
8/85	L1011	Dallas/Ft. Worth, TX	Landing	Microburst
8/85	MD80	Dallas/Ft. Worth, TX	Go-around	Microburst
11/85	B747	Over Greenland	33,000'	Clear air turbulence
3/86	B747	Offshore Hawaii	33,000'	Clear air turbulence
4/86	DC10	Jamestown, NY	40,000'	Wind shear
7/86	A300	West Palm Beach, FL	20,000'	Convective turbulence
9/87	L1011	Near Bermuda	31,000'	Convective turbulence
11/87	A310	Near Bermuda	33,000'	Convective turbulence
1/88	B767	Chicago, IL	25,000'	Convective turbulence
3/88	B767	Cimarron, NM	33,000'	Clear air turbulence

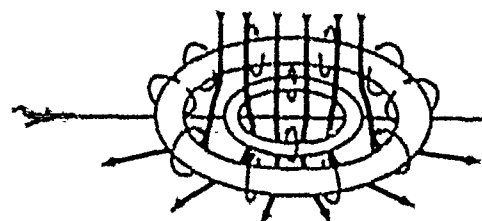
High-altitude turbulence (Fig. 1a) results from the growth and breakdown of stratified shear layers (Refs. 2-7). This disturbance is usually referred to as "clear-air turbulence" and is associated with a strong inversion in air temperature and a strong vertical shear in horizontal winds. These conditions are often in the regions of the tropopause and the associated jet streams. The most severe encounters are frequently above mountains or thunderstorms. Some of the severe clear-air turbulence encounters for airliners equipped with the DFDR are discussed in Refs. 8-10.

Microbursts (Fig. 1b) are intense downdrafts that impact the surface and cause strong outflows (Refs. 11-13). They are associated with thunderstorms, and usually occur during the summer. The accident of Delta Airlines flight 191 in August 1985 involved a microburst at the Dallas/Fort Worth airport (DFW). This aircraft and the following American Airlines flight 539, which made a go-around through the DFW microburst, were both equipped with DFDRs. Some background information about the DFW microburst can be found in Refs. 14-20.

This paper considers the usefulness of DFDR data in analyzing aircraft encounters with clear-air turbulence and low-level microbursts, and presents some findings regarding the nature of these phenomena. In particular, it is shown that the winds encountered in both types of atmospheric disturbances can be modeled deterministically. In the case of clear-air turbulence, the winds are represented by a Kelvin-Helmholtz vortex-array model. In the case of the DFW microburst, the winds are represented by a multiple-vortex-ring model. The method used to analyze the flight records is described first. Its application to clear-air turbulence encounters is presented, followed by an analysis of the DFW microburst encounter.



(a) HIGH-ALTITUDE TURBULENCE



(b) LOW-LEVEL MICROBURST

Figure 1. Two types of severe atmospheric disturbances.

2. ANALYSIS METHOD

Airliners certified in 1969 or later are equipped with DFDRs which record an extensive set of variables (Table II). These digital flight records, along with ATC tracking data, can be used to determine the time histories in the three components of the winds along the aircraft flightpath (Ref. 1). In this analysis the accelerations measured aboard the aircraft are integrated to determine the time history of the flightpath that provides the best match to the ATC radar position data and the DFDR barometric altitude data. The wind velocity is computed as the difference between the vehicle inertial velocity and its velocity with respect to the airmass. A block diagram of the general analysis procedure is shown in Fig. 2.

The equations of motion are in an Earth frame with the x-axis pointing north, the y-axis pointing east, and the h-axis vertical (z axis down):

$$\ddot{x} = a_x \cos \phi \cos \psi + a_y (\sin \phi \sin \phi \cos \psi - \cos \phi \sin \psi) + a_z (\cos \phi \sin \phi \cos \psi + \sin \phi \sin \psi)$$

$$\ddot{y} = a_x \cos \phi \sin \psi + a_y (\sin \phi \sin \phi \sin \psi + \cos \phi \cos \psi) + a_z (\cos \phi \sin \phi \sin \psi - \sin \phi \cos \psi)$$

$$\ddot{h} = a_x \sin \phi - (a_y \sin \phi + a_z \cos \phi) \cos \phi - g$$

where a_x , a_y , and a_z are the body-axis accelerations, and ϕ , θ , and ψ are the body-axis Euler angles. Integration of these differential equations provides estimates of inertial velocity ($\dot{x}, \dot{y}, \dot{h}$) and position (x, y, h). A set of initial conditions and bias corrections is determined by matching the calculated x and y time-histories to ATC radar position data and by matching the calculated h time history to the DFDR barometric altitude data.

TABLE II - TYPICAL DIGITAL FLIGHT DATA RECORDER MEASUREMENTS FOR DIFFERENT AIRCRAFT.

VARIABLE	MEASUREMENT RATE, per sec					
	L1011	DC10	MD80	B747	B747SP	B767
Normal acceleration	4	4	8	4	4	4
Lateral acceleration	4	4	4	4	4	4
Longitudinal acceleration	4	1	4	4	4	1
Roll angle	1	1	1	1	1	1
Pitch angle	1	1	1	1	1	1
Heading angle	1	1	1	1	1	1
Angle-of-attack vanes	2	-	-	-	2	2
Pressure altitude	1	1	1	1	1	1
Indicated airspeed	1	1	1	1	1	1
Elevator deflection	1	1	1	1	1	1
Rudder deflection	2	2	2	2	2	2
Engine thrust	1/4	1/4	1	1/4	1/4	1
Air temperature	1/2	1/2	1	-	-	1

The wind vector is computed as

$$W_x = \dot{x} - V \cos \gamma_s \cos \gamma_a$$

$$W_y = \dot{y} - V \sin \gamma_s \cos \gamma_a$$

$$W_h = \dot{h} - V \sin \gamma_a$$

where the true airspeed V is computed from the flight records, and the wind-axis Euler angles (γ_s , γ_a) are computed using the identities

$$\sin \gamma_s = \cos \alpha \cos \beta \sin \theta - C \cos \theta$$

$$\tan(\gamma_a - \psi) = (\sin \beta \cos \phi - \sin \alpha \cos \beta \sin \phi) / (\cos \alpha \cos \beta \cos \theta + C \sin \theta)$$

$$C = \sin \alpha \cos \beta \cos \phi + \sin \beta \sin \phi$$

where α is the angle of attack and β is the angle of sideslip.

The angle of attack α was derived from onboard-recorded vane angles. For aircraft without recorded vane angles, the angle of attack α was determined through the equation

$$C_L = C_{L_1}(\alpha, \delta_f) + C_{L_2} \delta_e + C_{L_3} \dot{q}/2V$$

where $C_{L_1}(\alpha, \delta_f)$, C_{L_2} , and C_{L_3} are based on the aircraft aerodynamic characteristics, and the lift coefficient C_L was calculated using the aircraft weight along with the lift acceleration and dynamic pressure from the DFDR. The flap position δ_f , elevator position δ_e , and pitch rate \dot{q} were derived from the DFDR, leaving the angle of attack α as the variable to be determined. (This method of deriving unmeasured flow angles is discussed further in Ref. 21.)

In a similar manner, the angle of sideslip β was determined through the equation

$$C_Y = C_{Y_1} \beta + C_{Y_2} \delta_r + C_{Y_3} \dot{r}/2V$$

where C_{Y_1} , C_{Y_2} , and C_{Y_3} are based on the aircraft aerodynamic characteristics, and the side-force coefficient C_Y was calculated using the aircraft weight along with the side acceleration and dynamic pressure from the DFDR. The rudder position δ_r and the yaw rate \dot{r} were derived from the DFDR, leaving the angle of sideslip β as the variable to be determined.

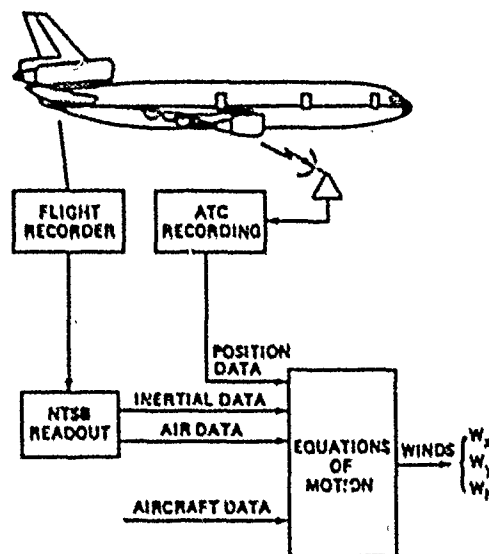


Figure 2. Reconstruction of severe winds from flight and ATC records.

3. APPLICATIONS

3.1 High-Altitude Turbulence

High-altitude clear-air turbulence encounters usually occur in the region of the tropopause. The tropopause altitude varies with the season and the location. The upper plot in Fig. 3 shows recent severe turbulence encounters as a function of altitude and time of year. Also shown are the average tropopause heights for 30° and 45° N. lat. (Ref. 22). Generally, this distribution of turbulence encounters follows the trends for the average tropopause heights. That is, the encounters occur at lower altitudes in the winter months and at higher altitudes in the summer months. The lower plot in Fig. 3 presents the distribution of 12,678 reports of moderate to severe turbulence, from a special survey of airline pilots taken in 1960-62 (Ref. 7). These data indicate that turbulence occurred most often in the winter months, peaking in February. At the time of the survey, airliners usually cruised at altitudes of 31,000 to 33,000 ft, and would be in the region of the tropopause primarily in the winter months. However, many of today's aircraft cruise at higher altitudes, and spend more time in the region of the tropopause throughout the year. At altitudes from 35,000 to 41,000 ft the aircraft are in the region of the tropopause in the fall and spring.

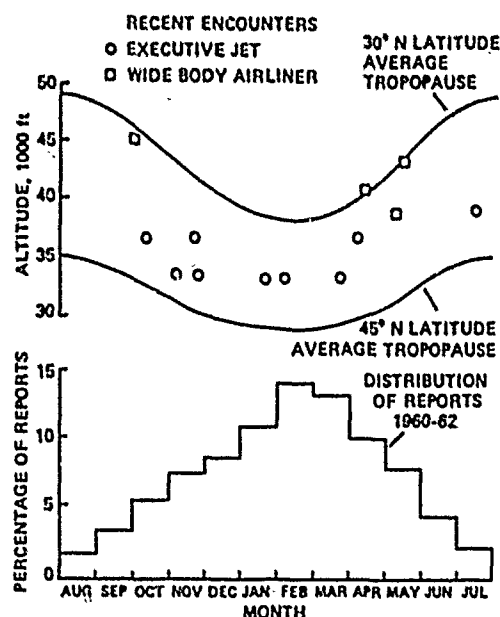


Figure 3. Severe turbulence encounters shown with altitude and time of year.

Many clear-air-turbulence encounters occurred near or over a landmass where meteorological soundings provide wind and temperature profiles, ground weather radar observations provide information about nearby convective activity, and ATC radar records provide information about the aircraft track. Representative encounters are illustrated in Fig. 4. Note that the encounters were associated with low-level barriers such as mountain ranges or thunderstorm lines. The encounters were found to occur at about 15 to 30 miles downwind of these low-level obstacles.

Temperature profiles for the encounters of Fig. 4 are presented in Fig. 5. The sounding records in Fig. 5 indicate a strong temperature inversion at the tropopause. Previous studies (Refs. 2-4) have noted that a strong temperature inversion becomes a destabilizing influence when the streamlines are tilted. The encounters analyzed here involved temperature inversions in conjunction with lower-level barriers that could have tilted the streamlines and triggered Kelvin-Helmholtz instability (Refs. 2-4).

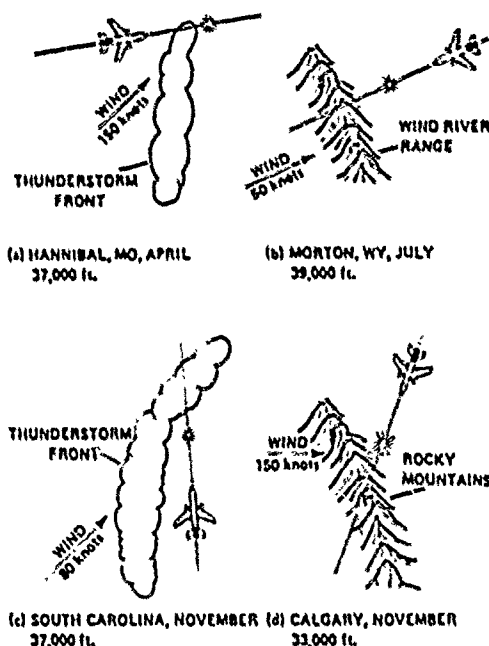


Figure 4. Overview of severe turbulence encounters at cruise altitudes.

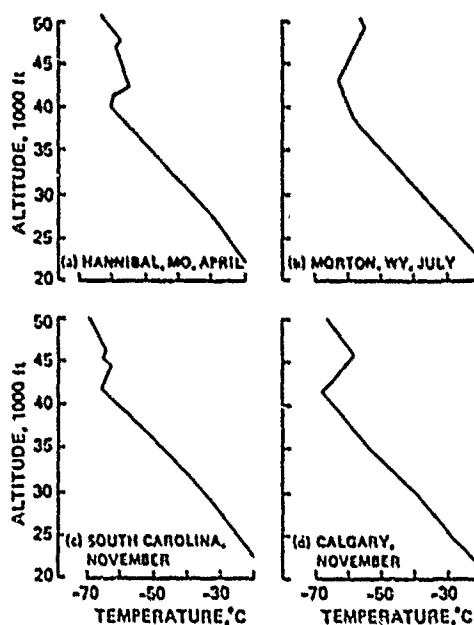


Figure 5. Temperature inversion at the tropopause associated with severe turbulence.

A representative case is that of Fig. 4a, in which a DC-10 encountered severe turbulence while cruising in an easterly direction at 37,000 ft in the jet stream in April near Hannibal, Missouri (Ref. 8). The encounter occurred shortly after the aircraft passed over a developing line of thunderstorms with cloud tops reported at about 30,000 ft. Using the technique described in the previous section, the horizontal wind W_x and vertical wind W_y were estimated. These estimates and the normal acceleration from the DFDR are presented in Fig. 6. The horizontal wind is shown to increase as the aircraft passes over the line of thunderstorms about 2.5 min before the turbulence encounter. The vertical winds in the period of severe turbulence appear as sharp up-and-down gusts about 5 sec apart. The severity of the turbulence is apparent from the wide fluctuations in the normal acceleration from +1.7 to -1.0 g.

These results appear consistent with previous studies (Refs. 2-6) in which the formation of Kelvin "cat's eyes" patterns in clear air was noted. To determine whether the derived winds could be accounted for by patterns of this type, an analysis was conducted to duplicate the time histories with vortex-array models (Refs. 8, 23). The DFDR-derived wind data were used with parameter identification techniques to determine the strength, size, and spacing of the vortex arrays. A vortex model for the Hannibal case is shown in Fig. 7. As shown in the lower graph, the general nature of this model is a vortex array located on the downslope with respect to the prevailing wind. The large spikes in vertical velocity are caused by the passage of the aircraft through the solid-body cores of two vortices. These spikes provide significant evidence about the size and strength of the vortices. Each vortex has a diameter of 1,000 ft and a circumferential velocity of 87 ft/sec. The distance between the centers of the two significant vortices is 3,400 ft. A comparison of the modeled vertical and horizontal wind perturbations (solid lines) with the measured winds (dashed lines) shows reasonably good agreement. This vortex model provides a means of studying the effects of these wind hazards on aircraft behavior and g load.

Simulations have been done to provide information on the effects of these reconstructed vortices on the flight behavior for three types of aircraft: a remotely piloted vehicle (RPV), an executive jet, and a large commercial airliner. As shown in Fig. 8, the RPV undergoes a large change in pitch angle. With its relatively low speed, it has time to align with the local airspeed vector, and the pattern of the pitch angle variation is similar to the (inverse) pattern of the vertical wind. The executive aircraft exhibits periodic variations in pitch angle and g load. These variations are dependent upon the relationship between the time span of the vortex traverse and the aircraft's short oscillatory period. The large airliner exhibits only a small variation in pitch angle, because of the short time in vortex traverse and a long oscillatory period. The pattern of the g-load variation is similar to the pattern of the vertical wind.

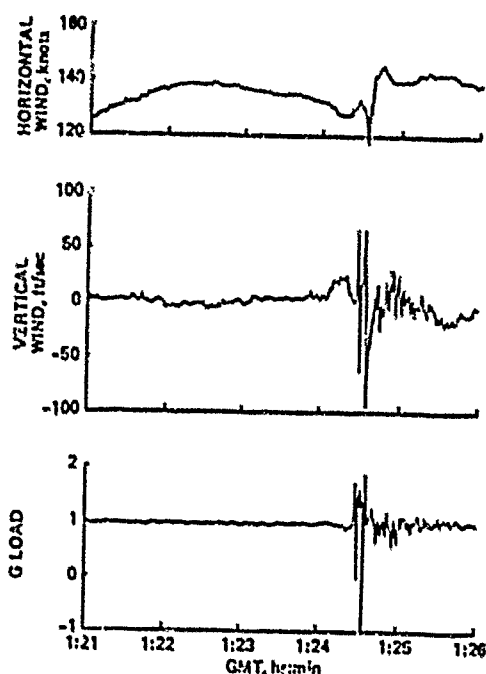


Figure 6. Time-history data for a severe turbulence encounter over Hannibal, MO, April 1981.

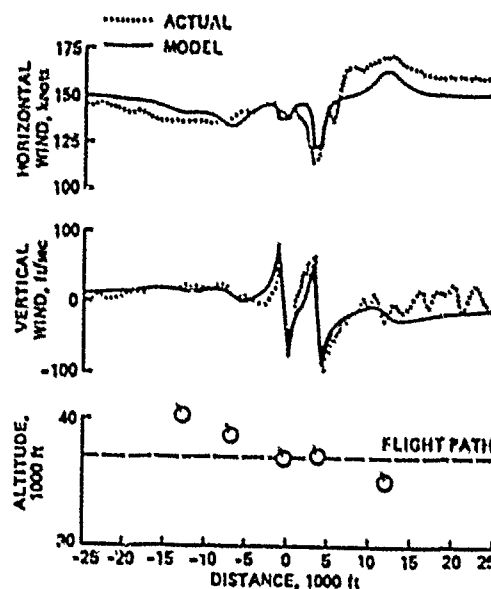


Figure 7. Vortex-array model for a severe turbulence encounter over Hannibal, MO, April 1981.

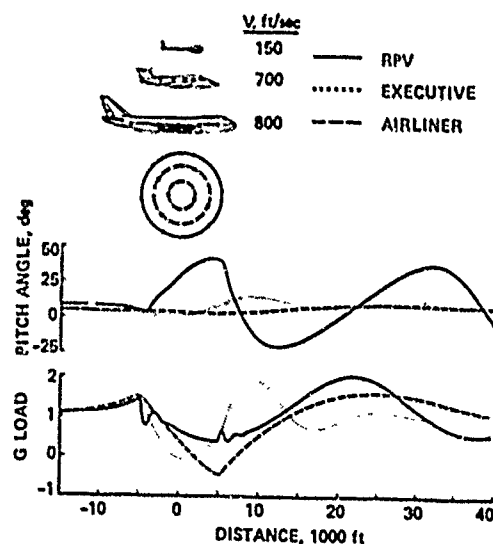


Figure 8. Simulation of a vortex encounter for different aircraft.

3.2 Low-Level Microbursts

Flight and radar records from two airliners that penetrated the 1985 DFW microburst have been analyzed. The first aircraft, Delta Airlines flight 191, encountered the microburst on final approach and contacted the ground about 1 mile short of the runway. The following aircraft, American Airlines flight 539, made a go-around and flew through the microburst about 2,500 ft above the ground. The results of the analysis are shown in Fig. 9. The data for the two aircraft are presented as a function of altitude and position with respect to the runway. The horizontal and vertical wind components (W_x and W_z) are superimposed as vectors on the flightpaths.

As Delta 191 descended through 900 ft approaching the runway, the vertical wind component W_z increased to about 15 ft/sec and the horizontal wind component W_x increased to a headwind of over 50 ft/sec. The aircraft then encountered a strong downflow followed by a rapid change in vertical wind direction, followed by further changes about 5 sec apart. In the period of major downflow, the aircraft experienced vertical winds of -10 to -40 ft/sec. During the encounter, the 50-ft/sec headwind changed to a tailwind of over 50 ft/sec.

American 539, the following aircraft, executed a go-around at 1400 ft above the ground and then climbed to an altitude of 2500 ft where it penetrated the microburst. The analysis shows that the aircraft first experienced an updraft W_z of about 15 ft/sec and a headwind W_x of 15 ft/sec. The aircraft then encountered a strong downflow over a fairly large distance, followed by a strong updraft. In the period of major downflow, the aircraft experienced vertical winds of -10 to -40 ft/sec. During this encounter, the 15 ft/sec headwind changed to a tailwind of over 25 ft/sec.

In comparing the magnitudes of the changes in the horizontal winds W_H , we can see that Delta 191 was nearer the ground and experienced the stronger horizontal divergence from the microburst. The data indicate that there was a headwind-tailwind change of 100 ft/sec for Delta 191, and 40 ft/sec for American 539. Note that the overall change from a headwind to a tailwind occurred at nearly the same location over the ground for the two aircraft. This suggests that the center of the microburst had not changed location appreciably between the times that the two sets of measurements were made. American 539 passed through the center of the microburst about 110 sec after Delta 191 did.

It can be observed that the region of the downflow measured for American 539 is larger than that for Delta 191. American 539 entered the region of the downflow about 0.5 n. mi. farther out from the runway than did Delta 191. Also, the data from American 539 indicate that portions of the downflow had extended to near the end of the runway. The total region of downflow measured by American 539 was about 3 n. mi. in diameter. This indication of an expanding microburst is consistent with meteorological data gathered at the DFW airport (Ref. 16) and with a numerical simulation of the DFW downburst (Ref. 19). These studies indicate that the storm had reached the end of the runway and had expanded to about 3.7 n. mi. in diameter near ground level when American 539 traversed the microburst.

The Ames analysis shows several rapid and large changes in winds within the microburst. Previous studies (Refs. 12, 24-26) have indicated that microbursts might involve vortices that induce variations in the internal winds. Those studies indicate that when a vortex nears the ground its vorticity increases, providing a mechanism for large fluctuations in wind velocity.

A multiple-vortex-ring model has been developed to represent the wind pattern in the DFW microburst (Ref. 27). The vortex model for American 539, which made a complete passage through the microburst, is shown in Fig. 10. As shown in the lower graph, the general nature of this model is a large outer ring with a smaller inner ring near the center of the microburst. The outer ring has a diameter of 15,000 ft with a vortex core diameter of 3000 ft. The inner ring has a diameter of 2500 ft with a vortex core diameter of 900 ft. A comparison of the modeled vertical and horizontal wind perturbations (solid lines) with the measured winds (dashed lines) shows reasonably good agreement. The multiple-vortex-ring model provides a way to mathematically describe the wind pattern within the microburst. The model provides a deterministic, rather than random, means of analyzing the internal velocity fluctuations.

4. CONCLUDING REMARKS

Analysis of a series of cases involving severe turbulence at cruise altitudes has shown that the aircraft encountered vortex arrays generated by wind-shear layers associated with strong temperature inversions near the tropopause. The destabilization of the wind-shear layers was caused by low-level barriers such as mountain ranges or thunderstorm lines. The wind pattern in these severe turbulence encounters have been identified through the development of vortex-array models. The analysis identified the strength, size, and spacing of the vortex arrays, providing a means of studying the effects of these severe wind hazards on operational safety. Modern aircraft are spending more time at higher altitudes near the tropopause, where this severe turbulence occurs. Simulation studies have shown that small RPV and executive aircraft are more prone to violent dynamic behavior than are large airliners during encounters with high-altitude vortices.

Data from the Delta 191 accident show that the aircraft encountered a strong microburst downflow followed by a strong outflow accompanied by large and rapid changes in vertical wind. Data from American 539 recorded during the go-around indicate a broad pattern of downflow in the microburst, with regions of upflow at the extreme edges. The combined results indicate a microburst that was increasing in size with vortex-induced velocity fluctuations embedded in a strong outflow near the ground. The wind pattern in the DFW microburst has been identified through the development of a multiple-vortex-ring model. The results show a large vortex ring at the leading edge of the microburst and a smaller vortex ring embedded in the downflow. The study provides a realistic model of the wind field that can be used in flight simulators to better understand the control problems in severe microburst encounters.

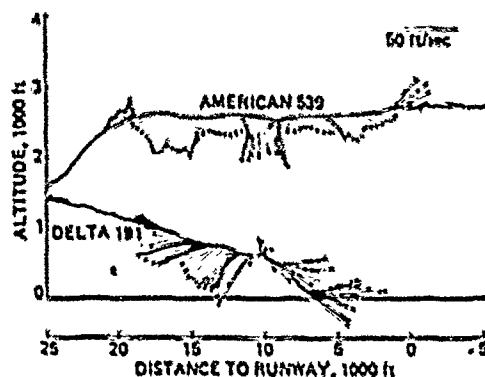


Figure 9. Wind vectors at the Dallas/Ft. Worth Airport, August 1985, reconstructed from flight records of two aircraft.

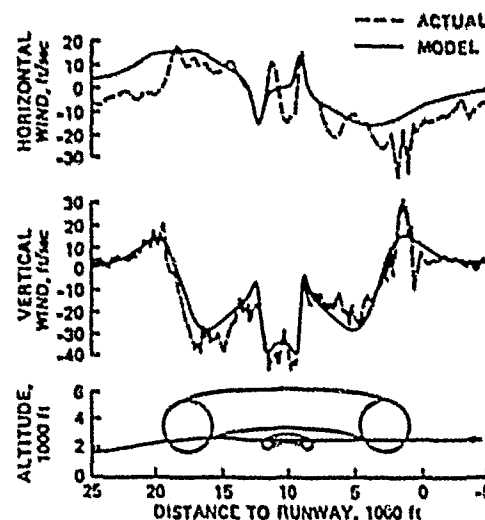


Figure 10. Multiple-vortex-ring model of the DFW microburst.

3. REFERENCES

1. Bach, R. E. and Wingrove, R. C., "Applications of State Estimation in Aircraft Flight Data Analysis," *J. Aircraft*, Vol. 22, No. 7, July 1985, pp. 347-354.
2. Storer, R. S., "Environmental Aerodynamics," Wiley, New York, 1978.
3. Godard, E. E. and Hooke W. H., "Waves in the Atmosphere," Elsevier Scientific Publishing Co., New York, 1975.
4. Clark, J. W., Stoeffler, R. C., and Vogt, P. O., "Research on Instabilities in Atmospheric Flow Systems Associated with Clear Air Turbulence," NASA CR-1604, 1970.
5. Hopkins, R. H., "Forecasting Techniques of Clear Air Turbulence Including That Associated with Mountain Waves," WSAF Technical Note No. 155, 1976.
6. Hardy, K. R., "Studies of the Clear Atmosphere Using High Power Radar," *Remote Sensing of the Troposphere*, V. E. Dettl, ed., NOAA, Boulder CO, 1972, chap. 14.
7. Colson, DeVer, "Summary of High-Level Turbulence Over United States," *Monthly Weather Review*, Vol. 91, No. 12, 1963, pp. 605-609.
8. Parks, E. K., Wingrove, R. C., Bach, R. E., and Mehta, R. S., "Identification of Vortex-Induced Clear Air Turbulence Using Airline Flight Records," *J. Aircraft*, Vol. 22, No. 2, Feb. 1985, pp. 124-129.
9. Lester, P. F. and Bach, R. E., "An Extreme Clear Air Turbulence Incident Associated with a Strong Downslope Windshear," *AIAA Paper 86-0329*, Jan. 1986.
10. Lester, P., Sen, O., and Bach, R. E., "The Use of DFDR Information in the Analysis of a Turbulence Incident Over Greenland," *Monthly Weather Review*, accepted for publication June 1989.
11. "Low-Altitude Wind Shear and its Hazard to Aviation," National Academy of Sciences, National Academy Press, Washington, D.C., 1981.
12. Fujita, T. T., "The Downburst," SMRP Research Paper 210, U. Chicago, Chicago Ill., 1985.
13. "Windshear Training Aid," Federal Aviation Administration, Washington, D.C. 1957.
14. Bach, R. E. and Wingrove, R. C., "Analysis of Windshear from Airline Flight Data," *J. Aircraft*, Vol. 26, No. 2, Feb. 1989, pp. 103-109.
15. Wingrove, R. C. and Bach, R. E., "Severe Winds in the DFW Microburst Measured from Two Aircraft," *J. Aircraft*, Vol. 26, No. 3, March 1989, pp. 221-224.
16. Fujita, T. T., "DFW Microburst," SMRP Research Paper 217, U. Chicago, Chicago Ill., 1985.
17. Caracena, F., Ortiz, R., and Augustine, J., "The Crash of Delta Flight 191 at Dallas-Fort Worth International Airport on 2 August 1985: Multiscale Analysis of Weather Conditions," NOAA Technical Report ERL-430-ESG 2, Dec. 1986.
18. Aircraft Accident Report, "Delta Air Lines Inc., Lockheed L-1011-385-1, N726DA, Dallas/Fort Worth International Airport, Texas, August 2, 1985," NTSB AAR-86-05, 1986.
19. Proctor, F. H., "The Terminal Area Simulation System, Volume II, Verification Cases," NASA CR 4047, April 1987.
20. Bray, R. S., "Aircraft Performance in Downburst Wind Shear," SAE Paper No. 861698, 1986.
21. Bach, R. E. and Parks, E. K., "Angle-of-Attack Estimation for Analysis of CAT Encounters," *J. Aircraft*, Vol. 24, No. 11, Nov. 1987, pp. 789-792.
22. Roe, J. M., "A Climatology of a Newly-Defined Tropopause Using Simultaneous Ozone-Temperature Profiles," AFGL-TR-81-0190, May 1981.
23. Mehta, R. S., "Modeling Clear-Air Turbulence with Vortices Using Parameter-Identification Techniques," *J. Guidance, Contr. Dynam.*, Vol. 10, No. 1, Jan. 1987, pp. 27-31.
24. Caracena, F., "Is the Microburst a Large Vortex Ring Imbedded in a Thunderstorm Downdraft?" *Eos*, Vol. 63, 1982, p. 899.
25. Woodfield, A. A. and Woods, J. F., "Worldwide Experience of Wind Shear During 1981-1982," AGARD-CP-347, Oct. 1983.
26. Bedard, A., "Microburst Vorticity," *AIAA Paper 87-0440*, 1987.
27. Schultz, T. A., "A Multiple-Ring-Vortex Model of the DFW Microburst," *AIAA Paper 88-0685*, Jan. 1988.

ACKNOWLEDGMENT

The authors thank Dennis Grazi and others on the staff at the National Transportation Safety Board, Washington, D.C., for their aid in obtaining the data used in this report.

SYSTEMS FOR AIRBORNE WIND AND TURBULENCE MEASUREMENT

by
 Dr. Peter Vörmann
 President
 Aerodata Flugmesstechnik GmbH
 Rebenring 33
 D-3300 Braunschweig
 Federal Republic of Germany

SUMMARY

For many years aircraft have been equipped for research in wind and turbulence measurements. Very often the system installation consisted of sensors and recording hardware which was spread all over the aircraft. This paper will describe a modern system solution, where all components are integrated in an external pod for aircraft and helicopter applications.

After a brief description of the principles for airborne wind measurements, advantages and disadvantages for different system solutions will be discussed. The presented pod solution includes a software and hardware concept, which allows to determine all three components of the wind vector in real time on-board the aircraft.

Flight test results are presented, which demonstrate the achievable accuracies for the horizontal and especially the vertical wind component. This includes the effects of dynamic aircraft maneuvers. Finally an outlook is given, what kind of precision can be achieved in the future, when satellite navigation systems will be available on a 24 hour basis.

LIST OF SYMBOLS

q	dynamic pressure
R	gas constant
T_t	total temperature
x_1, y_1, z_1	earth fixed coordinate system (positive sense: north, east, downward)
u_1, v_1, w_1	true airspeed components in the earth fixed coordinate system
u_{t1}, v_{t1}, w_{t1}	components of horizontal velocity in the earth fixed coordinate system
u_{a1}, v_{a1}, w_{a1}	wind speed components in the earth fixed coordinate system
\underline{V}	true airspeed vector
\underline{V}_h	horizontal velocity
α	angle of attack
β	angle of sideslip
γ	flight path angle
Δ	sensor or wind component error
θ	pitch angle
ϵ	ratio of specific heat
ψ	bank angle
χ	true heading

1. INTRODUCTION

The results of airborne turbulence measurements have been very useful in the past for aeronautical engineers, for example, to establish models for simulators and to perform fatigue and load analyses. Lately the need for real-time measurements has increased significantly by users from other scientific communities, e.g. meteorologists and air chemists.

Modern airborne atmospheric and environmental survey systems require not only airchemical sensors but also a complete sensor package for wind and turbulence measurements. Such a system is capable of performing the necessary in-situ investigations to find out the actual transport of polluted air and the turbulent transports of momentum, heat, and moisture.

As a subsystem for aeronautical and environmental research aircraft the Aerodata company has developed an airborne wind and turbulence system for aircraft and helicopters. The system is called METEOPOD and is currently flying on-board the German polar research aircraft of the Alfred-Wegener-Institute (German Institute for Polar- and Marine Research). Figure 1 shows the pod under the wing of the Polar 4, a Dornier Do 228 aircraft.

2. THE PRINCIPLE OF AIRBORNE WIND AND TURBULENCE DETERMINATION

From an aircraft wind can not be measured directly. Only by taking the vector difference (fig. 2) between the inertial velocity V_a and the aircraft movement relative to the air, the true airspeed V , the wind vector V_w may be computed (ref. 1).

$$(u_w, v_w, w_w)_e = (u_a, v_a, w_a)_e - (u, v, w)_e$$

One should note that the magnitude of the wind vector differs to the others by at least one order. Therefore an accurate measurement of the inertial velocity and the true airspeed must be insured.

The horizontal components of the inertial velocity can be taken from a suitable inertial navigation system. The inherent drift and Schuler-error of such a system can be eliminated in the future by combining it with a satellite navigation system like GPS (Global Positioning System) through Kalman filtering techniques. Then the good dynamic behavior of the inertial system is supported by the excellent long term precision of GPS. Thus an accuracy of 0.1 m/s can be expected for the total frequency band.

The vertical channel of inertial systems is principally unstable, unless it is stabilized with external altitude information. In order to reconstruct vertical speed, it is state of the art to stabilize the integration of the vertical accelerometer using a barometric altimeter (ref. 2), where in future the altimeter may be replaced by the altitude output of the GPS-signal.

While the inertial components can be gathered from one box, the inertial navigation system, there is no one box system for true airspeed. To obtain the magnitude of the true airspeed vector, it is most common to derive it from dynamic pressure, static pressure, and total temperature.

$$V = \sqrt{2R_0 \frac{\rho}{\rho_0} \left[1 - \left(\frac{p_0}{p_0 + q} \right)^{\frac{\gamma-1}{\gamma}} \right]}$$

In order to characterize the direction of the airflow, it is necessary to measure angle of attack and angle of sideslip of the aircraft. Before the vector difference between inertial velocity and true airspeed can be computed, the true airspeed vector has to be transformed into the earth-fixed coordinate system, which by nature is the system in which the wind vector is defined.

The complete transformation includes two rotation processes. First the true airspeed vector is transformed into the aircraft-fixed coordinate system using angle of attack and angle of sideslip as rotation angles. The final rotation into the earth-fixed system is performed with the attitude angle of the aircraft: roll, pitch, and true heading.

The resulting equations for the true airspeed components contain numerous SINE- and COSINE functions, see references 3 and 4. These references also describe how wind component errors depend on individual sensor errors.

3. CONVENTIONAL SYSTEMS

Currently most research aircraft throughout the world use instrumentation packages for wind and turbulence measurements, which are specifically adapted to the aircraft in use. There is no portability from one aircraft to another without major modifications of the aircraft and the measuring system.

Figure 3 demonstrates a typical example of a conventional turbulence measuring system. It pictures the system of the DO 28 research aircraft of the Technische Universität Braunschweig, Germany, (ref. 4). This aircraft was used as a test bed to develop sensor know-how and real-time technology for wind and turbulence measuring systems. This technology was later transferred to design the Meteopod system which is described in the following chapter.

Conventional systems, see fig. 3, often use a nose boom in order to measure the undisturbed airflow ahead of the aircraft. In order to really measure undisturbed airflow the nose boom should be as long as possible. However, a design compromise has to be made between desired boom stiffness, boom weight, and aircraft operability.

Stiffness is a very important design criteria. Low eigen-frequencies of elastic booms often show up as peaks in turbulence spectra and therefore disturb the measurement. Thus there seems to be a trend to change from a nose boom installation to

airflow sensing in the nose of the aircraft. This can be achieved by installing a 5 hole probe in the nose (ref. 5), where differential pressure measurements yield angle of attack, angle of sideslip, and total pressure.

Certainly the airflow around the nose is more disturbed than at the tip of a nose boom, but it seems possible to calibrate the flow and correct for nonlinear effects in real-time by the computer.

Even though all airflow and temperature sensors as well as inertial systems can be concentrated around the nose within short distance of each other, which is a prerequisite for turbulence measurements, there is the need for further integration and quick-change systems that handle turbulence algorithm in real-time.

4. THE METEOPOD SYSTEM

The Meteopod is an integrated system solution to combine all sensing units necessary for airborne wind and turbulence measurements in one external compartment. The sensor configuration allows the registration of the long term values as well as the turbulent fluctuations of wind, temperature, and humidity.

Figure 4 gives a schematic presentation of the hardware location of sensors and data acquisition and control units in the pod. The pod itself is of fibre glass construction. Its cigar shaped body measures about 4 meters in length and has a diameter of about 50 centimeters. The total weight depends on the actual system configuration. A typical weight including the pod with its equipment but excluding the aircraft pylon is about 100 kg.

In table 1 a typical list of suitable sensors and devices for a wind and turbulence measuring system is given as it is realized in the Meteopod system. The total power requirement for all sensors, power converters, control units, and preprocessors is in the order of 500 Watts.

The hardware is mostly mil-specified as far as the temperature range is concerned. However, some sensors are only available as commercial hardware with limited temperature range. There is a need to operate the system in cold weather environments, as it is planned to fly it in German Antarctic missions. Therefore the pod has been equipped with a temperature controlled heating system. To heat the inside of the pod and the five-hole airflow probe at the tip in icing conditions another 2000 Watt have to be supplied. Primary power is supply is 115 V/400 Hz and it is supplied from the inside of the cabin through the wing and pylon to the pod. AC/DC Power converters then generate all other voltages required inside the pod.

The main advantages of the Meteopod system compared to conventional ones are manifold:

The first advantage is the short distance of 0.5 meters between the flow sensing head, the temperature and humidity probes, and the inertial navigation or reference system. At an assumed true airspeed of 50 m/s and a sampling rate of 100 Hz it is possible to measure the turbulent transports of momentum, heat, and moisture for micrometeorological applications.

Spectral results from conventional systems very often contain resonance frequencies, which often originate from nose boom oscillations in the order of 5 to 20 Hz. Sensors themselves may also cause resonances and therefore disturb the turbulence spectrum. The dynamic behavior of flight logs (ref. 3 and 4) and tubings between air flow pressure ports and pressure sensors are typical examples for this problem, where tubings create the so-called "organ pipe" effect.

Both problems do not occur in the Meteopod. The tube lines are very short, only about 40 centimeters in length. This results in a resonance frequency well above 100 Hz, which is the current sampling rate for the system.

The pod does not have a boom. The fibre glass construction for the nose tip is very stiff. Thus no peaks are to be expected in turbulence spectra due to mechanical elasticities.

One of the most practical features of the Meteopod is its variability concerning the operating aircraft. The pod can not only be mounted together with a pylon on several aircraft. In the near future it can also be operated by helicopters, where the pod is flying as an external load hanging on a rope about 5 to 15 meters below the helicopter. Figure 5 shows the prototype version of the helicopter pod with its stabilizing fins.

As an integral part the Meteopod package includes data acquisition and modern real-time processing and monitoring systems as well as a post-processing software for spectral analysis. Thus the Meteopod is a complete engineering solution from the sensor to post-flight analysis. Due to today's necessity to perform more and more processing on-line, the following separate chapter is dedicated to describe the real-time needs to compute turbulence data.

5. REAL-TIME PROCESSING OF WIND DATA

An airborne data system for wind and turbulence measurements requires special attributes to execute an effective flight test. The operator must have a good insight into all sensor data, the status of each sensor, the computed results, and the actual flight condition of the aircraft. Only with this capability at the operator's hand it is possible to influence further flight operations and ensure the success of each test flight. Therefore the system must perform in real-time.

A flight test aircraft equipped for wind and turbulence measurements is a complex and an expensive testbed and sensor platform. Only a real-time system can keep development and operating costs down to a minimum. The computer system has to be powerful, flexible, and modular in its hardware and software design, see reference 6.

Figure 6 shows the hardware concept for the total metapod system. In the pod itself there is a preprocessor, which collects all analog, synchro, and digital data. It also receives and sorts data from the high speed ARINC 429 bus of the inertial navigation system in the pod. It supplies accelerations, body rates, inertial velocities, attitude angles, and position data. All data is then transmitted at a rate of 100 samples per second via pulse code modulation (PCM) to the main computer in the aircraft cabin.

Inside the cabin a powerful computer system can be installed that performs the necessary real-time calculations, e.g. the transformation of the true airspeed vector into the earth-fixed coordinate system (ref. 6 and 4). Besides the data processing and data registration, the on-board software has to perform another important task: monitoring.

The software is the heart of a modern turbulence measuring system. The software package MODAMS (Modular Data Acquisition and Monitoring System) performs all required tasks, especially the monitoring tasks, and can be implemented due to its modular concept on all current and wide-spread computer systems like DEC LSI 11/73, DEC MicroVax, VME-Bus, and PC's (see ref. 6 and 7).

The software written in MODULA 2 has to execute parallel processes, which are handled by the job scheduler, see figure 7. These are the high priority real-time process and the lower priority processes like monitoring, dialogue with the operator, tape recording, terminal I/O, printer output for a screen hardcopy and the output of a continuous flight test protocol.

Data storage on streamer tapes as well as alphanumeric and graphical monitoring is performed in engineering units. Figure 8 is a sample hard copy of an altitude temperature profile collected on-line during a meteorological mission with the Polar 4 in 1988. The temperature inversion in this figure can be clearly seen. Thus ad hoc flight altitudes could be chosen that depended on the inversion layer.

Figure 8 also pictures three windows that should be accessible to the operator during flight test. The upper left hand corner represents the dialogue window. It is used like a small terminal, where the operator inputs instructions into the system. The status window can be seen in the upper right hand corner. It continuously displays to the operator all important system states, e.g. status of data transfer from the Metapod preprocessor, realtime load, time information, event counter, tape status and printer status as well as graphical monitoring status. The bottom part of the screen is the monitoring window, where the operator can switch between 10 alphanumeric and 6 graphical menus.

6. FLIGHT TEST RESULTS

An efficient hard- and software system like the one presented in the preceding chapter is a prerequisite to perform successful wind and turbulence measurements. It can greatly support the quality assurance of the computed data.

Two examples for the quality assurance of the in real-time computed wind data will be presented. The flight maneuvers have been chosen in a way, which allow to find out specific sensor errors or miscalibrations. The first one is a 360 degree turn by the aircraft. This is the typical maneuver to check out the quality of the computed horizontal wind components. The vertical wind component is mostly influenced by extreme vertical maneuvers of the airplane (ref. 3 and 9). Therefore the phygoid motion of the aircraft can be excited as a good check-out procedure.

Figure 9 shows the north and east wind component as well as the true heading for two consecutive 360 degree turns. One can clearly note the sinusoidal behavior of the two wind components, which contain a 90 degree phase shift between the two components. Assuming that there is no wind change during this maneuver, there must be a sensor error or miscalibration present.

Quite a few sensor errors result in true heading dependent wind component errors (see ref. 3 and 4). This is the case here. Using a linear error model (ref. 3), the following equations for the wind component errors can be derived for a turn maneuver:

$$\Delta u_{y_2} = V_R \sin \theta_R (\dot{\theta} + \dot{\epsilon} - \dot{\theta}_R \sin \theta_R \dot{\theta}) \\ - \Delta V \cos \theta_R + \Delta u_{y_1}$$

$$\Delta v_{y_2} = -V_R \cos \theta_R (\dot{\theta} + \dot{\epsilon} - \dot{\theta}_R \sin \theta_R \dot{\theta}) \\ + \Delta V \sin \theta_R + \Delta v_{y_1}$$

Taking a look at the phase of the wind component errors in figure 9, it can be seen that the maxima and minima occur at 0° , 90° , 180° , and 270° . Therefore it can be concluded that no major errors are present in angle of sideslip, angle of attack, heading, and bank. In this specific example the equations reduce to:

$$\Delta u_{y_2} = -\Delta V \cos \theta_R + \Delta u_{y_1}$$

$$\Delta v_{y_2} = \Delta V \sin \theta_R + \Delta v_{y_1}$$

Assuming that the inertial velocity errors u_{i_1} and v_{i_1} did not change during the turn maneuver, the true airspeed error can be calculated from the following, very simple relationship.

$$t = 180^\circ, 360^\circ: 115 \text{ m/s} - \Delta u_{y_2} = 5.5 \text{ m/s}$$

$$t = 90^\circ, 270^\circ: 115 \text{ m/s} - \Delta u_{y_2} = 5.5 \text{ m/s}$$

Thus during this calibration flight there was a true airspeed error in the order of 5.5 m/s. Errors like this can usually be tracked back to false calibration curves of the pressure transducer, false calibration parameter inputs into the real-time system, or a false pitot-static calibration of the pressure ports.

Figure 9 just served as an extreme, but clear example, how sensor errors can be detected during a turn maneuver. For this actual flight the assumed pitot-static correction was wrong. After inserting the correct values on the ground, figure 10 demonstrates that no significant changes in wind speed as a function of true heading are any longer detected during the turn.

The first Meteopod trials were flown with the research aircraft of the Technische Universität Braunschweig, a Dornier 128. Figure 11 shows the results for the computed vertical wind speed during the phugoid motion. Drawn in this figure are: The inertial vertical velocity computed by an observing algorithm from earth-fixed vertical acceleration and barometric altitude (see ref. 4), the vertical true airspeed component (inverted in sign), and the resulting vertical wind speed component.

It is of interest to note that the vertical wind speed (curve 3) shows a sinusoidal behavior with time, which is not acceptable for quality measurements. The other interesting fact is that there is an apparent phase lag between the vertical components of true airspeed and inertial velocity. After some investigation it was found that the output signal for the earth-fixed vertical acceleration of the inertial reference system was low-pass filtered. Reconstructing the "original" acceleration signal by a digital filter with inverse characteristics, before it entered the observing algorithm for vertical speed estimation, was the cue to reverse the phase shift problem.

This example shows that it is not only necessary to carefully calibrate sensors, especially the airflow sensors, but is also necessary to identify resonance frequencies of the installed sensors and as in this case identify the time behavior of the signals used. Otherwise the resulting wind components may be quite erroneous. Figure 12 represents the corrected results for the vertical wind speed using the high-pass filter mentioned above. Even though extreme vertical speeds of up to 20 m/s were flown in this maneuver, the vertical wind speed could now be correctly computed.

Typical accuracies, which are currently achieved in the Meteopod system, are in the order of 1 m/s for the horizontal wind components and 0.3 m/s for the vertical wind component. This is the total error calculated from a Gaussian error propagation model including sensor offsets, drift, temperature effects, etc. The error of the horizontal component is mostly due to the drift and Schuler-error of inertial navigation system. However, turbulent fluctuations are measured far more precisely because they do not depend on offsets, for example. Their accuracy for all components is in the order of 0.1 m/s. As an example for the possibilities of the system figure 13 presents the results of a vertical sounding for the three wind components, static temperature, and relative humidity.

7. CONCLUDING REMARKS

The paper briefly discussed the theoretical background for determining the wind and turbulence vector on-board of aircraft. After describing conventional systems for the measurement of wind and turbulence, a new-integral system approach was presented, where the Meteopod system permits high resolutional micro and mesoscale atmospheric measurements.

All data can be monitored in engineering units on screens in alphanumeric and graphical form. With the mentioned software concept, the flexibility of the computer

system and its monitoring capabilities the operator is able to undertake a flexible flight planning. No longer rigid prefixed flight patterns have to be followed, which after tedious off-line calculations often have proven to be wrong in the past.

Computation power can be further increased in the near future. The addition of small and fast vector processors will allow real-time sampling and computation of turbulence data in the order of up to 200 Hz and higher. Now no longer the computer is the bottleneck, it is the slower response time of some sensors.

A helicopter version of the Meteopod system is under development, which will be completely independent on helicopter power and which will have a telemetry link for data transmission between the pod and the computer system in the helicopter. Thus, by simply flying an external load under a helicopter, wind and turbulence measurements will be possible in remote areas in the near future. This is of special interest e.g. for helicopter operations from ships in Antarctica and Arctica.

Besides this promising outlook, the most challenging new feature in wind and turbulence measurements will be the availability of satellite navigation systems. With their position and groundspeed accuracy it will be achievable to measure all wind components with a precision of 0.1 m/s. Thus airborne measurements will fall into the same precision category as ground based anemometer data.

3. REFERENCES

- [1] D.H. Lenschow The Measurement of Air Velocity and Temperature Using the NCAR Buffalo Aircraft Measuring System. NCAR-TN/EDD-74, 1972.
- [2] A. Redeker
P. Vörsmann Precise Vertical Speed Reconstruction Based on Vertical Acceleration and Barometric Altitude. Z. Flugwiss. u. Weltraumforschung, 2, 4, 1985.
- [3] P. Vörsmann Ein Beitrag zur bordautonomen Windmessung. Doctoral thesis, Technische Universität Braunschweig, 1984.
- [4] P. Vörsmann An on-line Realization for Precise Wind Vector Measurements on Board the DO 28 Research Aircraft. ICAS-84-5.10.1, Toulouse, France, 1984.
- [5] E.N. Brown
C.A. Friehe
D.H. Lenschow The use of Pressure Fluctuation on the Nose of an Aircraft for Measuring Air Motion. Journal of Climate and Applied Meteorology, Vol. 22, January 1983.
- [6] A. Redeker
P. Vörsmann An Airborne Realtime Data Processing and Monitoring System for Research Aircraft. AIAA 4th Flight Test Conference, San Diego, USA, 1988.
- [7] A. Redeker Datenerfassung im Flug. Deckblatt 10/1987, Markt & Technik Verlag, Haar bei München.
- [8] H. Haverland Die PDP lernt fliegen. Deckblatt 8/1988, Markt & Technik Verlag, Haar bei München.
- [9] D.H. Lenschow
C.A. Cullian
R.B. Friesen The Status of Air Motion Measurements on NCAR Aircraft. 4th Symposium on Meteorological Observations and Instrumentation, American Meteorological Society, Denver, USA, 1978.



Fig. 1: Meteoropod under the wing of the Polar 4 (Dornier DO 228)
of the Alfred-Wegener-Institute for Marine and Polar Research

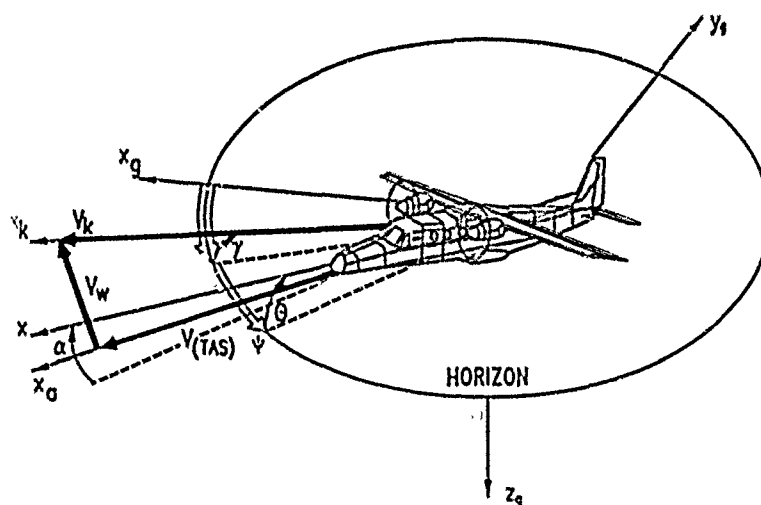
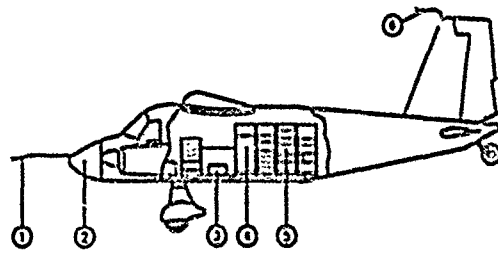


Fig. 2: Determination of the Wind Vector



- 1 Nose Boom with Air Flow Sensors
- 2 Temperature Sensor
- 3 Inertial Navigation System
- 4 Pressure Sensors
- 5 Data Acquisition and Processing System
- 6 Pitot Tube

Fig. 3: Conventional Wind and Turbulence System with Nose Boom Installation

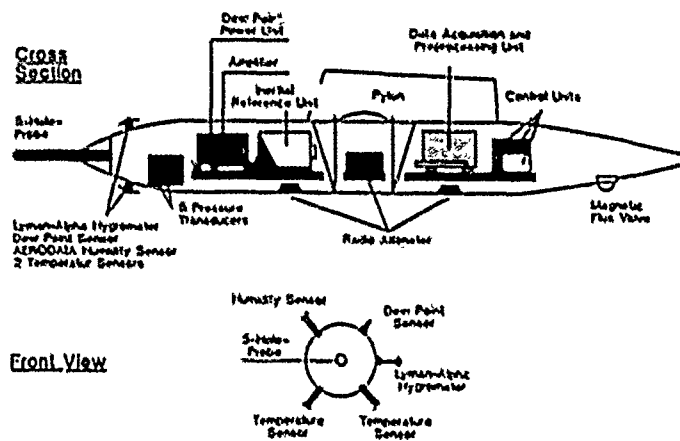


Fig. 4: Cross Sections of the Meteopod System with Hardware Locations of Sensors, Data Acquisition and Control Units



Fig. 5: Helicopter version of the Meteopod

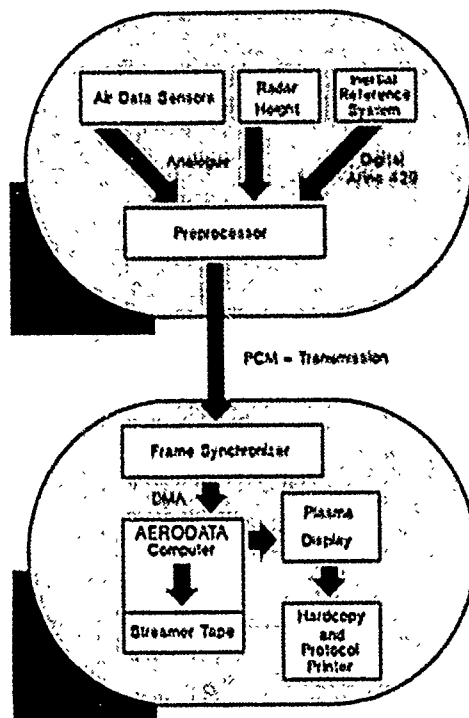


Fig. 6: Signal Flow between Meteoropod and Aircraft Cabin

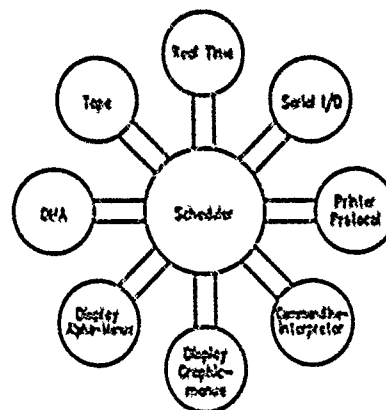


Fig. 7: System Processes handled by the Job Scheduler

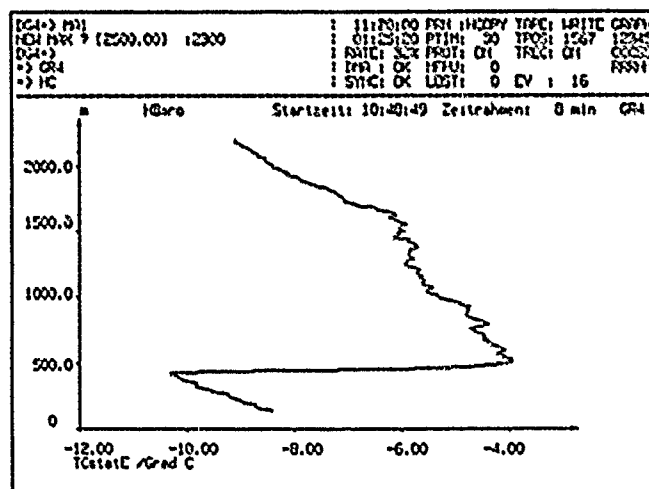
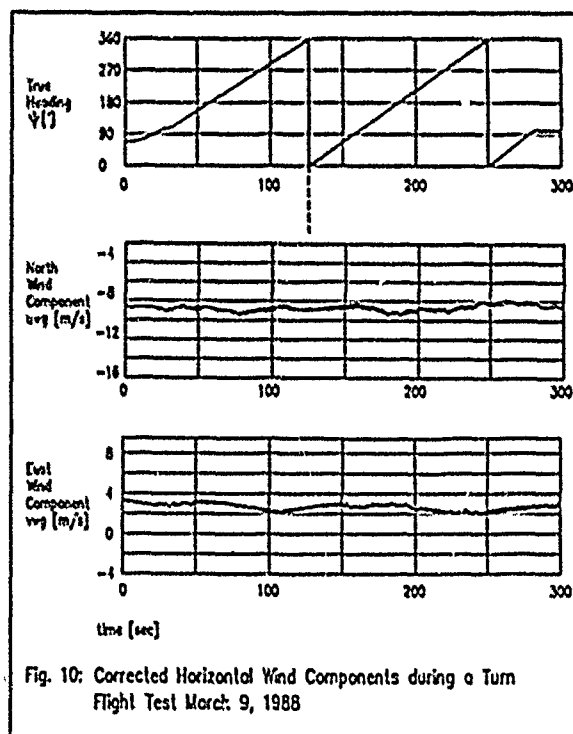
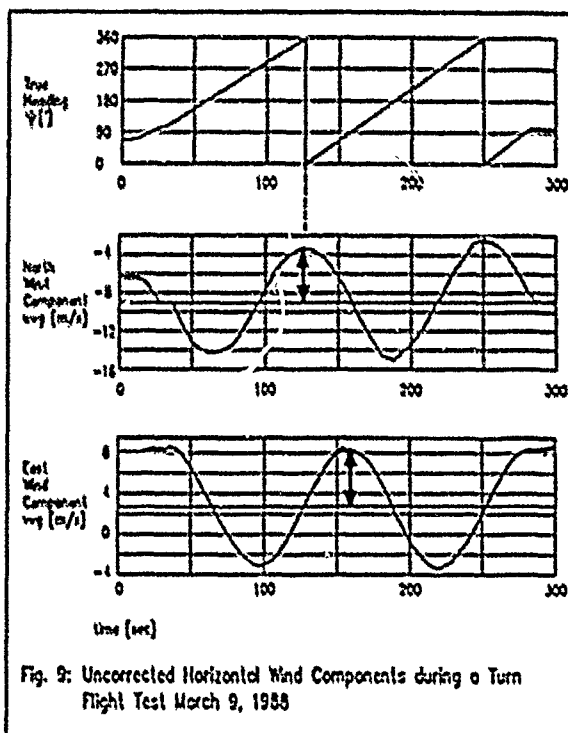
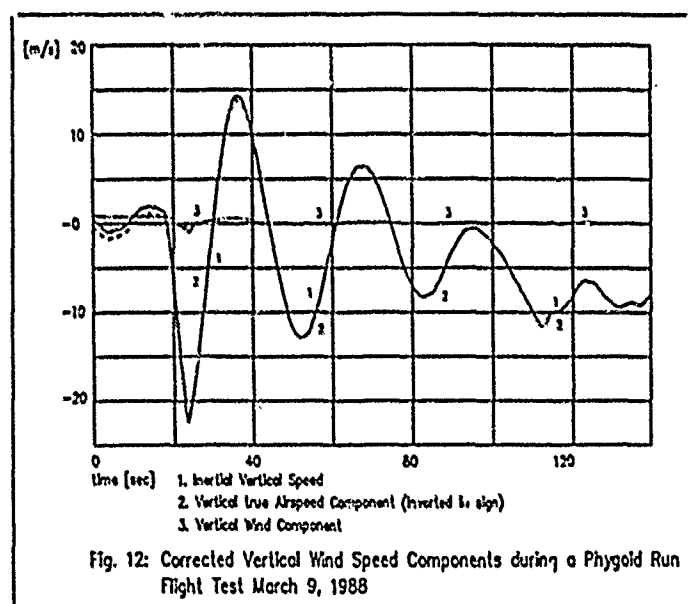
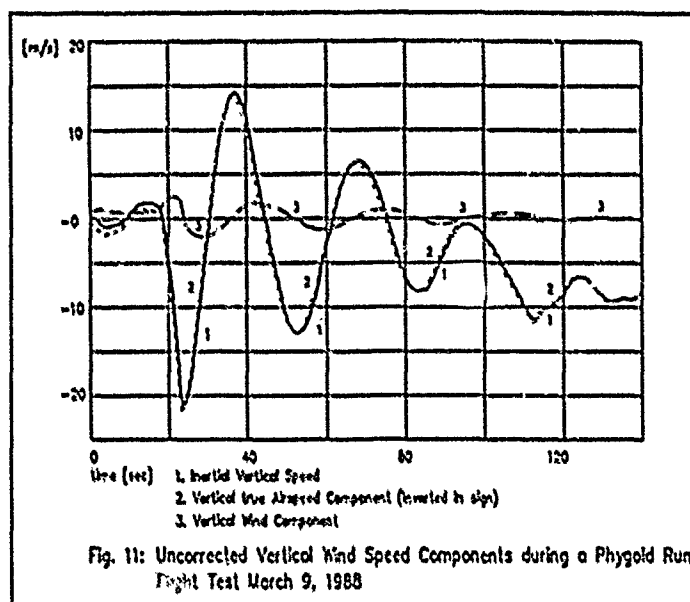
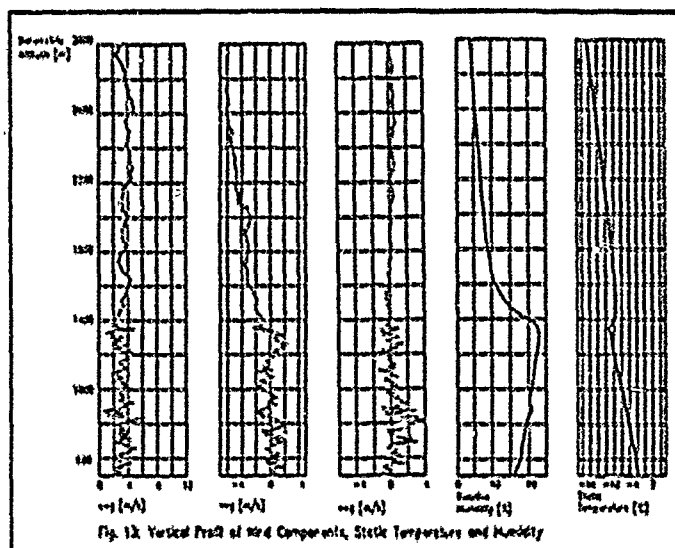


Fig. 8: Sample Real-Time Hard-Copy of Vertical Temperature Profile







THE UNITED STATES AIR FORCE APPROACH TO ALL-WEATHER TESTING

by
Clifford D. Tompkins
and
James A. Ford
6520 Test Group/CHAS
Edwards AFB California, U.S.A. 93523-5000

SUMMARY

All-weather test programs historically reveal design deficiencies that impact the operational capabilities of the vehicle involved. Therefore, testing is required to ensure that Air Force weapon systems can be effective under varying or extreme environmental conditions. The major purpose of all-weather testing is to determine to what extent a weapon system, its essential support equipment and crews, can accomplish the design mission in the required climatic conditions.

This paper addresses the requirements, purposes, and methods for conducting ground and flight tests under simulated and actual climatic extremes. The ideal all-weather test program is discussed in sufficient detail for an overall understanding of the major phases. The United States Air Force (USAF) approach to all-weather testing is presented, including regulatory requirements. The current methods of planning, extent of participating test organization involvement, and need for concurrent testing in USAF all-weather test programs of new weapon systems are discussed.

INTRODUCTION

Necessity for environmental testing of U.S. military equipment dates back to 1934 when a military review board recommended that tactical units be trained in various areas of the United States under winter conditions, and that at least one composite squadron undergo all-year training in Alaska on a continuing basis. This recommendation was based on problems that were found in arctic conditions. Typical problems included difficulty in starting engines, hardening of seals and gaskets, fuel leaks, increased fluid viscosities, and extended warm-up times. Other environmental extremes also presented problems, and the involvement of U.S. military forces in North Africa during World War II, and in Southeast Asia from 1960-1970, reinforced the requirement for worldwide operational capability. Bombers located in North Africa experienced problems such as lubricant breakdown, rubber deterioration, sand erosion, and subsystem overheating during exposure to the hot desert climate. Problems encountered in the Southeast Asia tropical environment included compartment seal deficiencies, water entrapment and subsequent freezing at altitude, corrosion, mold, and mildew difficulties. These problems emphasized the need for designing equipment to withstand all expected environmental conditions and the need for operationally testing weapon systems to evaluate the effectiveness of these designs.

Two men, Colonel H. O. Russell and Lieutenant Colonel A. C. McKinley, were mainly responsible for developing climatic test policies and facilities in the United States. Lieutenant Colonel McKinley, because of his experience in ferrying aircraft to the Soviet Union, suggested that all U.S. aircraft and equipment be operable at temperatures as low as -65 degrees F, and that a refrigerated hangar be constructed at Eglin Air Force Base (AFB) Florida to produce such an environment under controlled conditions. The reasons for such a testing facility were numerous. By 1944, the U.S. had become a global power with forces deployed worldwide, and the future demanded a force capable of operation in all global environments. Further, since testing at remote sites was expensive and had produced only meager results, Lieutenant Colonel McKinley reasoned that testing under controlled conditions would be far superior in useful results and up to ten times more economical. The weapon system could subsequently be deployed to selected extreme weather sites and flown to evaluate the areas not possible in a static, ground environment.

OBJECTIVES

The major objective of all-weather testing is to determine to what extent a weapon system, including its essential support equipment, maintenance personnel and aircrews can accomplish the design mission in the required climatic extremes using technical order (T.O.) procedures. Specific objectives of all weather testing include defining the effects of the environment on the integrated system, suggesting/developing corrective actions including design changes and workaround procedures, assessing operational impacts such as system effectiveness, safety, and operating/maintenance costs, and initiation of changes at an early stage of the program.

IDEAL ALL-WEATHER TEST PROGRAM

An ideal all-weather test program would consist of several consecutive Developmental Test and Evaluation (DT&E) phases. The program would begin with climatic laboratory

tests, then proceed to in-flight icing/rain and climatic deployments. This ideal program would allow a buildup approach to all-weather testing. The climatic laboratory tests would provide preliminary data during ground tests and identify possible problem areas before beginning climatic flight tests. The in-flight icing/rain tests would provide a simulation of icing or rain conditions that may be encountered by the test vehicle. The climatic deployments would then allow for testing the test vehicle in an operational environment in climatic extremes.

McKinley Climatic Laboratory:

The McKinley Climatic Laboratory at Eglin AFB Florida is normally used for the first test phase. The laboratory is an insulated hangar having a total enclosed volume of approximately 3,282,300 cubic feet. The size of the main chamber permits testing of very large items (e.g., C-5A) of equipment and complete weapon systems. Also, several tests can be conducted simultaneously depending on the size and complexity of the individual items. Tiedown rings are installed in the concrete floor for anchoring test vehicles and other equipment. Usable floor space in the main chamber is 55,000 square feet. Tasks accomplished in the climatic laboratory are:

1. Identification of any potential climatic related safety of flight deficiencies.
2. Verification and adequacy of T.O. procedures related to ground operation and maintenance functions.
3. Support equipment adequacy and compatibility with the weapon system under test.
4. Human factors evaluations during test vehicle operation and maintenance activities.
5. Establishment of subsystem baseline data under controlled conditions.
6. Development of workaround procedures for problems encountered.

Component and subsystem qualification tests in extreme conditions should have been completed by the contractor prior to testing of the complete air vehicle and, therefore, are not usually included in climatic laboratory tests. However, components/subsystems which have been identified as marginal or critical for extreme climatic operation during qualification testing, are subject to special attention during climatic laboratory testing. Problems which are identified during climatic laboratory testing are documented and immediately submitted on appropriate forms to the System Program Office (SPO) for corrective action. Major deficiencies are corrected, if possible, prior to deployment to natural extreme environment test sites, so that these corrections can be evaluated. If deficiencies are not corrected, workaround procedures are used, where possible. Potential safety of flight problems, however, are resolved prior to further deployment.

The weapon system to be tested is configured as close to production as possible. Any deviations from production configuration are noted and these deviations corrected as soon as possible. The most appropriate time is usually between deployments to subsequent test sites when the test vehicle can be returned to the airframe manufacturer's facility. Quick response "fixes" are sometimes incorporated in the climatic laboratory so that an evaluation of the effectiveness can be made prior to deployment to a natural extreme weather test site.

Functional tests of the test vehicle systems (with engines operating) and its support equipment are conducted to the fullest extent possible within the scheduled time constraints and limitations of the laboratory and test setup. Some activities involve a degree of simulation and some T.O. procedures may require modification to be compatible with the limitations of the Laboratory.

Use of the climatic laboratory can save time and cost by highlighting design deficiencies and manufacturing faults before testing in actual environments begin. Also, when deployment tests take place, comparison with climatic laboratory test results will give added confidence in the test results.

In-flight Icing and Rain Simulation

The next test phase following the climatic laboratory evaluation consists of in-flight icing and rain simulation. These tests are an in-flight simulation of adverse weather conditions. The tests are conducted using the KC-135A water spray tanker located at the Air Force Flight Test Center (AFFTC) at Edwards AFB California. Icing tests are conducted using a buildup approach with regards to icing cloud severity and time of exposure. The test vehicle is flown into the formed icing cloud with only the area under test exposed (e.g., engine, windscreen). After a predetermined amount of time, the test vehicle exits the cloud and a photo chase documents the ice accumulations. A descent is then made, with photo chase, to document ice shedding characteristics. If ice is ingested, the test vehicle returns to base and an inspection carried out. These in-flight icing tests identify icing problem areas prior to operational use.

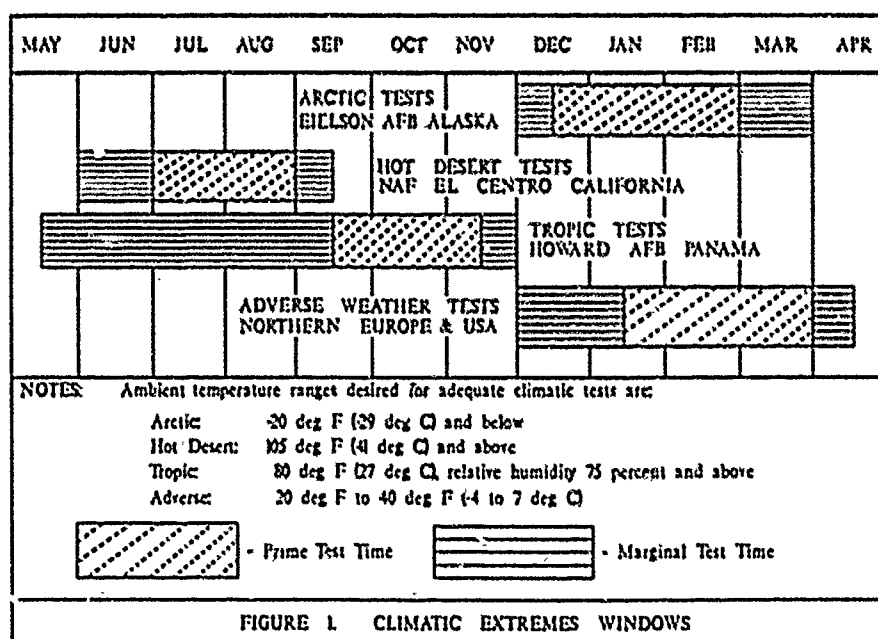
In-flight tests are also conducted using the water spray tanker to simulate flight through a heavy rain. Tests include evaluation of the engine's capability to ingest water without stalls or flameout, the ability of the windshield to resist erosion, and the extent of clear vision areas provided by the rain removal system.

Climatic Deployments:

When climatic laboratory and in-flight icing tests are completed, and after safety of flight problems are resolved, the test vehicle is deployed to extreme weather test sites for continuation of all-weather testing. The particular test site (arctic, hot desert, tropic, or adverse weather) depends on using command requirements and the season of the year. Cold weather testing is done during winter months at a location such as Eielson AFB Alaska, or Cold Lake and Yellow Knife, Alberta, Canada. Hot weather testing is done during the summer months at locations such as the Naval Air Facility (NAF), El Centro, California, or the Marine Corps Air Station (MCAS) Yuma Arizona. High humidity testing is done under moderate temperature, high humidity, and tropical rain conditions, which are typical during the autumn months at locations such as Howard AFB Panama, or Clark AFB Philippines. Adverse weather testing is that testing conducted under simulated and actual weather conditions which are detrimental to the operation or performance of the system under evaluation. It includes corrosive environmental testing of systems under conditions involving atmospheric pollutants and/or natural corrosive processes. This type of testing has been conducted in northwestern Europe. Adverse weather tests can be conducted during cold and tropic weather testing when suitable conditions permit. Adverse weather tests of aircraft include:

1. Wet, slushy and icy runway/taxiway performance and handling qualities.
2. Operation after freezing rain exposure.
3. Engine water ingestion on the ground and in-flight.
4. Evaluation of Instrument Flight Rules (IFR) capability.
5. Evaluation of the effects of corrosive atmospheric pollutants.

Tests are conducted at remote sites under natural extreme weather conditions to exercise a complete weapon system in an operational environment and to test under conditions not possible in the climatic laboratory. Normally, there is only a short time available for test accomplishment. If the extreme conditions are not experienced in a given season, it probably will not be possible to repeat the test until the following year. Therefore, every effort is made to obtain the maximum amount of valid data in the shortest possible time. Typical test time for exposure to climatic extremes of a given area are shown in figure 1.



Cold Weather

Cold weather (arctic) tests in the northern hemisphere are normally conducted from mid-December to the end of February. The test approach is to cold soak the test vehicle for extended periods at extremely low temperatures, then demonstrate response to various design mission requirements (alert, self-sufficiency, etc.) using current T.O. procedures. Cold weather related problems will usually begin at 0 degrees F (-10 degrees C) and there will be an indication of the most severe problems by the time -20 degrees F (-29 degrees C) is reached. However, at extremely low temperatures (-40 to -65 degrees F) (-40 to -54 degrees C), inability to start without using workaround procedures and total system failures are likely.

The test vehicle is operated from snow, slush or ice covered runways to satisfy adverse weather test requirements when conditions permit. Test flights are made to exercise the systems in dynamic conditions not possible in the climatic laboratory. Emphasis is placed on evaluating engine starting, hydraulic system operation, environmental control system (ECS) effectiveness and avionics system (including radar) functions.

Hot Desert Tests

Hot weather (hot desert) tests in the northern hemisphere are usually conducted from mid-June to the end of August. The desired conditions are 105 degrees F (41 degrees C) with high solar radiation. System specification requirements are usually 120 degrees F (49 degrees C) and 355 British Thermal Units per square foot (1119 watts per square meter) per hour solar radiation. The best sites are usually those close to sea level altitude where high solar radiation occurs and ambient temperatures remain high overnight such that total systems heat soaking occurs.

The test approach is to heat soak the test vehicle for extended periods of time in the extreme hot temperature and solar radiation, then demonstrate response to various design mission requirements at worst-case conditions. Indications of the most severe hot weather related problems will begin to appear at 105 degrees F (41 degrees C).

The test vehicle is ~~soaked~~ up and parked in the open with the nose facing south to maximize solar radiation through the cockpit. The complete weapon system, including critical ground support equipment such as air conditioning and electrical ground power units, is operated during periods of peak solar radiation and ambient temperature. Taxi time is maximized and heavy gross weight takeoffs are conducted to tax the engines and secondary power systems in the extreme heat. Flight at low altitude is conducted consistent with mission requirements to exercise the ECS, avionics, and other critical subsystems such as air/oil heat exchangers in the most stringent hot weather conditions.

High Humidity

High humidity (tropic) tests in the northern hemisphere are usually conducted from mid-September to mid-November. The test approach is to soak and then operate test vehicle systems in a moderate ambient temperature, high humidity environment. Test flights are conducted at peak ambient temperature and during or immediately after tropical rainstorms. Throughout the test period, an evaluation of corrosive effects of moisture from condensation or rainfall and material deterioration as mildew growth progresses is made. Emphasis is placed on ECS system performance, water intrusion/entrapment, electrical equipment performance, effects of trapped water freezing at altitude, rain removal systems, mildew growth, avionics equipment cooling, effectiveness of rain removal solutions or pneumatic systems, and erosion of windscreens or their protective coatings. Adverse weather tests such as IFR procedures, wet runway operations, and lighting effects during flight through rain are also accomplished.

Adverse Weather

Adverse weather tests are normally conducted in the late winter or early spring in a climate usually experienced in Canada, northern Europe and some parts of the United States. The test approach is to expose the test vehicle to rain, sleet, snow, and freezing rain, and then operate it on slippery taxiways and from runways with a runway condition reading as low as six. Other conditions desired during adverse weather testing are:

1. Crosswind components up to 20 knots during taxi, takeoff and landing.
2. High surface winds over salt water.
3. Instrument meteorological conditions for in-flight evaluations.
4. Temperature/humidity combinations conducive to airframe/engine icing during ground operations.

Instrumentation and Data Acquisition

Adequate data acquisition is essential for the conduct of a thorough climatic test program. Environmental parameters (temperature, humidity, solar radiation, rainfall,

etc.) must be documented to define climatic conditions during the tests. Extensive temperature/pressure instrumentation along with key operating parameters are installed within the test vehicle to track subsystem conditions during testing, document environmental conditions in case of failure, help in fault analysis, and aid in determining any corrective action or modification required as a result of subsystem or component failure. This information is also useful to designers of future systems through accurate knowledge of present subsystem performance during extreme environmental conditions. Airborne data acquisition, with quick-look data reduction capability, climatic laboratory systems, and weather recording are the primary systems available to the climatic test engineer.

Engine oil temperatures and pressures, hydraulic system temperatures and pressures, crew and avionics compartment temperatures, and fuel temperatures and flow rates are typical examples of instrumented parameters. Selection of specific instrumentation parameters is based on past climatic test experience and particular engineering requirements determined for the specific weapon system to be tested. Because it is not feasible to instrument every conceivable item, subsystems with histories of problems and those with marginal qualifications should be of prime interest (e.g., hydraulic systems nearly always leak at extremely low temperatures). Consideration should be given to parameters required to determine mass temperatures during soak periods. These parameters are used to determine thermal stabilization. Typical mass temperatures would be the hydraulic fluid reservoir, engine oil reservoir, main fuel cell, and large internal metal mass. Ambient air temperatures should be obtained near the extremities of the test vehicle, especially large aircraft, and should include, as a minimum, the vehicle nose, tail, tip of vertical stabilizer, wingtips, and wheel well area. In the climatic laboratory these temperatures will be used to control the laboratory conditioning to ensure approximately the same soak temperature for the entire test vehicle.

The actual environment to which the test system is exposed during deployment to remote sites must be recorded to document test conditions. Weather services and individual pieces of weather instrumentation are used to gather this data. Since manual data recording and reduction from individual instrumentation sensors is too time consuming, a portable, automatic recording weather station is essential to achieve the required accuracy and shorten data reduction time.

Photographic documentation of testing is an important tool in engineering analysis of events occurring in the course of the tests. It provides a vivid portrayal of the test activity to management, and is useful when preparing future tests. Black and white stills, color stills, 16mm color motion picture, and color video are the primary types of documentation required.

A portable microcomputer type data processing system is deployed with the test team to the climatic laboratory and most remote sites. It consists of a tape recorder with time search capability compatible with the test vehicle recorder, an analog-to-digital system for driving strip charts and data identification, a microcomputer display and processor system, and a printer/plotter. At the climatic laboratory, it is used both for real-time strip-out of selected parameters and processing final report data in tabular or plot formats. At remote sites, strip-out of data is done after each flight. Final report-quality plots can be generated within hours after a flight or test run if plot parameter arrangement, parameter scales, and calibration data have been predetermined and put into the computer prior to testing.

CURRENT USAF APPROACH

Today's austere program budgets and limited test assets mandate concurrent testing of new weapon systems. Subsystems testing, for example, is accomplished in piggyback fashion with performance and flying qualities or avionics tests, where possible, to save the cost of flying separate test missions. All-weather testing is no exception, and the ideal all-weather program must be modified using this approach. Climatic laboratory and extreme weather site deployments do require a dedicated test vehicle; however, that vehicle may be used for other testing before and between the all-weather test periods (during the climatic off-seasons). The current USAF approach to all-weather testing is to instrument a test vehicle for several types of DT&E testing, to be determined early in the formulation phase of the program. Other testing to be accomplished on the designated all-weather test vehicle is jointly decided upon by the SPO, Air Force Operational Test and Evaluation Center (AFOTEC), using command (HAC, SAC, or TAC), and the prime test vehicle contractor.

Detailed Test Plan

Review of the applicable regulations, military standards (MIL-STD), and air vehicle specifications is necessary prior to preparing a detailed test plan for ground and flight testing under extreme environmental conditions. The air vehicle design specifications provide most of the detailed information on climatic conditions/extremes for which a particular air vehicle was designed. Frequently, the design specifications reflect requirements of earlier versions of military standards. This information has to be supplemented with assumptions based on known operational requirements. The primary USAF regulation (AFR) and military standards as they apply to all-weather testing are:

1. AFR 80-31 (Reference 1). This regulation is the primary authority for all-weather testing and states that the USAF must have the capability to conduct operations in all types of environmental conditions. Additionally, it states that effects of the natural environment must be considered in the design, development, testing, and procurement of systems or material which may be operated, maintained, stored, packaged, and transported under a wide range of natural environmental conditions.

2. MIL-STD-210 (Reference 2). This standard establishes uniform climatic design criteria for military material which is intended for worldwide usage. It does not apply to design of material to be used only in specific areas or environments. Extreme climatic conditions contained in this standard apply broadly to all items of equipment and systems.

3. MIL-STD-810 (Reference 3). This standard establishes uniform environmental test methods for accelerated testing to determine the resistance of equipment to the effects of natural and induced environments peculiar to military operations.

Planning the all-weather test programs can take several months to several years, depending on the scope and complexity of the program. An engine qualification or new hydraulic fluid qualification test may take only six months planning effort, while a program such as the D-18 Climatic Laboratory test or the F-16 All-Weather program may require two years or more. A detailed test plan is initiated by the AFPTC as the Responsible Test Organization (RTO). This plan is accomplished in draft form as soon as enough detailed knowledge of the new test vehicle systems becomes available. The plan is circulated to all Participating Test Organizations (PTO), the prime contractor, and the SPO for review and comments. The final draft, along with the safety package containing the test risk level and hazard minimizing procedures, is usually approved by the AFPTC Commander 60 days before scheduled first test date.

Test Plan Working Group

Overall planning effort for the program, including spares, logistics, support equipment, etc., is done through a series of Test Plan Working Group Meetings (TPWG) chaired by the SPO and held alternately at various RTO, PTO and contractor plant locations. Action items are discussed and assigned to participants with deadlines for resolution. The TPWG meetings are usually held every three to six months, as dictated by the test schedule and urgency of action items. On large new programs such as the C-17, advanced all-weather planning is done as part of the TPWG for the entire flight test program, so that test vehicle disposition, appropriation of assets, etc., can be properly addressed and tracked as a part of the whole program.

Test Conduct

Over the years, USAF all-weather testing of a new weapon system has evolved into a joint effort by the AFPTC, AFOTEC, and using command, with technical assistance by the prime contractor. The lead organization conducting the tests is the AFPTC.

The aim of the extreme weather deployments is to demonstrate the ability of the test vehicle and all its systems, in all its mission roles, to operate in the extreme environments likely to be met. The safety, reliability, maintainability, and operational effectiveness need to be examined at ground level temperatures, but they can only be adequately confirmed during operational scenarios. While the climatic laboratory is an excellent facility for obtaining quantitative data under controlled conditions, it is not a complete test of the weapon system. It must be complemented by deployments to extreme weather test sites to ensure that the system is really operable under all expected conditions. The current approach is to conduct comprehensive ground tests before flying the test vehicle, during which critical areas or components are identified. At the end of the deployment tests, it is necessary to recommend ground level temperature limits, precautions and operating limitations which absolutely must be incorporated in operational T.O.s. Two important points should always be kept in mind. First, the individual component environmental type tests conducted during the manufacturer's development work do not give an exact and conclusive representation of actual service conditions. They may show a high degree of confidence that the components will function satisfactorily in the field when assembled into a complete system; however, testing is needed to confirm this confidence. Second, a test vehicle parked in the open and soaked in the environment undergoes a much more stringent test than when warmed up and airborne, particularly during cold weather tests.

Deployments to extreme weather sites are currently done as combined Initial Operational Test and Evaluation (IOT&E) and DT&E efforts. If the using command can schedule it, an operational "mini squadron" of several uninstrumented production vehicles, along with the instrumented all-weather test vehicle, are deployed to the test site along with a combined team of using, command and Systems Command crewmembers and maintenance personnel. Operational experience is gained first-hand in the real environment using this approach. Dedicated test points are flown on the instrumented test vehicle; however, every effort is made to fly operationally representative missions when possible. A much better data base, including reliability and maintainability information, is possible through this combined approach than is possible with a single, instrumented test vehicle.

CONCLUSIONS

Today's austere program budgets and limited assets mandate concurrent testing of new weapon systems. All-weather testing is no exception. Thorough planning must include review of the detailed test plan by all participating organizations. Test Planning Working Group Meetings must be held to define overall support required and determine methods for obtaining it. The safety, reliability, maintainability and operational effectiveness of a weapon system all need to be examined at ground level temperatures, but they can only be confirmed during operational scenarios. While the climatic laboratory is an excellent facility for obtaining quantitative data under controlled conditions, it is not a complete test of the weapon system. It must be complemented by deployments to extreme weather test sites to ensure that the system is really operable under all expected conditions. A combined approach to deployments using both Systems Command and using command personnel in a "mini-squadron" will produce a much better data base, including reliability and maintainability, than is possible with a single, instrumented test vehicle.

Environmental testing of weapons systems is a vital necessity in our global military effort and an important benefit is the improvement in overall system reliability. As our operational theaters continue to expand and systems become more complex, reliability and operational capability must be maintained. Through environmental testing, we are afforded an opportunity to study and understand the mechanics of failure and thus improve weapon system reliability.

REFERENCES

1. All-Weather Qualification Program for Air Force Systems and Materiel, AF Regulation 80-11, 23 September 1975.
2. Climatic Information to Determine Design and Test Requirements for Military Systems and Equipment, MIL-STD-210, 9 January 1987.
3. Environmental Test Methods and Engineering Guidelines, MIL-STD-810, 19 July 1983.
4. Hendrickson, C.L., Flight Testing Under Extreme Environmental Conditions, AGARDograph Flight Test Techniques, Vol. 8, Series No. 300, June 1988.

INFLUENCE OF WINDSHEAR, DOWNDRAFT AND TURBULENCE ON FLIGHT SAFETY

by

Gunther Schänzer
 Director of the Institute for Flight Guidance and Control
 Technical University Braunschweig
 Hans-Sommer-Str. 66
 3300 Braunschweig
 FRG

ABSTRACT

Wind shear, downdraft and turbulence influences flight safety especially in take-off and landing approach. For a better understanding of the relevant problems, the typical aircraft response in gust and in wind shear will be pointed out and will be compared with real flight situations. In general the airspeed deviation of an aircraft in a wind shear situation is relatively small in contrast to flight path deviations and flight performance is not the limiting factor. Flight simulator studies have shown that it is difficult for the cockpit crew to identify a wind shear situation without any additional display of relevant information in order to control throttle and elevator in a correct manner. A wind shear warning display, based on energy deviation and energy rate can assist the pilot to overcome severe wind shear.

LIST OF SYMBOLS

\bar{c}	mean aerodynamic chord	V_w	change in windspeed
C_D	drag coefficient	u_w	} wind components
C_L	lift coefficient	v_w	
D	drag	w_w	
g	earth acceleration	u_{wz}	} wind gradients
h	height	u_{wy}	
\dot{h}	rate of climb	w_{wy}	
\ddot{h}	vertical acceleration	u_{wx}	} change in horizontal wind speed
h_E	energy height	W	
\dot{h}_E	time derivation of energy (specific excess power)	x	} position coordinates
h_s	surface roughness height	y	
k	von Karman constant	z	
L	lift	α	angle of attack
n	load factor	α_w	wind angle
T	thrust	γ	flight path angle
T_H	cycle time of the phugoid mode	λ_{ph}	wavelength of the phugoid mode
u_s	friction velocity	θ	pitch attitude
V	airspeed		
V_E	flight path speed (ground speed)		
V_w	wind speed		

1. INTRODUCTION

Accidents caused by wind variation e.g. turbulence, gusts, downdraft and wind shear are very rare but in most cases will lead to a catastrophic end. In general wind shear accidents and incidents result from the fact that the wind shear phenomenon is not understood by the pilot due to his training condition and the cockpit instrumentation. In such situations the pilot is not able to act in the correct way. Therefore it can be suspected that a considerable amount of wind shear accidents will be interpreted wrongly as pilots error. Only in some rare situations, especially during take-off, hazards may be caused by limited flight performance without any chance for the pilot to respond properly. Numerous investigations have been made in order to solve the wind shear problem. Many of these proposals will fail

because the physical phenomena are not understood completely, neither by the pilots nor by the investigators of wind shear warning systems. This problem will be illuminated by the fact that some of the correct safety procedures in wind shear contradict the pilots feeling of how controlling an aircraft.

This paper tries clarifying step by step some physical backgrounds of the wind shear phenomena including adequate flight safety procedures to overcome the problems.

3 METEOROLOGICAL WIND PHENOMENA

3.1. DEFINITION

The influence of wind and turbulence on aircraft design and flight safety is of great importance. But only in relative simple cases a calculation of wind and turbulence is possible. Wind shear and turbulence are generally correlated with a flow field afflicted with friction. The solution of the correlated nonlinear Navier - Stokes equations of motion for a three dimensional friction afflicted flow field is even up today only possible for very simple situations. For example the separation of low frequency wind alternation and turbulence yields to the mathematical problem of stochastic functions with a time varying mean value. In Fig. 1 we find the trial separating an in flight measured windspeed into low frequency wind shear and turbulence [1]. In order to solve engineering problems for practical applications we use segments with constant mean value or apply bandpass-filters. It is useful to vary the filter parameters in such a manner that the parameters of the turbulence power density spectrum become constant.

Another approach separating wind shear and turbulence is to take advantage of the different response of an aircraft in wind shear and gust. In contrast to gust and turbulence it is very difficult to formulate a definition concerning wind shear. Different persons are using different definitions. The translation of "wind shear" into other languages has created an international confusion. It is usual to combine different meteorological phenomena that will influence flight safety in the one term "wind shear". Therefore these less precise definitions ask for more differentiated advises for flight safety improvement, as each meteorological phenomenon requires a specific response.

A well known example for a one dimensional shear flow is a viscous flow in a channel (Fig. 2). The shear gradient is an indicator of the spatial speed variation and a function of the stress. In the atmosphere the flow is usually three dimensional. The windspeed vector \underline{V} , with the components u_x, v_y, w_z and the position vector (x,y,z) forms a nine element gradient tensor.

$$\text{grad } \underline{V} = \begin{vmatrix} \frac{\partial u_x}{\partial x} & \frac{\partial u_x}{\partial y} & \frac{\partial u_x}{\partial z} \\ \frac{\partial v_x}{\partial x} & \frac{\partial v_x}{\partial y} & \frac{\partial v_x}{\partial z} \\ \frac{\partial w_x}{\partial x} & \frac{\partial w_x}{\partial y} & \frac{\partial w_x}{\partial z} \end{vmatrix} \quad (1)$$

Only three of these nine elements are dominant in wind shear accidents.

$$\frac{\partial u_x}{\partial z} = u_{wz} \quad \text{windvariation with height}$$

$$\frac{\partial u_x}{\partial x} = u_{wx} \quad \text{windvariation along the flight pattern}$$

$$\frac{\partial w_x}{\partial y} = w_{wy} \quad \text{spanwise windvariation creates rolling moments}$$

An aircraft passing a spatial orientated wind field with the ground speed V_g creates a time varying windspeed $V_w(t)$ along the flight path. The wind field itself may move with an average wind speed V_w . For the aircraft response the following wind speed components are relevant

$$\dot{u}_{w1}(t) = u_{w1} \cdot V_g = u_{w1} \cdot \dot{H} \quad (2)$$

$$w_{w2}(t) \quad (3)$$

The variation of the horizontal wind speed component $\dot{u}_{w1}(t)$ due to time depends on the aircraft's ground speed V_g and the vertical speed \dot{H} . As in general the ground speed V_g is two orders of magnitude greater than the vertical speed \dot{H} , the efficiency of the gradient u_{w1} is much greater compared with u_{w2} . Measurements of gradients demonstrate (2,3), that u_{w1} is one or two orders of magnitude smaller than u_{w2} . The aircraft response itself is comparable in spite of the great differences of the gradients. If the gradients $|u_{w1}|$ are greater than 0.1 s^{-1} and $|u_{w2}|$ greater than 0.005 s^{-1} , the safety margin is critical. The ICAO [4] defines gradients of u_{w1} as

$$|u_{w1}| \geq 0.2 \text{ s}^{-1} \quad \text{dangerous}$$

$$|u_{w1}| \geq 0.13 \text{ s}^{-1} \quad \text{difficult}$$

$$|u_{w1}| \geq 0.066 \text{ s}^{-1} \quad \text{significant}$$

Additionally flight safety will be influenced by the time variable vertical wind $w_{w2}(t)$ or by downbursts.

To illustrate the different wind shear phenomena some examples will be demonstrated. A well known wind shear phenomenon is the earth surface boundary layer wind shear (Fig. 3). In the early thirties, L. Prandtl investigated an adequate formulation of this phenomenon. In an adiabatic atmosphere with constant density and stress close to the ground we get the exponential formula:

$$V_w = \frac{1}{k} \cdot u_* \cdot \ln \frac{H}{H_0} \quad (4)$$

$$\frac{dV_w}{dH} = -u_{w1} = \frac{1}{k \cdot H} \cdot u_* \quad (4a)$$

The approximation of the flight measurement (2) by the exponential law is adequate. This example gives an indication that ground measurements of the windspeed give only a poor extrapolation for the wind distribution in greater altitudes. The gradient u_{w1} becomes extremely large close to the ground (Equ. 4a). Despite the fact that the gradient is large, the situation is not critical as there is no time for significant flight path deviations. Our investigations show that the critical elevation of a wind shear occurrence is in the range between 120 m and 80 m. In greater elevation the pilot has time enough to control the disturbances and closer to the ground the flight path deviations are small.

Figure 4 demonstrates a typical low level jet, that occurs in the plains of northern Germany in 20% of all nights. The level of turbulence is extremely small. Correlation of flight and tower measurement show, that the low level jet is a large spreaded phenomenon. The strongest gradients occur in the critical elevation of approximately 100m. Although the situation is potential critical, only one accident has been reported (Soviet Union) [2]. The reason for the low probability of accidents may be the low flight traffic during night.

The flow field of safety critical fronts is less investigated (Fig. 5). Still uncertain is the knowledge of the physical background of a wind shear situation measured at Frankfurt airport (Fig. 6). With a measured wind direction of 10° , the airport is in the lee of the Frankfurt city buildings. Separated lee-eddies may be the cause of this critical phenomenon.

The most well known and dangerous wind shear and downdraft phenomenon is a thunderstorm downburst. The knowledge of the physics are relative good. A great variety of similar models have been developed (Fig. 7, 8) [1,3].

An approximately vertical orientated stagnation flow can give an impression of the situation. Critical wind shear gradients u_w and w_w , as well as immense downdrafts have been obtained. Each of this three elements can be very dangerous, the combination of all is threatening.

In the frame of this paper there is no space to discuss in detail the response of an aircraft in the different meteorological situations. In order to explain the aircraft response and the pilot reaction it seems to be sufficient to eliminate all the complex wind models by a very simple wind model (Fig. 9) of a ramp shape.

4. AIRCRAFT RESPONSE DUE TO WIND ALTERNATION

4.1 FUNDAMENTALS

The dynamic response of an aircraft in a variable wind field is a very difficult problem, which we can solve with time variant, non linear, strongly coupled equations of motion. It is state of the art to solve those problems with numerical simulation. If we concentrate on the significant response, a lot of couplings, non linearities and unsteady aerodynamics can be eliminated. In the appendix the simplified equations of motion have been derived. These equations become relative simple and can be used for the interpretation of the simulation results.

In order to demonstrate the typical response of an aircraft due to gust, turbulence and wind shear, the simple but powerful windmodel of Fig. 9 consisting of a spatial ramp function will be used (Fig. 9a). The wind gradient is given by the wind change ΔV_w and the rise distance Δx

$$V_w = \frac{\Delta V_w}{\Delta x} \quad (5)$$

If the aircraft enters the windfield (Fig. 9a) the space variable wind will be transformed into a time variable wind, that will change first the aerodynamic flow field (airspeed, angle of attack) of an aircraft. The resulting aerodynamic forces and moments will accelerate the aircraft.

The response of the aircraft varies very much with the rise distance related to relevant aircraft parameters. If the rise distance is less than ten times of the mean aerodynamic chord, we obtain a typical high frequency gust response. This response will be demonstrated with a heavy transport aircraft at a typical approach speed of $V = 70 \text{ m/s} \approx 140 \text{ kts}$ for a vertical gust in Figure 10 and a horizontal gust in Figure 11. A rise distance of $\Delta x = 30 \text{ m}$ or $\Delta x = 5\bar{c}$ is typical for a gust response.

Immediately after the gust occurrence the aerodynamic flow condition is heavily disturbed (see the deviation in airspeed ΔV and angle of attack $\Delta \alpha$). The angle of attack deviation is mainly compensated after a time period of the well damped aircraft short period motion. The reduction of the angle of attack deviation is the stronger the greater the static stability of the aircraft is. The airspeed deviation ΔV is reduced primarily after a time period of the poorly damped phugoid motion.

The pitch attitude response $\Delta \theta$ is primarily of interest immediately after the gust occurrence. Due to the static stability and unsteady aerodynamic effects the aircraft will pitch down in an updraft. In a headwind gust the aircraft is firstly pitching down due to unsteady aerodynamic downwash delay effects and then pitching up. In a headwind gust situation, the angle of attack deviation $\Delta \alpha$ and the wind angle deviation $\Delta \alpha_w$ are negligibly small ($\Delta \alpha \approx 0$, $\Delta \alpha_w \approx 0$), so that Equ. (A3) can be simplified to

$$\Delta \theta \approx \Delta \gamma$$

The pitch angle $\Delta \theta$ is primarily correlated with the flight path angle $\Delta \gamma$. The major deviation in flight path (vertical speed ΔH , height ΔH) is evident a phugoid period after the gust occurrence. Concerning the speed response, we obtain for short rising distances and strong gradients u_w , a sudden rise of airspeed V and no significant deviation of ground speed.

$$\lim_{u_{w1} \rightarrow \infty} \Delta V = \Delta u_{w1} \quad \lim_{u_{w1} \rightarrow \infty} \Delta V_k = 0 \quad (6)$$

If the rise distance of the horizontal wind will be significantly greater than the wavelength λ_{r2} of the phugoid motion we obtain the typical wind shear response. With the well known phugoid mode cycle time

$$T_H = \pi \cdot \sqrt{2} \cdot \frac{V}{g} \quad (7)$$

we get the wavelength

$$\lambda_{r2} = T_H \cdot V = \pi \cdot \sqrt{2} \cdot \frac{V^2}{g}$$

For the heavy transport aircraft with an approach or take off speed of approximately $V = 70$ m/s we achieve a cycle time of half a minute and a wavelength of ≈ 2200 m

For demonstration the rise distance has been preselected by $\Delta x = 3000$ m (Fig. 12a, b).

In contrast to the gust response, the speed deviation is small and the ground speed is proportional to the wind speed. For large rise distances or small gradients u_{w1} we can indicate

$$\lim_{u_{w1} \rightarrow 0} \Delta V_k = \Delta u_{w1} \quad \lim_{u_{w1} \rightarrow 0} \Delta V = 0 \quad (8)$$

Even if we obtain strong deviations in kinetic $\left(\frac{V_k \cdot \dot{V}_k}{g}\right)$ and potential (\dot{H}) energy (see appendix), the variation of total energy is negligibly small.

$$\lim_{u_{w1} \rightarrow 0} \Delta \dot{H}_k = 0 \quad (9)$$

Investigations on energy transfer between wind and aircraft [5,9] have shown that energy based on inertial speed and height is fairly constant at small flight path angles. This is true for all transport aircraft in normal flight regimes. Only glider aircraft can transfer significant energy from the wind in extreme flight manoeuvres, as for example in dynamic soaring flight [9]. The flight of an albatross in the surface boundary layer of the sea is a wellknown example for the application of this principle in nature. P. Krauspe [10] pointed out that wind shear induced by flight path deviations can be approximated by simple analytical functions (Fig. 13). A fundamental result of this investigation demonstrates that the aircraft response in wind shear is to a great extent independent of aircraft characteristics. The major parameters of influence are airspeed and lift to drag ratio. It should be noted that the earth-fixed wind shear can extensively modify the phugoid stability [10]. Krauspe's numerical calculations have been verified in a moving cockpit simulation.

An explanation for the unexpected small deviation of airspeed in a wind shear situation is the static stability of an aircraft. The higher the static stability the faster is the reduction of deviations of angle of attack and airspeed. In wind shear situations with small gradients the aircraft has response time enough, to reduce airspeed deviations. This typical behaviour of an aircraft is even more significant, if a pilot or an autopilot controls the airspeed.

In a real wind shear situation, we obtain rise distances that are between the typical gust response and the typical wind shear response. A typical strong wind shear situation is given in Fig. 9. We obtain a windspeed variation of 12,5 m/s in a shear layer thickness of 50 m and therefore a gradient of $u_{w1} = 0,25$ s⁻¹. Such a gradient is defined as dangerous [4]. If an aircraft is approaching with a typical flight path angle of $\gamma = -3^\circ \approx -0,05$ rad the rise distance for passing the vertical shear layer is

$$\Delta x = \frac{\Delta H}{|\gamma|} = \frac{50}{0,05} = 1000 \text{ m} \quad (10)$$

The aircraft response for this rise distance is demonstrated in Fig. 14. The deviation of airspeed V and ground speed V_g is of the same order, and the total energy variation even small.

4.2. TAKE OFF

After take off, our reference aircraft may pass a shear layer in an elevation of $H = 100\text{m}$ (Fig. 15). Layer thickness and gradient are the same as in Fig. 9. The increasing tailwind will accelerate the aircraft. The airspeed deviation is small, but the height loss relative to the undisturbed flight path is approximately $\Delta H = 200\text{ m}$. It is remarkable, that the main height loss occurs outside the shear layer. If we expand the shear layer thickness from 50 m to 75 m at the same gradient, the aircraft will touch the ground in a distance of 3 km behind the take off point. In a comparable downburst situation a transport aircraft had a fatal accident in Denver [11] (Fig. 16). The core of the downburst was positioned above the take off point. At a distance of 1 km behind break release a weak headwind changed to an immense tailwind of $u_w = 40\text{ m/s}$ (Fig. 16a). After the pilot's decision to take off, an accident could not be avoided in such a serious situation. The advice to pilots is trivial but powerful: do not start under such downburst conditions, and put up with the delay. Figure 16b demonstrates problems beside the primary effects which can irritate the pilot. At the point of break release the pilot will obtain a small tailwind that will be caused by recirculation of the downburst flow field. During the acceleration phase, the wind will change into power increasing headwind and the pilot gets a feeling of more safety. At last 2.5 km behind break release, the wind will change again into a dramatic situation. Additionally and probably unnoticed by the pilot the aircraft will be affected by a downdraft shortly after take off. The flight path of an piloted transport aircraft in a simulator run demonstrates Fig. 17. The downburst was the reconstructed Denver [11] situation. Most of the pilots did not realize the dangerous ground proximity. An explanation of this effect may be the poor visibility at high pitch angles during take off. Tailwind and downdraft become the stronger and more dangerous the greater the climb gradient is. Amazingly powerful aircrafts are more affected due to their greater climb gradient. A small chance to survive may exist, if the pilot will recognize the situation and change immediately to a flight close to earth surface in order to avoid the critical windfield areas in the climb phase [12]. In Fig. 18 such a procedure is demonstrated. This advice to fly close to the ground with heavy transport aircraft is more academic, as the recognition of the situation is difficult with today's cockpit instrumentation (especially the identification of the downdraft). Additionally obstacles may handicap a low level flight and the advised procedure will contradict the pilots feeling.

4.3. APPROACH AND LANDING

In comparison with take off we obtain a quite different situation for approach and landing. Flight safety will be primarily influenced during take off by limited flight performances and during landing approach by limited handling qualities. An aircraft response with fixed controls in the simple wind shear model (Fig. 9) has been demonstrated in Fig. 19. The flight path differs from decreasing tailwind (headwind shear) and decreasing headwind (tailwind shear). Decreasing tailwind gives similar effects as well as increasing headwind. Both effects shall be called: "headwind shear". In a headwind shear situation the aircraft climbs relative to the undisturbed glide path (Fig. 19). Again we achieve the greatest flight path deviations after passing the shear layer. The headwind shear situation is comparably uncritical, if the pilot decides to go around in good time. In contrast a tailwind shear leads to an undershoot (Fig. 19). The phugoid mode will be excited in the shear layer. The eigenfrequency of the phugoid mode differs between headwind- and tailwind shear (see chapter 4.1. and Fig. 13). In Fig. 19a a fictitious runway has been drawn for the most critical situation. The description of a typical wind shear accident is fairly precise. The aircraft will touch down with a moderate rate of descent approximately 2 km prior the runway threshold. As discussed as well in chapter 4.1. as later in Fig. 21 and Fig. 22, the airspeed deviation is small. The aircraft will touch down at the main landing gear with a usual pitch attitude. When the ground at the touch down point would be prepared, the landing could be said as hard but not dangerous. But usually the area prior 2 km of the runway threshold is quite unqualified (forest, obstacles, water) and in the worst case densely populated. A touch down of an aircraft in this area will lead to a catastrophic crash. The critical height of shear layer above the runway is again in the range between 80 and 120 meters.

The prior discussed aircraft response in wind shear may look academic, because the wind model is very simple and the aircraft is flying with fixed controls without any pilot response. The basic remarks are even true for piloted aircraft in realistic wind shear situations. A sensational and well known wind shear situation is the downburst, where a Boeing 727 crashed in New York, 1975 [11,13]. Fujita [14] measured and modelled the wind field of the downburst. This wind model has been implemented in a flight simulator and fourteen airline pilots have been tested on this and other different wind models [5]. The typical response of an experienced airline pilot demonstrates Fig. 20. The flight

path was nearly identical with the reconstructed flight path of the crash. Approximately 1.3 km prior to the desired touch down point, the aircraft touched the ground. The critical elevation of the effective wind field was again 100 m. The airspeed deviation ΔV is less than 10 m/s even under this unfavourable conditions. The influence of airspeed deviation is negligibly small. This typical pilot response underlines the statement, that airspeed deviations are small and not critical. The displacements of elevator and throttle are even small. The similarity to a flight with fixed elevators is significant. The responses of the experienced pilots were comparable. The reason for this response without significant pilot actions may be the standard cockpit instrumentation of the flight simulator. A less experienced airline pilot (2000 flying hours) (Fig. 21) reacts busier than the experienced pilot, the airspeed deviation is again small and the critical ground contact can not be avoided.

5. PROCEDURE TO IMPROVE FLIGHT SAFETY

The technical requirement for safe flights in wind shear is nearly trivial:

THE PRESELECTED FLIGHT PATH AND AIRSPEED MUST BE KEPT PRECISELY.

This requirement we can formulate very simple:

$$\begin{aligned} \text{flight path deviation } \Delta \gamma &\stackrel{!}{=} 0 \quad \text{or} \quad \Delta \gamma \stackrel{!}{=} 0 \\ \text{airspeed deviation } \Delta V &\stackrel{!}{=} 0 \end{aligned}$$

The requirement for precise speed control leads to some important consequences. As derived in the appendix, the ground speed V_g is the superposition of airspeed V and windspeed V_w . The time derivatives of Equ. (A1.1) leads to the acceleration terms

$$\dot{V}_g = \dot{V} + \dot{V}_w \quad (11)$$

If the airspeed deviation vanishes, $\dot{V} = 0$, and we get

$$\dot{V}_g = \dot{V}_w \quad (11a)$$

Equation (11a) states, that an aircraft with precise speed control has to be accelerated or decelerated with the wind field. This requirement can be fulfilled very easy, if the aircraft has a sufficient static stability and the pilot or the autopilot controls the airspeed. The relevant equation of motion will be derived from Equ. (A 11); appendix

$$\Delta \gamma = \Delta \left(\frac{T}{W} \right) - n \cdot \Delta \left(\frac{C_D}{C_L} \right) + n \cdot \alpha_w - \frac{\dot{V}_w}{g} \quad \dot{V} = 0 \quad (12)$$

A deviation of the flight path angle can only be avoided, if a thrust or drag variation is possible. In a take off position, thrust setting is at maximum level and airspeed as well as flaps are optimized for take off performances. A control of the flight path during take off is very limited. If thrust and drag are constant, the corresponding flight path angle deviation becomes:

$$\Delta \gamma = n \cdot \alpha_w - \frac{\dot{V}_w}{g} \quad (12a)$$

By introducing Equ. (2) and (A2.1) we get

$$\Delta \gamma = -u_{w1} \cdot \frac{V_g}{g} + u_{w1} \cdot \frac{\dot{V}_g}{g} - \frac{w_{w1}}{V} - \frac{u_{w1}}{V} \cdot \gamma \quad \begin{aligned} n &= 1 \\ \dot{V}_w &= \dot{u}_{w1} \end{aligned} \quad (13)$$

We obtain two contradicting effects of speed. The greater the ground speed and rate of climb are, the greater is the deviation of the flight path due to the wind shear gradient. The effect of horizontal and vertical wind speed is alleviated by airspeed. Therefore, the usual increase of airspeed for a better safety margin is in agreement with the pilots' feeling but creates the adverse effect in wind shear.

If a pilot enters a wind shear field during take off it can be his only chance, if he reduces airspeed down to stall speed to avoid ground contact [12].

In landing approach, flight performances are not a significant problem. The requirement of precise flight path control ($\Delta\gamma = 0$) can be fulfilled in principle. For $\Delta\gamma = 0$ we get the required thrust from Equ. (12)

$$\Delta\left(\frac{T}{W}\right) = \frac{\Delta u_w}{g} = n \cdot \sigma_w \quad (12b)$$

$$\Delta\left(\frac{T}{W}\right) = (u_{w1} - u_{w2} \cdot \gamma) \frac{V_k}{g} + \frac{w_{w2}}{V} \cdot \frac{u_{w2}}{V} \cdot \gamma \quad (12a)$$

It is again remarkable, that the required thrust variation will be increased with increasing ground speed (see discussion on take off). We eliminate the thrust by specific excess power (see appendix)

$$\dot{h}_k = \Delta\left(\frac{T}{W}\right) \cdot V_k \quad (13)$$

and get

$$\dot{h}_k = (u_{w1} - u_{w2} \cdot \gamma) \frac{V_k^2}{g} + \frac{w_{w2}}{V} \cdot V_k + \frac{u_{w2}}{V} \cdot \dot{h}_k \quad (14a)$$

If the aircraft will pass a windfield as shown in Fig. 9, we can calculate the required thrust or the specific excess power from Equ. (14a). The result is drawn in Fig. 22, curve R. The step increase of the required thrust corresponds with the gradient u_{w1} . The ramp shaped term describes a change of the wind angle σ_w or $\int (u_{w2} \cdot \gamma \cdot V_k \, dt)$. Deviation in airspeed and height are eliminated by this type of thrust control.

For comparison, the response of an aircraft with a modern flight control system (autopilot, autothrottle) is demonstrated for the same wind field (Fig. 22, curve A). The thrust response is more smooth and delayed approximately ten seconds compared with ideal thrust control. The maximum deviation of energy height is moderate (Fig. 22). The maximum deviation in airspeed ($\Delta V = 5 \text{ m/s}$) and flight path ($\Delta \gamma = 5 \text{ m}$) is not critical. An improved automatic control system [16,17] will reduce the residual deviations down to acceptable values.

In a simulator campaign, the deviation from the ideal thrust or specific excess power has been displayed to the pilots. Figure 23 and 24 show the response in a low level jet. As expected, no deviation occurs with ideal thrust command. In contrast to this ideal thrust response, both pilots produced a time delay of approximately ten seconds. Even under this circumstances, the airspeed and flight path deviations are still moderate.

Application problems of the ideal thrust control appear in Fig. 25 and 26. Busy wind profiles produce non acceptable throttle activity, that has to be avoided by the following reasons:

- thrust variations are coupled with engine revolution speed variations. This produces noise variations, that may bother inexperienced passengers who expect an engine failure. Additionally the cabin pressure will change with frequent thrust variation that can not be controlled properly by the cabin pressure controller. This additional pressure variation will strike the passengers with fear.
- experienced pilots use the throttle rarely but precise. Pilot students vary the throttle more frequently. The beginner like behaviour of the active automatic throttle control system is very unpleasant for experienced pilots.
- besides these psychological reasons the reduction of engine life time by frequent throttle variation plays a less important role.

From this report we may learn, that thrust should then and only then be varied if necessary. Thrust variation causes

primarily total energy changes. As frequent energy variations are meaningless in general, we should ask for low throttle activity that can be handled without delay. With the assistance of complementary filtering this problem can be solved significantly [17].

As the dynamic response of jet engines is said to be slow, the undelayed thrust variation is still called in question. The thrust step response of a fan engine is demonstrated in Fig. 27. The engine can vary the thrust from idle to maximum thrust in eight seconds. If we increase the thrust only by a smaller increment, e.g. from 50% to 75% the time constant is significantly reduced down to 0.7 s. For an adequate go around manoeuvre the minimum accepted thrust level will produce a sufficient quick engine response. On the other hand we have discussed that a delay time of 10 seconds of an autothrottle control system (Fig. 22) can be tolerated. Summarizing we can state, that engine dynamic is not a limiting factor for wind shear response alleviation. The phase diagram (thrust rate versus thrust) of a fan engine is presented in Fig. 28 for thrust rate and thrust limitations. Additionally the ideal thrust (see Equ. 12a) for an approach in the critical New York downburst (Fig. 20, 21) has been calculated and demonstrated in Fig. 28. Neither the limits for the maximum thrust nor for the maximum thrust rate will be touched. Even if these constraints would be touched for 10 or 20 seconds, the consequences for airspeed and flight path deviation would be small. This example demonstrates that with a correct thrust control the accident in New York could have been avoided.

6. WIND SHEAR WARNING INFORMATION

Previous discussions have shown, that proper control of throttle and control stick during approach and landing in wind shear can avoid accidents. Investigations of more than 20 accidents gave the same result, except one in a low level yet in the Soviet Union the flight performance was the limiting factor [3]. In contrast to the landing approach a take off in a strong wind shear is always extremely dangerous. The pilot has no information concerning the undisturbed flight path. In a wind shear encounter the flight path angle should be as low as possible and before touching the ground the airspeed should be reduced down to the stall speed.

In general only larger transport aircraft are involved in wind shear accidents. These aircrafts are well equipped with excellent cockpit instrumentations. In principle the pilot has all the necessary information available to respond in a correct manner. The question is still not answered why pilots do not react correctly or if they can, handle correctly. I assume that pilots are not able to filter the relevant informations out of the large amount of available data, or they have problems of adequate interpretation.

Additionally some correct procedures contradict the pilots feeling, e.g. speed reduction in a downburst and at the same time pull up and throttle setting to maintain the flight path. Events have been reported where the pilot had switched off the automatic flight control system in a wind shear situation. The pilot misinterpreted the correct response of the flight control system as a system failure. The switch over from an automatic to manual control in very dangerous meteorological situations may cause accidents in general. These remarks may demonstrate, that the pilots trust in the correct response of the automatic control system is very important for flight safety. So reliable control systems and intensive training are required. Additionally the pilot should be informed in a critical situation with all relevant information, which have to be displayed in an adequate manner. It should be noticed that miswarnings can destroy the basis for good will quickly.

In this paper some aspects could be presented about the information which is required by the pilot, in order to respond correctly in wind shear to supervise the correct action of the automatic flight control system. The main information concerns the flight path deviation. This is available as a standard for an instrument landing approach in the cross pointer instrument or the "flight director". For good visual ranges the risk exists that the pilot switches over from instrument to visual flight too early. The critical height range is between 120 m and 80 m. Additionally the pilot needs a display of the energy situation. For small energy deficits (20 m) no response of the pilot is necessary to act the throttle. For greater energy deficits an immediate thrust control is required, even if the passenger comfort may be disturbed for a short period. If there is a need for throttle activity, the display of the required thrust change, e.g. the change of specific excess power, is helpful. The display for energy and energy rate must be placed in a central position of the instrument panel to enable a scanning of the displays more frequently than every five seconds.

The concept of displaying airspeed based on energy and energy rate [5] (chapter 5) has been tested in a moving cockpit simulator by a joint team of the Bodenseewerk Gerätetechnik, the Deutsche Forschungs- und Versuchsanstalt

für Luft- und Raumfahrt (DLR) and the Technical University Braunschweig. This research was sponsored by the German Ministry of Transportation (BMV) [18]. Fourteen airline pilots flew approaches in different wind shear and turbulence situations. The downburst that caused the crash of the B 727 in New York in 1975 created the severest difficulties although gradients, energy variations and requested flight performances could be said moderate. All of the fourteen pilots caused a crash in the simulator in this downburst. In Figure 29 the approach passing the downburst has been demonstrated. In this simulator campaign, the energy deficit has been displayed in a modified fast slow indicator of the flight director. This specific excess power has been indicated in an additional pointer in the vertical speed indicator.

Before entering the downburst the aircraft is in a trimmed flight condition on the glide path (phase A in Fig. 29). In phase B the downdraft causes despite an increasing headwind a loss of power (dotted pointer in the vertical speed indicator). The total energy condition (modified fast slow indicator) is still comfortable and no pilot response is required. When passing the eddy layer into the core of the downburst, the immense increasing headwind leads to a surplus of energy and a moderate overshoot of the flight path (phase C). An attentive pilot would reduce thrust now. Shortly after the aircraft achieves the core of the downburst, the indicated loss of power is dramatically indeed, but the energy condition is still balanced. Only seconds later (phase D) the immense loss of power worsened the energy condition drastically. Now an immediate action (maximum thrust, go around) is demanded. Certainly many pilots have problems, shortly after the decision to reduce the thrust to revise this decision. The tricky sequence of power variation as well as the relative small deviations in airspeed and flight path in phase E hinder the pilot with a conventional cockpit instrumentation to identify the situation and handle correctly. With the assistance of the displayed energy and power deficit indicator, ten of the fourteen pilots were able to arrange a safe go around (Fig. 20 and 21). The question why four pilots did not follow the advice of the indicator and caused a simulator crash is still not answered. Probably the unfavourable position of the indicators plays an important role. The fast slow indicator has a relative small size and the vertical speed indicator is placed outside the pilots central range of vision and had been scanned in the experiments only every seven seconds. The wind shear problem is more or less a man machine interface problem. It appears difficult to supply the pilot with another information in view of the great burden of control task he has in a landing approach. The question arises whether to install additional instruments or to modify already existing displays. This is more or less a question of philosophy, that is certainly going to answer itself, when new or modified instruments fulfill the one demand, only warn the pilot when it is necessary, and that will give him appropriate guidance when he needs it.

So the main results of the simulator studies are as follows:

- pilots (both well or less experienced) are not able to make a safe landing under severe wind shear conditions without additional support of an automatic flight control system or an adequate wind shear warning display;
- sufficient display quality is required to persuade the pilot to response in the correct manner
- if there is enough training available, pilots can adapt themselves to specific wind shear profiles. It is therefore necessary to expose the pilot to different wind shear situations. A general ground based wind shear warning is worthwhile but not sufficient;
- an adequate wind shear warning display can support the pilot in the most severe wind shear situations.

7. CONCLUSIONS

Wind shear during take-off, go around and missed approach is a pure flight performance problem. Pilots should avoid to take off into thunderstorms. Moderate wind shear induced by orographic lee effects can be overcome by increasing the thrust to weight ratio, especially in engine failure conditions. In unexpected dangerous situations the pilot is advised to reduce the airspeed safety margin in order to increase the obstacle clearance. Wind shear accidents during landing and approach could generally be avoided if the pilot keeps the automatic flight control systems in operation and if he is informed by an adequate wind shear warning display. Wind shear is particularly dangerous if it occurs in a height of approximately 80 - 120 m.

A ground based wind shear warning is worthwhile but not sufficient. Measuring the gradients is still a problem. Significant is the energy and energy rate and this will be varied by combinations of different gradients and the

downdraft. The efficiency of the gradients differ very much. Small gradients can be overcome by sufficient control. A major parameter of influence is the airspeed, as the aircraft creates the windvariation only when passing a windfield. In contrast to the general opinion, a higher airspeed may increase the unfavourable wind shear situation. Pilots should be advised to keep the preselected flight path as precise as possible.

REFERENCES

- [1] Schänzer, G. Abschätzung von stochastischen Risiken unter Berücksichtigung in-
stationärer Luftkräfte
Z. Flugwiss. Weltraumforsch. 9 (1985) Heft 3, S. 167 - 178
- [2] Swolinsky, M. Beiträge zur Modellierung von Scherwind für Gefährdungsuntersau-
chungen
Thesis, Techn. University Braunschweig, 1986
- [3] Swolinsky, M. Wind Shear Models for Aircraft Hazard Investigation
2nd International Symposium on Aviation safety 18. - 21. Nov. 1986,
Toulouse
- [4] Hadner, J. Low level Wind Shear: A Critical Review NOAA Techn. Memor. NWS
FCST - 23
National Oceanic and Atmospheric Administration Silver Spring, Md.,
Apr. 1979
- [5] König, R.
Krauspe, P.
Schänzer, G. Procedures to Improve Flight Safety in Wind Shear Conditions .
Proceedings of the 12th Congress of the Aeronautical Sciences, Mu-
nich, Germany, Oct. 1980
- [6] Swolinsky, M.
Krauspe, P. Windbestimmung aus Flugmeßdaten eines Linienflugzeuges.
Meteorologische Rundschau
- [7] Hahn, K.-U. Take-off flight path along the lee side of a flat mountain ridge under
flight safety aspects.
2nd International Symposium on Aviation Safety 18. - 21. Nov. 1986,
Toulouse
- [8] König, R.
Krauspe, P. The Influence of Wind Shear and Vertical Winds on Take-off and
Go-around.
Airport Forum Nr. 5/1981
- [9] Schänzer, G. Dynamic Energy Transfer between Wind and Aircraft.
Proceedings of the 13th Congress of the International Council of the
Aeronautical Sciences, Seattle 1982, Paper Nr. ICAS 82-3.4.1.
- [10] Krauspe, P. Beiträge zur Längsbewegung von Flugzeugen in Windscherungen.
Thesis, Techn. University Braunschweig 1983
- [11] - Aircraft Accident Report - Continental Air Lines, Boeing 727 - 224,
N88777, Stapleton International Airport, Denver, Colorado, 5. August
1975
National Transportation Safety Board, NTSB - AAR - 76 - 14, May
1976
- [12] Hahn, K.-U. Beiträge zur Flugleistungsbestimmung beim Startsteigflug unter Be-
rücksichtigung variabler Windinflüsse
Thesis, Techn. University Braunschweig, 1988

$$\sin \alpha_w = -\frac{w w_E}{V} \cos \gamma - \frac{u w_E}{V} \sin \gamma \quad (A2)$$

$$\alpha_w = \alpha + \gamma = 0 \quad (A3)$$

$$\dot{h} = V_E \sin \gamma$$

For small angles, that are usual in transport aircraft Equ. (A2) and Equ. (A1) can be simplified to

$$\alpha_w = -\frac{w w_E}{V} - \frac{u w_E}{V} \gamma \quad (A2.1)$$

$$V_E = V + V_w \quad (A1.1)$$

A2 AIRCRAFT EQUATION OF MOTION

The basic forces as lift L , drag D , thrust T and weight W are defined in Fig. (A2)

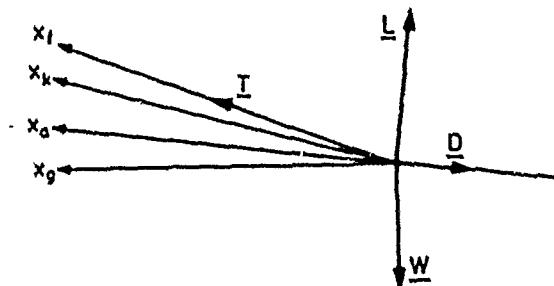


Fig. A2 : Forces action on an aircraft

For small angles we get the component equations parallel and perpendicular to the flight path

$$m \cdot \dot{V}_E = T + L \cdot \alpha_w - D - W \cdot \gamma \quad (A5)$$

$$m \cdot \dot{h} = L - W \quad (A6)$$

With definition of the energy height

$$H_E = \frac{V_E^2}{2g} + h \quad (A7)$$

we derive the specific excess power

$$\dot{H}_E = \frac{dH_E}{dt} = \frac{V_E \cdot \dot{V}_E}{g} + \dot{h} \quad (A8)$$

and the total energy angle

$$\gamma_E = \frac{\dot{H}_E}{V_E} = \frac{\dot{V}_E}{g} + \gamma \quad (A9)$$

- [13] - Aircraft Accident Report - Eastern Air lines Inc. Boeing 727 - 225 N884SE, John F. Kennedy International Airport, New York, June 24th, 1975;
National Transportation Safety Board NTSB-AAR-76-8, March 1976
- [14] Fujita, Th. Spearhead Echo Downburst near the Approach End of John F. Kennedy Airport Runway,
New York City, The University of Chicago, Department of the Geophysical Sciences, SMRP-Paper 137, March 1976.
- [15] Schänzer, G. The Effect of Gust and Wind Shear for Automatic STOL Approach and Landing.
AGARD Conference Proceedings CP 140, "Flight in Turbulence", Bedfordshire 1973.
- [16] Schänzer, G. Design Criteria for Multi-Loop Flight Control Systems,
AGARD, 42nd Guidance and Control Panel Symposium, Brussels, June 1986
- [17] Rejzker, A. Real Time Processing and Display,
AGARD Flight Mechanics Panel Symposium, Aircraft Testing Techniques, Edwards, California
- [18] - Untersuchung technischer Möglichkeiten zur Erhöhung der Sicherheit bei Scherwindanflügen.
Bundesministerium für Verkehr, BMV, L-5/79, Bonn, März 1983

APPENDIX

SIMPLIFIED EQUATION OF THE AIRCRAFT MOTION IN A WINDFIELD

A1 VELOCITY VECTOR GEOMETRIE

The aircraft moves with the airspeed \underline{V} relative to atmosphere. The atmosphere itself moves with windspeed \underline{V}_w relative to the earth surface. The flight path speed \underline{V}_K (ground speed) is the sum of airspeed and windspeed

$$\underline{V}_K = \underline{V} + \underline{V}_w \quad (A1)$$

This vector equation is demonstrated in Fig. (A.1) for a symmetrical flight (vector plain is perpendicular to the horizon).

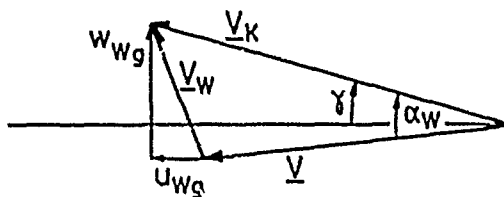


Fig. A1: Wind speed vectors

The important wind angle α_w is as well a function of the horizontal and vertical wind speed components u_w , w_w , as of the flight path angle γ . From Fig. A 1 we get

7.14

Introducing the load factor

$$n = 1 + \frac{H}{k} \quad (A10)$$

we get from Equ. A.5 and A.6

$$\frac{\dot{V}_s}{k} = \frac{T}{W} - n \cdot \frac{C_0}{C_L} + n \cdot \alpha_v - \gamma \quad (A11)$$

or

$$\gamma_L = \frac{T}{W} - n \cdot \frac{C_0}{C_L} + n \cdot \alpha_v \quad (A11.1)$$

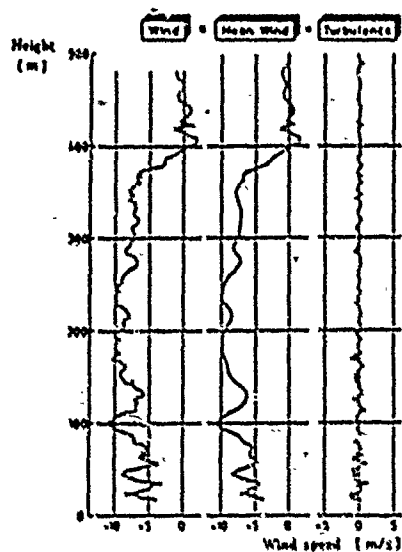


Fig. 1: Separation of turbulence and wind shear measured on board

AIRPORT: BREMEN
DATE: 22.10.80
TIME: 18:22 GMT
RUNWAY: 108
SURFACE WIND: 12.5 m/s / 130°

- METAR, Bremen airport
- NEW tower, Marnes (SIS) GMT
- NEW tower, Stade

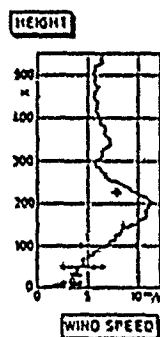


Fig. 4: Low level jet

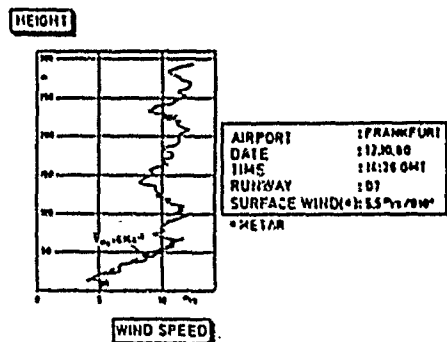


Fig. 6: Surface boundary layer wind shear with separated eddies

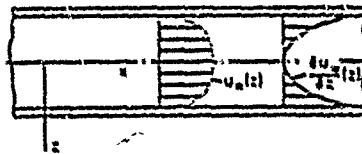


Fig. 2: Viscous flow in a channel

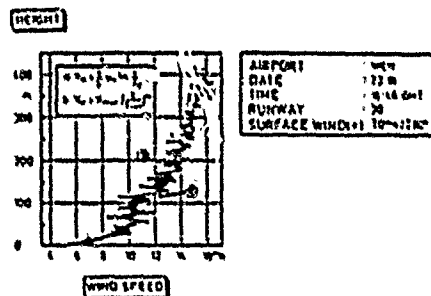


Fig. 3: Surface boundary layer wind shear

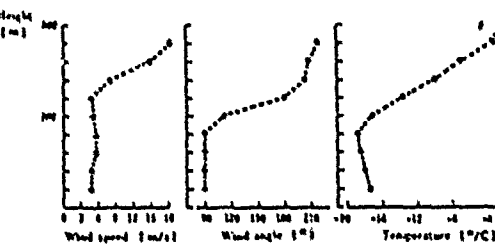
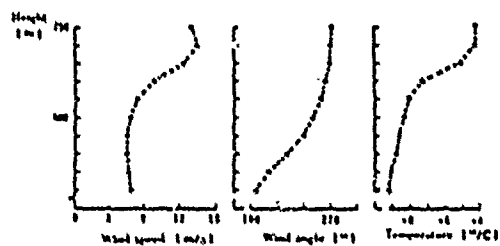


Fig. 5: Wind and temperature in the flow field of a front

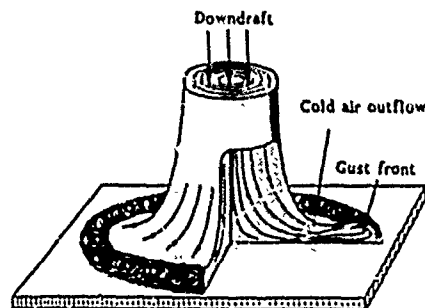


Fig. 7: Model of the flow field in a downburst

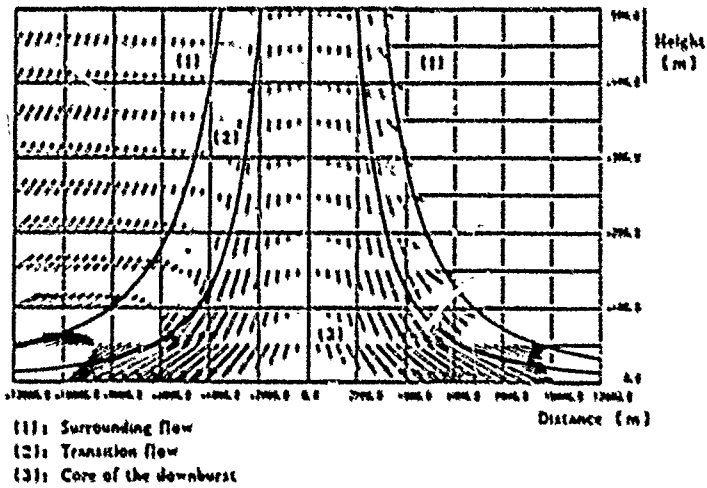


Fig. 8: Mathematical model of a downburst

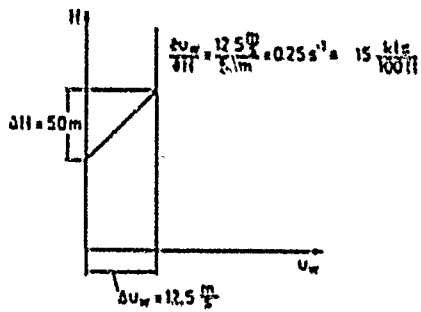


Fig. 9: Simple wind shear model

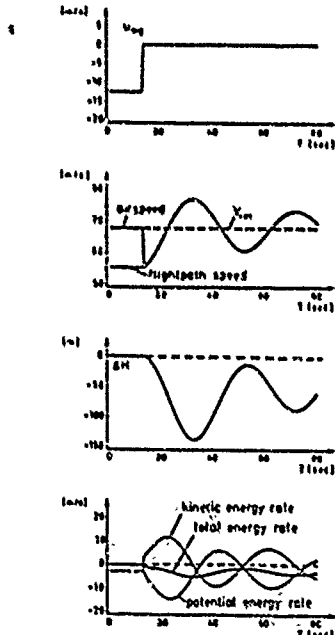
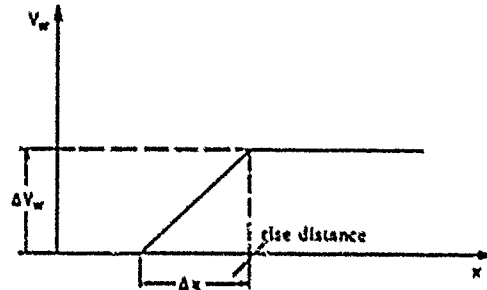
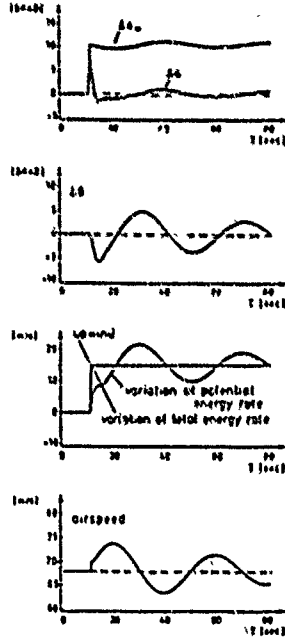
Fig. 10: Aircraft response due to a horizontal gust (rise distance $\Delta x = 30m$)

Fig. 9a: Wind variation as a ramp function

Fig. 11: Aircraft response due to a vertical gust (rise distance $\Delta x = 30m$)

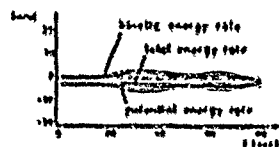
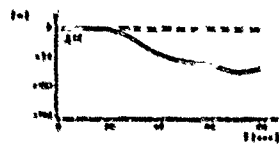
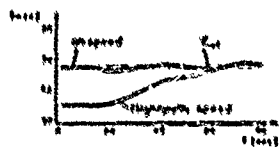
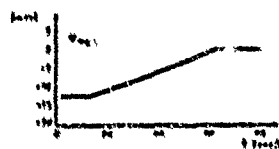


Fig. 12a: Aircraft response in a horizontal wind shear (rise distance $\Delta x = 3000\text{m}$)

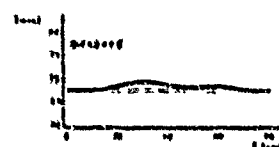
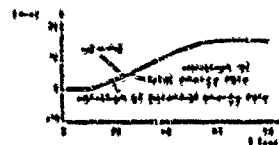
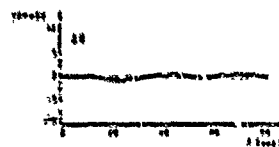


Fig. 12e: Aircraft response in a vertical wind shear (rise distance $\Delta x = 3000\text{m}$)

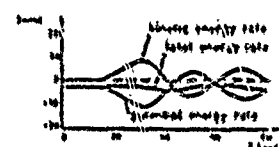
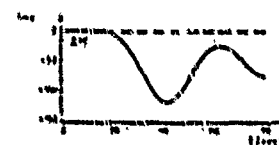
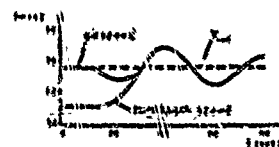
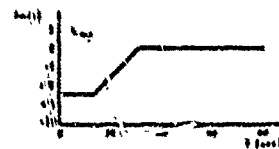


Fig. 12i: Aircraft response in a horizontal wind shear (rise distance $\Delta x = 1000\text{m}$)

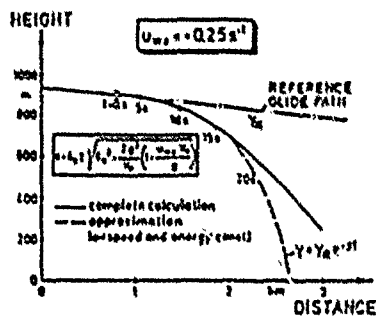


Fig. 13: Flight path of an aircraft with fixed controls in a constant vertical wind shear gradient

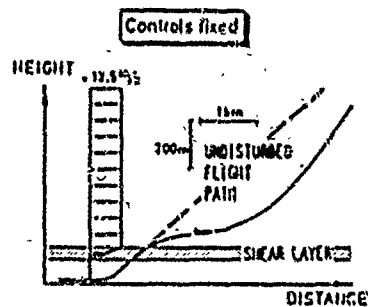


Fig. 15: Take off flight path in tailwind shear, controls fixed

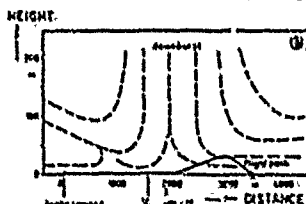


Fig. 16: Analysis of wind shear effect in an aircraft take-off accident:
a. Horizontal wind component along the flight path
b. Reconstructed waves of windstream flow and aircraft flight path

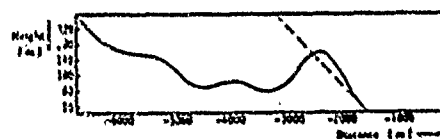


Fig. 17: Take off in a downburst (simulator run)

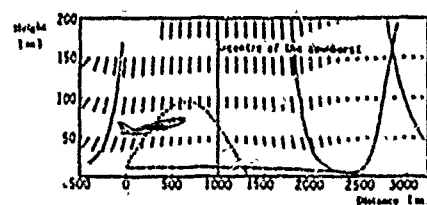


Fig. 18: Escape manoeuvre in a downburst

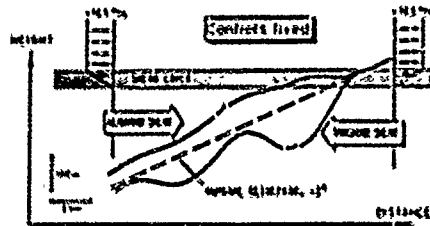


Fig. 19: Landing approaches in headwind / tailwind shear (fixed controls)

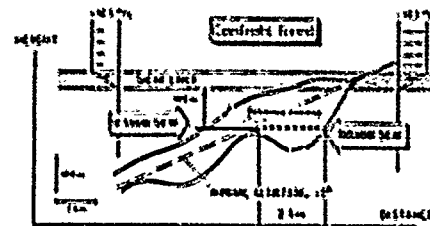


Fig. 19a: Landing approaches in headwind / tailwind shear with a fictitious runway (fixed controls)

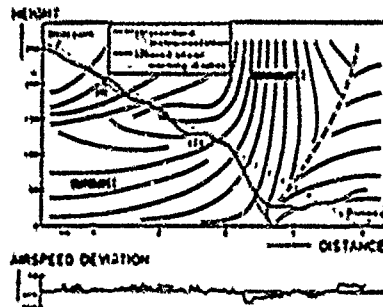


Fig. 20: Flight simulator approach in wind shear conditions, experienced airline pilot

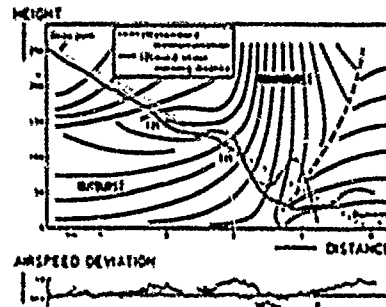


Fig. 21: Flight simulator approach in wind shear conditions, less experienced airline pilot

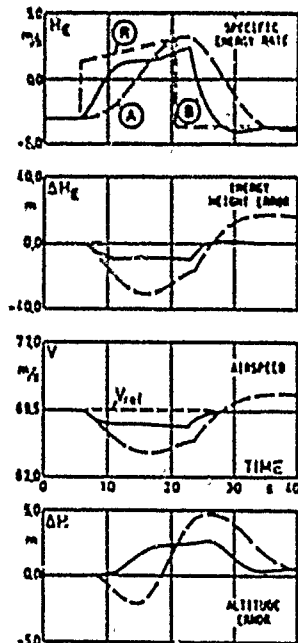


Fig. 22: Effects on flight control activity in linear tailwind shear
R: Required specific energy rate
A: Conventional automatic flight controls
B: Specific energy rate management

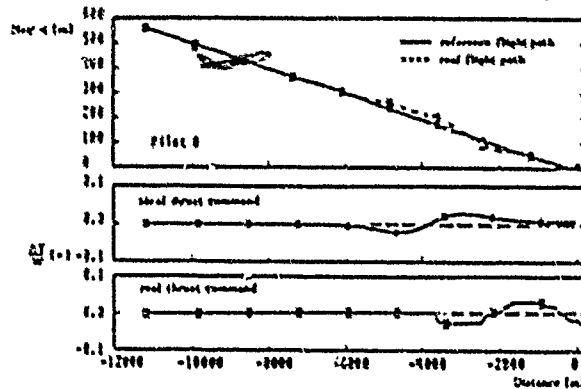


Fig. 23: Landing approach in a low level jet (Pilot A)

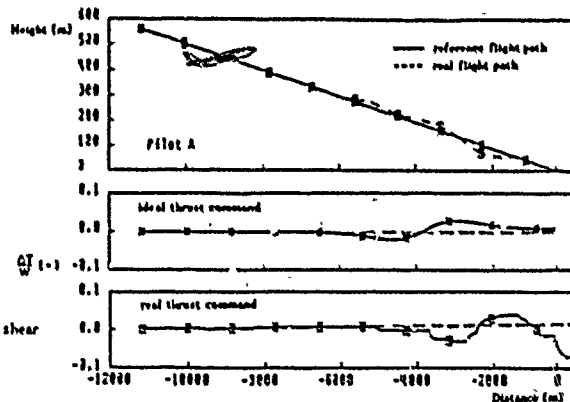


Fig. 24: Landing approach in a low level jet (Pilot B)

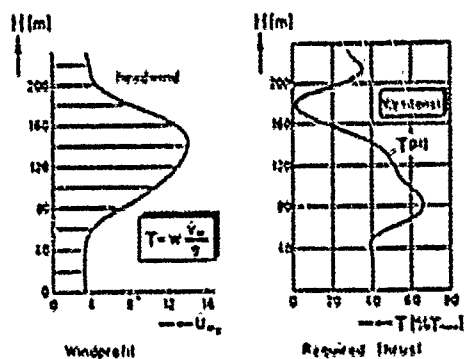


Fig. 25: Wind profiles and required thrust

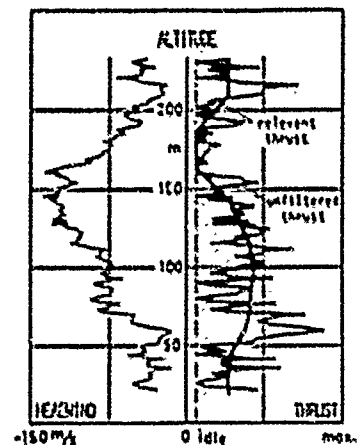


Fig. 26: Measured wind profile and commanded thrust

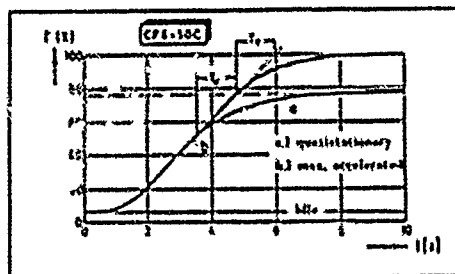
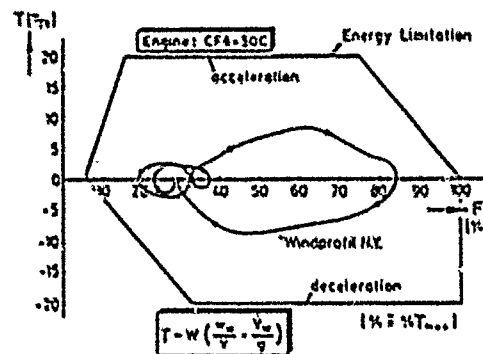
Fig. 27: Step response of a jet engine for
a.) small
b.) great thrust variations

Fig. 28: Required thrust and thrust rate

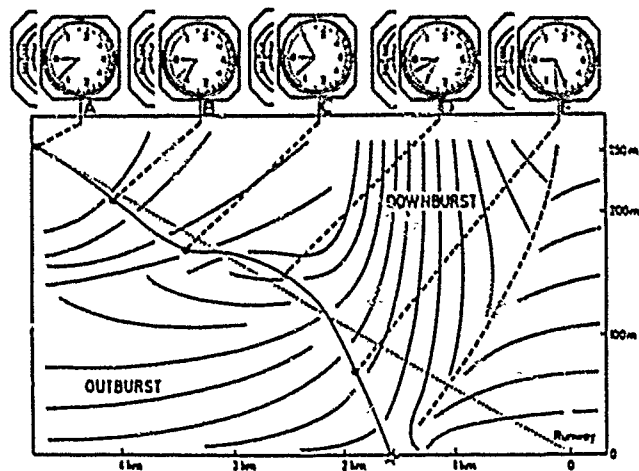


Fig. 29: Energy and energy rate display for a landing approach in a downburst

CLASSIFICATION OF WIND SHEAR SEVERITY

by

A A Woodfield
Royal Aerospace Establishment
Bedford, MK41 6AE
United Kingdom

SUMMARY

A simplified model of aircraft and pilot response to wind shear is used to identify the potential height loss during wind shear encounters. This potential height loss is directly related to the possibility of unscheduled ground contact and is proposed as a primary indicator of wind shear severity. Key factors of wind shear strength and aircraft performance which influence the potential height loss are identified using this simple model. This helps to provide a better understanding of the complex interactions between the pilot/aircraft and the wind shear.

Various practical severity factors are examined in relation to both the potential height loss and the probability of encountering various shears. It is shown that severity factors based on pseudo Energy Rate have fundamental problems in resolving the conflict between false alarms and providing timely information to a pilot, when used with current sensors on aircraft or sensors that scan and probe (such as Doppler Radar or Laser). An improved severity factor based on the potential height loss analysis is shown to have a low risk of false or missed alarms, and appropriate threshold values are easily identified for all aircraft types. This improved severity factor requires probe and scan sensors.

1 INTRODUCTION

Wind shear is a phenomenon which has resulted in several major aircraft accidents and loss of lives. It can be defined in general terms as —

'any change of wind or updraught causing a change of flight path that requires significant pilot action for recovery'

The words 'changes of wind' are particularly significant as steady winds or changes in aircraft direction do not produce wind shear.

These significant changes of wind in wind shear are part of the wide spectrum of wind variations from Turbulence through Wind Shear to Weather. In aviation terms these can be classified as —

Turbulence

Disturbances which require little or no pilot action to maintain the desired flight path within acceptable limits. Generally short duration events, typically, less than 3sec.

Wind Shear

Disturbances requiring significant pilot action to maintain flight path within acceptable limits. Generally events between about 3sec and 40sec in length.

Weather

Long term and large scale events with little effect on flight path.

Within this wide spectrum there are all possible combinations of size of wind change and length (time or distance). For practical application of wind shear measurements in aviation it is essential to find factors (Wind Shear Severity Factors) that directly relate the wind shear characteristics of wind change and length to the potential hazard for particular aircraft or classes of aircraft. It is also important that such factors should be easy to identify during the onset of a wind shear encounter by sensors on an aircraft so as to provide information to the pilot in a timely manner. Finally the information must be clearly and simply related to an aircraft's response capability, ie the pilot must be able to take immediate action of the appropriate magnitude without further assessment or calculation.

In addition to these practical application issues, it is also important that the severity factor and sensor systems should not generate many false alarms, nor seriously underestimate severity (at least not within the range of probable wind shears).

To evaluate proposals for Wind Shear Severity factors, it is necessary to have a measure of the potential disturbance to aircraft from any wind shear, and, also, knowledge of the probability of encountering these wind shears. Probabilities are well defined for Headwind shears in Ref 1, where nearly 10000 landing approaches are analysed from worldwide operations. The evaluation of potential disturbances is considered in this paper.

The method developed to evaluate potential disturbances provides a basis for better understanding of the importance of various wind shear and aircraft performance parameters. Then, finally, some wind shear severity factors are studied in the light of potential disturbances and probabilities of encounter.

2 ESTIMATION OF POTENTIAL DISTURBANCE

Among various measures that could quantify the severity of the effect of wind shear on an aircraft, there is little doubt that loss of height relative to the desired flight path is the most important. It is loss of height that determines whether or not there will be an unscheduled contact with ground. This paper considers height loss produced by wind shear as a direct measure of its severity.

In general wind shear duration will be many seconds, or even tens of seconds, and there is time for pilots to take action to counter the effects of the wind shear. Thus any estimate of height loss must include the effects of pilot actions to make corrective manoeuvres such as adding power and pulling up. In addition the time scale is also long enough to take into account normal stabilising control inputs from the pilot (or autopilot). Indeed it is essential that these stabilising inputs are included because the natural response of aircraft includes an almost neutrally stable long period oscillatory speed and flight path response mode (the Phugoid) Ref 2, which is easily stabilised by controlling pitch attitude. With pitch stabilisation (automatic or manual) the natural modes are changed to a very stable non-oscillatory flight path mode with a time constant of 1-2sec, and, at normal approach and take off conditions, an almost neutral non-oscillatory speed mode. (This speed mode is neutrally stable at minimum drag speed).

Several studies have illustrated the difference between stick-fixed and controlled flight through wind shear (Refs 3 & 4 are examples). They all clearly show large Phugoid oscillations when controls are fixed. These oscillations are almost completely absent when pitch control is used, although there are still flight path deviations related to the wind shear. It is clear that any estimates of wind shear effects on flight path must include pitch stabilisation.

Because pitch stabilisation results in almost neutral speed stability and a rapid response flight path mode it is possible to produce a simple and yet close approximation to an aircraft's response to wind shear by assuming —

- constant pitch attitude, ie perfect pitch stabilisation
- neutral speed stability, ie ground speed only varies in response to engine thrust changes and not in response to changes in headwind
- instant flight path response, or more rigorously that shear duration is long compared with the flight path response time constant of 1-2sec.

Using this approximation has the major advantage of providing direct insight into the factors influencing height response to wind shears of all kinds. The following sub-sections study the height response to headwind shears and up/down draughts respectively.

The influence of delays in pilot recognition and response to the shear, and in engine thrust response to throttle inputs are included in the studies.

2.1 Potential height loss because of Headwind shear

Consider the height loss, Fig 1 caused by a Headwind shear of ΔV s over T_s seconds of flight at an initial ground speed of V_i when the pilot applies a step throttle input demanding an aircraft acceleration of A at a time T_a seconds after the start of the shear. The engine has a first order response of thrust to throttle with a time constant of τ

In the Appendix, it is shown that

$$\frac{H}{L_s C_L} = \int_0^{T_s} r \left(\frac{\Delta V}{\Delta V_s} \right) d \left(\frac{t}{T_s} \right)$$

$$\text{where } r \left(\frac{\Delta V}{\Delta V_s} \right) = \left(\frac{\Delta V}{\Delta V_s} \right) \left(\frac{2}{\Delta V_s \sqrt{t}} + \frac{\Delta V}{\Delta V_s} \right) / \left(\frac{1}{\Delta V_s \sqrt{t}} + \frac{\Delta V}{\Delta V_s} \right)^2 \quad \text{---(10)}$$

ΔV = Airspeed change at time 't'

T_s = Time when $\Delta V = 0$, $t \neq 0$

a = Lift curve slope per radian

C_L = Lift coefficient at $t = 0$, $C_L = \frac{m \cdot g}{0.5 \cdot \rho \cdot V_i^2 \cdot S}$

m = aircraft mass

g = gravitational acceleration

ρ = air density

V_i = airspeed (= initial groundspeed)

S = reference wing area

L_s = Wind shear duration distance, $V_i \cdot T_s$

H = Height increase

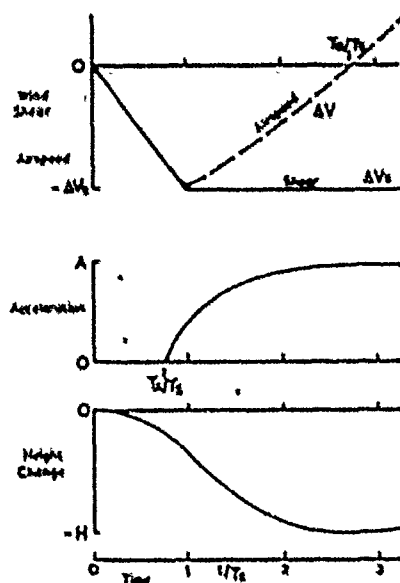


Fig. 1 Headwind Shear-Response

$$\text{and } \frac{\Delta V}{\Delta V_s} = f_1 \left(\frac{t}{T_s} \right) + \frac{f_2 (V/T_s)}{(\Delta V_s/A \cdot T_s)} - \frac{(V/T_s)}{\Delta V_s/A \cdot T_s} (1 - e^{-A/V T_s (V/T_s)})$$

$$\text{where IF } V/T_s < 1.0, \text{ THEN } f_1 \left(\frac{t}{T_s} \right) \approx \frac{t}{T_s}, \text{ ELSE } f_1 \left(\frac{t}{T_s} \right) \approx 1.0$$

$$\text{and IF } V/T_s > T_s/T_s, \text{ THEN } f_2 \left(\frac{t}{T_s} \right) \approx \frac{t}{T_s} - \frac{T_s}{T_s}, \text{ ELSE } f_2 \left(\frac{t}{T_s} \right) \approx 0$$

It should be noted that the relationships are non-linear functions of $(\Delta V/\Delta V_s)$ which means that for a given change of airspeed relative to V_t there is a much greater rate of descent for an airspeed decrease than there is rate of climb for the same airspeed increase, eg a -20% change produces a rate of descent 1.84 times larger than the rate of climb from +20%. This means that there will be a net loss of height in penetrating a symmetrical microburst (ie with equal headwind and tailwind changes) if a pilot takes no corrective action.

It is informative to study the influence of the various parameters on the non-dimensional potential height change function

$$I(H) = \frac{H}{L_s} \frac{a}{C_L}$$

This function could imply that the potential height loss, H , will be proportional to Lift Coefficient, ie it will reduce if an aircraft increases its flight speed. However, flight speed is also implicit in all the other non-dimensional parameters and it is not possible to deduce a simple effect from flight speed in response to Headwind shears.

First consider the effects of varying each of the three non-dimensional constants in turn with the other two held fixed. Fig 2 shows the contours of $I(H)$ while varying the Shear Gradient to Aircraft Acceleration ratio. Because of the complexity of the ratios it is not easy to interpret these contours (the solid lines). However it is straightforward to construct contours of constant shear length and airspeed and these (the dashed lines) show clearly that, height loss increases approximately as the square of the wind shear speed change and inversely as the square of the aircraft acceleration.

This demonstrates how the effects of shear increase dramatically (as the square of the wind shear speed change). This helps to account for some of the apparently large differences in response between competitive aircraft encountering shears on a landing approach which should not have increased greatly during the few minutes between each encounter. It also indicates why wind shear is not such a problem with high performance military aircraft as these usually have much more acceleration available than civil aircraft.

The effects of engine response time constant, Fig 3a, and of pilot action delay, Fig 3b, are much less significant than the shear and acceleration terms in Fig 2 (note that the scale of $I(H)$ is the same in all these Figs). The changes are almost linear in Fig 3 and the relatively gentle increases mean that any studies will not be particularly sensitive to the choice of engine or pilot

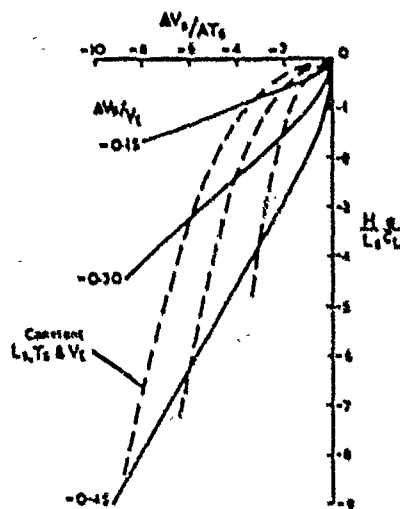
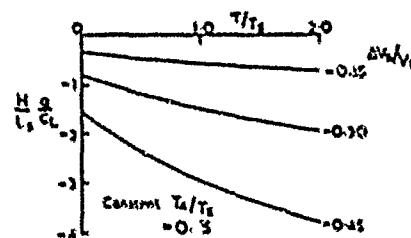
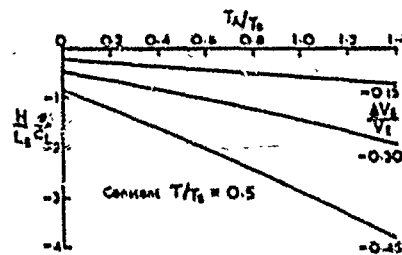


Fig. 2 Variation of H with ΔV_s at constant $T_A/T_s = 0.75$ & $\tau/T_s = 0.5$



a. H variation with T



b. H variation with T_A

Fig. 3 Variation of H with T and T_A at constant $\Delta V_s/AT_s = -1.5$

response. It is worth noting that there is a height loss at zero pilot response time in Fig 3b because the shear gradient is greater than the aircraft acceleration in this example.

To study other aspects of response to wind shear it is helpful to construct a graphical base relating wind shear gradient, $\Delta V_s/T_s$, and the ratio of the wind shear speed change to aircraft speed. Such a form is presented in Fig 4. The basic dimensions are all powers of acceleration and the axes relate two key wind shear parameters to aircraft speed. At constant airspeed, the horizontal axis is Shear Length and the vertical axis is a Wind Shear function,

$$\Delta V_s / [L_s \cdot V_t^{1/2}]$$

which relates directly to the probability of encounter, Ref 1. The shear gradient and speed ratio both relate directly to aircraft performance characteristics. For example, aircraft are required to have specific acceleration capabilities in approach and take-off configurations to cope with engine failure. This means that most aircraft have around 1 to 1.5m/s² acceleration available (NB 1m/s is approximately 2 knots). The other parameter of speed ratio relates directly to the ratio between the aircraft's speed

and its stall speed, which is usually about 1.2 on the approach and about 1.3 at normal climb speed. It should be noted that, although a shear speed ratio of 0.3 could imply that an aircraft would stall, the pilot's reactions with the throttle will reduce the actual loss of speed except for very short shear lengths. It is interesting to note also that the Wind Shear function is a product of shear gradient and the square of shear speed ratio, which reflects the joint importance of these two parameters. This Wind Shear function was suggested as a wind shear severity measure in Ref 1. Finally, as observed in Ref 1, in the limit it would be expected that severity would be almost entirely dependent on the speed change ratio when shear gradient is significantly greater than the acceleration available to the aircraft, ie at a short shear lengths, and severity would be almost entirely dependent on shear gradient when that is less than the aircraft acceleration, ie at long shear lengths.

Returning to the potential height change estimates, it is possible to add contours of a H height function, also in acceleration dimensions, to the graph for any fixed value of aircraft acceleration. Fig 5 shows such contours for an acceleration of 1 m/s^2 . (NB as the H height function varies very nearly as the inverse of the square of acceleration, it is easy to convert contours to other acceleration levels, eg at an acceleration of 1.4 m/s^2 the height function contour values will be halved). It is immediately noticeable in Fig 5 that the contours tend to be parallel to speed ratio at short shear lengths and parallel to shear gradient at large lengths as predicted in the previous paragraph.

A further important feature identified is that height is proportional to $V_i^2 C_L$ as the lift curve slope 'a' varies little between aircraft types. Now $V_i^2 C_L$ is directly proportional to Wing Loading and, thus, Height loss is directly proportional to Wing loading. This shows that the trends over the years towards higher wing-loading for transport aircraft have increased susceptibility to wind shear, and helps to explain why wind shear accidents have appeared as a modern phenomenon. (Improved accident recorder systems have also helped to identify wind shear where it might have gone undetected in the past). It also means that classification of different aircraft in terms of susceptibility to wind shear will be a simple function of Wing Loading and Available Acceleration.

Fig 5 also indicates that the effects of increasing flight speed for a given aircraft, ie at constant Wing Loading, and given wind shear, ie constant ΔV s and L_s , will be more height loss at long shear lengths and slightly less height loss at short shear lengths. This is not unexpected as increasing flight speed will increase the shear gradient, which is the most critical factor at long shear lengths. At short shear lengths the wind change is most important (and unchanged), which means that some relief can be gained from the shorter duration of the wind shear event.

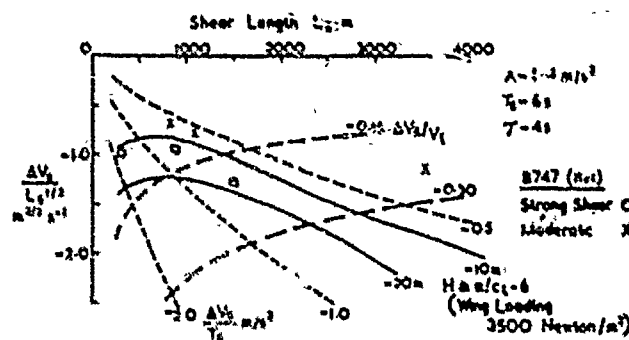


Fig. 6 Potential Height Loss and Headwind Shear at $V_t=75$ m/s

Taking specific examples will illustrate the height change contours. The first example, Fig 6, is for a V_t of 75 m/s (about 150 knot), an a/c_L of 6, an engine response time constant of 4s, and a pilot's response delay of 6s. These figures correspond to a wing loading of about 3500 Newton/m² (70 psf) and would be typical of a B747 type of aircraft. An acceleration of 1.4 m/s² is taken as being representative for a B747; but height loss values may easily be scaled for other cases. Also included on Fig 6 are the larger shear cases measured by Tel 1 where analysis of nearly 10000 landings by British Airways B747 aircraft throughout the world provided probability statistics for wind shear encounters and several examples of moderate and strong shears. These data suggest that the -10m contour could be an appropriate boundary between moderate and strong shears. The strong shear at around 1500m L_s was close to an accident axis, thus, the -20m contour could be suitable for the boundary between strong and severe shears.

In Fig 7 a case at a lower Wing loading is shown. All the parameters are the same except for V_t which is reduced to 55 m/s, which is equivalent to a Wing loading of about 1900 Newton/m² (40 psf). The scales in Fig 7 are the same as Fig 6 and show that the height change contours peak at a shorter shear length and a greater shear strength is needed to cause the same height loss. The contours for the two wing loadings are compared in Fig 8.

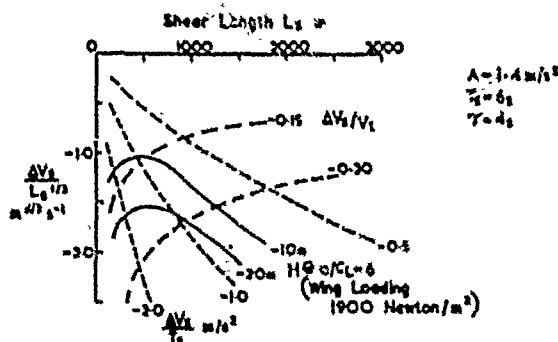


Fig. 7 Potential Height Loss and Headwind Shear at $V_t=55$ m/s

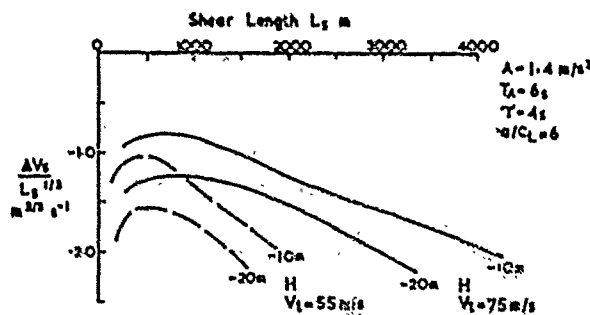


Fig. 8 Potential Height Loss and Headwind Shear. Comparison at $V_t=75$ and 55 m/s

2.2 Potential height loss because of Downdraught shear

At constant pitch attitude and speed the rate of descent of an aircraft is equal to the instantaneous downdraught. Height loss is then the integral of the downdraught, or

$$H = \int_0^{T_w} V_w dt = \int_0^{L_w} (V_w/V_t) dx$$

where H = Potential height loss

T_w = duration of the shear = L_w/V_t

L_w = Shear length

V_w = Instantaneous downdraught at distance 'x'

Thus in contrast to Headwind shear, the higher the airspeed the lower is the potential height loss for all shear lengths.

The effects of pilot actions on the throttle are identical to the Headwind shear case and need not be added again. In most cases downdraughts near the ground are associated with significant headwind shears and last no longer than the headwind shear. In these circumstances the effect of the downdraught may be added directly to the effects of the headwind shear and pilot's throttle responses.

3 SELECTION OF SEVERITY FACTOR

The choice of a severity factor can be made on various criteria. The most commonly used to date being the 'F' factor, Ref 5, which is based on pseudo Specific Energy rate and that the energy of an aircraft is given by its kinetic energy based on airspeed and potential energy from height. Whilst this is true in steady wind conditions, kinetic energy does not change with airspeed in changing wind conditions (wind shear). The usual form of the factor based on pseudo Energy Rate is

$$F = (dV_s/dt)/g = V_w/V_t$$

This 'F' factor does not include any specific reference to the length or duration of the shear, although Ref 6 suggests that shear length improves the correlation between the 'F' factor and the characteristics of microburst wind shears.

The analysis in Section 2 has shown that at long shear lengths the use of shear rate, dV_s/dt is directly related to potential height loss, Fig 5, and, as mentioned earlier, it is logical that this will be the main performance parameter when the available aircraft acceleration is greater than the shear rate. However, as shear rate approaches and exceeds aircraft acceleration, the shear rate would be expected to be less important with the emphasis transferred to the total change in headwind. This expected change is seen in the potential height loss factor. Furthermore, the pseudo Energy Rate factor gives no indication of the effects on any given aircraft and thus separate studies must be made to choose boundary conditions for various aircraft.

The potential energy term, V_w/V_t , again has some of the necessary terms to relate to height disturbances. However, potential height loss calculations would be related to $(V_w/V_t) \times$ (Shear length). It is to be expected that Shear length would be important as a high value of (V_w/V_t) over a short shear length would not cause a significant disturbance. Indeed, high values of (V_w/V_t) are not uncommon in turbulence.

A further problem with the F factor is that it can only be calculated if the airspeed of the aircraft is known. Ideally any severity factor should be calculated on the basis of the wind shear without any aircraft terms so that it can be applied to a wide range of different aircraft types using measurements of the shear from any sensors, i.e. a single severity factor can be identified and presented to all aircraft who will then compare it with the critical values for their particular aircraft and condition. Potential Height Loss severity can be directly related to terms containing only wind shear characteristics.

One perceived advantage of the F factor is that the shear rate term can be determined without any knowledge of shear length by direct measurements on board an aircraft, as can an estimate of the downdraught component. The Potential Height Loss method requires knowledge of shear length. However, as shown in Section 2, the shear length is an important factor in determining wind shear severity.

However, these ideal considerations of the F factor and Potential Height loss factor are only part of the picture. It is also important to consider practical measurement with various types of sensors on aircraft and on the ground, and to consider the probability of encountering the various types of wind shear, as this will determine the probabilities of false alarms or significant underestimates of shear severity (missed alarms).

3.1 Considerations of the probability of wind shear encounters.

It is convenient to consider probabilities first so that they can be included when considering practical measurements. Very clear statistics of the probability of encounter of headwind shear are presented in Ref 1. These show, Fig 9, that at the longer shear lengths there is a linear relationship between the logarithm of the Shear strength parameter of Figs 6 and 7 and the encounter probability in travelling one shear length. This is translated into the probability of encounter during a landing approach in Fig 10.

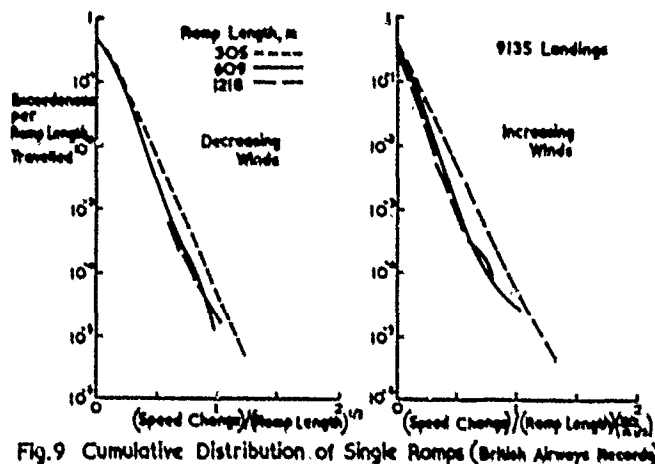


Fig.9 Cumulative Distribution of Single Ramps (British Airways Records)

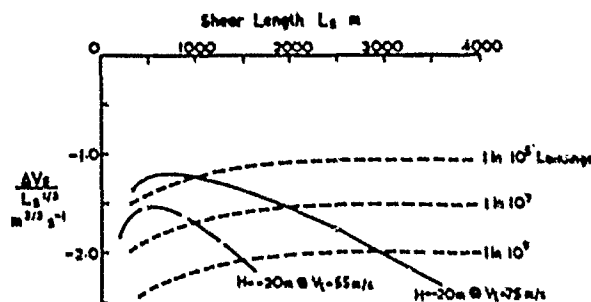


Fig. 10 Potential Height Loss and Headwind Shear. Comparison with Worldwide Probability of encounter.

Unfortunately there are no comparable statistics on the probability of encountering downdrafts, nor on joint probabilities. However, it would seem from the larger events studied in Ref 1, that headwind shears can occur without significant downdrafts, and significant downdrafts do not seem to occur close to the ground without significant headwind shear. Thus the overall probability of downdrafts will be less than headwind shear. It may be possible to establish a useful model, where downdraft is a constant proportion of the headwind change, for use with sensor systems that only measure headwinds. This would imply a small penalty in a lower threshold when downdrafts are absent, but this may be acceptable. A possible proportion could be 0.25 and this would give a downdraft of 4m/s (800ft/min) when ΔV_s was ~ 16 m/s (32kn), which is a reasonable model for the severe microburst case.

3.2 Practical measurement considerations

For the purposes of this study, all practical measurement systems may be classified into two types:

- point measurement systems where instantaneous information on winds is gathered at one or a group of fixed points as a time history. The fixed point may be an aircraft or on the ground.
- scan and probe measurement systems where wind measurements are taken almost instantaneously over a range of distance or volume. Again the system can be carried on an aircraft or on the ground.

The important difference between them is that there is no information on shear length from the point system until the end of the shear is reached. This may be after travelling several kilometres and will frequently be too late for a timely warning from systems carried on an aircraft. The scan system instantaneously measures both shear strength and length directly, and usually before an aircraft encounters a shear if it is an airborne system.

The F factor does not include shear length and can be measured by point systems on an aircraft. Fig 11 shows the component of F from a headwind shear. In this case a contour of $\Delta V_s / T_s = -1.0 \text{ m/s}^2$. At very short shear lengths this F factor corresponds to small changes in V_s which are insignificant. To reduce the false alarm rate that would result from the direct calculation of F, it is usual to apply a low pass filter. Fig 11 shows the effect of such filters and their use will improve the match between the F factor and the Potential Height loss contour. However, to give a timely response the filter should not have a delay of more than 4s on any aircraft based system. With this level of delay the F factor shows a significant region where warnings will be generated for

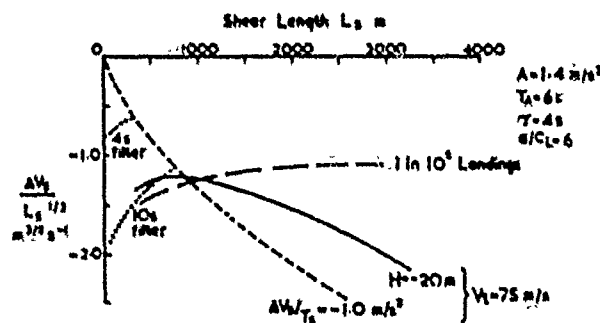


Fig. 11 F factor characteristics

shears that are as small as half the strength (or about 1/4 the height loss) of the critical boundary suggested by the potential height loss for short shear lengths (c. 750m in the example of Fig 11). The probability of encountering these shears is also much higher than those which correspond to the potential height loss contour. At greater shear lengths it requires a significantly greater shear strength to reach the F factor than that to give the potential height loss. Also the probability of encounter is much lower for the F factor. This will mean that a significant number of encounters which are critical in potential height loss will be missed by the F factor. Beyond a shear length of 3000m in the case of Fig 11, the probability of encountering critical shears falls below about 1 in 10^5 landings. If the F factor critical value is reduced it is possible to get a much closer fit between it and the potential height loss contour, but unfortunately only at the expense of increasing the size of the region at short shear lengths where false alarms are likely.

It is also unfortunate that the F factor does not contain any shear length in the downdraught term. This will increase the false alarm rate for short shears and the missed alarm rate for long shears.

For ground based systems, it may be impossible to use 'point systems' because the time taken for a shear to pass the sensor depends on the mean wind speed, which can be very low, and this also complicates measurement of shear length. The use of multiple 'point sensors' can partially overcome this problem, as in the Low Level Wind Shear Alert System in use in the USA. However, the spacing of the sensors determines the lengths of shears that can be satisfactorily measured, and there are other problems from fixed locations and the low height of the sensors compared with aircraft flight paths. A knowledge of aircraft speed and shear length are needed before an F or Potential Height factor can be calculated from ground based measurements.

Thus, the use of the F factor and point sensor systems on an aircraft is liable to generate significant false alarms and miss many serious shears. The false alarm rate will be difficult to identify because it is likely to occur relatively infrequently at around 1 in 10^5 landings compared with real critical shear probabilities of around 1 in 10^3 landings. However this is still high enough to eventually bring F factor point sensor systems into disrepute.

The use of scanning sensors, such as Doppler Radar or Laser systems, provides instant information on shear length as well as strength. This allows the potential height loss contours to be used directly from airborne sensors, and inputs for both the F and Potential Height Loss factors can be measured from the ground.

3.3 Proposed severity factor

A reasonable match between Potential Height Loss and a severity factor for Headwind shear can be obtained by using the numerically higher of the shear gradient and the shear to airspeed ratio. This requires two shear parameters to be combined with the airspeed of the aircraft. The speed change, ΔV_s , and the length, L_s . As Potential Height Loss is equal to the shear gradient at large shear lengths, it is possible to use the height loss function as a basis for a severity factor X.

From the characteristics identified in this paper, X may be empirically defined as

$$X = -2.2 * (-f(H))^{1/3}$$

$$\text{where } f(H) = \frac{H a}{V_0^2 C_L} = 0.5 * \rho_0 * \frac{a}{(W/S) \sigma} * A^2 * H'$$

H = Potential Height Loss at $A = 1.0 \text{ m/s}^2$

H' = Actual Potential Height Loss for factor threshold

ρ_0 = Air density at standard sea level conditions

σ = Relative air density

It is found that there is a good match to the shear/airspeed ratio for $-X^{3/4}$. Thus boundaries can be expressed as

$$Vt * (\Delta V_s / L_s) = \Delta V_s / T_s = X$$

and

$$\Delta V_s / V_t = -X^{3/4}$$

A boundary is exceeded

$$\text{IF } Vt * (\Delta V_s / L_s) > X, \text{ AND } \Delta V_s / V_t < -X^{3/4}$$

The analysis of the British Airways data in Ref.1, which is shown in Fig.6, suggests Potential Height Losses of 10 and 20m for boundaries between Moderate & Strong and between Strong & Severe respectively. Fig.12 presents the variation of the X factor with Wing Loading for these boundaries at an available aircraft acceleration of 1.4 m/s^2 and also 2.0 m/s^2 . Although account must be taken of Wing Loading changes, they do not have a dramatic effect on the X factor. Thus it should be possible to use constant values of X to cover all the normal variations for a given aircraft and situation. However there is a dramatic effect from the increase in available acceleration.

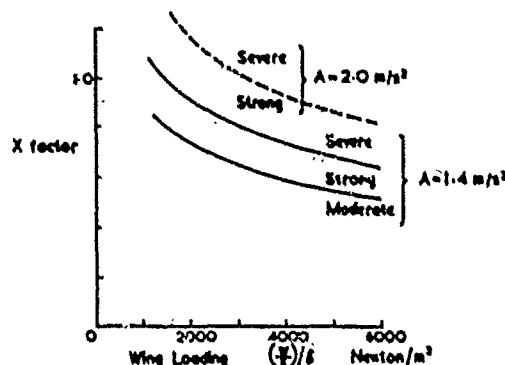


Fig. 12 X Shear factor vs Wing Loading

The close match between X factor boundaries and potential height loss is shown in Figs.13 & 14 for two very different wing loadings of 3500 Newton/m^2 and 1900 Newton/m^2 respectively (The same cases as Figs.6 & 7). The differences from the potential height loss contours is small and much less than that for the filtered F factor in Fig.11. It is recommended that the X factor should be used to reduce the risks of false alarms and missed detections inherent in the F factor. To do this on board an aircraft will require the use of scanning systems.

4 CONCLUSIONS

Potential height loss is a major indicator of wind shear severity and can be readily calculated for the representative case of an aircraft whose pitch attitude is controlled. Derivation of the equations and calculations demonstrate (Fig.2) that the primary factors in height response to headwind shear are the the squares of the wind speed change in the shear and the available acceleration of the aircraft, and the shear length. The delays in pilot and engine response, (Fig.3) have significant but less dramatic effects on the potential height loss.

A general graphical relationship between wind shear and aircraft performance parameters is established (Fig.4). This is also in a form which relates directly to the probabilities of encountering various wind shears (Fig.10). It is shown that a potential height loss parameter can also be plotted on this graph (Fig.5) and this identifies that the main aircraft parameters for categorising response to wind shear are Wing Loading and available acceleration. This suggests that there may well have been an increase in wind shear encounters in recent years because of the steady trend to increase wing loading. Comparison of the potential height loss contours with moderate and strong wind shears analysed (Ref.1) from British Airways worldwide operations with B747 aircraft shows a probable correlation (Fig.6) with the potential height loss contours. Fig.8 shows the contrast between potential height losses for aircraft with widely differing wing loadings of 3500 and 1900 Newton/m^2 .

The effects of downdraughts are shown to be easily calculated as an addition to any headwind shear by integrating the downdraught over the period while the aircraft is under its influence. Thus the length of the shear is particularly important and the effects are reduced by increasing airspeed.

The characteristics of the most commonly used severity factor based on pseudo specific energy rate and generally known as the F factor are compared with the potential height loss calculations. These show (Fig.11) that, even when filtered to reduce false alarm tendencies, the F factor is a poor match to the potential height loss. In particular it will have a significant false alarm rate in response to the shorter shears and will miss severe shears when their length is long. It is also shown that the lack of a shear length term in the portion of the F factor dealing with downdraughts will lead to false alarms and missed alarms. It is also noted that the F factor has not been explicitly identified with the various aircraft performance parameters and, thus, it is not possible to define appropriate values for specific aircraft or conditions of flight.

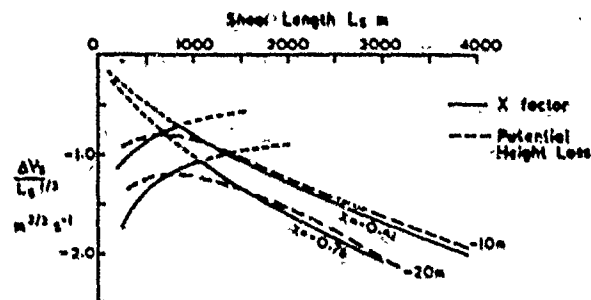


Fig. 13 Comparison of Shear factor X with Potential Height Loss.
Wing Loading = 3500 Newton/m²

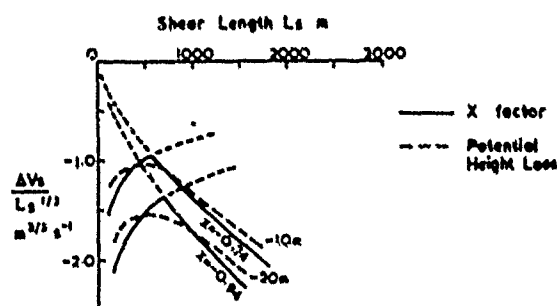


Fig. 14 Comparison of Shear factor X with Potential Height Loss.
Wing Loading = 1900 Newton/m²

An alternative wind shear severity factor X is identified which has explicit aircraft performance parameters and can readily be calculated from information on the wind speed change and length of a headwind shear. It is in the form of a potential height loss and any downdraught height loss may be added directly to it, if it is known. Figs. 13 & 14 show that the X factor gives a good match to the potential height loss for widely differing aircraft. However, to use the X factor with sensors on board an aircraft requires a scanning sensor. Point source sensors cannot produce information on the total size of a wind shear until after it has occurred. This is too late to help a pilot.

REFERENCES

- 1 A A Woodfield
J F Woods Worldwide experience of Wind Shear during 1981-1982. AGARD FMP Conference 'Flight Mechanics and System design lessons from Operational Experience' May, 1983. AGARD Conference Proceedings No. 347
- 2 B Etkin Dynamics of Flight. John Wiley & Sons, New York, 1959. Chap. 6.
- 3 B S Turkel
W Frost Pilot-Aircraft System Response to Wind Shear. NASA Contractor Report 3342, 1980
- 4 W Frost
B S Turkel
J McCarthy Simulation of Phugoid Excitation due to Hazardous Wind Shear. AIAA 20th Aerospace Sciences Meeting, Jan 1982. AIAA-82-0215
- 5 R Bowles
R Tarr Wind shear detection and avoidance: Airborne systems perspective. 16th Congress of the International Council of the Aeronautical Sciences, Jerusalem, Israel, 1988
- 6 K L Elmore
W R Sand A Cursory Study of F-Factor Applied to Doppler Radar. 3rd International Conference on Aviation Weather Systems, American Meteorological Society, Jan 1989

Appendix: Calculation of Height Change in response to a Single Ramp Headwind Shear

The response of an aircraft to longitudinal disturbances when pitch attitude is perfectly controlled by a pilot or autopilot has a 2nd Order Characteristic Equation and the basic response modes are an almost neutral exponential speed stability mode and a very stable exponential flight path response mode with a time constant of 1 to 2sec (proportional to Wing Loading/Flight Speed). The almost neutral speed stability mode means that the groundspeed tends to remain constant when headwind changes. Thus Headwind Shear has a direct effect on airspeed. The stable flight path mode means that the aircraft rapidly stabilises at a new flight path in response to wind disturbances and the transients can be ignored if the event time is much longer than 1 to 2sec. In these circumstances the following basic assumptions may be used in calculating flight path responses:

1. Constant pitch attitude
2. Neutral speed stability, i.e. only thrust changes affect groundspeed
3. Instant flight path response, i.e. Lift = Weight

Comparing lift at conditions where the airspeed has changed by ΔV and the Angle of Attack by $\Delta\alpha$ from the datum at the start of the wind shear encounter ($t=0$) gives

$$2W = \rho V_t^2 S a(\alpha_0 - \alpha_0) = \rho (V_t + \Delta V)^2 S a(\alpha_0 + \Delta\alpha - \alpha_0) \quad (1)$$

$$\text{or} \quad -\Delta\alpha (1 + \Delta V/V_t)^2 = (\Delta V/V_t) (2 + \Delta V/V_t) (\alpha_0 - \alpha_0) \quad (2)$$

where W = aircraft weight
 ρ = air density
 V_t = true airspeed at $t=0$
 V = change in true airspeed
 S = reference wing area
 a = lift curve slope
 α_0 = angle of attack at $t=0$
 α_0 = angle of attack for zero lift
 $\Delta\alpha$ = change of angle of attack

$$\text{now} \quad \alpha_0 - \alpha_0 = C_L/A \quad (3)$$

where C_L = lift coefficient at $t=0$, $= 2W/\rho V_t^2 S$

Thus eqn.(2) becomes

$$\Delta\alpha = - (C_L/a) (\Delta V/V_t) (2 + \Delta V/V_t) / (1 + \Delta V/V_t)^2 \quad (4)$$

For small speed changes eqn.(4) approaches the more familiar form

$$\Delta\alpha = -2(C_L/a) (\Delta V/V_t) \quad (5)$$

but speed changes are often large in wind shear situations and the full eqn.(4) is used here.

At constant pitch attitude, θ , the relationship between angle of attack and flight path angle, γ , is

$$\theta = \alpha_0 + \gamma_0 = (\alpha_0 + \Delta\alpha) + (\gamma_0 + \Delta\gamma)$$

$$\text{or} \quad \Delta\alpha = -\Delta\gamma \quad (6)$$

Height Deviation from the flight path is given by

$$H = \int_0^t V \Delta\gamma dt \quad (7)$$

where

V = groundspeed $= V_t - V_x + \Delta V - \Delta V_x$
 V_x = headwind at $t=0$
 ΔV_x = change in headwind at time t

(NB It should be noted that

$$H \neq \int_0^t \Delta h dt$$

where Δh = change of rate of climb,

because changes in groundspeed without changing flight path angle will change Δh without any deviation from the flight path)

For this study the initial headwind is set to zero to establish the primary height loss. This can also be a reasonable approximation for many wind shears occur in calm conditions. The affect of an initial headwind will be to reduce any height loss to about $(1 - V_x/V_i)$ of the estimated value.

The $(\Delta V - \Delta V_x)$ term is also ignored. By definition it is zero for $0 < t < T_a$, then (see Fig 1) the aircraft starts to accelerate and the term increases to be equal and opposite in sign to the wind shear, ΔV_x , when ΔV reaches zero again. Thus this term will increase the height loss by approximately $(-\Delta V_x/4V_i)$ times the estimated height loss.

Thus, from eqns (4), (6) & (7) the height change is

$$H \approx (C_L \cdot V_i / a) \int_0^{T_0} (\Delta V / V_i) (2 + \Delta V / V_i) (1 + \Delta V / V_i)^2 dt \quad (8)$$

where T_0 = time when $\Delta V = 0$ ($t \neq 0$)

Thus, from eqns (4) & (6), T_0 corresponds to $\Delta V = 0$ ($t \neq 0$), and is the point of maximum height deviation from the flight path. If T_s is the time for the headwind shear to reach its maximum of ΔV_x , then eqn (8) can be rearranged as

$$(H/a / T_s \cdot V_i \cdot C_L) \approx (H/a / L_s \cdot C_L) \approx \int_0^{(T_0/T_s)} (\Delta V / V_i) (2 + \Delta V / V_i) (1 + \Delta V / V_i)^2 \cdot d(t/T_s) \quad (9)$$

where L_s = wind shear length ($= T_s \cdot V_i$)

$$\text{or} \quad \frac{H/a}{L_s \cdot C_L} \approx \int_0^{f_1(t/T_s)} \left(\frac{\Delta V}{\Delta V_x} \right) \left(\frac{2}{\Delta V_x / V_i} + \frac{\Delta V}{\Delta V_x} \right) \left(\frac{1}{\Delta V_x / V_i} + \frac{\Delta V}{\Delta V_x} \right)^2 \cdot d(t/T_s) \quad (10)$$

From Fig 1 it can be shown that

$$\frac{\Delta V}{\Delta V_x} \approx f_1 \left(\frac{t}{T_s} \right) + \frac{f_2(t/T_s)}{(\Delta V_x / A \cdot T_s)} - \frac{\tau/T_s}{(\Delta V_x / A \cdot T_s)} [1 - e^{-\tau/T_s \cdot f_1(t/T_s)}] \quad (11)$$

where

$$\text{IF } t/T_s < 1.0, \text{ THEN } f_1(t/T_s) = t/T_s, \text{ ELSE } f_1(t/T_s) = 1.0$$

$$\text{and} \quad \text{IF } t/T_s > T_a/T_s, \text{ THEN } f_2(t/T_s) = t/T_s - T_a/T_s, \text{ ELSE } f_2(t/T_s) = 0$$

$$\text{Thus} \quad \frac{H/a}{L_s \cdot C_L} \approx f \left[\frac{\Delta V_x}{V_i}, \frac{\Delta V_x}{A \cdot T_s}, \frac{T_a}{T_s}, \frac{\tau}{T_s} \right] \quad (12)$$

Non-dimensionalising the various parameters has reduced the total number of variables by 2, and considerably eases the analysis and understanding of the problem.

HOW TO FLY WINDSHEAR USING THE FLY-BY-WIRE CONCEPT

BY

J. L. BOURVE

DEPUTY SYSTEMS PROSPECTIVE MANAGER

AEROSPATIALE

316, Route de Bayonne

Toulouse

FRANCE

ABSTRACT

In the past three years, AEROSPATIALE has developed windshear warning and guidance systems for the A310 and the A300-600 ; these systems are either newly designed or constructed around the Speed Reference System designed for the A300 and exploited in revenue flight since 1975 ; they are in accordance with certification rules, mainly AC 25.12, and have been installed on board the A300-600 since April 88.

In today's conference we present in the first part : AEROSPATIALE's warning and guidance philosophy regarding the conventional AIRBUS, then we analyse the fly-by-wire concept.

The fly-by-wire concept improves the general aircraft situation, and we take advantage of these new capabilities in the warning and guidance elaboration : this is the theme of the second part of today's conference.

Systems will be adapted for the A320 certified and installed onboard in the near future.

In the past three years AEROSPATIALE has developed windshear warning and guidance systems for the A310 and A300-600 ; these systems are either newly designed or constructed around the speed reference system designed for the A300 and exploited in revenue flight since 1975 ; the new systems are in accordance with the certifications rules, mainly AC25-12 and have been installed on board the A300-600 since April 88.

In today's conference we shall present, in the part A : AEROSPATIALE's warning and guidance philosophy regarding the conventional AIRBUS, then in part B we shall analyse the A320 Fly-by-wire concept and windshear warning and guidance adaptation.

A- AIRBUS WINDSHEAR WARNING AND GUIDANCE SYSTEM FOR CONVENTIONAL AIRCRAFT

A.1- Windshear Guidance Strategies

Analog A300's and digital A310's and A300-600's (AFCS standards 5-6-7) have a very well known and similar SRS guidance law (Basic 1975 situation).

From our experience we confirm that this strategy is precise enough to survive many shears. In some strong shear cases it is however completed by an OEB (Operator Engineering Bulletin) procedure

Safetywise, analog and digital systems also comply with AC 25-12.

The basic Airbus Windshear guidance is satisfactory but can be improved.

We therefore defined a fully adaptive system that is able to cope with strong shears without any special procedure (compared to the basic system).

Initially we tried to develop an optimal guidance system but we very quickly reached impossible solutions :

First : optimal procedures really are different from one shear to another, in some cases the system initially even demands diving.

Second : guidance is really optimal if we have full knowledge of the whole shear pattern before entering it.

Third : Much in fact is the conclusion of the second point : in any shear encounter an optimal guidance system is a bet on the future.

For all these reasons we developed a repetitive and adaptive survival strategy (Figure 1) adapted to all performance problems in typical shear conditions.

The system is derived from the A300 SRS System (Figure 2) improved by a vertical speed floor protection, climb protection and stall protection.

This Control law ensures the survival strategy (Figure 3) whatever the longitudinal or vertical shear stressing the aircraft capability in take-off or go-around conditions.

The Control law implemented in the FCC's SRS take-off/go around mode is available with the flight director, CWS or command mode.

In shear conditions and when the shear intensity stresses the aircraft capability, the SRS law will progressively adapt its control to a survival strategy (see figure 2 and 3) :

- 1- The Basic vote (N°1) will control airspeed (Vvel-10Kt) with a vertical speed decreasing to zero.
- 2- Vote N°2 then overrides vote N°1 and commands a slightly positive vertical speed with an airspeed decreasing to V stick-shaker plus a small
- 3- Vote N°3 then overrides vote N°2 and vote N°1 and controls airspeed at V_{ss-A}. Altitude will be reduced until the shear decreases.

Whatever the commanded strategy, the pitch attitude demand is limited by a stall protection to avoid any impending stall situation.

A 2- Airbus Guidance Situations

The most severe shears proposed in AC 120.41 windfield models were simulated in the take-off phase both with the initial A300 SRS system and with the newly developed windshear guidance system (called here control of aircraft's energy).

Comparing figures 4 and 5 we conclude that the new system really does improve the situation but that the initial A300 SRS was already very effective in this capability to cope with a real encounter.

Figures 6 and 7 emphasize the advantages presented by the new system in theoretical shear conditions : an adaptive control law maintains the aircraft inside the operational flight envelope and uses maximum airplane capability to achieve this.

The control law has been implemented in the A300-600 AFCS since A/C Serial Number 420 and for the A310 it will be implemented early in 89. In principle the control law is available for retrofit in all aircraft on the digital fleet.

From simulation experience we know that for take-off with derated power or for the landing case a successful escape manoeuvre can be accomplished if a max-power or go-around decision is made promptly upon entering the shear.

This remark is just to focus on the absolute need for a tool to trigger the crew's decision-making process to initiate escape.

Windshear detection can provide this valuable help ; but what do we have to detect or not detect ? What nuisance warning level should we reach to maintain an acceptable level of crew confidence with regard to the warning ?

All these aspects were borne in mind when defining an Airbus windshear warning philosophy from in-flight incident/accident analyses.

A 3- Airbus Windshear Warning

Airbus targets (Figure 8) enhance AC 25-12 advice in detection, non-detection and performance nuisance warnings.

An evident design philosophy with regard to the warnings was to define a wind severity factor computation (SF).

$$\frac{d \text{Energy}}{dt} = \text{Weight} \left[C_{te} \cdot \text{Airspeed} \times \frac{d W_x}{dt} + g \cdot W_z \right]$$

$$SF = \frac{d W_x}{dt} - \frac{g}{\text{Airspeed}} \times W_z$$

Obviously this reflects the instantaneous loss of energy due to the global shear (longitudinal & vertical) if $SF > 0$.

W_x = longitudinal wind (< 0 IF headwind)

W_z = vertical wind (< 0 IF down)

C_{te} = function of A/C propulsion and aerodynamics (typical of each airplane)

g = gravity acceleration

SF = could be filtered and compared to a fixed threshold of 2.5 Kts/sec or 0.13g typically

This conventionally adopted solution was however rapidly abandoned owing to a high level of nuisance warnings.

Wind variation knowledge is in fact the only parameter for a shear intensity evaluation, but it can never be the unique item of information in a windshear warning without duly taking the aircraft energy situation into account.

Windshear Warning computed without considering present aircraft energy will lead, in certain cases of shear encounter, to very early warnings (the crew should identify them as nuisance warnings) or too late warnings endangering an escape manoeuvre.

A good crew confidence level and a satisfactory escape manoeuvre capability can both be achieved by a windshear warning as a reasonable compromise between "SF", actual aircraft energy and a safe minimum energy.

A.4- Wind Shear Warning (NSW) Computation Principle

The NSW is activated when the predicted aircraft energy is below a predetermined minimum energy threshold (Figure 9).

This threshold corresponds to still air α' floor protection according to Flap and Slat position.

$$\alpha' = \alpha \cdot \alpha'_{W} \text{ is the predicted aircraft energy.}$$

The predicted aircraft energy, depends on α' which is obtained considering filtered angle of attack ($\Delta \alpha$ or α') corresponding to the present aircraft energy situation increased by equivalent angle of attack estimates ($E \cdot \Delta \alpha$, $E(\alpha'_{W})$).

α'_{W} is an estimate of the energy loss foreseeable in the near future.

Note that the higher the $\Delta \alpha$ (α') the lower the actual aircraft energy, and the higher the $E \cdot \Delta \alpha$, $E(\alpha'_{W})$ the higher the future loss of energy.

α'_{W} is obtained by a combination of equivalent angles of attack estimates:

$$\alpha'_{W} = a + d \cdot (b - c) \text{ if } a > 0$$

a - is the $E \cdot \Delta \alpha$, E due to instantaneous tailwind shear

b - is a memorized $E \cdot \Delta \alpha$, E of the recent headwind shear

Generally a strong headwind is precursor of a strong decreasing shear

c - is an $E \cdot \Delta \alpha$, E decrease according to the mean wind observed in order to alleviate nuisance turbulence warnings

d - is an $E \cdot \Delta \alpha$, E related to the observed vertical downward wind.

a, b, c, d, $E \cdot \Delta \alpha$, E 's cannot be negative

b minus c cannot be negative

This windshear warning mechanism is schematized on figure 10.

In areas I, II and III, $E \cdot \Delta \alpha$, E 's are computed but α'_{W} is identical to $\Delta \alpha$ since $a = 0$ (no tail wind shear).

α'_{W} combines $\Delta \alpha$ and W In area IV when vertical wind becomes negative: $d > 0$.

In area V $V_{Q/N}$ increases when tailwind shear appears.

In this case the MSW threshold is reached. It could have been reached in area IV if vertical wind intensity had been higher. Similarly, it could also have been reached in area V with tailwind shear depending on shear intensity.

Simulator experience shows that shortly after lift-off below 250 ft it is useful to trigger the MSW according to the tail shear for the case of a small margin respect to $1.2 V_h$. For clarification purposes, this function is not shown on these figures but it should be borne in mind that from lift-off to 250 ft, MSW can occur from Q/N or from the α branch only, compared to a smaller threshold if $V_0 < 1.2 V_h + 3 Kt$.

A.5- Performance Warning

A.5.1- Performance Missance Warning

We considered both take-off and landing cases but we are intentionally limiting our evaluation here to the most disturbing case for air traffic and aircraft utilisation: the landing case.

Missance warning probability per approach had been evaluated by simulating 500 automatic landings in tower wind conditions up to 40 Kts according to AC 20.37 A advice (automatic landing performance evaluation). Results are plotted on figure 11.

Missance warning probability per approach for Airbus windshear warning and for the conventional windshear warning (properly filtered "SF" by $\geq 4s$ lag referred in section 3) are compared in Figure 11.

We remind the reader that a conventional windshear warning leads to a nuisance level of 10^{-3} per landing with a recommended threshold of 0.13 g or 2.5 Kts/sec. We also note that the Airbus windshear warning leads to a nuisance level of 10^{-6} per landing with its implemented threshold of 11.5°. It is interesting to remember here that the US in service observed windshear probability encounter is about 10^{-6} .

A.5.2- Normal performance warning

The Airbus MSW will alert the crew after an initial loss of longitudinal airspeed. The closer the selected airspeed to $1.3 V_h$ the smaller this initial loss before the warning is triggered (Figure 12).

Airbus MSW merely alerts the crew but has no activity on throttles or go-around mode, the crew will decide according to the situation to pursue or to abort when landing, or to trigger max power or not at take-off.

α /floor protection is maintained on Airbus, it is the ultimate protection if the crew underestimates the situation at MSW. α /FLOOR protection gives automatically the full thrust if aircraft's energy is below a safe level.

For a windshear encounter case the general situation of Airbus MSW and α /FLOOR are plotted on figure 13. One can notice the remaining energy margin at MSW and at α /FLOOR.

In case the pilot wrongly selects too low a speed ($1.25 V_h$ for example autothrottle OFF) the α /FLOOR will in some cases of shear conditions intervene before the warning itself.

A.6- Airbus MSW and Guidance Implementation

The MSW is implemented in dual, aural and visual warnings can be tested on the ground with the engines not running (Figure 14). In case of shear encounter, aural warning is activated and a red visual windshear message displayed on each PFD. Warning can be activated at take-off from lift-off to 1,000 ft and at landing from 1,000 ft to 50 ft, the visual warning will remain for a minimum of 15 s.

The general architecture is given on figure 15.

B- WINGING WARNING AND GUIDANCE ADAPTATION TO THE A320 FLY-BY WIRE

OBJECT

B.1- Fly-By-Wire advantages

Thanks to its original definition the Fly-by-Wire concept first developed for the A320 commercial airplane provides the crew with many advantages in order to cope successfully with a shear.

We mainly note : pitch attitude protection, full stall protection, short term flight level hold, constant stick force per g whatever be.

These main threads considerably increase flight safety throughout the flight envelope including shear encounter.

The interesting capabilities of the A320 are associated with implementation of the side stick (Figure 16) whose characteristics are recalled here-after.

A Fly-by-Wire aircraft is stabilized on all three axes and sidestick control inputs are only required to change the flight path and not to maintain it.

Pitch control, which is the main concern for this paper is shown figure 17. Pilot orders are electrically transferred to the control surfaces by computers. These digital computers are designed to control longitudinal aircraft motion according to pilot sidestick orders through the C^{Law} in normal flight.

Side stick force is constant in the whole flight envelope and the C^{Law} has the following main features :

- Load factor demand associated with load factor protection according to the aircraft configuration (-1 +2,5g in clean configuration 0+2g with flaps extended).
- Autotrim function and neutral stability within the normal flight envelope
- Short term platform stability
- Aircraft response almost unaffected by speed, weight or center of gravity location
- Bank angle compensation up to 33°.

B.2- Fly-by-Wire protections

As today's presentation is limited to shear encounter, we shall just provide a brief reminder of the A320 Longitudinal Low speed protections.

B.2.1- Pitch attitude limitation

To enhance the effectiveness of angle of attack (AOA) protection, in extreme conditions, one parameter can easily be limited : attitude angle (θ) (figure 18).

This limitation is only a part of the basic C^{Law} which starts to reduce the pilot order 5 degrees below θ_{max} .

These limits are 15 degrees pitch-down and 25 degrees pitch-up within the whole flight envelope except in very low speed where the pitch-up demand limit is reduced to 22,5 degrees. These limits are more than enough to provide the pilot with ample manoeuvre capability even in extreme conditions. This limitation is very close to the stall protection specially included in conventional aircraft shear guidance law as explained before. But in the Fly-by-Wire system, this protection can be automatically activated not only in the shear escape manoeuvre but in the whole flight envelope whatever the piloting process.

B.2.2- High angle of attack protection

Protection against stall without penalizing aircraft manoeuvrability had always been a deep concern for handling quality engineers (Figure 19).

It is clear for the designer that angle of attack control provides a real protection. The potential offered by Fly-by-Wire is a real advantage for feed back of that function.

The A320 AOA protection law offers : dynamic and static stability compensation at low speed in the limits of the flight envelope providing a first stick-free protection :

- manoeuvres in normal speed free of interference
- aircraft protection against stall in dynamic manoeuvres or shear escape
- high CL flight with adequate roll manoeuvrability
- Load factor demand and C_L feedback are still computed even in AOA protection in order to limit elevator demand whatever the first limitation activated angle of attack or load factor.

This principle is very similar to the Vain protection in a conventional aircraft shear avoidance control law, but it is effective in the whole flight envelope and does not need special pilot training for the A320.

AOA protection is fully automatic owing to Fly-by-Wire capabilities and is available whatever the piloting purpose ; it should be noted that if AOA protection is reached when the autopilot is on, the autopilot is automatically disconnected but the Flight director remains controlled by the unchanged control law.

B.3- Shear escape control law adaptation to Fly-by-Wire concept Figure 20 (FBW Guidance Law)

The initial shear guidance (SPS) control law previously developed for conventional aircraft can be simplified owing to the Fly-by-wire advantages developed above.

Firstly : pitch demand limit (stall protection) included in FBW is not necessary in the Flight director control law.

Secondly : Vain control is superseded by Q/MAX control ; although the flight parameter is not the same the resulting energetic situation is equivalent : the aircraft can be controlled within its maximum capabilities.

Third : However one recommendation is necessary : whatever the control law, and mainly SPS, the crew has to follow the flight director bar demand. In the shear encounter case the crew does not have to pull the stick, fully back immediately : the pilot will follow the FD demand. AOA protection will be automatically activated at the end of the escape manoeuvre, if necessary.

In such shear encounter case the flight director displays a pitch-up demand impossible to achieve even with the stick fully back.

The survival strategy achieved by the A320 control law is equivalent to the strategy defined for the conventional aircraft, the main difference being the fully automatic protection when flying Vain on the A320. This help in extreme conditions can be considered to be an important increase in the flight safety whatever the crew's skill. The A320 windshear guidance control law is implemented basically from first delivery.

B.4- Windshear Warning Adaptation

The Fly-by-Wire system alone does not justify a modification of the conventional energy level of the windshear warning. The flight safety margins of the A320 are defined in exactly the same way as for conventional Airbus for take-off and for landing. However for landing a special speed control law, specifically defined and patented for Airbus, allows the A320 to fly with an increased flight safety margin, mainly in a shear encounter case. This specific speed control is called autospeed or ground speed min or managed speed.

B.4.1- Managed speed principle

According to Captain Jack BLISS, (ground speed min principle (figure 21)) the aircraft engine power demand will be associated with the airspeed target minus present airspeed or the ground speed target minus present ground speed whichever is the greater.

This principle smoothes engine rating variations and pitch attitude modifications, increases flight passengers comfort, allows a better glide slope control (ground slope) and increases airspeed margin when entering a shear.

An example of ground speed min benefits is shown on Figure 22, 23, 24 where a real automatic landing performed during flight tests without ground speed min control is simulated again using ground speed min concept.

A comparison between figures 23 and 24 clearly shows the advantages associated with the managed speed principle : advantages for passengers comfort. Lower pitch variations, lower engine ratings variations and advantages for flight safety (increased stall margin).

Managed speed is basically implemented on the A320. Speed can be managed automatically by the autothrottle function or manually by the crew by following the airspeed bug demand and speed trend vector displayed on the Primary flight display.

Managed speed is not the only speed control possibility for landing. The crew can select the classical constant airspeed control or the managed speed. Managed speed is advised by FCOM especially in shear condition.

If the crew selects the classical constant airspeed control, the A320 stall margin is equivalent to the conventional aircraft margin and the windshear warning setting remains identical, Fly-by-Wire airplanes or not.

B.4.2- Windshear warning adaptation to managed speed

As explained on Figure 21, managed speed increases the aircraft kinetic energy automatically when entering a shear mainly in a down burst encounter because the precursor phenomenon of a down burst is a large head wind increase.

Doing so managed speed avoids a throttle reduction allowing an airspeed increase before the tail wind appears but if the windshear warning threshold remains identical to the thresholds developed for constant airspeed control, the crew will be alerted later in the shear, which is not a good solution for coping successfully with the shear in an escape manoeuvre.

In order to earn maximum benefit from the managed speed principle, windshear warning thresholds will be set to a higher minimum energy than for constant airspeed approach.

The nuisance performance warning level will remain equivalent, but survival capabilities will be improved according to the increased minimum energy when the warning occurs.

C- CONCLUSION

Windshear warning and guidance systems are certificated for the A310 and A300-600 and are available for retrofit. The improved analog A300 system is in development and is planned for certification in early 1990. The A320 windshear warning is at the final development stage and certification is planned for the second part of 1989 again increasing flight safety for the Airbus winning breed.



SRS STRATEGIES

DIVISION AVIONS

NO SHEAR CONDITIONS

1	High thrust to weight ratio	<ul style="list-style-type: none"> SRS controls pitch attitude $\max \theta = 18^\circ$ Climbing slope = cte VC increases $\Rightarrow VZ = 10 \text{ Kts}$
2	Low thrust to weight ratio	<ul style="list-style-type: none"> SRS controls airspeed $VC = VZ = 10 \text{ Kts}$ ($VC = VZ$ or VZF if $VZF > VZ$) EP case (Vertical speed $> 2,44, \theta < 18^\circ$)

FIGURE 1

SHEAR CONDITIONS

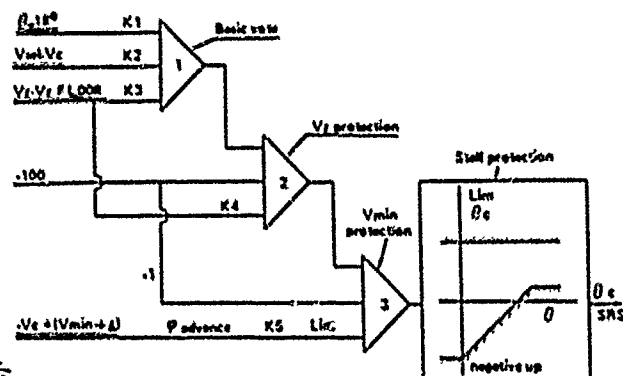
3	Shear does not stress aircraft capability	Strategy 1 or 2 will control AC according to shear intensity and thrust to weight ratio
4	Shear intensity stresses aircraft capability	Control strategy is self adapted to AC flight parameters : <ol style="list-style-type: none"> 1. $VC = VZ = 10 \text{ Kts}$ control ($VZ = 0$) 2. $VZ \neq 0$ control ($VC = VSS + \Delta$) 3. $VC = VSS + \Delta V$ control $VZ < 0$ until shear decreases.



NEW SRS CONTROL LAW PRINCIPLE

DIVISION AVIONS

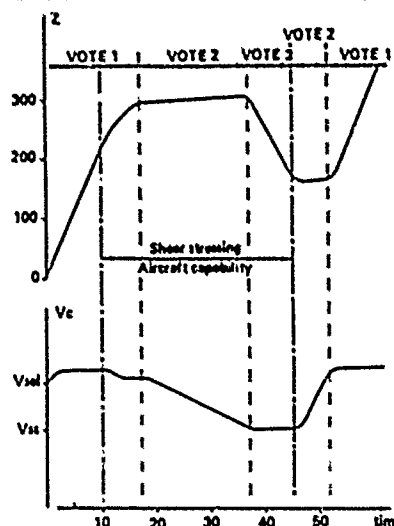
FIGURE 2



S.R.S. SURVIVAL STRATEGY

DIVISION AVIONS

FIGURE 3





1975 BASIC SYSTEM

DIVISION AVIONS

TAKE-OFF F/S 20/30 M=150 t XG=35 Y₂=154.5m

AC 120.41 WIND FIELD Nr 8

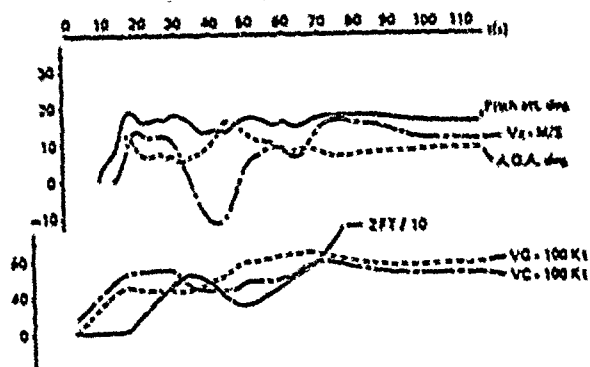


FIGURE 4



NEW SRS

DIVISION AVIONS

TAKE-OFF F/S 20/30 M=160 t XG=35 Y₂=154.5m

AC 120.41 wind field Nr 8

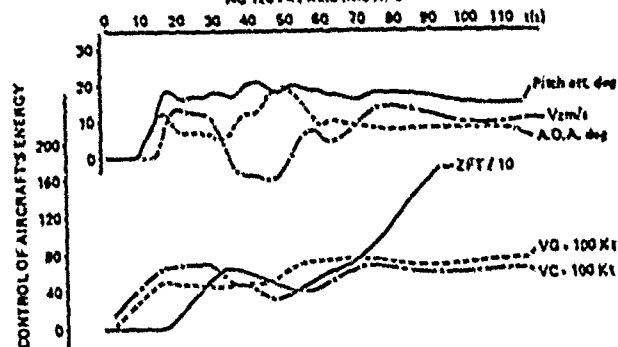
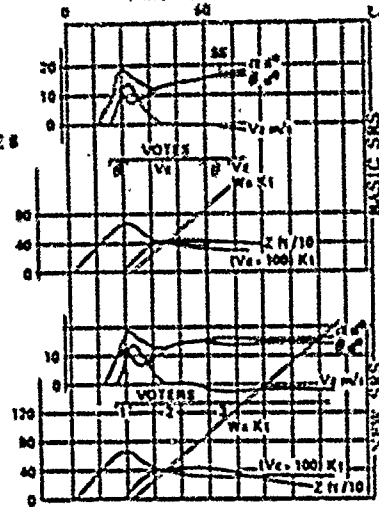


FIGURE 5

LONGITUDINAL TAIL SHEAR

A310 - S / F 30 / 30 - 140 000 KG 25%
TAKE-OFF ISA SL

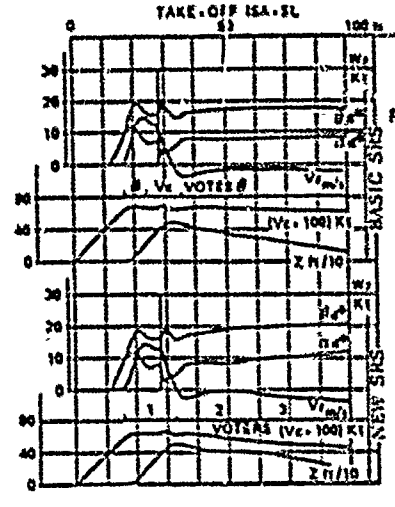
FIGURE 6



VERTICAL DOWN WIND

A310 - S / F 30 / 30 - 140 000 KG 25%

FIGURE 7



AIRBUS WSM SYSTEM TARGETS

DIVISION AVIONS

Performance

FIGURE 8

- Detect 10^{-4} or $< 10^{-4}$ simulated cases
- If no detection show the good behaviour of the aircraft.

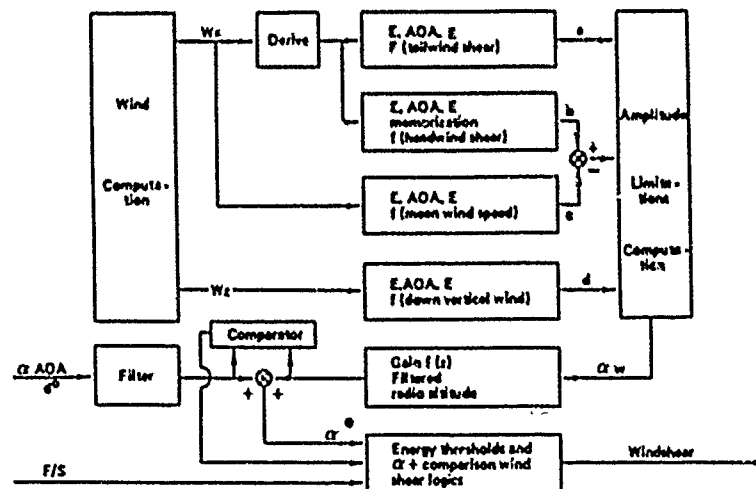
Nuisance

Warning due to active Failure $5 \cdot 10^{-4}$ /approach or take off
 Lack of warning due to latent Failure $5 \cdot 10^{-4}$ /approach or
 take off Performance nuisance warning 10^{-4} /approach.

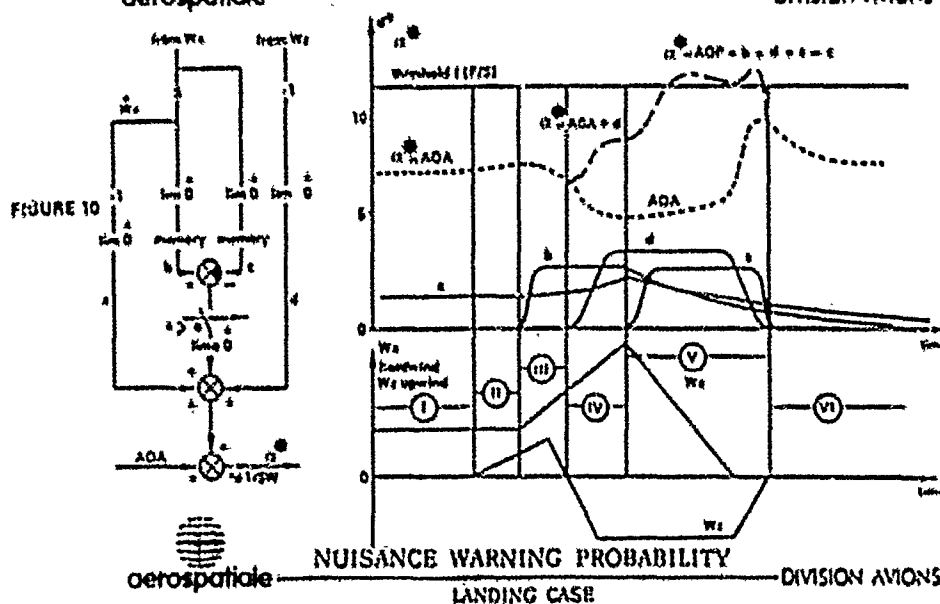
E.AOA.E = EQUIVALENT
ANGLE OF ATTACK ESTIMATE
AEROSPATIALE WINDSHEAR WARNING
COMPUTATION PRINCIPLE

DIVISION AVIONS

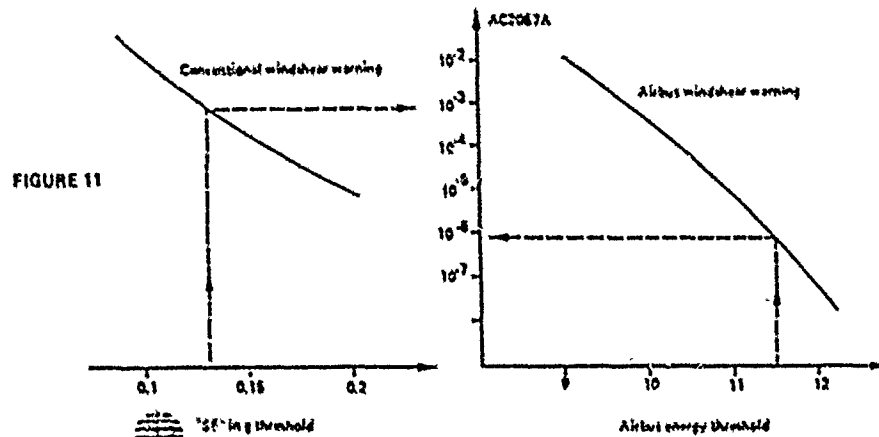
FIGURE 9



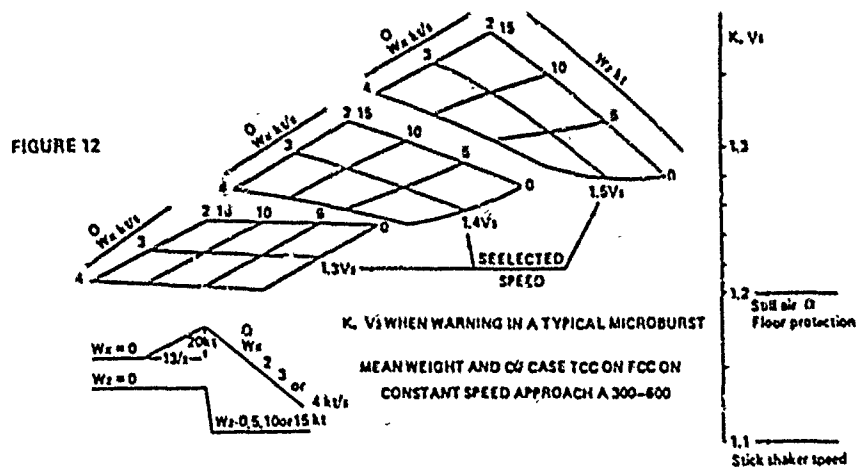
aerospatiale WINDSHEAR WARNING PRINCIPLE DIVISION AVIONS



aerospatiale NUISANCE WARNING PROBABILITY DIVISION AVIONS



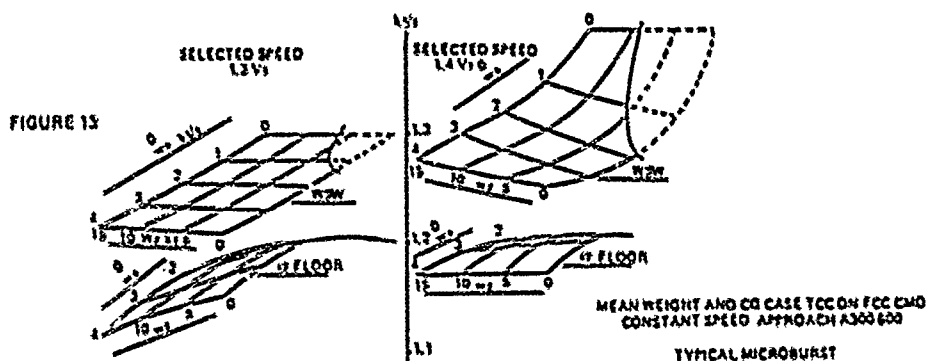
aerospatiale K. VS SITUATION AT WARNING DIVISION AVIONS





WARNING AND FLOOR COMPARED SITUATION

DIVISION AVIONS

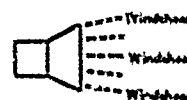
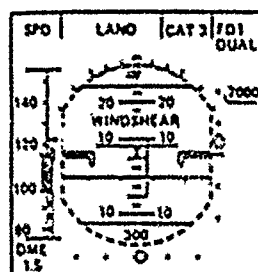


AUDIO AND VISUAL WARNING

GROUND TEST 1 or 2 FAC ENGAGED
Engine not running, perform Lamp test

DIVISION AVIONS

FIGURE 14



Windshear encounter non clean config.
and (from take off to 1000 Ft or from 1000 Ft to 50 Ft)
and WSW available 1 or 2 FAC ENGAGED.

Aural :Windshear 3 times when WSW gets on either FAC 1 or 2.

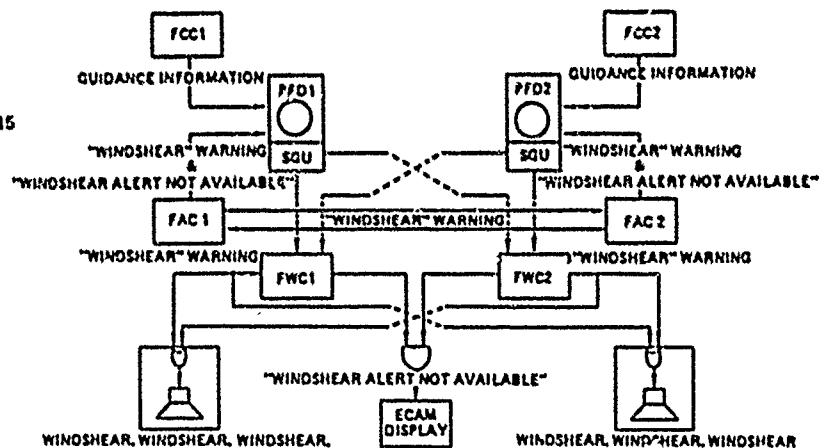
Visual :Windshear red on both PFD when WSW gets on either FAC 1 or 2 until WSW condition gets off both FAC 1 and 2 plus 15 s.



GUIDANCE AND WARNING ARCHITECTURE

DIVISION AVIONS

FIGURE 15



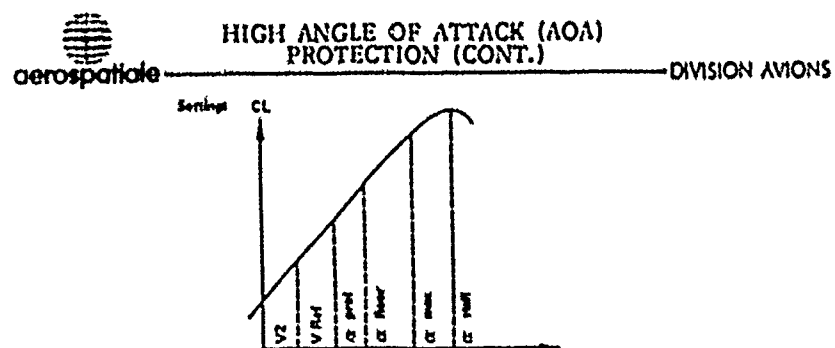
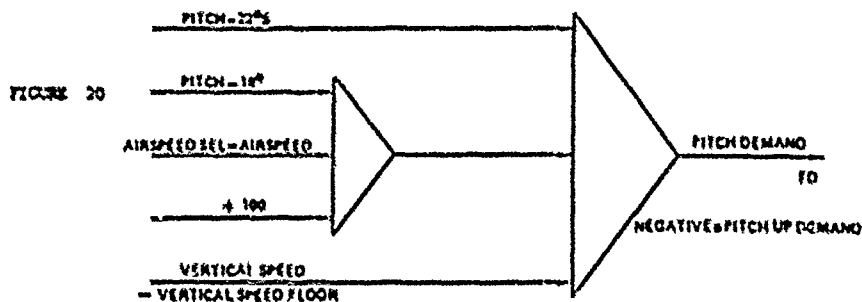


FIGURE 19



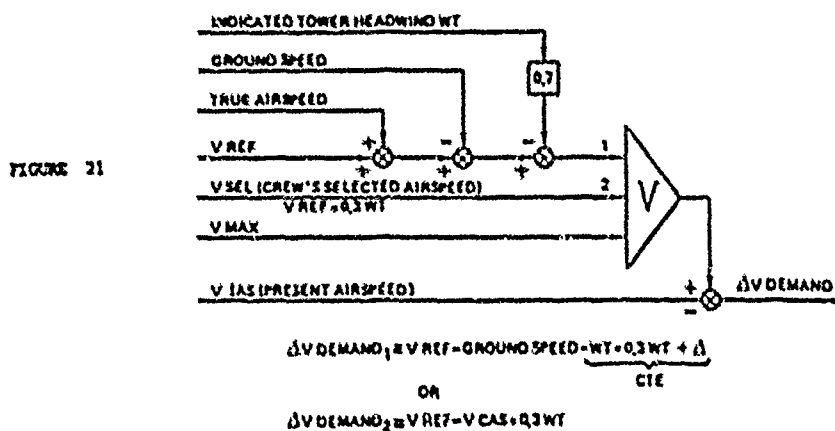
A320 SPEED REFERENCE CONTROL LAW

DIVISION AVIONS



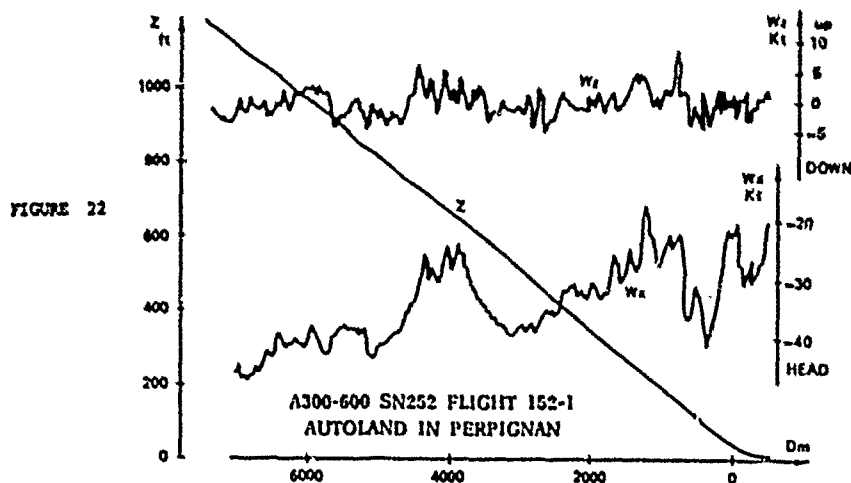
A320 MANAGED SPEED DEMAND-PRINCIPLE

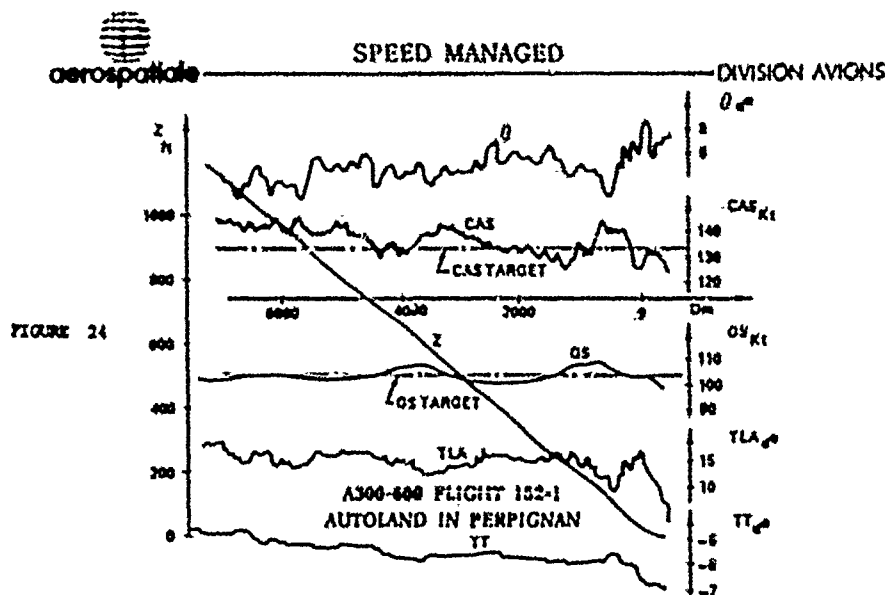
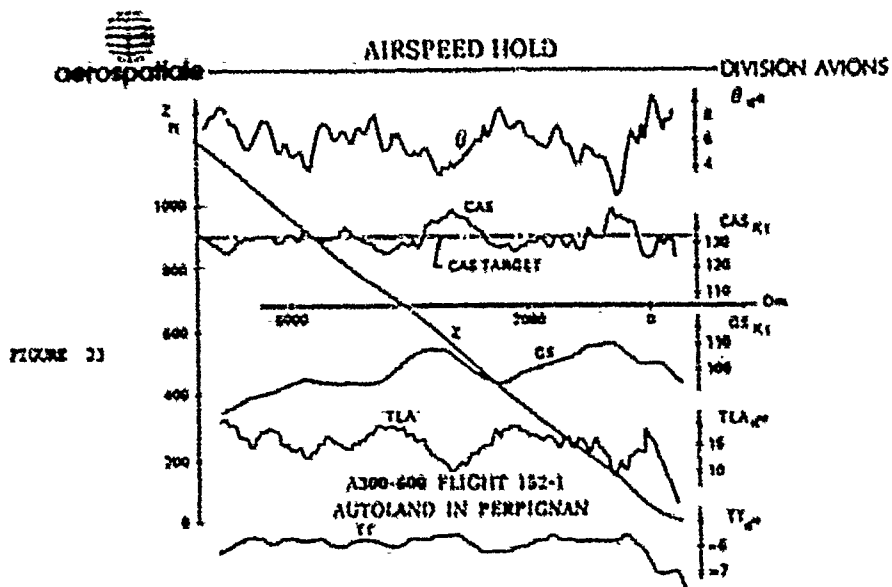
DIVISION AVIONS



RECORDED WIND

DIVISION AVIONS





A pitch control law for compensation of the phugoid mode induced by windshear

by L.M.B.C. Campos, A.J.N.M. Aguiar & J.R.C. Azeiteira,

Instituto Superior Técnico, 1096 Lisboa Codex, Portugal

In a previous paper (Ref. [1]) we have described the development of a flight test facility in Portugal, with support from AECAS, NLR in the Netherlands and Braunschweig University in Germany. This reference mentioned briefly some of the research projects for which the facility would be initially used, including among others studies in non-linear pitch stability and aircraft response to atmospheric disturbances. The purpose of the present paper is to discuss in more detail the flight mechanical theory which underlies these research projects: the comparison of theory with flight test data will have to await the availability of the CASA 212 Aviocar aircraft, which is at present already having all sensors installed but is still undergoing final check-out of instrumentation racks. The present theory starts with the presentation of a simple aircraft model describing pitch stability for flight along a constant glide slope, taking into account the phugoid but neglecting the short period mode. The model is solved to find pitch control laws for two problems: (i) the non-linear problem of keeping an aircraft on a constant glide slope in still air starting from an arbitrary initial velocity, possibly far removed from the steady flight condition; (ii) the linearized problem of keeping an aircraft on a constant glide slope in the presence of longitudinal and vertical winds of peak velocity up to 30% of the aircraft velocity, which provide a representation of a moderately strong windshear.

List of symbols

a	coefficient (8a) in total force
b	" (8b) & (13a) in total force
c	" (8c) & (13b) "
f	perturbation of ground speed (21a)
f ₀ , f ₁	coefficients in thrust law (6)
g	acceleration of gravity
k	coefficient for induced drag (4)
L	lengthscale of windshear (29,30)
m	mass of aircraft
q	perturbation of airspeed (27a)
r	" of incidence (27b)
s	lengthscale for stability (47a)
t	time
u	wind component along the flight path
w	" transverse to flight path
Δ	discriminant in (38a,b)
C _D	drag coefficient (3)
C _{Df}	form drag coefficient (4)
C _L	lift coefficient (2)
D	drag force (3) & (5)
F	total dimensionless force along flight path (7)
L	lift force (2)
P	dimensionless perturbation of groundspeed (31)
Q	" " " airspeed (32)
R	" " " incidence (33)
S	reference area (2)
T	thrust (1)
U	ground speed in still air (1)
U ₀	initial ground speed (41)
U ₁	ground speeds for steady flight (38a)
U _{nd}	minimum drag speed (39b)
U _u	groundspeed for steady horizontal flight (11)
U _w	" in the presence of wind (14)
V	ratio of groundspeed to minimum drag speed (49a)
V ₀	" initial groundspeed to minimum drag speed
V ₁	" steady flight speeds to minimum drag speed (50a,b)
V _w	airspeed in the presence of wind (15)
X	distance along flight path divided by windshear scale (34a)
Y	" lengthscale for stability (49a)
Z	time divided by timescale for stability (48b)
γ	glide slope angle (Figure 1)
δ	correction for non-elliptic loading
Δ	angle of airflow relative to flight path (16)
λ	coefficient of asymmetry of lift-drag polar (4)
A	aspect ratio
u	windshear susceptibility parameter (34b) & (35)
ρ	mass density of air (2)
θ	angle of incidence relative to angle of zero lift
θ ₀	initial angle of incidence
θ ₁	angles of incidence for steady flight
θ _u	angle of incidence for steady horizontal flight
θ _w	" " " in the presence of wind

θ_{nd}	angle of incidence for minimum drag
τ	time scale for stability (47b)
ζ	distance along flight path (figure 1)
v	coefficient in (22) and (23)

§1 - Introduction

It is well-known that an aircraft flying in still air in a constant glide slope has two steady flight speeds, one U_+ stable and above the U_{nd} the minimum drag speed U_{nd} , and the other U_- unstable and below U_{nd} the minimum drag speed. If an aircraft is put in a dive at a velocity distinct from the steady flight speeds, and if the stick is kept fixed, it will enter a phugoid motion [2,3], which exchanges periodically kinetic and potential energy. In the present paper we will consider the inverse problem, viz. finding the pitch control law which will exactly compensate the phugoid mode, by keeping the aircraft on a straight flight path, for arbitrary initial velocity, even if it is far removed from the steady flight speeds.

This problem is of practical interest in a variety of situations such as: (Problem A) an aircraft flying horizontally spots an objective of interest, and dives to track it accurately. The dive will most likely have started at a velocity distinct from the stable steady flight speed, and it will be necessary to use pitch control to keep on a constant glide slope. If the initial velocity is far removed from the steady flight speed, the pitch control law will be non-linear, and one problem we will consider (in Part III) is its determination. This pitch control law allows the aircraft velocity to stabilize on a constant glide slope, for the most accurate store delivery.

Another situation (Problem B) in which it is necessary to keep a constant glide slope, is, of course, the approach to land. In this case the preceding control law indicates how a constant glide slope can be maintained for an aircraft starting an emergency landing at an airstrip of opportunity, from an initial velocity which may be different from the normal approach speed. In a more normal scheduled approach to land, the aircraft starts at a steady speed, but may be perturbed from it by longitudinal or vertical winds, e.g. in a windshear (Problem C). In this latter case the phugoid mode is induced not by initial conditions (as in Problem A and B), but rather by atmospheric winds (Problem C), but an adaptation of the same aircraft model (Part I), will also determine the pitch control law for windshear compensation (Part III).

Part I - Mathematical model of aircraft for non-linear pitch attack

The determination of the pitch control law for exact compensation of the phugoid mode induced by windshears (Part II) or by initial conditions (Part III), is based on the same aircraft model which is presented first (Part I). We adopt the simplest aircraft model (52) which accounts for non-linear stability, so that it becomes possible (53) to obtain analytical solutions both for flight in moderate winds and for non-linear stability in still air.

§2 - Aerodynamic laws for lift and drag and thrust characteristic

We consider (Figure 1) an aircraft flying along a constant glide slope γ , acted upon by its weight W , the aerodynamic lift L and drag D , and the thrust T , which we assume to lie along the flight path. We denote by ζ the distance along the flight path, and the velocity $U = d\zeta/dt$ in still air is determined by balancing the inertia force, equal to mass times acceleration:

$$m \, dU/dt = T - D - W \sin \gamma, \quad (1)$$

against the thrust T , minus the drag D and the longitudinal $W \sin \gamma$ component of the weight W .

We could introduce in (1) the other aerodynamic force, namely, the lift L , by noting that it is balanced by the transverse component of the weight $W \cos \gamma$, where g is the acceleration of gravity:

$$mg \cos \gamma = L = \frac{1}{2} \rho S U^2 C_L(\theta); \quad (2)$$

In (2) we have expressed lift as usual [4,5] in terms of mass density ρ , velocity U (in still air we need not distinguish groundspeed and airspeed), reference area S (or 'corrected' wing area), and the lift coefficient C_L which is a function of incidence θ relative to the angle of zero lift (it equals the pitch angle relative to that for zero lift). The drag is given by a formula similar to (1), viz.:

$$D = \frac{1}{2} \rho S U^2 C_D(\theta), \quad (3)$$

where the drag coefficient consists of three contributions:

$$C_D(\theta) = C_{Df} + k (C_L(\theta))^2 + \lambda C_L(\theta), \quad (4)$$

namely: (i) the form drag, due to friction, which is independent of lift; (ii) the induced drag, which is proportional to the lift coefficient squared, through the coefficient k , which is minimum for elliptic loading, when it is given in terms of the aspect ratio A by $k=1/\pi A$, and a correction δ for non-elliptic loading may be applied in the form $k=(1+\delta)/\pi A$; (iii) the third term accounts for the non-parabolic, or non-

-symmetric lift-drag polar, and is proportional to the lift coefficient through the constant λ .

On substitution of (4) into (3), and using (2), it is found the dependence on velocity of the three components of total drag:

$$D = \frac{1}{2} \rho S U^2 C_{Df} + 2 (l/\rho S) (m g \cos \gamma)^2 U^{-2} + \lambda m g \cos \gamma. \quad (5)$$

viz.: (i) the form drag is proportional to the square of velocity; (ii) the induced drag is inversely proportional to the square of velocity; (iii) the asymmetry term for the drag polar is to a constant drag independent of velocity. Since we have neglected wave drag, the present mathematical model applies only to subsonic flight. We complete the model with simple thrust-versus-velocity law:

$$T(U) = (f_0 - f_1 U^2)/mg. \quad (6)$$

where f_0, f_1 are constants, viz. f_0 is the static thrust to weight ratio of the aircraft $f_0 T(0)/mg$, and f_1 specifies the reduction of thrust with velocity, and depends on density or altitude.

§3 - Velocity and incidence as functions of distance or time

In the mathematical model expressed by equations (1,2,3,4,6) there is an important implicit assumption, namely, the neglect of rotational inertia. Thus we have excluded the short period mode, and allowed only the phugoid mode, implying that the incidence needed to keep the aircraft on a constant glide slope can be obtained almost instantaneously through pitch control. This assumption is consistent with the aim of the present work of studying the compensation of the phugoid mode in isolation; the possible effects of the short period both as regards flight test records and the mathematical modelling of the data are considered in the discussion (§9). Since the motion on a constant glide slope is one-dimensional, and incidence is related to velocity by (2), the whole mathematical model can be reduced to a single differential equation of first-order.

One form of this equation specifies velocity as function of time, and follows from (1) on substitution of (5,6), viz. it states that the acceleration of the aircraft normalized to that of gravity:

$$g^{-1} dU/dt = F(U) = a - b U^2 - c/U^2. \quad (7)$$

equals a total dimensionless force $F(U)$ along the flight path, which depends only on velocity, as stated in (7) where the coefficients are given by:

$$a \equiv f_0 - \sin \gamma - \lambda \cos \gamma, \quad (8a)$$

$$b \equiv f_1 + (\rho S/2mg) C_{Df}, \quad (8b)$$

$$c \equiv 2 (l/\rho S) m g \cos^2 \gamma. \quad (8c)$$

We may express the acceleration in terms of distance ξ along the flight path using:

$$dU/dt = (dU/d\xi) (d\xi/dt) = U dU/d\xi, \quad (9)$$

to obtain an alternative form of (7), viz.:

$$(U/g) dU/d\xi = F(U) = a - b U^2 - c/U^2, \quad (10)$$

which expresses velocity as a function of distance.

Once the velocity has been determined, as a function of time by integrating (7), or as a function of distance by integrating (8), the incidence can be determined from the constancy (2) of the product of the square of velocity by the lift coefficient:

$$U^2 C_L(0) = \cos^2 \gamma \bar{U}^2 C_L(\bar{\theta}), \quad (11)$$

where $\bar{U}, \bar{\theta}$ refer to steady horizontal flight at the same weight. Comparing (11) with (2) we conclude that:

$$2mg/\rho S = \bar{U}^2 C_L(\bar{\theta}), \quad (12)$$

so that we can re-express the coefficients (8b,c) of the total force, in a form:

$$b = f_1 + (C_{Df}/C_L(\bar{\theta}))/\bar{U}^2, \quad c = k C_L(\bar{\theta}) \bar{U}^2 \cos^2 \gamma, \quad (13a,b)$$

involving $\bar{U}, \bar{\theta}$ instead of m, ρ, S .

Part II - Compensation of the phugoid mode induced by windshears

The preceding deduction applies to non-linear stability in still air, but it can be readily modified to account for the effects of arbitrary wind (§4). The linearization for 'moderate' wind of velocity not exceeding 30% of the groundspeed of the aircraft,

allows explicit analytic solution (§5). Taking as a windshear model a sinusoidal change from head to tailwind, superimposed with a half-sinusoidal downflow, we obtain (§6) the pitch control law which needs to be implemented to keep the aircraft on the same glide slope throughout the windshear encounter.

§4 - Non-linear pitch stability in the presence of arbitrary winds

In the preceding arguments concerning non-linear pitch stability in a dive in still air, the term velocity was used to designate indiscriminately the groundspeed and airspeed, since they coincide. They are distinct in the presence of wind, and in order to re-write the equations of motion in this case we must first choose a reference frame. We choose inertial axis fixed to the ground, so that the inertia force involves the acceleration of the groundspeed U_g , and it is balanced by the longitudinal component of weight and thrust minus drag expressed in terms of airspeed V , viz.: (7) in still air is replaced by:

$$g^{-1} dU_g/dt = F(V_g) = (U_g/g) dU_g/d\xi, \quad (14)$$

in the presence of arbitrary longitudinal u and transversal w winds (Figure 2), which relate:

$$V_g^2 = (U_g + u)^2 + w^2, \quad (15)$$

the groundspeed U_g to the airspeed V_g .

In the presence of a transversal wind in the vertical plane $w \neq 0$, the airspeed no longer lies along the flight path, but rather makes an angle α with it given by:

$$\alpha = \arctan \{w/(U_g + u)\}. \quad (16)$$

This must be added to the incidence when calculating the lift coefficient in (11), which is replaced by:

$$U^2 C_L(\theta) = V_g^2 C_L(\theta_0 + \alpha), \quad (17)$$

which specifies the dependence of the lift coefficient on wind velocities. If the aircraft flies at an incidence below the stall, the lift coefficient is proportional to that incidence (measured from the incidence for zero lift), and (17) simplifies to:

$$U^2 \alpha = [(U_g + u)^2 + w^2] (\theta_0 + \arctan \{w/(U_g + u)\}), \quad (18)$$

where the longitudinal u and transversal w wind appear explicitly.

We may summarize as follows the non-linear pitch stability problem in the presence of arbitrary winds: (i) the wind components $u(\xi)$, $w(\xi)$ along the flight path are assumed known; (ii) the total dimensionless force along the flight path is given by (7), in terms of the airspeed (15), with coefficients (8a: 13a,b); (iii) the differential equation (14) is integrated to specify the groundspeed $U(\xi)$ along the flight path; (iv) substituting this into (15) we obtain the airspeed $V(\xi)$ along the flight path; (v) the incidence along the flight path follows from (17) in stalling conditions, or (18) away from the stall. The key step is (iii) the integration of the stability equation, which can be performed: (i) numerically, in the extreme case of winds of velocity comparable to the groundspeed, which is very rare and hazardous; (ii) even in strong storms, the wind speed does not usually exceed 30% of the groundspeed, and in this case analytic integration is possible, as we proceed to show.

§5 - Flight with a constant glide slope in moderate winds

We consider a 'moderate' wind to be one not exceeding 30% of the groundspeed, so that the square of the wind velocity $0.3^2 = 0.09 \ll 1$ is negligible compared with the square of the groundspeed:

$$U^2 \gg (u+w)^2 \geq u^2, w^2, u w. \quad (19)$$

Applying this approximation in (15) and (18) it follows that:

$$V_g = U_g + u, \quad \alpha = w/U_g, \quad (20a,b)$$

the airspeed (20a) is affected only by the longitudinal wind, and the change of incidence (20b) is due only to the transverse wind.

We denote by U the groundspeed in still air (7), and by U_g the groundspeed in the presence of wind (14), so that the perturbation in groundspeed due to wind (21a):

$$f \equiv U_g - U, \quad g^{-1} df/dt = F(V_g) - F(U), \quad (21a,b)$$

satisfies (21b). The assumption of moderate wind implies that $f^2 \ll U^2$ as will be checked later, and allows the linearization of the right-hand-side of (21b):

$$F(V_g) - F(U) = (dF/dU)(V_g - U) = (U/g) v (f+u), \quad (22)$$

where we have used: (1) for the coefficient (7):

$$v \approx (g/U) dF/dU = -2g (b-c/U^4); \quad (23)$$

(11) for the difference of airspeed (20a) in the presence of wind and groundspeed in still air (21b):

$$V_x - U = (V_x - U_x) + (U_x - U) = f + u. \quad (24)$$

Substituting (22) into (21b) we obtain:

$$df/d\xi = v [f + u(\xi)], \quad (25)$$

as the linearized stability equation, where A is a constant calculated for the groundspeed in still air.

If the longitudinal wind along the flight path $u(\xi)$ is given, then the perturbation of groundspeed it causes is specified by the forced solution of (25), viz.:

$$f(\xi) = v e^{v\xi} \int_0^\xi e^{-v\eta} u(\eta) d\eta. \quad (26)$$

where the start of the wind is taken as position $\xi=0$. The perturbation of airspeed equals that of groundspeed (26) plus (20a) the longitudinal wind (27a):

$$q(\xi) = f(\xi) + u(\xi), \quad r(\xi) \approx \theta_0 - \theta = -(u(\xi) + 20 u(\xi))/U. \quad (27a,b)$$

whereas the perturbation of incidence (27b) involves also the transversal wind $w(\xi)$ to U . The latter expression was obtained by linearizing:

$$0 = V_x^2 (\theta + \theta_0) - U^2 \theta = (U^2 + 2uU)(\theta_0 + \theta/U) - U^2 \theta = U^2(\theta_0 - \theta) + 2uU\theta + wU. \quad (28)$$

where we have used the constancy of (18) to determine the difference between the incidence θ in still air and θ_0 in the presence of wind.

36 - Application to wind profiles typical of a windshear

Meteorological observations of windshears show that they can be modelled [6,7] by (Figure 3) a toroidal vortex above the ground, producing a downflow through the core, which is deflected into low-level jet. For an aircraft flying through the windshear the windfield appears (Figure 4) as a superposition of a longitudinal wind of maximum strength AU , changing from a head to a tailwind:

$$u(\xi) = A U \sin (2\pi\xi/L). \quad (29)$$

at the peak of a downflow of amplitude $8BU$:

$$w(\xi) = -8 U \sin (\pi\xi/L). \quad (30)$$

where L denotes the scale of the windshear.

Substituting (29) into (26; 27a,b) specifies the dimensionless perturbations of groundspeed:

$$P(X) \equiv f(\xi)/U = A/L(1+\pi) [u(1-\cos(2\pi X)) - \sin(2\pi X)], \quad (31)$$

airspeed:

$$Q(X) \equiv (u(\xi) + f(\xi))/U = P(X) + A \sin (\pi X). \quad (32)$$

and incidence:

$$R(X) \equiv r(\xi)/\theta_0 - 1 = -2 Q(X) - 8 \sin (\pi X). \quad (33)$$

as function of dimensionless distance (34a) along the flight path:

$$X \equiv \xi/L, \quad u \equiv 2\pi/vL, \quad (34a,b)$$

where the aerodynamics of the aircraft are specified by the parameter u (34b).

Using (23) and (13a,b) the windshear susceptibility parameter is given by:

$$\mu = \pi/(g(c/U^4 - b)) = \pi U^2/(gL[k C_L(\theta_0) - C_{Df}/C_L(\theta_0)]). \quad (35)$$

where we have assumed constant thrust $f_1=0$ equal to the maximum available as it is recommended to apply full throttle during a windshear. We consider a lengthscale $L=1000-2000$ m for the windshear, approach speed $U=30-60$ m/s, acceleration of gravity $g=9.80$ m/s², lift coefficient about unity $C_L=1$ for approach, when induced drag dominates form drag; the coefficient $k=(1+\delta)/\pi A$ uses a correction $\delta=0.25$ for non-elliptic loading, and an aspect ratio $A=2-8$ depending on the type aircraft, e.g. we are lead to a windshear susceptibility parameter taking a minimum value $\mu=1$ for a slow light aircraft of large aspect ratio ($U=30$ m/s, $A=8$), to a maximum $\mu=13$ for a large jet transport ($U=60$ m/s, $A=8$), and intermediate values $\mu=6$ for a jet fighter ($U=60$ m/s, $A=2$). The plots

in Figure 5 correspond to various values of U_1 for a windshear with peak headwind 25% of the groundspeed and peak downflow 15% of the groundspeed multiplied by approach incidence. They show that in order to retain a constant glide slope it is necessary (top plot) to increase the groundspeed in the tailwind phase of the windshear, so as to avoid (middle plot) to large a drop of airspeed from the head to the tailwind phase; this requires (bottom plot) decreasing incidence in the head-wind phase and increasing it in the tailwind phase.

Part III - Compensation of the phugoid mode induced by initial conditions

The pitch control law in Figure 5 (bottom) for compensation of the phugoid mode induced by windshears is only achievable if the incidence remains below the stall value θ_{st} . The same applies to the pitch control law for compensation of the phugoid mode induced by initial conditions, which we calculate next.

§7 - Evolution curves for non-linear stability and instability

If an aircraft starts a dive in still air at a velocity far removed from the steady flight speeds U_1 , we have a non-linear pitch stability problem, for which the equations (7) or (10) have to be integrated exactly. They can be re-written in the form:

$$g^{-1} dU/dt = -(b/U^2) \{ (U^2 - U_+^2) (U^2 - U_-^2) \} = (U/g) dU/dt. \quad (36)$$

where U_{\pm} are the steady flight speeds, for which the acceleration vanishes ($U=U_{\pm}$ implies $dU/dt=0$). The steady flight speeds are the roots of:

$$0 = (bU^4 - aU^2 + c) = b (U^2 - U_+^2) (U^2 - U_-^2). \quad (37)$$

and are specified by (38a):

$$U_{\pm}^2 = (a \pm \sqrt{\lambda})/2b, \quad \lambda \equiv a^2 - 4bc \geq 0. \quad (38a, b)$$

where the condition (38b) must be satisfied for steady flight to be possible. The equality sign specifies the minimum thrust to weight ratio needed for steady flight:

$$f_0 \geq \sin \gamma + \lambda \cos \gamma + 2\sqrt{\lambda} C_{Df} \cos \gamma. \quad (39a)$$

at the minimum drag speed:

$$U_{md} = a/2b = \sqrt{\lambda/C_{Df}} \cos \gamma C_L(\gamma) U, \quad (39b)$$

where we have used (8a; 13a, b) with constant thrust $f_1=0=f_2$. In the case of horizontal flight $\gamma=0$ and symmetric drag polar $\lambda=0$, we obtain the usual [8] formula $f_0=2\sqrt{\lambda} C_{Df}$ for the minimum thrust-to-weight ratio needed for steady flight.

The motion at velocity distinct from U_{\pm} is unsteady, as shown (28) by the signs of the acceleration:

Case	$U < U_-$	$U_- < U < U_+$	$U > U_+$	
acceleration	$dU/dt < 0$	$dU/dt > 0$	$dU/dt < 0$	(40)

The table shows that: (i) the upper steady flight speed U_+ is stable, because a deviation below causes an acceleration, and a deviation above a deceleration, until the velocity U_+ is regained; (ii) the lower steady flight speed U_- is unstable, because a deviation below causes further deceleration, and a deviation above further acceleration, so that in both cases there is no return to the steady state. These stability characteristics are known [9, 10], and we proceed to calculate the evolution curves describing the approach to the stable U_+ and deviation from the unstable U_- steady flight speeds.

The equation (36) may be integrated to specify the distance along the flight path ξ :

$$\exp(-2bg\xi) = \{ (U(\xi)^2 - U_+^2) / (U_0^2 - U_+^2) \}^{1/(1 - U_-^2/U_+^2)} \times \{ (U_0^2 - U_-^2) / (U(\xi)^2 - U_-^2) \}^{1/(U_+^2/U_-^2 - 1)}, \quad (41)$$

as a function of velocity $U(\xi)$, with $U_0 \equiv U(0)$ denoting the initial velocity. Since the function $U(\xi)$ is highly non-linear it is not simple to invert (41), and it is preferable to leave it in inverse form, with distance as function of dimensionless ratios of velocities, both in the bases and exponents. We can also obtain time elapsed as function of velocity:

$$\exp(-2bg(U_+ + U_-)t) = \{ (U(t) - U_+)(U_0 + U_+) / (U_0 - U_+)(U(t) + U_+) \}^{1/(1 - U_-/U_+)} \times \{ (U_0 - U_-)(U(t) + U_-) / (U(t) - U_-)(U_0 + U_-) \}^{1/(U_+/U_- - 1)}. \quad (42)$$

by integrating the first equation (36). The laws specify the way in which the velocity U must evolve as a function of time t (42) or distance ξ (41) so as to keep a constant glide slope, from an arbitrary initial velocity U_0 . The corresponding laws for incidence are obtained by making the substitutions:

$$U(t), U_0, U_+, U_{md} \rightarrow 1/\sqrt{\theta(t)}, 1/\sqrt{\theta_0}, 1/\sqrt{\theta_+}, 1/\sqrt{\theta_{md}}, \quad (43)$$

because away from the stall we have $U^2 \theta = \text{const.}$, where the constant may be omitted because (41,42) involve only ratios.

§8 - Computation of model for comparison with flight test data

The preceding solutions may be linearized for short times or distances, i.e. when the velocity U is relatively close to the initial velocity U_0 , and still far from the steady flight speeds:

$$(U^2 - U_0^2)^2 \ll (U_+^2 - U_0^2)^2, \quad (44)$$

in this case the evolution of the velocity is exponential with distance:

$$(U(z))^2 = U_0^2 + (U_+^2 - U_0^2)(1 - U_+^2/U_0^2)(1 - e^{-z/s}), \quad (45)$$

and in time:

$$U(t) = U_0 + \frac{1}{2}(U_+ + U_-)(U_+^2/U_0^2 - 1)(1 - U_+^2/U_0^2)(1 - e^{-t/T}), \quad (46)$$

with lengthscale s and timescale T given by:

$$s = 1/2bg, \quad T = s/(U_+ + U_-). \quad (47a,b)$$

These length and time scales apply only to short distances and times, viz. $U=U_0$ in (45) for $z \ll s$, and $U=U_0$ in (46) for $t \ll T$, but these expressions do not hold for $z \gg s$ or $t \gg T$.

For long distances and large times we must use the exact response curves (41,42); for $t \gg T$, $z \gg s$ the left-hand sides vanish and the right-hand sides show that either $U \rightarrow U_+$, i.e. the stable steady flight speed U_+ is approached or $U \rightarrow U_-$ and there is a large deviation from the unstable steady flight speed U_- . The non-linear stability curves for approach to U_+ , and instability curves for deviation from U_- , are readily calculated for each initial velocity U_0 , by giving values to the velocity U , and finding the distance z (41) and time t (42) when it is attained. The curves are plotted in Figure 6 top (bottom) where distance z (time t) is normalized to the lengthscale (48a) [timescale (48b)]:

$$Y \equiv z/s, \quad Z \equiv t/T, \quad (48a,b)$$

and the velocity is normalized to the minimum drag speed (49b):

$$V \equiv U/U_{md}, \quad U_{md}^2 = (U_+^2 + U_-^2)/2, \quad (49a,b)$$

and it follows from (30a, 31b) that the square of the minimum drag speed is the arithmetic mean of the squares of the steady flight speeds (49b); thus if we choose a stable steady flight speed 30% above the minimum drag speed (50a):

$$V_+ \equiv U_+/U_{md} = 1.3, \quad V_- \equiv U_-/U_{md} = \sqrt{2 - V_+^2} = 0.748, \quad (50a,b)$$

the unstable steady flight speed (50b) is 25% below the minimum drag speed.

We may now discuss the comparison of the stability curves in Figures 6 and 7 with flight test data. Suppose we put the aircraft in a dive at a glide slope angle γ such that the upper steady flight speed lies 30% above the minimum drag speed. If: (i) the initial velocity lies above the steady flight speed $V_0 > V_+$, viz. $V_0 > 1.3$ then the aircraft should decelerate, e.g. along the curve starting at $V_0 = 1.5$ and tending to $V_+ = 1.3$; (ii) the initial velocity is $V_0 = 1.3$ it should remain constant; (iii) the initial velocity lies between the two steady flight speeds $0.75 < V_0 < 1.3$, then the aircraft should accelerate towards the higher value, e.g. along the curve starting at $V_0 = 1.1$ and tending to $V_+ = 1.3$; (iv) the initial velocity is below the minimum drag speed, then there is an inflexion in the stability curve, corresponding to the inversion of controls at the minimum drag speed, e.g. along the curve starting at $V_0 = 0.9$ and tending to $V_+ = 1.3$; (v) initial velocity at or slightly below the unstable steady speed is a dangerous condition leading to rapid divergence or loss of speed towards the stall. In the flight tests the aircraft should be kept on a constant glide slope, e.g. using the ILS beams as reference, and applying pitch control as necessary. The records of velocity as function of distance (time) would then be compared with the curves in Figure 6 top (bottom) to check the agreement or disagreement with the theoretical predictions.

§9 - Discussion

The flight tests just described should be performed later this year, using the Portuguese BAFR (Basic Aircraft for Flight Research) described elsewhere [1]. This is a CASA 212 Aviocar of the Portuguese Air Force, fitted with flight test instrumentation offered by the NLR of Netherlands, in an installation designed and tested at the Aeronautics Laboratory of I.S.T. of Lisbon Technical University, with cooperation of the Braunschweig Technical University in Germany. At the present the aircraft is at OGMA (Oficinas Gerais de Material Aeronáutico) where all sensors have been installed, and fitting out of the main equipment rack is taking place, prior to final testing at the aeronautics laboratory, and first flights from Sintra airfield. Since we must defer to a future occasion the comparison of the present theory of pitch stability with

flight test data, we conclude with some remarks on the method we have used and possible further developments.

The study of flight in the presence of windshears has been directed at the reconstruction of particular incidents [11,12], to devise escape procedures or maximize chances of survival [13]. The methods used are usually numerical, and allow the simulation of complex aircraft models and windfields, although the flight mechanical process of interaction between the aircraft and the perturbed atmosphere is not always clear from the final output data. Analytical models, although limited to simple aircraft and aerodynamic models, give a better insight into the physical processes of interaction between the aircraft and wind [14-16]. In the present paper we have derived pitch control laws which maintain a constant glide slope in the presence of a model sinusoidal windshear. Since this theory cannot be readily compared with flight data, the comparison can be made using another application of the same theory, viz. the prediction of the evolution with time and distance of the velocity or incidence for an aircraft flying in still air on a constant glide slope from an arbitrary initial velocity, possibly far removed from the steady flight speeds. This non-linear stability problem should provide a significant test of the theory once flight data becomes available for comparison.

Pending the performance of the intended flight tests, we conclude with some speculative thoughts on further developments of the present theory. Its main restriction is likely to be the neglect of rotational inertia or the short period mode. This should become apparent in flight test data, viz. the difference between the evolution of velocity versus time recorded in flight and the theoretical prediction, should give evidence as to the importance of the short period mode relative to the phugoid mode. In the unlikely case they are of comparable magnitude, a non-linear theory involving rotational inertia would be needed. If, as is likely, flight test data shows that the short period mode to have a smaller effect than the phugoid mode, then it should be possible to linearize the equations of motion including rotational inertia, about the non-linear solution without rotational inertia presented here. This improved theoretical model, including rotational inertia, could then be compared with flight test data, to check whether it provides improved agreement. The method which we have adopted here, and propose to extend further in the future, is based on direct integration of the equations of motion; in the linear case it gives the same results as the method of linear stability derivatives, which is in most widespread use [17,18], e.g. for the problem discussed in Part II. For non-linear problems, such as that discussed in Part III, the direct integration [19,20] of the equations of motion is simpler and more accurate than the use of stability derivatives say to second or third order. Since we wished to use the same method to discuss (i) linear response to windshears and (ii) non-linear pitch stability, the direct integration of the equations of motion was adopted as a common starting point.

References

- [1] L.M.B.C.CAMPOS, H.F.RAMOS & A.A.FONSECA, "On the development of a flight test capability in Portugal and some related research projects", AGARD CP- , paper 28.
- [2] F.W.LANCHESTER, Aerodnetics, Constable, London 1908, 2nd ed. 1945.
- [3] R.VON MISES, Theory of Flight, McGraw-Hill 1945, repr. Dover 1961.
- [4] L.M.MILNE-THOMSON, Theoretical Aerodynamics, MacMillan 1960, repr. Dover 1975.
- [5] L.D.LANDAU & E.F.LIFSHITZ, Fluid Mechanics, Pergamon 1960.
- [6] A.A.WOODFIELD & J.F.WOODS, Worldwide experience with windshear during 1981-2, AGARD CP-347, paper 11.
- [7] S.ZHU & B.ETKIN, A fluid dynamic model of a downburst, Univ. Toronto Aerospace Dep., Rep. 271 (1983).
- [8] M.J.LIGHTHILL, Informal introduction to fluid mechanics, Oxford University Press 1986.
- [9] S.NEUMARK, Problems of speed stability below the minimum drag speed, and the theory of stability under constraint, A.R.C. Report 2983, 1953.
- [10] W.J.G.PINSKER, Glide path stability of an aircraft under speed constraint, A.R.C. Report 3705, 1971.
- [11] G.SCHANZER, Influence of windshear on flight safety, AGARD CP-347, paper 12.
- [12] T.T.FUJITA, Microburst windshear at New Orleans International Airport, Louisiana, on July 9, 1982. Univ. of Chicago; SMRP Res. paper 199, 1983.
- [13] A.MIELE, T.WANG & W.W.MELVIN, Optimization and guidance of landing trajectories in a windshear, ICAS Symposium 1988, proceedings p.445-462.
- [14] L.M.B.C.CAMPOS, On the influence of atmospheric disturbances on aircraft aerodynamics, The Aeronautical Journal, paper 1085, June/July 1984, pages 257-264.
- [15] L.M.B.C.CAMPOS, On the disturbance intensity as indicator of aircraft performance

degradation in a perturbed atmosphere. 2nd Int. Conf. on Aviation safety, Toulouse 1986. proceedings Cepadues Editions, pages 175-190.

- [16] L.M.B.C. CAMPOS. On aircraft flight performance in a perturbed atmosphere. The Aeronautical Journal, paper 1305, October 1986. pages 302-312.
- [17] G.H. BRYAN. Stability in Aviation. MacMillan 1911.
- [18] A.W. BARISTER. Aircraft dynamic stability and response. Pergamon Press 1980.
- [19] P. PAINLEVÉ. Etude sur le régime normal d'un aéroplane. Technique Aeronautique 1(1910). 3-11.
- [20] L.M.B.C. CAMPOS. On the compensation of the phugoid mode induced by windshears and initial conditions. ICAS Symposium 1988. proceedings p.435-444.

Legends for the figures

Figure 1: Descent with unsteady velocity $U = dC/dt$ with a constant glide slope γ , where t is time and C is the distance along the flight path, related to horizontal x and vertical y distance by $x = sec\gamma \cdot C$ and $y = C \sin\gamma$. Neglecting the angle between the thrust axis and the flight path, the thrust is balanced by drag, inertia force and component of weight along flight path; the transverse component of weight is balanced by lift. In this case, of unsteady motion with constant glide slope in still air, the velocity may be interpreted equivalently as groundspeed or airspeed.

Figure 2: The distinction between groundspeed U and airspeed V becomes necessary in the case when the unsteady motion along the constant glide slope is due to wind, whose velocity we split into components parallel w and orthogonal v to the flight path. If the glide slope γ is small these do not differ much from respectively the horizontal and vertical wind components.

Figure 3: An atmospheric event of concern to safety and involving strong wind changes, is the windshear, which may be represented by a toroidal vortex above the ground. A cross-section by a vertical plane passing through the axis of the torus shows two opposite vortex centers, inducing between them a downflow, which is deflected horizontally near a stagnation point, where the ground intersects the axis of the torus.

Figure 4: The simplest representation of the windfield due to the windshear is the superposition of: (i) a longitudinal wind, of amplitude a fraction A of the unperturbed groundspeed of the aircraft, changing from headwind to tailwind as the aircraft flies under the axis of the toroidal vortex; (ii) a downflow, with amplitude a fraction B of the product of unperturbed groundspeed and incidence, which peaks under the axis of the toroidal vortex, where the longitudinal wind reverses direction.

Figure 5: In order to keep a constant glide slope in a typical windshear, it is necessary (top) to start to increase groundspeed before the transition from head to tailwind, so that (middle) the airspeed is higher in the headwind phase than in the tailwind phase, and (bottom) the control inputs should be pitch-down before and pitch-up after the peak downflow. The magnitude of the control inputs, and their exact location along the windshear, depend on the windshear susceptibility parameter μ , which varies from about unity for a lightplane, to about then for a large jet transport, with values about half-way for a high-performance fighter.

Figure 6: Another type of control law applies in still air, when the perturbation of steady flight, along a constant glide slope, is due not to wind, but to an initial velocity V_0 far removed from either of the steady flight speeds V_{\pm} . In this case we plot instead of incidence, the ratio of velocity to the minimum drag speed, as a function of dimensionless (top) distance divided by lengthscale, and (bottom) time divided by timescale. These length and timescales apply to the non-linear evolution curves, shown for 15 different initial flight speeds, which demonstrate convergence to the upper stable steady flight speed V_{+} , divergence from the lower unstable steady flight speed V_{-} , and inflexion due to control inversion at the minimum drag speed.

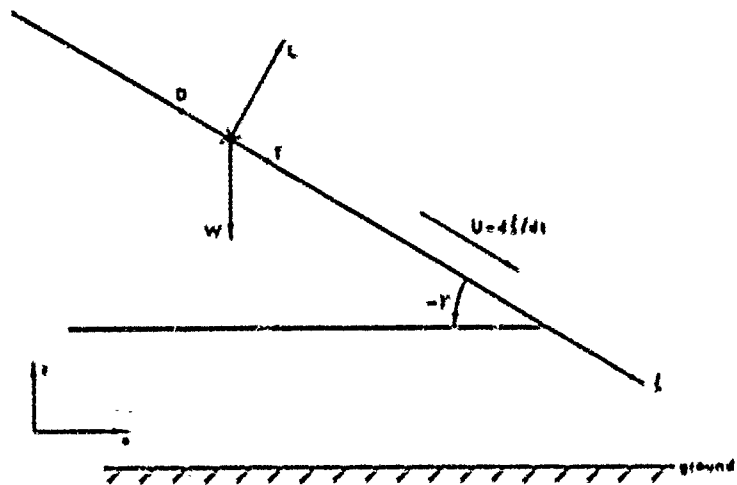


FIGURE 1

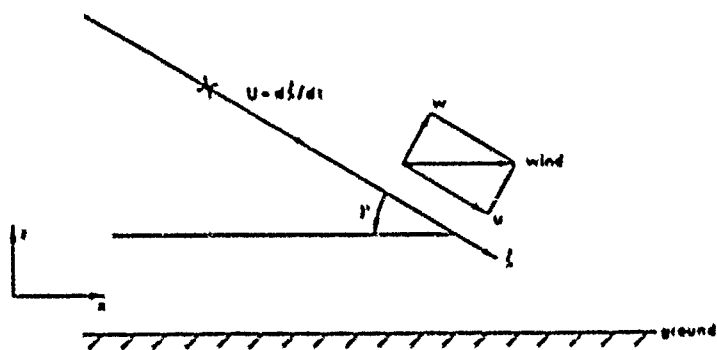


FIGURE 2

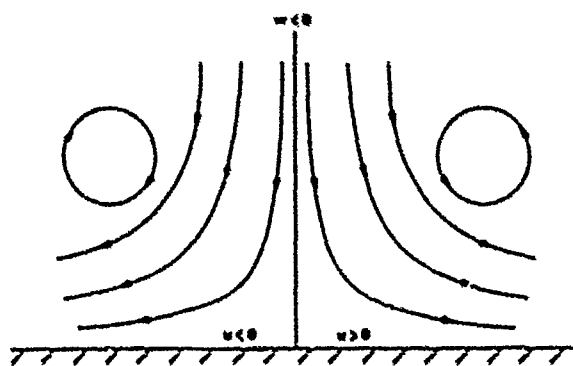


FIGURE 3

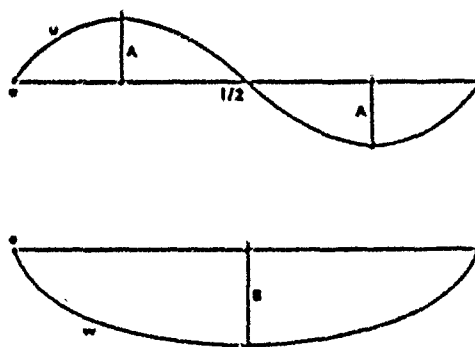
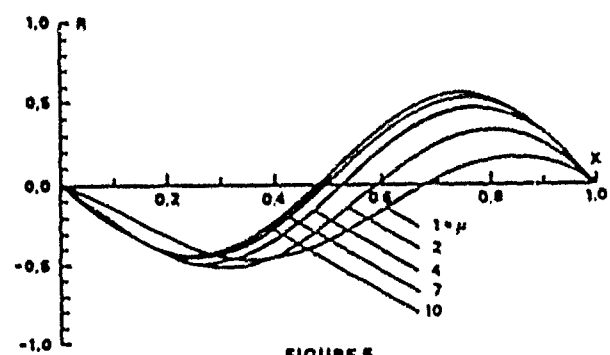
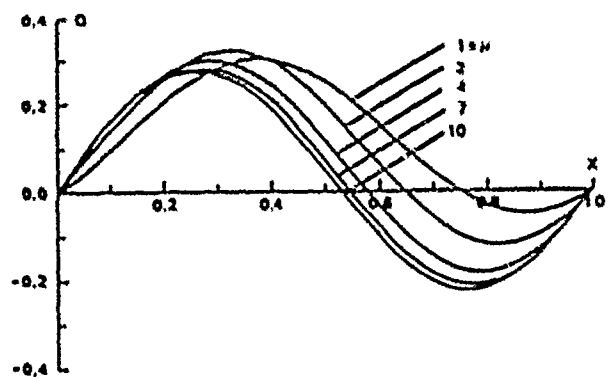
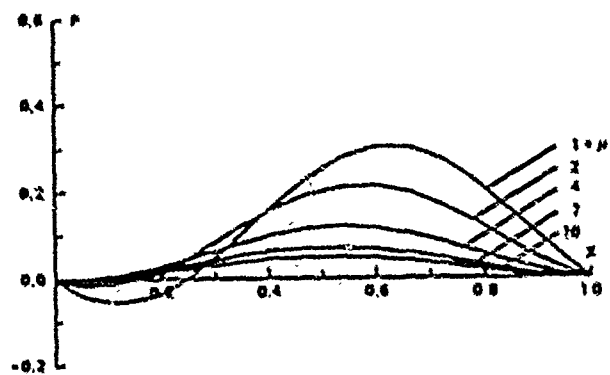
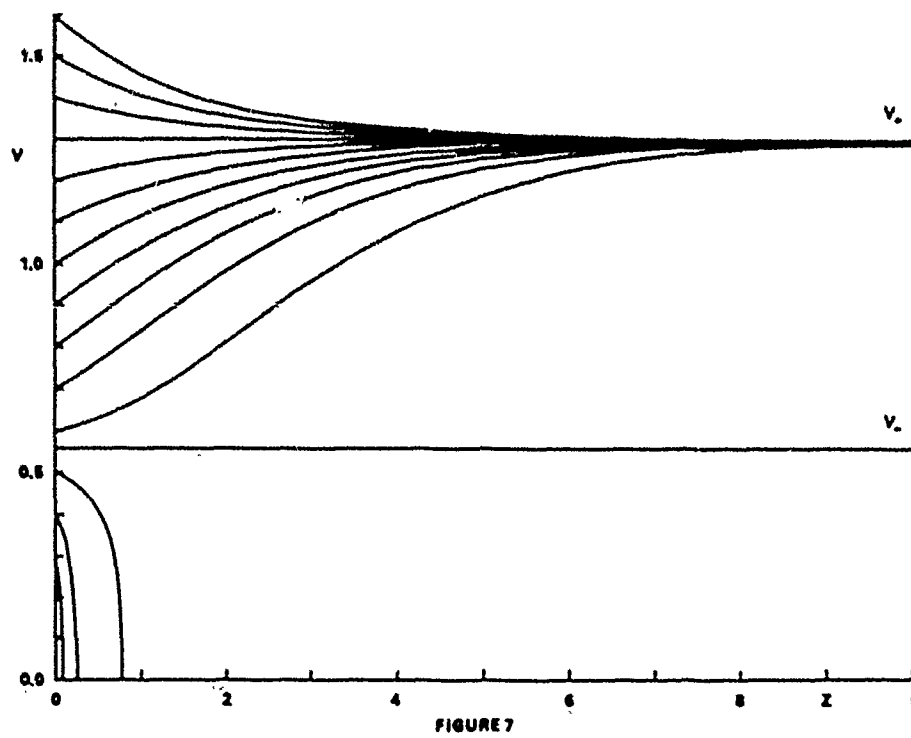
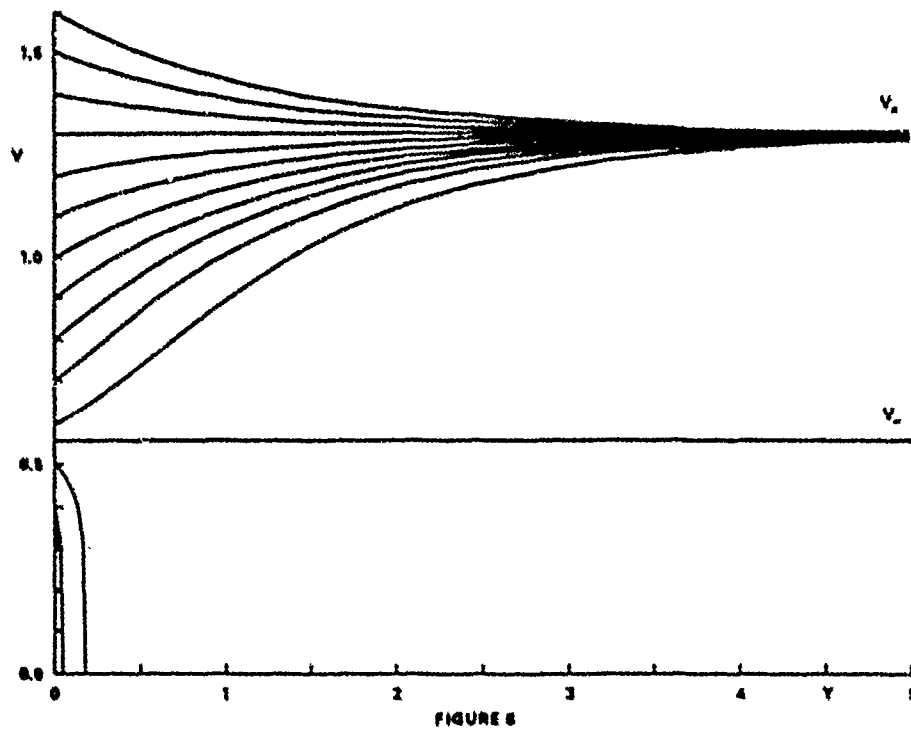


FIGURE 4

$$A = 0.25 \pm 0.15 \pi$$



FIGURES



ADVERSE WEATHER OPERATIONS DURING THE CANADIAN ATLANTIC STORMS PROGRAM

by

J. I. MacPherson
Flight Research Laboratory
National Aeronautical Establishment
National Research Council
Ottawa, Ontario, K1A 0N6
Canada

G. A. Isaac
Cloud Physics Research Division
Atmospheric Environment Service
Downsview, Ontario, M3H 5T4
Canada

SUMMARY

For cooperative research programs with the Atmospheric Environment Service of Canada, the NRC Twin Otter Atmospheric Research Aircraft has been instrumented to measure the motion and thermal structure of the atmosphere and the microphysics of cloud and precipitation. In 1986 the aircraft was flown in the Canadian Atlantic Storms Program to investigate large east-coast storms that typically account for the bulk of the winter-time precipitation in the Maritime provinces, and cause havoc for airborne and surface transportation. A variety of adverse flight conditions were experienced in this project, including heavy snow contributing to limited IFR alternates, airframe icing, wind shear and crosswinds on landing. The paper presents examples of these incidents analyzed from both a flight research and meteorological perspective using aircraft-recorded data. For this project, additional specially-designed deicing boots were installed on the Twin Otter's vertical tail and the wing and landing gear struts. The performance of the enhanced aircraft deicing system will be discussed using data from three icing encounters.

1. INTRODUCTION

The East Coast of Canada is frequently lashed by severe cyclonic winter storms in which winds can reach gale force and precipitation rates can be high. Precipitation types can vary among rain, snow and freezing rain. Canadian east coast storms can be expected to differ from storms on the west coasts of North America and Europe. The latter storms have had a long track over the ocean and have just encountered land. In contrast, many of the Canadian east coast storms are newly developed and most have been significantly affected by land. In addition, these Canadian storms are typically characterized by subfreezing conditions at the surface or by periods of such conditions. Although forecasts have improved in the last decade, the track, movement and often rapid intensification of these storms are not adequately handled by existing weather prediction models. Canada has undertaken a long term program, the Canadian Atlantic Storms Program (CASP), to study winter storms in the Atlantic Region. The general objectives of the first CASP field experiment held from January 15 to March 15, 1986 were to study storm behaviour, embedded mesoscale features and complementary oceanographic phenomena. The project was supported by the Federal Panel on Energy Research and Development (PERD).

The Twin Otter Atmospheric Research Aircraft (Fig. 1), fully instrumented for air motion and cloud physics measurements, flew 31 missions in this program, operating from Canadian Forces Base Shearwater near Halifax, Nova Scotia. Its recorded measurements form an important component of a comprehensive dataset from a variety of coordinated sensing systems focused on these storms (Ref. 1). These included a second aircraft (Canada Centre for Remote Sensing DC-3), satellites, three weather radars, meteorological towers, oceanographic buoys, ships, radiometers and an enhanced radiosonde network. The experiment was timed to coincide with a similar investigation in the United States, the Genesis of Atlantic Low Experiment (GALE), so that provision could be made to study storms that traversed both the American and Canadian project areas. Figure 2 shows the composite tracks of the storms that occurred in the Canadian project area during CASP.

In normal aircraft operations, pilots attempt to avoid the very conditions that were the subject of this research program. Great care had to be taken in the planning and operation of the research flights to ensure safety, while at the same time collecting important data on atmospheric motion and precipitation within the storms. The paper outlines measures taken to improve the deicing capabilities of the NAE Twin Otter, and presents example results for icing encounters during the CASP flights. Illustrations of other storm-related hazards experienced during these flights are given, including high winds, crosswind landings, wind shear and turbulence.

2. AIRCRAFT RANGE

For operation of the Twin Otter in major east-coast storms, the first limitation to be considered had to be the range of the aircraft in IFR conditions. The Twin Otter has a fuel capacity of 2450 lb. However, with the scientific instrumentation required for CASP, a crew of four and survival gear, only 2200 lb of fuel

could be carried at takeoff for the majority of the project flights. In normal cruise, the aircraft burns about 600 lb/hour and has a maximum true airspeed of 140 knots. Clearly, the operational range is small relative to the scale of Atlantic storms, so particular care had to be given to go/no-go decisions and the selection of a safe alternate airfield.

For IFR flight, a sufficient fuel reserve must be carried to allow for diversion to the alternate and 45 minutes of holding. When this reserve is subtracted from the 2200 lb takeoff fuel, the result is the amount available for project operations from takeoff to initial approach at the project base (CFB Shearwater). Figure 3 depicts the available flight endurance for project use as a function of the alternate airfield. For example, if 3 hours of project flight time was required, then this could be done only when Halifax International was an available alternate. On the other hand, if Moncton was the only alternate above limits, then an approach to the base at Shearwater would have to be made after about two hours of IFR flight, to allow enough fuel to divert to Moncton. Two hours of data collection was considered a minimum to meet scientific objectives, with a preference for 2-1/2. The figure shows that this imposes a serious restriction on the available alternates. Furthermore, given the size of the storms, it often happened that several of these potential alternates were below limits simultaneously.

Although these restrictions caused some flight delays, and cancellation in two or three cases, the Twin Otter did accomplish 31 project flights in ten storms during CASP. The careful flight planning and weather forecasting contributed to the fact that on none of these flights was diversion to an alternate required.

3. ICING

The NAE and the NASA Lewis Research Center have kept in close touch for the last 6 or 7 years because both operate Twin Otter aircraft in atmospheric research roles. The NASA aircraft is used primarily in airframe icing research. To record cloud droplet sizes and concentrations, it carries particle spectrometers similar to those operated by NAE/AES mounted on identical under-wing pylons.

NASA developed the capability to selectively deice airframe components to determine their contribution to the total drag increase due to icing. Aircraft performance losses in terms of lift and drag coefficient changes were obtained by flying in icing conditions for up to an hour, then exiting cloud to do steady level speed-versus-power measurements, while progressively deicing selected airframe components. Engine inlet and propeller icing were excluded from this study, as their deicing systems must be run continuously during icing conditions.

Data reported in References 3 to 5 show aircraft lift coefficient decrements from 7 to 17 percent in the NASA studies. Aircraft drag coefficients at normal operating speeds increased from 30 to 75 percent over un-iced baseline measurements. Figure 4 shows results from a flight in mixed rime/glaze icing, where the aircraft drag coefficient C_D increased about 33%, and a flight in glaze icing, in which C_D was up by nearly 50%. The shape of aircraft ice accretion is the principal factor influencing performance. Glaze ice is produced at the warmer temperatures nearer 0 deg C, so freezing is slower and the resulting surface rougher. In the cases shown, the glaze ice case produced the greater drag increase although the exposure time was lower and cloud water concentration was only half that of the mixed-icing case. The temperature was -5.0 deg C, however, 4.5 deg C warmer than during the mixed rime/glaze-icing case.

Figure 4 illustrates significant differences in the proportion of the drag due to icing of the different airframe components. This had important implications in plans to operate the NAE Twin Otter in CASP where glaze icing was anticipated. On the standard Twin Otter, only the wing and horizontal tail have deicing boots. In the glaze icing case shown, operating the standard boots will only shed ice responsible for 40 percent of the additional drag; 60 percent of the drag is due to ice on the remainder of the aircraft. A standard Twin Otter similarly iced would have, at best, a very limited capability of climbing should an engine be lost. Figure 4 shows that if the vertical tail, wing struts and wheel struts are also deiced, then nearly 3/4 of the drag due to ice can be shed in the glaze ice case, with an even higher proportion removed in rime icing. Deicing of the vertical tail also improves its performance in engine-out, asymmetrical flight.

NASA put us in touch with the suppliers of their custom-built deicing boots (B. F. Goodrich, Akron, Ohio), and a similar system was produced and installed on the NAE aircraft prior to CASP. Total cost was less than \$5000 U.S. and the weight penalty was only 33 lb. It should be mentioned that FAA or Transport Canada type-approvals were not sought for these installations. NASA and NAE operate their aircraft in an experimental category and are responsible for the safety of their own modifications.

During the CASP experiment, the Twin Otter encountered significant icing on three flights. On each occasion, the full deicing system was used including the newly-installed boots on the struts and the vertical tail, and fully satisfactory results were obtained from a safe-flight point of view. There appeared to be notable differences in the adherence of the ice, however, which was considered interesting from a meteorological perspective. Since the aircraft was fully instrumented to measure droplet spectra and cloud water concentrations, a further analysis of these events was undertaken.

Table 1 summarizes the cloud characteristics during the three icing encounters. For each case, the three minute period in which the liquid water content (LWC) was highest was selected for comparison. The liquid water content was measured using a PMS King probe. The concentration of droplets and precipitation particles in the size ranges from 2 to 30 μ m and from 200 to 6400 μ m were measured using PMS FSSP and 2D-P

probes respectively. The maximum one-second FSSP droplet concentrations and King LWC are also listed, as well as the droplet mean volume diameter (MVD) as determined from the FSSP data.

Figures 5 and 6 illustrate the major difference in the ice properties between the February 18 and March 2 flights. On February 18, about 2 cm of a rough glaze ice built up on the aircraft, as shown by the reverse flow temperature probe in Fig. 5a. On this occasion, activation of the pneumatic deicing boots removed all of the ice on the boots (Fig. 5b). On both flights on March 2, however, much of the ice remained tenaciously attached to the deicing boots even after landing, as shown by the photograph of the wing strut in Figure 6b. The crew reported ice forming in streaks on the cockpit side windows, indicating slow freezing that leads to glaze icing.

The most severe of the icing encounters occurred on the second flight of March 2. Figure 7 shows analog traces of liquid water content, static pressure, temperature, true airspeed and angle of attack during this event. The aircraft was flying at 8000 ft wsl on an easterly heading into the rear of the same storm sampled on the earlier flight. An indicated airspeed (IAS) just above 122 knots (143 knots true airspeed) was being maintained in conditions of light snow. A sudden onset of icing occurred at 1957:10, and airspeed started to fall and angle of attack increased. The slowing of the aircraft as a result of that initial burst of cloud liquid water is fairly typical of the Twin Otter in icing. Five minutes later, at 2002:10, the pilot commented on the voice-tape that the IAS was down to 112 knots and that the deicing system had not yet been activated. Only 40 seconds later, the cloud started to thicken and the pilot announced "107 knots" and deicing was commenced. By 2003:30 CMT, the liquid water content reached 0.1 g m^{-3} and was increasing rapidly to a peak above 0.6 g m^{-3} (Figure 7). Comments were made on the tape that the ice had considerable tensile strength and was adhering to the struts. There was little improvement in airspeed, and at 2007:30 the IAS had decreased further to 104 knots despite application of maximum continuous power. At 2009 a descent and turn was commenced as the pilot felt it was necessary to exit the storm.

It is interesting to note that on this second flight on March 2, when the most severe conditions were encountered, the temperature at the flight level was -9°C , that is, colder than the February 18 case then the temperature was near -5°C . However, the mean volume diameter (MVD, Table 1) of the cloud droplets was considerably higher on March 2. The NASA results (References 3 to 5) would suggest that the glaze icing would be worse at the warmer temperatures where the water would flow and freeze more slowly. However, in our case here, the problem was mainly the inability of the boots to shed all of the ice at the colder temperatures. The larger droplet sizes and the presence of snow in significant concentrations may have led to the "stickiness" of the ice on the boots.

The icing conditions encountered in these three cases were compared with the FAA design envelopes for stratiform cloud icing conditions (Ref. 6). The design envelopes consider the mean effective droplet diameter, the air temperature and the horizontal extent of the icing cloud. Using the microphysical conditions as outlined in Table 1, the liquid water content on February 18 reached 60 percent of the maximum proposed by the FAA, while the first flight on March 2, it was only 10 percent of the maximum. However, in correspondence with the pilot's comments and actions, the second flight on March 2 was the most severe, reaching 90 percent of the FAA design envelope maximum liquid water content.

4. SNOW

Heavy snowfall presented the obvious problem of reduced visibility and flight delays because conditions were below IFR limits. Although unavoidable, this was sometimes frustrating because these meteorological conditions were of scientific interest to the program and airborne measurements of the cloud and precipitation were highly desirable. Various strategies were employed to achieve as many flights in snow as possible. Sometimes the aircraft would be flown upstream to meet the precipitation, complete the sampling and land prior to the airport going below limits. On other occasions the aircraft would be launched as soon as possible after the snowfall diminished, and then flown into the rear quarters of the retreating storm. The latter case usually meant a takeoff in light snow. Caution had to be exercised because towing the warm aircraft out of the hangar into snow and below freezing conditions would cause ice and sticky snow to adhere to the wings as the aircraft cooled down. Opening the hangar doors for 30 minutes to cool the aircraft prior to towing usually did not alleviate the problem. In most cases the aircraft had to be deiced with a spray of warm deicing fluid.

This hazard was amply demonstrated by an incident during CASP that involved the second aircraft used in the experiment, a DC-3. A night-time flight was to be made in a snowstorm traversing the area from the southwest. The Twin Otter was unable to fly because of a lack of an available alternate within range, but the DC-3, with its 6-hour endurance, could use Quebec City as an IFR alternate. As it was snowing at the airport, the wings and tail of the DC-3 were deiced using standard techniques and a glycol-water solution. On the subsequent takeoff attempt the aircraft would not lift off, due to a heavy snow build-up on the port wing in an area not visible from the cabin or the cockpit. The takeoff was successfully aborted and the flight cancelled, but the danger of the situation was well recognized.

5. HIGH WINDS

The strongest winds ever measured by the MAE Twin Otter were experienced during the CASP experiment. This occurred on January 28, 1986 when a strong jet stream from the south-southwest was blowing up the entire east coast of North America (Reference 7). At 1800 GMT, a 975 mb low was situated just north of the Gulf of St. Lawrence, with a cold front trailing down across Nova Scotia. This explosively deepening storm has been further described by Stewart and Donaldson in Reference 8.

The effect of these winds on a slow speed aircraft such as the Twin Otter is dramatically illustrated by the flight track in Figure 8. The mission was flown to the northeast (downwind) of Halifax and included a climb to 14000 ft, level flight to the turn point, then a descent to 9000 ft for most of the return leg. At 1720 GMT another climb was made to 14000 ft, followed by a descent sounding to the Shearwater Airport. The outbound leg took 26 minutes (including the climb to 14000), while the return portion took 90. The spacing of the 5-minute markers on the ground track demonstrate the wind's effect on groundspeed. Over the period marked 'A' on Fig. 8, average groundspeed at 14000 ft was 229 knots and winds averaged 178 deg at 111 knots. The peak 4-sec average wind was 132 knots. On the portion of the return leg marked 'B', average groundspeed at 9000 ft was 61 knots and the winds were measured as 190 deg at 94 knots.

Figure 9 shows atmospheric profile data measured by the Twin Otter during the descent sounding from 14000 ft. The plotted wind vectors and the hodograph show winds at the top of the sounding were southerly near 100 knots, but southwesterly and considerably weaker (30 knots) below 3000 ft. Temperature and dew point show an inversion above a saturated layer at 740 mb with a stable, isothermal layer from about 740 to 670 mb (7400-10200 ft). About half of the wind shear occurred in this layer, the remainder in another stable layer near 870 mb. The upper shear layer is clearly illustrated by the virga shown in Figure 10. This photo was taken at 9000 ft looking west from the position indicated on the flight track plot (Fig. 8). This crosswind view shows precipitation from the faster moving upper air falling into the slower air below the flight level. The high winds encountered were oriented along the nearby surface cold front, which was a relatively common occurrence during CASP (References 9 and 10).

6. WIND SHEAR, CROSSWIND LANDINGS

During CASP, there were two landings that were made quite difficult by crosswinds and wind shear. The first of these occurred on the January 28 flight with the high winds discussed above. Figure 9 showed the wind profile during the descent sounding right down to the landing. This plot indicates that winds on approach were SSW at about 30 knots. The tower called the winds as 220/250 deg true at 15 to 20 knots one minute before landing on the runway which had a true heading of 265 deg (true headings are quoted here to correspond with the plots from the flight-recorded data). Perhaps due to the effects of hangars, the actual winds encountered in the landing had a considerably more southerly (crosswind) component than reported by the tower. The Twin Otter has a low wing loading (approximately 24 psf) and a very large vertical tail, which can be troublesome when landing in crosswinds in excess of 15 knots. The approach was made, therefore, with a reduced flap setting (15 deg) and a target touchdown speed of about 90 knots. After touchdown, the pilot had difficulty maintaining runway heading as the aircraft attempted to weathercock into wind. Consequently, he decelerated cautiously so as to maintain rudder effectiveness, and a landing ground roll almost twice the normal distance resulted. Heavy braking of the starboard mainwheel required to assist in directional control produced considerable tread wear on that tire.

Data recorded during this approach and landing are shown as analog traces in Figure 11. The bottom two traces show the headwind and crosswind components of the total wind vector. Note that the aircraft instrumentation is also capable of measuring winds during the rollout on the ground. The centreline of the heading trace represents the runway heading (265 deg true). During the approach, the wind direction averaged about 200 deg, but with a gradual shearing to a more southerly direction. The magnitude of the headwind decreased during the approach, but the crosswind remained strong, fluctuating about a 15-knot mean during the last 40 seconds before touchdown. It was quite turbulent with gusts of about 10 knots.

The heading trace on Figure 11 shows that during the approach, the aircraft was pointing left of the runway centreline to compensate for the wind, with correction to the runway heading at touchdown (Point 'B' on the plot). Shortly after touchdown, there was a significant increase in the crosswind to about 20 knots. The aircraft heading then began to veer to the left, reaching a heading nearly 9 deg left of the runway heading at 'A' about 11 seconds after touchdown. Recovery was then effected. Note that the time of this recovery coincides with a change in wind direction, and a resultant decrease in the crosswind component at Point 'A' on Figure 11.

The second case study involves the approach after a snow sampling flight on February 22, 1986. During this storm (Ref. 7), snowfall accumulations in some parts of Nova Scotia exceeded 75 cm, breaking 100 year records. Near the time of landing, there was a low pressure centre of 993 mb southwest of Nova Scotia. There were also some interesting precipitation patterns occurring around that time. Halifax International Airport received 30 cm of snow, while 25 km away, only a few centimetres of snow fell at Shearwater before the precipitation changed to freezing rain for one hour followed by 40 mm of rain. The region of rain was over the water while the snow region was over land. There were strong directional wind shears and accelerations linked to the coastline (Ref. 9).

Analog plots like those discussed in the above case are presented in Figure 12. Runway 11 (true heading of 085 deg) was in use. Winds down to a height of about 100 m on the approach averaged 020 deg at

about 27 knots. At this point, the aircraft began to encounter a directional wind shear as the wind shifted to a more northerly heading. It also became very turbulent, with gusts in excess of 15 knots for the remainder of the approach. The wind shear is further demonstrated by the bottom two traces in Figure 12, where the headwind component died off, but the mean crosswind component remained above 10 knots until the aircraft height was down to 40 m, and then decreased to about 8 knots by 5 seconds prior to touchdown. At this point ('B' in the figure), the radar altimeter height was about 5 m and the wind was an almost pure crosswind from about 140 deg true. The measured wind is then seen to increase, with the crosswind component exceeding 15 knots during the touchdown and subsequent ground roll. After touchdown, the wind sheared further to the northwest, giving a tailwind component in addition to the substantial crosswind. Some difficulty was experienced maintaining runway heading, but the ground roll was less than half that in the case above. As can be seen in the true airspeed plot, touchdown in this case was made at near 60 knots, suggesting that the normal landing flap configuration was used.

Again in this case, the winds reported by the tower were significantly different from those experienced by the pilot and recorded by the aircraft wind-measuring system. The last tower report on the voice tape quoted winds from 030 deg true at 15 knots. When the aircraft was at about 5 m altitude, the aircraft-measured wind direction was actually about 350 deg. The approach end of Runway 11 was, however, downwind of a hill and was displaced at least a half mile from the tower that measured the airfield winds. Wind shear and local topographical effects can account for the differences experienced during both these cases.

7. TURBULENCE

During the CASP flight program, the Twin Otter did not experience any severe turbulence encounters. Two incidents of light-to-moderate turbulence were found to be interesting from a meteorological point of view. The first occurred early in the first flight on March 2, which was one of the icing flights discussed in Section 3. The aircraft was making cloud physics measurements at 8000 ft in a banded radar echo structure (Fig. 13) typical of those responsible for much of the precipitation produced by east-coast storms. Three minutes after the radar photo was taken, the aircraft entered the clearing between the bands ('A' in Fig. 13). In about 30 seconds of flight (about 2 km), both the temperature and dew point increased 4-5 deg C (Figure 14). This was accompanied by an increase in wind speed of about 10 mps, and some light to moderate turbulence. Peak vertical gust velocities were about 3 mps, and vertical acceleration excursions were of the order of 0.2 to 0.3 G.

The second case was recorded on February 5, 1986 just after the aircraft levelled off at 10000 ft from a climb through clouds. Figure 15 shows the sudden onset of light turbulence superimposed on noticeable waves in the traces of the orthogonal wind components and the measured static temperature. The period of the waves is approximately 30 seconds, which corresponds to a wavelength of about 2 kilometres, since the aircraft was flying almost directly into the wind. A photograph taken during this event showed waves on the top of the clouds 500-1000 m below the flight level. Data from the sounding recorded 15 minutes earlier are shown in Figure 16. The waves and turbulence were encountered at a pressure level of 680 mb, just above a small inversion indicated at point 'B' on the tephigram. The wind data show a considerable amount of shear associated with a much larger inversion below 800 mb.

8. CONCLUSION

The Canadian Atlantic Storms Program was a challenging research environment in which to make airborne atmospheric measurements because of the adverse weather conditions experienced. As has been shown, it offered a variety of weather-related operational difficulties that face airline and military pilots every winter in Canada. Since the Twin Otter was fully instrumented for aircraft motion, wind and cloud physics measurements, this presented the opportunity to examine and report some of these encounters in detail from both a flight research and a meteorological perspective. Plans are being made for a second CASP experiment in 1992, probably based at St. Johns, Newfoundland.

The installation of specially-designed deicing boots on the vertical tail and the wing and landing gear struts provided an extra margin of safety during flights in CASP. Operators of Twin Otter aircraft in areas subject to a high incidence of airframe icing might want to consider the benefits provided by this enhanced deicing system.

9. REFERENCES

1. Stewart, R. E.
Shaw, R. W.
Isaac, G. A. Canadian Atlantic Storms Program: The Meteorological Field Project. Bulletin of the American Meteorological Society, Vol. 68, No. 4, April 1987, pp. 338-345.
2. MacPherson, J. I.
Baillie, S. W. The NAE Atmospheric Research Aircraft. AGARD Report No. 734, The Flight of Flexible Aircraft in Turbulence, December 1987, pp. 4-1 to 4-19.
3. Mikkelsen, K. L.
McKnight, R. C.
Ranaudo, R. J. Icing Flight Research: Aerodynamic Effects of Ice and Ice Shape Documentation with Stereo Photography. NASA TH-86906 and AIAA-85-0468, January 1985.

4. Ransudo, R. J.
Mikkelsen, K. L.
McKnight, R. C.
Ide, R. F.
Reehorst, A. L. The Measurement of Aircraft Performance and Stability and Control After Flight Through Natural Icing Conditions. NASA TM-87265 and AIAA-86-9750, April 1986.
5. Ransudo, R. J.
Mikkelsen, K. L.
McKnight, R. C.
Perkins, P. J. Performance Degradation of a Typical Twin Engine Commuter Type Aircraft in Measured Natural Icing Conditions. NASA TM-83564 and AIAA-84-0179, January 1984.
6. Airworthiness Standards: Transport Category Airplanes. FAA Part 25, Section 25.1419 and Appendix C, 1980.
7. Strapp, J. W.
Power, J.
McDonald, K. CASP Field Summary. Atmospheric Environment Service Internal Report.
8. Stewart, R. E.
Donaldson, H. R. On the Nature of Rapidly Deepening Canadian East Coast Storms. Atmosphere-Ocean, Vol. 27, pp. 87-107.
9. Stewart, R. E.
Lin, C. A.
Macpherson, S. H. Mesoscale and Microscale Processes in a Winter Storm Linked to the Nova Scotia Coastline. To be submitted to Monthly Weather Review.
10. Stewart, R. E.
Macpherson, S. H. Winter Storm Structure and Melting-Induced Circulations. Atmosphere-Ocean, Vol. 27, pp. 5-23.

TABLE 1 MICROPHYSICAL CONDITIONS DURING ICING EVENTS IN CASP

DATE TIME GMT	ALT. KFT	TEMP. C	LWC g/m3	MAX. LWC g/m3	FSSP cm-3	MAX. FSSP cm-3	MVD MICRON	2D-P m-3	PERCENT FAA MAX. LWC
FEB 18 1753-1758	7.1	-5.2	0.47	0.58	139	195	18.3	344	60
MAR 2 1614-1617	13.7	-11.7	0.04	0.31	21	42	19.5	380	10
MAR 2 2005-2008	8.0	-8.0	0.42	0.79	52	90	22.9	710	90

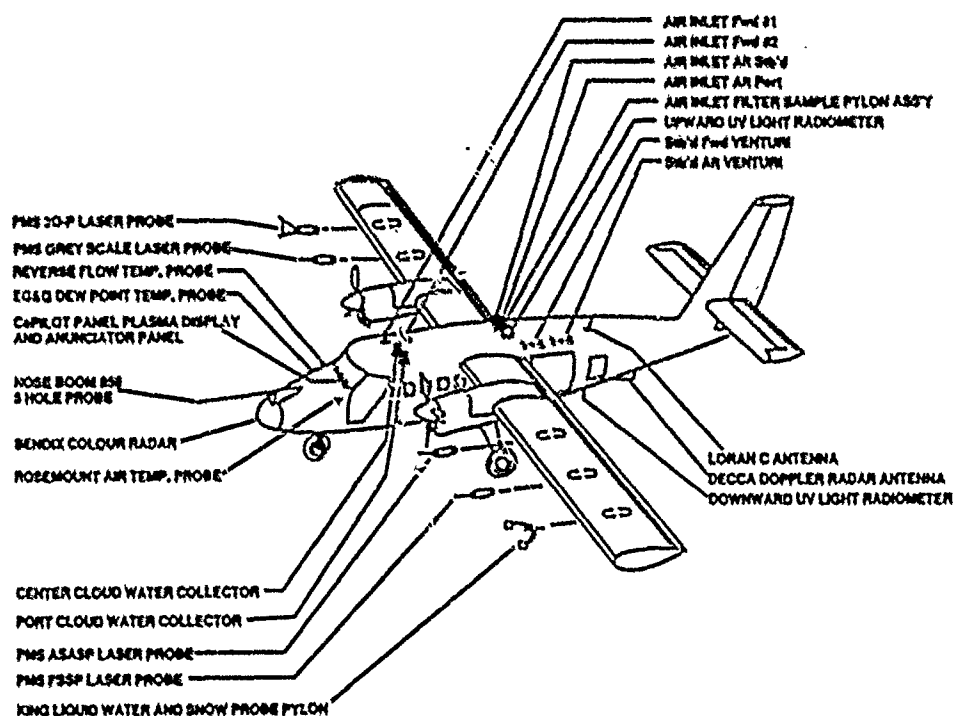


FIG. 1: NAE TWIN OTTER ATMOSPHERIC RESEARCH AIRCRAFT AS INSTRUMENTED FOR CLOUD PHYSICS MEASUREMENTS

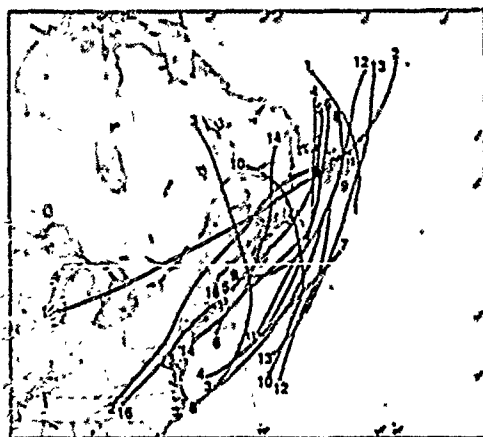


FIG. 2: TRACKS OF THE LOW PRESSURE CENTRES FOR THE STORMS STUDIED IN CASP

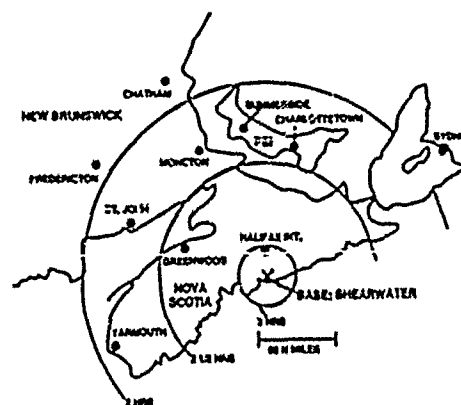


FIG. 3: THE CASP OPERATIONAL AREA SHOWING THE LOCATIONS OF THE PROJECT BASE AT CFB SHEARWATER AND POTENTIAL IFR ALTERNATES FOR THE TWIN OTTER. MAXIMUM AVAILABLE PROJECT FLIGHT TIME IS DEPENDENT ON ALTERNATE SELECTED.

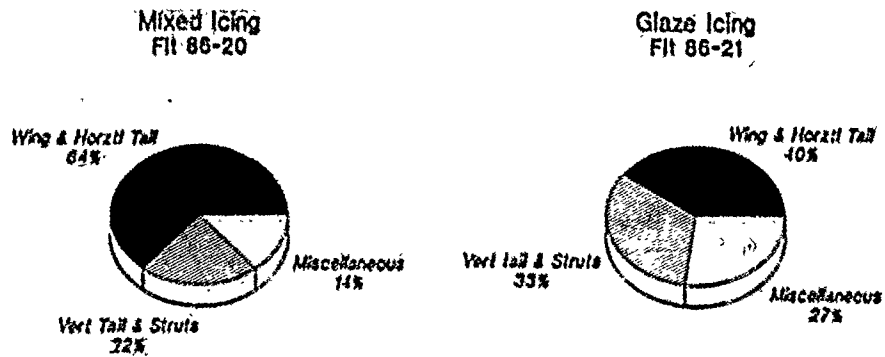


FIG. 4: PROPORTION OF DRAG INCREASE DUE TO ICING ON DIFFERENT AIRFRAME COMPONENTS FOR A CASE OF MIXED ICING AND GLAZE ICING. DATA WERE MEASURED ON A TWIN OTTER BY NASA (REFS. 3-5).

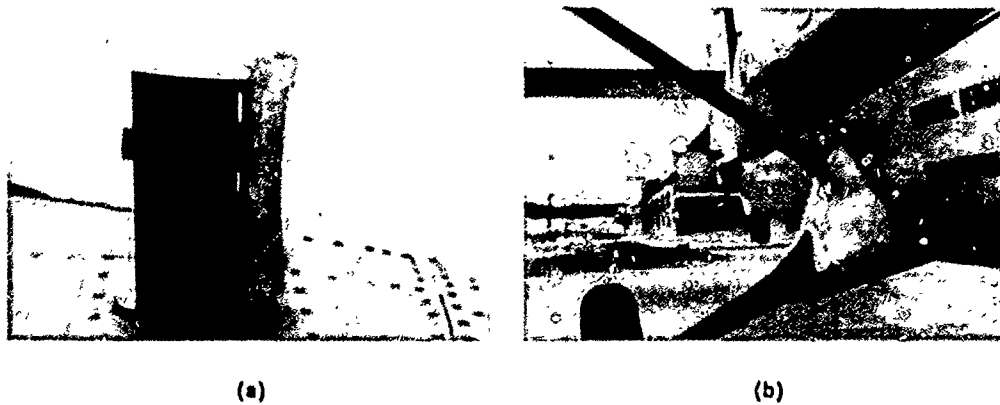


FIG. 5: ICING CASE ON FEBRUARY 18 SHOWING (a) REVERSE FLOW TEMPERATURE PROBE AND (b) DEICING BOOTS ON HORIZONTAL TAIL, WING STRUT AND LANDING GEAR STRUT



FIG. 6: ICING CASE FOR FIRST FLIGHT ON MARCH 2 SHOWING ROUGH ICE (a) ON AIRCRAFT NOSE AND (b) ADHERING TO THE WING STRUT DEICING BOOT AFTER LANDING

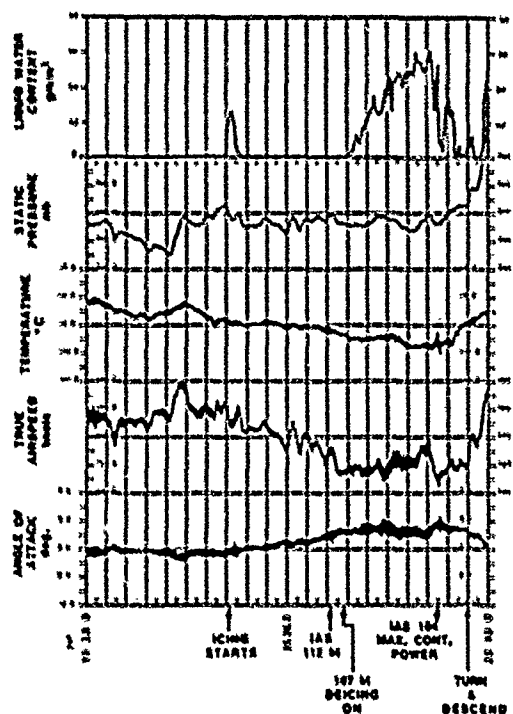


FIG. 7: DATA RECORDED DURING ICING ENCOUNTER ON SECOND FLIGHT OF MARCH 2

Trim Other Track Plot
 CASP FLIGHT 01
 Reference Point HALIFAX RADAR
 44 57 2 0330 0
 Flight Date 28-JAN-85
 Segments (Lines)
 Start 10:30 End 10:30
 Data Descending from 10
 Range 1000 to 2500 km
 Scale (m/min) = 1:2500
 x = Start/end of test
 Caps = Turn out
 o = 5 min CUT
 u = Photo event

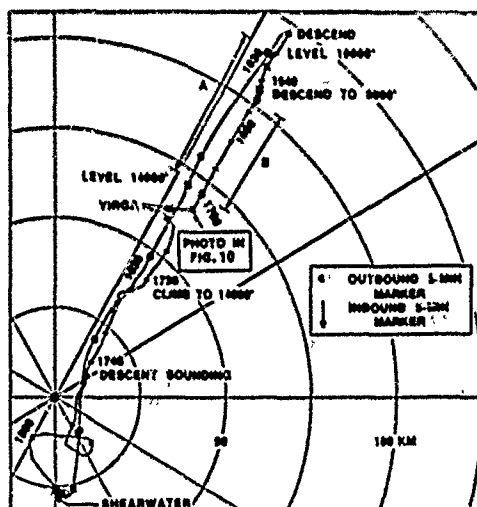


FIG. 8: GROUND TRACK FOR JANUARY 28, 1986 FLIGHT IN HIGH WINDS

Twin Otter Sounding
 Flight date 28-JAN-86
 Start 174200 End 180740

Doppler Winds

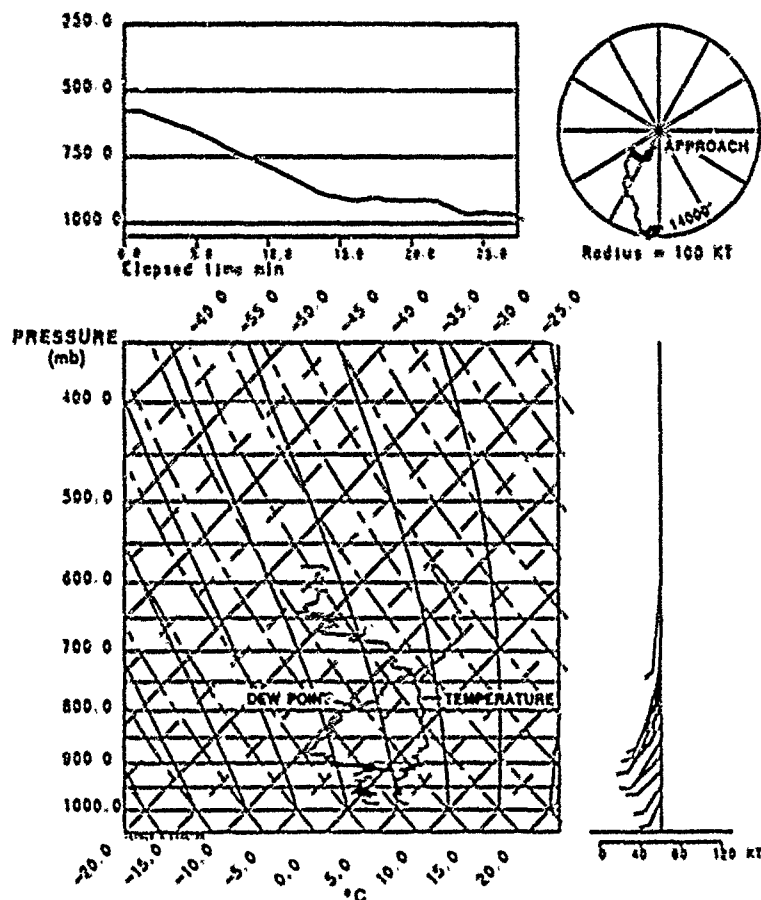


FIG. 9: ATMOSPHERIC PROFILE RECORDED DURING DESCENT FROM 14000 FT AND APPROACH ON JANUARY 28, 1986



FIG. 10: WIND SHEAR ILLUSTRATED BY PHOTOGRAPH OF VIRGA TAKEN AT 9000 FT ON JANUARY 28, 1986. VIEW IS LOOKING CROSSWIND TO THE WEST FROM THE POSITION MARKED ON THE FLIGHT TRACK IN FIG. 8.

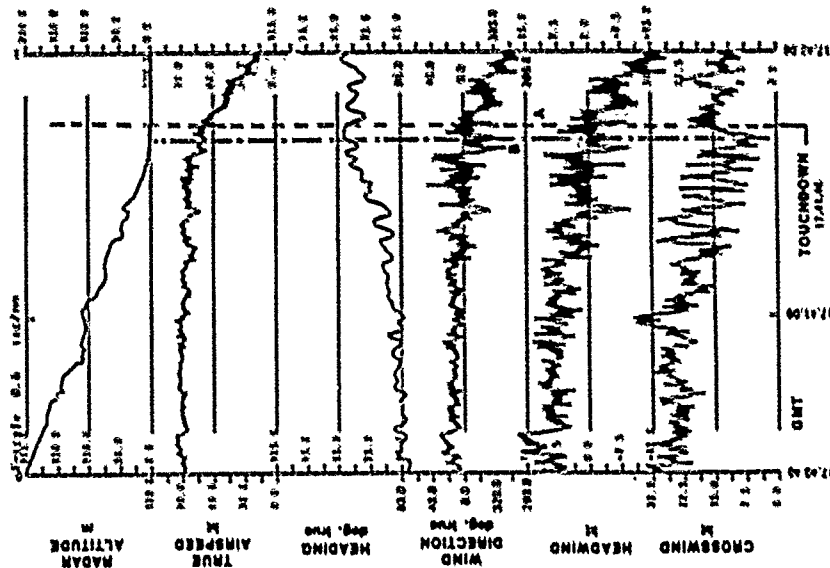


FIG. 11: DATA RECORDED DURING CROSSWIND LANDING ON JANUARY 26, 1966

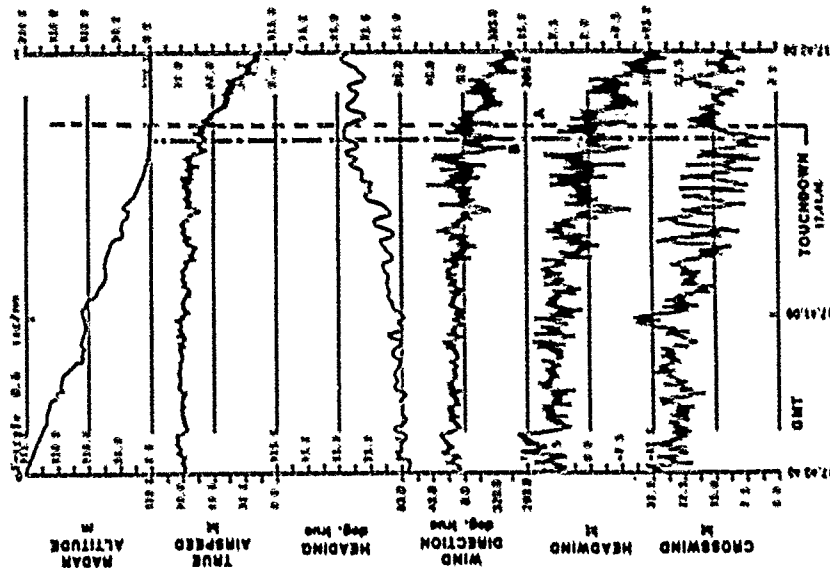


FIG. 12: DATA RECORDED DURING CROSSWIND LANDING ON FEBRUARY 22, 1966

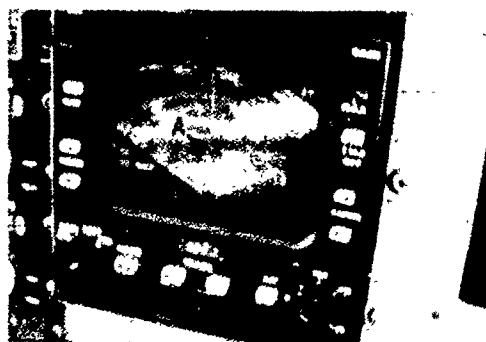


FIG. 13: RADAR PHOTO TAKEN AT 8000 FT
AT 1459 GMT ON MARCH 2, 1986.
TURBULENCE AND TEMPERATURE
RISE WERE ENCOUNTERED WHEN
AIRCRAFT REACHED POINT 'A' IN
THE GAP IN THE PRECIPITATION BANDS.

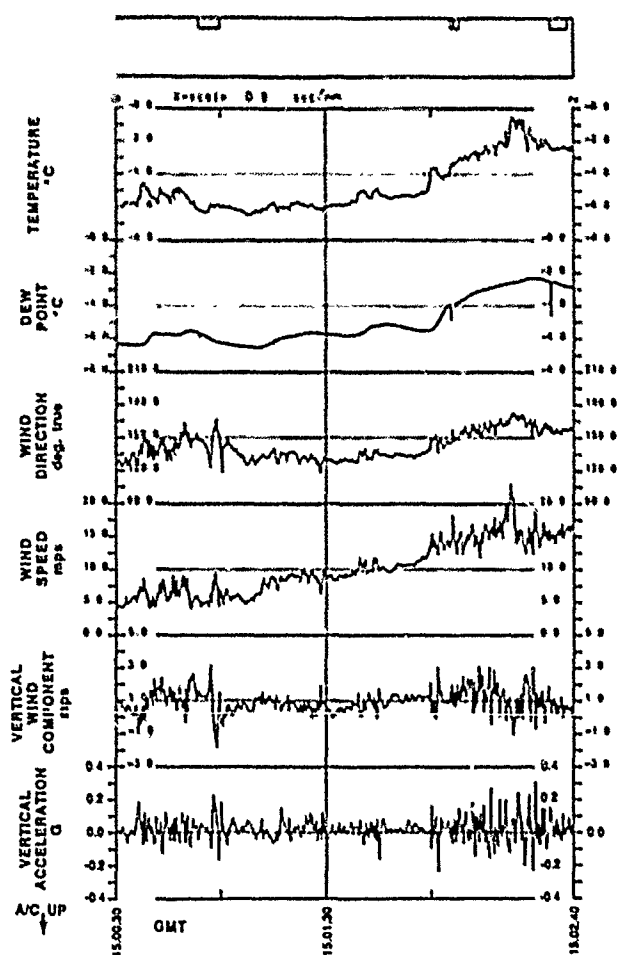


FIG. 14: TRACES SHOWING TURBULENCE AND TEMPERATURE
CHANGE ENCOUNTERED AT 8000 FT ON MARCH 2, 1986

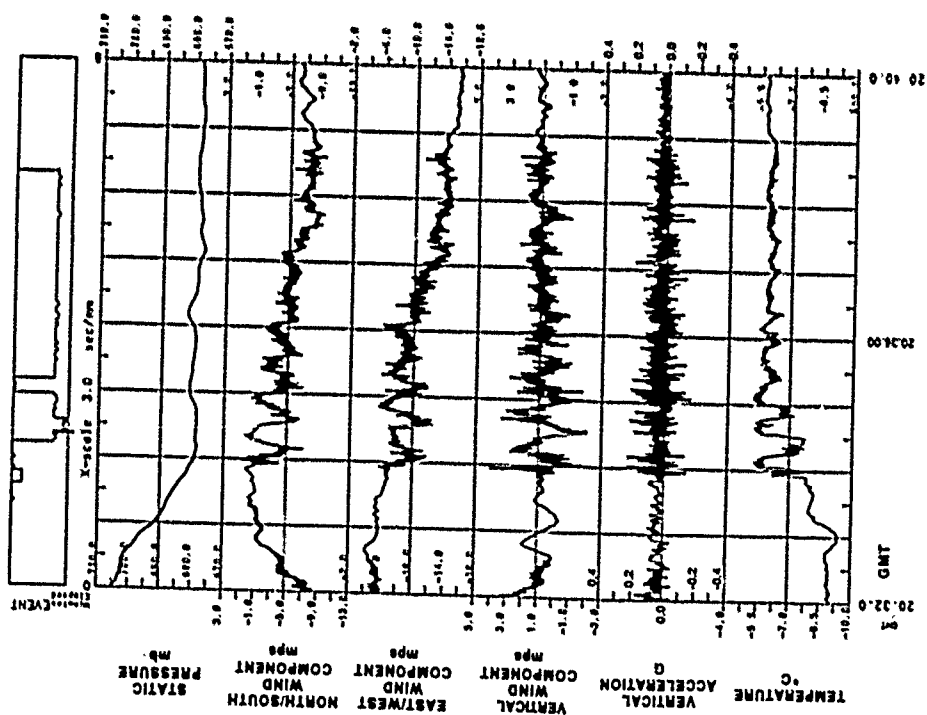


FIG. 15: TURBULENCE AND WAVES MEASURED AT 10000 FT ON FEBRUARY 5, 1966

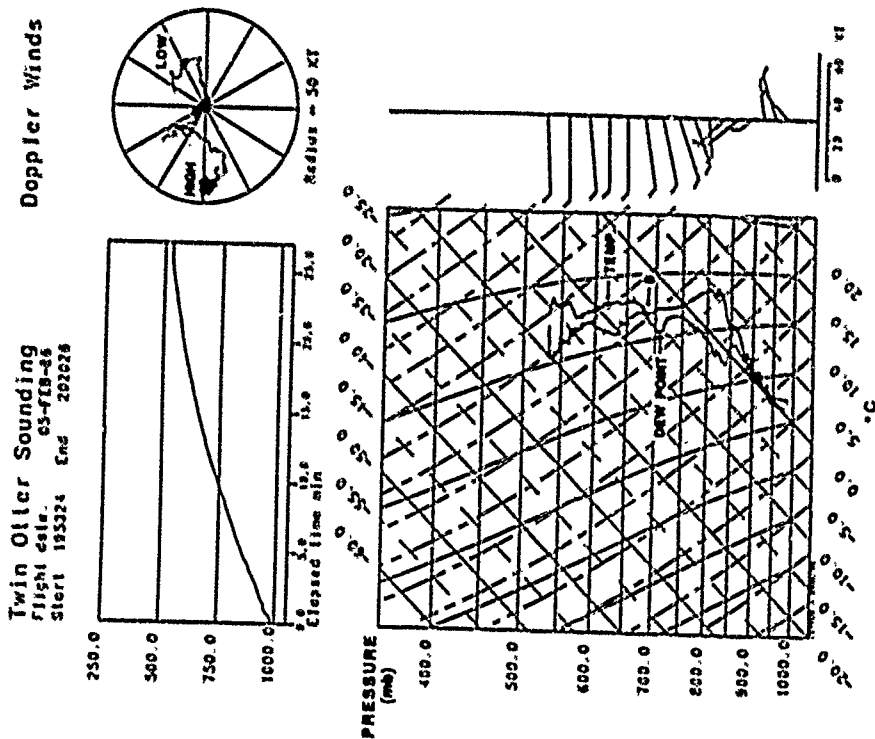


FIG. 16: ATMOSPHERIC PROFILE MEASURED BY TWIN OTTER ON FEBRUARY 5, 1966. WAVES ON PREVIOUS FIGURE WERE ENCOUNTERED AT LEVEL 'B' INDICATED.

CANARD VERSUS AFT-TAIL RIDE QUALITIES PERFORMANCE AND PILOT COMMAND RESPONSE

L.V. Cioffi, L. Mangiacasale
Flight Mechanics and
Automatic Control Dpt.
AERMACCHI S.p.A.
Via Sanvito, 80
21100 - Varese
ITALY

SUMMARY

A comparison between a Close-Coupled Canard configuration and a Close-Coupled Tail configuration has been developed in terms of Ride Qualities and Pilot Command response in turbulence.

Parameters of the study are the mass factor of the airplane, the static stability and the sign of the trailing-edge flap effectiveness (only for the aft-tail airplane). The known Ride Quality criteria are used in order to assess the Flying Qualities of the airplane.

Interesting conclusions are derived in terms of configuration sensitivity and attenuation capabilities. Further research is needed in order to add structural flexibility and unsteady aerodynamics to the design model. Pilot command responses are in agreement with the current Flying Qualities parameters, but a special purpose control law has to be designed for good tracking in presence of discrete gusts.

1. INTRODUCTION

The design of an airplane is a task which requires the analysis of a large number of parameters and constraints.

In this paper a very limited problem is discussed, which concerns the Ride Qualities of two configurations as shown in Fig. 1:

- a close-coupled canard with relaxed static stability
- a close-coupled tail with two free parameters; i.e. the static stability (negative or positive) and the sign of the trailing-edge flap effectiveness ($C_{m\dot{\delta}} \neq 0$).

The Ride Qualities are assessed with reference to the following criteria:

- Exposure Time (CALSPAN CRITERIA, Fig. 2 from Ref. [1])
- Discomfort Index (DI, Table I from Ref. [2])
- Crew-Mission-Performance Limitation (CMPL, Table II from Ref. [3])
- Ride-Bumpiness ($N_{1/2}$ /minute from Ref. [4]).

Since the baseline configuration of both airplanes is statically unstable stabilization is achieved by using active control.

In other words, control laws are designed to stabilize the airplanes and optimize their Ride Qualities.

For the analysed configurations the control laws are also tested versus the pilot input (stick force) in order to demonstrate their quality in terms of maneuver command response.

2. DESIGN PARAMETERS

The following parameters have been taken into account in the design:

- the mass factor $\mu = W/(S\bar{C} C_{L_a})$ which is a leading parameter in the Ride Qualities of airplanes
- the static stability which, in terms of Static Margin, is:
 - $4\% \bar{c}$ (unstable) for the canard
 - $4\% \bar{c}$ (unstable) and $4\% \bar{c}$ (stable) for the aft-tail

- the trailing-edge flap effectiveness (tail configuration only) which can be positive ($C_{m\delta F} > 0$) or negative ($C_{m\delta F} < 0$).

The Flight Condition is:

- Mach number $M = .9$
- Altitude $H = 15000$ ft
- Turbulence input Dryden Spectrum

The control surfaces (Fig. 1) are:

- canards and inboard flaperons for the canard configuration
- trailing-edge flap and tail for the aft-tail configuration

3. CONTROL LAW DESIGN METHOD AND CONTROL SYSTEM LAYOUT

The control law design (synthesis) has been developed with the use of the well known method called the Linear Quadratic Regulator (LQR): this method offering the following advantages:

- it easily handles complex systems where multiple control surfaces and multiple outputs are to be controlled (MIMO Systems),
- it handles large dynamic systems (large number of state variables),
- it allows fast trade-offs and generates a large bulk of information with limited effort and time expense.

Without entering the details of the formal developments, the designed control laws have the following properties:

- they are of a Model Following type (in the presence of pilot commands)
- they generate good level of turbulence attenuation
- they generate a Proportional + Integral + Filter (PIF) compensation
- they are developed including the control actuation systems (actuators) in the design model.

In the evaluations of Discomfort Index, Crew Mission Performance Limitations and Ride Bumpiness, the Power Spectral Density Analysis has been implemented in the computational procedure.

Although the LQR methodology generates a large number of feedbacks (equal to the number of state variables used in the dynamic system description), a simplification has been applied so that many feedback gains can be nulled with no sensible impact on the airplane performance.

The most important feedbacks retained in the control system are:

- inertial angle of attack (α)
- normal load factor (n_z)
- pitch rate (q)
- gust angle of attack ($\hat{\alpha}_g$) and rate ($\dot{\hat{\alpha}}_g$) which can be estimated by on board computation.

The system lay-out is simply sketched in Fig. 3, where all the control compensations and computations are included in the "computer" block.

Moreover, during the flight in turbulence and in absence of Pilot commands the Altitude Autopilot (Hold Mode) is closed in order to avoid large altitude excursions.

4. RIDE QUALITIES PERFORMANCE

The Ride Qualities of the configurations in term of Bumpiness and CMPL are summarized in Fig. 4 and 5 where the limits of Refs. [4] and [3] are also indicated. Figure 4 shows the trend of Bumpiness versus the airplane mass factor μ , the airplane stability (SM) and the trailing-edge flap effectiveness (for the aft-tail configuration).

The following points have to be highlighted:

- for the same mass factor μ , the canard configuration is the "most sensitive" to turbulence,
- the stable aft-tail is the "least sensitive"

- the unstable aft-tail is more sensitive than the stable aft-tail, and a negative T.E. flap effectiveness worsens the behaviour.

Fig. 5 shows the CNPL trend versus the same parameters. This Ride Quality seems to be in good agreement with the Sumpiness Characteristics. Other Ride Qualities such as the Discomfort Index, are shown in Table III. Here information can be found in terms of Root-Mean-Square (RMS) of the airplane states as:

- attitude (θ)
- pitch rate (q)
- normal load factor at the Pilot station (n_{zpil})
- altitude (h)

Indications are also supplied concerning:

- control surfaces actuation rate (maximum value)
- control surfaces deflection (maximum value).

From the data in Table III it is evident that the canard configuration featured the "lowest attenuation capability" among those analysed. A simple explanation can be drawn from Fig. 6. In the canard configuration it is in fact evident that the "main attenuation surface" (which is the inboard flap) generates a pitching moment in the wrong direction, in the aft-tail architecture the main attenuation surface (which is the TE flap) can generate a pitching moment in the right direction. Another aspect that can be noted from Table III concerns the canard control rate which rapidly saturates in the attempt to counteract the wrong pitch action of the inboard flaperons.

Also the aft-tail architecture with $C_{m4} < 0$ is affected by the same drawback, and the general behaviour is not better than the canard because of the tail surface lower control rate allowed.

In the present design the following maximum values have been retained for the control surfaces rate:

CANARD CONFIGURATION

$$\dot{\delta}_{CAN,max} \leq 50^\circ/sec, \dot{\delta}_{FLAP,max} \leq 20^\circ/sec$$

AFT-TAIL CONFIGURATION

$$\dot{\delta}_{FLAP,max} \leq 40^\circ/sec, \dot{\delta}_{TAIL,max} \leq 20^\circ/sec$$

These values are of course lower than the maximum values, the current technology would permit, the reason for this is that have been margins kept for superimposed pilot commands and discrete gust encounters.

The responses to a discrete bell-shaped gust ($1-\cos$) with a maximum intensity of $\alpha = 2.6$ deg and wave length of 306 m, are shown in Fig. 7a for the canard configuration and in Fig. 8a for the tail configuration with $C_{m4} > 0$.

It is evident that the control surfaces maximum rates are within the desired limits and the control surfaces maximum deflections are within the limits of known airplanes.

From the airplane attitude (θ) time history it is easy to draw the preliminary conclusion that the designed control law has a poor performance in terms of target tracking in the presence of discrete gust.

In order to demonstrate the attenuation behaviour of the two configurations in the frequency domain the Power Spectral Densities are shown in Fig. 7b for the canard and in Fig. 8b for the tail.

5. PILOT COMMAND PERFORMANCE

The responses to a pilot command (Stick force input = 10 lbs) are shown in Fig. 7c for the canard configuration and in Fig. 8c for the tail configuration with $C_{m4} > 0$. The reference Model is built according to the MIL-F-8785C with the following characteristics:

- $C_{SP,MOD} = 1.0$ for the canard
- $C_{SP,MOD} = .80$ for the tail
- $CAP = 1$ for both configurations

$$\omega_{SP,MOO} \approx 10 \text{ rad/sec}$$

The Flying Qualities of the controlled airplane are assessed in terms of:

- Time Response Parameter (T.R.P. as in Ref. [5])
- Equivalent Q/P (as in Ref. [6])
- Attitude Dropback (as in Ref. [7])
- Flight path angle delay
- Frequency Response (as in Ref. [8]).

The obtained performance is shown in Table IV and indicates that the control law designed for turbulence attenuation purposes performs well also in presence of pilot commands.

The responses are well damped and the control surface rates are well within the limits; the design, therefore, seems to be well balanced for commands and turbulence attenuation.

The Frequency Responses to a pilot stick force are shown in Fig. 7d and 8d and are in good agreement with those suggested in Ref. [8] for good pitch tracking.

6. CONCLUSIONS AND FURTHER WORKS

A comparison between a canard configuration and an aft-tail configuration has been presented in terms of Ride Qualities.

The trade-off demonstrates that a close-coupled canard is more sensitive to the atmospheric turbulence than a close-coupled tail.

The airplane stability has an important impact on the performance since the stable tail alleviates the turbulence effects better than the unstable tail.

The mass parameter (μ) is the leading parameter, but other important parameters are:

- stability margin
- pitch moment of inertia (J_y)

Results not reported in this paper indicate that an increase in the pitch radius of inertia (ρ_y) has a positive impact on bumpiness if the configuration is statically unstable.

The Ride Quality criteria today available represent a good guideline in the preliminary design of a modern airplane. If the basic configuration is statically unstable then the impact of the automatic control system becomes very important and an integrated design (aerodynamics plus control system) is necessary.

The control law designed for turbulence attenuation generates good airplane response to pilot commands. This aspect obviously requires more study because the Handling Qualities should be assessed also in terms of other tasks. Nevertheless the control law designed in this study should allow the pilot to perform a pitch tracking task in presence of atmospheric turbulence with good results.

More work of course is needed in this field.

Adding structural flexibility and unsteady aerodynamics should improve the design model quality and generate more credible information in terms of effective alleviation, and more realistic values for the maximum control surface rates.

In terms of control law it should be necessary to demonstrate, with Man-in-the-Loop simulations, the real tracking capabilities in presence of turbulence. The airplane pointability in presence of discrete gust also is an important problem and should be addressed; but the attitude time history in Figs. 7a, 8a demonstrates that the designed control law is not well suited for Air-to-Air Gunnery or Strafe Mode where a tighter control of the airplane attitude is required.

Therefore, a special purpose control law has to be designed for this task.

7. REFERENCES

- [1] R.C.A'Harrish, Low Altitude, High Speed and Riding Qualities, AGARD, Report 443, April 1963
- [2] Background Information and User's Guide for MIL-F-9490
- [3] M.Hacklinger, Design Problems of Military Aircraft as Affected by Turbulence, AGARD CP-140 (Flight in Turbulence), 1973
- [4] J.Becker, Gust Load Prediction and Alleviation on a Fighter Aircraft, AGARD Report 726, September 1985

- [5] D.J.Moorhouse, R.J.Woodcock, Background Information and User Guide for MIL-F-8785C, AFVAL TMB1-3109, July 1982
- [6] D.E.Niechoff, The Definition of Short Period Flying Qualities Characterization via Equivalent Systems, J. of Aircraft, Vol. 2, n. 6, June 1983
- [7] J.C.Gibson, Piloted Handling Qualities Design Criteria for High Order Flight Control Systems, AGARD CP335 (Criteria for H.O. of Military Aircraft)
- [8] M.P.Bland, F.J.Shirk et al., Alternative Design Guidelines for Pitch Tracking, Paper 87-2289, AIAA Atmospheric Flight Mechanics Conference, Monterey, Aug. 1987

TABLE I - DISCOMFORT INDEX (USER'S GUIDE MIL-F-9490)

RISE DISCOMFORT INDEX, D_1	FLIGHT PHASE DURATION (EXPOSURE TIME)	PROBABILITY OF EXCEEDING RMS TURBULENCE INTENSITY
LONG TERM	OVER 3 HOURS	0.20
REQUIREMENT	FROM 1.5 TO 3 HOURS	0.20
	FROM 0.5 TO 1.5 HOURS	0.20
SHORT TERM	LESS THAN 0.5 HOUR	0.01
REQUIREMENT		

TABLE II - CREW-MISSION PERFORMANCE LIMITATIONS (C.M.P.L.)

CMPL	AIRCRAFT ACCEPTABILITY	MISSION PERFORMANCE & CREW EFFORT
.07	ACCEPTABLE FOR UNLIMITED EXPOSURE TIME	MISSION PERFORMANCE NOT AFFECTED
.14	ACCEPTABLE NORMAL OPERATION	MISSION PERFORMANCE ADEQUATE
.21	ACCEPTABLE NORMAL OPERATION NOT EXCEEDING ALLOWABLE EXPOSURE TIME	ADEQUATE FOR MISSION SUCCESS, REASONABLE PERFORMANCE REQUIRES CONSIDERABLE CREW CONCENTRATION
.28	UNSATISFACTORY FOR NORMAL OPERATIONS, UNACCEPTABLE WHEN EXCEEDING ALLOWABLE EXPOSURE TIME	ADEQUATE FOR MISSION SUCCESS, BUT REQUIRES MAX. AVAILABLE PILOT/CREW CONCENTRATION TO ACHIEVE ACCEPTABLE PERFORMANCE
.35	UNACCEPTABLE EXCEPT FOR EMERGENCY CONDITIONS	INADEQUATE PERFORMANCE FOR MISSION SUCCESS, AIRCRAFT CONTROLLABLE WITH MINIMUM COCKPIT DUTIES
.42	UNACCEPTABLE, DANGEROUS	AIRCRAFT JUST CONTROLLABLE REQUIRING MAX. PILOT SKILL, MISSION SUCCESS IMPAIRED

TABLE III - RIDE QUALITIES PERFORMANCE

CONFIGURATION PERFORMANCE	CANARD	UNSTABLE TAIL ($C_{H^*F} +$)	UNSTABLE TAIL ($C_{H^*F} -$)	STABLE TAIL ($C_{H^*F} +$)
ATTITUDE (DEG) RMS	.15	.09	.1	.1
PITCH RATE (DEG/SEC) RMS	.3	.46	.42	.48
NORMAL LOAD FACTOR (g) RMS	.23	.21	.23	.19
ALTITUDE (ft) RMS	4.5	3.7	5.2	4.2
FORWARD DEFLECTION (DEG) MAX	6.5	3	4	2.75
AFTERWARD DEFLECTION (DEG) MAX	2.5	.7	1.42	.9
FORWARD RATE (DEG/SEC) MAX	47.5	40	42.5	40
AFTERWARD RATE (DEG/SEC) MAX	17.4	12.2	21.5	13.56
$N_{1/2g}$ BUMPS/MIN	18±20	12±15	21±24	5±7
DISCOMFORT INDEX	.24	.21	.23	.18
C.M.P.I.	.2	.17	.2	.15

TABLE IV - PILOT COMMAND PERFORMANCE

CONFIGURATION PERFORMANCE	CANARD	UNSTABLE TAIL ($C_{H^*FL} +$)	UNSTABLE TAIL ($C_{H^*FL} -$)	STABLE TAIL ($C_{H^*FL} +$)
CONTROL ANTICIPATION PARAMETER	.512	.5	.51	.46
TIME RESPONSE PARAMETER	.13	.14	.15	.13
DROPPACK	.15	.12	.16	.15
SLOPE TIME CONSTANT	.25	.20	.17	.19

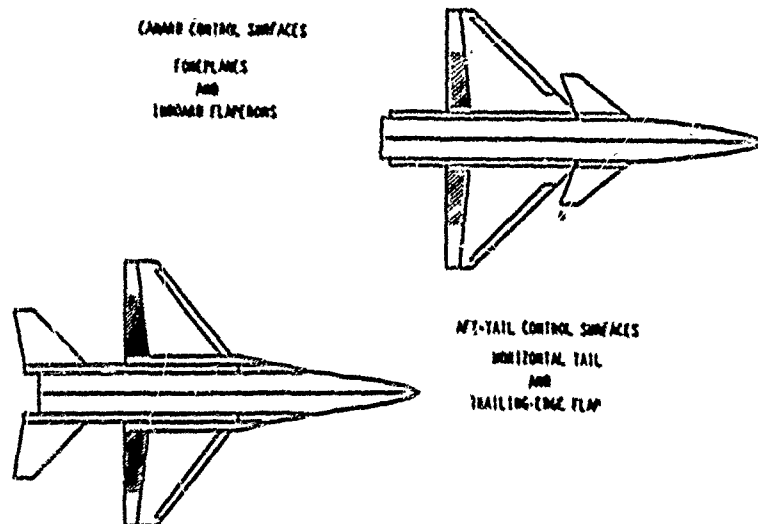


FIG. 1 - AIRCRAFT CONFIGURATIONS

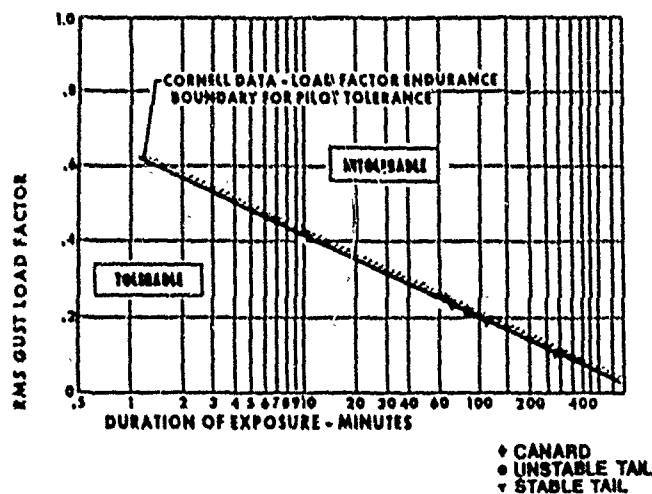
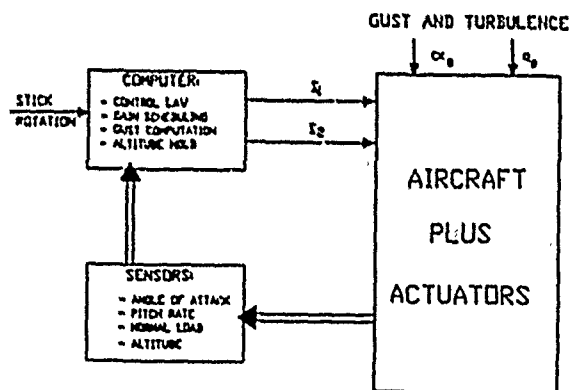
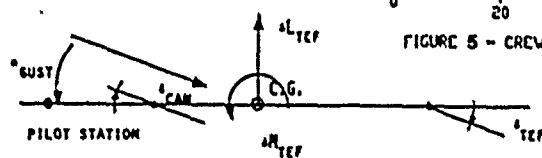
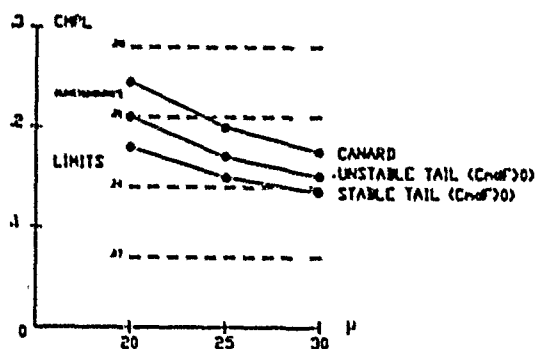
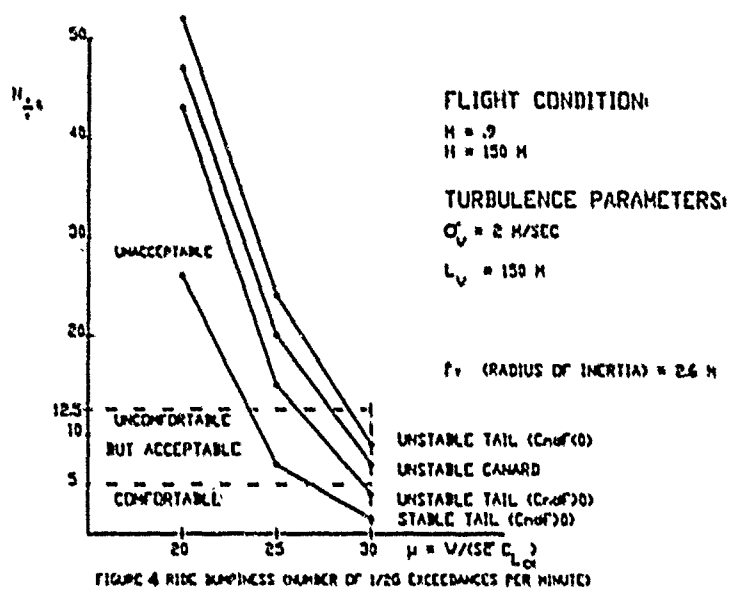


FIG. 2 - CALSPAN CRITERIA

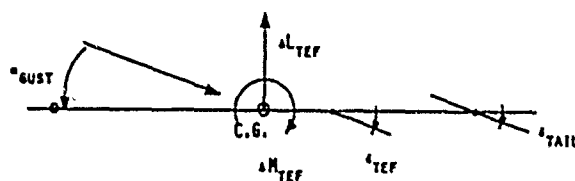
FIG. 3 - CONTROL SYSTEM LAY-OUT



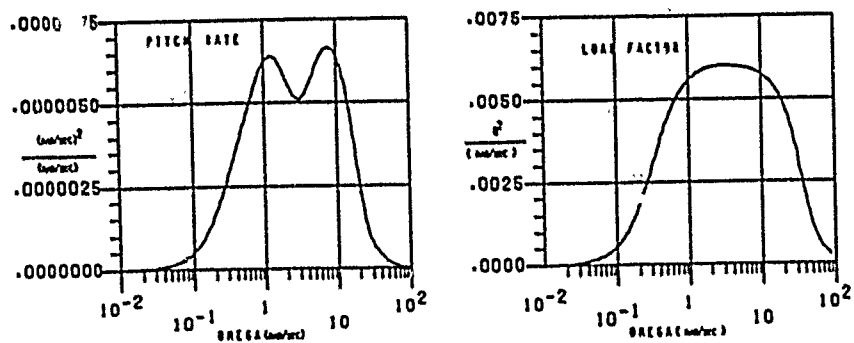
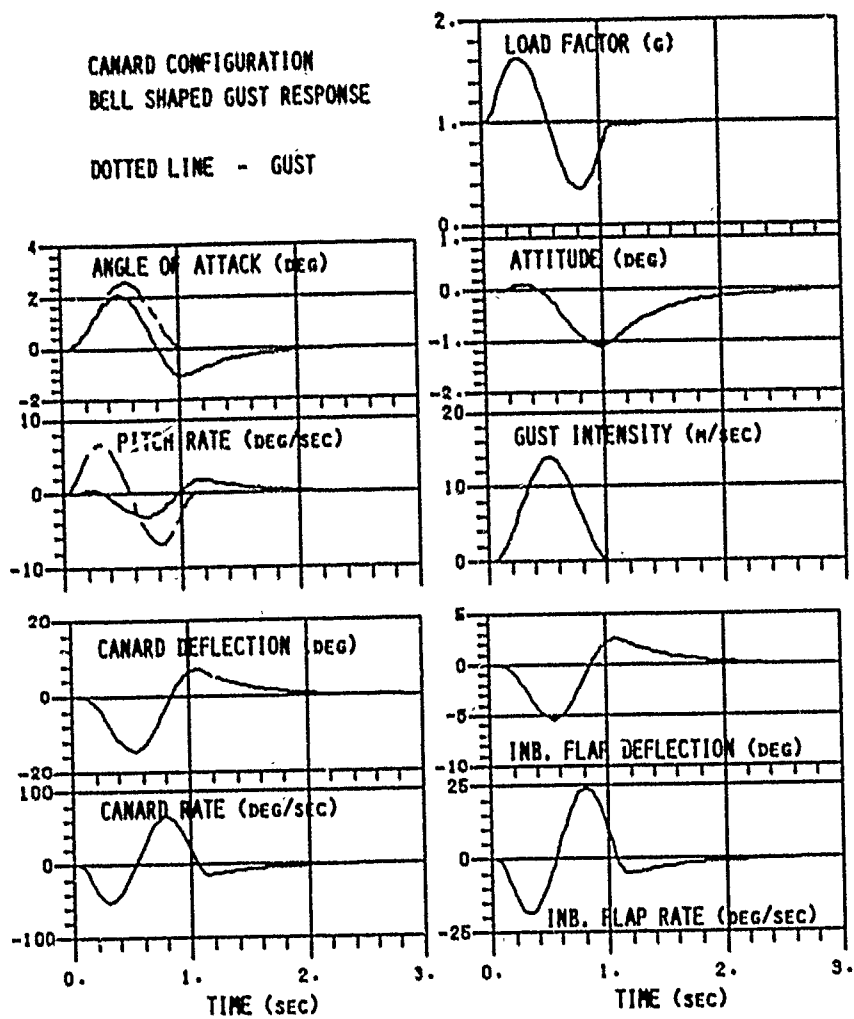


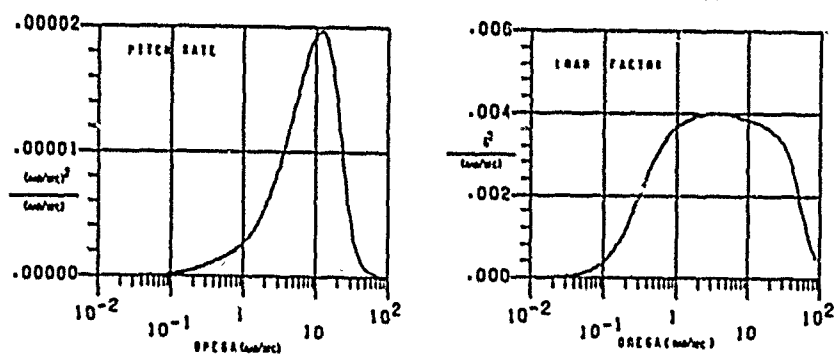
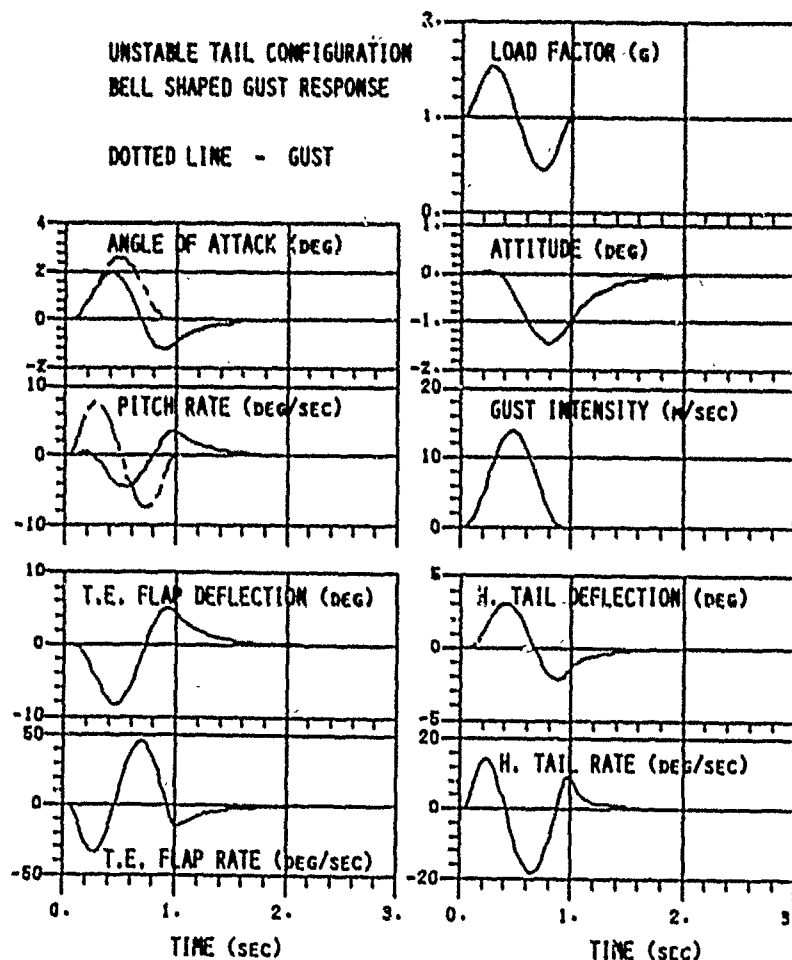
CANARD CONFIGURATION
 $C_{H_{TEF}} < 0$

FIG. 6 - CONTROL SURFACES
 EFFECTIVENESS



AFT-TAIL CONFIGURATION
 $C_{H_{TEF}} > 0$





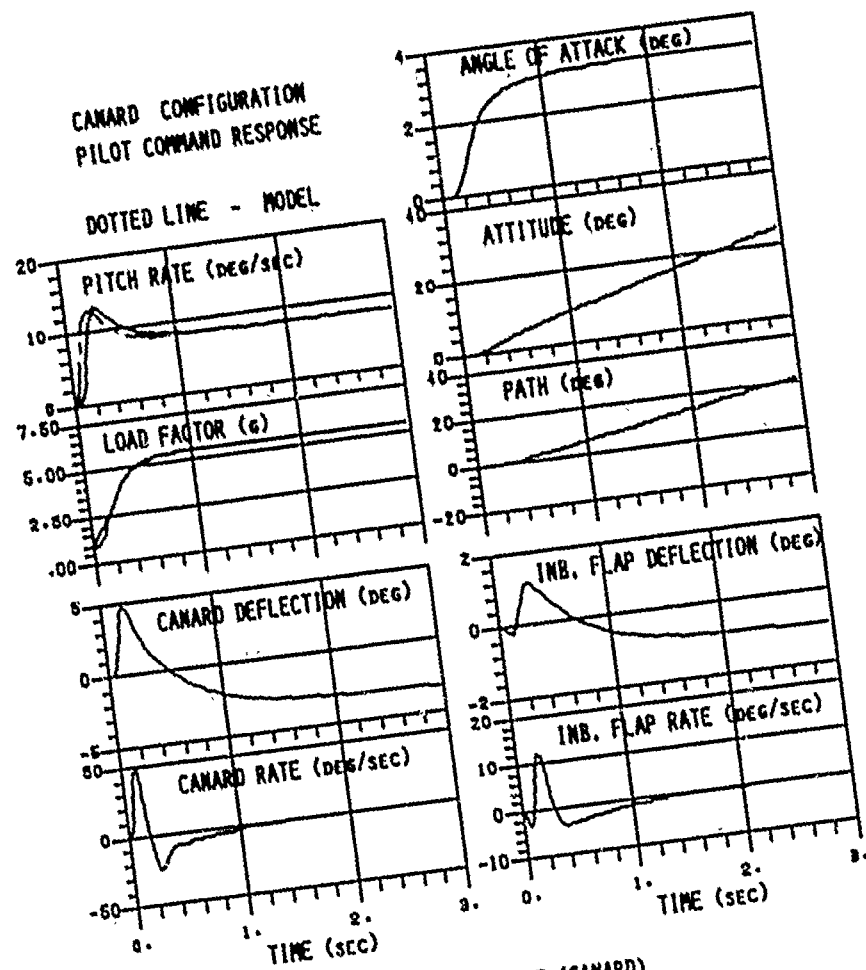


FIG. 7c - PILOT COMMAND RESPONSE (CANARD)

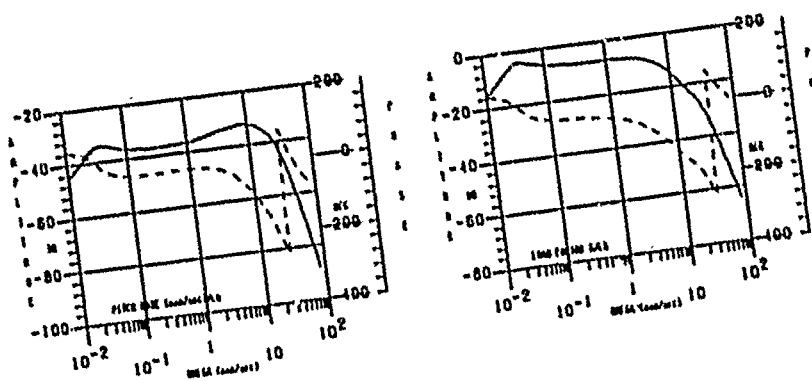


FIG. 7d - FREQUENCY RESPONSE (CANARD)

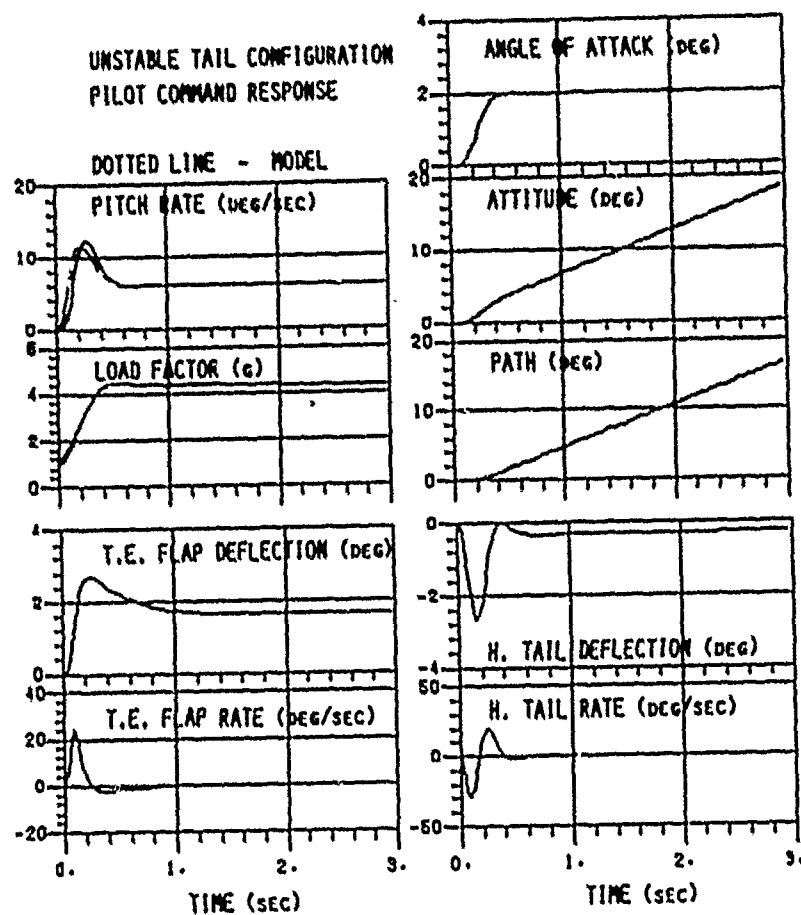


FIG. 8c - PILOT COMMAND RESPONSE (AFT-TAIL)

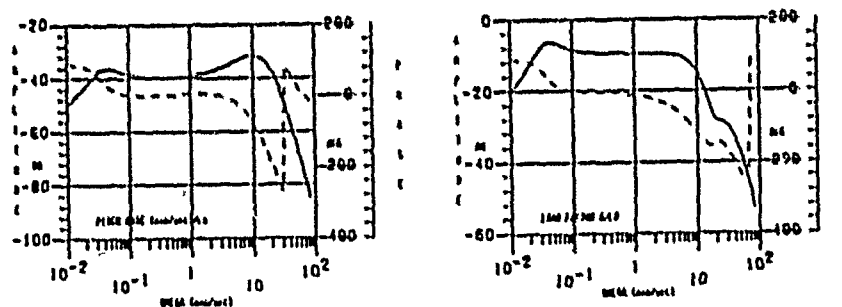


FIG. 8d - FREQUENCY RESPONSE (AFT-TAIL)

The Interference of Flightmechanical Control Laws with those of Load Alleviation and its Influence on Structural Design

by

M. Molzow, Head of Structural Dynamics
R. Moebest, Head of Loads Department
MBB GmbH UB-Transport- u. Verkehrsflugzeuge
Dynamic Department-TE 24
P.O.Box: 950109
Kreiselag 10
2103 Hamburg 95
West Germany

Abstract

Today modern A/C designs use fly-by-wire together with control laws to make the A/C comfortable for handling in service. In addition, this implies an attractive chance for a lot of protections and limitations with the aim to improve handling quality characteristics or to protect the aircraft against overloading. Examples are

- Overspeed protection
- Load factor protection
- Stall protection

Another chance is the implementation of Load Alleviation Functions (LAF).

To optimize the overall A/C design a close cooperation between the different disciplines like

- Systems
- Handling Quality
- Aerodynamics
- Loads
- Stressing

is needed, not to cancel the benefits in one discipline by handicaps or additional weight in others.

This lecture describes the different problems, which have carefully to be watched in relation of interference to each other to reach an overall optimum.

Table of Contents

1.0 Introduction	14-3
2.0 Example of a Systems Layout of a Today Transport Aircraft	14-4
3.0 Design Concept	14-6
3.1 Handling Quality	14-6
3.2 Structures	14-6
4.0 Aircraft Protection Systems	14-13
4.1 Overspeed Protection System	14-14
4.2 Load Factor Protection System	14-14
4.3 Stall or Low Speed Protection System	14-15
5.0 Aircraft with Load Alleviation	14-16
5.1 Gust Load Alleviation	14-16
5.2 Maneuver Load Alleviation	14-18
6.0 Conclusion	14-19
7.0 References	14-20
8.0 Acknowledgement	14-20

List of Illustrations

Figure 1. Flight Control Surfaces	14-4
Figure 2. EFCS Installation	14-5
Figure 3. Pitch Control Arrangement	14-5
Figure 4. Lateral Control Arrangement	14-5
Figure 5. Gust Load Alleviation Function	14-6
Figure 6. Unchecked Maneuvers Stickdeflection	14-7
Figure 7. Unchecked Man. Elevator Deflection w. and w.o. CL	14-7
Figure 8. Unchecked Maneuver A/C-Loadfactor NZ	14-7
Figure 9. Unchecked Maneuver Tailplane Root Bending	14-8
Figure 10. Unchecked Maneuver Tailplane Root Torque	14-8
Figure 11. Checked Maneuver Stickdeflection	14-8
Figure 12. Checked Maneuver Loadfactor Command NZC	14-8
Figure 13. Checked Maneuver Elevator Deflection	14-8
Figure 14. Checked Maneuver Response Loadfactor NZ	14-8
Figure 15. Checked Maneuver Tailplane Root Bending	14-9
Figure 16. Checked Maneuver Tailplane Root Torque	14-9
Figure 17. A/C Development Cycles	14-10
Figure 18. Tailplane Bending Moment Ratio VG/V _M for conventional A/C	14-11
Figure 19. Tailplane Bending Moment Ratio VG/V _M for EFCS/CL-A/C	14-11
Figure 20. Tailplane Root Bending	14-11
Figure 21. Safety factor at time of failure / Active Failure	14-12
Figure 22. Safety factor after failure / Passive Failure	14-12
Figure 23. Wing Bending Envelope Failure Cases / Non Failure	14-13
Figure 24. HTP Bending Ratio Failure / Non Failure	14-13
Figure 25. Fuselage Torque Envelope Failure Cases / Non Failure	14-13
Figure 26. Overspeed Protection System	14-14
Figure 27. Altitude Loss versus Load Factor Demand	14-15
Figure 28. Time Delay versus Load Factor Demand	14-15
Figure 29. Low Speed Protection Settings	14-16
Figure 30. Gust Load Alleviation	14-17
Figure 31. Wing Shear Conventional A/C, GLA- and FBW-Effect	14-18
Figure 32. Wing Bending Conventional A/C, GLA- and FBW-Effect	14-18
Figure 33. Wing Torque Conventional A/C, GLA- and FBW-Effect	14-18
Figure 34. HTP Bending Conventional A/C, GLA- and FBW-Effect	14-18
Figure 35. Scheme of MLA	14-19
Figure 36. Change of Wing Bending due to MLA	14-19
Figure 37. System effect on Loads/Structures	14-20

Abbreviations

Abbreviation	Description	Abbreviation	Description
A/C	Aircraft	V_c	Cruising Speed
HTP	Horizontal Tailplane	V_{MO}	Maximum Operating Speed
S/F	Slats/Flaps	M_{MO}	Maximum Operating Machnumber
FBW	Fly by Wire	V_D	Dive Speed
EFCS	Electrical Flight Control Systems	Φ	A/C-Bank Angle
LAF	Load Alleviation Functions	Φ_c	Bank Angle Command
GLA	Gust Load Alleviation	Φ^*	A/C - Roll Velocity
MLA	Maneuver Load Alleviation	Φ_c^*	Roll Velocity Command
CL	Control Law	NZ	A/C - Vertical Load Factor
HQ	Handling Qualities	NZ Φ	A/C-Load Factor induced by banking
SF	Safety Factor	ΔNZ_c	Load Factor Command
LL	Limit Load	Θ	A/C-Pitch Attitude
UL	Ultimate Load	Θ^*	A/C-Pitch Velocity
J	Failure State	r	A/C - Yaw Velocity
P	Failure Probability	β	A/C - Sideslip
		ΔM_x	Reduction or Increase of Bending Moment relative to defined Basis

1.0 Introduction

The progress in electronics and computer-techniques and the decrease of prices in this field let the designers in the civil Aircraft Industry start thinking about the attractions the usage of this could have in civil aviation.

Based on the experience in the military fighter area and supersonic civil transports they came to the conclusion that there is a big amount of attractions, if the standards of

- Reliability
- Safety
- Inspection Intervals

usual in civil aviation can be at least guaranteed or better improved.

Further investigations showed that this would be the case if some conditions are accepted. These conditions result mainly from the extremely high interference between different technical disciplines designing an A/C with electrical flight control systems (EFCS), control laws and possibly load alleviation functions (LAF).

The competitive situation in the civil A/C market is such, that an A/C design must be an overall optimum to be successful. It is therefore not acceptable, as it was sometimes in the past, to have an optimum in one discipline, say aerodynamics and only suboptima in the other fields.

To have an overall optimum requires a close cooperation of several disciplines from the early beginning to have a chance to meet this target.

Our experience is, that this has to be learned and trained again and again before it can be really realized. So it is a danger to install EFCS and all these features with the only target, to reach attractive handling qualities without realizing what this could mean to loads, flutter, structures, and to structural weight.

This presentation deals with the interference between the systems and structural layout of a today civil A/C design.

2.0 Example of a Systems Layout of a Today Transport Aircraft

European aircraft manufactures made a big step forward in introducing in their now delivered civil transport A/C generation

Electrical Flight Control Systems (EFCS)

already known from the military fighters as "Fly By Wire" (FBW) together with control laws but especially fitted to the "civil world".

Figure 1 shows the overall arrangement for the total A/C and the control surfaces with their partially multifunction.

In Figure 2 on page 14-5 a scheme is given, explaining the EFCS installation in its different axis

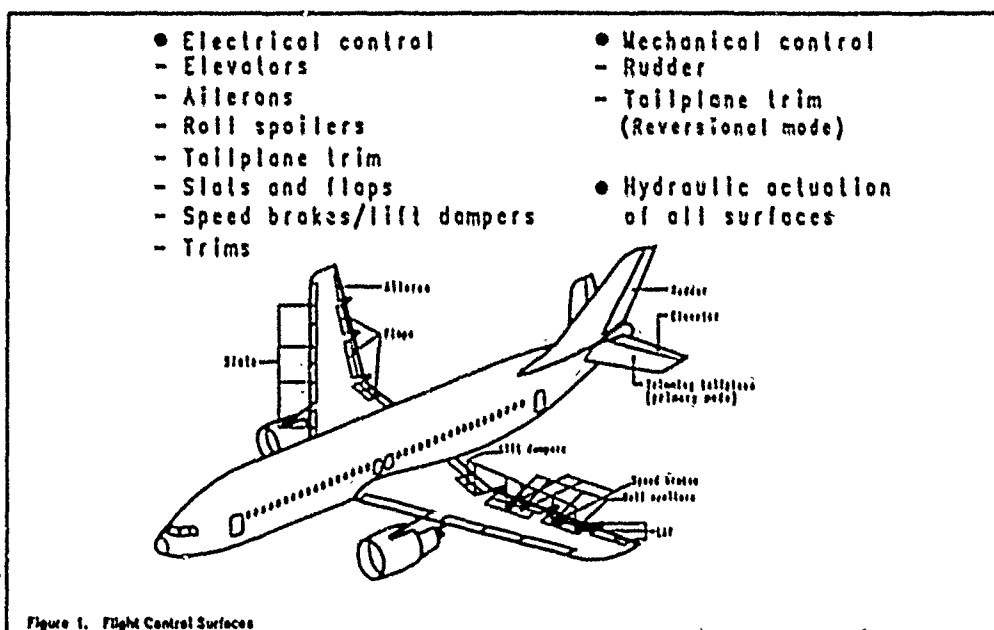
- Pitch Control
- Roll Control
- Yaw Control

and the

- Loads Alleviation Function (LAF)

integrated in the pitch control string.

Figure 3 on page 14-5 shows in more detail the pitch control from the side stick via C-Star Law to the tailplane and elevator.



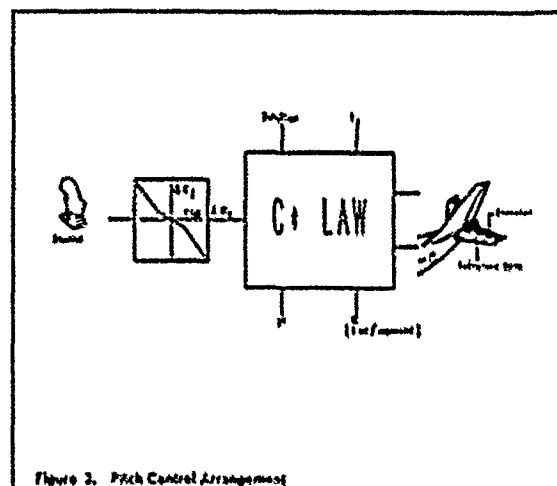
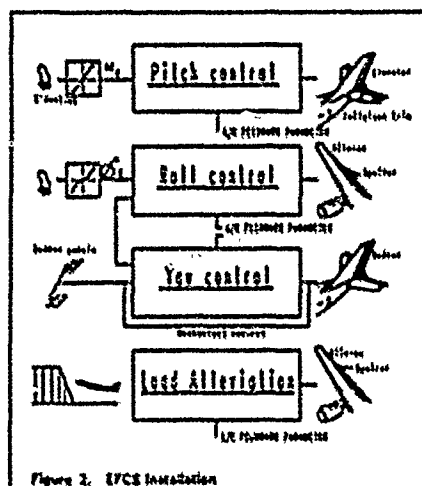
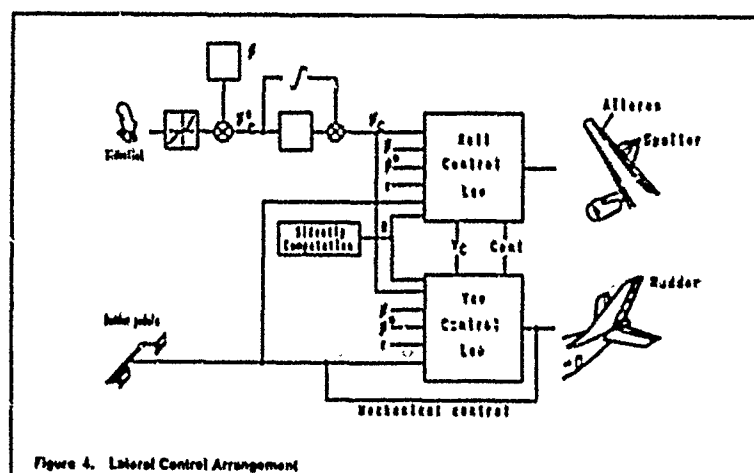
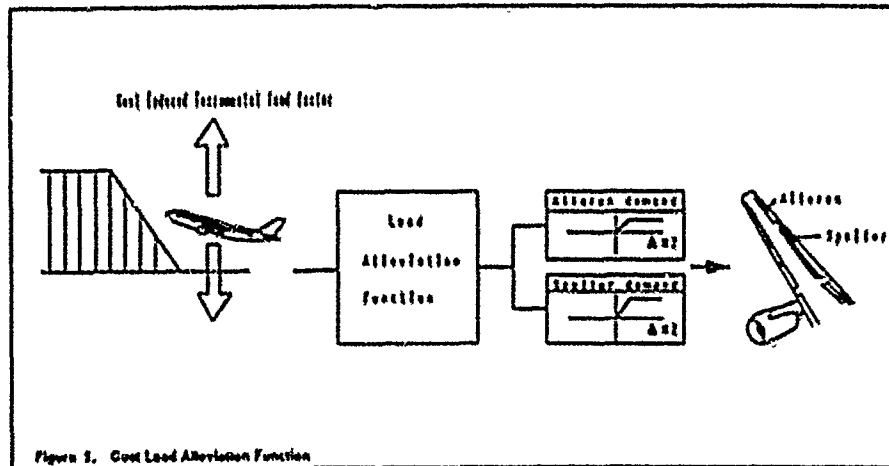


Figure 4 shows the scheme of the lateral controls in the combination of roll and yaw axis. Also here a control law is installed, which works as a combination of roll and yaw control law, depending upon the fact from where the excitation (stick or pedal) is coming. In this EFCS layout the string from the pedals to the rudder is mechanically linked. In Figure 5 on page 14-6, a scheme for a Gust Load Alleviation (GLA) as a function of the existing pitch control law is shown, working on the two outer spoilers and an outer aileron. The target of this GLA is to reduce wing bending by destroying part of the additional lift induced by a vertical discrete gust.

The reduction of the wing root bending has the order of magnitude of about 15 % of the gust increment. The system becomes active after overriding a threshold of $\Delta N Z = 0.3 g$.





3.0 Design Concept

3.1 Handling Quality

It is easy to understand, nearly obvious to regard EFCS, FBW, and control laws as a chance to give an *A/C* attractive handling qualities (HQ), because the control law gives nearly no limitations in doing so.

The first step in the overall control law/systems layout therefore will be to specify an attractive HQ and establish a control law concept, which has a chance of realization in soft- and hardware. This first concept will be established without being influenced by the structures discipline. One handicap already arises from the fact, that the gains, time constants and time delays are highly depending on the aerodynamic data used, which will be not very well settled in this early stage of the program.

It was found to be recommendable to investigate as a reference basis always the *A/C* without control laws (reference *A/C*). Furthermore it was found necessary to undertake sensitivity studies to give all involved disciplines an idea what margins of variation could arise from development of HQ-requirements and what this means as impact on structural weight.

3.2 Structures

The situation of the structural design must be regarded from the history. It has to be reminded, that static design of structure was done in the past based on static design loads resulting from artificial severe design condition as *A/C* response in

- Design Gusts
- Design Maneuvers
- Design Landing Conditions.

In these calculations the *A/C* was modelled precisely in

- Geometry
- Masses
- Flexibility
- Aerodynamics

and responding due to a defined excitation as function of time or frequency in its rigid and flexible body modes taking into account steady distorted and unsteady aerodynamics. Non linearities were taken into account as far as relevant for that problem. This shows that the *A/C* realization is very realistic, which had to be validated by flight test, but the artificial part was the excitation input. This input normally defined as

- Control Surface Deflection as $f(t)$
- Gust Shape and Intensity
- Rate of Descent

resulting from the airworthiness requirements JAR/FAR 23 had to be taken into account extremely severe and far beyond operational or handling needs.

The introduction of control laws led to the situation where this control surface deflection became, depending on the control laws, such different from the old required ones that their further use was felt to be too unrealistic and too far from what happens at the surface after a pilot input. As an example the unchecked maneuver might be mentioned. Figure 6 and Figure 7 show the different time-histories with and without Control Law (CL). Without CL the surface deflection equals the column movement, with CL the stick deflection (pilot command), and consequently aileron deflection is totally different, producing naturally also different A/C behaviour and tailplane loads as shown in Figure 8 to Figure 10 auf Seite 14-8.

A similar behaviour of deflections and reactions can be observed in Figure 11 auf Seite 14-8 to Figure 16 auf Seite 14-9 for a checked design maneuver like a sinusoidal movement of sidestick respectively elevator.

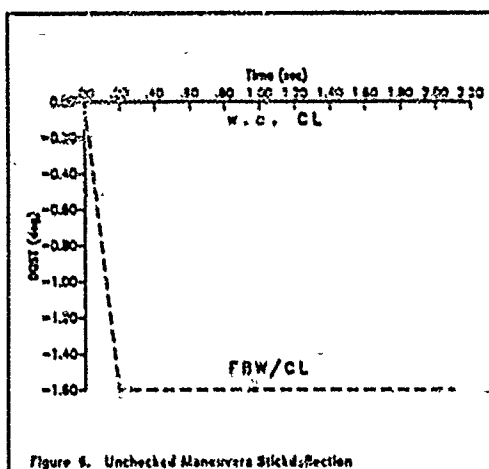


Figure 6. Unchecked Maneuver Stick Deflection

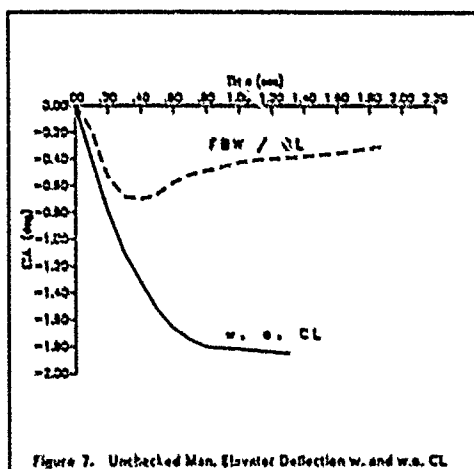


Figure 7. Unchecked Man. Elevator Deflection w. and w.o. CL

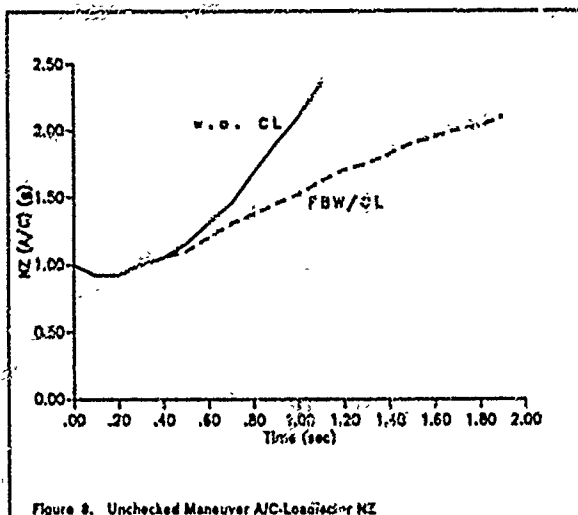
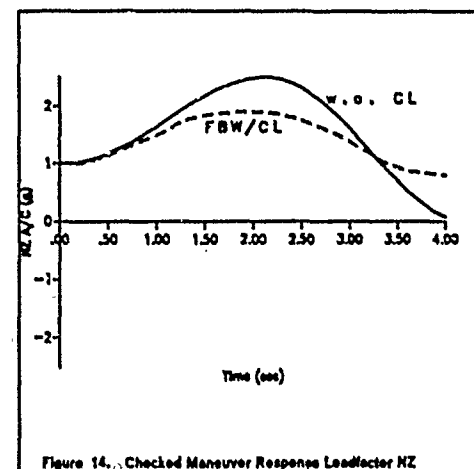
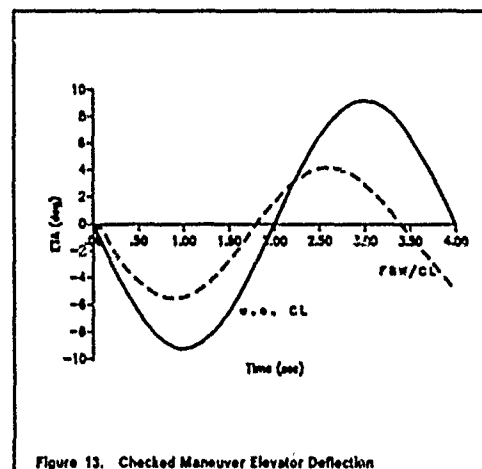
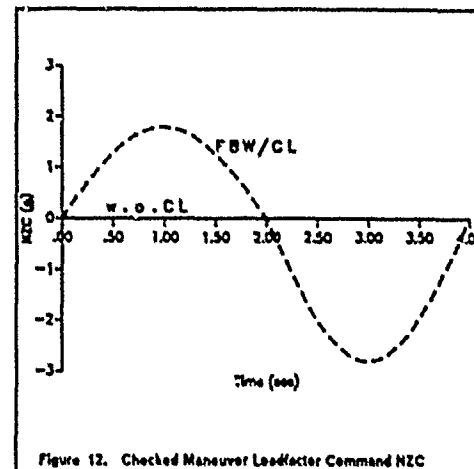
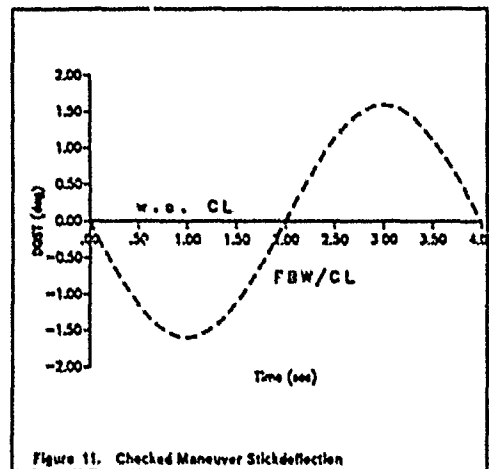
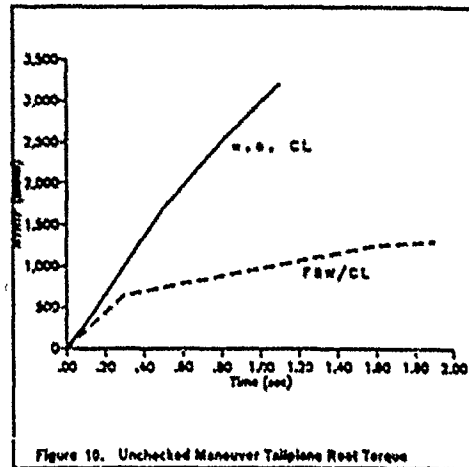
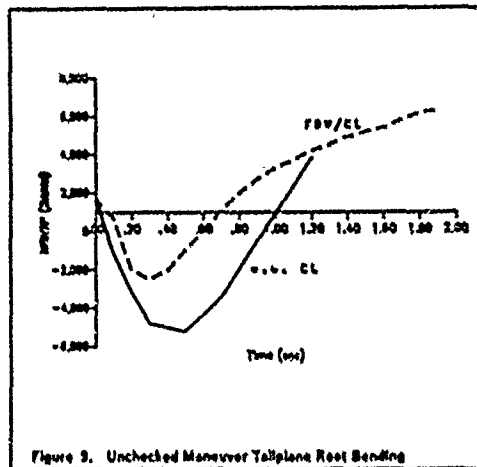


Figure 8. Unchecked Maneuver A/C Load Factor NZ



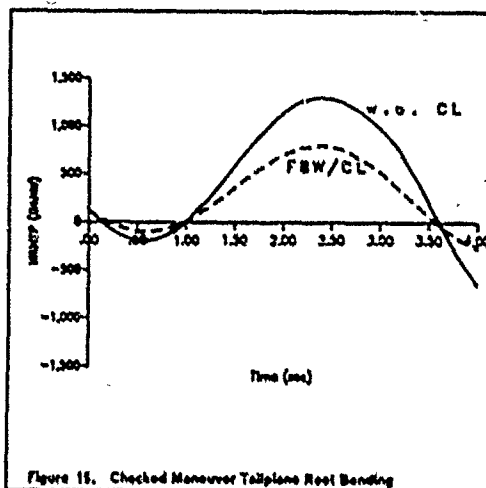


Figure 15. Checked Maneuver Tailplane Root Bending

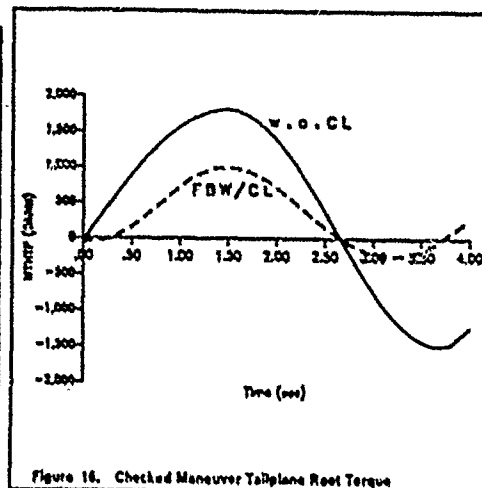


Figure 16. Checked Maneuver Tailplane Root Torque

Therefore, we had to agree with the airworthiness authorities about a stick input as function of time or frequency to be used for design maneuvers for such an "unconventional A/C". This was done in 1985 during the design phase of Airbus A320 and is laid down in special condition (SC-A2.2.2) as replacement of JAR 25.331(C)(1) and (C)(2), and addition to (C)(3) and replacement of JAR 25.349 (a).

With this new situation we were faced with modified needs for establishing design loads. Now it was necessary to increase the A/C modelling by

- Systems Architecture and
- Systems-Parameters.

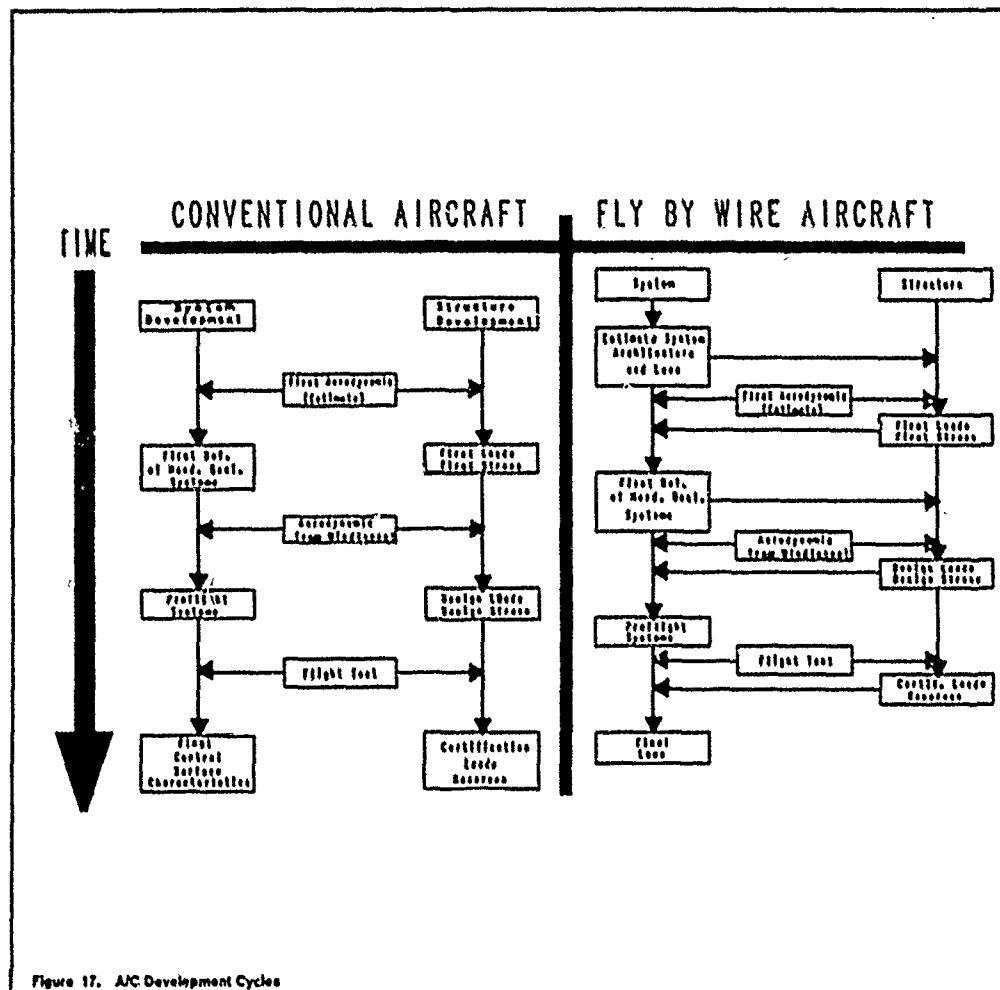
Here it is felt necessary to say that with this development a totally new way of interdisciplinary work was requested. Figure 17 on page 14-10 shows in a flow chart the development-cycles of an aircraft.

In the design philosophy of a conventional A/C, it was acceptable that the different disciplines worked nearly independent from each other in parallel with linear models.

The system controlled A/C requests because of the high interaction of

- Aerodynamics
- Handling Qualities
- Systems
- Structures

a close cooperation of these disciplines in all phases of design. Taking into account the different non-linearities is now a "must".

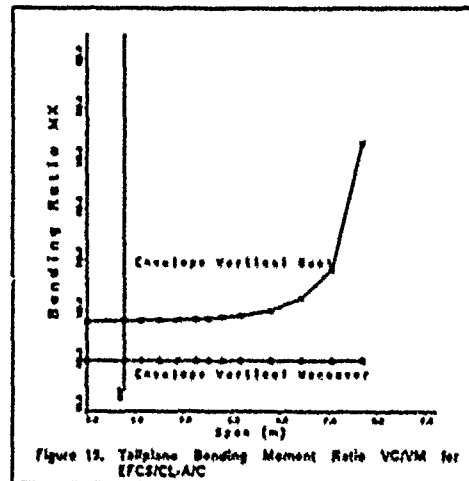
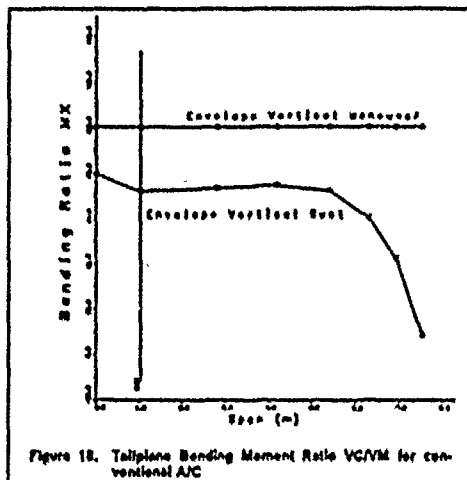


Because the control law will make the excitation smoother than in the old maneuver design conditions, we could expect in general for the EFCS/CL-A/C a lower maneuver design load level for the non-failure condition than for the conventional A/C. This is an important aspect in the light of reducing A/C weight and improve the overall A/C efficiency.

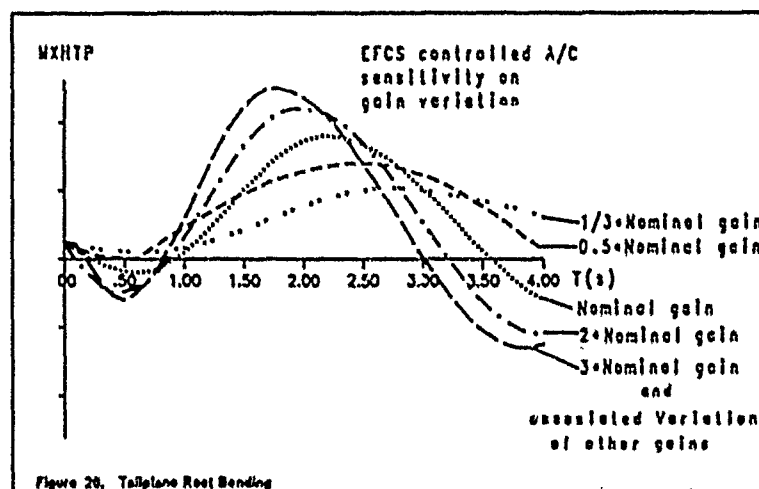
Having stated this the handling quality/systems expert might not understand why close cooperation with loads/structures is required.

However, systems supported A/C's also tend to fly in stability regions, which would not have been used for conventional airplane. This produces on the other hand higher loads, for instance from gusts because the damping imposed by system is just enough for handling quality criteria but for the special selected critical cases for structural design it could be here and there very limited and though increasing gust loads over maneuver loads for HTP, a component which is conventionally designed by vertical maneuvers (see Figure 18 on page 14-11 and Figure 19 on page 14-11).

This requires that an acceptable compromise between HQ-aspects and structural implications has to be found, not to penalize the structural design by optimization only to HQ-aspects.



As an example for the effect of different gains in Figure 20 is shown the resulting tailplane bending time histories for different sets of gains and time constants. It can be seen that the variation in the load is up to 100 % higher load than the load associated with the gain producing the minimum load level.



On top of that let's say "normal dependency" between systems and structures we encountered the

• System Failure Cases

as influencing effect from systems to structures and vice-versa.

Using the system behaviour for reducing design loads makes necessary to have a systems reliability, which in case of system failures does not eat the benefits. If this is the case or not depends highly upon the system failure probabilities, for which also the structure has to be designed. Therefore again in the design phase of the A320 we worked out together with the airworthiness authorities a concept "How to handle system failures, which have structural implications." This is reflected in a special condition SC-A2.1.1. This paper defines the safety factor as function of system failure probability (see Figure 21 on page 14-12 and Figure 22 on page 14-12).

The safety factor, which for non failure conditions is $SF = 1.5$, to transfer Limit Load to Ultimate Load

$$L_{UL} = 1.5 \times L_{LL} \quad (\text{non failure})$$

can under special circumstances become $SF < 1.5$ depending upon system failure probability using SC-A 2.1.1. philosophy

$$L_{UL}(j) = SF(p_j) \times L_{LL}(j) \quad (\text{failure state})$$

where

- L : load quantity
- SF : safety factor
- LL : limit load
- UL : ultimate load
- j : failure state
- p : failure probability

This relationship shows the high influence of a systems layout with respect to failure probabilities on the ultimate design load level.

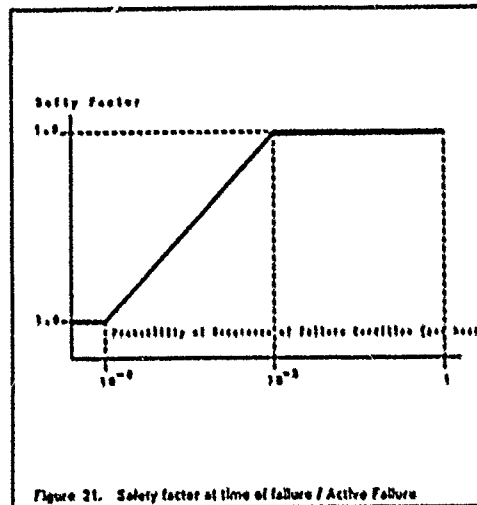


Figure 21. Safety factor at time of failure / Active Failure

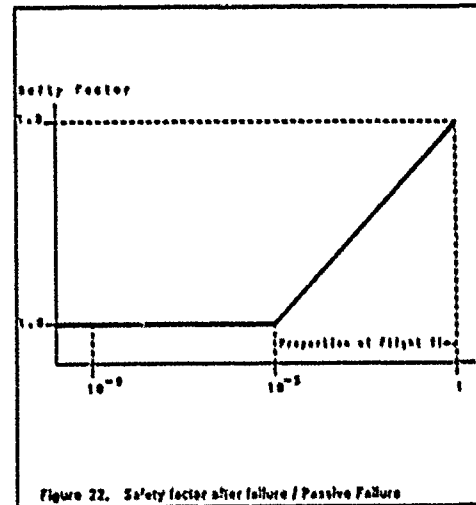


Figure 22. Safety factor after failure / Passive Failure

Figure 23 on page 14-13 to Figure 25 on page 14-13 illustrate the loads situation between non failure envelope and system failure envelope achieved for different components after a strong interdisciplinary work between handling quality-, systems- and loads-experts. The work started with the system failure definition but for systems side this is a defect of hardware.

- What does this defect mean, for instance, on deflection rates of surfaces, behaviour of control laws, and so on?
- Does the pilot know about the failure and can he do anything to avoid critical situations?
- How in detail, the special behaviour of aircraft in system failure state can be transferred into loads?

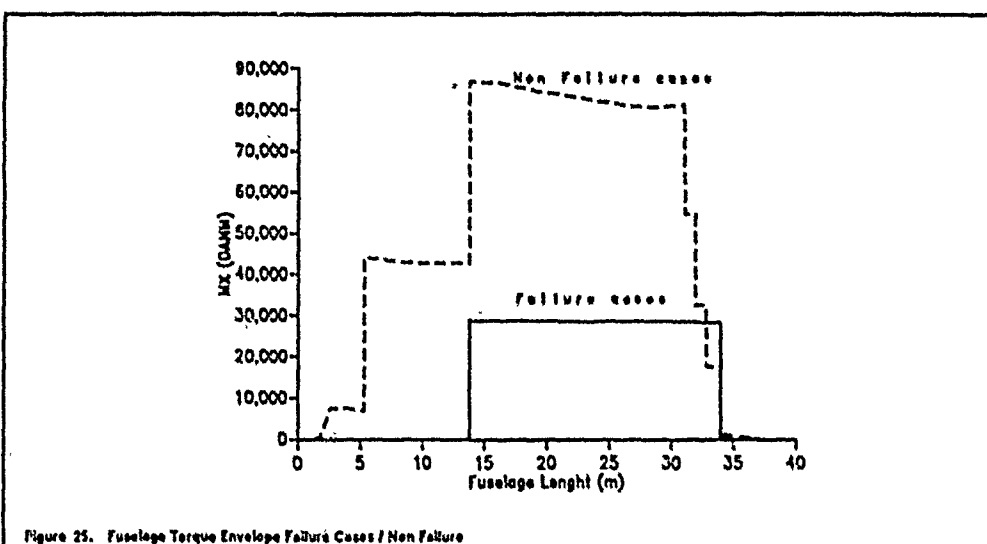
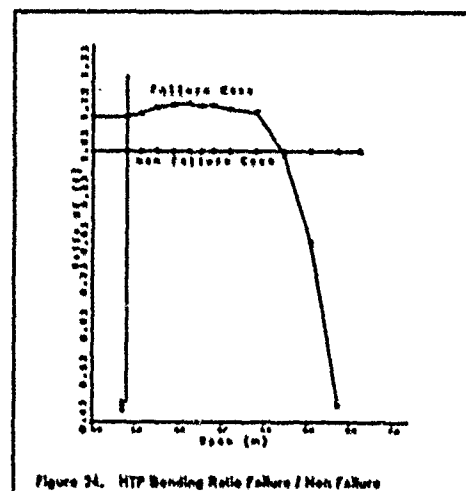
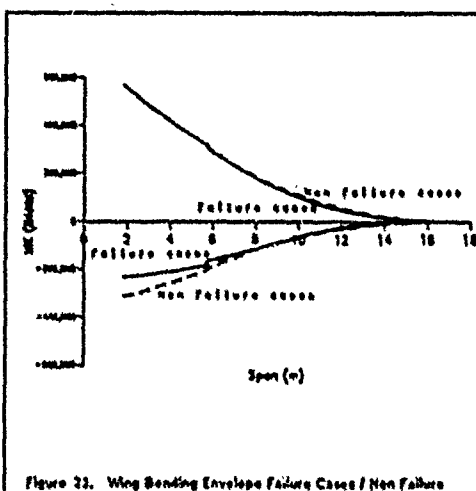
Always, if the answers could not be given precisely a conservative estimate had to be used in this process to ensure aircraft safety even in system failure state, but very often it was possible to reduce the consequence of a failure by extensive rig testing to an acceptable level from structural point of view.

So it can be seen that at the wing (Figure 23 on page 14-13) the failure case level is about the same as the non failure envelope. This was achieved by careful layout of gust alleviation system including possible failures right from the beginning of system design.

For the fuselage (Figure 25 on page 14-13) the failure level is well below the non failure level except for the attachment area of HTP (horizontal tailplane). This is produced by unsymmetrical runaway of elevator and has to be further treated as a design case because it was not possible to avoid this case.

Also for HTP (Figure 24 on page 14-13) it can be seen that the failure level in downward direction overrides the non failure case level by about 10 %. Also here the reason was a system driven runaway of one elevator which could not be avoided.

The cases producing higher loads for aircraft failure state were covered by structural margins available by chance from other reasons. However, the structural optimization might reduce this chance in future A/C designs further. Therefore, the system failure cases have to be controlled very carefully right from the beginning of a new design.



4.0 Aircraft Protection Systems

The installation of EFCS and Control Laws offers another chance to improve safety of the A/C against the standards of a conventional one by protections against

- Overspeed
- Load Factor
- Stall

The targets of these protections are:

- The A/C shall self recover against full pilot input.
- The A/C cannot be broken in pitch maneuvers.
- The A/C cannot be stalled, therefore no loss of control up to maximum angle of attack.

4.1 Overspeed Protection System

The objective of this system is to protect the A/C against speed overshoot above VMO/MMO. The overspeed will be limited by an automatic elevator recovery maneuver, which leads to a VD (protected) of about

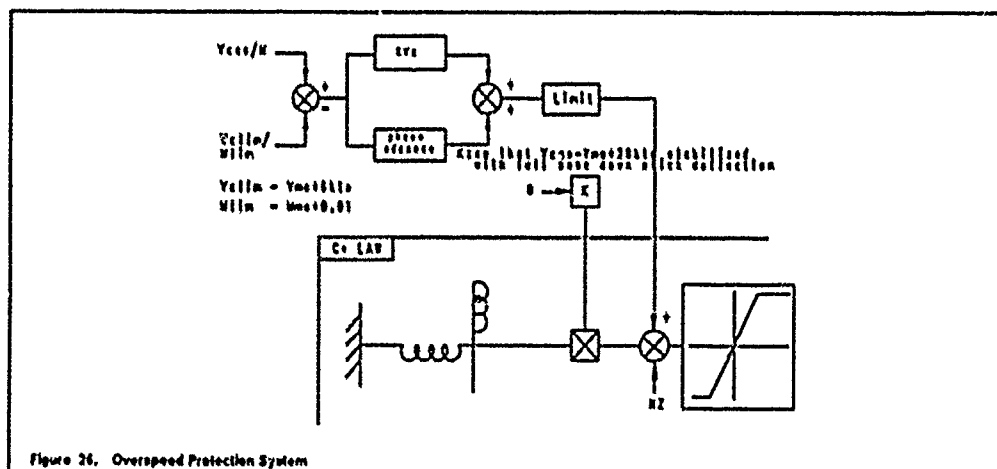
$$VMO + 33 \text{ kts}$$

This margin is about half of that between VMO and VD for a conventional A/C.

The system further limits the maximum bank angle above the overspeed warning to a defined value. The stick free bank angle will smoothly be reduced to zero.

Besides this positive aspect in handling, there are further benefits in demonstrating flutter freedom and in loads in cases, where normally VD-cases produce the critical design conditions.

Figure 26 shows the architecture of such an overspeed protection system.



4.2 Load Factor Protection System

The objective of such a system is to minimize the probability of hazardous events when from a handling point of view high maneuverability is needed.

This means in reality, that the pilot is free to act in a critical situation as he feels he should, without the need to care for another problem as in the conventional A/C.

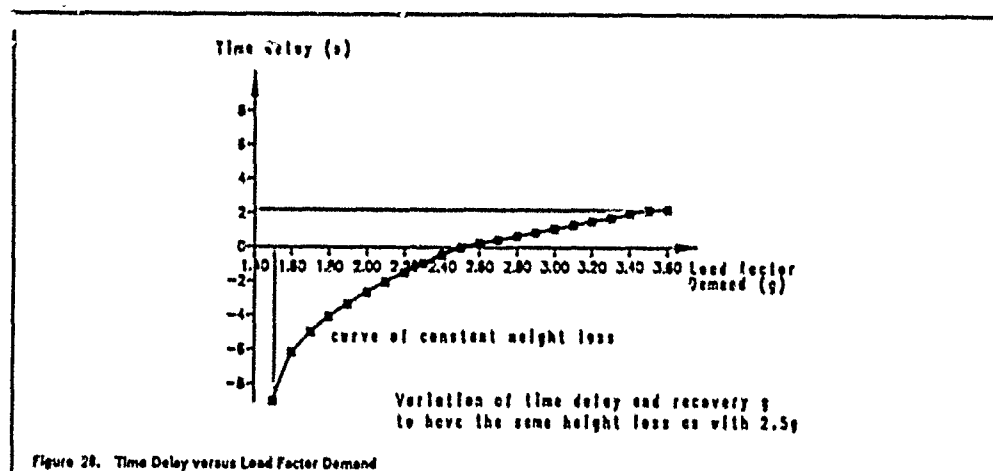
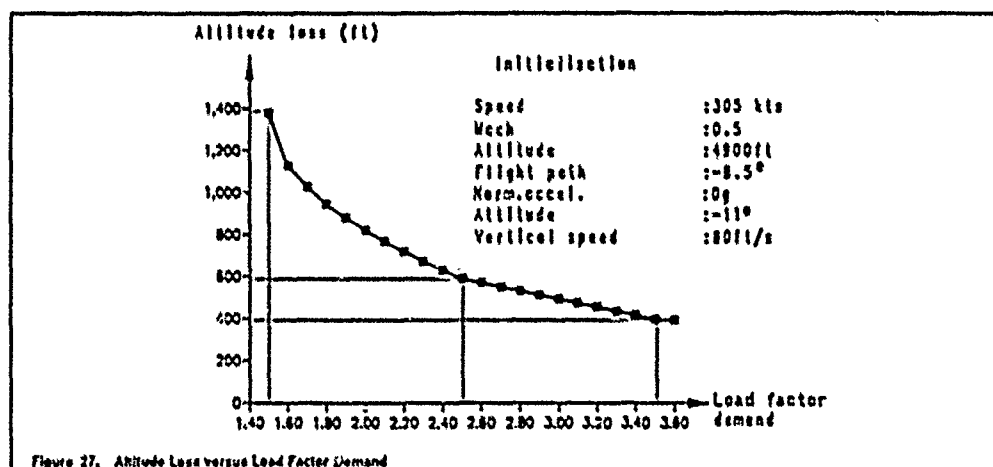
This is regarded as a big improvement in safety, because it can be shown by past experience, that A/C's were broken by pilot actions during recovery from a critical situation.

Such a system could for example ensure that the loadfactor is limited to

- $+2.5 \text{ g/-1 g}$ for clean configuration
- $+2 \text{ g/0 g}$ for flaps extended

It can be shown that a rapid pull to 2.5 g knowing the A/C cannot be broken leads to a more effective A/C reaction than a cautious pull to a higher loadfactor and taking care that the A/C will not be broken.

These facts are demonstrated in Figure 27 on page 14-15 and Figure 28 on page 14-15.

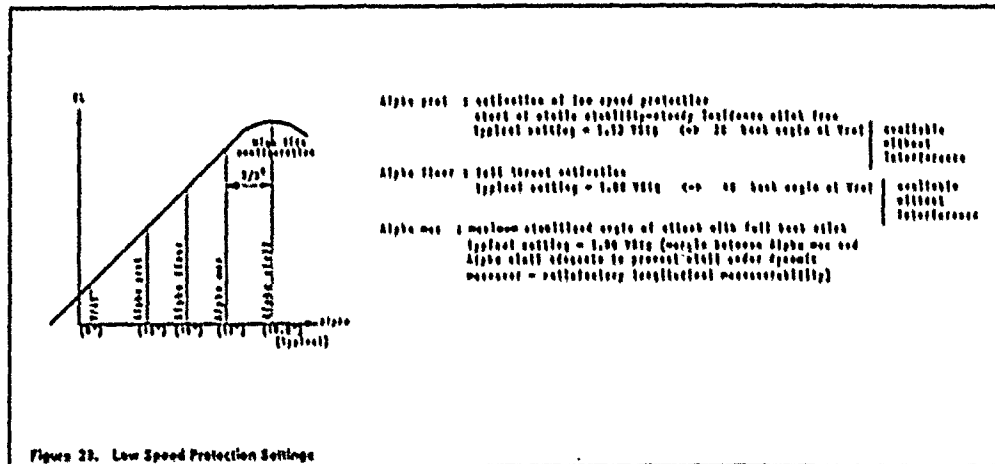


4.3 Stall or Low Speed Protection System

The objective of this system is to

- protect the A/C against stall in high dynamic maneuvers and gusts.
- give the A/C the possibility of a high lift side stick full back without exceeding a defined maximum angle of attack and without the risk of stall
- give the A/C a good rolling maneuverability
- Improve the windshear survivability by reaching a safe lift in conjunction with early full thrust availability under Alpha-floor command.

A scheme of the settings is given in Figure 29 on page 14-16.



5.0 Aircraft with Load Alleviation

Besides the improvement of the HO a FBW-A/C inclusive control laws implies the big chance to implement different load alleviation functions.

Depending upon the A/C category (short, medium, long range) the critical wing design condition can be gust or maneuver.

Saving structural weight means reducing or changing the critical design loads which in principle can be done by

- Gust Load Alleviation (GLA)
- or
- Maneuver Load Alleviation (MLA)

or both.

More or less all these systems are aiming at reducing design loads at the wing and not increasing at the same time the design loads at other components to maintain a positive overall weight reduction balance including additional weight for systems installation.

The philosophy and the expenses to be spent are very different as shown in the following subchapters.

5.1 Gust Load Alleviation

The target of a GLA is to destroy parts of the gust incremental load at the wing. Depending upon the wing design conditions in gust the system must work on

- Discrete Gusts
- Stochastic Gusts

both has to be demonstrated.

Realistic margins of reduction have the order of magnitude up to 20 % reduction of wing root bending.

The GLA works per layout for upgusts because the higher gust level is produced in that direction.

As controls in this function generally the symmetrical use of ailerons and spoilers is possible. High deflection rates of about 200 deg/s are requested, therefore additional hydraulic power is needed. It has further to be ensured that there will be no unacceptable interactions during pilot demanded maneuvers.

Such a system will normally operate under

- clean configuration
- speed higher than a defined value
- beyond a defined load factor threshold

A scheme of such a GLA is given in Figure 30.

As mentioned under item 3.2 also such a GLA-Function can fail for several systems reasons and therefore if the structural design of the wing is optimized to the reduced loads produced by the system the failure cases have to be carefully watched right from the beginning of the systems development.

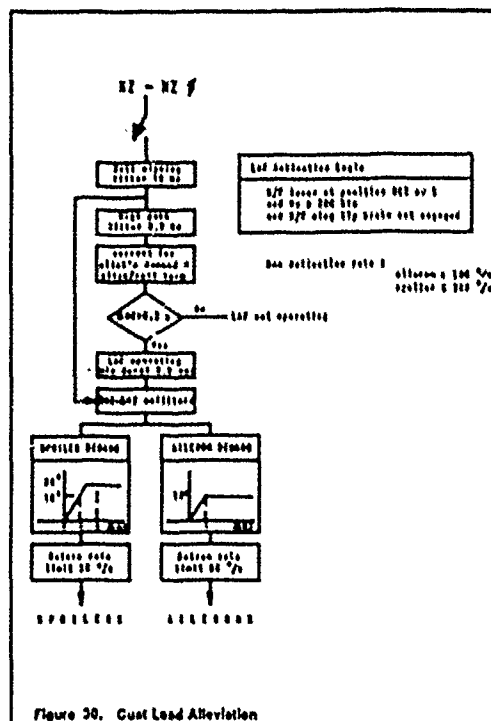


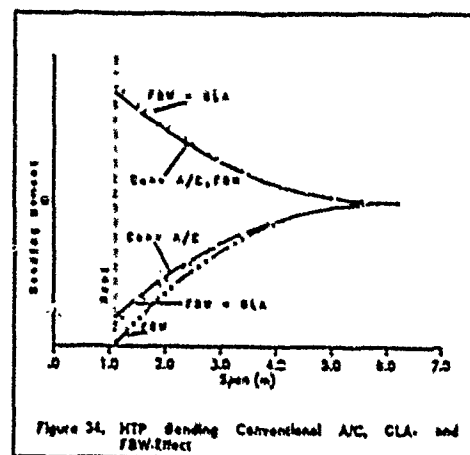
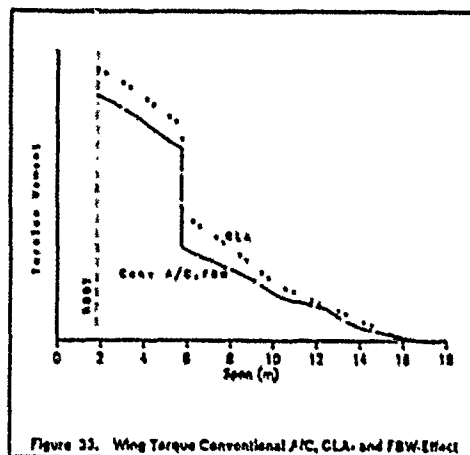
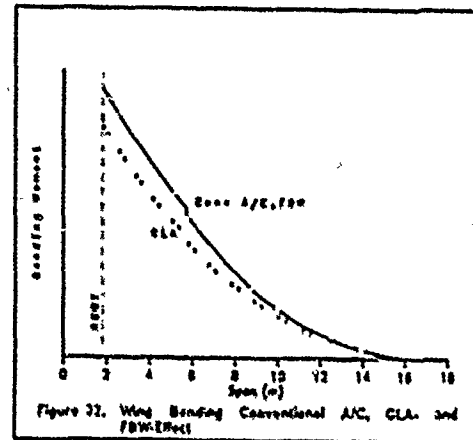
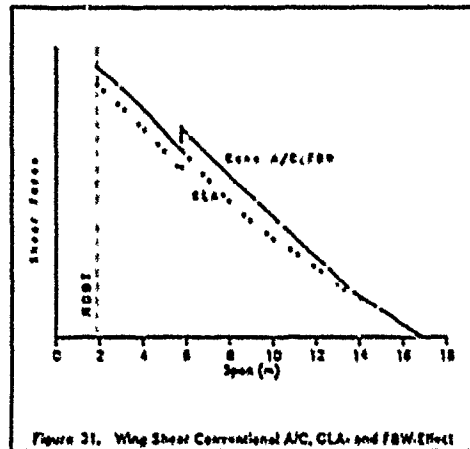
Figure 30. Gust Load Alleviation

Figure 31 on page 14-18 to Figure 34 on page 14-18 present the effect of GLA on wing and tailplane compared to a conventional A/C (mechanical link between pilot and surface) and to a FBW-A/C which has only the control law installed.

The wing upbending in Figure 32 on page 14-18 shows the expected reduction versus span, whereas one cannot distinguish conventional and FBW-A/C. The effect on wing torque of GLA is adverse, i.e. torque is increased due to the surfaces used for alleviation.

The HTP-bending in Figure 34 on page 14-18 shows that one has to distinguish the load directions in judging on the system effect. For downward tailplane load the FBW-A/C presents the highest load level, this is then reduced by additional use of GLA. However, the lowest level is presented from the conventional A/C. For the upward load direction the A/C with CL and GLA presents the highest load level, FBW-A/C and conventional cannot be distinguished.

In this example the absolute highest level was obtained in upward direction. What can be said generally is that due to System Effect (EFCS and GLA) the HTP loads were increased and an exchange from vertical maneuver to vertical gust cases has taken place as already shown under item 3.2. This certainly effects the rear fuselage too.



5.2 Maneuver Load Alleviation

The aim of a MLA is to redistribute for maneuvering necessary lift to the inner part of the wing and by this reducing only the wing bending. In doing so the overall A/C-balance will be disturbed and has to be regained by elevator reaction. It is easily to be seen that by this the MLA influences the tailplane- and rear fuselage loads too.

Realistic wing root bending margins which can be gained by MLA have the order of 10 %. That means the MLA is less efficient compared to the CLA. However this efficiency is achieved by far less complicated system and needs no additional hydraulic power. It can be realized using the system performance already available for HQ of an EFCS equipped A/C. Therefore it is principally possible to add this feature to such an A/C for further development reasons.

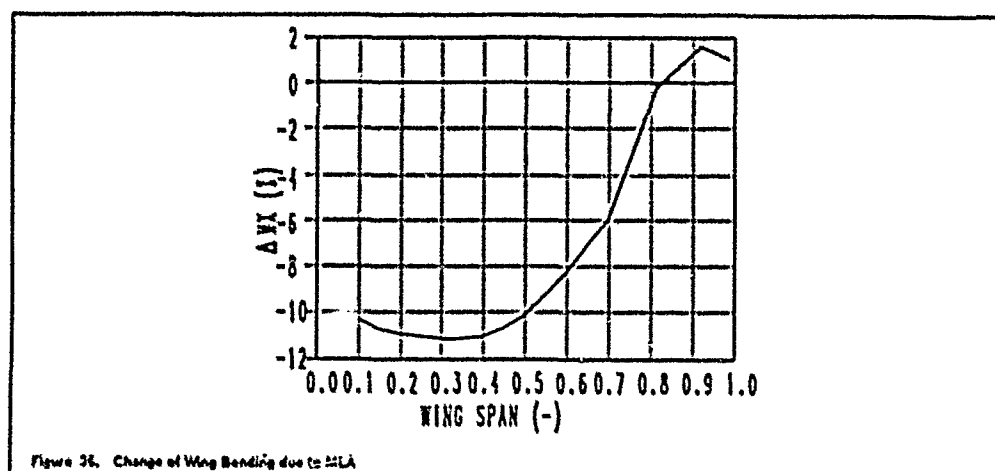
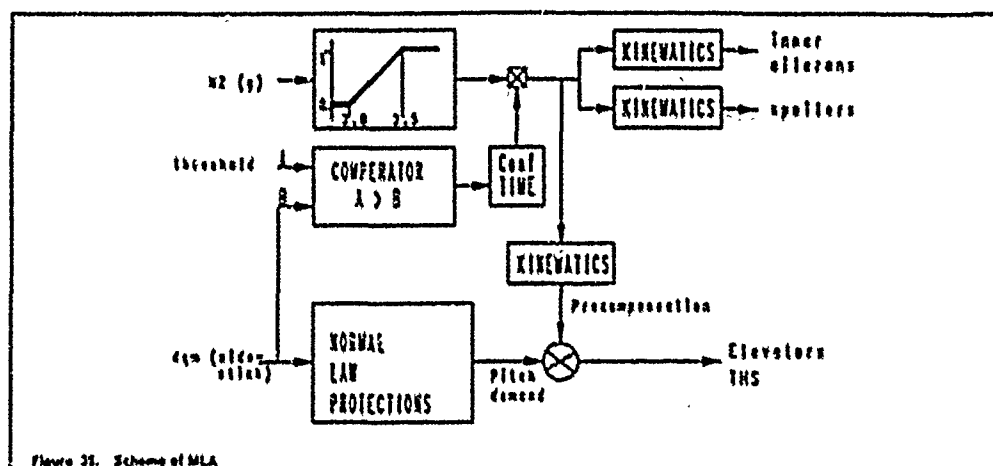
A scheme of MLA is given in Figure 35 on page 14-19.

It can be seen that the ailerons, outer spoilers and the elevator are used, in a symmetrically sense naturally, and that there is a certain threshold in elevator demand and load factor.

The reduction of wing bending versus span is presented in Figure 36 on page 14-19

However this reductions has to be balanced with possible higher loads for tailplane and rear fuselage. The MLA tends to make the A/C sluggish in checked maneuvers. This could make it necessary from HQ point of view to modify the gains in such a way to regain the A/C maneuverability without MLA. The consequence of this could be an increase of tailplane loads up to 30 %.

Again here it is an clear interaction of HQ, Loads, Stressing to find a from all concerned disciplines acceptable compromise.



6.0 Conclusion

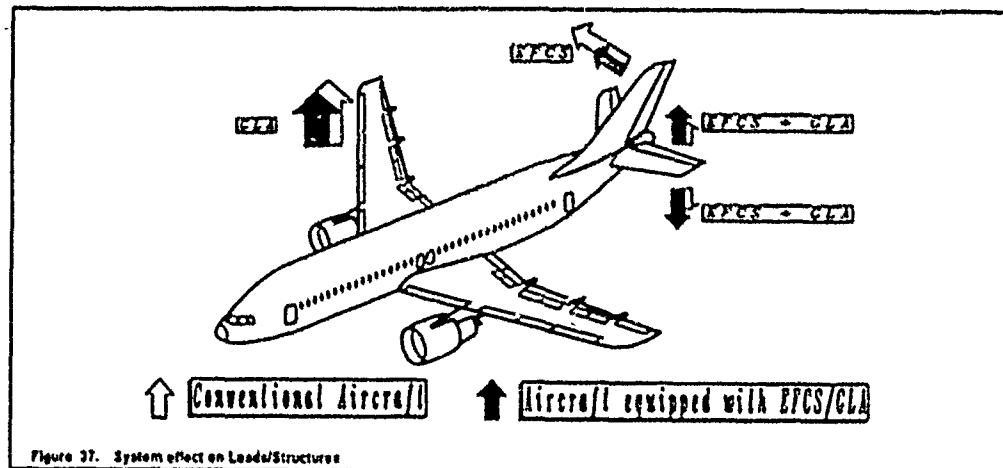
The presentation has shown that there are advantages and disadvantages available from the system effects on structures as it is summarized in Figure 37 on page 14-20.

The target in future developments shall be to avoid the disadvantages as far as possible while keeping the advantages.

Because of the strong interaction between

- Aerodynamics
- Handling Qualities
- Systems
- Loads
- Stressing

In today A/C-Design as presented here, the only future solution can be an intensive cooperation of the before mentioned disciplines during the total design phase in a "closed loop".



7.0 References

1. MBB note T-I-TE242/01-87
C.L.Tanck, M.Besch 1987
2. ICAS-86-2-1-2
Influence of EFCS-Control-Laws on Structural Design of Modern
Transport Aircraft
M.Besch, C.L.Tanck 1986
3. MBB note TN-TE2403/01-89
Study to Check Influence of MLAF on Design Loads of
Non-Wing-Structure
G.Beuck, G.Rollwagen 1989

8.0 Acknowledgement

The authors like to express their acknowledgements to their staff who has supported this paper, especially to Mr. Mesercknecht who has much contributed for the efficient establishment of this paper

TURBULENCE EFFECTS ON AIRCRAFT FLIGHT DYNAMICS AND CONTROL

Robert L. Swain, Ph.D., P. E.
 Professor of Mechanical and Aerospace Engineering
 Oklahoma State University
 Stillwater, OK 74078
 USA

SUMMARY

Design of aircraft flight control systems requires consideration of many factors including maneuvering, ride and handling qualities, stability augmentation, and control power requirements as well as several others. All the mentioned factors, however, are strongly influenced by the atmospheric turbulence environment through which the aircraft must fly. A unified analytical design method is described which systematically accounts for three-component gust velocity spatial distribution effects, handling qualities in terms of needed closed-loop stability augmentation systems, and the maneuvering and stabilization three-axis control power required. These factors are all interrelated. State variable formulations of modern system theory are used for the aircraft and turbulence dynamic models and in stability augmentation system synthesis. Both homogeneous and heterogeneous turbulence are considered. Homogeneous models are described in a statistical sense. Heterogeneous turbulence is discrete due to vortex patterns generated by obstacles such as trees, buildings, mountains, etc. and has been known to result in aircraft upsets and structural failure.

INTRODUCTION

An airplane has six rigid-body degrees of freedom--vertical, forward, and sideways translation of the center of gravity and yaw, pitch, and roll rotations. These are usually referenced to an orthogonal axis system fixed at the center of gravity. The overall control problem is conveniently divided into the guidance function, concerned with control of linear position and velocity of the airplane to cause it to follow a desired flight path time history, and the attitude control or stability augmentation function. The guidance system obtains position and velocity information from the navigation system and uses this data to generate velocity commands, which in turn are implemented by maneuvering the aircraft through displacement of appropriate aircraft controls. In order for the guidance function to be carried out, the airplane must be stable along its flight path. In other words, it must not exhibit divergent oscillations which would cause it to depart from the desired flight path. All VTOL and most CTOL high performance airplanes require such stability augmentation, provided by either an automatic system, or by the pilot working harder to stabilize by control inputs as well as maneuver the vehicle with additional inputs from the same controls.

The quality of the attitude stability is referred to as the "handling qualities" or "flying qualities" of the airplane, and there has been much research devoted to determination of what these should be for various classes of airplanes in various flight conditions. The handling qualities specifications for CTOL airplanes are given in Ref. 1 and VSTOL airplanes is in Ref. 2. Pilot opinion ratings obtained in simulations or from actual flight test are always used in assessing whether the airplane does have satisfactory handling qualities.

The source of turbulence-generated aerodynamic forces and moments acting on aircraft are the three orthogonal components of wind relative velocity referenced to a body-fixed coordinate system. The components contain mean wind values U_0 , V_0 , W_0 and turbulence stripes u_g , v_g , w_g , which are functions of time and spatial position relative to the aircraft (Fig. 1). The forces and moments are created by (1) Kutta-Joukowski law of circulation and (2) momentum transfer between the turbulence and the airframe.

For aircraft in conventional flight, circulation lift is predominant. For winged VTOL aircraft in hovering flight, momentum transfer becomes significant. The turbulent air is of two types, (1) Homogeneous and (2) Heterogeneous. Homogeneous turbulence is that which can be described statistically. Heterogeneous is non-statistical turbulence and refers to discrete gusts such as thunderstorm downbursts, wind shears, and vortex patterns off mountains, buildings and other obstacles. The momentum transfer approach is appropriate for vortex and shear inputs to the aircraft. Figures 2 and 3 show a possible vortex model and velocity profile for use in momentum transfer calculations. A nose-to-tail traverse would cause rapid pitch and yaw reversals, depending on the orientation of the vortex axis relative to the aircraft. Likewise, a wing tip-to-wing tip traverse would result in rapid roll and yaw reversals. Severe disturbances of this type put extreme demands on the control system. Reference 9 describes a detailed application of this vortex method, as well as etc. etc.

CONTROL POWER

A number of VTOL crashes have been attributed to a lack of sufficient control power to stabilize the aircraft in turbulence. Control power is most often defined as the angular acceleration produced by a control input. For example, instantaneous yaw control power is given by

$$Cp(t) = N_{\delta_r} \delta_r(t) \quad (1)$$

where $\delta_r(t)$ is the yaw control, usually rudder deflection or its equivalent in terms of reaction jet thrusting, and N_{δ_r} is the control sensitivity (change in yawing moment due to unit δ_r divided by aircraft yaw mass moment of inertia). Similar expressions give control power in roll and pitch. This definition applies to the control power needed for maneuvering and that needed for stability augmentation about a trimmed flight condition.

There is a need for better methods of determining the minimum levels of control power necessary to provide adequate stabilization and maneuverability for VTOL aircraft. An insufficient amount is unsafe and an excess reduces the available lift engine thrust, as control power is obtained by bleeding air or modulating thrust from the propulsion system. The amount needed for maneuvering is generally independent of aircraft size and dynamic characteristics. However, that needed for stabilization is strongly dependent on aircraft size, open-loop dynamics, the type and amount of stability augmentation provided, and the turbulence environment. An analytical design method is available which structures the stability augmentation system required for satisfactory aircraft handling qualities, while simultaneously yielding the minimum required values of stabilization control power. Ride quality by suppression of rigid-body and elastic modes can also be incorporated in the design method.

The literature and the CTOL and VTOL aircraft built to date have not recognized the importance of the type of feedback control system used on the resulting control power requirements. Most three-axis stability augmentation systems have employed conventional attitude and rate feedback loops with no regard for what this control law structure means in terms of stabilization control power levels. For example, most vehicles in a hovering mode have minimum phase transfer functions and require unnecessarily high control power levels when stabilized by conventional servomechanism design techniques. It has been shown that modern linear state variable control synthesis methods can be used for direct synthesis of stability augmentation systems yielding prescribed handling qualities and minimum stabilization control power.¹⁰

UNIFIED DESIGN METHOD

An easily formulated and convenient form of aircraft dynamic equations of motion is the vector-matrix form

$$\dot{x} = Ax + Bu + G\eta_g \quad (2)$$

where x is an $(n \times 1)$ matrix of the physical aircraft variables, u is an $(m \times 1)$ control input vector, and η_g is an $(k \times 1)$ matrix of the gust velocity state variables. A , B , and G are $(n \times n)$, $(n \times m)$, and $(n \times k)$ coefficient matrices, respectively. Elastic mode degrees of freedom can be included in x .

The variables in the gust matrix η_g satisfy the vector-matrix equation, where coefficient matrices A_g and G_g can be determined from Dryden gust velocity power spectral density math models; r is scalar, zero mean, unit white noise

$$\dot{\eta}_g = A_g \eta_g + G_g r \quad (3)$$

If gust spatial distribution effects are included, $\eta_g = [u, v, w, r, q, p]$, where r, q, p are equivalent yaw, pitch and roll angular velocities due to the spatial effects. By augmenting the aircraft state vector x with the gust states, an alternate form of Eq. (2) is

$$\begin{bmatrix} \dot{x} \\ \dot{\eta}_g \end{bmatrix} = \begin{bmatrix} A & 0 \\ 0 & A_g \end{bmatrix} \begin{bmatrix} x \\ \eta_g \end{bmatrix} + \begin{bmatrix} B \\ 0 \end{bmatrix} u + \begin{bmatrix} 0 \\ G_g \end{bmatrix} r \quad (4)$$

For almost all stability augmentation system (SAS) control laws, from simple rate feedback to full state, the control input vector u can be expressed as

$$u = -Kx \quad (5)$$

where K is an $(m \times n)$ matrix of feedback gains. By use of Eq. (5), Eqs. (2) and (4) become Eqs. (6) and (7):

$$\dot{x} = [A - BK]x + G\eta_g \quad (6)$$

$$\begin{bmatrix} \dot{x} \\ \dot{n}_g \end{bmatrix} = \begin{bmatrix} \lambda - BK & 0 \\ 0 & A_g \end{bmatrix} \begin{bmatrix} x \\ n_g \end{bmatrix} + \begin{bmatrix} 0 \\ 0 \end{bmatrix} n \quad (7)$$

To simplify the notation in what follows, let \dot{x}^* , B , and F now be used to indicate the augmented system of Eq. (7), or

$$\dot{x}^* = Dx^* + F_n \quad (8)$$

Many conventional aircraft stability augmentation control philosophies use a single control input, usually elevator in the longitudinal case and rudder in the lateral-directional case. Since the ride quality analysis can be divided into separate longitudinal and lateral-directional cases, then the feedback gain matrix K in Eq. (5) becomes a $(1 \times n)$ row matrix.

In the scalar control input case, a powerful method for setting the feedback gains to achieve specified handling qualities is first to transform the aircraft states to phase variable canonical (companion) form.¹¹ If the system in Eq. (2) is completely state controllable, then there exists a transformation matrix T in $x = Ty$, which yields a phase variable canonical form in the vector y .

$$T\dot{y} = ATy + Bu + G_n n_g \quad (9)$$

and

$$\dot{y} = [T^{-1}AT]y + [T^{-1}B]u + [T^{-1}G]n_g \quad (10)$$

where

$$[T^{-1}AT] = \begin{bmatrix} 0 & 1 & 0 & 0 & \dots & 0 \\ 0 & 0 & 1 & 0 & \dots & 0 \\ 0 & 0 & 0 & 1 & \dots & 0 \\ \vdots & \vdots & \vdots & \vdots & \ddots & \vdots \\ 0 & 0 & 0 & 0 & \dots & 0 \\ -d_0 & -d_1 & \dots & \dots & \dots & -d_{n-1} \end{bmatrix} \quad (11)$$

and

$$[T^{-1}B] = \begin{bmatrix} 0 \\ \vdots \\ \vdots \\ \vdots \\ \vdots \\ 1 \end{bmatrix} \quad (12)$$

The d coefficients in Eq. (11) are the coefficients of the bare-airframe characteristic equation (13).

$$|sI - A| = s^n + d_{n-1}s^{n-1} + \dots + d_1s + d_0 = 0 \quad (13)$$

The $(n \times n)$ matrix T is formed as follows¹¹

$$T = [t_1 t_2 \dots t_n] \quad (14)$$

where

$$\begin{aligned} t_n &= B \\ t_{n-1} &= At_n + d_{n-1}t_n \\ t_{n-2} &= At_{n-1} + d_{n-2}t_n \\ &\vdots \\ t_1 &= At_2 + d_1t_n \end{aligned} \quad (15)$$

The scalar SAS control law is

$$u = -Kx = -KTy \quad (16)$$

and Eq. (10) becomes

$$\dot{y} = T^{-1}[A-BK]Ty + [T^{-1}G]n_g = \lambda^*y + [T^{-1}G]n_g \quad (17)$$

A^* is given by Eq. (18).

$$A^* = \begin{bmatrix} 0 & 1 & 0 & \dots & 0 \\ 0 & 0 & 1 & \dots & 0 \\ \vdots & \vdots & \vdots & \ddots & \vdots \\ 0 & 0 & 0 & \dots & 1 \\ (-d_0 \ k_1) & (-d_1 \ k_2) & \dots & (-d_{n-1} \ k_n) \end{bmatrix} \quad (18)$$

The last row of A^* contains the coefficients of the desired closed-loop characteristic equation. Handling qualities are strongly influenced by the roots of the characteristic equation. Therefore, if the desired closed-loop characteristic equation is specified by selecting all of the roots for good handling qualities, the coefficients e , as in Eq. (19), then are known and are related to those in A^* by Eq. (20).

$$s^n + e_{n-1}s^{n-1} + \dots + e_1s + e_0 = 0 \quad (19)$$

$$\begin{aligned} -e_0 &= -d_0 + k_1 \\ -e_1 &= -d_1 + k_2 \\ &\vdots \\ -e_{n-1} &= -d_{n-1} + k_n \end{aligned} \quad (20)$$

The k 's then are calculated easily, given the d 's and e 's. The k row matrix is obtained from Eq. (21), using Eq. (12).

$$-T^{-1}BKT = \begin{bmatrix} 0 & 0 & \dots & 0 \\ \vdots & \vdots & \ddots & \vdots \\ 0 & 0 & \dots & 0 \\ k_1 & k_2 & \dots & k_n \end{bmatrix} \quad (21)$$

$$K = [k_1, k_2, \dots, k_n] = [-k_1, -k_2, \dots, -k_n][T^{-1}] \quad (22)$$

Calculating the BK square matrix allows determination of the augmented D matrix in Eqs. (7) and (8).

Since sensors can measure only combinations of physical output variables, which are usually less than the order of the state vector, we have

$$z = Cx \quad (23)$$

where the z outputs are a $(p \times 1)$ vector, C is a $(p \times n)$ matrix of numbers and $p < n$. Each row of C is made up of the coefficients of the transfer function numerator polynomials of each output variable in the z -to- u transfer functions.¹⁰ Since matrix C is not square, its inverse does not exist, and the control law given by Eq. (24) cannot be realized.

$$u = -Kx + u_0 = -KC^{-1}z + u_0 \quad (24)$$

u_0 is the scalar maneuvering control deflection from pilot input. However, by forming additional equations by using derivatives of the z states and a technique described in Ref. 10 of using real-valued left half-plane transfer function numerator zeros, C can be made of size $(n \times n)$ and the inverse in Eq. (24) can be obtained.

A block diagram of the SAS implementation of Eqs. (3), (6), and (24) is shown in Figure 4.

RIDE QUALITY ANALYSIS

Once the SAS is designed for good handling qualities, the ride quality can be considered, although there are some trade-offs to be made between handling and ride in any design.¹²

The commonly used ride quality parameter is the vertical and lateral normal acceleration rms responses at selected fuselage stations. In terms of perturbation of flight path angle γ ; pitch angle θ ; roll-angle ϕ ; yaw angle ψ ; sideslip angle β ; symmetric elastic mode shapes and generalized coordinates ϕ_s and ξ_s ; and antisymmetric mode shapes and coordinates ϕ_a and ξ_a , the vertical and lateral normal acceleration load factors as a function of fuselage station l_x (positive forward of the c. g.) are

$$n_z(t_x, t) = \frac{1}{8} \{ U_0 \ddot{t} - t_x \ddot{\theta} - \sum_{i=1}^n \ddot{t}_i(t_x) \ddot{t}_i(t) \} \quad (29)$$

$$n_y(t_x, t) = \frac{1}{8} \{ (k + \dot{t}) U_0 - t_x \dot{t} - \sum_{j=1}^m \ddot{t}_j(t_x) \ddot{t}_j(t) \} \quad (26)$$

and U_0 is the true airspeed. Reference 13 contains details of a method of analysis compatible with the SLS design method and notation above. Only a brief presentation of the method is made here.

The vertical or lateral load factor (i.e., Eqs. (25) or (26) can be expressed as

$$n_{z,y}(t_x, t) = P x^* \quad (27)$$

where P is a $(1 \times n + k)$ row matrix of deterministic coefficients (different for n_z and n_y), which makes n_z or n_y a scalar. The mean square or expected value of $n_{z,y}^2$ is obtained by squaring and averaging.

$$n_{z,y}^2(t_x, t) = [P x^*][P x^*]^* = [P x^*][P x^*]^* \quad (28)$$

where $[]^*$ indicates the matrix transpose. Since $[P x^*]$ is a scalar, then $[P x^*]^* = [P x^*]$, and

$$\begin{aligned} n_{z,y}^2(t_x, t) &= [P x^*][x^{*T} P^T] = P x^{*T} P^T \\ &= [p_1, p_2, \dots, p_{n+k}] [x^{*T} P^T] \begin{bmatrix} p_1 \\ p_2 \\ \vdots \\ p_{n+k} \end{bmatrix} \end{aligned} \quad (29)$$

The mean square value then is the expected value $E[]$:

$$E[n_{z,y}^2(t_x, t)] = P E[x^{*T} x^{*}] P^T \quad (30)$$

where $E[x^{*T} x^{*}]$ is a symmetric square $(n + k) \times (n + k)$ state covariance matrix, which can be determined as follows. From Eq. (8),

$$E[\dot{x}^{*T} \dot{x}^{*}] = DE[x^{*T} x^{*}] + E[x^{*T} \dot{x}^{*}] \quad (31)$$

Also,

$$\dot{x}^{*T} = [D x^*] + [F \eta]^T = x^{*T} D^T + \eta^T F^T \quad (32)$$

and

$$x^{*T} \dot{x}^{*} = x^{*T} x^{*T} D^T + x^{*T} \eta^T F^T \quad (33)$$

$$E[x^{*T} \dot{x}^{*}] = E[x^{*T} x^{*}] D^T + E[x^{*T} \eta^T] F^T \quad (34)$$

It can be shown with fundamental stochastic analysis that, for a linear system driven by unit white noise, as Eq. (8), the correlation between x^* and η is ¹³

$$E[\eta x^{*T}] = F^T / 2 \quad (35)$$

and

$$E[x^{*T} \eta^T] = F / 2 \quad (36)$$

Thus,

$$E[\dot{x}^{*T} \dot{x}^{*}] = E[x^{*T} \dot{x}^{*}] + DE[x^{*T} x^{*}] + E[x^{*T} x^{*}] D^T + FF^T \quad (37)$$

For statistically time stationary (constant rms value) systems,

$$(d/dt)E[x^{*T} x^{*}] = 0 = E[\dot{x}^{*T} \dot{x}^{*}] + E[x^{*T} \dot{x}^{*}] \quad (38)$$

This is true in the present case as $t \rightarrow \infty$, if the system in Eq. (8) is stable. Thus, Eq. (37) becomes the algebraic matrix-Riccati equation

$$DE[x^{*T} x^{*}] + E[x^{*T} x^{*}] D^T + FF^T = 0 \quad (39)$$

Given D and F , Eq. (39) has a unique solution for the elements of the symmetric covariance matrix, which then can be used in the evaluation of Eq. (30). Equation (39) usually must be solved numerically, and various computer algorithms exist for doing so. One method, with fast convergence on aircraft ride quality problems, is described in Ref. 14.

STABILIZATION CONTROL POWER

The pitch, yaw and roll minimum safe levels of control power (angular accelerations) needed to stabilize the aircraft in homogeneous turbulence of known intensities can be expressed as

$$CP_{pitch} = 3\sigma_{\delta_e}^2 (\delta_{e_{RMS}})^2 \quad (40)$$

$$CP_{yaw} = 3\sigma_{\delta_r}^2 (\delta_{r_{RMS}})^2 \quad (41)$$

$$CP_{roll} = 3\sigma_{\delta_a}^2 (\delta_{a_{RMS}})^2 \quad (42)$$

These "three-sigma" values mean that an instantaneous value of control power about any axis would exceed these values only 0.27 percent of the time. This is considered safe in that it is only an instantaneous value which would pass in fractions of seconds in a worse case scenario.

The RMS (root mean square) values of equivalent elevator, rudder and aileron control deflections in Eqs. (40), (41) and (42) can be determined as follows:

$$u = \begin{bmatrix} \delta_e \\ \delta_r \\ \delta_a \end{bmatrix} \quad (43)$$

$$E\{uu^T\} = E \begin{bmatrix} \delta_e^2 & \delta_e \delta_r & \delta_e \delta_a \\ \delta_r \delta_e & \delta_r^2 & \delta_r \delta_a \\ \delta_a \delta_e & \delta_a \delta_r & \delta_a^2 \end{bmatrix} \quad (44)$$

$$\delta_{e_{RMS}} = [E(\delta_e^2)]^{1/2} \quad (45)$$

$$\delta_{r_{RMS}} = [E(\delta_r^2)]^{1/2} \quad (46)$$

$$\delta_{a_{RMS}} = [E(\delta_a^2)]^{1/2} \quad (47)$$

The elements of Eq. (44) and, thus, Eqs. (45)-(47) can be obtained from the control law given by

$$u = -Kx \quad (48)$$

$$\{uu^T\} = [-Kx][x^T] \quad (49)$$

or

$$\{uu^T\} = Kxx^TK = K[xx^T]K^T \quad (50)$$

$$\text{and } E\{uu^T\} = KE[xx^T]K^T \quad (51)$$

$E[xx^T]$ in Eq. (51) can be obtained from the covariance matrix $E[x^*x^{*T}]$, which is the solution of Eq. (39), as the upper left partition matrix in $E[x^*x^{*T}]$.

$$E[x^*x^{*T}] = \begin{bmatrix} E[xx^T] & E[x\eta^T] \\ E[\eta x^T] & E[\eta\eta^T] \end{bmatrix} \quad (52)$$

The elevator is the primary control for augmenting the longitudinal dynamics and placement of the roots of Eq. (19). The rudder is the primary control for implementing a yaw damper function and placement of the lateral-directional dynamics desired roots of Eq. (19). The method of scalar control and exact pole placement can be applied separately to both perturbation equations of motion, with the usual assumptions that uncouple the two sets of equations. The matrix of gains K in Eqs. (48) and (51) would be a $(2 \times n)$ matrix when δ_e and δ_r are the SAS controls used. Each row of K comes from Eq. (22) for the two sets of dynamics.

STRUCTURAL ELASTIC MODE SUPPRESSION

For aircraft where the elastic mode terms dominate the normal accelerations in Eqs. (25) and (26), a structural mode control system may be needed to provide acceptable ride quality. The USAF B-1 has such a system.¹⁶

By locating the accelerations which sense the motion at the same location as the aerodynamic force used to suppress the structure motion, phase margin can be assured for stable operation under reasonable parameter variations.¹⁷ Eigenspace assignment methods can also be used to design such systems.¹⁸ Care must be taken, however, to not adversely affect the aircraft handling qualities and to ensure a fail-safe system.

CONCLUDING REMARKS

The design method presented to account for atmospheric turbulence in minimizing control power requirements and achieving specified closed loop roots is simple to use and requires very little, if any, trial-and-error to arrive at a suitable design. A compatible ride quality analysis can be accomplished within the framework presented.

REFERENCES

1. Anon, "Flying Qualities of Piloted Vehicles", MIL-STD-1797, Wright-Patterson AFB, OH, Mar. 31, 1957.
2. Anon, "Military Specification, Flying Qualities of Piloted V/STOL Aircraft," MIL-F-33300, Wright-Patterson AFB, OH, Dec. 31, 1970.
3. Cooper, G. E. and Harper, R. P., Jr., "The Use of Pilot Rating in the Evaluation of Aircraft Handling Qualities," NASA TN D-3153, Ames Research Center, Moffett Field, CA, Apr. 1969.
4. Etkin, B., "The Turbulent Wind and Its Effect on Flight, UTIAS Review No. 44, University of Toronto Institute for Aerospace Studies, Aug. 1980.
5. Etkin, B., "A Theory of the Response of Airplanes to Random Atmospheric Turbulence," Journal of the Aero/Space Sciences, Vol. 26, No. 7, 1969, pp. 409-420.
6. Eggleston, J. H. and Phillips, W. H., "The Lateral Response of Airplanes to Random Atmospheric Turbulence," NASA TR R-74, National Aeronautics and Space Administration, 1960.
7. Houbolt, J. C., Steiner, R. and Pratt, K. G., "Dynamic Response of Airplanes to Atmospheric Turbulence Including Flight Data on Input and Response," NASA TR R-199, National Aeronautics and Space Administration, June 1964.
8. Swaim, R. L. and Connors, A. J., "Gust Velocity Spatial Distribution Effects on Lateral-Directional Response of VTOL Aircraft," Journal of Aircraft, Vol. 5, No. 1, January-February 1968, pp. 53-59.
9. Gogonsa, O. R. and Moriarty, T. E., "The Response of a Hovering V/STOL Aircraft to Discrete Turbulence," CCC/EE/67-7, Air Force Institute of Technology, Wright-Patterson Air Force Base, OH.
10. Swaim, R. L., "Minimum Control Power for VTOL Aircraft Stability Augmentation," Journal of Aircraft, Vol. 7, No. 3, May-June 1970, pp. 231-235.
11. Perkins, W. R. and Craig, J. B., Jr., Engineering of Dynamic Systems, Wiley, N. Y., 1969, pp. 421-431.
12. Roberts, P. A., Swaim, R. L. and Schmidt, D. K., "Relationships Between Augmented Handling Qualities and Ride Qualities for Flexible Aircraft," Proceedings of the Twelfth Annual Conference on Manual Control, May 25-27, 1976, University of Illinois at Urbana-Champaign.
13. Swaim, R. L., et al., "An Analytical Method for Ride Quality of Flexible Airplanes," AIAA Journal, Vol. 15, No. 1, January 1976, pp. 4-7.
14. Bryson, A. E., Jr. and Ho, Y. C., Applied Optimal Control, Wiley, N. Y., 1975, pp. 328-334.
15. Gelb, A. (ed.), Applied Optimal Estimation, The M.I.T. Press, Cambridge, MA, 1974, pp. 136-138.
16. Wykes, J. H., Mori, A. S. and Borland, C. J., "B-1 Structural Mode Control System," AIAA Paper 72-772, Stanford, CA, August 1972.
17. Wykes, J. H., "Structural Dynamic Stability Augmentation and Gust Alleviation of Flexible Aircraft," AIAA Paper 68-1057, Philadelphia, PA, October 1968.
18. Schmidt, D. K. and Davidson, J. B., "Flight Control Law Synthesis for an Elastic Vehicle by Eigenspace Assignment," AIAA Paper 65-1898, Snowmass, CO, August 1965.

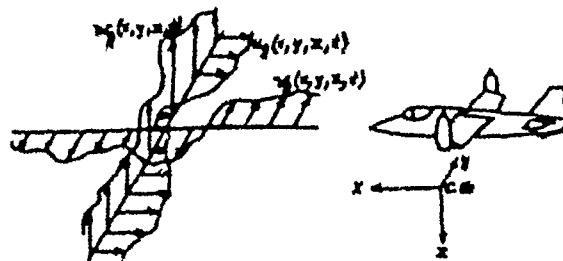


FIGURE 1. Turbulence Components

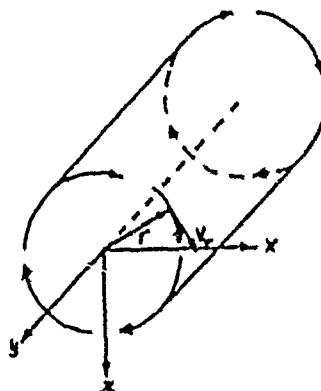


FIGURE 2. Vortex Model

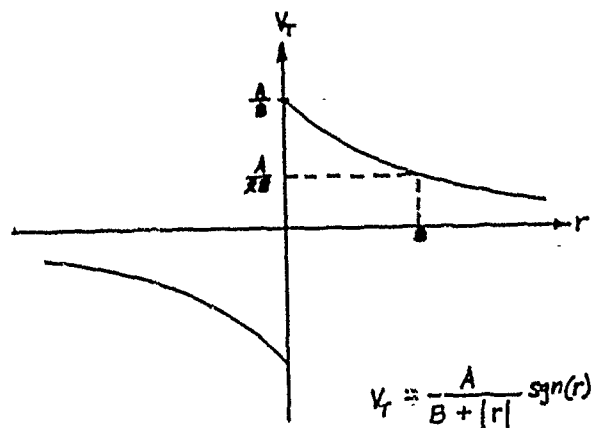


FIGURE 3. Vortex Velocity Profile

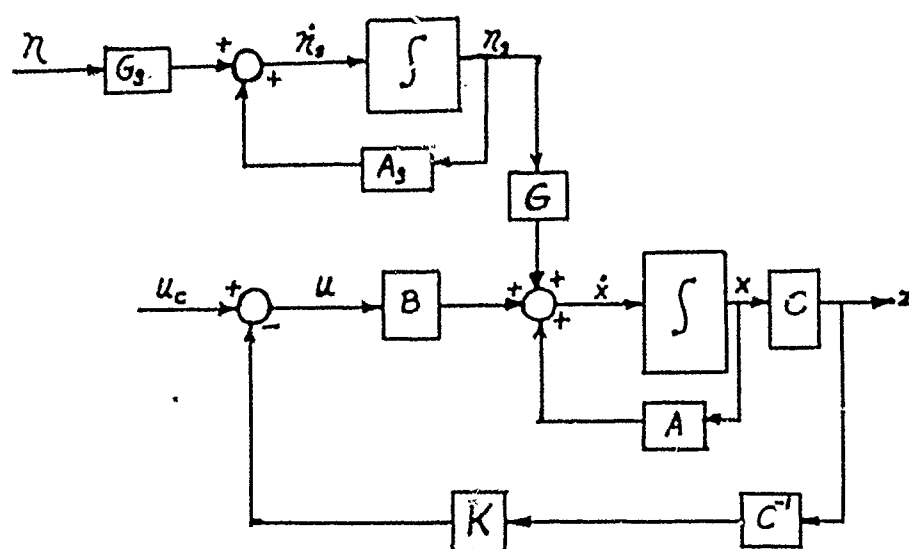


FIG. 4 SAS DIAGRAM

ACTIVE CONTROL SYSTEM FOR GUST LOAD ALLEVIATION AND STRUCTURAL DAMPING

by
Hartmut Böhrer Dr. Joachim Winter
Dornier-Luftfahrt GmbH, BN 40
Postfach 13 03
D-7990 Friedrichshafen 1
FRG

SUMMARY

Based on the Do 328 regional airliner, the improvement in passenger comfort provided by the gust load alleviation system OLGA under adverse weather conditions is shown. The problem of excited structural vibrations is solved with an active structural damper, which eliminates the adverse effect of the gust load alleviation system on structural vibrations and, additionally, diminishes their excitation by maneuvers and gust loads.

ABBREVIATIONS

OLGA Open Loop Gust Alleviation
RDI ride discomfort index
SD active structural damper
TNT Tragflügel Neuer Technologie (Advanced Technology Wing)

NOMENCLATURE

A system matrix
A(f) frequency response
 α angle-of-attack
B input matrix
C output matrix
F feed-forward gain matrix (OLGA)
f frequency [Hz]
K feedback gain matrix (SD)
L coupling matrix (structural dynamics/rigid aircraft)
n load factor
R disturbance matrix (gusts)
u input vector
v noise input vector
w noise state vector
x state vector
y output vector
z vertical displacement

1. INTRODUCTION

For regional airliners and general aviation aircraft, flying under adverse weather conditions has a dimensioning influence on the structure and is a significant measure of passenger comfort. Further improvements to the economy and flight performance of future aircraft designs constitute exacting requirements to aircraft configuration and, in particular, structural weight parameters. Structures become increasingly elastic. Commuter aircraft featuring modern wings of high aerodynamic efficiency are sensitive to gusts which is inconsistent with the also requested improvements in ride quality. Additionally, on account of excited elastic modes of wing and fuselage the problem has spread to a higher frequency range.

The degree of ride quality achieved by means of a system to improve the passenger comfort is indicated by the so-called ride discomfort index (RDI) [1]. This index is based on the 'von Karman' gust power density spectrum. The acceleration reactions of an aircraft to this gust excitation are weighted and added according to frequency. In Fig. 1, the weighting factors of vertical acceleration values are shown.

Studies have shown that the passengers' susceptibility to airsickness does not only depend on the intensity of gusts, but to a high measure also on gust frequency. In Fig. 1, this fact has been taken into consideration by the high weighting in the frequency range between 0.1 Hz and 0.3 Hz. Unfortunately, there is also a maximum for the vertical acceleration intensity caused by gusts in this frequency range, since the eigenfrequency of short period motion varies between 0.3 Hz and 0.6 Hz, depending on flight altitude and speed.

Medical studies have revealed that the eigenfrequency of the fundamental mode of man's vertebral column is approximately at 6 Hz. Therefore the frequency range from 4 Hz to 8 Hz has been weighted higher in the diagram. Unfortunately the eigenfrequency of the first wing bending mode generally is within this range.

The aim is to reduce vertical accelerations for the two heavily weighted frequency

ranges by means of control measures. The gust alleviation system OLGA will be employed for the low frequency range of up to 2 Hz and an active structural damper for the frequency range above 2 Hz.

This paper provides a brief description of the OLGA system and the achieved flight test results and a more detailed description of the system extended by an active structural damper.

The design goal for the overall system is to combine the advantages provided by the OLGA system (based on a rigid-body model) with those of the structural damper (based on an elastic model).

2. GUST LOAD ALLEVIATION SYSTEM OLGA

There are two gust load alleviation principles:

- Open Loop Gust Load Alleviation (OLGA)
- Closed Loop Gust Load Alleviation

With the "open loop" principle, which is primarily considered in this paper, the time history of gusts (gust angle-of-attack) must be calculated directly from the sensor signals. Depending on this gust angle, the lift-changing control surfaces must be deflected so as to compensate for the lift-changing effect of gusts (Direct Lift Control, DLC). The advantage of this principle is that handling qualities remain unchanged while the disadvantage is its complexity and, by this, limited accuracy of gust angle calculation.

With the "closed loop" principle, not the gusts are measured but rather the aircraft response to gusts. The sensor signals deflect the control surfaces to minimize this response. The advantage of this principle is that the gust angle is not calculated while the disadvantage is that this system changes aircraft handling qualities. With this system, the aircraft responds more sluggishly to flight path changes initiated by the pilot.

Fig. 2 depicts the functional structure in line with the following design philosophy (2, 3):

- Calculation of the gust angle-of-attack from the sensor signals (angle-of-attack, pitch attitude, flight path angle)
- Symmetrical aileron deflection to compensate for the changed lift produced by gusts
- Simultaneous deflection of the elevator to compensate for the pitching moment of the symmetrical ailerons
- Delayed deflection of the elevator to compensate for changed lift on the horizontal tail produced by gusts.

Excellent results with respect to systems efficiency were expected on account of the extensive investigations in systems theory and wind tunnel tests. The results, however, also revealed the limits of real systems (measuring accuracy, delays, limited deflection speed).

The expected efficiency of the OLGA system was tested by simulation runs in the wind tunnel and by numerical simulation of the rigid aircraft model including hardware-in-the-loop (actuators, sensors). The reduction in vertical acceleration above the frequency range produced by gusts is used as evaluation criterion. For the simulation runs, the time history of gusts was determined by the so-called Dryden spectrum in flight direction, which defines gust intensity as a function of frequency and, by this, simulates to a satisfactory degree of accuracy the natural conditions. As the stochastic behaviour of gusts could be reproduced accurately, a cost-effective optimization of the system parameters was possible. The simulation runs showed the effects of non-linearities, but not of the elastic modes of wing and fuselage, because of the rigid aircraft model.

The first flight test showed an excitation of the first wing bending mode at 5.7 Hz and a relatively slight gust load alleviation in the low frequency range. Fig. 3 depicts the power density spectrum of vertical acceleration in this flight with the OLGA system switched on and off. The clearly visible excitation of structural vibration at approximately 7 dB was provoked by the phase shifting between the gust signal and the OLGA aileron deflection. In the eigenfrequency range of the first wing bending mode it achieved 180°.

Flight testing has also shown that, by reducing vertical accelerations in the low frequency range of up to 2 Hz, the passengers' susceptibility to airsickness in the frequency range between 4 and 8 Hz seems to be increased, since the latter range now represents a dominant portion of the frequency spectrum.

To solve this problem, technical equipment modifications (reduction of phase shift, notch filters) had to be performed.

Flight testing of this new configuration revealed a marked improvement in system performance. Fig. 4 shows the vertical acceleration spectrum after modification in one of the flights and demonstrates:

- satisfactory gust load alleviation in the low frequency range by approximately 10 dB
- negligible excitation of structural vibrations in the 3-4 Hz frequency range
- passive system behaviour in the higher frequency range.

The description of the OLCA development status has shown that the frequency range including the first bending mode of wing and fuselage, must be taken into account, in order to improve passenger comfort. This means that the frequency range between 0.1 Hz and 15 Hz must be considered. To attain this goal, a structural vibration damper must be designed in addition to the gust load alleviation system. For this purpose, the dynamics of the elastic aircraft must be modelled.

2. MATHEMATICAL MODEL OF AN ELASTIC AIRCRAFT

The dynamics of an elastic aircraft is being described at first in two steps based on Duncan's 'semi-rigid method'.

In a first step, the aircraft is considered as a rigid body with its mass concentrated in the centre of gravity. The centre of gravity moves on the flight path. At an arbitrary point of the flight path, the so-called steady state, the equations of motion of minor deflections of the rigid aircraft related to the stability axes can be indicated in linear form.

In a second step, the structural vibrations of the elastic degrees of freedom of the airframe are described in the form of aircraft-fixed coordinates.

Via the unsteady aerodynamic forces, the rigid aircraft model is then coupled with the structural model.

3.1 Rigid Aircraft Model

The rigid aircraft model is generated for the longitudinal motion of the Do 228 aircraft. In this case, the frequency spacing between the short period motion ($f_{sp} = 0.3$ Hz) and the phugoid mode ($f_{ph} = 0.01$ Hz) is so big that, by approximation, both motions can be considered as decoupled. As the static longitudinal stability is determined by the airframe design and the frequency spacing is very big between phugoid and structure bending modes ($f_{ph} = 3$ Hz, $f_{ph} = 12$ Hz), the phugoid motion can be neglected.

The subsystem characterized by the short period motion is described by

$$\dot{x}_R = A_R x_R + B_R u_R \quad (1)$$

with the state vector $x_R^T = (\alpha, q)$ in state representation.

3.2 Structural Vibration Model

The mathematical model for structural vibrations of the airframe is generated in aircraft-fixed coordinates for the position on the flight path which is described by the equations of motion of the rigid aircraft.

The aircraft structure, which moves freely in the airspace, is studied now. Its equations of motion are based on the following assumptions:

- Compared with the dimensions and motion of the rigid aircraft, elastic deformation is small, and MOORE's law is applicable. Then, the elastomechanical behaviour can be described by means of linear equations.
- The assumed structural weight is invariant (fuel consumption, for instance, is not considered).
- The elastic structure with an infinite number of degrees of freedom is replaced by a system with a limited number of degrees of freedom.

The model of the elastic degrees of freedom is generated by means of the dumbbell model approach by discretizing the airframe into five masses (Fig. 5). The resulting submodels of wing and fuselage comprise the rigid body motion 'heave' and the first (symmetrical) and second (asymmetrical) natural bending modes.

As the rigid-motion has already been described by the rigid-aircraft model, it must be eliminated from the structural model. The elimination of the rigid-body motion leads to static vibration equations which are used for the studies of dynamic response by structural mechanics. Wing and fuselage vibration frequencies are known from static vibration tests conducted on Do 228 aircraft. In the frequency range of up to 15 Hz, which is of interest here, the first bending modes of wing ($f_{w1} = 3.4$ Hz) and fuselage ($f_{f1} = 12$ Hz) have been identified as a major influencing factor. Therefore, the structural model can also be reduced by the other vibration modes included.

For this purpose, the following proceeding was devised:

- 1st step: Calculation of the eigenvalue problem for the undamped submodels
- 2nd step: Order reduction of submodels
- 3rd step: Superimposition of submodels
- 4th step: Elimination of the rigid-body motion 'heave'.

For the two submodels the calculations of step 1 provide the natural modes and assign them definitely to the eigenfrequencies. As a structural dynamics model is required which correctly reproduces the first bending modes of wing and fuselage, it is important to

preserve their eigenfrequencies despite the reduction.

In step 2 this requirement is fulfilled by an order reduction which corresponds to an incomplete modal transformation. Conditional equations for the required coordinate transformations can be determined from the orthogonality relations of the eigenvectors by means of the diagonal mass matrix of mechanical systems. The reduction by the 2nd bending mode for the individual submodel can be performed in this step.

The rigid body motion can only be eliminated in step 4 for the model superimposed in step 3, since it is this coordinate transformation that couples wing and fuselage motion.

The structural model reduced to the coordinates of wing mass m_W and tail mass m_T and with the state vector $x_E = (z_W \dot{z}_W z_T \dot{z}_T)$ in state representation is:

$$\begin{bmatrix} \dot{x}_W \\ \dot{x}_E \end{bmatrix} = \begin{bmatrix} 0 & I \\ A_{E21} & A_{E22} \end{bmatrix} \begin{bmatrix} x_W \\ x_E \end{bmatrix} + \begin{bmatrix} 0 \\ B_E \end{bmatrix} u \quad (2)$$

3.2 Model of Unsteady Aerodynamic Forces

Vibrations of the wing are excited by unsteady aerodynamic forces (e.g. caused by gusts). They are classified as a self-excited, non-linear, dynamic oscillator. As the air flow supplies the energy, special, flow self-excited oscillations are induced.

Incident flow is considered as constant. Lift changes, therefore, depend on the lift coefficient which, in turn, primarily depends on the angle-of-attack. With the rigid aircraft, the time-variant angle-of-attack is assumed to be constant over the complete wing. This does not apply to a vibrating wing as a result of the deformation. In the latter case, the angle-of-attack or directly the pressure distribution must be considered as time-variant and dependent on location.

As regards the test aircraft Do 323, a method must be chosen for the calculation of the unsteady aerodynamic forces in the subsonic range which describes the behaviour of the aerodynamic forces with a satisfactory measure of accuracy and comparatively low calculation efforts. The easiest way is to assume quasi-stationary aerodynamic forces. The equations of motion are then linear.

As the discrete masses of the wing move independently, only the masses moved down at a certain moment generate additional lift, while the others decrease lift. This is recorded by means of superimposition in the changing overall angle-of-attack which is distributed according to mass discretization.

The rigid aircraft model is then superimposed with the reduced-structural model. On account of the additionally recorded vertical acceleration of the wing, the structural dynamics is coupled to the rigid-aircraft model via the changing overall angle-of-attack, and is coupled vice versa via the unsteady aerodynamic forces.

Any transformation related to the wing model must, therefore, also be applied to the aerodynamic model.

The resulting model (including additive noises) represents stable dynamics:

$$\begin{bmatrix} \dot{x}_R \\ \dot{x}_W \\ \dot{x}_E \end{bmatrix} = \begin{bmatrix} A_R & 0 & L_{R0} \\ 0 & 0 & I \\ L_{ER} & A_{E21} & A_{E22} \end{bmatrix} \begin{bmatrix} x_R \\ x_W \\ x_E \end{bmatrix} + \begin{bmatrix} B_R \\ 0 \\ B_E \end{bmatrix} u + \begin{bmatrix} R_{RD} \\ 0 \\ R_{ED} \end{bmatrix} v$$

$$\begin{bmatrix} \dot{x}_R \\ \dot{x}_E \end{bmatrix} = \begin{bmatrix} A_R & L_{RE} \\ L_{ER} & A_E \end{bmatrix} \begin{bmatrix} x_R \\ x_E \end{bmatrix} + \begin{bmatrix} B_R \\ B_E \end{bmatrix} u + \begin{bmatrix} R_{RD} \\ R_{ED} \end{bmatrix} v \quad (3)$$

3.4 Elastic Aircraft Simulation

Linear simulation is intended to verify whether the mathematical model approximates the vertical acceleration spectra (Fig. 3 OLGA OFF) recorded in flight testing with a satisfactory measure of accuracy.

In hardware-in-the-loop simulation, vertical excitation gusts were determined by the mathematically easier Dryden spectrum in flight direction, as there is only a minor difference between the two spectra. As a power density spectrum can be generated by many mathematical subfunctions, it is sufficient for technical applications to have the same power density spectrum for original and simulation functions. The simulation function is generated by a first-order time-lag filter from the Gauss-distributed random numbers (white noise).

Given the noise quantity $w = a_G$ and the noise input $v = a_{G0}$ the following noise model in state representation results:

$$\dot{v} = \bar{A}_D v + \bar{B}_D u \quad (4)$$

The following result is provided from (3) for the overall system:

$$\begin{bmatrix} \dot{x}_R \\ \dot{v} \\ \dot{x}_E \end{bmatrix} = \begin{bmatrix} A_R & R_{RD} & L_{RE} \\ 0 & \bar{A}_D & 0 \\ L_{ER} & R_{ED} & A_E \end{bmatrix} \begin{bmatrix} x_R \\ v \\ x_E \end{bmatrix} + \begin{bmatrix} B_R & 0 \\ 0 & \bar{B}_D \\ B_E & 0 \end{bmatrix} \begin{bmatrix} u \\ v \end{bmatrix} \quad (5)$$

The calculated frequency response $A(f) = \bar{n}_2(f)/\bar{u}_D(f)$ is depicted in Fig. 5. In consideration of the heavily reduced model and the location of the vertical accelerometer which was 1.50 m aft of the centre of gravity in the test aircraft, a comparison between measured and calculated power density spectra (Fig. 3) revealed satisfactory agreement.

The OLGA feed-forward control

$$u = u_{AD} = F_D v \quad (6)$$

is determined from the steady state requirements of the rigid aircraft from $R_{RD} + C_R F_D = 0$.

In consideration of the electromechanical actuators ($f_{AD} = 5$ Hz) for the symmetrical ailerons δ_a and the elevator η used in the flight testing by means of the dynamics of a second-order time-lag element

$$\dot{x}_{AD} = A_{AD} x_{AD} + B_{AD} u_{AD} \quad (7)$$

$$y_{AD} = C_{AD} x_{AD}$$

(5) together with the coupling $u = x_{AD}$ yields:

$$\begin{bmatrix} \dot{x}_R \\ \dot{v} \\ \dot{x}_E \\ \dot{x}_{AD} \end{bmatrix} = \begin{bmatrix} A_R & R_{RD} & L_{RE} & B_R C_{AD} \\ 0 & \bar{A}_D & 0 & 0 \\ L_{ER} & R_{ED} & A_E & B_E C_{AD} \\ 0 & B_{AD} F_D & 0 & A_{AD} \end{bmatrix} \begin{bmatrix} x_R \\ v \\ x_E \\ x_{AD} \end{bmatrix} + \begin{bmatrix} 0 \\ B_D \\ 0 \\ 0 \end{bmatrix} v \quad (8)$$

A closer look at the system matrix in (8) explains the flight test results according to which the OLGA system has first excited the aircraft structure. The inevitable effect of the OLGA feed-forward control on the structural dynamics corresponds to a positive feedback, which becomes apparent only above the frequency of 2 Hz, because the eigenfrequencies of the structural dynamics are in this order of magnitude.

A comparison between the calculated frequency response $A(f)$ (Fig. 7) and the corresponding results from the first flight test (Fig. 3) clearly shows the explained coupling effect between the OLGA gust alleviation system designed for the rigid aircraft and the elastic aircraft structure.

The calculated frequency responses confirm that the mathematical model reproduces the effects to be investigated to a satisfactory degree of accuracy.

4. DESIGN OF THE ACTIVE STRUCTURAL DAMPER

Gust-excited structural vibrations shall be suppressed by an active vibration damper in the range of the eigenfrequencies of the first bending modes of wing and fuselage. The frequency response $A(j\omega)$ of the load factor of the central mass is again selected as a measure for the vibration intensity. The passenger comfort can be measured directly by this load factor response. The control target thus consists in reducing the amplitudes of this frequency response within the range from 2 Hz to 15 Hz.

In order to minimize the technical means it is intended to make use of control surfaces that exist already on the aircraft as far as this is possible. With a view to integrating the OLGA system, symmetrical ailerons and an elevator are planned for the Do 14.8. Since these control surfaces are decoupled as far as the actuator influence on the structural vibrations is concerned the vertical speeds of wing and tail mass can be fed back to the associated control surface. Both controller states can be measured with accelerometers, which are the most suitable sensors for this purpose.

The control law to be calculated reads:

$$u = u_{AE} = -K_0 y_E - K_0 C_E x_E \quad (9)$$

with the output feedback matrix

$$K_0 = \begin{bmatrix} k_{11} & 0 \\ 0 & k_{11} \end{bmatrix}$$

and the measuring matrix $C_E = \begin{bmatrix} 0 & 1 \end{bmatrix}$.

In order that the control parameters can be optimized directly towards the target mentioned above the deviation of the frequency response $A(j\omega)$ from a given, optimal frequency response $A_{opt}(j\omega)$ is minimized in the form of a penalty function.

Another penalty function of the eigenfrequency deviations between controlled and uncontrolled system is to avoid that the algorithm makes the eigenvalues move towards infinity. However, the calculation has to be carried out in conjunction with the overall mathematical model for the aircraft (5). In principle, all dynamical portions which may occur (e.g. actuators) can be taken into account that way. The frequency response values are computed directly from the state representation.

The dynamics of the structural damper actuators compared to the aircraft movement cannot be neglected since the eigenfrequencies are within the model frequency range. In principle, there are two possibilities of solving the problem:

- Application of quicker actuators.
- Suitable signal feedback via the actuator.

The effect of the actuator dynamics on the presented control concept has to be verified in any case. For this purpose, the dynamics of the actuators is expressed as second-order time-lag elements

$$\dot{x}_{AE} = A_{AE} x_{AE} + B_{AE} u_{AE} \quad (10)$$

$$y_{AE} = C_{AE} x_{AE}$$

Inclusion of the coupling $u = y_{AE}$ results in the model

$$\begin{bmatrix} \dot{x}_R \\ \dot{v} \\ \dot{x}_E \\ \dot{x}_{AE} \end{bmatrix} = \begin{bmatrix} A_R & R_{RD} & L_{RE} & B_R C_{AE} \\ 0 & R_D & 0 & 0 \\ L_{ER} & R_{ED} & A_E & B_E C_{AE} \\ 0 & 0 & -B_{AE} K_0 C_E & A_{AE} \end{bmatrix} \begin{bmatrix} x_R \\ v \\ x_E \\ x_{AE} \end{bmatrix} + \begin{bmatrix} 0 \\ B_D \\ 0 \\ 0 \end{bmatrix} v \quad (11)$$

For the preliminary assumed actuators with a proportional behaviour (Fig. 8) the amplitude reduction for the eigenfrequency of the first bending mode is 7.6 dB on the wing at 5.4 Hz and 7.5 dB on the fuselage at 12 Hz. This corresponds to a reduction of the load factor to less than half the value, but has to be paid with a small amplitude rise in the frequency range from 6 Hz to 8 Hz.

Investigations showed that consideration of the actuator dynamics greatly influences the results. It is, for instance, possible to prove by way of the eigenvalues that the use of actuators with a cut-off frequency of less than 10 Hz results in unstable dynamic characteristics. The physical reason for this phenomenon is the higher first bending mode of the fuselage ($f_y = 12$ Hz).

In case actuators with an eigenfrequency of 30 Hz are available, the amplitude of the fuselage eigenfrequency can be diminished by ≈ 5 dB according to Fig. 8.

With a structural damper, a slight amplitude reduction of approximately 2 dB is additionally achieved in the frequency range below 2 Hz.

This represents an important improvement with regard to the acceleration weighting (Fig. 1).

5. COMBINATION OF GUST LOAD ALLEVIATION AND STRUCTURAL DAMPING

On account of the results, obtained with the OLGA gust alleviation system in the frequency range from 0.1 Hz to 2 Hz and with the active structural damper in the frequency range from 2 Hz to 15 Hz, a combination of both methods is aimed at, which offers both advantages.

Based on the state equations (8) and (11) the dynamics of the complete system can be expressed as follows (Fig. 9):

$$\begin{bmatrix} \dot{x}_R \\ \dot{v} \\ \dot{x}_E \\ \dot{x}_{AD} \\ \dot{x}_{AE} \end{bmatrix} = \begin{bmatrix} A_R & R_{RD} & L_{RE} & B_R C_{AD} & B_R C_{AE} \\ 0 & R_D & 0 & 0 & 0 \\ L_{ER} & R_{ED} & A_E & B_E C_{AD} & B_E C_{AE} \\ 0 & B_{AD} F_D & 0 & A_{AD} & 0 \\ 0 & 0 & -B_{AE} K_0 C_E & 0 & A_{AE} \end{bmatrix} \begin{bmatrix} x_R \\ v \\ x_E \\ x_{AD} \\ x_{AE} \end{bmatrix} + \begin{bmatrix} 0 \\ B_D \\ 0 \\ 0 \\ 0 \end{bmatrix} v \quad (12)$$

Since the feed-forward control of OLGA (6) excites the elastic dynamics of the airframe (2), and, in turn, the structural damper (9) does not take the OLGA feed-forward control into account, simple addition of both systems does not lead to the desired result.

On the contrary, experience showed that a two-stage optimization strategy - neglecting the actuator dynamics - is the right way. Here, the

- first step is represented by the optimization of the feed-forward control without the structural damper, while the
- second step consists in the optimization of the structural damper with the feed-forward control being fixed.

Fig. 10 gives the resulting frequency response $A(f)$ for the assumption that symmetrical ailerons and an elevator are available as control surfaces for the OLGA system and the active structural damper. The feedback signals which actively influence the structural vibrations are mixed with those of the feed-forward controller of the OLGA system. In the frequency range between 0.1 Hz and 2 Hz, the control concept results in an amplitude reduction between about 5 dB and 15 dB (refer to paragraph 2, Fig. 4). With regard to the eigenfrequency of wing and fuselage, the frequency response is reduced by 7.5 dB. As far as the load factor is concerned, this corresponds to a reduction of between 40 % and 80 % for frequencies below 2 Hz, and up to 60 % above this frequency.

The first bending modes are completely eliminated. In the frequency range above 15 Hz, which has not yet been included in the mathematical model, the amplitude peak increases depending on the actuator frequency of the structural damper and due to the feedback gain (see Fig. 8). Every increase in actuator frequency by 10 Hz entails a reduction of the amplitude peak by 5 dB.

Considerable improvement of these results can be expected, if separate control surfaces can be applied to gust load alleviation and structural damping.

For this purpose, additional trailing edge flaps are used. The control signals of the OLGA feed-forward control are coupled to the trailing edge flaps and the elevator, while the symmetrical ailerons and the elevator remain the control surfaces of the structural damper.

The frequency response (Fig. 11) now shows the expected reduction of the amplitudes in the whole frequency range from 0.1 Hz to 15 Hz. Below 1 Hz, the reduction is almost constant at 15 dB (80 %). With regard to the eigenfrequency on the wing, the frequency response is reduced by 10 dB (70 %), and on the fuselage by 7.5 dB (60 %). The problems of the actuator frequency of the structural damper, however, remain unchanged.

The design goal, which consists in combining the advantages of the OLGA system in the low frequency range with those of the active structural damper in the upper range, is thus achieved.

6. CONCLUSIONS

For regional airliners like the Do 228, bad weather conditions represent a significant measure of passenger comfort. The achieved degree of passenger comfort can be indicated by the ride discomfort index (RDI). For the calculation of this index, aircraft acceleration reaction due to gusts is taken into consideration by applying certain weighting factors which particularly evaluate the passengers' susceptibility to airsickness in the frequency range between 0.1 and 2 Hz, and the fundamental mode of man's vertebral column at frequencies from 4 to 8 Hz.

In the present contribution, a system for ride quality improvement has been presented, consisting of the OLGA gust load alleviation system for the lower frequency range up to 2 Hz, and an active structural damper for the frequency range between 2 and 15 Hz.

The OLGA system was developed applying the open loop principle (open loop gust alleviation); it was subjected to comprehensive simulation runs and flight tests.

Gust alleviation is achieved by direct lift control via the symmetrical ailerons and the elevator whose deflections depend on the time-history of the gust angle-of-attack, calculated in the digital signal processing unit.

The OLGA system improves the passenger comfort clearly by reducing the gust-excited vertical acceleration in the frequency range from 0.1 Hz to 2 Hz.

Another flight test result was the finding that reduction of the vertical accelerations in the frequency range below 2 Hz caused an apparent increase in the sensitivity of the human body at frequencies between 4 Hz and 8 Hz. This problem caused by the excitation of structural vibrations were solved with the design of an active structural damper.

To keep the order of the required mathematical model low the model of the elastic degrees of freedom was reduced to the first bending modes of wing and fuselage. The unsteady aerodynamic characteristics were greatly simplified and assumed to be quasi-stationary. Accelerometers were used as sensors in the wing and tail. The control signals of the active structural damper were mixed with the OLGA control signals.

The simulation showed that the frequency response of the model corresponds well with the response measured during the Do 128 TNT test flights and that the effect of the first bending modes of wing and fuselage can be suppressed completely. These prerequisites include the availability of highly efficient actuators with a high eigenfrequency (> 20 Hz), but with low amplitudes.

A further considerable improvement of the passenger comfort could be reached in the whole frequency range from 0.1 Hz to 15 Hz by using trailing edge flaps as additional control surfaces.

REFERENCES

- [1] J.L. Townsend, K.T. Raymond
Background Information and User's Guide for MIL-F-9490
Rep. No. AFFDL-TX-74-116, 1975
- [2] B. Krag, D. Rohlf, H. Wünnenberg
OLGA, a Gust Alleviation System for Improvement of Passenger Comfort of General Aviation Aircraft
ICAS Proceedings, 1980
- [3] N. Böhrer, B. Krag, J. Skudridakis
OLGA - an Open Loop Gust Alleviation System
AGARD, Conference Proceedings No. 384, Toronto, 1984, paper 13
- [4] W. Alles, N. Böhrer, H. Wünnenberg
Integrated Control Technology for Computer Aircraft Experimental Results and Future Potential
ICAS Proceedings Vol. 1, Jerusalem, 1988, pp. 178 - 183

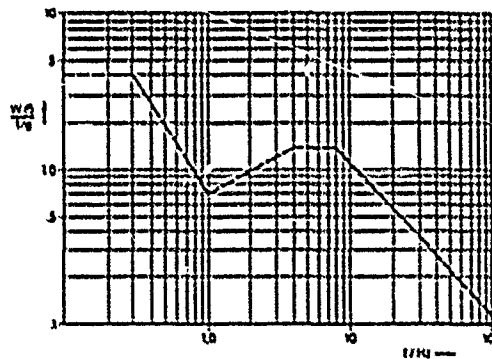


Fig. 1: Acceleration Weighting of the Vertical Vibration MIL-F-9490D (USAF) [1]

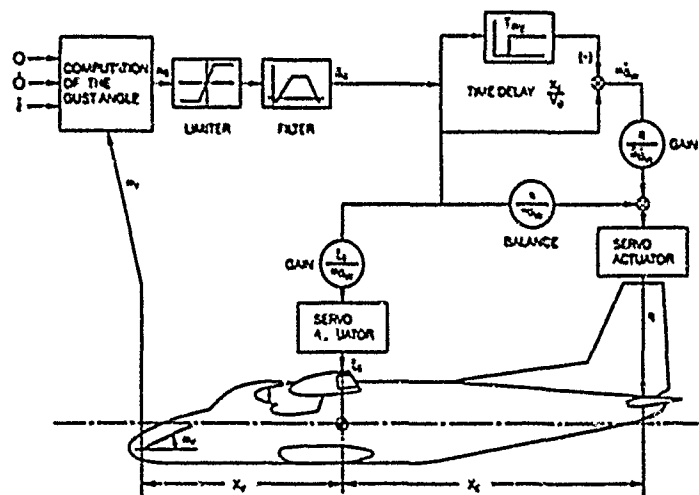


Fig. 2: Functional Diagram of the Gust Alleviation System OLGA

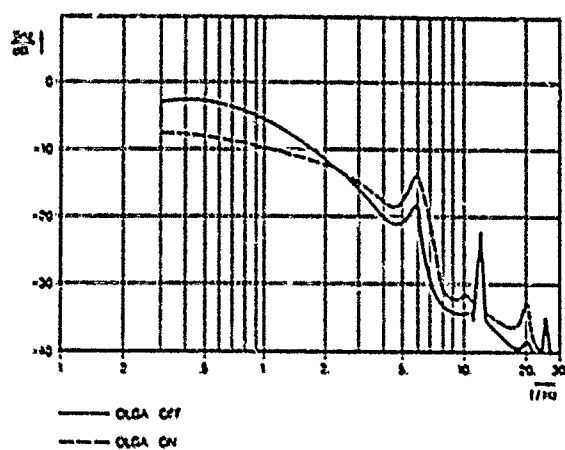


Fig. 3: Spectrum of the Vertical Acceleration (First Flight Test)

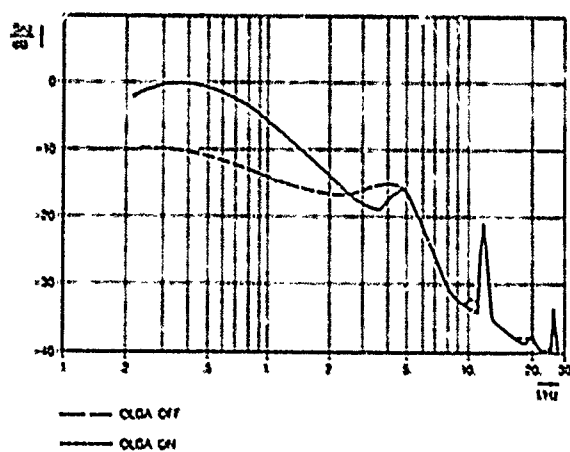


Fig. 4: Spectrum of the Vertical Acceleration (Final Flight Test)

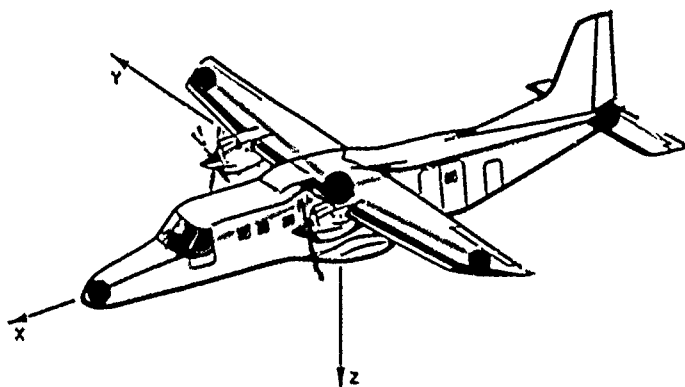


Fig. 5: 5-Masses-Model of the Elastic Aircraft

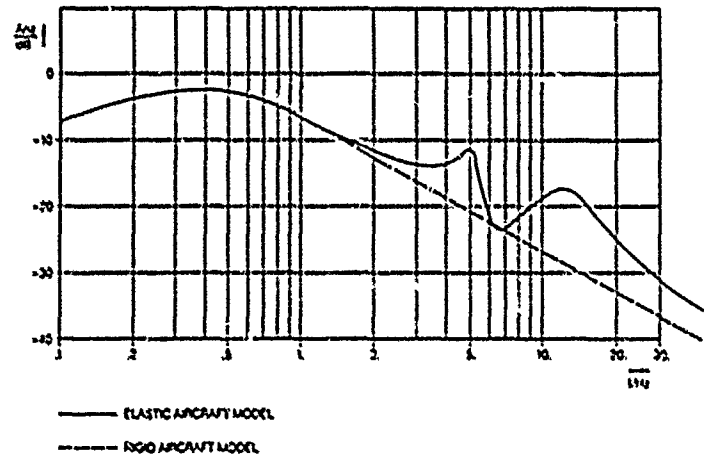


Fig. 6: Mathematical Model
frequency response of the vertical acceleration

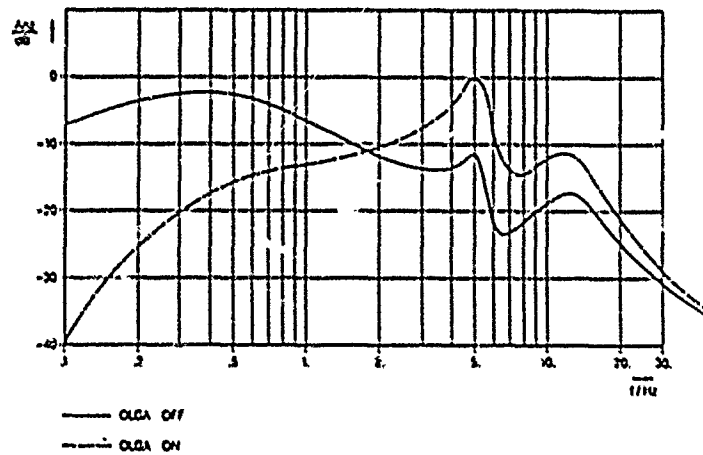


Fig. 7: Elastic Aircraft Model with OLGA (sym. ailerons, elevator)
frequency response of the vertical acceleration

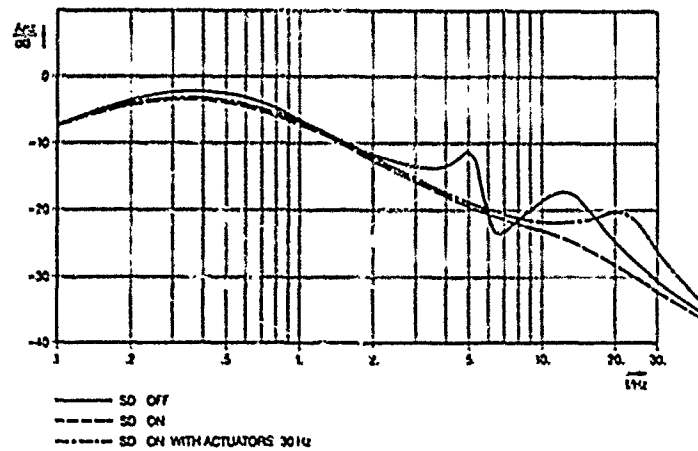


Fig. 8: Elastic Aircraft Model with SD (sym. ailerons, elevator)
frequency response of the vertical acceleration

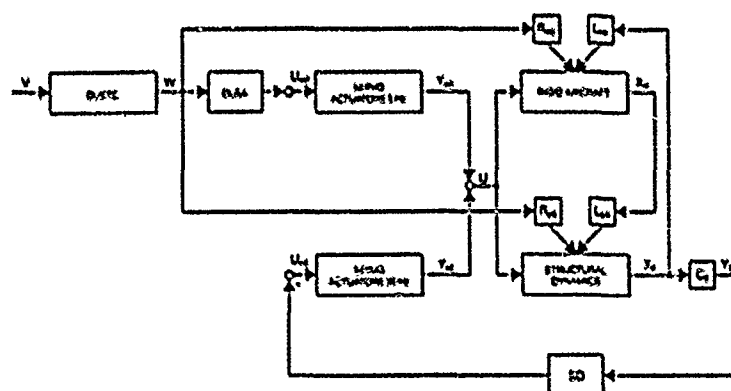


Fig. 9: Block Diagram of the Controlled Elastic Aircraft

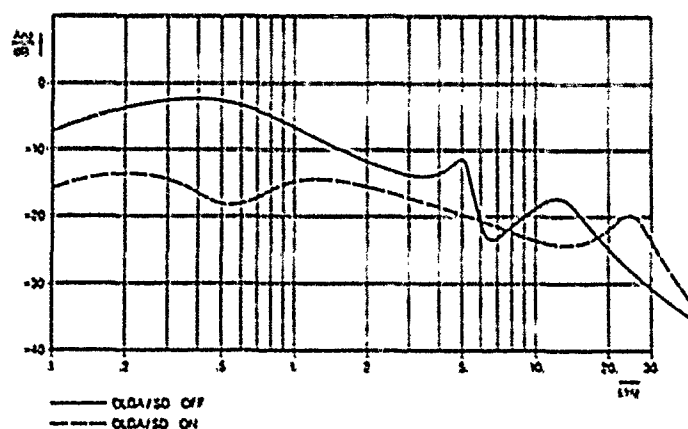


Fig. 10: Elastic Aircraft Model with OLGA and SD (syn. ailerons, elevator) frequency response of the vertical acceleration

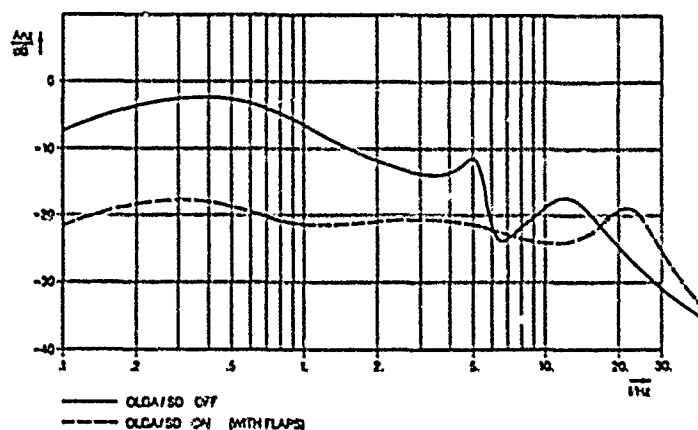


Fig. 11: Elastic Aircraft Model with OLGA and SD (syn. ailerons, elevator, trailing edge flaps) frequency response of the vertical acceleration

Aircraft Response and Pilot Behaviour During a Wake Vortex Encounter Perpendicular to the Vortex Axis

by

Reinhard König
Institut für Flugmechanik
Deutsche Forschungsanstalt für
Luft- und Raumfahrt e.V. (DLR)
D-3300 Braunschweig, Postfach 32 67
Federal Republic of Germany

SUMMARY

Vortex systems can be hazardous to trailing aircraft which encounter them in flight. The greatest hazard occurs in areas where aircraft from a wide range of classes operate and where the flight paths are close to the ground. Upwash velocities induced by the wake vortices can be equivalent to the design gust velocities. Furthermore different types of hazardous effects exist when encountering the vortex system, such as imposed rolling and pitching moments, a loss of rate of climb, a loss of altitude and structural loads.

This paper describes an investigation of aircraft response and pilot behaviour during takeoff when a wake vortex is encountered perpendicular to the vortex axis. The aircraft response is calculated by nonlinear digital simulation with a mathematical model of a wake vortex system close to the ground. This real-time vortex model is also used in the Boeing B737 simulator of Deutsche Lufthansa in order to examine the pilot behaviour. Close to the ground, the wake vortex system induces additional horizontal velocities. There exists a critical flight path where very large g-loads are induced by vertical and horizontal vortex velocities and normal vertical acceleration shortly after takeoff. Often the pilot will attempt to counteract these g-loads, but this produces only a small effect.

List of Symbols

b	wing span
C_L	lift coefficient
C_{L_R}	reference lift coefficient
C_{L_α}	lift derivative
DR	vortex rotation direction
G	aircraft weight
H	aircraft altitude
k	lift distribution factor
n_{zI}	vertical g-load
q	pitch rate
q_a	relevant aerodynamic pitch rate
q_w	rotation rate due to disturbances
R	radius
R_C	vortex core radius
R_H	aircraft vertical location from vortex center
R_X	aircraft horizontal location from vortex center
S	wing surface
t	time
u_{Vg}	component of tangential vortex velocity along flight path direction
u_{Wg}	component of wind velocity along flight path direction
V	flight velocity
V_R	reference flight velocity
V_{VC}	tangential velocity at the edge of the vortex core
V_{Vh}	horizontal component of tangential vortex velocity
V_{Vh}	vortex motion velocity
V_{Vt}	tangential vortex velocity
w_{Vg}	vertical component of tangential vortex velocity
w_{Wg}	vertical component of wind velocity

α	angle of attack
Γ	circulation
Γ_c	circulation at the edge of vortex core
Δ	variation
η	elevator deflection
θ	pitch attitude
ρ	air density

Indices

C	core
V	vortex
t	tangential
h	horizontal
∞	infinity
g	geodetic
H	height, altitude
R	reference
X	horizontal distance

1. INTRODUCTION

Every aircraft generates a pair of counter rotating vortices trailing from the wing tips which can be hazardous to other aircraft encountering them in flight. The greatest hazard occurs in areas where aircraft from a wide range of classes operate and where the flight paths are close to the ground. The existence of wake vortices restrict the number of airport operations (takeoffs and landings) to an increasing degree. Release for takeoff can not be given before all potential encounters near the ground are excluded. Likewise during the landing approach, the aircraft must be separated from each other to avoid such encounters. Reduction of the distance between aircraft during the landing approach, better utilization of parallel runways and specified release for takeoffs require precise knowledge about the vortex intensity, shape and movement. Furthermore, the aircraft's and pilot's behaviour is of interest during the vortex encounter.

A vortex encounter can be classified into one of the forms: The encounter along the vortex axis direction, which imposes rolling moments, a loss of rate of climb and a loss of altitude; and the encounter perpendicular to the axis, which imposes pitching moments and structural loads [1] (Figure 1).

The second form can be possible near the ground, when the airport has crossed runways, and when a takeoff occurs shortly after a landing (Figure 2).

The Institut für Flugmechanik of the Deutsche Versuchsanstalt für Luft- und Raumfahrt (DLR), in cooperation with the Deutsche Lufthansa (DLH), carried out investigation of aircraft response and pilot behaviour during takeoff when a wake vortex is encountered perpendicular to the vortex axis. The aircraft response was calculated by nonlinear digital simulation using a simple mathematical model for a wake vortex system close to the ground. In order to examine the pilot behaviour, this model was used in the D737 moving cockpit simulator of DLH. The pilot inputs and the aircraft response were monitored during 43 simulated encounters.

2. A SIMPLE MATHEMATICAL MODEL OF A WAKE VORTEX SYSTEM NEAR TO THE GROUND

2.1 THE SINGLE VORTEX

2.1.1 COMPARISON OF MODELS

The simplest vortex model is the potential-vortex well-known from the fluid dynamics. The circulation of the potential vortex is described with the following equation:

$$\Gamma = 2\pi V_{vt} R$$

The tangential velocity V_{vt} decreases to zero as the distance from the vortex center increases to infinity. In reverse V_{vt} increases to infinity as the distance decreases to zero.

$$V_{vt} = \frac{\Gamma}{2\pi R}$$

The potential-vortex assumes that there is no friction in the flow. This model is not valid near to the vortex center because the friction can not be neglected.

Another simple model is the RANKINE model [2] which describes the tangential velocity within the vortex core in a linear form. At the edge of the core the velocity has the same magnitude as the potential-vortex. Outside the Rankine and potential vortex models are identical.

$$V_{Vt} = \frac{r_c}{2 \cdot R}$$

$$r_c = 2 \cdot V_{VC} R_c$$

$$V_{Vt} = V_{VC} \frac{R_c}{R} \quad R > R_c$$

$$V_{Vt} = V_{VC} \frac{R}{R_c} \quad R < R_c$$

Other models exist such as the exponential LAMP-model and the logarithmic KUHN/NIELSEN-model which will not be described in detail [2]. In the represented investigation an empirical model was used. The tangential velocity of this model has the following form:

$$V_{Vt} = \frac{2 V_{VC} R_c R}{R^2 + R_c^2}$$

The different vortex models are shown in Figure 3.

2.1.2 THE VORTEX STRENGTH

The strength or circulation of a wake vortex depends linearly on the aircraft lift which can in turn be equated with the aircraft weight when the flight path is level. Therefore, heavy aircraft generate intense wake vortices. Generally the circulation is a function of lift distribution, air density, wing span and flight velocity.

$$\Gamma_{\infty} = \frac{G}{k \cdot \rho \cdot b \cdot V}$$

In order to have a disadvantageous condition (worst case) a B747-200C was selected as the vortex generating aircraft. Under landing conditions with maximum landing weight, the induced circulation was 642 m²/s. To determine the core velocity V_{VC} and core radius R_c which are required to calculate the tangential velocity as a function of the distance from the center, one equates the calculated value of the circulation and the general expression:

$$\Gamma_{\infty} = 2 \Gamma_c = 4 \cdot V_{VC} R_c = 642 \frac{m^2}{s}$$

$$V_{VC} R_c = \frac{\Gamma_{\infty}}{4} = 51 \frac{m^2}{s}$$

To separate core velocity and radius from each other, it is necessary to have measurements [3], [4], [5], [6]. Table 1 shows values of measured velocity as a function of time after vortex generation and the calculated radius with the assumed circulation.

vortex age [s] (measured)	V_{VC} [m/s] (measured)	Γ_{∞} [m ² /s] (assumed)	R_c [m] (calculated)
5.4	43.2	641.6	1.18
16.8	34.1	641.6	1.49
25.6	31.1	641.6	1.64
47.6	25.9	641.6	1.97

Table 1: Measured vortex velocity and calculated radius with an assumed circulation

2.2 VELOCITIES OF A WAKE VORTEX SYSTEM NEAR TO THE GROUND

The simulation of the aircraft response to disturbances requires knowledge of the vertical and horizontal disturbance velocities. Normally a vortex system consists of a pair of wake vortices, but near to the ground it is necessary to assume a mirror pair (a counter rotating pair of the same distance and height, but under the ground, Figure 4). For each point of height and distance that the simulated aircraft can reach, the velocity components of the four vortices must be calculated and applied against the aircraft. The simplest way to accomplish this is by taking the dot and cross products using vector algebra. Figure 5 shows the decomposition of the tangential velocity into its horizontal and vertical components. The vector dot product yields:

$$\underline{R} \cdot \underline{V}_{Vt} = |\underline{R}| |\underline{V}_{Vt}| \cos 90^\circ = 0$$

$$\begin{bmatrix} R_x \\ R_{11} \\ 0 \end{bmatrix} \cdot \begin{bmatrix} V_{Vh} \\ V_{Vg} \\ 0 \end{bmatrix} = R_x V_{Vh} + R_{11} V_{Vg}$$

$$R_x V_{Vh} + R_{11} V_{Vg} = 0$$

In a left rotating vortex, one obtains the following vector cross product:

$$\begin{bmatrix} R_x \\ R_{11} \\ 0 \end{bmatrix} \times \begin{bmatrix} V_{Vh} \\ V_{Vg} \\ 0 \end{bmatrix} = \begin{bmatrix} 0 \\ 0 \\ R_x V_{Vg} - R_{11} V_{Vh} \end{bmatrix}$$

The absolute value of the new vector is:

$$\begin{aligned} |\underline{R} \times \underline{V}_{Vt}| &= R_x V_{Vg} - R_{11} V_{Vh} \\ &= |\underline{R}| |\underline{V}_{Vt}| \sin 90^\circ \end{aligned}$$

$$R_x V_{Vg} - R_{11} V_{Vh} = K V_{Vt}$$

Now we have two equations to calculate the components V_{Vg} and V_{Vh} :

$$\begin{aligned} V_{Vg} &= -DR \frac{R_x}{K} V_{Vt} & DR = 1: \text{left rotating} \\ & & DR = -1: \text{right rotating} \\ V_{Vh} &= -\frac{R_{11}}{R_x} V_{Vg} \end{aligned}$$

2.3 THE VORTEX MOTION

Wake vortices have a limited life cycle and do not remain at the place of origin. First they move downward and then they come apart. It is possible to calculate the motion using a numerical integration method (simulation). Additional conditions such as horizontal winds or boundary layer influences can be considered in a simple way. In order to simulate the motion, three induced velocities are added in the center of one vortex. The resulting velocity is then numerically integrated so that the center becomes a new position. During a short duration (less than one minute) one can assume that the circulation remains constant. Due to friction the vortex grows while the tangential velocity diminishes. The following equation can be used to estimate the vortex core radius as a function of time.

$$R_c(t) = \sqrt{R_c^2(t=0) + 5 \cdot 10^{-4} \Gamma(t=0) t}$$

Figures 6 and 7 show the results of a simulated vortex movement. During the simulation time of 60 s, the vortex pair moves downward to about half of its initial distance and then comes apart. The core radius grows from 1.2 to 3.5 m while the maximum tangential velocity shrinks from 40 to 15 m/s. The velocity of the vortex core was 2.3 m/s at the beginning, 1.3 m/s in the middle and again 2.3 m/s at the end of the simulation.

The movement depends strongly on the starting circulation and is decrease during the vortex life time. The vortex shape does not influence the motion. Crosswinds displace the vortex system as shown in Figure 8. If the magnitude of the crosswind has the same value as the horizontal core velocity near to the ground, one of the two vortices remains nearly stationary.

3. FLIGHT SIMULATION IN VORTEX ENVIRONMENT

3.1 AIRCRAFT BEHAVIOUR IN WIND DISTURBANCES

Aircraft behaviour in wind fields is characterized by an interaction between the flight path and the wind disturbances. The wind disturbs the flight path and the new resulting path is then affected by other wind velocities. A simulated flight through horizontal windshear (Figure 9) can be used to demonstrate this effect. A decreasing horizontal wind during a landing approach induces an increase in the vertical speed of the aircraft; this then increases the time-dependent windshear gradient resulting in an even greater increase in aircraft vertical speed.

$$\frac{du_{Wg}}{dt} = \frac{du_{Wg}}{dh} \cdot \frac{dh}{dt}$$

Wake vortex systems are also location-dependent velocity fields. Compared with horizontal windshear, they have even greater shear gradients. Therefore the aircraft response strongly depends on the initial flight path through the vortex system.

3.2 IMPROVEMENT OF AIRCRAFT SIMULATION MODELS THROUGH APPLICATION OF ROTATING GUSTS

In most aircraft models used in simulators, especially training simulators, the aerodynamic forces act upon the aircraft center of gravity. When the disturbance wavelength approaches the aircraft length, these models are no longer valid. The disturbed aerodynamic forces must then be separated into wing and tail forces to properly calculate the total lift and pitch moment. An improvement to the single point models can also be obtained by applying rotating gusts which are approximated from the difference in the velocities at the wing and tail locations (Figure 10).

$$q_a = q - q_w$$

$$q_w = - \frac{dw_{wg}}{dx_L}$$

The influence of this improvement is illustrated in Figure 11. Without such a "rotating gust", the simulated aircraft decreases in pitch attitude shortly after entering the step gust since the aircraft is statically stable. In the case with the rotating gust, however, the aircraft initially increases in pitch. Once the aircraft tail reaches the step gust, the pitch attitude then decreases in a manner similar to the first case.

3.3 AIRCRAFT BEHAVIOUR IN DEPENDANCE ON INITIAL FLIGHT PATH

To describe aircraft behaviour during a wake vortex encounter perpendicular to the vortex axis, a mathematical model of a B737-200ADV was used. The initial conditions were takeoff configuration, takeoff weight near the minimum (57 tons) and initial stationary flight path. Elevator and throttle settings remained constant during the simulation. The vortex parameters used were those mentioned above. Under the assumption that the vortex lifetime amounted to 30 s, the core radius was 2.5 m and the maximum tangential velocity 20.4 m/s. The vortex system location was fixed at a horizontal distance between the vortices of 52 m and a height of 50 m.

The aircraft behaviour due to the following initial flight path conditions were considered:

- 1) horizontal encounter
 - a) vortex center
 - b) core radius below vortex center
 - c) core radius above vortex center
- 2) encounter during climb
 - a) directly through both vortices
 - b) through the center of the left vortex
 - c) through the center of the right vortex

Due to the interaction between flight path and wind disturbances these desired paths were not obtained exactly.

Figure 12 shows the simulation results of an encounter during horizontal flight. The maximum vertical vortex velocity is nearly 20 m/s. Horizontal vortex velocities are quite small. They appear due to the updraft of the left vortex which produces a positive rate of climb and causes the aircraft to fly through this vortex half of a meter above the vortex center. The downdraft between the two vortices leads to a loss of altitude, but not before the aircraft passes through the right vortex. The horizontal vortex velocity disturbs the flight velocity, the vertical component disturbs the angle of attack; both lead to additional g-loads. The maximum of the lift coefficient is reached and the additional g-loads are between -1 g and +1 g. However the changes in flight path are small and even at low altitudes not critical. This is also the case with pitch attitude (11.5 degrees).

A horizontal encounter of the core radius below the vortices height results in large changes of flight velocity. The increase in speed and angle of attack produces additional g-loads up to 1.3 g while crossing the left vortex (Figure 13). In the case of an encounter of the core radius above the vortices height, the maximum g-loads occurred at the right vortex (Figure 14).

A simulated climb directly through both vortices is shown in Figure 15. The initial climb gradient is equal to 10 degrees. Since the aircraft encounters the left vortex below the center and the right vortex above the center, the flight velocity increases twice. But the disturbances to the angle of attack are smaller than in the case of the horizontal encounter. Furthermore, the left vortex produces a downward pitch of 2.5 degrees which is recovered when the right vortex is nearly passed through. Climbs that pass nearly through the center of the left or right vortex lead to the largest values of additional g-loads (Figures 16 and 17). The results show that the additional g-loads depend strongly on the flight path, and one can search for the critical path which produces the largest loads. A numerical method to determine the extrema of a given function is helpful for analyzing this problem [7]. The vertical g-load is coarsely described with the following equation:

$$n_{zf} = \frac{\rho}{2} (V_R + \Delta V)^2 \frac{S}{\sigma} [C_{ZR} + C_{Za} \Delta \alpha]$$

For higher frequency disturbances, such as turbulence or wake vortices, one can assume:

$$\Delta V = -\Delta u_{Vg} \quad \Delta u_{Vg} = V_{Vh}$$

$$\Delta \alpha = -\frac{\Delta w_{Vg}}{V_R + \Delta V} \quad \Delta w_{Vg} = w_{Vg}$$

The vertical g-load then obtains the following form:

$$n_{zf} = \frac{\rho}{2} (V_R - \Delta u_{Vg})^2 \frac{S}{\sigma} [C_{ZR} - C_{Za} \frac{\Delta w_{Vg}}{V_R - \Delta u_{Vg}}]$$

The results of searching the maxima and minima of this function inside the velocity field of the vortex system are shown in Figure 18. There exists respectively two locations of extreme values which can be reached during climb. An updraft of 16 m/s and head-velocity of 9 m/s are produced at the left side below the center of the left vortex, where the additional g-load is 1.7 g. The additional g-load minimum occurs above this vortex on its right side; the value is -1.8 g. For both cases a combination of vertical and horizontal vortex velocity is responsible for the extreme values.

During takeoff rotation near to the ground, the pilot produces further additional g-loads. Figure 19 shows the simulation results of the rotating phase after liftoff while encountering the vortex system. In order to determine the initial conditions leading to maximum g-loads, the above-mentioned numerical method is again used to search for extreme values. The maximum of the additional g-load is about 1.5 g, so that the g-load safety limit of 2.5 g is reached.

4. PILOT BEHAVIOUR

Simulations with fixed elevator and throttle settings during encounters with vortex systems have shown that the deviation in pitch and aircraft altitude remain small, but the g-loads can nearly reach the allowed limit. Unforeseen changes in pitch and g-loading, particularly near to the ground, can lead to either deliberate or unconscious pilot reactions. The question is whether the possible pilot inputs can be dangerous to flight. In order to describe pilot behaviour and its effect on flight safety, a moving-cockpit study on DLR B737 training-simulator was performed [8], [9]. Pilot inputs and aircraft response were monitored for 43 simulated encounters. Additionally, pilot questionnaires were completed.

The most important result of this study was that the pilot was unable to counteract the g-load within the two seconds it took to cross the vortex system. Partial elevator inputs were observed shortly after the encounter aimed at stabilizing or decreasing pitch attitude. During all encounters, the pilot inputs did not threaten the flight safety with conditions such as stall or significant altitude loss. On the other hand, the safety limit of additional g-load (1.5 g) was passed over repeatedly. Figure 20 shows the number of vortex encounters with special maximum or minimum g-loads. Nine encounters were above 1.5 g. A pilot reaction during and after a vortex encounter is shown in Figure 21. After a time delay of about 0.5 s, the pilot pushed the elevator downward to decrease pitch attitude; however he could not avoid additional g-loads of around 2 g. Disturbance with wavelengths near to the aircraft dimension could not be compensated by an elevator input, even if there were no time delay in pilot reaction, or if an autopilot were used. Only the use of direct lift control technology can counteract these disturbances.

The mathematical model used in the training simulator does not contain sections that describe the elastic behaviour of the aircraft and instantaneous aerodynamic effects. To assure that the calculation of g-loads is valid, these effects should be included.

5. CONCLUSIONS

Wake vortex systems can be described with simple mathematical models which are also valid near to the ground. These simple models are a basic requirement for investigating the aircraft and pilot behaviour in a real-time environment.

The present investigation leads to the result that the vortices created by a B747 at maximum landing weight can produce g-loads higher than the safety limit on a B737 during takeoff at minimum takeoff weight. Nevertheless, it is necessary to observe a specific flight path through the vortex system. On this flight path a special combination of horizontal and vertical vortex velocities affect the aircraft. As expected, the results of a simulator study have shown that the pilot cannot counteract the g-loads within the short time of passing through the vortex system. Fortunately critical flight states did not occur during simulations with either fixed controls or with pilot interaction.

6. REFERENCES

- [1] W.A. Mc Cowan Avoidance of Aircraft Trailing Vortex Hazards, 37th Meeting of the Flight Mechanics Panel of AGARD, Baden-Baden, 20-23 October 1970.
- [2] J.N. Hallock Aircraft Wake Vortices: A State of the Art Review of the United
W.R. Eberle States R&D Program DOT-TSC-FAA-77-4, Final Report, February 1977.
- [3] D.C. Burnham B747 Vortex Alleviation Flight Tests: Ground-Based Sensor Measurements. DOT-FAA-RD-81-99, DOT-TSC-FAA-81-19, Final Report, February 1982.
- [4] D.C. Burnham Ground-Based Measurements of the Wake Vortex Characteristics of
J.N. Hallock a B-747 Aircraft in Various Configurations. FAA-RD-78-146, Final
I.H. Tombach Report, December 1978.
M.R. Brashears
M.R. Barber
- [5] F. Köpp Untersuchung der Wirbelschleppen landender Flugzeuge am Flughafen
H. Klier Frankfurt. IB 552-13/83, DFVLR, Institut für Optoelektronik.
Ch. Werner
- [6] Ch. Werner Measurements of Aircraft Wake Vortices Using the DFVLR Laser Doppler
F. Köpp Anemometer. IB 552-13/84, DFVLR, Institut für Optoelektronik.
- [7] H.G. Jakob Rechnergestützte Optimierung statischer und dynamischer Systeme.
Springer-Verlag, Berlin, Heidelberg, New York, 1982.
- [8] R. König Untersuchung zum Pilotenverhalten beim Wirbelschleppendurchflug
quer zur Wirbelachse. IB 111-87/59, DFVLR, Institut für Flugmechanik.
- [9] R. König Zusammenstellung der Ergebnisse einer Simulatorstudie zum Wirbelschleppendurchflug quer zur Wirbelachse. IB 111-87/60, DFVLR, Institut für Flugmechanik.

FIGURES

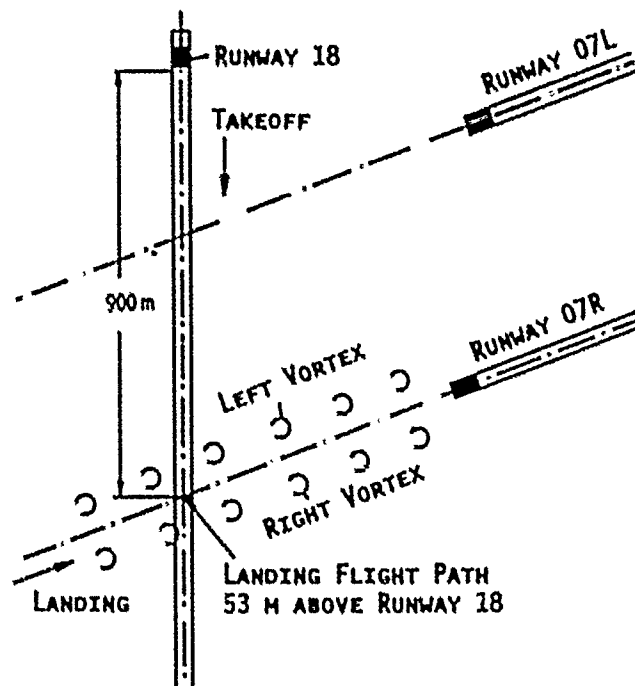


Figure 1: Possible scenario of a vortex encounter perpendicular to the vortex axis

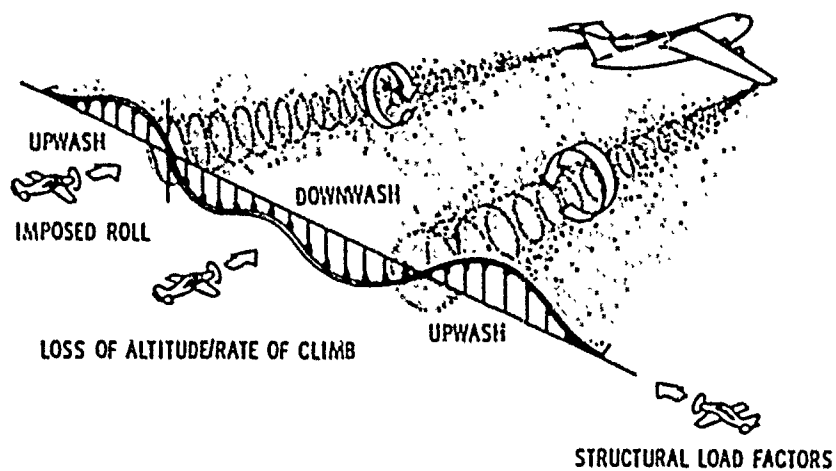


Figure 2: Potential hazards due to trailing vortices [1]

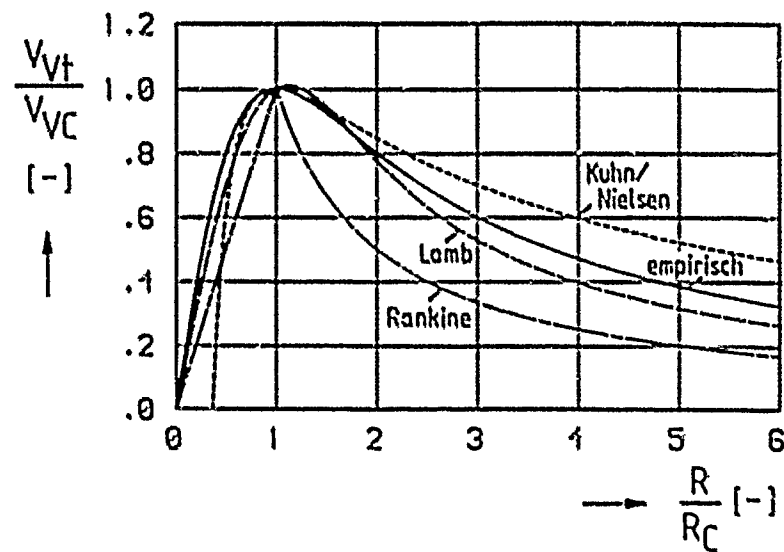


Figure 3: Comparison of vortex models

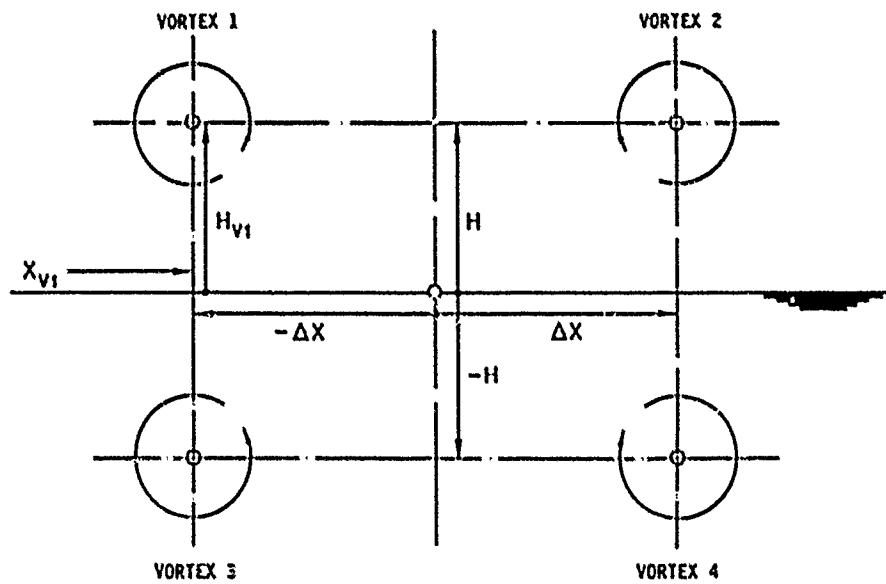


Figure 4: "Mirror vortices" used to describe the induced velocities near the ground

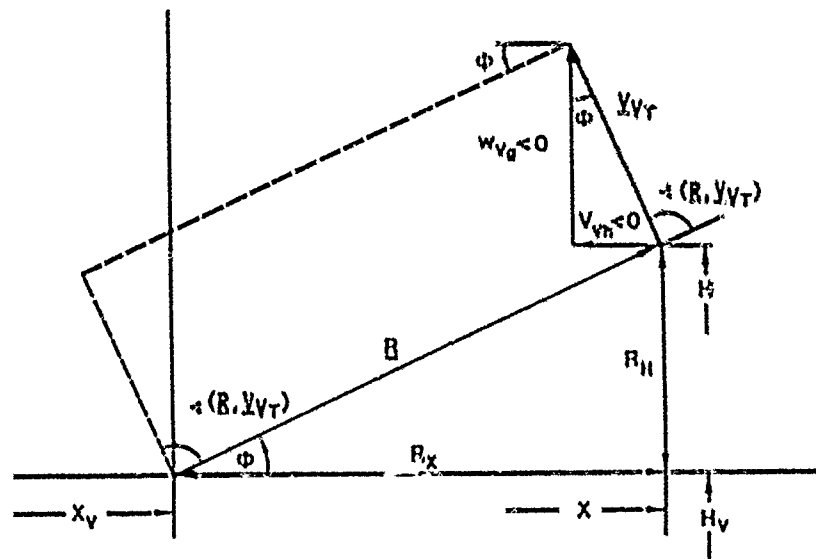


Figure 5: Decomposition of vortex velocity into horizontal and vertical components

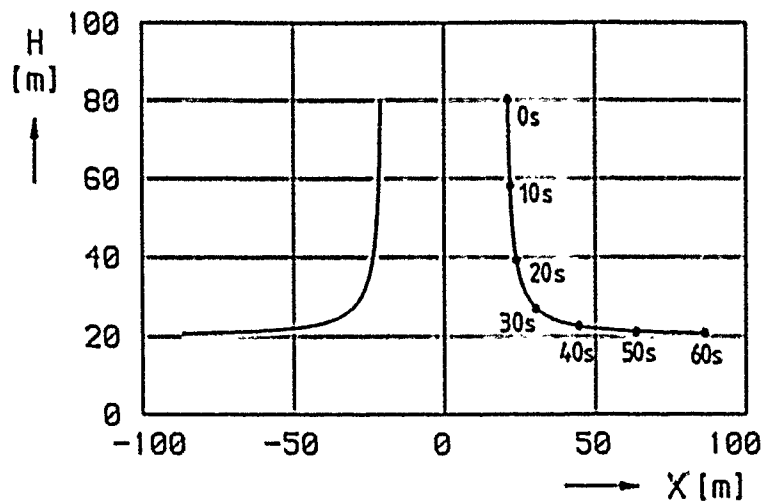


Figure 6: Vortex motion from simulation

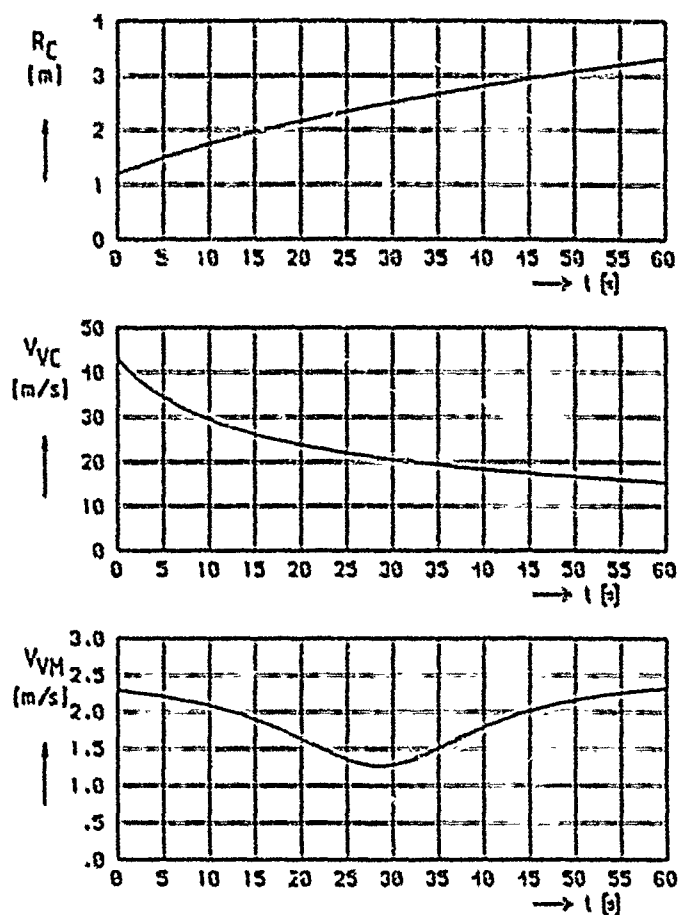


Figure 7: Characteristics of a vortex near the ground

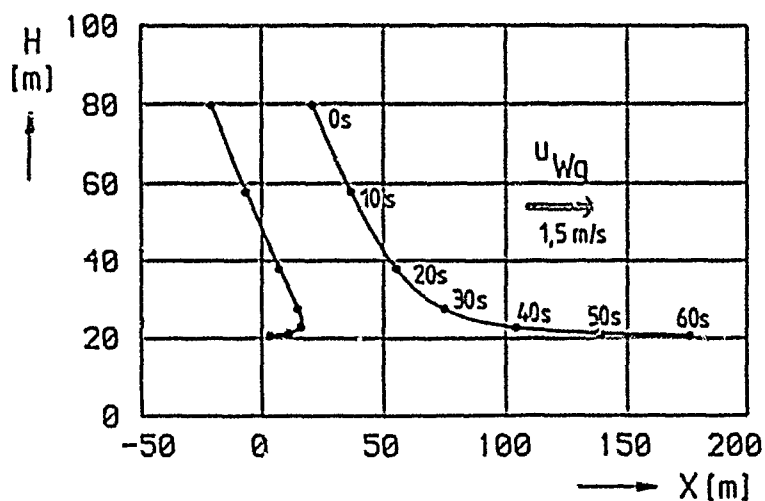


Figure 8: Vortex motion with crosswind

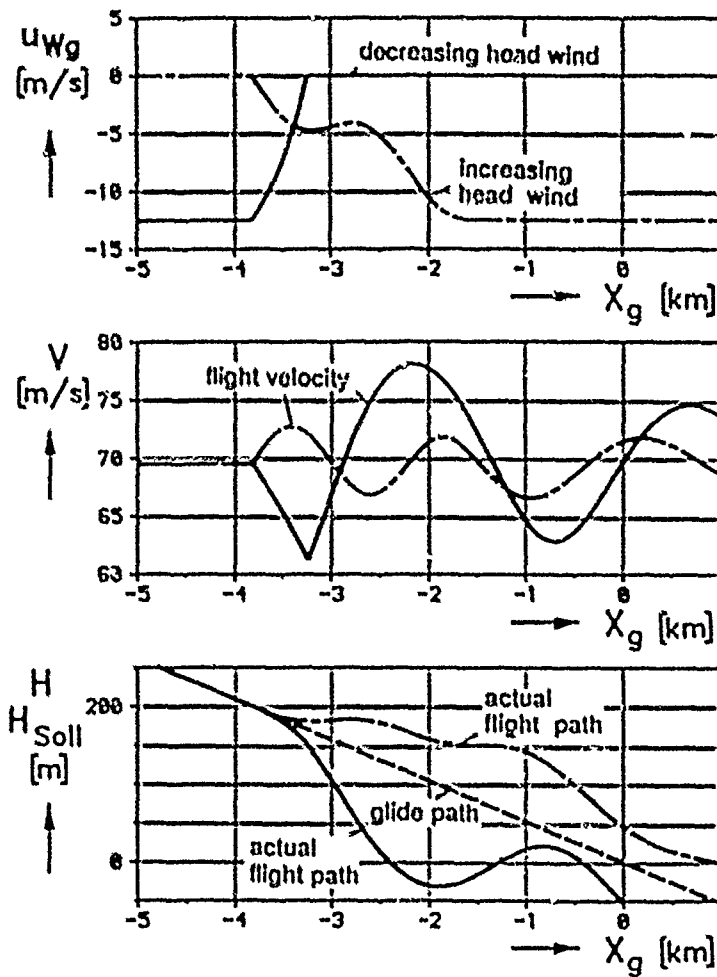


Figure 9: Aircraft behaviour during horizontal windshear

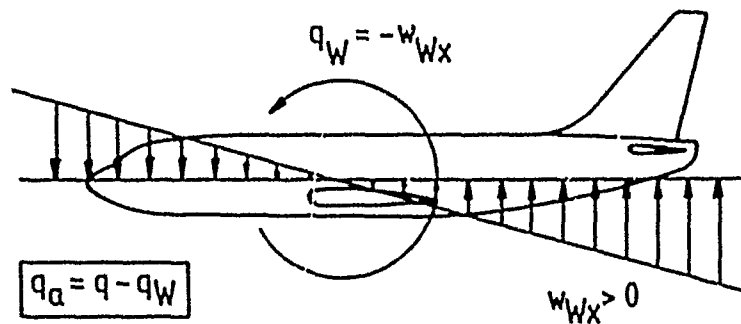


Figure 10: Relevant aerodynamic pitch rate

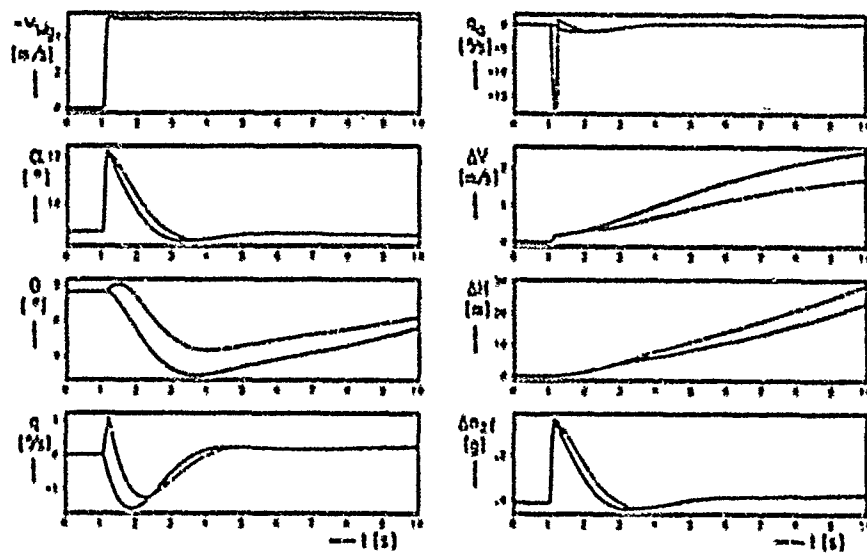


Figure 11: Step gust response
 — without q_W , --- with q_W

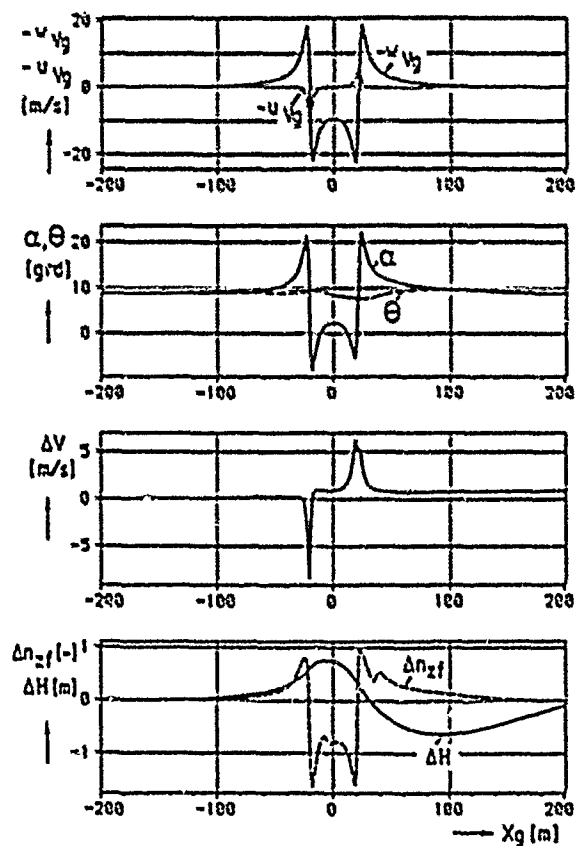


Figure 12: Horizontal encounter at vortex center

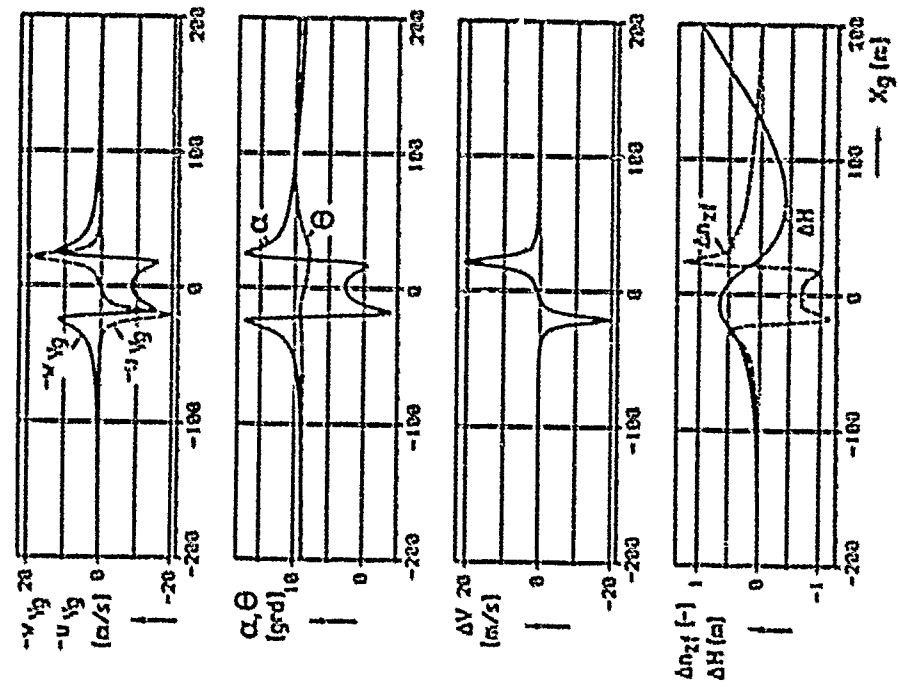


Figure 13: Horizontal encounter one core radius below vortex center

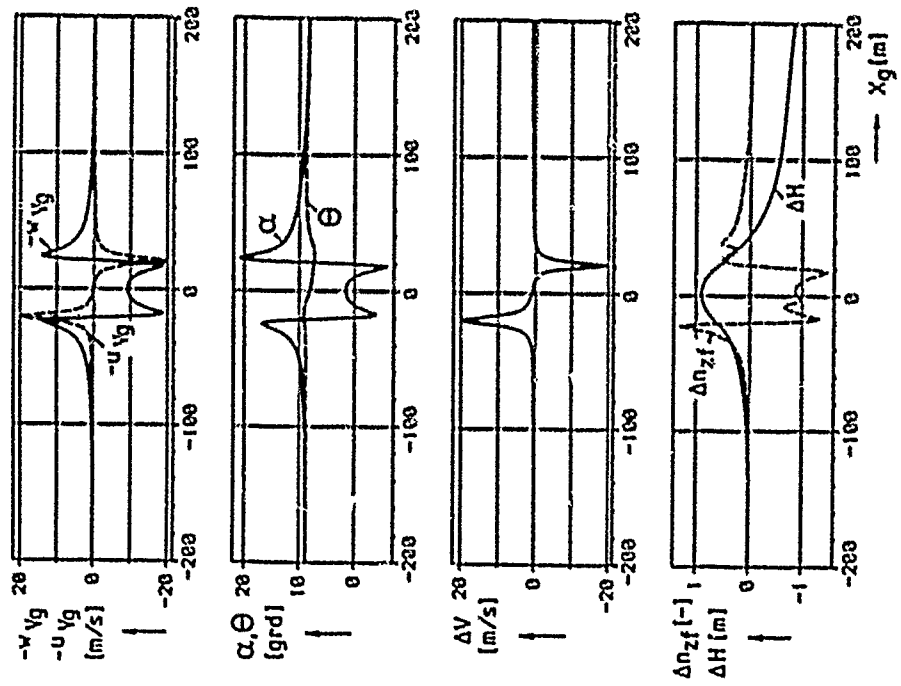


Figure 14: Horizontal encounter one core radius above vortex center

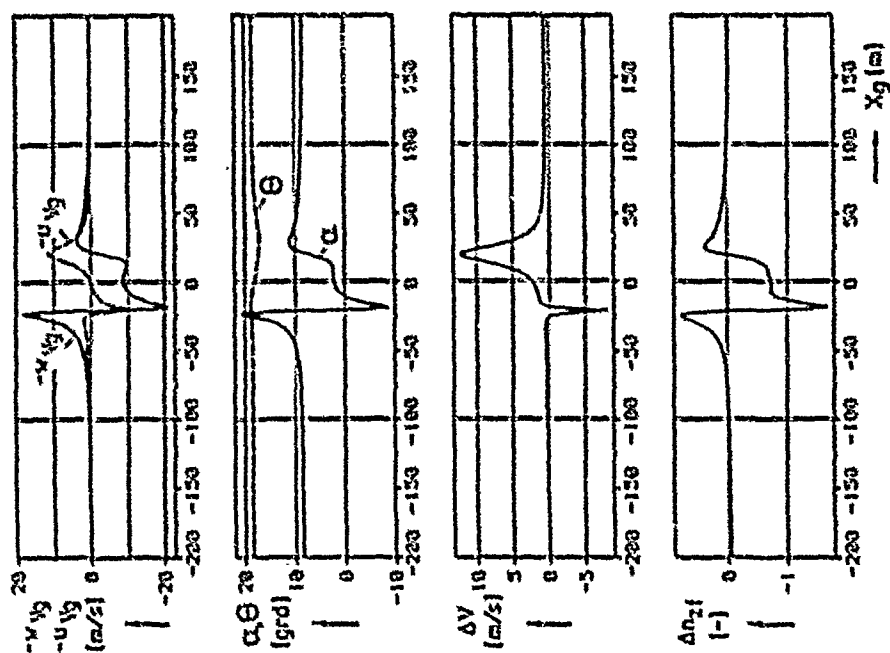


Figure 16: Encounter through center of left vortex during climb

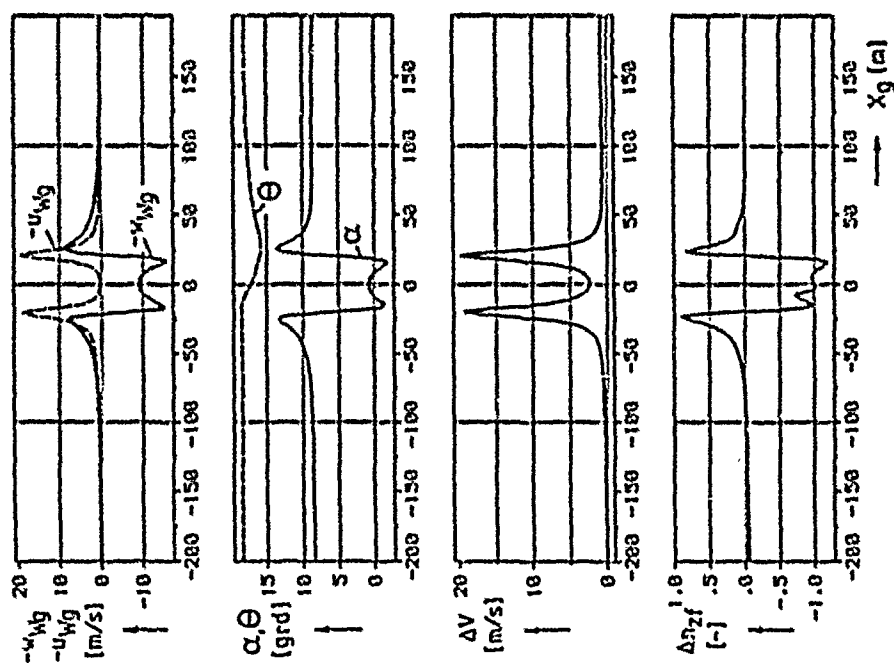


Figure 15: Encounter directly through both vortices during climb

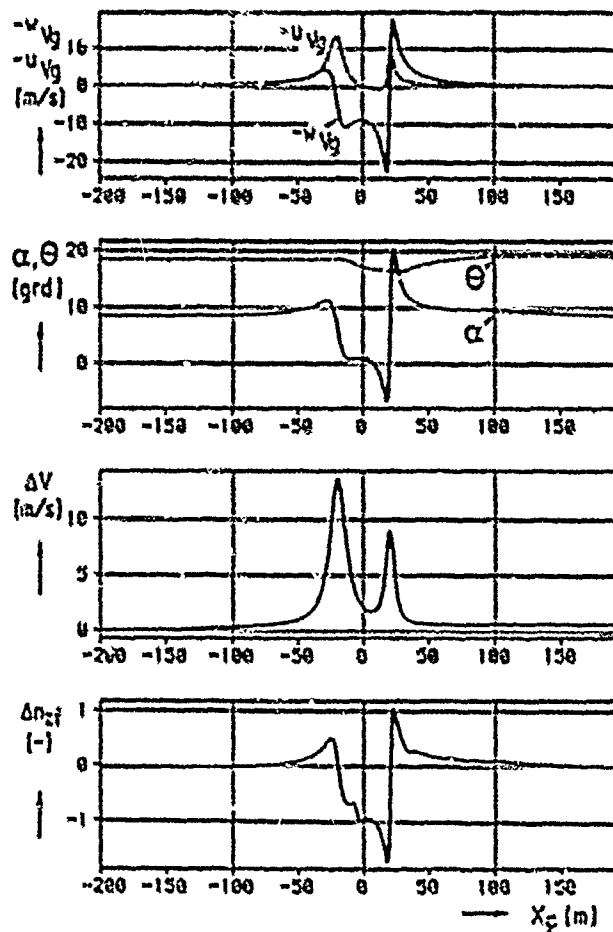


Figure 17: Encounter through center of right vortex during climb

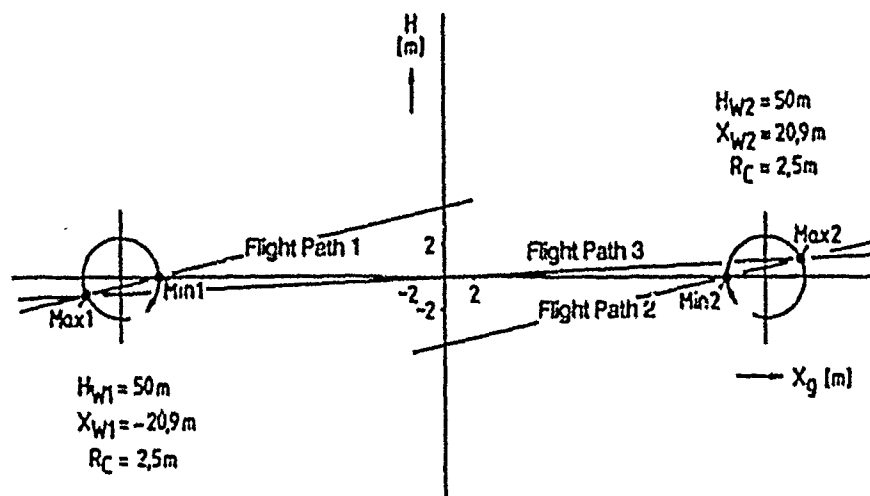


Figure 18: Flight paths and locations of extreme g-loads

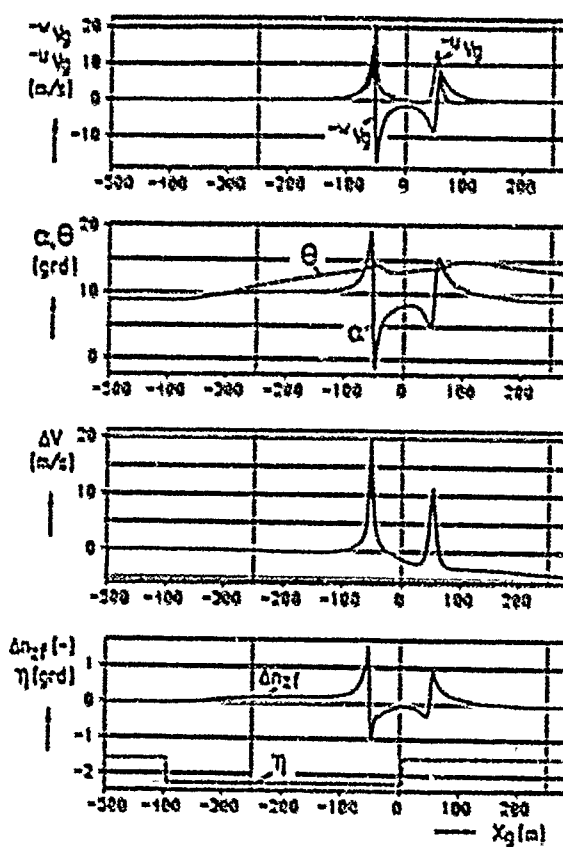


Figure 19: Maximum and minimum values of g-load during a simulated aircraft takeoff rotation phase

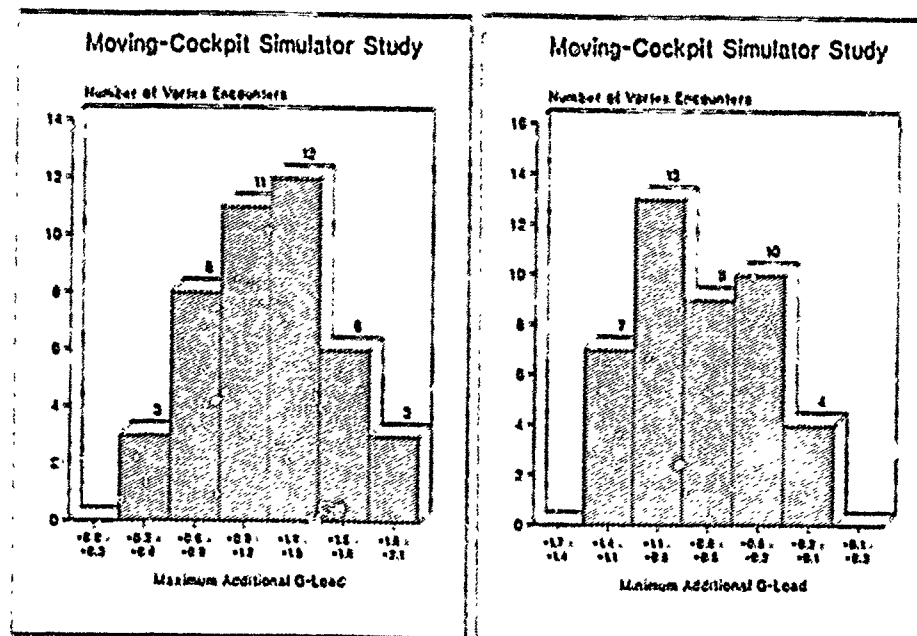


Figure 20: Extrema of additional g-loads monitored during simulator study

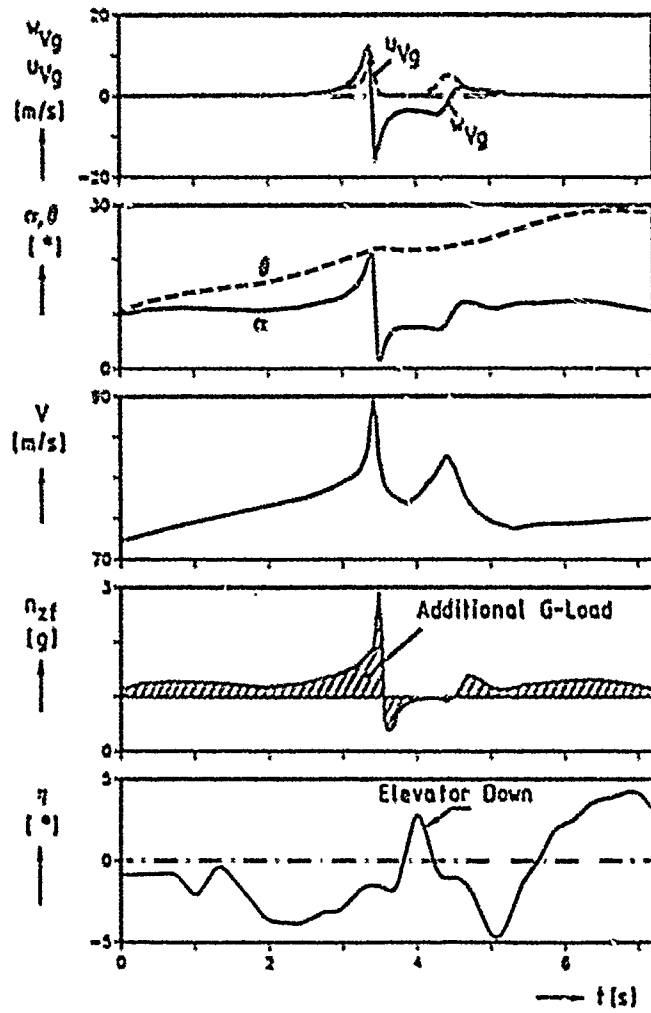


Figure 21: Maximum g-load and pilot reaction crossing the left vortex

A STUDY OF THE EFFECTS OF ROTATING FRAME TURBULENCE (RFT) ON HELICOPTER FLIGHT MECHANICS

by

D.P. Schrage, J.V.R. Prasad
School of Aerospace Engineering
Georgia Institute of Technology
Atlanta, Georgia 30332, USA

and

G.H. Gaonkar
Mechanical Engineering Department
Florida Atlantic University
Boca Raton, Florida 33431, USA

ABSTRACT

The turbulence actually experienced by a helicopter blade-element significantly differs from the space-fixed free atmospheric turbulence. The turbulence in the rotor disk requires a rotationally sampled description in a rotating frame of reference. It is referred to as the rotating frame turbulence or RFT, which exhibits a striking phenomenon. The RFT spectral density versus frequency shows high peak values at $1P$, $2P$, $3P$, etc., frequencies. The energy increase at these peaks is balanced by an energy decrease primarily at the lower-than- $1P$ frequency range. Particularly for low altitude flight regimes of pure helicopters, such as the nap-of-the-earth maneuvers, the conventional space-fixed description of turbulence is not a good approximation, since the turbulence scale length can have values comparable to the rotor radius. Accordingly the flight mechanics characteristics with RFT description are compared with those based on the conventional space-fixed turbulence description. The results demonstrate that the RFT qualitatively and quantitatively affects the prediction of helicopter flight mechanics characteristics in turbulence. Such comparisons should play an important role in the new development of handling qualities specifications for helicopters.

INTRODUCTION

The modern helicopter is no longer a vehicle used for simple missions where only its hovering capability is required. The helicopters are ever-increasingly faced with complex missions which push the aircraft to its design limits. One emerging requirement is stabilized flight through moderate, or even severe atmospheric turbulence to accomplish high workload mission tasks.

Rotorcraft, both civilian and military, now compete on a commercial basis with many other forms of transportation and have often shown greater reliability and productivity in mission performance. For example, as stated in [1], nearly all of the lighthouses and lightships around the British coastline are now relieved by helicopters. This is because they have demonstrated higher mission reliability, that is, completing the specified mission *on time*, than the former relief boats, which were often up to seven days late. Helicopters are also based on off-shore oil platforms in the North Sea to provide daily routine inter-rig support and to provide rescue services. These helicopters commonly operate to and from landing pads with restricted access in severely turbulent atmospheric winds as high as 55 knots. Military rotorcraft of the U.S. Navy and Marine Corps operating from ships frequently encounter harsh turbulent winds. These rotorcraft are required to perform missions such as hovering over and landing on moving ships, in moderate or severe turbulence, at speeds up to 50 knots while stormy seas induce ship motion up to 15 degrees yielding oscillations on the landing deck in excess of 20 feet [2]. Given these flight conditions which both military and civilian rotorcraft encounter routinely, it is essential to accurately predict rotorcraft performance in a turbulent atmosphere. This capability would allow both passive and active methods of control to be considered early in the preliminary design process. Thus, rotorcraft designers will be able to address the influence of atmospheric turbulence adequately.

We now address the lack of an adequate low-altitude turbulence model to assess helicopter flight mechanics characteristics, loads and vibrations. In fact this lack, particularly for the nap-of-the-earth maneuvers, has been identified as a critical gap in the recent NASA/Army study to develop new han-

handling qualities specifications for helicopters. There are two aspects to modeling turbulence in the rotor disk. The first one is the space-fixed turbulence models based on the studies by Taylor, von Karman, Dryden, Kaimal and others [3]-[6]. Here, the modeling assumptions include stationarity, homogeneity, isotropy and momentarily time-wise frozen concept of the turbulence field. In rotorcraft applications, these assumptions are retained. Further, the assumption that self-induced turbulence in the rotor disk is negligible as compared to the free atmospheric turbulence is required as well, for details see references [3]-[6]. Recent relations between the predicted and measured turbulence excitations on wind turbines show that such an approach to modeling in the rotorplane is fairly valid [7, 8]. The second one is the significant difference between the space-fixed turbulence as experienced by a fixed point in the rotor disk and the turbulence that is actually experienced by a rotating blade element. This 'actual' turbulence in a rotating environment requires a rotationally sampled and non-Eulerian description and is referred to as the rotating frame turbulence (RFT) [6]. The impact of RFT effects on high speed compound rotorcraft in forward flight and wind turbines is well explored in the literature [6]-[8]. For example, reference 6 explains the two contrasting findings: negligible influence of RFT effects on compound rotorcraft during high speed flight regimes [6], and the dominant influence of RFT effects on wind turbines [7, 8]. Reference 6 also shows that for pure low-speed helicopters, RFT effects should be included while modeling turbulence in the rotor disk.

A noteworthy feature of wind turbine studies is the concordant corroboration of predictions by test data on turbulence excitations and turbulence induced vibrations and loads. This wind turbine experience shows that atmospheric turbulence can contribute decisively to the life-time load spectrum and that the RFT effects cannot be neglected. Concerning low speed conventional or pure helicopters, the past studies of turbulence effects on flight mechanics have all neglected the RFT effects. It has been assumed that the entire disk experiences a spatially uniform turbulence velocity field identical to that felt at the rotor hub center. Outside the earth's boundary layer where the turbulence length scale is 600 feet or more as compared to a rotor diameter which is 80 feet or less, this assumption seemed to be reasonable. With this assumption, random loads and vibration were found to be relatively insignificant as compared to the deterministic dynamic loads and vibrations from steady and maneuvering flights. Within the earth's boundary layer and depending on the ground texture, the turbulence length scale has values that are comparable to the rotor diameter so that the assumption of space fixed turbulence is not a good approximation. Therefore, the treatment of turbulence effects for low-altitude flight regimes such as the nap-of-the-earth maneuvers require inclusion of RFT effects. Accordingly this study addresses the RFT effects on low frequency helicopter response with particular emphasis on handling qualities. Such a study should serve as a valuable reference point for the future development of handling qualities specifications for helicopters in turbulence.

TURBULENCE MODELS

For helicopter applications, the vertical turbulence velocity $g(t)$ is the most dominant component. Therefore, in the present treatment, the fore-to-aft and side-to-side turbulence velocity components in the rotor plane are neglected.

In the stochastic treatment, a stationary vertical turbulence velocity $g(t)$ is described by (auto) spectral density function $S_g(\omega)$ or autocorrelation function $R_g(\tau)$. There are many forms of atmospheric turbulence models quoted in the literature. The two widely used models are the von Karman and the Dryden models. The following equations describe the power spectral density function for the vertical turbulence velocity component according to von Karman and Dryden:

von Karman:

$$S_g(\omega) = \sigma_g^2 \frac{L}{2\pi} \frac{1 + \frac{1}{2}(1.34 L\omega)^2}{[1 + (1.34 L\omega)^2]^{\frac{5}{4}}} \quad (1)$$

Dryden:

$$S_g(\omega) = \sigma_g^2 \frac{L}{2\pi} \frac{1 + 3(L\omega)^2}{[1 + (L\omega)^2]^2} \quad (2)$$

In equations 1 and 2, ω is the spacewise circular frequency given by $\omega = 2\pi k$, where k is the wavenumber per unit length, and L is the scale length of the fore-to-aft or longitudinal turbulence component. This turbulence scale length L is given by

$$L = \frac{2}{\sigma_z^2} \int_0^\infty R_z(x) dx \quad (3)$$

It is mentioned in passing that the scale length of the vertical turbulence velocity is equal to $L/2$.

The von Karman power spectrum (equation 1) is generally preferred but the analysis simplifies considerably when the Ornstein-Uhlenbeck model is used without appreciable sacrifice in accuracy of results. In this work, the Ornstein-Uhlenbeck model is used according to which

$$S_z(\omega) = \sigma_z^2 \frac{2L}{\pi} \frac{1}{[1 + (L\omega)^2]} \quad (4)$$

In the development of the RFT model, we define the following rotorcraft parameters.

$$\mu = \frac{V \cos(\alpha)}{\Omega R} \quad (5)$$

$$\lambda = \frac{V \sin(\alpha) + v}{\Omega R} = \mu \tan(\alpha) + \lambda_i \quad (6)$$

$$\lambda_i = \frac{C_T}{2\sqrt{\mu^2 + \lambda^2}} \quad (7)$$

In equations 5, 6, and 7 μ is the advance ratio, λ is the total inflow, and λ_i is the induced inflow (see Figure 1). For hover we have, $\alpha \approx 0.0$, $V \approx 0.0$, $\lambda = \lambda_i$, and $T \approx W$. Thus, we can simply compute the thrust coefficient, downwash velocity, and the induced inflow using the following equations.

$$C_T = \frac{W}{\rho A V^2} \quad (8)$$

$$v = \Omega R \sqrt{\frac{C_T}{2}} \quad (9)$$

$$\lambda_i = \frac{C_T}{2\lambda} \quad (10)$$

Then, as done in reference [6], the out of plane velocity through the rotor, w , is approximated as

$$w = K \lambda_i \Omega R \quad (11)$$

In hover, we set $K = 1.0$. Thus, in the present exploratory study, we neglect the role of mean turbulence velocity and axial flight velocity. Then, in non-dimensional form, w is given by \tilde{w} .

$$\tilde{w} = \lambda_i \quad (12)$$

Using Taylor's hypothesis, i.e. the frozen field concept, in conjunction with the Ornstein-Uhlenbeck power spectrum, we can write the autocorrelation function as a function of the spatial separation between two time intervals. Consider the rotor disk shown in Figure 1. At the $0.7R$ blade station, the blade section encounters the following velocity components:

$$\frac{dx}{dt} = V + 0.7\Omega R \sin \Omega t \quad (13)$$

$$\frac{dy}{dt} = 0.7\Omega R \cos \Omega t \quad (14)$$

$$\frac{dz}{dt} = w \quad (15)$$

Integration of equations 13, 14, and 15 from t_1 to t_2 results in the following equations.

$$x(t_2) - x(t_1) = V(t_2 - t_1) - 0.7R(\cos \Omega t_2 - \cos \Omega t_1) \quad (16)$$

$$y(t_2) - y(t_1) = 0.7R(\sin \Omega t_2 - \sin \Omega t_1) \quad (17)$$

$$z(t_2) - z(t_1) = w(t_2 - t_1) \quad (18)$$

In equation 18, w represents the total mean airflow perpendicular to the rotor disk in the z -direction due to axial flight velocity, mean vertical gust velocity and downwash velocity. From the frozen field concept, the turbulence autocorrelation function is simply a function of the spatial separation for the elapsed time ($t_2 - t_1$):

$$R_w(t_1, t_2) = \sigma_w^2 g(r) \quad (19)$$

Using the Ornstein-Uhlenbeck power spectrum the vertical turbulence autocorrelation function at the $0.7R$ blade station is now given by [3]-[5]

$$R_w(t_1, t_2) = \sigma_w^2 e^{-r/(L/2)} \quad (20)$$

In equation 20, r is the spatial separation of the $0.7R$ blade station during the elapsed time ($t_2 - t_1$) and is given by

$$r = \sqrt{(x(t_2) - x(t_1))^2 + (y(t_2) - y(t_1))^2 + (z(t_2) - z(t_1))^2} \quad (21)$$

Substituting equations 16, 17, and 18 into equation 21 we get

$$r = \sqrt{[V(t_2 - t_1) - 0.7R(\cos \Omega t_2 - \cos \Omega t_1)]^2 + [0.7R(\sin \Omega t_2 - \sin \Omega t_1)]^2 + [w(t_2 - t_1)]^2} \quad (22)$$

In terms of non-dimensional time, $\bar{t} = \Omega t$, non-dimensional flight velocity, $\mu = V \cos(\alpha)/\Omega R$, and non-dimensional total mean airflow, $\bar{w} = w/\Omega R$, we can define the following constants.

$$a = \frac{V \cos(\alpha)}{\Omega R(L/2)R} = \frac{2\mu}{L/R} = 2\frac{R}{L}\mu \quad (23)$$

$$b = 2\frac{R}{L}\bar{w} \quad (24)$$

$$c = 1.4\frac{R}{L} \quad (25)$$

Also, for simplicity of notation, the following definitions are introduced.

$$\tau = \bar{t}_2 - \bar{t}_1 \quad (26)$$

$$t = \frac{\bar{t}_2 + \bar{t}_1}{2} \quad (27)$$

Plugging into the expression for r given by equation 22, and dividing by $L/2$, results in the following expression after trigonometric simplification.

$$\frac{r}{L/2} = \sqrt{(a^2 + b^2)\tau^2 + 4ac\tau \sin t \sin \frac{\tau}{2} + 4c^2 \sin^2 \frac{\tau}{2}} \quad (28)$$

Substituting equation 28 into equation 20 yields the final expression for the nonstationary vertical turbulence autocorrelation function accounting for the rotating frame effects.

$$R_w(t, \tau) = \sigma_w^2 \exp[-\sqrt{(a^2 + b^2)\tau^2 + 4ac\tau \sin t \sin \frac{\tau}{2} + 4c^2 \sin^2 \frac{\tau}{2}}] \quad (29)$$

In a space fixed turbulence formulation, the stationary model for the vertical turbulence velocities simplifies to

$$R_w(t, \tau) = \sigma_w^2 \exp[-\sqrt{(a^2 + b^2)\tau^2}] \quad (30)$$

In hover $\mu = 0$, hence $a = 0$, and the stationary rotating frame vertical turbulence model is given by

$$R_w(t, \tau) = \sigma_w^2 \exp[-\sqrt{b^2\tau^2 + 4c^2 \sin^2 \frac{\tau}{2}}] \quad (31)$$

The corresponding space fixed vertical turbulence model in hover is simply

$$R_w(t, \tau) = \sigma_w^2 \exp[-\sqrt{b^2\tau^2}] \quad (32)$$

TURBULENCE FILTER IMPLEMENTATION

The main goal of the present research is to investigate in hover the effects of RFT on flight mechanics characteristics and compare them with those based on space fixed formulation. For the hover case, the autocorrelation function of the RFT, $R_w(r)$, is stationary [6, 4, 5, 3] and hence, the simplicity of this analysis facilitates an improved appreciation of the RFT *vis-a-vis* conventional space fixed turbulence.

In order to effectively assess different aircraft turbulence models, a combination of pilot, gust and helicopter model needs to be chosen such that all three models are of the same *texture* or level of detail. The helicopter model used for this investigation is the UH-60A Black Hawk helicopter. A generic blade element analysis flight simulation program [9] is used for response simulation.

The gust model used in this investigation is the continuous stochastic turbulence model approach as previously described. Basically, we begin with a power spectrum for the vertical atmospheric turbulence using the Ornstein-Uhlenbeck model given by equation 4. From the vertical turbulence power spectral density function, we seek to derive a turbulence filter system driven by white noise.

Consider, the space fixed turbulence autocorrelation function given by equation 32. The power spectral density function or Fourier transform is easily computed analytically. The space fixed power spectrum is given by

$$S_f(\omega) = \frac{2b}{\pi(\omega^2 + b^2)} \quad (33)$$

The turbulence filter is also easily deduced by decomposing $S_f(\omega)$ into a complex function multiplied by its conjugate. The turbulence filter is given by

$$F(i\omega) = \frac{1}{b + i\omega} \quad (34)$$

The final filter for the space fixed turbulence is obtained by normalizing the power spectral density function. The normalized filter, in transfer function form, is given by

$$F(s) = \frac{A}{s + b} \quad (35)$$

where A is the normalization constant.

For turbulence modeling the level of power must be parametric. The level of power is given by σ^2 where σ is the standard deviation representing the intensity of the turbulence. In order to compare different turbulence models, the total power spectrum must be normalized [10]. Following reference [10], the normalization requirement is:

$$\frac{T}{\pi} \int_0^\infty |F(i\omega)|^2 d\omega = 1 \quad (36)$$

where T is the sampling time. The normalization requirement for the first order filter becomes

$$\frac{A^2 T}{2b} = 1 \quad (37)$$

Thus, the constant A is given by

$$A = \sqrt{\frac{2b}{T}} \quad (38)$$

Consider the RFT autocorrelation function given by equation 31. The power spectral density function of equation 31 is difficult to compute analytically. Thus, a numerical technique is employed to compute the power spectral density function using fast Fourier transforms. The nature of the power spectral density function has been investigated in several papers [7, 6], and all find that the power spectral density function for the turbulence process contains *spikes* occurring at integer multiples of the rotor rotational speed. For handling qualities work, 1P modes are most important. Hence, when approximating a power spectral density function using the RFT approach, it is most important to accurately model the first two peaks in the power spectral density function (a low frequency approximation). To capture the first two peaks in the the power spectral density function a third order turbulence filter is employed where the natural frequency of the turbulence filter is chosen to be the frequency of the second peak in the power spectral density function and the damping of the filter system is given by

$$\zeta = \frac{1}{2Q} \quad (39)$$

In equation 39, Q is the amplitude of the first spike in the power spectral density function. The filter gain is chosen to match the dc-gain characteristics of the numerically computed power spectrum.

RESULTS

This section primarily compares the helicopter response results obtained using the RFT model and the space-fixed turbulence model.

Figure 2 shows the spectral density of vertical turbulence as experienced by a 0.7R blade station according to RFT and space-fixed formulations for $L/R=4$, that is when the turbulence scale length L is four times the rotor radius. It is significant that the turbulence spectral density has sharp peaks at 1P, 2P, 3P, etc. It is equally significant that the conventional space-fixed distribution fails to capture these peaks. The consequence of the presence or absence of these peaks on an isolated rigid blade flapping response is shown in Figure 3. The blade is flexibly hinged at the hub center and a Lock number of 8 is used. Since the rigid blade can respond only to 1P variation in the excitation, the strong peak at 1P in Figure 3 for the case of RFT is noteworthy. Equally noteworthy is the fact that the occurrence of such response peaks can not be captured by the space-fixed turbulence model.

The effect of turbulence on the Black Hawk helicopter response is considered next using a generic blade element analysis flight simulation program [9]. The helicopter is initially trimmed for zero wind hover. Then with the controls held fixed and with the flight control system turned off, the helicopter response due to turbulence excitation is obtained.

For the Black Hawk helicopter, the rotor diameter is 53.66 ft and the thrust coefficient (C_T) in hover is 0.00532. The turbulence scale length to rotor radius (L/R) is set to 1. For these values, the power spectral density function of the RFT is obtained by taking the fast Fourier transform of the autocorrelation function of equation 31 and the same is shown in Figure 4. As expected, the RFT spectral density function has sharp peaks at 1P, 2P, 3P, etc. Following the procedure described in the previous section, a third order filter is designed to approximate the first two peaks in the power spectral density function of the RFT.

With turbulence intensity set to 10 ft/sec, the sample functions of the RFT and the space fixed cases are obtained and the same are shown in Figure 5. It is interesting to note that, in general, the sample function for the RFT exhibits much larger peak-to-peak amplitude as compared to that of the space fixed case. The helicopter response to turbulence is obtained by assuming that the turbulence is represented by the sample functions of Figure 5. The effect of turbulence on the flap response of a reference blade is shown in Figure 6, wherein the change in flap response from trim is plotted versus time. From Figure 6, it is clear that the blade flap response for the RFT case is significantly different from that of the space fixed case.

The body accelerations and normal velocity in the body axes frame of reference are shown in Figures 7 through 10. It is to be noted that the body axis system used in this study has its x-axis to the front, y-axis to the right, and the z-axis down. The effect of turbulence on the body normal acceleration response is shown in Figure 7. The body normal acceleration response is strikingly different for the RFT case as compared to that of the space fixed case. The peak-to-peak amplitude of the normal acceleration is much larger than that of the space fixed case. The difference in response between the two cases, i.e., RFT and space fixed cases, highlights the necessity of treating turbulence in a rotating frame of reference for helicopter applications. The body longitudinal and lateral accelerations are shown in Figures 8 and 9, respectively. Though the general level of magnitude of longitudinal and lateral accelerations are small compared to the normal acceleration response, it is clear from Figures 8 and 9 that these accelerations are quite different for the RFT case as compared to the corresponding accelerations for the space fixed turbulence. The body normal velocity response is shown in Figure 10 from which it is clear that the normal velocity response is significantly different for the RFT case as compared to that of the space fixed case.

In order to assess the effect of turbulence scale length on the helicopter flight mechanics, the Black Hawk helicopter response simulation is repeated for a turbulence scale length (L/R) of 10. The change in flap response from trim of the reference blade due to vertical turbulence with $L/R = 10$ is shown in Figure 11 and the body normal acceleration response is shown in Figure 12. Though the turbulence

Intensity is the same, the general magnitude of response for the $L/R = 10$ case is reduced as compared to that of the $L/R = 1$ case. Also, from comparison of Figures 13 and 14 of the $L/R = 10$ case with the corresponding figures of $L/R = 1$ case (Figures 6 and 7), it is clear that the difference in response between the RFT and the space fixed case is reduced as L/R is increased. As noted in the introduction, with increasing L/R , the difference in responses between the RFT and the space fixed cases decreases.

CONCLUSIONS

It has been known for a long time that near-the-ground hovering in turbulence causes a loss of performance requiring great pilot skill and it causes additional loads and vibrations. A treatment of this phenomenon using the concept of RFT demonstrates the following:

1. blade response as well as the body response to turbulence excitations is strongly affected by RFT, and

2. the conventional space-fixed description fails to capture those effects.

Thus, the present treatment of turbulence in the rotating frame provides a means of describing turbulence effects on low frequency blade response and helicopter handling qualities both qualitatively and quantitatively.

REFERENCES

- [1] Dahl D.E., Faulkner A.J., "Helicopter Simulation in Atmospheric Turbulence," *Vertica*, Volume 3, pp. 65-78, 1979.
- [2] Carico D., McCallum K., Higman J., "Dynamic Interface Flight Test and Simulation Limitations," Presented at the 11th European Rotorcraft Forum, London, England, Paper Number 100, September 1985.
- [3] Gaonkar G.H., "Gust Response of Rotor and Propeller Systems," *Journal of Aircraft*, Volume 18, Number 5, pp. 389-396, May 1981.
- [4] Gaonkar G.H., "Random Vibration Peaks in Rotorcraft and the Effects of Nonuniform Gusts," *Journal of Aircraft*, Volume 14, Number 7, pp. 68-76, Jan. 1977.
- [5] Gaonkar G.H., Hohenemser K.H., "Flapping Response of Lifting Rotor Blades in Atmospheric Turbulence," *Journal of Aircraft*, Volume 6, pp. 496-503, November-December 1969.
- [6] Gaonkar G.H., "A Perspective on Modeling Rotorcraft in Turbulence," *Probabilistic Engineering Mechanics*, Volume 3, Number 1, pp. 36-42, 1988.
- [7] Kristensen L., Frandsen S., "Model for Power Spectra of the Blade of a Wind Turbine Measured from the Moving Frame of Reference," *Journal of Wind Engineering and Industrial Aerodynamics*, Volume 10, pp. 249-262, 1982.
- [8] Anderson M.B., Garard A.D., Hassan U., "Teeter Excursions of a Two Blade Horizontal-Axis Wind-Turbine Rotor in a Turbulent Velocity Field," *Journal of Wind Engineering and Industrial Aerodynamics*, Volume 17, pp. 71-88, 1984.
- [9] Howlett J.J., "UH-60A Black Hawk Engineering Simulation Program: Volume I - Mathematical Model," NASA CR-166309, 1981.
- [10] McFarland R.E., "Turbulence Filters at NASA Ames Flight Simulation Laboratory," NASA Ames Internal Report, March 1984.

ACKNOWLEDGEMENTS

We wish to acknowledge the help received from Mark Costello and Jamshed Riaz during the course of this study. This work is performed under the NASA-Ames University Consortium Grant No. NCA2-266.

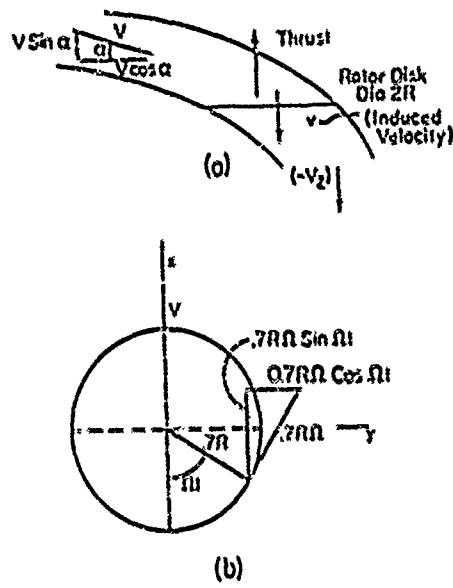


Figure 1. Rotor Disk Velocity Diagram.

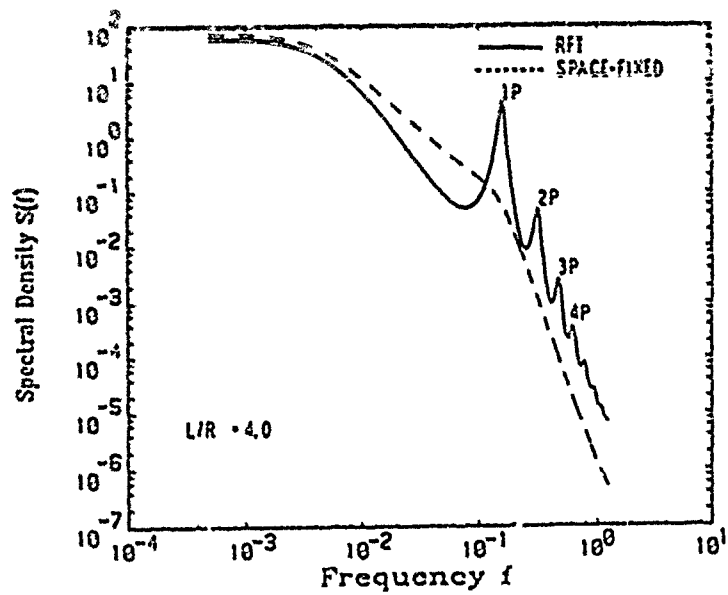


Figure 2. Comparison of RFT and Space Fixed Turbulence Models

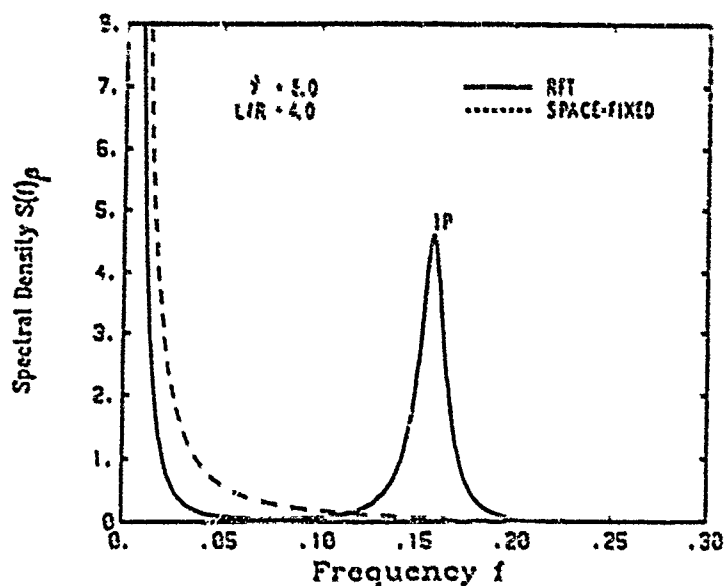


Figure 3. Effect of Turbulence on Isolated Blade Flap Response.

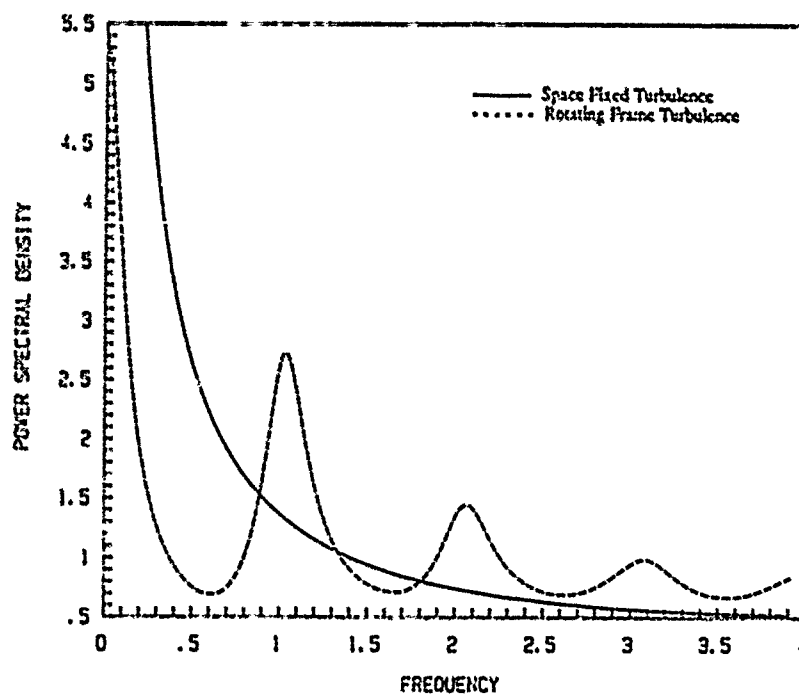


Figure 4. Turbulence Models for the Black Hawk Helicopter in Hover for $L/R = 1$.

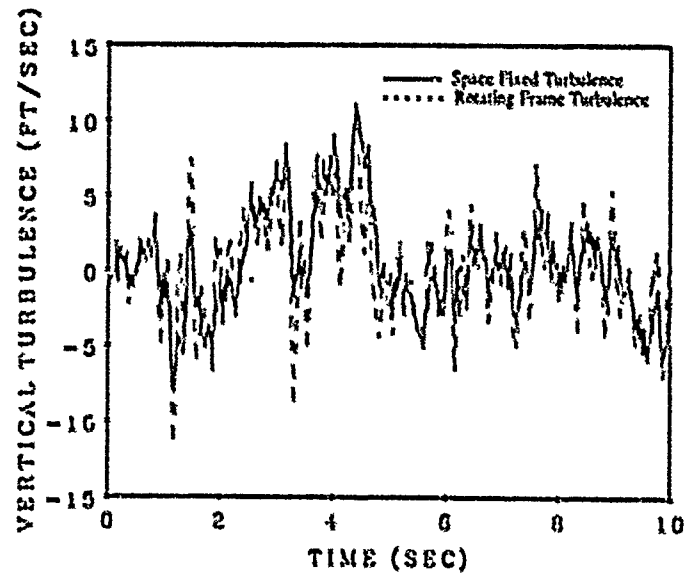


Figure 5. Vertical Turbulence Sample Functions for $L/R = 1$.

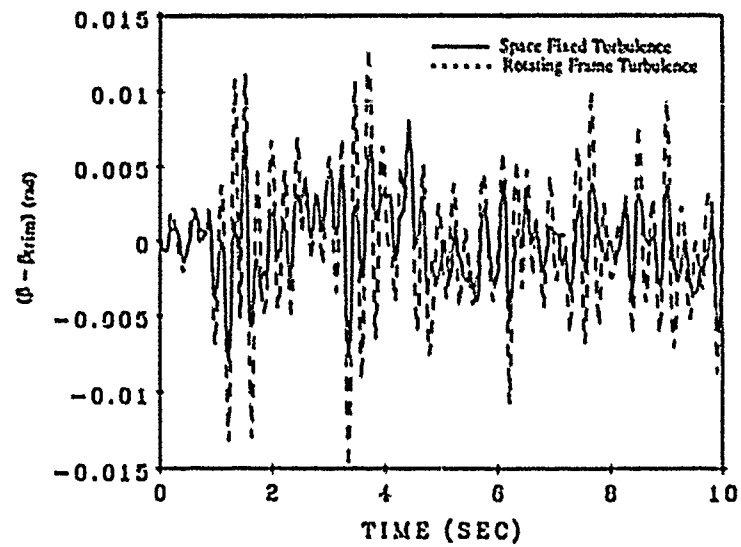


Figure 6. Effect of Turbulence on the Black Hawk Helicopter Rotor Blade Flap Response for $L/R = 1$.

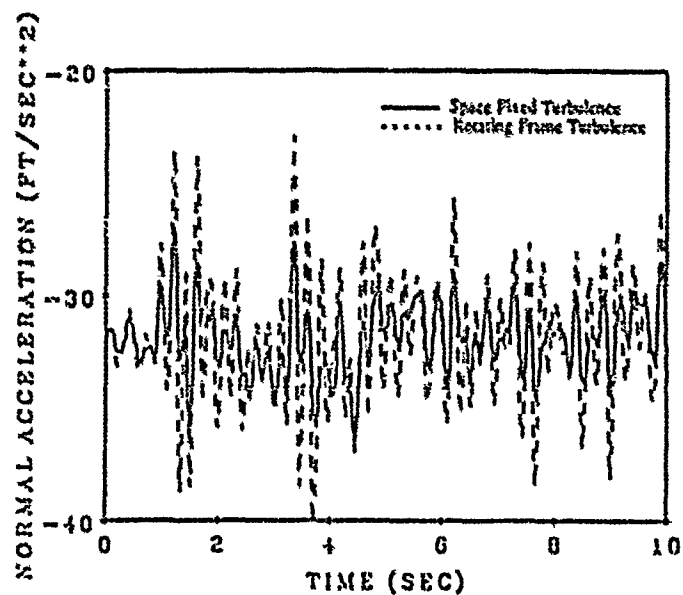


Figure 7. Effect of Turbulence on the Black Hawk Helicopter Normal Acceleration Response for $L/R = 1$.

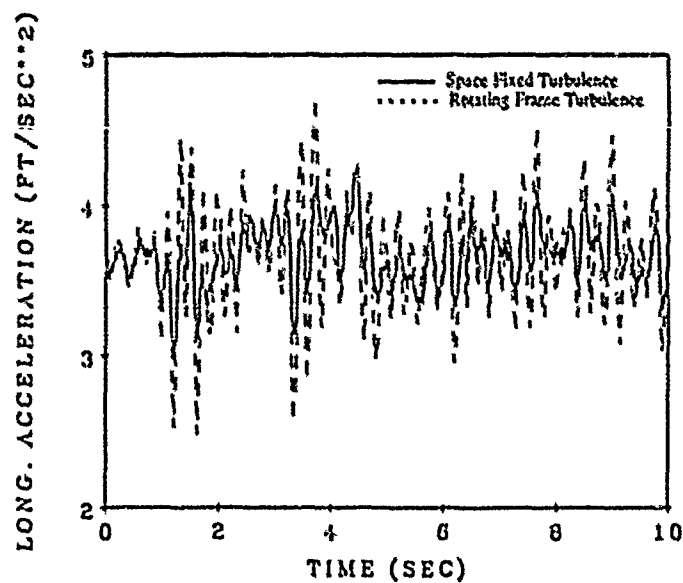


Figure 8. Effect of Turbulence on the Black Hawk Helicopter Longitudinal Acceleration Response for $L/R = 1$.

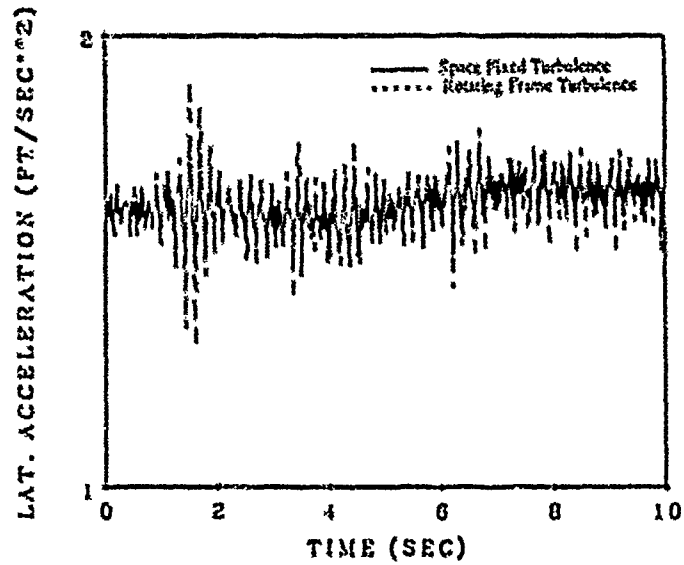


Figure 9. Effect of Turbulence on the Black Hawk Helicopter Lateral Acceleration Response for $L/R = 1$.

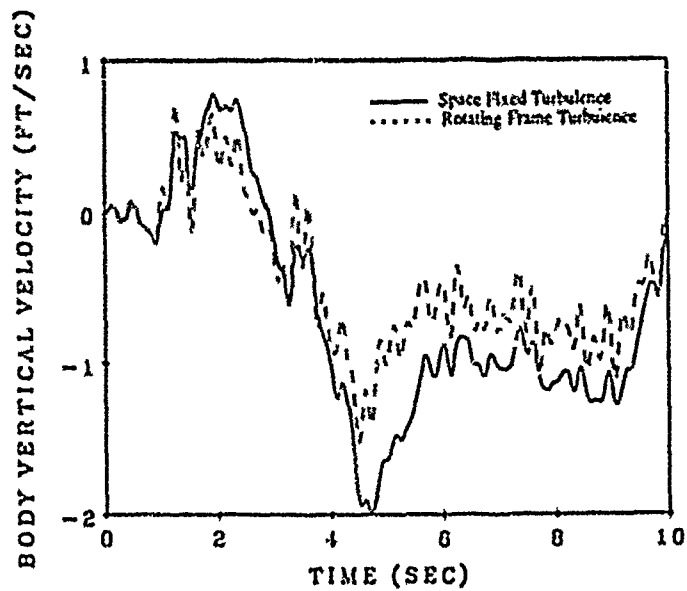


Figure 10. Effect of Turbulence on the Black Hawk Helicopter Body Vertical Velocity Response for $L/R = 1$.

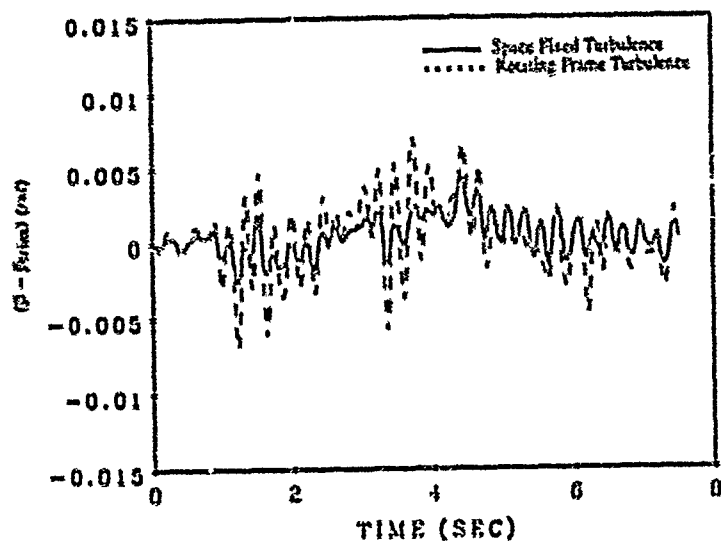


Figure 11. Effect of Turbulence on the Black Hawk Helicopter Rotor Blade Flap Response for $L/R = 10$.

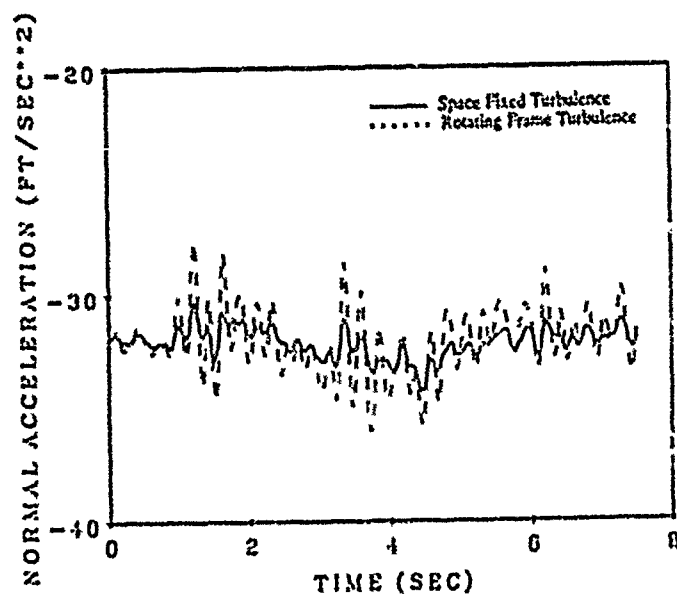


Figure 12. Effect of Turbulence on the Black Hawk Helicopter Normal Acceleration Response for $L/R = 10$.

Measurements of Horizontal Visibility in the Lowest 300 m over Northern Germany

R. Roth
A.H. Sinner
Institut für Meteorologie und Klimatologie der Universität Hannover
Herrnhäuser Straße 2
D-3000 Hannover 21
Federal Republic of Germany

Summary

In order to establish a climatology of the vertical structure of horizontal visibility in the lowlands of Northern Germany continuous measurements were carried out on a radio tower at six different levels up to 300 m above the ground for two and a half years between 1982 and 1985. Ten minute mean values of horizontal visibility, temperature and dewpoint at each level were recorded automatically as well as the cloud ceiling up to 1500 m above ground. For selected weather situations an additional high resolution vertical sounding system supplied more detailed data on the vertical structure.

A statistical analysis of the data was performed showing that there is a relationship between typical patterns of the diurnal variation of the vertical visibility profile and the large scale weather situations in Middle Europe classified according to schemes well established in meteorology.

Special cases have been examined to study the variation of the vertical visibility profile during fog formation, during the passage of atmospheric fronts and in cases of rapid visibility increases and decreases.

The physics of visibility

First of all, an object is only visible by its contrast to the surroundings. However, there is a difference if an object radiates light by itself, but those cases are not considered here.

By definition the range of horizontal visibility is the distance up to which a black object which is large enough and situated just above the horizon shows a contrast to the light which comes from the sky. Since the radiation of the sky is built up by scattered solar light the contrast between sky and object decreases as a function of the amount of light scattered within the column of air between the object and the observer.

The scattering elements for the visible light in the atmosphere are the molecules of oxygen, nitrogen and other gases of the air as well as aerosol particles. The first scatter according to the scatter law of Rayleigh while the second scatter in a different manner described first by Mie. Rayleigh-scatter shows no special variation according to the synoptic weather situation. It only limits the range of horizontal visibility to about 350 km. Mie-scattering is far more interesting because the aerosol concentration within the atmosphere is highly variable and the same is true for the material those particles are built of and the size they have. So within continental air masses the aerosol concentration is usually higher than within maritime air masses.

Furthermore the size of the aerosol particles shows a relation to the relative humidity - at least in the range between 80 and 100 %. In this range of the relative humidity the size of the aerosol particles increases due to the aggregation of water and therefore the visibility decreases. Since aerosol particles have a far larger density than the surrounding air they show another distribution with height than the air itself. Only in the case of a well mixed planetary boundary layer (PBL) the vertical aerosol gradient will be relatively small. For more details of the aerosol physics and the theory of visibility reference is to be made to classical textbooks.

By these facts it is clear that weather affects the horizontal visibility as we all know. The most effective influence on the visibility is exerted by the condensation of water vapour, that is the formation of fog and its disappearance.

The scatterometer

Since the aerosol concentration may be as high as several thousand particles per litre and since as a first approximation we may assume that the aerosol concentration and its spectral distribution mainly vary with height and less in the horizontal directions we may make the assumption of horizontal homogeneity. Therefore the horizontal range of visibility can be measured locally in a rather small scattering volume. This may be as small as a few litres and by measurements in this small volume visibility ranges up to 50 km can be measured (1).

In Fig.1 the scatterometer designed by Ruppertsberg is shown. Additionally to the commercially available instrument the heating of the optical system was improved so that there were no difficulties to operate it during wintertime.

The site

Six instruments of that type were used to measure a vertical profile of the horizontal visibility at a rural site in Northern Germany. The instruments were located at the heights of 2, 9, 60, 133, 223 and 297 m above the ground at a mast of a radio transmitter station. The coordinates of the site near the village of Sprakensehl are $52^{\circ} 48' N$ and $10^{\circ} 12' E$. This location of the site is given in Fig. 2, and the cross section (Fig. 3) showing the height of the terrain above sea level and the height of the tower demonstrates the relative flatness of the area.

In addition to the visibility measurements temperature and humidity were measured at the same heights. During some special observation periods the profiles of wind, temperature and humidity were also measured in 5 m vertical intervals by a tethered sonde system operated with a cable lift from the top of the mast down to the bottom. The horizontal distance of this system from the tower was for the most part of the entire altitude range large enough so that there was no significant influence by the tower itself. The site, the data acquisition system and the results of the investigation are described in detail by Pletzer (2).

The data

The time of operation of the system was from Sept '82 until May '85. The scanrate was 25 times within 10 minutes and the data were digitized immediately. Mean values for each 10-min period were recorded as well as maxima and minima. Furthermore for each data block covering 10 min the ceiling of clouds lower than 1500 m were recorded, both mean values and extrema.

The data were preprocessed at the measuring site and the status of the data acquisition system was monitored via phone and a modem. The phone also served for the data transfer to the institute at Hannover. For redundancy purposes all the mean values were also printed at the measuring site.

Results

First we shall look at typical vertical profiles of the horizontal visibility. In Fig. 4 the profiles of visibility, temperature and relative humidity within a well mixed daytime planetary boundary layer are shown, and in contrast in Fig. 5 nighttime profiles in a stable PBL are presented. In the first case the relative humidity increases with height and balances therefore the only slightly decreasing aerosol concentration in the well mixed planetary boundary layer so that the effect on the visibility is only very small, i.e. the visibility changes only little with height. During a night with clear sky the visibility is strongly affected by the height of the PBL which extends within the lowest 100 m. Below the inversion the relative humidity is rather high and so the visibility is low and even fog may form. Above the inversion the relative humidity is very low due to subsidence (in case of a high pressure system). In addition the subsidence rate of about 1 cm/s means that during the nighttime hours air which originally was situated a few hundred meters above will come down to the top of the inversion layer. Therefore the daytime aerosol gradient is increased above the inversion. For this reason the visibility increases during the night in the layers above the PBL. This case is typical for clear nights.

Because sometimes the vertical extension of the layer with low visibility is less than 100 m, the ground can be seen from an airplane flying at heights well above the PBL. However, when descending to land the horizontal visibility may be so poor that the landing operation is possible only by instrumental guidance. In one of those nights a pilot could see an airfield over a distance of more than 50 km when at the same time he was told that the visibility was too poor for landing.

Beneath a low cloud cover the visibility may decrease right from the bottom up to the ceiling level as shown in Fig. 6. But this only happens if aerosol concentration within the air is rather high. At high latitudes above water or snow surfaces situations may be observed, where the visibility is very good in the whole vertical range between ground level and cloud ceiling even if the relative humidity is very high.

For a night with ground based fog the development of the range of visibility with time is shown in Fig. 7. Here again the increase of visibility above the PBL can be seen very clearly. Later on in the morning when the mixing starts again the visibility in 300 m height decreases while at the same time it increases in lower heights. In Fig. 8 a nighttime situation with clear sky is shown when fog has formed. Here the subsidence is well documented by the increase of the temperature and the decreasing humidity above the PBL. Later on together with the formation of fog the windspeed increased and therefore the whole pattern changed.

A statistical analysis for the onset and termination of fog is presented in Fig. 9 and Fig. 10. Since these cases are not all the very same only the basic features of the typical structures are to be seen. Above the fog visibility increases during the first hours after the formation of fog, while visibility decreases well above the fog layer when the fog vanishes by surface heating.

A statistical analysis has also been done for cases of weather front passages. The results are shown in Fig. 11 (warm fronts, 7 cases) and Fig. 12 (cold fronts, 17 cases). In Fig. 13 an example is shown for a situation when the Sprakensehl site was within a warm sector, i.e. the area between the warm front and the cold front, for a few hours only. Again the typical structure of the visibility records during a frontal passage can be seen.

Next the results of the overall statistical analysis of the diurnal time behaviour of the vertical distribution of visibility in relation to summer (01.04.-30.09.) and winter (01.10.-31.03.) season and typical synoptic pattern is presented. The large scale weather patterns were categorized after a scheme suggested by Hess and Brezowsky (3). The combination of several of these synoptic weather patterns into classes has been done after a very careful investigation of the daily variation of visibility, of the vertical gradient of visibility and of the mean range. In Tab.1 and Tab.2 the grouping according to the synoptic weather conditions is given. For each group the reference to the figures where the composites are shown is added. The tables also indicate the number of cases. The wind directions in Tab.1 and Tab.2 are only to give a rough idea of the situation. The index a or z stands for anticyclonal or cyclonal geostrophic winds. The main structure of the results presented in the Fig.14a,b to 23a,b is summarized in Tab.3. The Fig.14a,b to 23a,b present the composites of the daily variation of the horizontal visibility for the heights given above. For each of these composites also the ceiling of clouds below 1500 m is added.

The material presented here is the only available for vertical profiles of horizontal visibility for Northern Germany on a nearly climatological basis. The statistics shown explain that the range of horizontal visibility and its vertical profile may well be grouped according to the synoptic situation and in relation to mesoscale structures such as fronts. The question under which circumstances either fog or dew will form in clear nights was not investigated up to now. However, there are some hints that this may be controlled by the divergence within the Föhl, which is related to the geostrophic vorticity. Hopefully this problem can be investigated in the future.

References

- (1) Ruppertsberg, G.H.: Registrierung der Sichtweite mit dem Streulichtschreiber. Beiträge zur Physik der Atmosphäre, 37, 1964, p.252-263.
- (2) Pietzner, B.: Die Vertikalstruktur der Horizontalsicht im Höhenbereich bis 300 m über Grund in Norddeutschland. Berichte des Instituts für Meteorologie und Klimatologie der Universität Hannover, 26, 1986.
- (3) Hess, P., Brezowsky, H.: Katalog der Großwetterlagen. Berichte des Deutschen Wetterdienstes, 15, No.113, 1969.

Tab.1: Definition and Statistics for Typical Visibility Patterns (Summer).

Number	Synoptic Situation	Number of Cases	Shown in Figure
1	TRM, IM, BM, TB (SW-Winds)	111	14
2	TRM, HB, NWa (NW-Winds)	72	15
3	Wz, Wa (W-Winds)	44	16
4	TM (variable)	29	17
5	NWz (NW-Winds)	12	18

Tab.2: Definition and Statistics for Typical Visibility Patterns (Winter).

Number	Synoptic Situation	Number of Cases	Shown in Figure
1	Wz, Wa, NWa (W/NW-Winds)	103	19
2	HB, BM, SWa, IM (SW-Winds)	81	20
3	SWz, WS (SW/W-Winds)	34	21
4	TB, Sa (S-Winds)	24	22
5	NWz (NW-Winds)	16	23

Tab.3: Typical features of the Visibility for the Classes Given in Tab.1 and Tab.2.

Group		Variation of the Horizontal Visibility with Time and Height
Summer	Winter	
1	2	Visibility rapidly increasing with height during the nighttime, weak increase during daytime.
2		Weak vertical gradients, but highly variable range between day and night, about sinusoidal.
3	1	Weak vertical gradients, range strongly increasing during the morning, slowly decreasing in the afternoon.
4		Weak vertical gradient during the night, during the day decreasing range with height, low visibility.
5	5	Visibility highly variable due to convective activity and clouds.
	3	Mediate increase of visibility with height, nearly no change with time, fair visibility.
	4	Weakly increasing with height, no change with time, poor visibility.

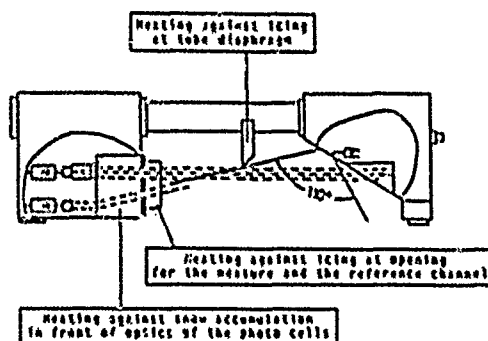


Fig.1 Position of the additional heating elements of the visibility meter

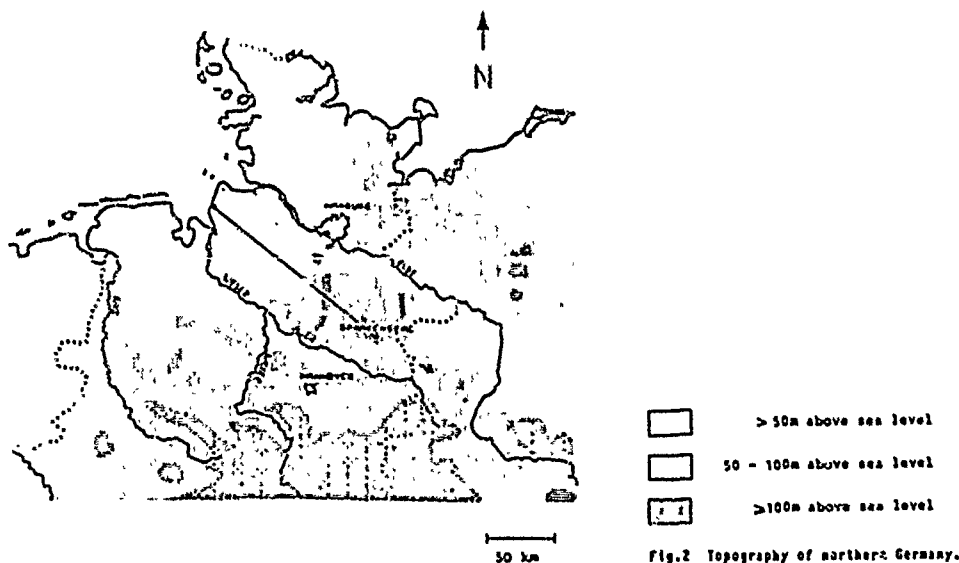


Fig.2 Topography of northern Germany.

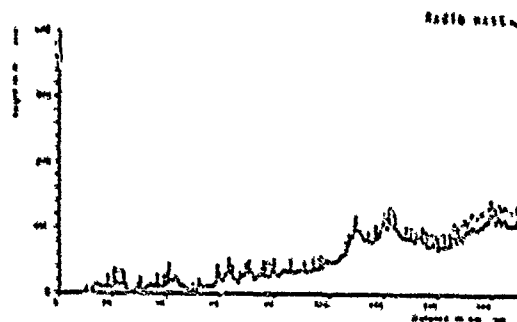


Fig. 2 Topographical cross section from the north sea to the radio mast at Spratonschl.

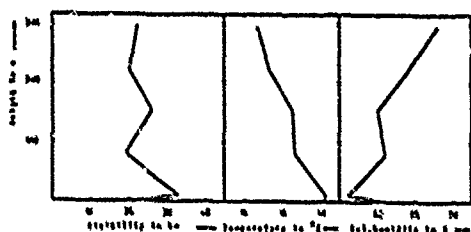


Fig. 4 Vertical profiles of visibility, temperature and relative humidity in an unstably stratified atmosphere (27 June 1981, 12.00 CET).

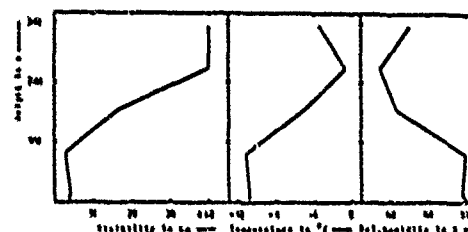


Fig. 5 Vertical profiles of visibility, temperature and relative humidity in an inversion type weather situation (11 Jan 1985, 12.00 CET).

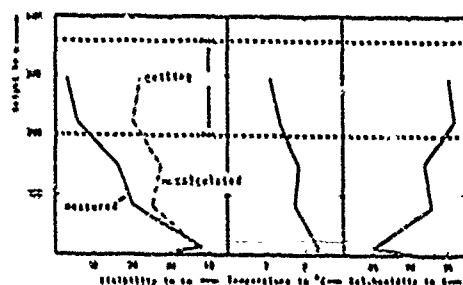


Fig. 6 Vertical profile of visibility (measured and computed after the formula below), temperature and relative humidity in a maritime breeze (4 July 1984, 01.00 CET). The dotted lines show the minimum ceiling during a 10-minute interval.

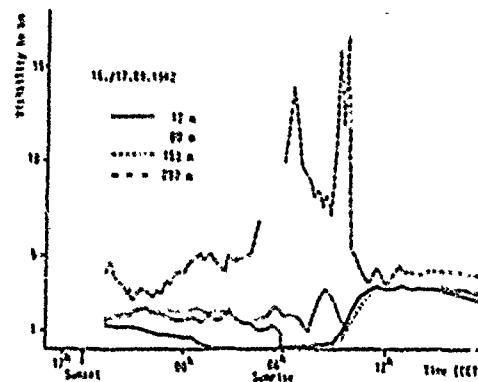


Fig. 7 Visibility data for different heights measured on 16-17 Sep 1982 at Spratonschl.

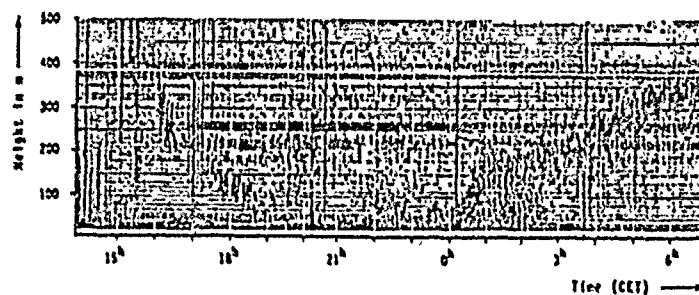


Abb. 24 Sodar measurements on 29-30 Oct 1983.

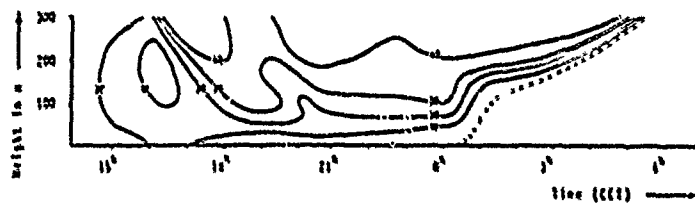


Abb.8a Isopleths of visibility in km (29-30 Oct 1983).

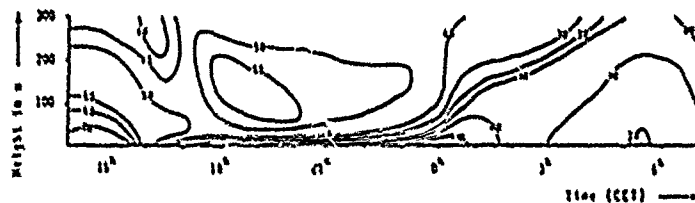


Abb.8b Isopleths of temperature in °C (29-30 Oct 1983).

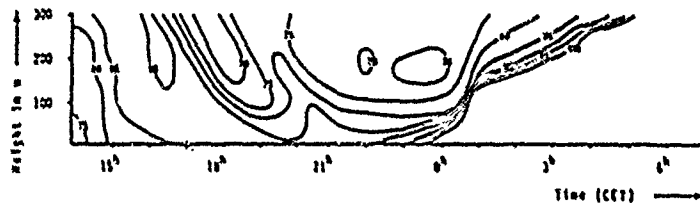


Abb.8c Isopleths of relative humidity in % (29-30 Oct 1983).

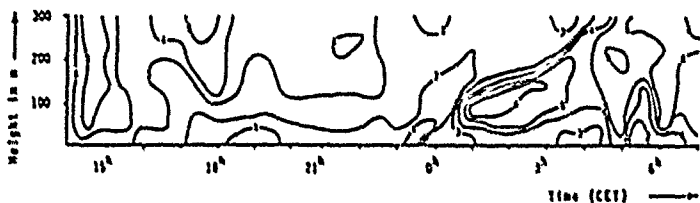


Abb.8d Isopleths of wind speed in m/s (29-30 Oct 1983).

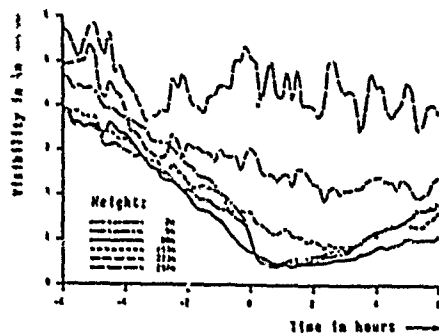


Abb.9 Mean time variation of the vertical profile of visibility during fog formation.

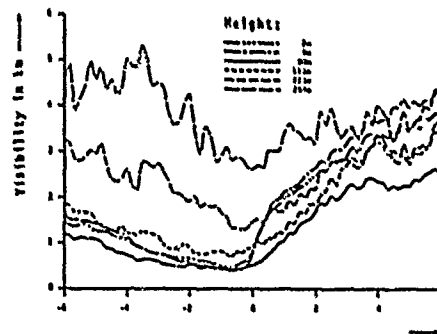


Abb.10 Mean time variation of the vertical profile of visibility during fog dispersal.

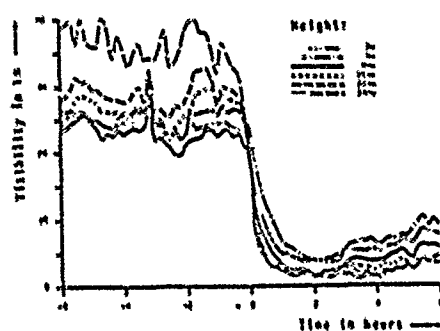


Abb. 11 Mean time variation of the vertical profile of visibility during the passage of a warm front.

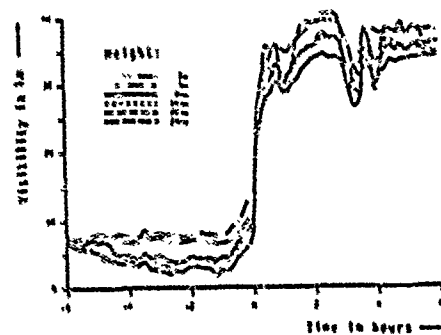


Abb. 12 Mean time variation of the vertical profile of visibility during the passage of a cold front.

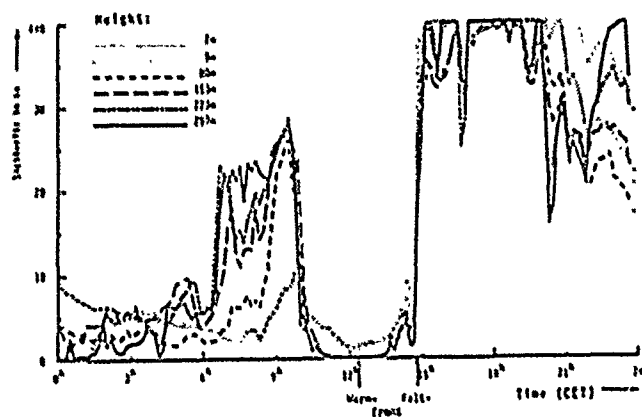


Abb. 13 Time variation of the vertical profile of visibility during the passage of a warm front and a subsequent passage of a cold front on 29 Nov 1983.

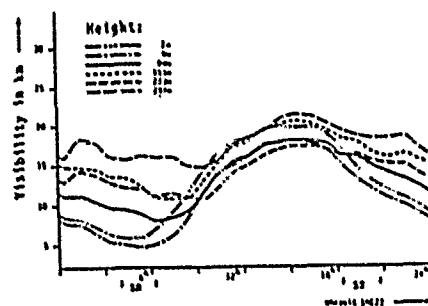


Abb. 14a Summer semi-annual period. Group 1: TRV, MN, BN, TB. Mean diurnal variation of the visibility profile.

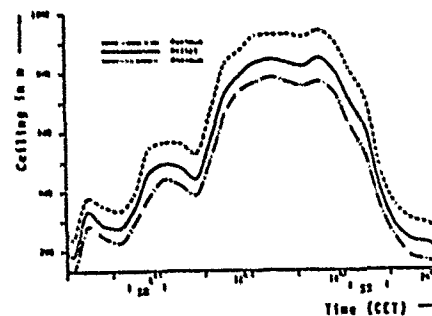


Abb. 14b Summer semi-annual period. Group 1: TRV, MN, BN, TB. Mean diurnal variation of ceiling and the diurnal variation of minima and maxima of ceiling registered during hourly intervals.

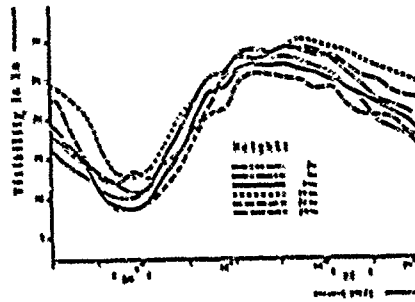


Abb. 11a Summer semi-annual period, Group 2: 18M, 18S, 18V. Mean diurnal variation of the visibility profile.

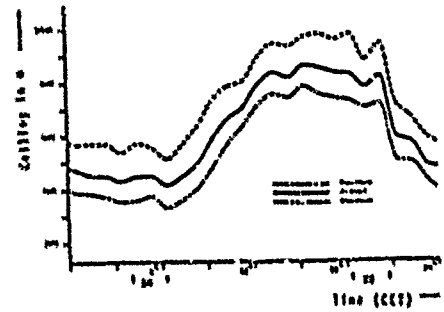


Abb. 11b Summer semi-annual period, Group 2: 18M, 18S, 18V. Mean diurnal variation of ceiling and the diurnal variation of minima and maxima of ceiling registered during hourly intervals.

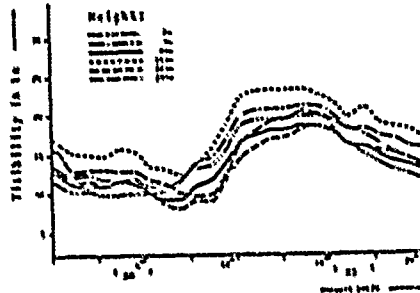
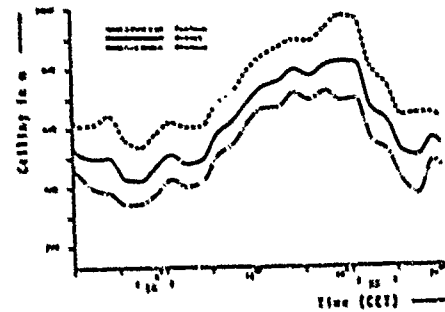


Abb. 12a Summer semi-annual period, Group 3: 12, 12S, 12V. Mean diurnal variation of the visibility profile.



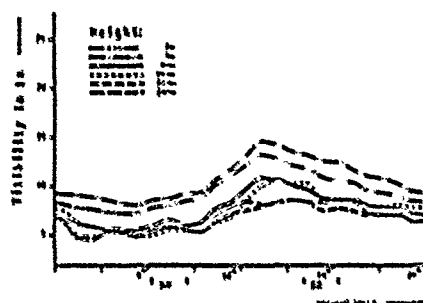


Abb.19a Winter semi-annual period. Group 1: W2, V2, NW. Mean diurnal variation of visibility profile.

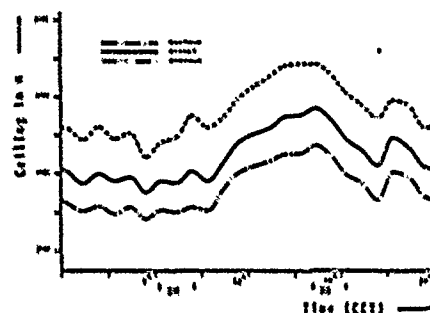


Abb.19b Winter semi-annual period. Group 1: W2, V2, NW. Mean diurnal variation of ceiling and the diurnal variation of minima and maxima of ceiling registered during hourly intervals.

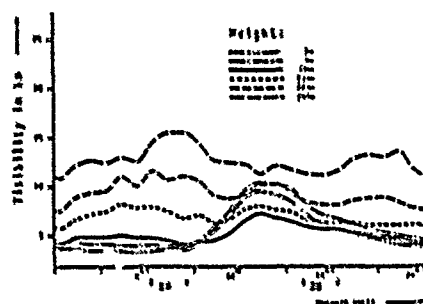


Abb.20a Winter semi-annual period. Group 2: W3, V3, NW. Mean diurnal variation of visibility profile.

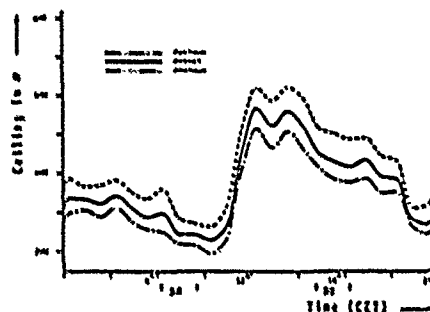


Abb.20b Winter semi-annual period. Group 2: W3, V3, NW. Mean diurnal variation of ceiling and the diurnal variation of minima and maxima of ceiling registered during hourly intervals.



Abb.21a Winter semi-annual period. Group 3: W4, V4, NW. Mean diurnal variation of the visibility profile.

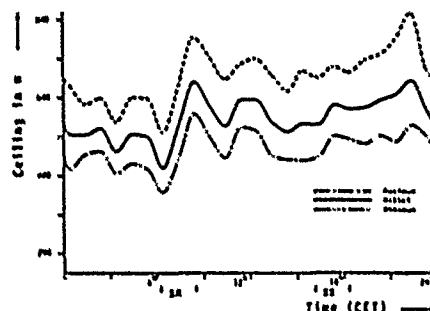


Abb.21b Winter semi-annual period. Group 3: W4, V4, NW. Mean diurnal variation of ceiling and the diurnal variation of minima and maxima of ceiling registered during hourly intervals.

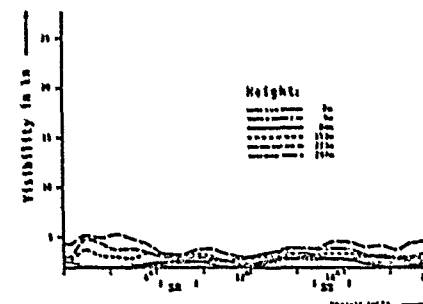


Abb.22a Winter semi-annual period. Group 4: W5, V5, NW. Mean diurnal variation of the visibility profile.

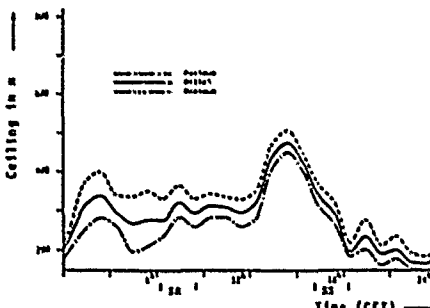


Abb.22b Winter semi-annual period. Group 4: W5, V5, NW. Mean diurnal variation of ceiling and the diurnal variation of minima and maxima of ceiling registered during hourly intervals.

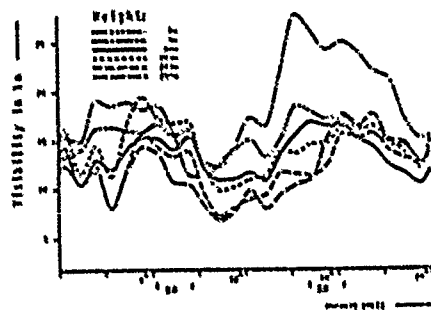


Abb.23a Winter semi-annual period, Group 51 MVZ.
Mean diurnal variation of the visibility profile.

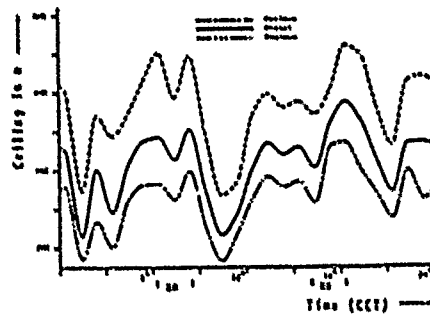


Abb.23b Winter semi-annual period, Group 51 MVZ.
Mean diurnal variation of ceiling and the diurnal
variation of minima and maxima of ceiling registered
during hourly intervals.

IMAGING PROBABILITIES, GEOMETRY AND ERGONOMICS IN LIMITED VISIBILITY HELICOPTER OPERATIONS

Robert H. Wright, Ph.D.
U.S. Army Research Institute Aviation R&D Activity
Fort Rucker, Alabama 36362-5334
USA

SUMMARY

Helicopter pilots using night vision systems have a low probability of seeing the best visual cues that are available for flight control. Even with good visual range, the forward view of current night vision systems looks where visual cues are geometrically insensitive to changes in vehicle states and motions. At terrain flight heights, best visual cues reflecting vehicle states and motions are located directly below the helicopter. As visual range attenuates, the best vision of the terrain retreats toward the same angles below the helicopter where the best flight control cues are found.

Image *z* hydraulic cues of night vision systems both preclude effective use of normal spatial-motion visual perception, which quickly processes the entire visual array in parallel with no or very low workload. Downward viewing display concepts should allow normal spatial-motion vision to function effectively, resulting in major reductions in pilot workload and training requirements, and safer flight control with poor visibility.

At terrain flight heights most tactical visual cues are visually compressed in elevation angle within just a few degrees at the horizon, but are widely dispersed in azimuth. Terrain obstacles to safe flight are also located within a few degrees of the horizon, but are well defined in azimuth by the velocity vector. It is concluded night vision systems could be improved by designing to better exploit geometric characteristics of visual cues and normal pilot spatial-motion visual processes.

INTRODUCTION

Helicopter pilot night vision systems enable terrain flight missions in limited visibility conditions that are not feasible with direct unaided vision. However, these systems impose high pilot workload, stress and fatigue, and require extensive training to develop and maintain proficiency at levels assuring combat effectiveness and flight safety. Attaining mission effectiveness with safety is especially demanding of pilots when visual range becomes severely limited by atmospheric attenuation.

Current helicopter night vision systems represent design compromises among the mission visual requirements for flight control, target acquisition and target engagement. The compromises have resulted in systems with characteristics which are not highly effective for any of the requirements. The system designs suggest the developers were not highly aware of either visual information requirements and characteristics, or the visual and mental processes of the pilots who will apply the systems in combat. Visual range attenuation, in particular, appears to have received little consideration in night vision system design decisions. Consequently, flight control capability can be lost entirely with substantial visual range attenuation, even when relatively good vision of the terrain still exists for some angles of view.

Except for the imaging technology, night vision system designs represent a close approximation to just a simple transfer of a home television picture to the pilot on a panel or helmet display. The sensor and display characteristics that would best satisfy each of the mission visual requirements need to be defined, without home TV constraints, for each of the major environments of day, night and limited visual range. In addition, evaluation criteria need to be defined for analysis and assessment of how well a given design satisfies the mission visual requirements. To the author's knowledge, these best characteristics and evaluation criteria have never been defined and used as guides for the design and development of night vision systems.

Developers of helicopter night vision systems and their improvements need to understand the relationships between vehicle states and motions, and the related changes in images for various sensor directions and fields of view. It appears developers have focused on the "form" aspects of night vision requirements, and virtually ignored the "spatial-motion" information requirements of pilots. Understanding is needed of the effects on acquisition probabilities of angular compression and dispersion of targets and threats, and effects of the interactions between fields of view and the limited duration of viewing opportunities for many tactical cues. This report will address some of these types of relationships, effects and aspects that may not have received systematic consideration in the design decisions of prior night vision system development and improvement efforts. Better reflection of such factors in night vision system designs should have a potential for major improvements in their flying safety, combat effectiveness and associated training requirements.

A thorough ergonomic analysis of night vision systems is not feasible within the allowable length for this paper. However, a few of the more significant ergonomic issues will be noted that relate to effective vision with and use of night vision systems, and to the effects of the extreme psychological stress of combat.

The geometric and ergonomic analyses reported here resulted from an effort to determine the causes for, effects of and approaches for reducing, the high pilot workload and training requirements of night vision systems. Maintaining a safe flight control capability with severe visual range attenuation was a major concern. The variables of line of sight orientation, fields of view and magnification, and sensor mounting and slaving will be considered in terms of effects on probabilities that pilots are provided the best visual cues to support their flying and fighting tasks. Typical night vision system characteristics are assumed. Finally, the conclusions reported apply equally to both intensifier and infrared imaging technology night vision systems.

BACKGROUND

The basic purposes of helicopter night vision systems and aids are to provide pilots an imaging capability during darkness that will enable:

- flight control and navigation
- avoidance of obstacles
- visual acquisition of targets, threats and friendly elements, and
- engagement of targets and threats.

There is a wide variety of factors that are important to designing and using night vision systems as they will serve their purpose in the most effective manner. These include the external environment, night vision system characteristics, vehicle characteristics, the pilot's visual and mental characteristics, and tactical considerations. In this section a few of these factors are briefly reviewed as an orientation for the reader who may be unfamiliar with night vision system helicopter operations or ergonomic aspects of their application.

Causes of Poor Visibility. Three causes of poor visibility exist that have substantially different consequences on helicopter terrain flight operational capabilities and night vision system requirements. One is darkness with little or no atmospheric attenuation of visual range. This forces use of night vision systems. A second is attenuation of visual range by contrast reducing atmospheric particulates such as clouds, fog, rain, dust, snow, smoke, haze and mist. They occur and will adversely affect operational capabilities in both daylight and darkness, but have a greater adverse effect when night vision systems are used. A third form of poor visibility peculiar to helicopters is the sudden, often complete masking of any vision of the terrain that can result from clouds of dust, snow or mist raised by the outflowing rotor downwash as the helicopter nears or maintains a hover in ground effect. It often forces a rapid switch to instrument flight control, or continuing a landing with no, or very poor, visual reference to the ground.

Characteristics of Night Vision Systems. There are two basic types of night vision systems: image intensifiers and infrared imagers. Image intensifiers use a photon amplification process over wavelengths covering the visible and near infrared, with peak sensitivities in the far red or infrared just beyond direct human visual sensitivity. Image intensification can be built into or coupled to a TV camera, but in helicopters is most often found in the form of night vision goggles attached to the pilot's head or helmet. Infrared imagers are more complex systems that detect temperature differences between objects. Their sensors usually are mounted on the nose, top or mast of the helicopter, and their images provided on panel displays, telescopic display units or helmet displays. Sensors may be manually aimed, slaved to helmet angles, or automatically stabilized in one or more axes. The pilot night vision system in the U.S. AH-64 Apache helicopter uses a nose mounted infrared sensor slaved to pilot helmet angles in pitch and yaw, but not roll. Offset of sensors from the center of rotation of the helicopter can produce anomalous image changes with vehicle state changes, which the pilot has to learn to recognize and compensate. Typical fields of view are circular diameter of 40 degrees for night vision goggles, and 30 by 40 degrees for other pilot sensors. These fields of view block most of the peripheral visual cues helicopter pilots believe they use extensively for flight control with direct vision in daylight.

Visual Changes in Flight Control. In very simplified terms, a helicopter flies because of lifting forces on the mast produced by the turning rotors. To accelerate or change position the lifting forces are tilted slightly by varying lift of the rotor at appropriate azimuths for appropriate durations, to produce a lateral or longitudinal component to the lift vector. Direction can be changed by either antitorque forces at the tail rotor, or by banking when forward speed exists. Large pitch or roll attitude changes occasionally may be used for short periods to produce large translational acceleration or deceleration forces, but much smaller angles are the norm for most maneuvers. For hovering, pitch and roll changes will usually be only a few degrees or less, with changes, on average, to shift or maintain a position often involving only a fraction of a degree. Perceiving such small attitude change angles are unlikely with night vision systems, and also unlikely with direct vision in daylight. It is probable the pilot keys on translational rates as his primary visual hover flight control cue, but perceiving these rates is difficult in the typical forward viewing night vision system image.

Visual Processes. Normal human vision combines three different perceptual processes into an integrated whole perception(1). These are:

- (1) a spatial and motion perception process,
- (2) a color perception process, and
- (3) a high resolution form perception process.

Encoding for all three processes occurs in the retina of the eye in a basic form, with no workload or attention involved (1, 2, 3,). Spatial-motion, color and form encoded signals are sent via the optic nerves to several midbrain nuclei, where they are relayed to visual areas of the cerebral cortex, or linked to motor neurons. At the cortical visual areas there are relatively direct links to motor areas and pathways, and also extensive ties to association areas of the cortex. Processing that extracts additional information occurs in both the midbrain and cortex. These basic forms of visual process encoding and their anatomically direct links with motor actions should involve virtually no workload, and be quite resistant to the adverse effects of stress on visual-motor performance.

Spatial-Motion Encoding: The spatial-motion encoding that occurs in the retina consists of a variety of different types of information. Included are nerve signal encoding reflecting the fact of motions of external objects and motions of self, and the directions of these motions. Motions not germane to survival of animals may not be reflected.

Form Masking. The form-like encoding that occurs in the retina and higher brain centers consists of localized (to a few degrees), directionally resolved (to a few degrees), spatial Fourier transform analyzer equivalents of image content. Unless separated by about 10 degrees visual angle or directional orientation differences of more than 15 degrees, forms with similar spatial Fourier transforms will be difficult to distinguish. Continued exposure to a form, especially bright or high contrast form, will mask or reduce sensitivity to a similar nearby form. This has the practical consequence that continued exposure to forms and edge orientations in night vision system symbology will mask or reduce sensitivity to adjacent image objects having similar shapes or edge orientations. Of particular concern is the extensive use of horizontal and vertical edges in symbology, when the dominant characteristics for recognition of obstacles and targets are also horizontal and vertical edges.

Form Recognition Causes Workload: Stress Will Increase. Form recognition is found only in higher animal species, and in humans appears to require attention (infer workload) to the form in combination with memory (infer workload) and some degree of higher mental processing (infer workload) involving association with memory. Form recognition will involve the association areas at the highest level of the central nervous system, the cerebral cortex. Each element in the symbology of night vision systems requires a form recognition process, a comparison of indicated value with memory for the desired value, and often integration with other elements for correct interpretation of vehicle state and needed control actions. Form recognition is not essential for basic helicopter flight control in daylight, but is required for flight control with night vision system images due to their small field of view. The extreme stress of actual combat should adversely affect the form recognition process, especially its memory and higher mental processing aspects.

Spatial-Motion Processes Limited By Night Vision Systems. Helicopter pilots report they use peripheral spatial-motion perceptual processes extensively for flight control with direct vision. They also report the limited field of view of night vision systems precludes normal use of these processes, and forces them to adopt alternative techniques for extracting the information they require for flight control. Pilots state that alignments and relative motions between foreground and background objects (parallax) are major cues used in flight control with direct vision, especially for hovering. These cues are lost when limited visual range masks the background objects from view by reducing their contrast below visual thresholds.

See Before Seen to Survive. Tactics used by all types of military forces include attempting to reduce enemy opportunity for detecting and observing their actions, while improving their own chances for detecting and observing the enemy. A large percentage of combat casualties probably result from successful application of this tactic, when it often enables unopposed attack with very high probability of success. Eighty percent of WW I air-to-air combat kills are reported to be the result of such attacks on unaware victims (4). It is logical to presume unaware victims will continue to account for a large percentage of casualties in both ground and air combat, including helicopters. To minimize chances of becoming unaware victims, helicopter night vision systems need to assure a high probability of rapid detection of both ground and air threats. Who sees whom first will have major impact on outcomes of combat engagements. Soldiers of all ranks fully understand this tactical truth, and weigh it heavily in their tactical decisions. Designers of night vision systems should also give heavy weight to probability of detecting the enemy before he detects us.

Duration of Tactical Visual Cues. A majority of the more critical tactical visual cues are momentary or of short duration. Examples include muzzle flashes, missile firing and burn plumes, short vehicle exposures for observation or weapon firing, and short soldier or vehicle exposures as they quickly move from concealment behind one object to concealment behind another object. Map-of-the-earth flying contributes to short viewing durations because of the masking of vegetation and terrain. A viewing gap must exist through the masking for any possibility of observation, and most will be quite short (5). Vantage points with good views will be used often, but any movement behind the mask will result in short viewing gaps having nearly random directions and durations. These viewing gaps represent opportunities for the enemy to observe us, as well as for us to observe him. If our sensors are not looking in the direction of the gap while it is open, the opportunity for observation will be lost.

RESULTS

The results in large part derive from straightforward geometrical consideration of locations and changes in flight control and tactical visual cues in night vision systems, for terrain flight heights with both good and limited visual range. To minimize complexity it will be assumed that visual range attenuation in poor visibility is a constant linear function, and that the terrain is a flat surface. The actual variation in visual range attenuation and terrain relief characteristics will produce only minor deviation from the results obtained with these assumptions.

Geometric Characteristics. The fundamental geometric relationships that form the basis for most of the results are illustrated in Figure 1, and a set of pertinent values are tabulated in Table 1.

In panel "a" of Figure 1, a profile view of elevation angles is shown, which applies to any relative direction of view. On the right side is sketched a typical night vision sensor 30 degree elevation field of view that is centered on the horizon. It may be noted the lower edge intercepts the terrain surface at a point "1" at a distance several times the viewing height. From the Table 1 values for 15 degrees dip angle, it may be found the terrain distance is 3.73 and the sightline is 3.86 times the viewing height. On the left side of panel "a" are lines separated by 15 or 30 degrees labeled A through E. It may be noted these equal angular separations result in unequal distances on the terrain surface (corresponding to a tangent function), with the last angle to the horizon impossible to represent due to its infinite value.

Panel "b" illustrates a plan view corresponding to panel "a," but illustrating the typical 40 degree azimuth field of view of a night vision sensor. The lower edge of the sensor intersects the terrain surface at the line "1," but the top edge of the sensor and all angles near the horizon will be indeterminate for this plan view. On the left the points corresponding to the 15 or 30 degree angular increments

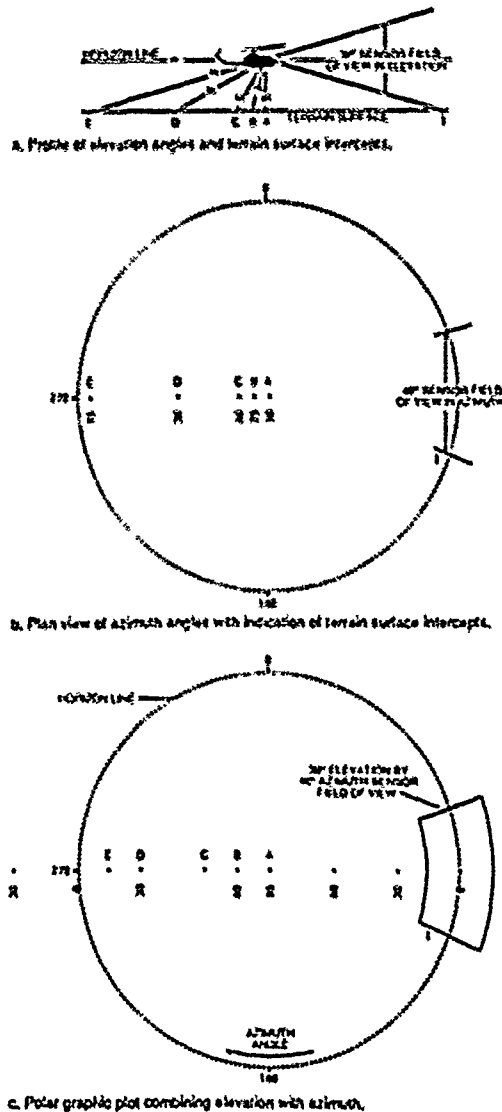


Figure 1. Angular representation of terrain viewing angles.

Head Slaving and Mounting. A helicopter pilot does not fly his head, he flies the helicopter. In view of this obvious fact, one may wonder why he is given sensors slaved to or mounted on his head as the source of information for controlling the helicopter. Although some advantages result from head slaving/mounting, major disadvantages result for acquiring flight control information. Flight control requires knowledge of locus, or more accurately change in locus, of visual cues with respect to helicopter axes. Head slaving/mounting has the effect of adding a large source of noise, or uncertainty, in the locus of visual cues with respect to helicopter axes. The amount of this noise or uncertainty for head angles appears typically to be on the order of 2 to 4 degrees, although at times it may reach 10 degrees or more.

The magnitude of this head angles noise equals, or may exceed by an order of magnitude, the rotational changes required for controlling a helicopter in a hover. It exceeds by one or two orders of magnitude the angular changes that occur in a forward viewing image that correspond with the typical "hover box" of a helicopter.

may be seen to fall at distances from the center equal to those in panel "a." This view accurately reflects azimuths, but provides no information about elevation angles near or above the horizon.

In panel "c" is found a polar plot combining azimuth and elevation angles information, with the center representing the downward vertical (or 90 degree dip angle). The circle represents the horizon, points outside it represent elevation angles above the horizon, and points falling inside it represent the entire viewable terrain surface that lies in the lower hemisphere. It provides equal spacing for equal elevation angles. However, azimuth angle scaling is equal to that for elevation at only one elevation angle, 57.3 degrees from the vertical.

Vision With Range Attenuation. The quality of a visual image of the terrain in poor visibility depends on the angle of view, the degree of range attenuation, and the viewing height. How far and how well one can see the terrain when visual range attenuation exists is an inverse linear function of range to points on the terrain. The points with the shortest sightline range will be seen best, and have the highest probability of being seen at all. The shortest sightline to the terrain is a vertical line below the helicopter. Assuming level terrain, ratio of length of sightlines to the terrain are defined by the secant of the angular difference from vertical. Table 1 shows these ratios for angles indicated both as differences from vertical and dip angle below the horizon.

The increase in sightline distance is seen to increase slowly with increasing angle from vertical. For example, at 25 degrees from vertical sightline has only increased by 10 percent, and at 30 degrees only by 15 percent. One can conclude that if the terrain can be seen at all at the vertical, a large 50 to 60 degree diameter cone of nearly equivalent vision of the terrain will be available. As sightline ratios exceed 150 percent at 40 degrees from vertical and beyond, the attenuation of contrast will begin to preclude terrain vision with severe range attenuation. The actual angle at which effective terrain vision is lost will, of course, depend on the degree of atmospheric attenuation. Whenever significant atmospheric attenuation exists, contrast reduction for any forward viewing sensor will be substantial. At the lower edge of a 30 degree elevation angle sensor centered on the horizon, for example, attenuation will be 386 percent of that for angles directly below.

Table 1

Ratios of Sightline, Surface Distance and Angular Change to Vertical for Various Angles of Regard of the Terrain

Angle From Vertical	Angle of Dip	Ratio of Sightline To Vertical	Ratio of Surface Distance To Vertical	Ratio of Sightline Angular Change*
0	90	1.00	0.00	1.00
10	80	1.01	0.17	0.97
20	70	1.06	0.36	0.88
30	60	1.13	0.57	0.77
40	50	1.21	0.78	0.67
50	40	1.32	0.99	0.57
60	30	1.45	1.20	0.47
70	20	1.60	1.41	0.37
80	10	1.76	1.62	0.27
85	5	18.47	18.47	0.0018
86	4	18.34	18.34	0.0049
87	3	19.11	19.09	0.0067
88	2	26.85	26.84	0.0012
89	1	57.50	57.29	0.0004
89.5	0.5	114.79	114.79	0.0001
89.6	0.4	143.24	143.24	0.00003
89.7	0.3	190.99	190.98	0.00001
89.8	0.2	286.48	286.48	0.00001
89.9	0.1	572.96	572.96	0.000001

* At sightline intercept of surface under projection of a level translational vector

Lack of knowledge of head angles appears to be much less of a problem for head mounted night vision goggles than it is for head slaved sensors such as the FNVs used in the *Adena*. This situation exists in spite of the fact FNVs use a symbol that conveys head angles information which is not available to night vision goggles. The reasons are not entirely clear, but it is suspected the cockpit framing obscures outlines, even though fuzzy with infinity goggles focus, may provide sufficient head angle cues in a natural low workload form. The lack of image offset from the eye with goggles may also contribute.

It should not be inferred that precise knowledge of head angles, or even helicopter angles, are essential for flight control. Over time, as drifts accumulate, velocities relative to the terrain should become evident. Precision hover control, however, should be promoted by visual cues that clearly convey position changes, rates and helicopter angles. Large uncertainties in these cues resulting from head angles uncertainty are certain to reduce hover precision, and require substantial workload in some form to compensate.

The major advantages of head mounting/inlaying are the simplicity of goggle design, and improved quick reaction engagement and crew coordination capabilities. In addition to head and visual cue location uncertainty, disadvantages include (in non-goggle designs), substantial complexity and system cost resulting from head slaving and display, and many fragile components, connections and adjustments that can adversely affect reliability.

Angular Change With Vehicle State Change. The largest angular changes for five of the six degrees of freedom of vehicle state change are found to be located directly below the vehicle. Directly below, angular change for vehicle pitch and roll changes equal the maximum changes for any other direction of view. Angular change directly below for vehicle yaw changes are less than that available at other viewing directions, but will be perceived easily for any practical imaging system. For all three translations, much larger angular changes will occur below the vehicle than at any other angles of view. With translations, the very short range to the terrain at nap-of-the-earth viewing heights emphasizes these angular changes in the downward image relative to other viewing directions. The viewing angles directly below the vehicle, therefore, provide in one location large, easily perceived image angular changes reflecting states of all six degrees of freedom needed for helicopter flight control. This is not true for any other direction of view, including the forward view now used for all night vision systems.

Rotations. There are two types of image change that result from rotations: A rotation or tilt of the entire image, and displacement of objects across the display that increases with separation from the axis of rotation. The image changes resulting from vehicle or sensor rotations can be defined by a set of general change rules and by formulas. The primary change rules and formula are:

No Relative Change Rule: No relative changes occur in the visual array of the world with just sensor rotations (ϕ). Relative positions of all elements in the array remain fixed. The effect of sensor rotation is only that it samples a different part of the fixed visual array.

Change Rules: For vehicle or sensor rotations about an axis of rotation:

- Rate of change in rotation around the axis as pivot.
- Image rotation is equal to vehicle/sensor rotation, when the axis of rotation is at the center of the image.
- Amount of displacement in the image resulting from rotation increases in proportion to sine of viewing angle offset from the pivot axis, to a maximum 90 degrees from the axis.
- Linear offsets of sensor from rotation axis produce displacement image changes proportional to the offset, while image rotation angles continue to equal vehicle or sensor rotations.
- For a sensor aligned on one axis of rotation, the other two rotations produce maximum displacement X-Y image changes proportional to vehicle angular change.

Change Formula: Angular change for an object in a viewport with rotation about an axis can be defined as in formula 1.

Rotational change formula:

$$\text{Angular Change} = \sin(\text{offset angle}) \times 2 (\sin(\text{rotation angle}/2)) \quad (1)$$

where angular change is in radians, and

Offset angle is the difference between the rotation axis and angle of regard.
Rotation angle is difference between two rotation states of vehicle or sensor.

For pitch and roll rotations, angular change directly below the vehicle equals the maximum change found at any other viewing angles. The magnitude of angular image change for vehicle pitch and roll rotations in a down-pointing sensor, will be identical to those for vehicle pitch and yaw changes with the same sensor pointing forward. The angular changes below the vehicle for yaw, however, are rotations around the vertical axis that provide less angular change than the maximum yaw angular changes which are found at the horizon in any direction. For the change rules, yaw angular changes are zero on the pivot axis, and increase with distance from the pivot axis. These will be perceived usually at moderate distances from the pivot, and have maximum displacement change at the edge of the display. These angular changes with yaw below are directly analogous to the changes at the forward horizon viewpoint with roll. At the forward horizon viewpoint the visual image pivots around the roll axis. The "visual gain" for yaw looking below is the same as for roll looking forward. It should be noted the maximum angular and displacement change for roll at the horizon, equal to that found for roll below, will be found in the lateral (90 and 270 degree) directions. For each rotation, maximum angular change is found on a plane perpendicular to the axis of rotation. For yaw, therefore, maximum angular change occurs at all points on the horizon.

Translations. Image changes resulting from vehicle translations can be defined by a set of general change rules and by formulas in either rectangular or polar coordinates. Only two ways of defining translation angular change, considered most germane to flight control vision, have been selected from the many available. Figure 2 illustrates the angular changes resulting from translation that will be considered. Only a few of the many related equivalent formulas have been selected. The primary rules and formulas are:

No Relative Change Points: Two points (or angles) of no relative change, or null points, exist in the visual array for any non-curved translations, change (?). One of these represents the velocity vector or spatial angle of advance, and the other the angle of retreat in the opposite direction.

Relative Change Rules: For linear translation along a vector:

- Any translational change of viewpoint produces angular relative change between the foreground and background elements composing the visual array of the world, except for the two no-change points on the velocity vector.
- A small part of the visual array may, or may not, contain changes in visual cues effective for conveying changes in one or more vehicle translational states.
- Magnitude of relative change for each element in the visual array is inversely proportional to its distance, for elements with large angular separation from the angles representing the velocity vector null points.
- Zero relative change exists between elements in the visual array falling on the vehicle velocity vector angle, and relative change between visual array elements increases with separation from this null point in accord with a function involving both distance and angular separation.

Change Formulas: Angular change of objects in the visual array for unit of translation along a flight path vector are defined for rectangular and polar coordinates by formulas (2), (3) and (4).

Change formula for unit translation; rectangular coordinates:

$$\text{Angular change} = \sqrt{H^2 + D^2 + L^2} \quad (2)$$

Change formula for unit translation; polar coordinates:

$$\text{Angular change} = \sin(\text{Azimuth angle}) / R \quad (3)$$

$$\text{Angular change} = (\sin(\text{Dip angle}))^2 / H \quad (4)$$

where: Angular change is in radians, and the terms are as defined in Figure 2.

For a point directly below these formulas reduce to angular change = $1/H$. If their solutions are multiplied by velocity the result will be angular velocity, and if multiplied by units of translational change the result will be approximate angular change for small translational changes (for exact solution, compute angles for start and end positions and take differences). It follows logically from these formulas that the maximum perceptible change for longitudinal and lateral translations will occur between

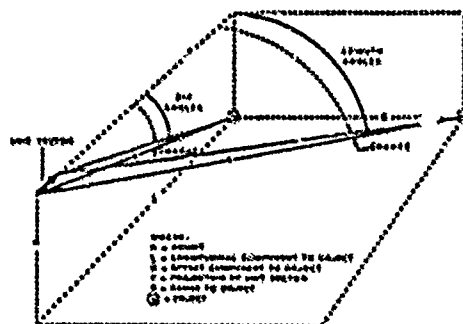


Figure 2. Illustration of dip and azimuth angles, and terms used in formulae.

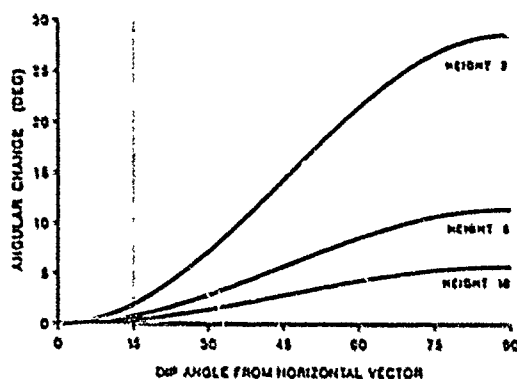


Figure 3. Elevation angular change of surface objects from level unit translational change, for dip angles and viewing heights of 2, 5 and 10 units.

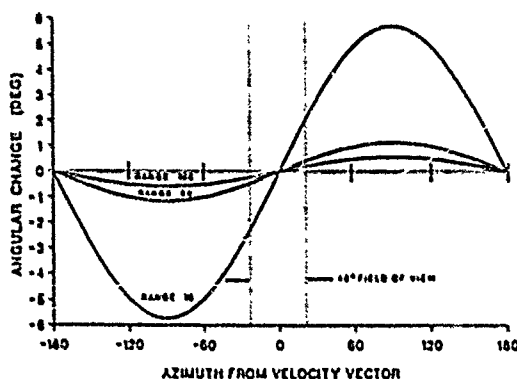


Figure 4. Angular change resulting from unit of translational change, for azimuth from velocity vector and slant ranges of 10, 50 and 100 units.

a downward image and a synthetic symbol representing the downward vertical axis. At low heights, vertical translations will also be very apparent around 10 degrees or more from the vertical axis, due to the short ranges producing significant amounts of angular change. Plots of these formulas in Figures 3 and 4 illustrate sensitivity of angular change in images resulting from a unit of translational velocity or change, as functions of angle from vector and height or range of view.

Figure 3 shows terrain object angular change for dip elevation angles at 2, 5, and 10 unit viewing heights for level flight using formula (4). The horizontal axis is the dip angle for sightline intercept of the terrain surface under a level translational vector. The curves for each viewing height reflect the ratios to maximum change at 90 degrees, as found in the right column of Table 1. Differences between viewing height curves reflect the inverse relationship between image angular change and viewing height. The sine squared function stays low for smaller dip angles, then builds rapidly with larger dip angles as the sine values approach unity. As the dip angles become large, range to terrain surface intercept becomes short as it approaches its minimum equal to height. At the lower edge of a typical forward sensor indicated by the dashed line at 15 degrees dip angle, it may be seen that only 6.7 percent of maximum potential image angular change will occur (for height = 2, angular change of 1.9 versus maximum change at 90 degrees dip of 28.6). At more typical image visual use areas of 10 to 5 degree dip angles, the image angular changes are, respectively, only 3.0 and 0.8 percent of maximum.

Figure 4 shows object angular change with azimuth difference from translational velocity vector for constant sightline ranges of 10, 50 and 100 distance units. Differences between the sightline range curves reflect the inverse relationship between image angular change and range. For a constant range, the changes shown are a sine function of the angular difference from the velocity vector. These functions have zero values at zero and 180 degree angular differences. Small angular differences from zero and 180 degrees could be vertical, lateral or any combination, but large angular differences would have to consist mainly of a directional azimuth component. It should be noted the width of the reduced change area is fairly wide in comparison to the 40 degree azimuth field of view typical of night vision systems, indicated by the pair of dashed vertical lines. At the edge of such a sensor for a given range, image angular change is only 34 percent of the maximum change that exists in directions perpendicular to the translational vector. At a more typical viewing angle of 10 degrees from vector, the change would be only 17 percent of maximum.

In both Figures 3 and 4, the powerful effect on angular change of range or height is evident. It is the much longer ranges to objects seen in a forward view image that will have the major adverse effect on perceiving angular changes reflecting vehicle translational changes. For azimuth, the most severe effects of the angular offsets

from the translational vector are restricted to within just a few degrees of the vector. Fifty percent of maximum change exists at 30 degrees offset, and 70 percent at 45 degrees. Along the forward terrain below a level translational vector where the sine squared function applies (Figure 3), angular change stays exceptionally small in comparison to its maximum in the downward view, until appreciable dip angle exists. From 6.7 percent of maximum at 15 degrees dip, it reaches 25 percent of maximum at 30 degrees, and 50 percent at 45 degrees dip angle.

Target Acquisition Angles and Dispersions. Geometric angles and dispersions in location of targets and threats have characteristics that can be expected to have substantial influence on probabilities of detection and identification.

Elevation Angles. At map-of-the-earth viewing heights of a few meters to a few tens of meters, geometric perspective results in compression in elevation angle of all objects, from a few hundred meters on out to the horizon, into just several degrees of visual angle directly below the horizon. For example, by multiplying Table 1 distance ratios by 10 to reflect viewing from a height of ten meters, it is found that everything on a flat surface from 191 meters to the horizon falls within just three degrees of the horizon. Similarly, everything from 573 meters to the horizon will fall within only one degree of the horizon. Due to the relatively long ranges involved, actual terrain relief seldom will increase these angles by more than a degree or two for complete elevation coverage. Due to terrain flight and low level profiles used for survival, virtually all air-to-air threats will also be found in this band or in a comparable band just above the horizon.

A very high probability exists, therefore, that nearly all targets and threats will be located geometrically in elevation angle within just a few degrees of the horizon. Spreading the vertical field of view above or below these few degrees in an acquisition sensor, will only reduce acquisition probabilities through corresponding reductions in resolution in the few degrees at the horizon where targets and threats are located.

Azimuth Angles. Geometric location of targets and threats in azimuth approaches a completely random distribution. A major intent of tactics is to reduce the uncertainty in azimuth of targets and threats. Seldom is this uncertainty, however, reduced to less than a 90 degree quadrant. Usually, azimuth location uncertainty for targets and threats will be about 180 degrees, and often it will be close to 360 degrees (such as in deep penetrations). A tactical requirement also exists for awareness of locations of the elements of friendly forces, and such awareness will normally require 360 degree azimuth sensor coverage.

A low probability exists, therefore, that a sensor with narrow field of view in azimuth will be pointed at only one moment in time, in the direction required for detection and identification of targets and threats. When targets and threats are oriented in almost any direction, it is not likely a narrow field of view sensor will be looking in the right direction. The enemy attempts to avoid detection and identification, and we attempt the same thing, through exploitation of cover and concealment. Both the enemy's and our own efforts result in clear line of sight, essential for visual detection and identification, being of short durations in most tactical engagement situations. Also, many of the most significant tactical cues, such as muzzle flashes from weapons firing, are momentary. The momentary and short duration of many of the cues required for target and threat detection and identification, in combination with a narrow sensor field of view in azimuth, will result in low probability these cues will be detected.

Poor Visibility Effects. As visual range attenuation increases, it is evident the angles for target acquisition viewing must shift downward to shorter ranges where image contrast is sufficient for discriminating targets from their background. As indicated in the fourth Table 1 column of terrain distance for sightline intersect, however, the angular shift will be quite small until attenuation becomes quite severe. For example, to center a sensor on 2000 meters viewing range at 10 meters viewing height (multiply table values by 10) would require less than 0.3 degree downward shift from the horizon. Five hundred meters would require only one degree, 250 meters only 2 degrees, and 100 meters only 5 degrees downward shift.

When severe visual range attenuation to tens or a hundred meters or so exists, then substantially larger downlook angles will be required for highest probability of target detection. Such targets will be very close, and blur will become a significant factor even for fairly slow speeds.

Marking by vegetation and man-made structures, when their density approaches one percent or more of the terrain on an area basis, impose a different form of visual range attenuation that is very similar in effect to atmospheric range attenuation. At terrain flight heights these objects will mask all but the closer targets and threats if their distribution approaches random (5). Consequently, large downlook angles similar to those for severe atmospheric visual range attenuation will result in best probability of target/threat detection. When terrain vegetation/structures marking reaches ten percent or more, steep downlook angles of 10 to 60/90 degrees will often give best detection probabilities. Ranges, of course, will be very short. Although distributions approaching random are common, for most terrain, distributions of both natural and man-made marking objects have stochastic characteristics. Tactical vantage points for exploiting these systematic characteristics can increase effective visual range significantly.

DISCUSSION

It is essential to look forward along the velocity vector to avoid obstacles. However, the results illustrate that a forward view, geometrically, is an exceptionally uninformative direction to look for vehicle state flight control information. The angular uncertainty resulting from sensor head slaving or mounting compounds the difficulty of acquiring good flight control cues from a narrow forward view. The results indicate a downward wide angle/panoramic view will have maximum sensitivity to, and clearly convey, all six degrees of freedom of vehicle motion. These results suggest incorporating a downward view should have potential for major improvements in flight control visual discriminations in night vision systems. Such a view would also assure maximum potential in poor visibility of seeing the terrain, and seeing it in a form that could be used effectively for flight control.

As visual range attenuation increases, decreasing contrast reduces the probability at high speeds that obstacles on the velocity vector will be detected at sufficient range for avoidance. Detecting and avoiding obstacles to safe flight in poor visibility appear likely to remain dependent on technology for solution. The nap-of-the-earth pilot's optimum for the present are either to perform a vertical recovery maneuver, or to slow down to speeds allowing obstacle avoidance for detection ranges in the existing visibility conditions. The latter requires sufficient terrain vision or symbolic cues to assure safe flight control, and is tactically preferable. This capability should be enhanced by designing night vision systems with characteristics that exploit the better terrain vision that exists directly below the helicopter. Viewing in this direction also should substantially enhance safe flight control capability when rotor downwash near a hover obliterates any terrain reference in a forward viewing image.

The complex higher mental processes required of pilots for flight control by both the image and symbology of night vision systems raises concern over the effects of the extreme psychological stress of combat on flying performance. Using the image appears to require cognitive processes known to be degraded by stress. Using the symbology requires numerous channels of complex higher mental processing that will be degraded by stress. In addition, most of the symbology has form characteristics certain to degrade perception of targets and obstacles in the image near the symbols. The most effective night vision systems will avoid dependence on stress degraded complex mental processes in the cues they provide for both flying and fighting tasks. Symbol design and location can be altered to minimize degradation of perception of the form cues characteristic of targets and obstacles. It appears feasible to design night vision systems using the above principles that should result in major improvements under the extreme stress of combat, in flying safety and fighting effectiveness. Improved vision capability and safety in poor visibility would also be expected. The sections below provide a general outline of one concept for integrated helicopter night vision system design that reflect these principles.

System and Information Integration. Several factors relevant to helicopter operational capabilities in poor visibility have been separately considered. However, a helicopter pilot must maintain awareness of all the factors relevant to fighting effectiveness and flying safety in an integrated manner. Combining the best poor visibility terrain visual cues with the best flight control cues in an integrated system is desirable, and appears to be feasible. Extension of the information integration approach to encompass tactical mission aspects is required. Incorporation of visual obstacle detection and avoidance information is, of course, essential.

Most pilots probably use a comprehensive mental framework, or cognitive "frame of reference," in which they place all the information relevant to flying and fighting. It is likely this frame of reference will match that inherently used by the spatial-motion visual process. Existing night vision systems do not provide a display with such a comprehensive frame of reference encompassing all flying and fighting cues and information. Instead, they provide only small field of view "snapshots" of the visual world, and force the pilot to mentally build up over time the comprehensive picture of the terrain and battlefield he requires for flying safety and fighting effectiveness. This imposes substantial cognitive workload on the pilot, in addition to his image and symbology interpretation workload.

It would be most desirable for night vision system design characteristics to provide the pilot with all the information he needs for both flying and fighting in a single fully integrated, or in a few highly related, display formats. The display format(s) should match or closely conform with the cognitive "frame of reference" normally adopted by pilots for battlefield and flight control spatial awareness. The downward vertical centered azimuth-elevation polar plot (Panel C of Figure 1) used in this report should represent a close approximation to this normal pilot frame of reference. Analyses of the ergonomic characteristics of such a display format suggest excellent potential for substantial reductions in pilot workload and errors in flying with night vision systems, and for reducing reaction times for responding to tactical cues. The natural visual-motor characteristics of this kind of format should have much better resistance to the adverse effects on performance of the severe psychological stress of combat, and of the stress of poor visibility during terrain flight. Such a format would accommodate direct incorporation of the clearest visual terrain cues for flight in poor visibility.

Integrated Poor Visibility Display Concept. The display concept outlined below is based on the premise that sensors and displays should provide pilots with the best visual cues technology can provide for flying and fighting tasks. It assumes independent sensors each designed to provide the best visual cues needed for flying and fighting tasks, rather than a compromise single sensor for providing all required cues. These separate sensors should provide redundancy desirable from a system reliability standpoint, and would not necessarily increase complexity and cost since each could be relatively simple in design. A combination of both panel and helmet mounted displays would be used similar to that now used in the AH-64. However, the panel display would be primary for flight control and target acquisition, and the helmet display primarily for weapons aiming and obstacle clearance.

Sensors. Three different sensors are required to convey to pilots the best visual cues they need for their flying and fighting tasks:

(1) The first is a downward pointing panoramic sensor fixed to the airframe that would convey the primary cues for flight control. It should be located beneath the helicopter and near its center of rotation. It could use refractive "fisheye" lens optics, but primarily reflective optics appear to have advantages. A center opening in the reflectors would be used to provide magnification near 1 to 1 directly below. A large optical aperture focusing on an image intensifier is envisioned, with intensifier output imaged by a video camera. This sensor has minimal resolution requirements; it just needs to convey motions, and the objects it images will usually cover large visual angles. The display of this sensor requires a vertical reference (attitude) symbol for maximum sensitivity to vehicle translational state changes. This sensor will assure maximum probability in poor visibility of imaging effective terrain cues for flight control.

(2) The second sensor is slaved to the vehicle velocity vector for the primary purpose of obstacle detection, and would normally be oriented in the forward direction. It would have two to five power magnification, and preferably should combine both image intensifier and far infrared imaging technologies. An alternate application for this sensor would be to couple it with the pilot's helmet for use in weapon aiming, crew coordination and close-in target acquisition.

(3) The third would be a high resolution long range target acquisition sensor providing continuous 360 degree scan of the target-rich area at the horizon, to which it would be slaved. It would provide updating at 10 to 100 times per second for each direction to assure imaging of short duration and momentary cues. Processors and displays for sorting and conveying to the pilot the relevant cues and information from the tremendous amount of visual content contained in such a sensor will be a challenge, but should be feasible with emerging technology.

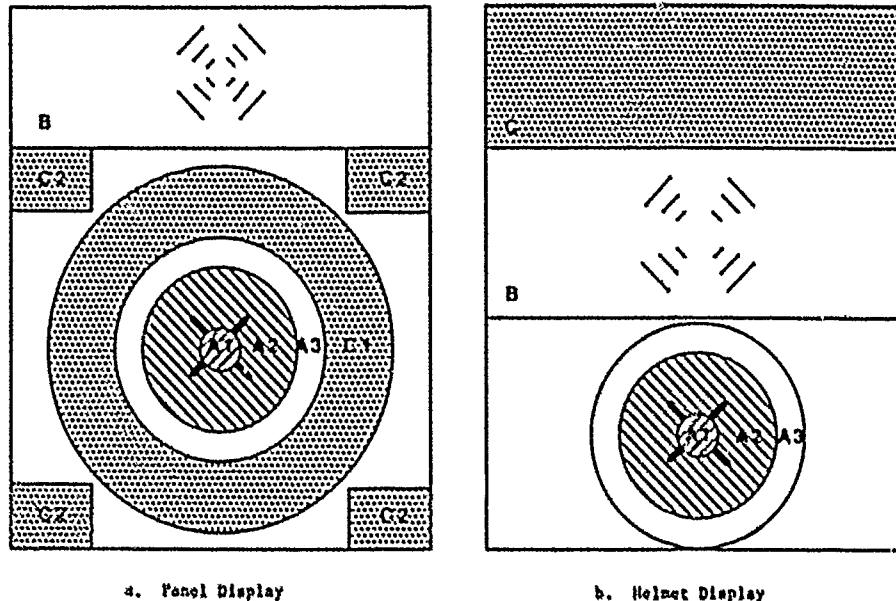


Figure 5. Display concept image areas. Areas labeled A are the downward panoramic image, with A1 the 1 to 1 magnification inset, A2 the terrain from below to the horizon, and A3 the sky above the horizon. Area B is the obstacle avoidance image. Area C1 is the high resolution horizon scanning target acquisition sensor, and C2 areas are area of interest outsets of this sensor.

Panel Display. Figure 5a illustrates the panel display concept in terms of visual areas. At the center of the lower section would be the downward panoramic sensor that would provide a fisheye type of image combining azimuth and elevation angles (A). Vertical downward would be at its center, and its edges at 10 to 30 degrees above the horizon. A 1:1 magnification inset (A1) at the center of this area will be used for a variety of ergonomic and information requirement reasons.

Surrounding the center downward panoramic view, would be an outer ring (C1) for displaying the high resolution long range target acquisition sensor imagery. This ring would be displayed at the panel with elevation magnification. At the eye this would probably result in a 2 to 5 factor magnification in elevation, and about a 4 factor minification in azimuth—a very substantial mismatch in magnifications. Nevertheless, it is believed valid reasons exist for continuously imaging the entire horizon, and that pilots could adapt to it quickly without significant problems. It is anticipated high magnification outsets (C2) with matched elevation and azimuth magnifications would be used for detailed viewing of suspect locations. These outsets could be defined automatically by smart sensors, or selected manually by the crew. These outsets could be provided in alternative locations and orientations, as long as their azimuth and elevation location was evident. These alternative locations for the outsets could be on the ring itself, inside it, or outside at the corners.

The obstacle detection image would be displayed at the top of the outer ring. It would provide clear indication of the velocity vector either through centering on it, or by an array of symbols that would flow out from it.

Helmet Display. The helmet display is envisioned to consist of three vertical layers in a format with the long dimension oriented vertical. The top layer would consist of aiming and target acquisition imagery (C). The middle layer would consist of the obstacle detection sensor image slaved to the velocity vector (B). The lower layer would consist of a small replica of the downward panoramic sensor panel display (A). Any of the layers could be shifted to the other levels in accord with task demands, as well as the magnifications used for each.

Mechanization. The number and type of sensor and display technologies to mechanize these concepts are a matter for future definition. There are a number of technologies and approaches to mechanization that should be within current state-of-the-art, and a variety of promising near-term technologies.

CONCLUSIONS

It is concluded a fundamental re-examination of design approaches with regard to information requirements and information change are needed for significant improvements in night vision systems. Major increases are needed in the probability the systems actually effectively convey to pilots the best available visual cues technology can provide for their flying and fighting tasks. When this is done, major improvements can be expected in the flying safety and combat effectiveness of night vision systems used under the extreme psychological stress of combat, and when used in poor visibility conditions.

REFERENCES

1. Livingstone, Margaret S., Art, Illusion and the visual system, *Scientific American*, 238 (1), Jan. 1988, 78-83.
2. Lattin, J. Y., Maturana, H. R., McCulloch, W. S., and Pitts, W. H., What the frog's eye tells the frog's brain, *Proc. Inst. Radio Engrs.*, 1957, 47, 1950-1951.
3. Barlow, H. B., Hill, R. M., and Levick, W. R., Retinal ganglion cells responding selectively to direction and speed of image in the rabbit, *J. Physiol.*, 173, 1964, 377-407.
4. Hays, Chris, *Top Gun and Beyond*, an INCA production in association with WGBH and Channel 4 Ltd for NOVA TV documentary series, U.S. Public Broadcasting System, Spring, 1988. Transcript: NOVA, Box 122, Boston, MA 02134; Video: Corner Film & Video, 108 Wilmet Road, Deerfield, IL 60015.
5. Wright, Robert H., and DeBoris, J. Nicholas., U.S. Army Aeromedical Research Laboratory, Object visibility patterns in low level flight, Sept. 1975, Report No. 76-5.
6. Gibson, James J., *The Ecological Approach to Visual Perception*, Boston, Houghton Mifflin Co., 1977, pp. 116-120.
7. Gibson, James J., *The Ecological Approach to Visual Perception*, Boston, Houghton Mifflin Co., 1977, pp. 122-123, 227-229.

THE ASSESSMENT OF VISIBILITY FROM AUTOMATIC CONTRAST MEASUREMENTS

by
A W Puffett
Flight Management Department
Royal Aerospace Establishment
Bedford MK41 6AE
UK

SUMMARY

This paper discusses the assessment of visibility and hence runway visual range through the passive and automatic measurement of contrast reduction in a dark target. Though limited to use from dawn through to dusk the method offers significant advantages over the more usual transmission, or scattering approaches. The advantages arise not only from the measurement process which is intrinsically more robust than that of the transmissometer, but also from the ratio-metric manner in which it can be implemented. The result is a self-compensating system which virtually abolishes any requirement for temperature and long term stability in the instrument. Unlike conventional scatter-meters the method may be used under a wide range of obscuring conditions without doubts in respect of its constancy of sensitivity.

Initial comparisons with a human observer have both produced good agreement and confirmed theoretical expectations of behaviour.

To overcome the night-time deficiency, suggestions are made for ways in which conventional measurements might be integrated into the system. The relaxation in design that would result from night-time only operation show this to be both a practical and economic alternative.

1 INTRODUCTION

The regulation of aircraft landings in reduced visibility conditions requires that an assessment be made of the visual range on the runway in order to ensure that adequate visual cues are available to permit a safe operation. There are 2 basic methods for assessing the Runway Visual Range (RVR). A human observer can gauge either directly, or indirectly through a TV camera the greatest range along the runway at which the runway lights, or markings can be seen. The alternative method utilises automatic instruments to assess atmospheric transparency as one of the parameters from which the performance of the visual aids and cues can be modelled. Both approaches are not without their problems but automatic instruments have an attraction for the operator, in terms of their round-the-clock availability and vigilance. World wide, there are perhaps in excess of a dozen different types of instruments used for RVR assessment, so why invent "a better mouse-trap"? Ideally, such instruments should be simple in design as well as construction and with a low cost of ownership in terms of capital expenditure and maintenance. In addition, they should make measurements which are both accurate, reliable and robust. In practice, all these goals are rarely achieved in a single instrument.

This paper describes the results of an investigation into a method of measurement which goes some way to achieving these goals under daytime conditions. It utilises an instrumental assessment of the reduction of contrast in a dark target, and suggests possible complementary methods for night-time use.

2 METHODS FOR THE ASSESSMENT OF RUNWAY VISUAL RANGE

2.1 Human assessment

The fundamental method of assessing the Runway Visual Range relies on a human observer estimating the number of runway centreline, or edge lights which are visible from a position on the runway centreline adjacent to the touch-down point. Such observations, when taken from an appropriate height, are as close to the situation experienced by a pilot as can be achieved. Even so, the observations cannot necessarily match the eye adaption and dynamic viewing conditions experienced by a pilot. Further, at busy airports, the observations must of necessity be made from outside the confines of the runway.

2.2 Automatic instrumental assessment

Automatic visibility instruments are generally designed to provide round the clock assessment of atmospheric transmissivity, or extinction coefficient. They do not in general produce a direct measure of the visibility or the visual range of lights. These are obtained by calculation and, in the case of RVR, require measurements or assumptions of other parameters.

The calculation of the visual range of lights is normally achieved through the application of Allard's Law² which implies knowledge both of the effective source intensity and the eye illuminance threshold. This latter is not directly measurable and is usually assessed through a measure of background luminance, either by a subjective assessment (ie day, night, twilight), or by a photometric measurement made adjacent to the runway. This data is then used to deduce the appropriate value of eye

illumination threshold through an assumed relationship. The method may be subject to significant errors, nevertheless a useful assessment can be made where the visual range of the lights is substantially greater than the visibility.

By comparison a good assessment of the visual range of runway markings is far more difficult to achieve, due to the complex nature of the visual scene. In this case recourse is usually made to Koschmeider's Law¹ which can be used to relate the reduction in target contrast to meteorological visibility. In these circumstances it is however, usual to employ a fixed value for the threshold eye contrast ratio. This approach would be expected to give a good assessment of the visibility of an idealised dark target against a fog background, but is quite inadequate in describing the visibility of markings of undetermined contrast viewed against a runway surface.

3 INSTRUMENTAL TECHNIQUES

3.1 Transmissometers

One type of instrument which is frequently used for the assessment of visibility, or visual range is the transmissometer. In its most rudimentary form this consists of a searchlight producing a narrow beam of light which is aimed at a telephotometer some distance away. This in turn has a narrow field of view and is aimed at the searchlight. The fog, or other obscuring media has the effect of reducing the amount of light from the searchlight arriving at the photometer. A good example of such is the transmissometer of Douglas and Young¹.

The behaviour of the transmissometer can be adequately described by Douger's Law². This Law assumes, however, that light once scattered from the beam plays no further part in the measurement. This then is one potential source of error. A further type of error may be induced by changes in the ambient light level, causing the detector's working point to change and thus interact with any non-linearity. In practice most designs attempt to eliminate the effects of the natural light field.

In visibility terms the output characteristic of a transmissometer will be logarithmic (Fig 1). The sensitivity to error in visibility may be seen to be a function of transmission and to increase with visibility as the slope of the characteristics reduces. The same is also true, to a lesser degree, at low visibilities where the measurement value approaches any zero offset, or noise level. As a consequence there are limits to the useful measurement range for any single path length, apart from any limitations in the electronic or optical engineering of the equipment. Any restriction in dynamic range can to some extent be overcome by either utilising high accuracy measurements with a shorter path, or by changing its length to suit the prevailing conditions. Where long paths are employed a further problem which will be encountered is that of scintillation of the source due to atmospheric turbulence. This phenomenon is not generally significant during the foggy conditions which it is desired to measure, but rather in the clear conditions which are necessary to the periodic calibration of the instrument. Analysis suggests that the minimum error tends to occur at 37% transmission and that the optimum path length will therefore be one third of the significant meteorological optical range.

One practical aspect of transmissometer design is the need for a periodic calibration. This requires that a measurement be made of the transmission value in clear air. This is then used over a period (of up to some days) as the reference for the readings in fog. This need for long term stability has a significant impact on the standard of design and engineering which is required.

3.2 Scatter meters

Another type of instrument used in visibility assessment is the scatter meter. These fall into 2 broad classes which may be termed polar and integrating. In the polar type, a narrow beam of light is used to illuminate a small volume of fog, the light scattered from this being measured at a particular angle, or over a range of angles⁴. Typically, these angles may range from 20° to 50° in the forward direction, or to approximately 180° in the backward direction. This scattered component can then be related to the volume scattering function and in turn to the visibility. In this case it is essential to choose the scattering angle to minimise the sensitivity of the measurements to any changes in the size distribution of the fog droplets. In the integrating scatter meter an attempt is made to assess the volume scattering function by measuring components of the scattered light over the full range of 0° to 180°. In principle this ought to eliminate any sensitivity to changes in droplet size distribution. The configuration of the instrument is such that a distributed volume of fog is illuminated over a wide range of angles by a discrete diffusing source, and then viewed parallel to the surface of the diffuser⁵.

Scatter meters normally have the advantage of a compact single unit construction. This enables the relatively easy monitoring of the intensity of the source, compared with the case of a transmissometer where the 2 head units may be separated by some tens of meters. A further advantage is obtained due to their linear response to the volume scattering coefficient. Consequently the error sensitivity at long visibilities might be expected to be less than that for a transmissometer operating to the same level of measurement accuracy. Experience however, shows that the advantages may be more than outweighed by residual sensitivity to variation in the

droplet size distribution, or by aerodynamic modification either of the droplets themselves, or through their selective presentation at the sampling volume. This underlines the necessity to expose sensors to a variety of conditions, or to have available means of modelling their response.

A further difficulty encountered with scatter meters is that of achieving a sensitivity calibration. Since in these instruments an infinite visibility produces a zero output this cannot be used for sensitivity scaling as is the case with the transmissometer. To overcome this problem it is necessary to use an artificial scattering volume which reproduces a dense fog. The angular scattering characteristics of this however, are unlikely to match those of a real fog, so that it is not possible to provide an absolute calibration. Thus, unlike the transmissometer where, given a basically sound engineering design, the error model goes a long way towards describing the behaviour of the instrument, this is not true of scatter meters where sampling errors are likely to predominate.

3.3 TV systems

Until recently the only known example of an operational TV system was used as a means of obtaining the remote assessment of RVR lights by a human observer⁶. It is understood however, that this has now been superseded by a system which makes essentially the same measurements with a non-imaging sensor⁷. In principle the video waveform of a scene can be analysed to extract information on the contrast from either natural, or man made objects in the scene and to use this to determine visibility and of course RVR⁸. The contrast of an object however, depends greatly on the way in which it and its background are lit. It is also dependent on the nature of the surfaces involved and, for instance on the extent to which they are wet or dry. These factors suggest practical difficulties in the implementation of such a technique.

The essential laws governing the apparent contrast of objects, or lights are those of Koschmeider and Allard². In the case of TV systems however, the design and performance of the camera will provide a major component in the error budget.

3.4 Contrast reduction meters

Another means of assessing the visibility in daylight, which is the main subject of this paper, is to measure the amount of ambient illumination which is scattered into the sight line of a human eye, or imaging detector. This is the mechanism by which the apparent contrast of a dark object is reduced in fog.

Automatic contrast meters are not seen in general operational service, though visual instruments such as the ED Instruments Visibility meter (a form of flicker photometer), and the GEC Disappearance Range Gauge (based on Waldram's design), have been produced. A suitable model to describe the behaviour of such a contrast meter is Koschmeider's Law. As with the transmissometer this model gives a fairly good description of the measurement technique, though unlike the transmissometer the measurement includes variations in both the spatial and directional components of the ambient light field. Like the transmissometer it would have the same logarithmic response (Fig 1) and as a consequence would be expected to obey the same error sensitivity function. There is however, an inherent advantage in the way in which these contrast measurements are made. This can be best illustrated by considering the assessment of a visibility which is many times longer than the measurement path. For a transmissometer the transmission factor would be calculated from the ratio of 2 values which are similar in magnitude, whereas contrast (the analogous parameter for a contrast meter) would be calculated from the ratio of greatly differing values. To demonstrate this, the errors for both types of instrument have been calculated in terms of the Meteorological Optical Range (MOR) (range for 5% transmission) for the same conditions (Fig 2). It can be seen immediately, that there are significant potential benefits from the contrast method, since the rate of increase in error with visibility is about half that for the transmissometer. The break even point in this example being at a visibility which is about 5 times the base-line. Even at the lowest ranges the transmissometer is not as good as would appear from the figure, since the effect of zero, or offset errors would cause the error in visibility to increase at low transmission values rather than to diminish to zero. A further benefit to the contrast system lies in the fact that the measurements are used in a ratio-metric manner. Thus, even though a clear air calibration value is required to establish the contrast datum for the target, it is formed from a ratio of readings taken over a short time interval. This means that unlike the transmissometer, drift in the contrast system over the medium to long term (ie minutes to days) is of no consequence.

3.4.1 Dark target design

It might be thought that in the ideal situation a dark target should have a negligible reflectance. This is by no means essential however, if the system parameters are sensibly optimised. Consider the case where the calibrating MOR is numerically 100 times the instrument baseline length and the photometric accuracy of instrument is 1%. Using these figures error curves can be plotted for various values of intrinsic target contrast (Fig 3). In the case of an MOR for assessment which is 30 times the baseline and a target whose reflectance is 0.1% then the error in MOR is some 6%. Should however, the reflectance be degraded to 3% the rise in error is only 1%.

In order to minimise deterioration and specular reflections it is best that the dark target be enclosed. One means of achieving this is to use some kind of box with an aperture in one side to allow viewing. Care, is of course, needed in order to avoid providing a perch, or nest box for furred, or feathered creatures. The choice of material for the dark target depends on its degree of exposure to the elements. The apparent contrast of the target may in practice appear greater than its intrinsic reflectance would indicate. This is due to the restricting effect of the viewing aperture and the reflective losses within the box.

3.4.2 Dark target photometry

The measurement of the luminance of a dark target is not as straightforward as might be thought due to lens flare. Though the main part of the sensor's response may be arranged to lie within the dimensions of the dark target, any residual response outside of this will respond to the background¹. Consider for instance, an unhooded camera lens. While the angular response of the sensor outside of the target may be small, the solid angle exposed to the background is large. By comparison, though the axial response of the sensor will be very much greater, the solid angle is small and the luminance of the target is less than that of the background by perhaps a factor of 100. Of course when the target is bright in comparison to the background this effect is less significant. In practice the effect is not disastrous, but makes the measurement of low reflectance targets more difficult and points to the need for careful choice of optics.

4 Field evaluation of contrast system

4.1 Experimental sensor

The instrument used in our research to make the measurements was manufactured specially for the purpose by Aeronautical and General Instruments (AGI) under contract to the UK Civil Aviation Authority. In essence it takes the form of a camera with an optical fibre pick-off in the image plane which is capable of being positioned anywhere in the picture format (Fig 4). The position of this fibre within the 'picture' is controlled by 2 lead screws at right angles which are driven by stepper motors. The resolution of this motion is 0.01 mm. This when coupled with a 100 mm focal length lens, gives an angular resolution of 0.344 minutes of arc, or 1 milli-radian. The total range of 60 mm in each axis is equivalent to 32', or 0.56 radian. The immediate field of view is defined by means of a small pinhole aperture fitted to the end of the optical fibre and is 1.9 minutes of arc, or 5.5 milli-radians in radius. The photodetector is a Peltier cooled and stabilized photomultiplier tube operated at -20°C, with a measurable output current over the range 10⁻⁹ to 10⁻⁵ amps. In operation the working range of the tube is normally constrained to lie between 10⁻⁷ and 10⁻⁵ amps. This compression is achieved through the use of selectable neutral density filters, inserted between the optical fibre and the photodetector. One of the filter positions in fact selects a blanking plate which can be used to protect the detector from exposure to excessive light levels and also allows any dark current to be monitored. In practice this is normally well below the 10⁻⁹ amps of the lowest point on scale, but is a useful indicator of failure of the Peltier cooler, or an inadequate warm-up period.

4.2 Dark target details

The prototype target used for these trials consisted of a wooden box 0.75 m high by 1.0 m wide and 1.25 m deep, painted matt black on the inside. At the end facing the instrument was a hole of 0.3 m diameter which was viewed by the telephotometer from a distance of 100 m. This primitive model was used throughout the trials, though its deficiencies later prompted the design and manufacture of an improved model.

4.3 Method for contrast measurements

The layout of the trials site as seen from behind the sensor and looking towards the dark target is shown in Fig 5.

Essentially the method of operation was first to measure the sky background a little to the side of the target, then the target itself and finally to repeat the first measurement. The first sky measurement was solely used to establish the optimum sensitivity range for the instrument, the second being to establish the contrast. In practice the co-ordinates used for positioning by the computer were obtained by visual observation through a sighting graticule in the instrument. In order to minimise the effects of any change in alignment the sensor was always aimed at the middle of the target, though in practice this was rarely found to vary by more than 1 or 2 steps (milli-radians). Finding the center of the target (with a non-imaging system) was tedious in the extreme and was generally accomplished by means of a specially developed centring routine in the control computer. In general, measurement cycles included both differing types of background, as well as of the dark target. In addition on some occasions a distant map was included which could be controlled by the computer. A further feature of the system was to enable a point in the cycle to be synchronised to a particular time (ie on the minute, half minute etc). This was intended to reduce timing uncertainty and skew when making comparison with other measurements, or observations.

The basic assumption made in the assessment of contrast, is that it is unaffected by absolute light levels over the normal operating range of the equipment. This was demonstrated by comparing the luminance of the target and a local background over the dawn period on a day when the sky was overcast, but the visibility was good. A correlation of 0.975 was achieved for log luminance over some 3 decades. This was very good considering the mismatch between the path to the dark target and that to the point of visual equilibrium for the background.

4.4 Calibration of target intrinsic contrast

As previously discussed the contrast reduction meter needs to be calibrated at a time when the visibility is substantially in excess of the required operating range. This procedure enables the influence of errors in the calibration to be significantly reduced when applied to the nominal operating range. In principle, a calibrating MOR which is 50 times the baseline and has an error of 20% has the same effectiveness as one which is 25 times the baseline and has an error of 10%. The problem is one of the choice of a representative background and the performance of the target rather than of instrumental stability. Consider the situation where the visibility may be some 30 or more kilometres, but where the dark target is situated at a quite modest distance of a few tens to several hundreds of metres. As a consequence the illumination of the air path to the point of visual equilibrium in the background may vary quite considerably from that to the target. For example, the conditions overhead the instrument may be overcast, while the background may consist of sunlit clouds.

An alternative form of background which was tried was a matt white board placed in proximity to the target. It is readily seen however, that when considering a strongly anisotropic light field in relatively good visibility the illumination at the board may be far from representative of that at the dark target, or the intervening air path. In particular, where a simple board is concerned there appears to be no way of achieving a non-specular response.

An expedient which was employed in order to get the system calibrated and to overcome the shortcomings of clear air calibration was to utilise a period of good uniform overcast conditions in moderate visibility. On a particular occasion the local meteorological office reported a visibility of 3700 m with good precision for 3 hours in succession. The analysis of the target and background data from the sensor confirmed the stability of the conditions and gave a mean reflectance of 0.1084 for the instrument. This resulted in a deduced intrinsic contrast for the target of -0.991 after allowance was made for an average observer's contrast threshold of 2%.

An alternative calibration background which was investigated was the use of an integrator placed in the vicinity of the target. The basis of this method is that in good visibility the angular scattering function is not strongly dependent on the scattering angle¹⁰. As a consequence, a summation of all the angular components of light incident at a given point should be expected to give a representative assessment of the total light incident along the measurement path and hence the scattering veil. A simple implementation of this technique took the form of a hollow white translucent glass globe which was mounted with its mouth downwards. This was viewed by the sensor looking into an angled mirror beneath the globe. By using the same sensor to view the integrator as the target a radiometric mode of operation was ensured, thus tending to eliminate any effects of drift in the sensor. The level of signal obtained from the device was close to that obtained in conditions of moderate visibility under an overcast sky. Though the principle appears sound, the effectiveness of the prototype in summing the light components did leave something to be desired. This was evidenced by the fact that cloud structure was still visible in the mirror when viewed from the position of the instrument. An alternative method which might be adapted to this purpose is that of viewing an externally reflecting sphere¹⁰.

4.5 Comparison techniques

The evaluation of any visibility sensor poses a fundamental problem since there is no primary standard. It had been planned to make a comparison with an Erwin Sick SM5 transmissometer but, in the event it was found that the one available had inadequate stability for the purpose. This left human observation as the only available means for comparison.

The problems encountered in using visual assessment as a means of comparison relate to the difficulty in calibrating the observer's effective contrast sensitivity and of standardising the observational technique.

The method of comparison adopted was to use the same target for both sensor and observer and to vary the distance of the latter. The variation of distance was achieved by the observer driving a small van which was initially backed away from the target until it was no longer visible and then driven slowly forward until the target achieved a certain level of conspicuity. The criterion used for the trials was that of 'clearly discernable'. This represented the greatest distance at which the shape of the target was unambiguous. Inevitably, there must be a tendency towards persistence in observed distance (ie the observer knows the position from which the last reading was taken). Nevertheless, with care, a good degree of precision and freedom from bias was achieved. The experiment was blind in that the observer had no way of knowing what the instrument was reporting, nor whether trends were being under, or over estimated.

The distance from the target was obtained from a locally designed and manufactured micro-processor based distance measuring equipment. This equipment was attached to the speedometer drive of the vehicle and produced a display scaled in metres. With reasonable care in driving, the slippage in position over a period of 20 minutes was no more than 1 m. The basic accuracy of the distance measuring system was of the order of 1%. Although a high degree of repeatability of observation was achieved the observer's contrast threshold was unknown. Difficulties were experienced in making observations in excess of 600 m, due to the temporal and spatial variability during the formation and decay phase of fog. Limiting visual resolution and an obscuring hump in the track also added to the difficulties in making successful observations at the longer ranges. It was expected that there might be some non-linearity in the comparison, since the instrumental system calculates range using a fixed contrast ratio, whilst the threshold contrast ratio for the observer might be expected to change with range. Application of the Blackwell data¹² suggests that over the range of 100 to 600 m the observer's threshold ratio might change by a factor of 10, the angular subtense of the dark target being insufficient to ensure a constant threshold. In practice, the results show no obvious signs of curvature, suggesting that either the observer was using the box and supporting framework as the target at the longer ranges, or that some other effect was coming into play.

4.6 Comparison parameters

There are a number of parameters that should be tested in the course of field testing an instrumental visibility system.

These are:

- 1 The reliability of the functional relationship.
- 2 The minute-to-minute correlation.
- 3 The day-to-day correlation.
4. The repeatability for all types of natural obscuring phenomena.
- 5 An understanding of the mechanisms of comparison failure.

The large variations which can occur in an observer's threshold contrast ratio, both day-to-day and between observers, suggest that items 3 and 4 would only be achieved through a large statistical trial. Nevertheless, with the techniques and resources discussed above, it should be possible to demonstrate items 1 and 2 on a day by day basis. If the observer's contrast threshold is sensibly constant during the period of the trial then the application of Koschmeider's Law leads naturally to a linear comparison in visual range. Under these circumstances the level of correlation achieved will apply regardless of the actual values of the thresholds employed. The slope of any regression line will not necessarily be unity and may well vary from trial to trial, though the line should pass through zero. The actual value of correlation which is achieved will depend on the spatial and temporal homogeneity of the fog as well as any averaging in either dimension which is applied by the measurements, or observations. One outcome of the comparison is that if the instrumental contrast measurements can be relied upon, then these could in fact be used to assess the observer's contrast threshold.

4.7 Trials logistics

The conduct of trials such as these, which are dependent on naturally occurring phenomena, pose severe logistical problems. Even today, the forecasting of fog is by no means certain, as small deviations from the forecast meteorological conditions can have a marked effect on its occurrence, duration, extent and density. As a result there were numerous occasions when the site was manned and fog did not occur. In addition, there were occasions when malfunctions of the sensor, communications, or controlling computer prevented data being acquired. Further, when fog did occur it was sometimes unsuitable in nature. So far as fog conditions are concerned there is little point in making comparisons between systems when the fog is either spatially, or temporally variable, because of the implicit assumption that both systems are assessing the same atmospheric condition. For instance, on one occasion the visibility along the track varied so rapidly that the observer simply could not vary the position of the vehicle quickly enough to achieve the necessary visual criterion. Other sources of difficulty to the observer were the extremes of light level which were encountered. On one occasion, although the light was adequate for the instrument, it was insufficient for the human observer (1 Nit). On another, a trial was abandoned because the light level was so high that the observer could not regard the target without watering of the eyes (5000 Nits).

4.8 Trials results

The number of occasions on which successful comparison of instrumental output with human observations were obtained, proved disappointingly small, being only 5 in all. The results obtained, however, give every encouragement to the use of the contrast reduction method. In general, excellent correlation was obtained and where this was not so, the departures can be explained.

The comparison shown in Fig 6 was made on the morning of 30 November 1985. Although the range of the data was small (125 to 255 μ CH), a very high level of correlation was achieved (0.99) and the points were well distributed about and along the regression or, 'best fit' line. The implication of this high level is that only 2% of the variance about the regression line is unexplained. Similarly the 'standard' error in the slope of the regression line is only 1.5% of its value and that of its intercept 3 m. Furthermore, there is no apparent tendency to curvature.

4.9 Discussion of trials technique

The weakness of the trials as conducted is seen to lie in the lack of a calibration for the threshold contrast ratio of the observer and the absence of information regarding the variability of the fog.

So far as the first aspect is concerned, one technique which may be capable of providing a field assessment of the observer's threshold is Ginsberg's Vision contrast test system⁽¹⁾). This is a variant of the sine wave grating technique and provides on a board a 2 dimensional array of gratings. These are graded in spatial frequency in one direction and contrast in the other. Though this method does not directly yield the contrast threshold for 'real' targets, it would allow the observer to be calibrated in the field for the current ambient lighting conditions.

Addressing the second deficiency, a method which might be used to assess the degree of variability in the different fogs is to compare the spectral content of their assessed extinction coefficient time histories.

Although the method used to make human observations has been seen to be capable of excellent short term repeatability, it is nevertheless slow and limited in duration to about 2 hours. This is due to the level of concentration required in the visual task and the fatigue of making repeated driving manoeuvres.

4.10 Discussion of trials equipment

The experimental sensor used for the trials does not reflect the approach which should be adopted for an operational system. So far as deployment against a single target is concerned, then the aim of the telescope could be fixed, with perhaps 2 detectors side by side, or a single detector with a rotating, or commutating stop which allows the target and background to be viewed in turn. Patently this is unsatisfactory where more than one target, or a hybrid system is involved (see section 5). A method which is found particularly attractive in this instance is to position the telescope vertically and to use a mirror steerable in 2 axes to select the appropriate point of regard. This would have the added attraction that apart from relaxing requirements on target placement on airports, the system could at the least be used for making assessments in both directions along the runway thus improving the sampling coverage.

The other element of the system, which is the dark target, has been given some thought in the light of trials experience. The shortcomings of the simple box construction are many. In particular, the lack of baffles means that oblique illumination can reach the target proper (the back surface of the box), without significant attenuation. A particularly good example of this occurred when driving snow collected on the floor of the box which then reflected oblique rays onto the target proper. In addition, birds have perched both on the front aperture and floor of the box, in the one case obscuring the target and in the other providing a secondary source. The basic design principles which have emerged are:

1. The box should be baffled, both to prevent internal reflections and to restrict the field of view of the target.
2. The entire internal surface should be coated with a good weather proof low reflectance paint.
3. The front entry should be knife edged in shape to prevent the accumulation of snow and the roosting of birds.
4. The front compartment of the box should be equipped with a sump and light proof drainage. Thus enabling any foreign matter which enters to fall far enough so as not to provide a secondary source of illumination for the target proper.
5. The target should be of a low reflectance non-specular material mounted in such a way that it can be removed for inspection and maintenance.

An improved dark target has been built with these aims in mind.

5. ALTERNATIVE METHODS FOR USE AT NIGHT

The method of contrast reduction as described is limited to daytime use and cannot readily be adapted for use after dark. In order to achieve round-the-clock operation it would be necessary to employ a hybrid system, preferably based on the hardware employed for the daytime use.

One candidate technique for the night-time component of the system is the low cost transmissometer. This could be achieved through the use of a light source perhaps mounted within the dark target unit and occulted by the dark target plaque.

One of the punitive aspects of transmissometer system design is the need to overcome and reject natural daylight from the measurement. In addition, a system which is geared to the reporting of HVN over the range 50 to 1500 m may well need to measure MORA over the range 10 to 1500 m. By restricting the use of the transmissometer to the hours of darkness, the need to reject daylight is removed. In addition the upper end of the required MORA range may be reduced to some 510 m, thus eliminating the need for error susceptible measurements at high transmittance values. This transmissometer however, unlike the contrast meter would not be self compensating in respect to drift in source output, or detector sensitivity.

Another method which has received some attention is the design of an integrating nephelometer which might be adapted to use the hardware and configuration of the contrast meter. As discussed previously one of the major criticisms of the integrating nephelometer is its inability to include measurements of scattering components at small forward angles. The configuration of the contrast meter however, suggests a form of open extended construction for an integrating nephelometer which might overcome this problem and yet yield a reasonably robust, self compensating system. This would use a circular, angularly weighted source placed in front of the dark target to illuminate the sight line over a wide range of angles. The circular nature of the source being used to compensate for any displacement in aim. In order to achieve a ratio-metric mode of operation it is necessary to measure the effective source intensity. In the case of daylight this was the background. In this case the angular weighting of the source means that only a small proportion of the light is directed towards the sensor. One way of obtaining a represent-ative measure of the light output would be to interpose a translucent diffusing screen immediately in front of the source. A preliminary analysis shows that this allows the compensation of the transmission losses involved in the 2 measurements and gives an appropriate functional relationship.

6 CONCLUSIONS

The method of contrast reduction described in this paper, is an adaption of the natural visual process for the daytime assessment of visibility for use by an automatic instrument. As such it makes use of a well established law due to Koehrmelder relating the apparent contrast reduction in a dark target to visibility. Distinct from other methods, it has the merit of being both a passive and a robust measurement process. In this respect it has been demonstrated that the process compares favourably to transmissometer techniques which are frequently used as a standard against which other methods are assessed. Again, contrary to other methods, it incorporates those aspects of the visual environment which are not normally considered. In particular, the reflectance of the surface about and below the measurement path and the directional qualities of the ambient light in the direction that the measurements are made. A further significant advantage is the self compensating nature of the measurements, whereby variations in source intensity (in this case the ambient light) and, or system sensitivity are automatically eliminated.

Another advantage of the method is that the target does not require accurate alignment and that the length of the measurement path can be varied widely, without the more usual restrictions arising from limitations in source power and detector sensitivity.

The comparisons made by a human observer to prove the technique have been highly successful over the range of exposure, although this range was small. Undoubtedly, the process of evaluation by field trials does pose problems, particularly in the longer visibilities, as it does with any method for visibility assessment.

An area of difficulty concerns the calibration of the system in good visibilities. This is due to the effects of spatial variability on widely differing path lengths. This problem also occurs whenever unassisted human observations are used to calibrate an instrumental visibility system. In this case means of making background measurements which are more representative have been suggested. The greatest shortcoming lies in the fact that the system is for use in daylight only, though in twilight conditions the relatively mediocre sensitivity of the prototype instrument outstripped that of a human observer. Notwithstanding, the method is unsuited for use after dark and alternative methods have been proposed to operate in this regime. At least one, if not both of these approaches could result in a round the clock system which would compare very favourably in accuracy cost and complexity with existing systems. While the pros and cons of the contrast reduction system are summarised in Table 1, more detailed results are to be published at a later date.

ACKNOWLEDGEMENTS

This paper is based on research which was funded by the UK Civil Aviation Authority and used equipment supplied by them. Valuable personal contributions were also made to the research by CAA personnel and the author would like to acknowledge the contribution of Mr W D Brown in particular.

Table 1Pros and Cons of the Contrast Reduction MethodAdvantages

- 1 Passive measurement.
- 2 Improved accuracy over equivalent transmissometer.
- 3 Unlimited length of measurement path (see below).
- 4 Compensates source/detector drift, no long term stability requirement.
- 5 Tolerant to deterioration in target reflectance.
- 6 Insensitive to mis-alignment, particularly of target.
- 7 Eliminates scattering defects in measurement.
- 8 Incorporates scene reflectance and light field anisotropy.
- 9 Insensitive to dirtying of optical window (see 4 above).
- 10 Potentially simple optics and electronics.
- 11 Easily adapted to use in many directions.

Disadvantages

- 1 Daytime to twilight use only, requires augmentation for night-time.
- 2 Clear visual path required to 1.5 times highest reported MOR.
- 3 Slant measurements must be made viewing upwards (see 2).
- 4 Requires means of sampling local light environment to aid calibration.
- 5 Dark target measurement requires optics with low veiling glare.
- 6 Large total dynamic requirement.

REFERENCES

<u>No.</u>	<u>Author</u>	<u>Title, etc</u>
1	J. Gorraiz H. Horvath	Influence of non-uniform ground reflectance on horizontal visibility. Applied Optics, Vol 22, No 21, 1983
2	M.E.K. Middleton	Vision through the Atmosphere. Toronto Press, 1958
3	G.A. Douglas L.L. Young	Development of a transmissometer for determining visual range. National Bureau of Standards, Report 17, February 1945
4	H.S. Muench E.Y. Moroz L.P. Jacobs	Development and calibration of the forward scatter visibility meter. Air Force Geophysics Laboratory, Cambridge, Mass, USA, Report No AFGL-TR-74-0145, March 1974
5	J.A. Garland J.B. Pse J. Phya	An integrating nephelometer for atmospheric studies and visibility warning devices. AFRE Harwell, England, E Sci Instr, 1970, Vol 1
6	H.A. Brousmiche I.L. Gajardin M.E. Etienne P. Rouet	Final report of tests on ACEC videometer in fog chamber at University of California, Berkeley California, US. Report No FAA-RD-67-32, Project No 430-302-01N, July 1967
7	M. Etienne P. Rouet C. De Swert B. Blave	Automatic videometer for the runway visual range measurement. Regies des Voies Aeriennes, Department Securite Service Meteorologique
8	M. Vizee W.E. Evans	Automated measurements of atmospheric viability. AIAA 21st Aerospace Sciences Meeting, AIAA-83-0436
9	H. Kondo Y. Chiba T. Yoshida	Veiling glare in photographic systems. SPIE Vol 274 Assessment of Imaging Systems: Visible and infrared, 1981
10	O.D. Barteneva	Scattering functions of light in the atmospheric boundary layer. Bull Acad Sci USSR Geophys. Series 12,1237 (1960), in English
11	D.S. Goodman	Illumination analysis with a reflecting sphere. Applied Optics, Vol 24, No 8, April 1985
12	H.R. Blackwell	Contrast thresholds of the human eye. JOSA, Vol 36, No 11, November 1946
13	-	Spot-on test for eyes New Scientist, 5th March 1987

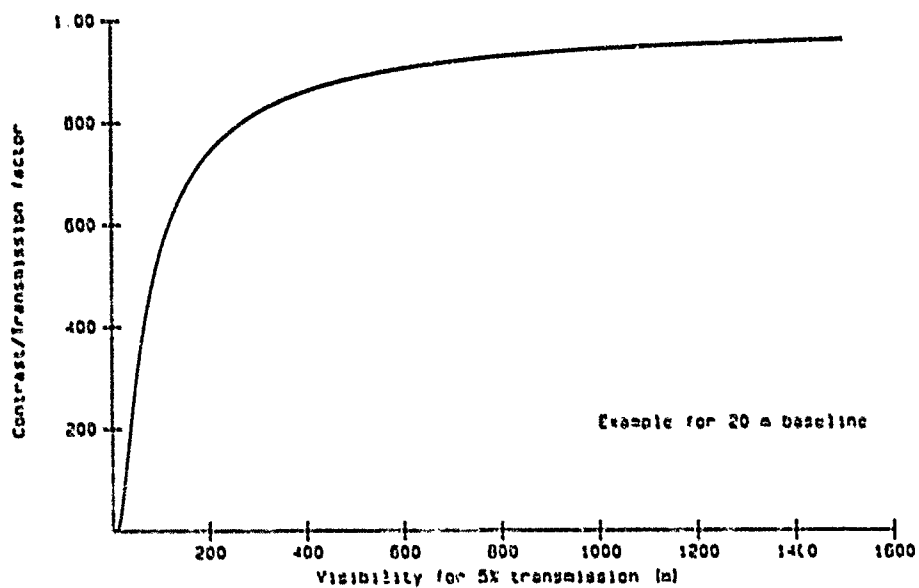


Fig 1 Contrast/Transmission Meter Characteristics

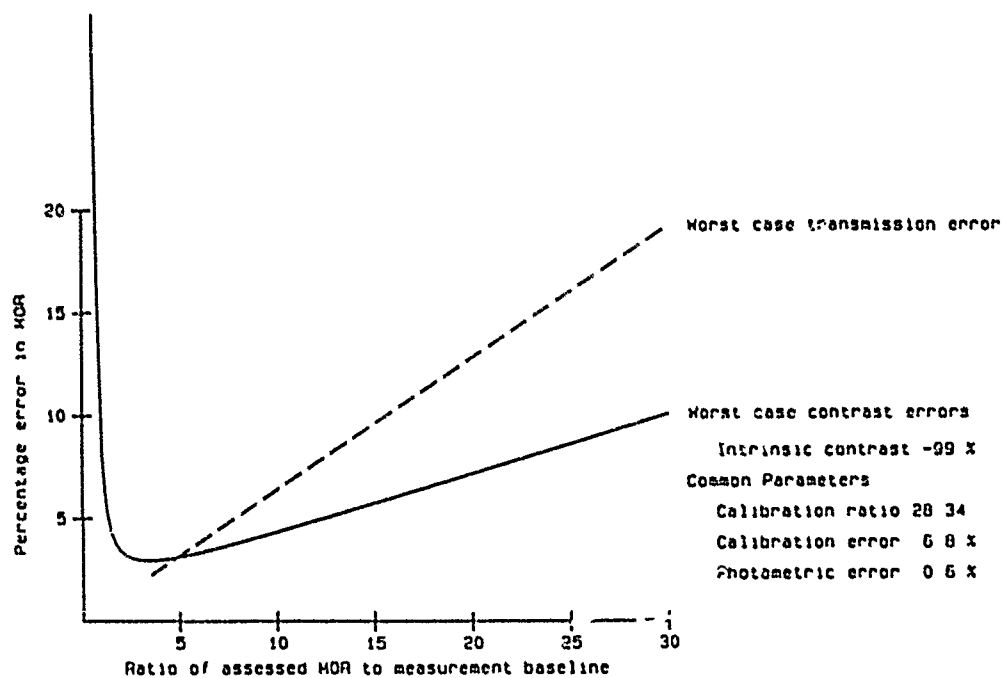


Fig 2 Comparison of System Errors.

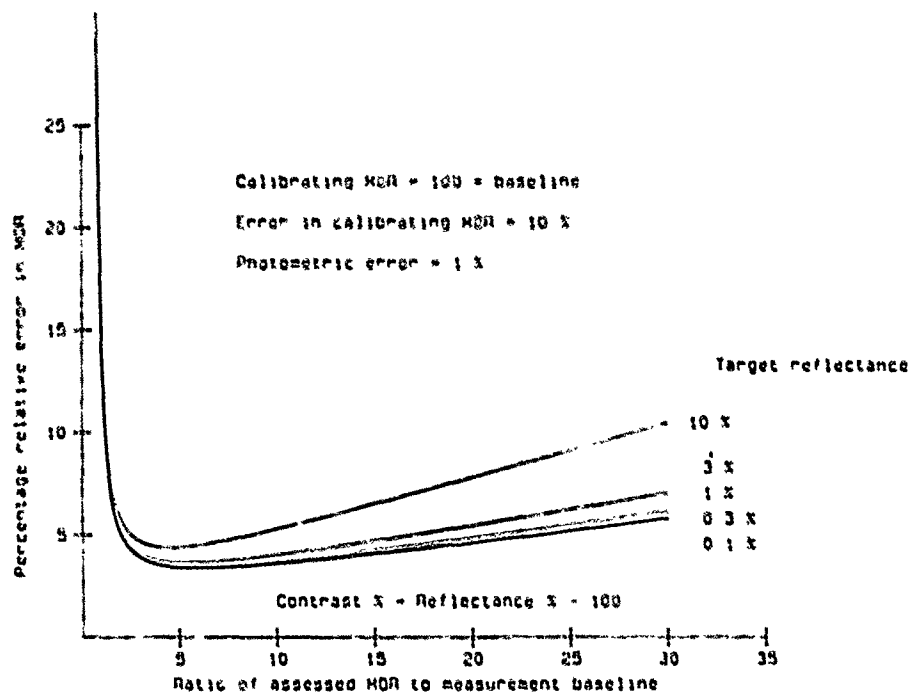


Fig 3 Contrast System Sensitivity to Target Contrast.

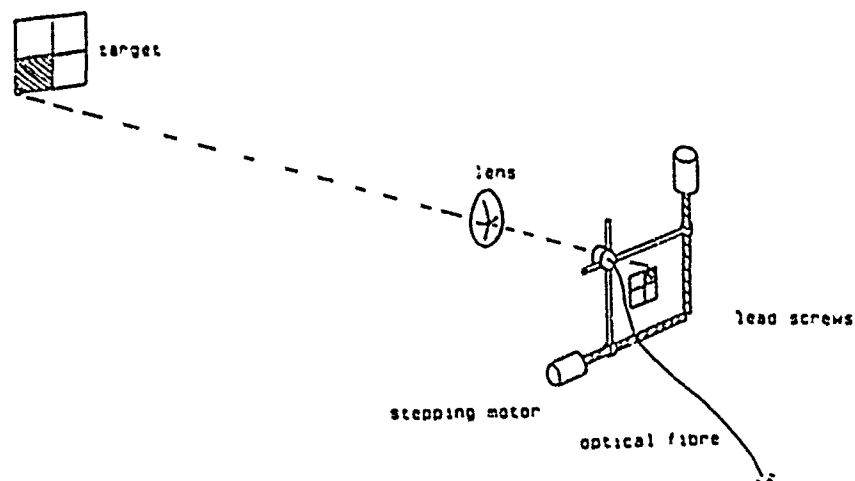


Fig 4 Principle of Experimental Sensor

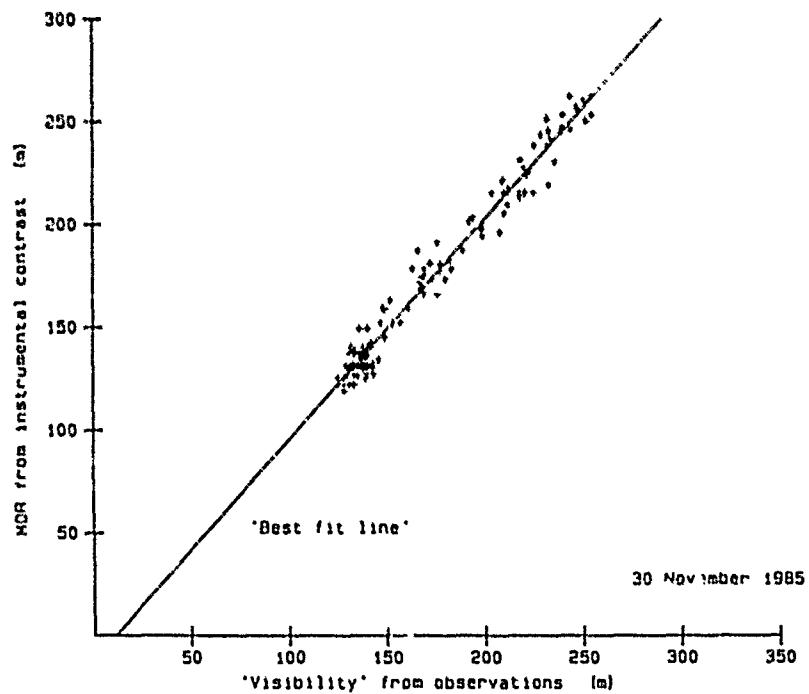


Fig 6 Comparison of Instrumental MOR with Observations.

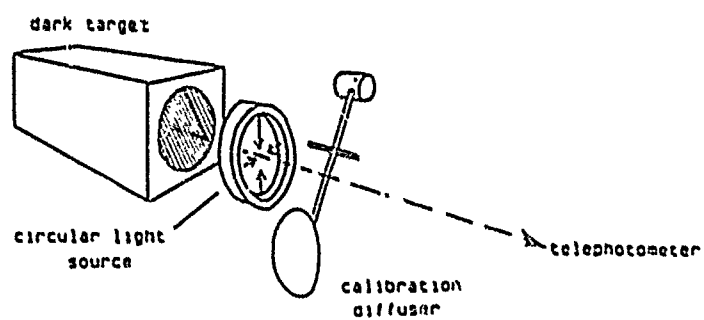


Fig 7 Possible Scheme for Scatter Meter.

NASA'S PROGRAM ON ICING RESEARCH AND TECHNOLOGY

John J. Reimann, Robert J. Shaw and Richard J. Kanaudo
National Aeronautics and Space Administration
Lewis Research Center
Cleveland, Ohio 44135 U.S.A.

SUMMARY

2637-3
This paper reviews NASA's program in aircraft icing research and technology. The program relies heavily on computer codes and modern applied physics technology in seeking icing solutions on a finer scale than those offered in earlier programs. Three major goals of this program are (1) to offer new approaches to ice protection, (2) to improve our ability to model the response of an aircraft to an icing encounter, and (3) to provide improved techniques and facilities for ground and flight testing. This paper reviews the following program elements: (1) new approaches to ice protection; (2) numerical codes for deicer analysis; (3) measurement and prediction of ice accretion and its effect on aircraft and aircraft components; (4) special wind tunnel test techniques for rotorcraft icing; (5) improvements of icing wind tunnels and research aircraft; (6) ground deicing fluids used in winter operation; (7) fundamental studies in icing; and (8) droplet sizing instruments for icing clouds.

INTRODUCTION

The icing problem is receiving more attention today than it has in any other period of the last 25 years. For example, at the NASA Lewis Research Center, testing activity in the Icing Research Tunnel (IRT) has increased steadily over the past 10 years, and in 1988 the IRT logged 1330 hr of test time, which is the highest annual usage on record since 1950.

There are many reasons for the current interest in icing: (1) the more efficient, high by-pass ratio engines of today and the advanced turboprop engines of tomorrow have limited bleed air for ice protection, so the airframers are seeking more efficient systems; (2) airfoil designers do not want their modern, high-performance surfaces contaminated with ice, so they are intensifying pressure to develop ice protection systems that minimize residual ice and thereby allow the airframer to keep airfoil surface area to the minimum; (3) new military aircraft requiring all-weather capability are currently under development; (4) some existing military aircraft, being used primarily for training missions, are experiencing foreign object damage (FOD) due to icing conditions they would not normally encounter in combat; (5) designers of high performance military aircraft want to avoid burdening the aircraft with ice protection, so they want to know where and how much ice will build on the aircraft and whether the aeroperformance penalties are acceptable; (6) designers of future high performance aircraft with relaxed static stability need to know how their aircraft will perform with contaminated aerodynamic surfaces; (7) little is known about the effects of ice accretion on the operation and performance of advanced turboprops, and whether or not ice protection will be required; and (8) the FAA has certified only one civilian helicopter for flight into forecasted icing, which implies a strong need for support of helicopter icing.

NASA's icing program was first reviewed in 1983 (Ref. 1). Many elements of the early program are still in progress, and they are brought up to date in this paper. Some new elements have been added, the most notable ones being the following: ice protection systems based on electro-mechanical impulses; effects of ground deicing fluids on wing aerodynamic performance during takeoff, upgrades and enhancements to the LEWICE ice accretion prediction code; applications of viscous flow codes to the icing problem; experimental observations of the ice accretion process; and structural and adhesive properties of impact ice.

Other review articles have been published on parts of the NASA aircraft icing program. Reference 2, published in 1984, gave an account of our aircraft icing analysis activities (analytical and experimental). Several review papers (Refs. 3 to 5) were published in 1988. Reference 3 gave an update of our icing analysis activities for ice accretion on unprotected airfoils. Reference 4 reviewed our analytical modeling, wind tunnel experiments, and flight testing and showed how they support our goal of modeling the effect of icing on the whole aircraft. Reference 5 reviewed the numerical codes that model the transient performance of electrothermal deicing systems.

This paper attempts to present the full scope of NASA's extensive program in aircraft icing research and technology. Three major goals of this program are (1) to offer new approaches to ice protection, (2) to improve our ability to model the response of an aircraft to an icing encounter, and (3) to provide improved techniques and facilities for ground and flight testing.

For several years, the Federal Aviation Administration (FAA) has contributed financial support to the NASA icing program, especially in the areas of ice accretion modeling, cloud droplet instrumentation evaluation and calibration, and icing scaling.

ICE PROTECTION SYSTEMS

Since the mid 1950's, jet transports have kept their critical lifting surfaces and engine inlets completely clear of ice by employing hot air anti-icing systems. But more recently, as jet engine manufacturers have begun increasing engine by-pass-ratios to achieve higher efficiencies, the engine cores have become smaller and the amount of hot bleed air available for anti-icing has shrunk significantly (Fig. 1). To cope with this loss of bleed air, airframers are (1) eliminating ice protection from selected components, or (2) developing the more energy-efficient deicing systems that require some buildup of ice before activation. Helicopters, general aviation, and light transport aircraft, all with relatively small payload fractions and low power margins, have always relied heavily on the more efficient deicing systems.

Always in demand are new ice protection systems that can offer any of the following improvements: lower weight, lower power consumption, more effective ice removal, more reliable operation, more easily retrofitted to existing components, smaller aero penalties, lower maintenance costs or lower manufacturing costs. NASA has selectively supported the development of ice protection systems, with emphasis on the more efficient deicing systems.

Next to pneumatic deicer boots, the most efficient mechanical deicing systems are those that employ electro-mechanical impulses. Typically, the power required for electro-mechanical deicing is about one percent of that used for evaporative anti-icing. Electro-mechanical deicers use about as much power as the aircraft's landing lights.

Three deicing systems employing electro-mechanical impulses have been supported by NASA. These are (1) the Electro-Explosive Separation System (EESS), (2) Electromagnetic Impulse Deicers (EIDI), and (3) Eddy Current Repulsion Deicer Boots (ECRDB). All three of these systems are energized by rapidly discharging a capacitor through electrical conductors whose currents set up opposing magnetic fields that force the conductors rapidly apart. The short discharge pulse, a fraction of a millisecond in duration, imparts an impulsive force to the ice that shatters, debonds, and expels it from the surface. The required power supplies and switching circuitry are nearly identical for the three systems.

Electro-Explosive Separation System

The EESS system was invented and patented by Mr. L. A. Haslim of the NASA Ames Research Center, Moffett Field, CA (U.S. Patent No. 4,690,353; September 1, 1987). Though it has undergone only limited icing testing to date, it appears to be an effective deicer. It seems to be especially effective for removing thin layers of ice. Thus the EESS can be activated after very thin layers of ice have built up, which should minimize the aeroperformance penalties caused by ice accumulated between activations or by residual ice left after activation. Because it can be easily manufactured as a thin boot and easily retrofitted by bonding to the outside of any component, several companies are interested in applying it to both civilian and military aircraft.

As shown in Fig. 2 the EESS conductors are arranged as a series of U-shaped ribbons such that the current flows into one leg of the U and out the other. When the capacitor discharges into the ribbon, the opposing currents in the two legs create opposing magnetic fields that force adjacent ribbons rapidly apart. The conductors are embedded in the elastomeric boot as shown in Fig. 3. Slits in the deicer boot allow the ribbon conductors to move rapidly apart and then they quickly collapse back to a thin layer.

The B. F. Goodrich Company tested the EESS system on board the NASA Twin Otter icing research aircraft, and Data Products of New England tested it in the NASA IRT, and on the Twin Otter.

Through a competitive bidding process, NASA has granted limited patent rights for the EESS to Data Products of New England, Wallingford, CT. Reference 6 provides a discussion of the improvements that Data Products of New England is currently carrying out on the EESS.

Data Products of New England offers blankets from 0.040 to 0.080 in. thick, smooth on both sides, and capable of being feathered into the surface on which they are installed. Thickness adds durability, but reduces blanket efficiency and may affect air flow. Blankets weigh between 0.7 and 1.1 lb/ft². Each rectangular area of approximately 70 in.² maximum is connected to one Blanket Driver Assembly (i.e., a capacitor and related switching circuitry). Five separate blankets were pulsed for a total of 50,000 cycles, with greater than 10,000 cycles being the highest on one blanket, with no discernible degradation.

Electromagnetic Impulse Deicer

NASA recently completed a development program on the EIDI system that began in 1982. Reference 7 is the final EIDI report that summarizes the program history, test results, technical accomplishments, and analysis and design procedures for the implementation of an EIDI system.

The physical form of the EIDI method is shown in Fig. 4. Flat-wound coils made of copper ribbon wire are placed just inside the leading edge of a wing's skin with a small gap separating skin and coil. Either one or two coils are placed at a given span

wise station, depending on the size and shape of the leading edge. Two methods of supporting coils are shown: support by a front spar or from a beam attached to ribs is generally used, but mounting to the skin itself is sometimes used.

Energy is discharged from a capacitor through the EIDI coil. The rapid discharge creates a rapidly forming and collapsing electromagnetic field which induces eddy currents in the metal skin. The magnetic fields resulting from current flow in the coil and skin create a repulsive force of several hundred pounds magnitude, but a duration only a fraction of a millisecond. A small amplitude, high acceleration movement of the skin acts to shatter, debond and expel the ice. Two or three such "hits" are performed sequentially, separated by the time required to recharge the capacitors, then ice is permitted to accumulate until it again approaches an undesirable thickness.

Deicing has been successfully accomplished in the icing wind tunnel and in flight for typical general aviation and transport wings and inlet nacelles under a wide range of velocities, angles of attack, icing rates and temperatures. Testing consisted of eleven sets of icing tunnel tests and two flight test programs. Fatigue tests were conducted for the wing skin and the EIDI components. Tests on electromagnetic interference (EMI) with other aircraft systems was also conducted. Both fatigue life and EMI emissions can be made acceptable.

EIDI's major advantage is that it does not alter the external surfaces of the aircraft, and therefore does not impose an aerodynamic performance penalty. Its limitation is that it does not adapt readily to retrofitting, since in most cases it must be considered a part of the original design of the component. The fundamental technology for EIDI is now established, and it is up to the various airframers and engine nacelle fabricators to adopt it. Those who have worked on the EIDI program are convinced that it is just a matter of time until it makes its way onto a next generation aircraft.

Eddy Current Repulsion Deicing Boot

The ECRDIB contains electrical conductors in an elastomeric boot that is bonded to the leading edge of a wing. When a capacitor is discharged through the conductors, eddy currents are induced in the skin of the wing, just as in EIDI. Opposing magnetic fields repel the boot rapidly away from the wing. No say that ECRDIB is EIDI applied on the outside rather than the inside of the wing. (ECRDIB differs from EESP in that EESP does not induce eddy currents.) NASA has a small contract with Electroimpact, Inc., Seattle, WA, to fabricate several ECRDIB units and test them on a large-chord and a small-chord wing section in the NASA IRT.

The ECRDIB conductors will be fabricated from stacks of thin, flexible circuit boards, with a coil conductor pattern that allows current to enter and exit the edge, rather than the center, of the circuit board. A sheet of elastomeric material will cover the circuit boards to form the boot. The inventor (Ref. 8) has calculated that for the same pulse of energy, the ECRDIB should deice about two to four times the area an EESS would deice.

The EESS and the ECRDIB systems are embedded in elastomeric boots that are applied over the outside of the airfoil. As with the pneumatic boot, these elastomeric outer surfaces will tend to get pulled away from the airfoil skin in the region of negative pressures or suction pressures, i.e., on the upper leading edge of the airfoil. This would cause upper surface distortion and an attendant aerodynamic performance penalty. Designers of pneumatic boots pull a vacuum on the inside of the boot to prevent the boot from staying inflated after the boots are activated. Pulling a vacuum on an EESS or ECRDIB seems impractical, and some other means must be found to overcome this problem. Data Products appears to have solved this problem for EESS.

The other issue with elastomeric materials is their ability to withstand rain and sand erosion. Erosion would be most serious near the outboard sections of helicopter rotors. Perhaps an acceptable solution for rotors would be a hybrid system consisting of EESS on the inboard sections and electrothermal on the outboard sections.

PREDICTIONS OF AIRFOIL AERODYNAMIC PERFORMANCE DEGRADATION DUE TO ICING

A major goal of the NASA aircraft icing program is to develop and experimentally validate a group computer codes that will predict the details of an aircraft icing encounter. The flowchart in Fig. 5 shows the many codes required to form such an overall icing analysis methodology and indicates the codes currently under development by NASA. Once validated, these codes can be used for (1) preliminary design studies to ascertain component sensitivity to icing, (2) performance predictions of proposed ice protection systems, (3) computer-based certification or qualification studies to reduce the amount of required icing flight testing, and (4) more realistic icing effects inputs for use in flight training simulators.

This section will review the progress on one goal of the overall activity, namely, to produce codes that predict the ice buildup on an unprotected airfoil and the resulting aerodynamic degradation. NASA has given the name LEWICE to its overall ice accretion code. (This section is a condensation of the material in Ref. 3 and also includes some more recent material).

Figure 6 illustrates the aerodynamic performance penalties caused by leading edge ice: (1) increased drag even at low angles-of-attack; (2) airfoil decambering due to a

thickened upper surface boundary layer; and (3) reduced C_{lmax} and premature stall due to separation of the airfoil upper surface boundary layer.

Overall Approach

Figure 7 shows the key physical processes that must be adequately modeled in any airfoil icing analysis methodology. In the LEWICE approach, ice is grown layer by layer, where each layer represents the ice accretion for one user-specified time increment. The overall approach for LEWICE is as follows: (1) a potential flow code calculates the flow field around the airfoil; (2) a droplet trajectory code, using the inviscid flow velocities, computes the local water flux around the airfoil; and (3) an ice accretion code, using the local water fluxes and inviscid velocities, calculates the local ice growth around the airfoil. At this point the code can loop back and re-run the potential flow analysis to determine the new inviscid flow field around the iced airfoil. Then a new droplet trajectory calculation and a new ice accretion calculation can be completed for the second time step, and so on. The looping process is repeated for as many time increments as required to reach the overall icing encounter time. If aerodynamic performance losses are required for the iced airfoil, then a viscous flowfield calculation is performed for the predicted ice shape.

It is highly desirable to replace the separate inviscid and viscous flow calculations with a single viscous flow calculation. However, we have not yet made the replacement because a viscous flow calculation requires far more computer time than does an inviscid calculation, so the total CPU time to calculate an ice shape would be impractical for routine calculations. Obviously as the ice shape grows and dominates the airfoil leading edge flowfield, viscous effects (boundary layer separation and reattachment) will become so important that the simplified inviscid analysis will no longer be appropriate.

The following sections will look at the modules in more detail.

Inviscid Flowfield/Droplet Trajectories

The inviscid flowfield code is a second order panel code. Droplet trajectories are obtained by integrating Newton's second law of motion using a predictor-corrector scheme optimized for stiff systems of equations.

An experimental droplet impingement data base is being obtained for use in validating the droplet trajectory prediction codes (Ref. 3). Comparisons between analysis and experiment are shown in Fig. 8. The comparisons show that the prediction, when using either inviscid or viscous flowfield velocities, is quite accurate for cases of small ice accretion, but not as accurate for large ice accretions that have massive flow separation with unsteady flow. Figure 8 shows that while the predicted collection efficiencies were lower when the viscous flow velocities were used in the trajectory calculations, they were not as low as those observed in the experiment. Since the Navier-Stokes codes overpredicts the velocities near the separation points, the next logical step seems to be to replace the actual model geometry with a geometry that follows the outer boundary of the separated flow region behind the horns. This geometry should not produce the higher velocities near the beginning of separation, and should begin turning the flow further upstream, thereby reducing the droplet collection efficiency. We plan to try this in the near future.

Ice Accretion

The ice shape module predicts ice shapes by solving the continuity and energy equations for differential control volumes on the surface of the airfoil as depicted in Fig. 9. The code determines the fraction of incoming water that freezes in each control volume. Any water that does not freeze in a control volume is assumed to flow back to the immediately aft control volume.

Figure 10 shows representative comparisons of predicted shapes versus actual ice shapes grown on a NACA 0012 airfoil in the NASA IRT. The agreement in predicted versus measured ice shape for both the rime and glaze ice was judged to be acceptable. Typically, LEWICE predicts rime ice shapes very well, but it can have difficulty with glaze ice predictions. Other comparisons with in-flight icing are given in Ref. 9.

The dependence of airfoil drag on ice formation temperature is shown in Fig. 11 (Ref. 10). Notice that at the warmer temperatures the drag is extremely sensitive to ice formation temperature. Also note that the mass of accreted ice stays relatively constant until the temperature approaches the freezing point of water, and then the mass drops off presumably because the runback water blows off the airfoil. The current NASA ice accretion module does not account for water blowoff.

A key part of the ice accretion module is the method used to predict heat and mass transfer convection coefficients. The convection coefficients are calculated by the integral boundary layer method (Ref. 3). The ability to model surface roughness as an equivalent sand grain roughness is an important feature of the integral boundary layer method. The predictions were compared with results from a heat transfer experiment in which ice shapes grown on a cylinder in the IRT were replicated in a wood model that was instrumented with surface heat flux gauges (Ref. 11). The predicted heat transfer coefficients shown in Fig. 12 do not agree favorably with the experimental data.

Figure 13 compares the experimental data with predictions made with a Navier-Stokes code that solves the energy equation and uses a distributed roughness model (Ref. 12). The agreement between analysis and experiment is good.

The icing process modeled in LEWICE follows closely the model given by Messinger (Ref. 13). The Messinger model, as depicted by Olsen (Ref. 14), is shown in Fig. 14. Olsen took closeup movies of the actual ice accretion process under a variety of ice formation conditions in the IRT, and his observations lead him to propose the new model shown in Fig. 15. In this model, water flows along the surface only during the initial moments of exposure to the icing cloud. After that, the water begins to form beads on the surface as shown in Fig. 16. Ice forms in the base of the beads and impinging water accumulates at the top of the beads.

Hansman (Refs. 15 and 16) later followed up on Olsen's work and basically confirmed Olsen's observations. Hansman observed several distinct zones of surface water behavior: a smooth wet zone in the stagnation region with a uniform water film; a rough zone where surface tension effects caused coalescence of surface water into stationary beads; a horn zone where roughness elements grew into horn shapes; a runback zone where surface water ran back as rivulets; and a dry zone where rime feathers formed. The location of the transition from the smooth to the rough zone was found to migrate with time towards the stagnation point. The behavior of the transition appeared to be controlled by boundary layer transition and bead formation mechanisms at the interface between the smooth and rough zones. Regions of wet ice growth and enhanced heat transfer were clearly observed with infrared video recordings of glaze ice surfaces.

Hansman formulated a three zone model and tested it by forcing the LEWICE ice accretion module to have three zones. A zone near the stagnation region was modeled by the original control volume approach. A second zone was modeled as freezing all the water that impinged on it. A third zone was modeled as a transition zone separating the other two zones. In the transition zone the control volumes had freezing fractions that varied linearly from the value at the edge of the first zone to a value of unity at the edge of the second zone. Figure 17 shows how an experimental ice shape formed on a cylinder compared with the predictions made by the unmodified approach and by the Hansman approach. Hansman's model gave results far superior to the unmodified approach.

Because this new multi-zone model holds promise of being more representative, NASA will continue to conduct fundamental experiments on the details of the ice accretion process, such as, closeup movies in natural icing clouds and infrared studies of the surface of the ice (Ref. 16).

Aerodynamic Performance

As noted earlier, it is highly desirable to replace the potential flow code in LEWICE with a viscous flow code that more accurately models the flowfield and also allows a direct calculation of lift, drag, and pitching moment. To this end, NASA is developing two viscous flow codes: (1) a Reynolds averaged thin layer Navier-Stokes code (ARC2D) (Ref. 17), and (2) an interactive boundary layer code (IBL) (Ref. 18). Both of these codes were designed to handle clean airfoils and are being extended to handle iced airfoils for which flow separation and reattachment at lower angles-of-attack is not uncommon. The IBL code is attractive for inclusion in LEWICE because it utilizes a potential flow code which requires far less computer power than the Navier-Stokes code.

A comprehensive experimental data base for validating the viscous flow codes is being developed as Fig. 18 illustrates. A NACA 0012 airfoil model was modified to have a leading edge ice shape that had the gross cross sectional features of an ice shape grown in the IRT, but also had a geometry that could be accurately digitized to allow inputting to flow analysis codes.

Figure 19 compares the predictions of the ARC2D and IBL codes with the experimental data base described by Fig. 18. At lower angles-of-attack, both codes compared well with experiment. At the higher angles-of-attack the IBL code underpredicted the measured drag levels. At these higher angles the ARC2D code predicted unsteady flow. Although the IBL code appeared inadequate at the high alphas for this case, Cobelli (Ref. 19) showed that the IBL code can do a good job on clean airfoils beyond stall.

NASA is supporting grid definition studies (Ref. 4) and also developing an adaptive grid generation code that should prove useful for generating a new grid for each new time step in the LEWICE ice accretion calculation. Another supporting effort for the ARC2D code is the testing of various turbulence models such as the Baldwin-Lomax model and the Johnson-King model, as well as a model developed in-house (Ref. 20).

Work is continuing on improving the two-dimensional viscous flow codes and on conducting experiments to validate them. The next step is to begin work on three-dimensional codes for application to modern swept-wing aircraft. To this end, NASA is conducting wind tunnel testing at the Ohio State University (Ref. 21) on three-dimensional rectangular and swept semi-span wings with and without attached ice shapes. A data base similar to the two-dimensional data base (see Fig. 18) will be acquired. NASA is also supporting development of a three dimensional Navier-Stokes code (Ref. 22) that will be validated against the experimental data.

Although a great deal of research still needs to be done on ice accretion modeling and aeroperformance penalties, the codes presented in this section are representative of the best available at this time. Many organizations in the U.S.A. are using these codes as research codes and are relaying their experiences with them to NASA and its grantees and contractors.

AIRPLANE PERFORMANCE AND STABILITY AND CONTROL CHANGES DUE TO ICING

Since ice will accumulate on selected surfaces of modern aircraft, and since failure of any ice protection system will result in ice accumulations, NASA has a major program element to study the effects of icing on aircraft performance and stability and control. The approach employs three interrelated elements: analysis, wind tunnel experiments, and considerable flight testing in natural icing clouds.

In the previous section, we reviewed NASA's research on the effects of icing on airfoil aerodynamics. In this section we will concentrate on flight testing in natural icing clouds.

Research Aircraft

The NASA Lewis icing research aircraft shown in Fig. 20 is a modified Bellavilland DH-6 Twin Otter (Refs. 23 to 25). The aircraft is equipped with electrothermal anti-icers on the propellers, engine inlets, and windshield. Pneumatic deicer boots are located on the wing outboard of the engine nacelles, on both the horizontal and vertical stabilizers, on the wing struts, and on the rear landing gear struts. The pneumatic deicers located on the vertical stabilizer, wing struts, and landing gear struts are nonstandard items that provide additional research capability for measuring component drag through selective deicing. The aircraft is equipped with several standard instruments for measuring icing cloud properties (Ref. 26).

Wing leading edge ice shapes are measured in flight with a stereo photography system. Wing section drag is measured with a wake survey probe mounted on the wing behind the region where the stereo photos are taken. A noseboom is used to measure airspeed, angle-of-attack, and sideslip.

A complete flight test system is being built up to measure flight dynamics along a flight path. The system will include a data acquisition system and an inertial package that contains rate gyros, directional gyros, and servo accelerometers.

Wing Ice Shapes and Drag

One purpose of the icing flight research program is to obtain inflight data that can be used to validate computer codes and to confirm that the NASA Lewis Icing Research Tunnel adequately simulates natural icing. We have flown numerous flights through natural icing clouds, in which ice was allowed to build up on the wing leading edge. The aircraft was then flown out of the cloud into clear air, where stereo photographs were taken of the ice shape and a drag wake survey probe was moved across the trailing edge of the wing behind the ice shape (Ref. 24). Figure 21 shows the ice shape derived from the stereo photos and Fig. 22 shows the increase in drag versus angle-of-attack.

Later this year, a section of a Twin Otter wing will be mounted in the IRT (Fig. 23), and ice shape and drag will be measured under the same conditions as in flight so that a direct comparison can be made between flight and the IRT.

Aircraft Performance

Airframe icing degrades aircraft performance by reducing lift and increasing drag. This results in higher stall speeds, lower angles-of-attack for stall, lower climb, lower cruise, and lower power margins for engine out performance. These performance degradations were measured on the icing research aircraft for a wide range of icing conditions. By deicing one airframe component at a time and taking a set of performance measurements after each deicing event, we obtained lift loss on the wing and relative values of drag increase for each airframe component. For some cases power required versus power available was measured to assess the effects on engine-out performance (Ref. 27).

Results from a flight in glaze icing conditions (Ref. 27) are shown in Fig. 24. The most noticeable changes in the lift curves due to ice are lower slopes and reduced C_{lmax} . The test aircraft has a C_{lmax} of approximately 1.4 in the clean, no flap configuration. With ice, C_{lmax} is reduced to something less than 1.0. The loss in lift that remains after deicing all components is largely because the portion of the wing between the engine nacelles and fuselage has no ice protection. Another factor, more difficult to evaluate, is the contribution to lift loss made by residual ice left on the wings after cycling the deicer boots.

Figure 24 also shows the drag increase due to airframe icing. To a pilot, this translates into degraded aircraft performance, especially in the event of an engine-out condition. Figure 25 shows the relationship between power required and power available under the glaze icing conditions. The increase in power required means lower climb rates, altitude potential, and cruise speeds. These factors become essential for the pilot to consider when planning his options under an engine-out condition.

Stability and Control

NASA is formulating a methodology that will predict the effect of ice accretions on the stability and control characteristics of aircraft. This methodology will be useful in aircraft design, safety and airworthiness analyses, flight control system design for relaxed static stability aircraft, and possibly in providing simulator software for pilot training.

Rather limited flight tests have been conducted so far. These tests were structured to determine whether the icing effects were measurable, and if so, what their values were. The stability and control flight tests investigated only the longitudinal characteristics (Ref. 25 and 28). For these tests the icing research aircraft was configured with a Styrofoam layer of simulated ice bonded to the leading edge of the horizontal tail as shown in Fig. 26.

The flight test maneuvers and data acquisition were designed to provide a statistically significant ensemble of data points that could be analyzed by a Modified Stepwise Regression (MSR) technique to yield estimates of the stability and control derivatives. The aircraft was flown in the clean (baseline) configuration and then later with the "Styrofoam ice" on the horizontal tail. Forty five repeat maneuvers were flown at identical conditions for each configuration.

The MSR technique (Refs. 28 and 29) accurately estimated the longitudinal stability and control derivatives throughout the flight envelope of the aircraft. Figure 27 shows how elevator control power was degraded over the range of attainable flight speeds at a constant power setting. Note that the estimated variations, or predicted bands of uncertainty, were less than the measured changes.

In a supporting analytical effort, the icing research aircraft geometry was paneled up for input to a three dimensional airflow code (VSAERO). The digital description included propellers and both the baseline and iced-tail geometry. The ARC2D (Ref. 17) code was also run to obtain a modified geometric definition of the iced tail for input to VSAERO. The initial VSAERO calculations predicted nearly the same decrease in stability due to ice as the flight test did. However, the calculated results also indicated that the nonlinear downwash due to the propeller must be better modeled in VSAERO to obtain the correct power effects.

ROTORCRAFT ICING RESEARCH

Helicopter companies use the NASA IRT and other icing tunnels for testing engine inlets, rotor ice protection systems on a stationary rotor blade (i.e., no centrifugal force), stabilizers, external stores, weapons systems, optical systems, velocity sensors, and other vulnerable parts of a helicopter. However, a full-scale, rotating main rotor will not fit into any known icing wind tunnel. Therefore, to prove that the main rotor and tail rotor can operate successfully in icing, manufacturers have no choice but to fly their helicopters in icing clouds.

Because helicopters are slow and have a short range, they must wait for the weather to come to their home base of operations. This dependence on local weather further aggravates the most difficult icing certification problem: finding clouds that cover the wide range of natural icing conditions required for certification -- a range that often seems unattainable due to the low probability of some of the conditions. Thus it requires years to acquire enough icing data for either FAA certification or military qualification. Since U.S. helicopter manufacturers want all-weather operational capability and want to overcome this heavy dependence on flight testing NASA has been working with them to develop an icing test capability for sub-scale helicopter rotors in the NASA IRT.

Model Rotor Testing in the NASA Icing Research Tunnel

We have recently completed an icing test of a rotating OH-58 tail rotor in the IRT. The OH-58 tail rotor has a 13.3 cm chord and a 1.57 m diameter. The primary purpose of this test was to develop the techniques for operating a model rotor in an icing wind tunnel. The secondary purpose was to acquire data for use in developing various computer codes that predict ice accretion, ice shedding, and rotor performance degradation due to ice on rotors.

Operational concerns addressed in the test program were as follows: model and tunnel startup; coordination of model and tunnel operation; model and tunnel shutdown; observation and documentation of the rotor ice accretion and shedding; safety and emergency procedures; reaction of the rotor to the accretion and shedding of ice, and the control of the model under these circumstances.

Video cameras recorded overall and closeup views of the rotor ice buildup and shedding processes. A remotely controlled 35-mm camera was also used for detailed photographs of the ice formations during the runs. After each run, photographs and tracings of the ice shapes were taken for each blade. For some selected ice shapes, molds were made from which castings of the ice will eventually be made.

A substantial and unique rotor ice accretion and performance data base was acquired in this test. The rotor blade ice shapes were found to be quite repeatable for a given set of conditions, and corresponding iced rotor torque values were also repeatable.

up to the onset of shedding. When ice did shed, the inboard radial extent from which ice never shed was relatively repeatable, but the shed times, locations, and quantities of ice shed varied substantially from run to run. Although considered preliminary, this data will be useful for comparisons with the predictions of ice accretion codes, rotor performance codes, and ice shedding models.

Figures 28 and 29 show photos of the OH-58 tail rotor rig and of ice accretions on the rotor. And Fig. 30 shows rotor torque versus time during a typical icing encounter. A detailed report of these tests is in preparation and will be published as Ref. 30.

The successful test of the OH-58 tail rotor has prepared the way for a more sophisticated model rotor test that will be run in the IRT later this year. In this test, a scale model of the UH-60 Blackhawk (Fig. 28) will be tested with four NACA 0012 rotor blades, and data will be acquired with a six-component force balance. All four major U.S. helicopter companies will participate in the test.

ADVANCED TURBOPROP ICING STUDIES

NASA Lewis Research Center has been the U.S. leader in managing the development of the new high speed, high efficiency aircraft propulsion system, called the advanced turboprop (ATP). The ATP can operate efficiently up to about 0.85 Mach numbers. One of the ATP technology issues that requires research is ice protection (Ref. 31). Although aircraft equipped with advanced turboprops will cruise at altitudes above the FAR Part 25 Appendix C icing envelope, they are expected to encounter icing conditions during ground operation, take-off, climb, descent, low altitude hold, and they may cruise with accreted ice obtained at the lower altitudes. Of primary concern is the potential performance degradation of ATP's in icing environments. Advanced turboprops are built so ruggedly that it is unlikely that asymmetrical ice sheds will pose a serious vibration problem, if any at all.

Whether the ATP will require ice protection is not known yet. At warmer icing temperatures, it is likely that the ice can be shed from the turboprop blades by simply increasing engine rpm. But the ice may not shed at the coldest icing temperatures where ice adhesion is known to be stronger. Even if the ice can be shed at the coldest temperatures, some residual ice may cling to the blades and cause a loss in lift and an increase in drag.

To study the effect of ice accretion on ATP performance, NASA, Hamilton Standard, and Pratt & Whitney jointly conducted an icing test program at the Fluidyne Icing Tunnel (Ref. 31). The testing consisted of evaluating the ice accretion characteristics and resulting aerodynamic degradation for two thin, two-dimensional airfoil sections that were representative of advanced turboprop airfoils. The tests were conducted over a wide range of icing conditions, angles-of-attack, and Mach numbers (0.3 to 0.8). At each test point, the accreted ice shape and weight were recorded. Airfoil drag and surface pressures were measured for each run.

This data can be used for several purposes: (1) to compare with LEWICE predictions of ice shape; (2) to compare with lift and drag predictions in the literature; (3) for predicting ATP performance in icing; and (4) for constructing a composite ice shape that could be bonded to the leading edge of ATP blades for measuring performance losses during flight.

Other proposed efforts under consideration for the longer term include testing of a scale-model ATP in the IRT. The goals of these tests would be (1) to measure performance changes due to icing, (2) record actual ice accretion shapes, (3) observe shedding characteristics, and (4) use the resulting data to validate propeller performance codes and ice shedding codes. It is unlikely that satisfactory icing scaling laws will be found for relating sub-scale model testing to full-scale. But if the sub-scale data can be used to develop fundamental computer models for predicting changes in performance and ice shedding characteristics, we may be able to bypass the scaling question and use these models to predict full-scale results.

GROUND DEICING FLUIDS FOR WINTER OPERATION

The Boeing Commercial Airplanes Company and NASA conducted a joint test program in the IRT to evaluate the Type I and Type II ground deicing fluids that are used by the Association of European Airlines (AEA) during winter operations (Ref. 32). Several experimental fluids were also tested as possible candidates to replace the then-current Type II fluids. The object of the tests was to assess the aerodynamic performance penalties that result when an airplane takes off with ground deicing fluids on its wings.

Type I fluids are propylene glycol, which have hold times similar to those of the ethylene glycol fluids used in the U.S.A. for removing ice and snow from aircraft prior to takeoff. Type II fluids are non-Newtonian (thixotropic) fluids whose viscosity varies inversely with the rate of shear applied to the fluid. The Type II fluid is also called a thickened fluid, because it has the viscosity of a gel when sitting on the wings of a grounded airplane. But during takeoff, the air rushing over the wings exerts a shear stress on the fluid, thus reducing its viscosity and allowing the fluid to flow off the wing.

Prior to the IRT tests, the AEA and Boeing had conducted a joint flight test program on a Boeing 737 aircraft to evaluate the Type I and Type II fluids during take

off. The results of those tests were as follows: During takeoff, as the airspeed over the wing increased, the fluid surface became wavy and the fluid began to run off the wing, but it also accumulated near the trailing edge. The waviness roughened the upper airfoil surface, and the fluid accumulation near the trailing edge disturbed the airfoil. Both of these effects caused a loss in lift, an increase in drag, and a reduced stall angle-of-attack. The last effect was observed later in the wind tunnel tests, but not in the flight tests because the aircraft was not flown into stall while so close to the ground.

Tests were conducted on two models in the IRT: (1) a 0.091 scale 3D half model of the Boeing 737-200 ADV aircraft, and (2) a 0.18 scale 2D airfoil section at the 45 percent span of the 737-200 ADV aircraft (Fig. 31 and 32 respectively). Wind tunnel test objectives were as follows: (1) correlate wind tunnel and flight test measurements of aerodynamic effects of de-/anti-icing fluids; (2) evaluate fluid effects that could not be safely performed during flight tests; (3) expand flight test results for parametric variations of temperature, airfoil configuration, and fluid formulation; (4) contribute to the data base for establishing aerodynamic acceptance standards for ground de-/anti-icing fluids; and (5) obtain data that contributes to a physical understanding of the lift loss mechanism.

The data obtained from the wind tunnel tests included (1) model force data from internal balances; (2) surface static pressures; (3) initial fluid film depth from a gap gauge; (4) fluid film depth from a relationship between depth and photographed fluorescent intensity (a fluorescent dye added to the fluid and illuminated with ultraviolet light); (5) video recordings of fluid flow-off characteristics; and (6) boundary layer velocity profiles.

Typical results are shown in bar chart form in Fig. 33 where the percent loss in lift at 8° angle-of-attack and also at stall are presented for the Type I (labeled 1) and Type II (labeled 3) fluids and eight experimental Type II fluids. All of the experimental fluids showed lower lift loss than the then-current Type II fluid, and the losses for the experimental fluids were comparable to the losses for the Type I fluid.

An important outcome of this test program was that the experimental Type II fluids tested in the IRT in April 1988 have now become the current operational fluids in Europe. Another significant outcome is that these quantifiable test results showed that these new Type II fluids do not degrade takeoff aerodynamic performance anymore than do the Type I fluids. The Type II fluids have been shown by the AEA to have far greater holdover times than the AEA Type I fluids.

NASA also is funding research by Dr. C.S. Yih at the University of Florida to derive an analytical model of the surface instability that causes the fluid waves on the airfoil. Dr. Yih has identified the instability as being driven by the large fluid-to-air viscosity ratio. He has also derived dimensionless parameters that should be preserved during scale model testing to assure that model test results will represent full-scale results. A paper on the analytical formulation and mathematical solution will be published later.

DROPLET SIZING INSTRUMENTATION FOR ICING CLOUDS

Very accurate droplet size data is needed to validate droplet trajectory codes, such as the one used in LEWICE. And automated droplet sizing systems are needed to calibrate the IRT in a shorter time and with far fewer personnel than were employed in the earlier calibration program of the 1950's. NASA's droplet sizing effort is divided into two parts: (1) research to devise methods of calibrating and checking the accuracy of existing droplet sizing instruments; and (2) development of a new instrument that promises to overcome some of the known problems of the existing instruments.

Calibration Devices for Existing Wind Tunnel and Flight Instruments

Reference 33 presents a detailed review of the droplet sizing research conducted to understand the calibration and operation of two instruments manufactured by Particle Measuring Systems, Inc. (PMS): the FSSP (forward scattering spectrometer probe) and OAP (optical array probe).

A rotating pinhole device (Fig. 34) was developed (Refs. 33 and 34) to check the calibration of the FSSP. A calibration curve of the FSSP using rotating pinholes is given in Fig. 35. The value of this device is that it can be inserted into the FSSP probe volume at anytime to check whether the instrument is scattering light into the correct droplet size bin. This device can uncover misalignment of the laser or its optical system, it can measure optical parameters such as depth-of-field and optical collection angles, it can detect dirt or other contamination on the laser optics, and it can detect problems with the electronics systems. The device has proved invaluable in the recent calibration of the IRT, where it was demonstrated that such a calibration device is absolutely essential to the proper field operation of the FSSP.

NASA has checked the sizing accuracy of the FSSP by three methods: (1) pinholes, (2) glass beads, and (3) a water droplet generator. The results of these checks are shown in Fig. 36 where it can be seen that at the mid to upper range of the FSSP, the measured droplet size begins to depart significantly from the actual size. Thus in clouds with large droplets, the FSSP would undersize the median volume diameter 5 to 10 μm .

The Optical Array Probe (OAP) is used to measure droplets from 10 to 620 μm . NASA has developed a rotating reticle calibration disk for the OAP that provides absolute calibration over the entire size range of the OAP (Refs. 33 and 35). Figure 37 shows the calibration curve for the OAP using the rotating reticle.

When calibrating the icing cloud in the IRT, both the FSSP and the OAP were required because the droplet size range extended beyond the range of the FSSP alone. Thus results from the OAP and FSSP had to be spliced together to obtain a continuous droplet distribution. Unfortunately, the splicing process is not exact, and since the median volume diameter (MVD) of the cloud is extremely sensitive to the number of larger droplets, the measurement of the larger MVD's has an indeterminate uncertainty.

Development of a Wind Tunnel and Flight Instrument

A newer instrument developed by Aerometrics, Inc., named the Phase Doppler Particle Analyzer (PDPA), shows promise of eliminating some of the limitations we have in calibrating the IRT with the FSSP and OAP (Ref. 36). NASA has worked very closely with Aerometrics to upgrade the laboratory PDPA instrument. These upgrades, which center on the signal processor, will result in the following improvements: (1) measurement of particles with velocities representative of flight speeds; (2) increase in dynamic size range from 35 to 50 (dynamic size range is the ratio of largest particle size to smallest particle size); and (3) greater size accuracy at high speeds and dense sprays. These upgrades, when completed, should allow us to use a single instrument for measuring the entire operating envelope of the IRT cloud.

Currently, the PDPA is a laboratory instrument that can probe clouds up to about 2 ft in depth. But in its present form, it cannot be used in the IRT, whose test section is 1.82 by 2.74 m (6 by 9 ft). Nor can it be used in an aircraft to sample clouds. To convert the laboratory PDPA for use on aircraft or the IRT, Aerometrics was awarded Phase I and Phase II Small Business Innovative Research contracts. For the flight version, a small transmitter and receiver unit will be placed in the cloud and the laser light will be sent to and from the unit by fiber optic cables. The Phase II contract is for 2 years and is just getting under way.

EXPERIMENTAL ICING FACILITIES

The NASA Icing Research Tunnel has for several years been one of NASA's most heavily scheduled wind tunnels, with tests scheduled up to two years in advance. In 1988, the tunnel logged 1330 test hours, which is the highest annual usage on record since 1950. The IRT is the largest refrigerated tunnel in the world. The test section is 1.82 m high by 2.74 m wide by 6.09 m long (6 ft high by 9 ft wide by 20 ft long). Its maximum airspeed empty is 134 m/sec (300 mph), and its maximum airspeed with a model installed depends on the model blockage. The IRT can provide tunnel total temperatures from 0 to -35 °C (+32 to -30 °F). Two different sets of nozzles are available for producing supercooled icing clouds that cover most, but not all, of the FAA Part 25 Appendix C icing envelopes.

Recent Rehabilitation of the NASA Icing Research Tunnel

Two years ago, the IRT underwent extensive renovations aimed at improving its reliability and productivity. The major improvements are as follows: (1) a new spray bar system, which has eight bars to provide a more uniform cloud than did the original six bars; (2) a new 3.73 MW (5000 hp) drive motor; (3) new solid state controls for the drive motor; (4) a new distributed process control system, which provides programmable, digital control of the drive motor, the refrigeration system, the spray bar system, and other support systems; (5) a three-times-larger control room with vastly improved acoustics; (6) new electrical power supplies for operation of aircraft test models while in the IRT; and (7) replacement of all wooden floors with concrete floors.

Figure 38 shows a schematic of the IRT flow circuit and identifies the components that were rehabilitated. These improvements not only have increased productivity, but also have provided new test capabilities. For example, the Boeing/NASA ground deicing fluids test program, which required ramping the IRT airspeed to simulate takeoff, could not have been done with the old drive motor and controls.

Recalibration of the NASA Icing Research Tunnel

The purpose of the IRT is to simulate a flight through natural icing clouds. The quality of that simulation depends on its calibration for the following parameters: the aerothermodynamic variables of airspeed, temperature, and turbulence level; and the icing cloud variables of liquid water content and droplet size. Other simulation issues, such as scaling, are resolved by analyses and experimental technique.

The recent calibration included all of the above parameters. Figure 39 shows a preliminary droplet size calibration for the IRT "standard" nozzles. Figure 40 shows the IRT operating envelope for both the "standard" and "mod 1" nozzles at a tunnel airspeed of (112 m/sec) 250 mph. This was the first recalibration of the spray nozzles since 1956. One improvement over the old calibration is that the upper limit on calibrated MVD droplet size has been increased from 20 to 40 μm .

Tunnel Simulation Versus Natural In-Flight Tests

Flow turbulence level is always an element of concern in an icing tunnel because both the physical blockage of spray bars and the water and air that come out of the spray bars should affect turbulence. Since turbulence level in the IRT would affect both the ice accretion process and the evaluation of thermal ice protection systems, users often want to know about the IRT's turbulence level and if it adequately simulates inflight conditions.

The turbulence level in the IRT test section, as measured by VanFossen (Ref. 37) with hot wires, is about 0.5 percent when the water and air to the spray bars are turned off. Obviously, the turbulence level cannot be measured with the cloud on because the water droplets striking the hot wires would invalidate their readings. But we have tried to measure the turbulence level with the hot (180 °F) spray bar air turned on. At first it appeared that a valid hot wire reading was possible, but after careful study, VanFossen decided that filaments of the hot spray bar air may have been hitting the hot wires and giving incorrect readings.

To address the heat transfer question for the IRT, NASA measured heat transfer performance on a NACA 0012 airfoil (53.3 cm (21 in.) chord) in the IRT (with hot spray bar air turned on) and compared it with heat transfer performance on the same model in flight (Ref. 38). The model was extended out the overhead hatch of the Twin Otter as shown in Fig. 41. Figure 42 shows a plot of Frossling number versus location on the airfoil for data taken in flight and in the IRT (Ref. 39). The figure shows that there is no distinguishable difference between heat transfer in flight and in the IRT.

FUNDAMENTAL STUDIES IN ICING

NASA maintains a strong effort in icing fundamentals, which is the backbone of any program that is developing new computer codes and new test techniques. We have already described several fundamental studies, for example, in formulating a new description of the ice accretion process, and in obtaining fundamental flowfield data for flow over ice shapes that cause flow separation and reattachment. In this section we review work on two important problems: icing scaling laws, and structural and adhesive properties of in-flight ice.

Icing Scaling Laws

The proposed or desired test matrix for an icing test usually involves the following variables: airspeed, outside air temperature, altitude, cloud liquid water content, cloud droplet size distribution or median volume diameter, and model size or scale. In a flight test in natural icing, or in an artificial cloud behind an in-flight spray tanker, chances are that the exact set of variables desired will be unattainable. In a wind tunnel test, certain combinations of variables also will be unattainable. For example, most icing wind tunnels have maximum airspeeds far below the speeds of modern transport or military aircraft. And due to the practical limits on nozzle turn-down ratios and nozzle droplet size ranges no wind tunnel can achieve the full FAA Part 25 Appendix C operating envelopes over the full speed range of the tunnel.

If the desired test variables cannot be met, the experimenter must resort to some form of scaling. Various objectives can be imagined for any particular scaled test: (1) a geometrically similar ice shape; (2) an equivalent drag coefficient for the ice shape/model combination; (3) the same water flux around the airfoil leading edge; (4) the same heat transfer results for a thermal ice protection system; (5) time icing conditions (i.e., all water must freeze immediately upon impact); and so on. Scaling laws have always been used, but never rigorously validated (Ref. 40). This does not mean the tests were done incorrectly, for icing has been and always will be part science and part art. This is why inflight testing in natural icing clouds always will be a required part of the certification/qualification process.

Reference 40 gives a good bibliography of the work done previously on scaling. Most of these works on scaling rely on an analysis of the ice accretion process described by Messinger (Ref. 13) over 30 years ago. New insights into the ice accretion process by Olsen (Ref. 14) and Hansman (Refs. 15 and 16) have led Bilanin (Ref. 41) to apply the Buckingham pi theory to the ice accretion problem. Bilanin showed that the normalized thickness of the ice accreted on the airfoil is a function of 18 nondimensional groups. Although many of the groups are satisfied in any scaling test, there exists a problem holding Mach, Reynolds and Weber number constant between tests. He concluded that the old Messinger formulation may be inadequate, and that improved ice accretion scaling may require a better match in Reynolds number and consideration of the physics of water film and droplet splash dynamics on the airfoil surface.

In Ref. 41 Bilanin concluded that competing physical effects do not in general allow a rigorous scaling methodology, but an acceptable approximate scaling scheme may be possible. He has suggested a series of tests on rotating and nonrotating cylinders to validate the approximate schemes. NASA plans to participate in a joint Air Force/FAA/NASA program to carry out these suggested tests later this year.

Structural and Adhesive Properties of In-Flight Ice

Over the past 5 years, NASA has supported a considerable, but low-level effort to study the structural properties of ice formed in flight. This work is described in References 42 to 47. Ice formed in flight or in a tunnel results from

supercooled water droplets impacting a surface at light speed or wind tunnel airspeed. We refer to ice so formed as 'impact' ice. Impact ice can vary in type over a wide range, depending on the liquid water content and droplet size distribution in the cloud, on the outside air temperature, and on the droplet velocities. The adhesion of ice to a surface depends not only on the type of ice formed, but also on the roughness, porosity, and other fundamental properties of the surface. The statistical variation of ice properties from one test to the next is a real phenomenon, and it must be accounted for in the design of systems that depend on ice shedding for their operation.

The overall objectives of the project are (1) to measure the structural properties of impact ice, such as, basic tensile properties, adhesive characteristics, and peel properties and (2) to develop finite element analytical methods for use in the analysis and design of deicing systems and icing testing apparatus.

Test apparatuses have been designed to measure each of the three basic mechanical properties: (1) tensile (Young's modulus (E), and ultimate tensile strength of impact ice in a direction transverse to the direction of ice growth); (2) shear (adhesion); and (3) peeling. Data has been obtained on both adhesive shear strength of impact ices and peeling forces for various icing conditions. Being studied are the influences of key parameters, such as, tunnel temperature, wind velocity, water drop size, substrate material, substrate surface temperature, and ice thickness. A finite element analysis of the shear test apparatus was developed in order to gain more insight into the evaluation of the test data.

Measurements indicate that surface roughness has a major effect on the adhesive shear strength. Additional adhesive shear strength tests are planned in which the surface roughness will be systematically varied.

Fixed airfoils, rotor blades, and propellers are being studied. In these studies, the adhesive shear strength of the impact ice is an important parameter. Surface roughness and the statistical nature of the data must be considered. For rotating surfaces, not only is the adhesive strength important but also the tensile strength of the ice perpendicular to the direction of growth. At the present time, the finite element analysis of rotating airfoils is being emphasized. Analytical results will be compared to recent data from the OH-58 tail rotor tests in the IRT. The statistical nature of the fracture of impact ice will be considered in the analysis.

The NASTRAN finite element code was also used to predict deicing of an EIDI ice protection system, for which experimental data was available (Ref. 46). Even though additional correlations with other data are needed, results from this initial study were encouraging.

There is a possibility that a fracture mechanics approach could be used to predict the peeling of ice from deicing systems such as a pneumatic boot. Data obtained from peeling measurements is being reduced to obtain the critical stress intensity constant of fracture mechanics.

REFERENCES

1. Reinmann, J.J., Shaw, R.J., and Olsen, W.A.; "Aircraft Icing Research at NASA," June 1982, NASA TM-82919.
2. Shaw, R.J.; "Progress Toward the Development of an Aircraft Icing Analysis Capability," Jan. 1984, AIAA Paper 0105.
3. Shaw, R.J., Potapczuk, M.G., and Bidwell, C.S.; "Predictions of Airfoil Aerodynamic Performance Degradation Due to Icing," Fourth Symposium on Numerical and Physical Aspects of Aerodynamic Flows, Jan. 1989.
4. Ranaudo, R.J., Reehorst A.L., and Potapczuk, M.G., "An Overview of the Current NASA Program on Aircraft Icing Research," Oct. 1988, SAE Technical Paper 881386.
5. Keith, T.G., DeWitt, K.J., Wright, W.B., and Masiulaniec, K.C., "Overview of Numerical Codes Developed for Predicted Electrothermal De-Icing of Aircraft Blades," Jan. 1988, AIAA Paper 88-0288.
6. Goldberg, J., and Lardiere, B., "Developments in Explosive Separation Ice Protection Blankets," Jan. 1989, AIAA paper 89-0774.
7. Zumwalt, G.W., Schrag, R.L., Bernhart, W.D., and Friedberg, R.A., "Electro-Impulse De-Icing Testing Analysis and Design," 1988, NASA CR-4175.
8. Zieve, P.S.; private communication.
9. Berkowitz, B.M., and Riley, J.T., "Analytical Ice Shape Predictions for Flight in Natural Icing Conditions," 1988, NASA CR-182234.
10. Olsen, W.A., Shaw, R.J., and Newton, J., "Ice Shapes and the Resulting Drag Increase for a NACA 0012 Airfoil," Jan. 1984, NASA TM-83556.

11. Van Fossen, G.J., Semonian, R.J., Olsen, W.A., and Shaw, R.J., "Heat Transfer Distributions Around Nominal Ice Accretion Shapes Formed on a Cylinder in the NASA Lewis Icing Research Tunnel." Jan. 1984, AIAA Paper 84-0017.
12. Scott, J.N., Gielus, T.P., and Hankey, W.L., "Navier-Stokes Solutions of Flowfield Characteristics Produced by Ice Accretion," Jan. 1988, AIAA Paper 88-0290.
13. Messinger, B.L., "Equilibrium Temperature of an Unheated Icing Surface as a Function of Airspeed," Journal of Aeronautical Sciences, Jan. 1958.
14. Olsen, W., and Walker, E., "Experimental Evidence for Modifying the Current Physical Model for Ice Accretion on Aircraft Surfaces," May 1980, NASA TM-87184.
15. Hansman, R.J., and Turnock, S.R., "Investigation of Microphysical Factors Which Influence Surface Roughness During Glaze Ice Accretion," Fourth International Conference on Atmospheric Icing of Structures, Sept. 1988.
16. Hansman, R.J., Yamaguchi, K., Berkowitz, D., and Potapczuk, M., "Modeling of Surface Roughness Effects on Glaze Ice Accretion," Jan. 1989, AIAA Paper 89-0734.
17. Pulliam, T.H., "Euler and Thin-Layer Navier-Stokes Codes: ARC3D, ARC3D," Notes for Computational Fluid Dynamics User's Workshop, The University of Tennessee Space Institute, Tullahoma, TN, 1984.
18. Cebeci, T., "Effects of Environmentally Imposed Roughness on Airfoil Performance," June 1987, NASA CR-179639.
19. Cebeci, T., Jau, J., Vitiello, D., and Chang, K.C., "Prediction of Post-Stall Flows on Airfoils," Fourth Symposium on Numerical and Physical Aspects of Aerodynamic Flow, Jan. 1989.
20. Potapczuk, M.G., "Personal Communication on Doctoral Dissertation. NASA Lewis Research Center, Cleveland, OH.
21. Bragg, M.B., and Khodadoust, A., "Effect of Simulated Glaze Ice on a Rectangular Wing," Jan. 1989, AIAA Paper 89-0750.
22. Sankar, L., Chiu, J., and Huff, D., "Evaluation of Three Turbulence Models for the Prediction of Steady and Unsteady Airflows," Jan. 1989, AIAA Paper 89-0609.
23. Mikkelsen, K.L., McKnight, R.C., Ranaudo, R.J., and Perkins, P.J., Jr., "Icing Flight Research: Aerodynamic Effects of Ice and Ice Shape Documentation With Stereo Photography," Jan. 1985, AIAA Paper 85-0468.
24. Mikkelsen, K., Juhász, H., Ranaudo, R., and McKnight, R., "In-Flight Measurements of Wing Ice Shapes and Wing Section Drag Increases Caused by Natural Icing Conditions," Apr. 1986, NASA TM-87307.
25. Ranaudo, R.J., Mikkelsen, K.L., McKnight, R.C., Ido, R.F., and Reehorst, A.L., "The Measurement of Aircraft Performance and Stability and Control After Flight Through Natural Icing Conditions," Apr. 1986, AIAA Paper 86-9758.
26. Ido, R.F., and Richter, G.P., "Comparison of Icing Cloud Instruments for 1982-1983 Icing Season Flight Program," Jan. 1984, NASA TM-83569.
27. Ranaudo, R.J., Mikkelsen, K.L., McKnight, R.C., and Perkins, P.J., Jr., "Performance Degradation of a Typical Twin Engine Commuter Type Aircraft in Measured Natural Icing Conditions," 1984, NASA TM-83564.
28. Ranaudo, R.J., Batterson, J.G., Reehorst, A.L., Bond, T.H., and Omara, T.M., "Determination of Longitudinal Aerodynamic Derivatives Using Flight Data From an Icing Research Aircraft," Jan. 1989, AIAA Paper 89-0754.
29. Batterson, J.G., and O'Mara, T.M., "Estimation of Longitudinal Stability and Control Derivatives for an Icing Research Aircraft From Flight Data," Mar. 1989, NASA TM-4099.
30. Miller, T.L., and Bond, T.H., "An Icing Research Tunnel Test of a Model Helicopter. To be presented at the American Helicopter Society 45th Annual Forum and Technology Display, Boston, MA, May 22-24, 1989.
31. Pike, J.A., Wainauski, H.S., and Boyd, L.S., "Prop-Fan Airfoil Icing Characteristics," Jan. 1989, AIAA Paper 89-0753.
32. Hill, E.G., Zierston, T.A., and Runyan, J.J., "Results of a Flight and Wind Tunnel Investigation of Aerodynamic Effects of Aircraft Ground De-/anti-Icing Fluids," Effect of an Adverse Environment on Flight, (AGARD Flight Mechanics Panel Symposium), Gol, Norway, May 1989.
33. Hovanec, E.A., "Droplet Sizing Instrumentation Used for Icing Research: Operation, Calibration, and Accuracy; Phase I Final Report," NASA CR- (to be published jointly by NASA and FAA).

34. Hovenac, E.A., and Ide, R.P., "Performance of the Forward Scattering Spectrometer Probe in NASA's Icing Research Tunnel," Jan. 1989, AIAA Paper 89-0769.
35. Hovenac, E.A., Hirleman, E.D., and Ide, R.P., "Calibration and Sample Volume Characterization of FMS Optical Array Probes," International Conference on Liquid Atomization and Spray Systems, July 1985.
36. Bachalo, W.D., and Houser, J.J., "Phase Doppler Spray Analyzer for the Simultaneous Measurements of Droplet Size and Velocity Distributions," 1984, Optical Engineering, Vol. 23, no. 5, pp. 583-590.
37. VanFossen, G.J., "Private Communication. NASA Lewis Research Center, Cleveland, OH.
38. Newton, J.E., VanFossen, G.J., Poinsett, P.E., and deHart, K.J., "Measurement of Local Convective Heat Transfer Coefficients From a Smooth and Roughened NACA-0012 Airfoil Flight Test Data," Jan. 1988, AIAA Paper 88-0787.
39. Van Fossen, G.J.: Private Communication. NASA Lewis Research Center, Cleveland, OH.
40. Bilanin, A.J., "Proposed Modifications to Ice Accretion/Icing Scaling Theory," Jan. 1988, AIAA Paper 88-0203.
41. Bilanin, A.J., "Problems in Understanding Aircraft Icing Dynamics," Jan. 1988, AIAA Paper 89-0745.
42. Chu, M., Scavuzzo, R.J., and Olson, W., "Measurement of Adhesive Shear Strength of Impact Ice in an Icing Wind Tunnel," Proceedings of 3rd International Workshop on the Atmospheric Icing of Structures, May 1986.
43. Scavuzzo, R.J., Chu, J.L., and Lam, P.D., "Development of a Composite Technique in the Determination of the Tensile Strength of Impact Ices," Proceedings of 3rd International Workshop on the Atmospheric Icing of Structures, May 1986.
44. Scavuzzo, R.J., Chu, M.L., and Olson, W.A., "Structural Properties of Impact Ices Accreted at Aircraft Structures," Jan. 1987, NASA CR 179500.
45. Kharkhato, A.A., Scavuzzo, R.J., and Chu, M., "A Finite Element Study of the EIDI System," Jan. 1988, AIAA Paper 88-0022.
46. Chu, M., Scavuzzo, R.J., and Zian, X.T., "Hybrid Finite Element-Experimental Technique for Determination of Ice/Impact Ice Tensile Strength," Proceedings of the 4th International Conference on Atmospheric Icing of Structures, 1988.
47. Scavuzzo, R.J., Chu, M.L., and Brikmann, C.K., "Adhesive Peel Strength of Artificial Ice," Proceedings of the 4th International Conference on Atmospheric Icing of Structures, 1988.

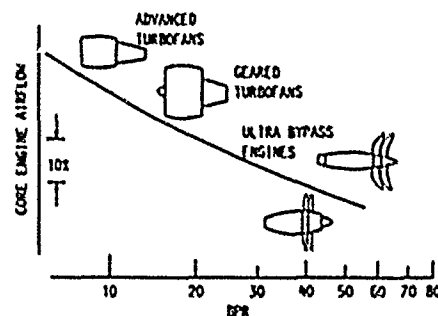


FIGURE 1. - ENGINE PERFORMANCE TRENDS; CORE ENGINE AIRFLOW VERSUS BY-PASS RATIO.

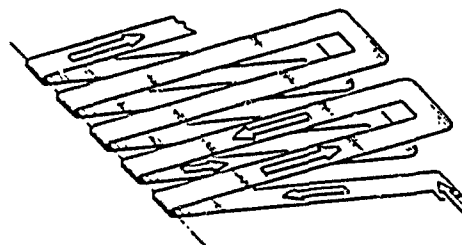


FIGURE 2. - EESS CONDUCTOR GEOMETRY.

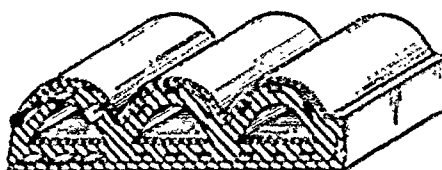


FIGURE 3. - RESISTORS EMBEDDED IN ELASTIC MOUNT.

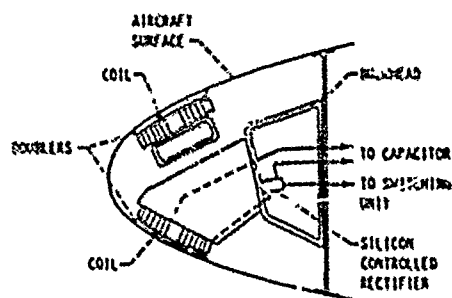


FIGURE 4. - EIDI COILS IN LEADING EDGE.

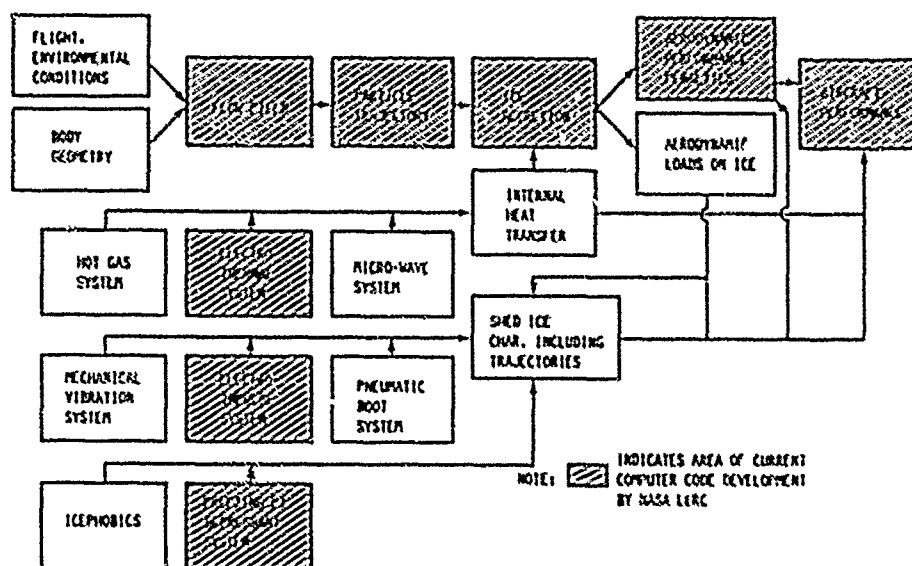


FIGURE 5. - AIRCRAFT ICING ANALYSIS METHODOLOGY.

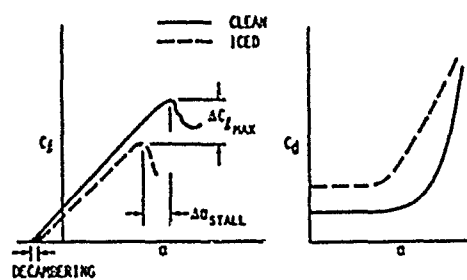


FIGURE 6. - AERODYNAMIC PERFORMANCE DEGRADATION DUE TO ICING.

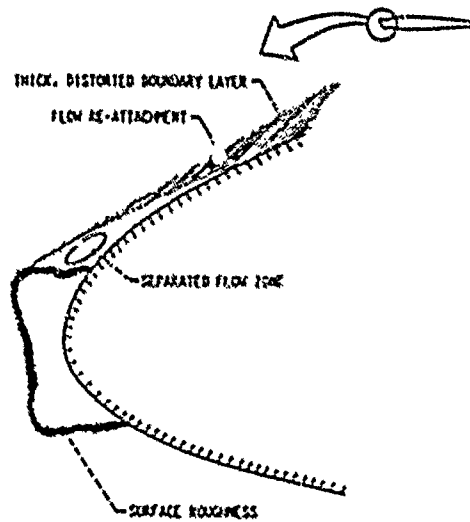


FIGURE 7. - KEY ASPECTS OF AIRFOIL ICING.

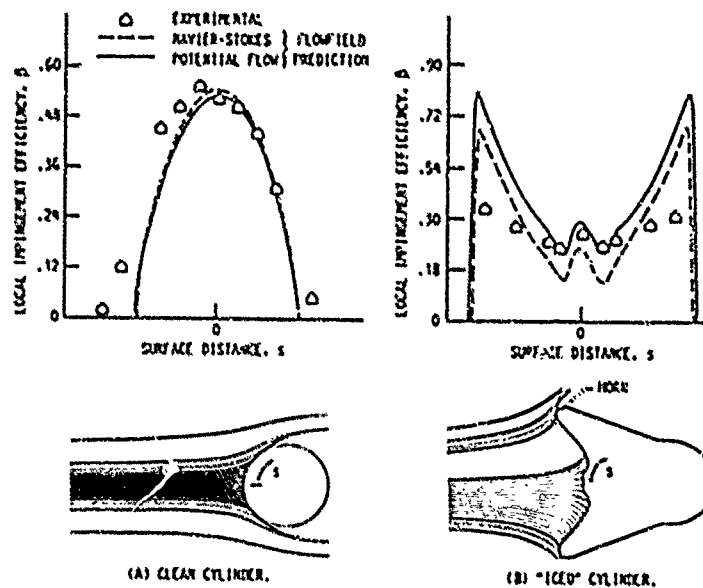


FIGURE 8. - DROPLET COLLECTION EFFICIENCY COMPARISONS.

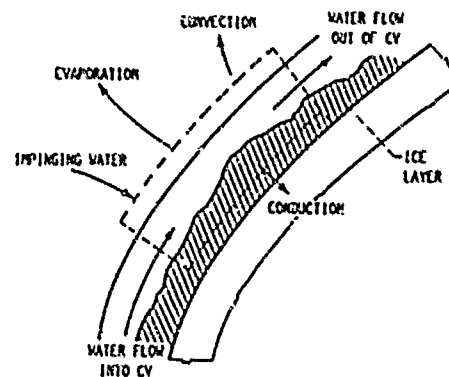


FIGURE 9. - CONTROL VOLUME ANALYSIS OF ICE ACCRETION PROCESS.

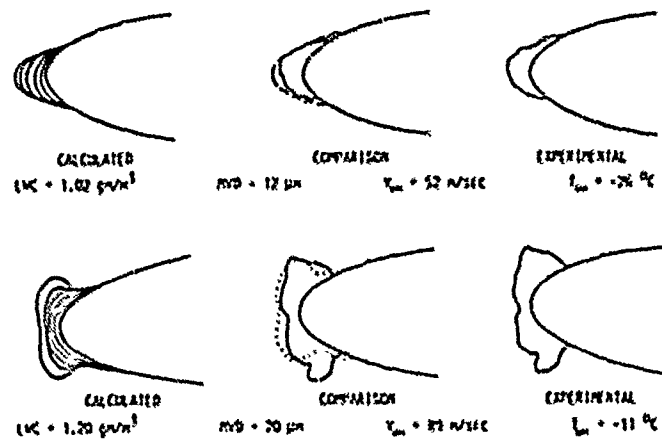


FIGURE 10. - COMPARISON OF ICE SHAPE PREDICTIONS WITH AIRFOIL ICING DATA.

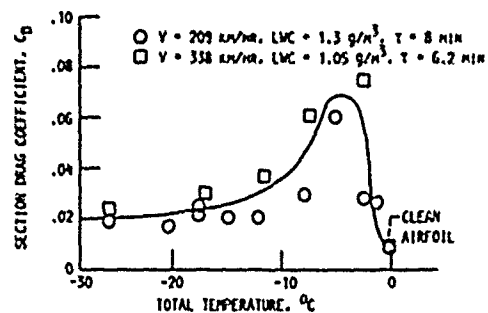
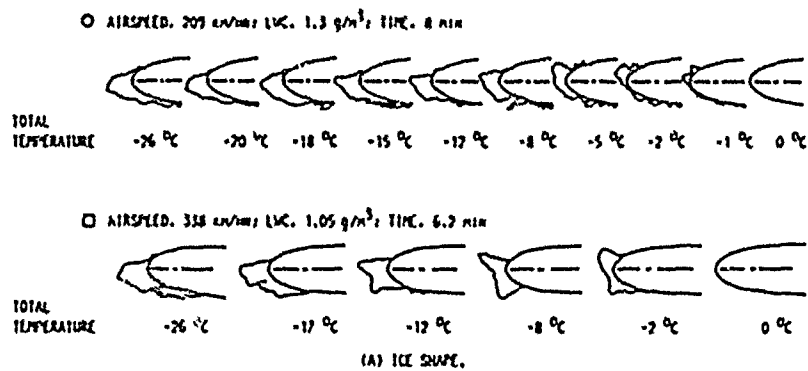


FIGURE 11. - EFFECT OF TOTAL TEMPERATURE ON ICE SHAPE AND DRAG.

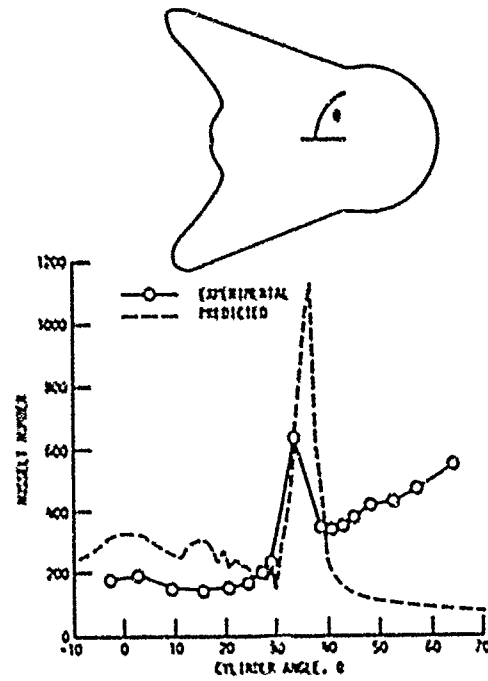


FIGURE 12. - NUSSLETT NUMBER PREDICTION BASED ON INTEGRAL BOUNDARY LAYER METHOD.

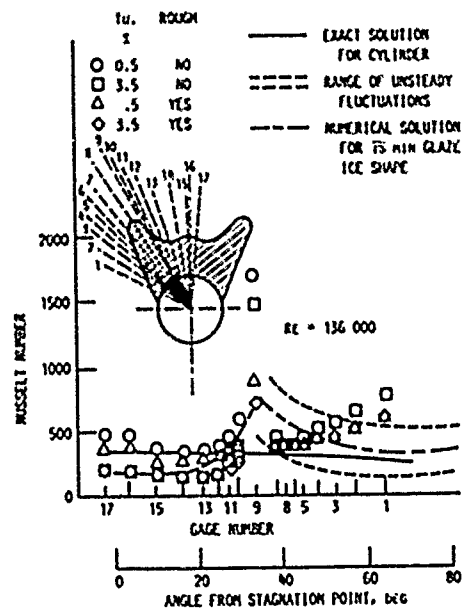


FIGURE 13. - NUSSLETT NUMBER PREDICTION BASED ON NAVIER-STOKES SOLUTION OF ENERGY EQUATION.

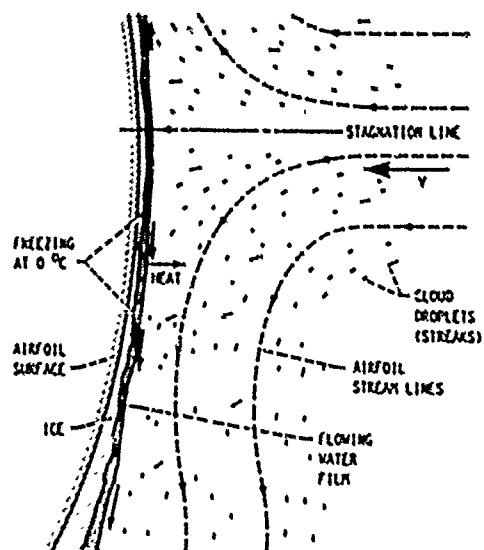
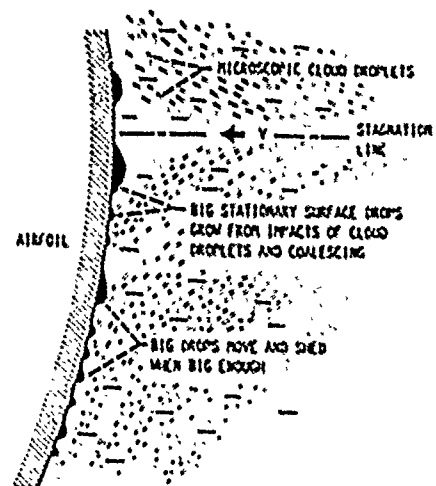
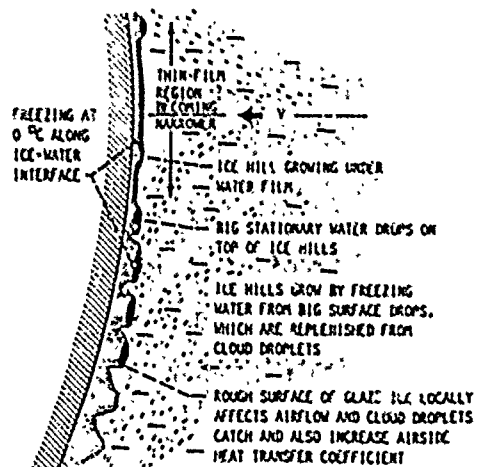


FIGURE 14. - EXISTING PHYSICAL MODEL FOR ICE ACCRETION.



(A) NO FREEZING OCCURRING (ABOVE 0 °C OR BEFORE FREEZING STOPS SURFACE DROPS).



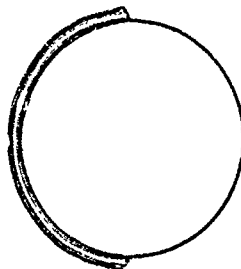
(B) FREEZING OCCURRING.

FIGURE 15. - PROPOSED NEW PHYSICAL MODEL FOR ICING PROCESS.

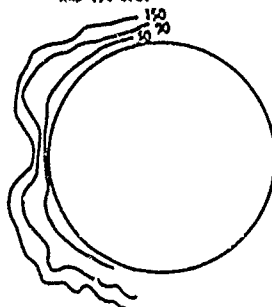


T = 20 SEC

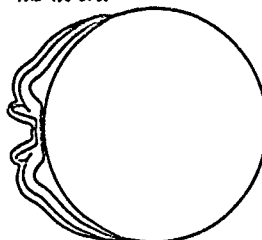
FIGURE 16. - CLOSE-UP PHOTO OF ICE FORMED AT -2°C .



(A) NORMAL LEVICE AT 45, 105, AND 150 SEC.



(B) EXPERIMENTAL RESULT AT 30, 90, AND 150 SEC.



(C) MODIFIED LEVICE AT 45, 105, AND 150 SEC.

FIGURE 17. - EXPERIMENTAL ICE SHAPE COMPARED TO MODIFIED LEVICE PREDICTIONS.

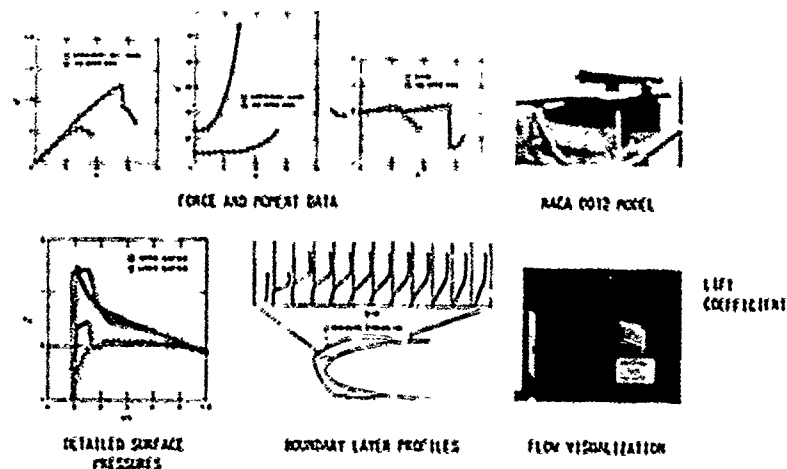


FIGURE 18. - CODE VALIDATION DATA BASE FOR ICED AIRFOIL PERFORMANCE.

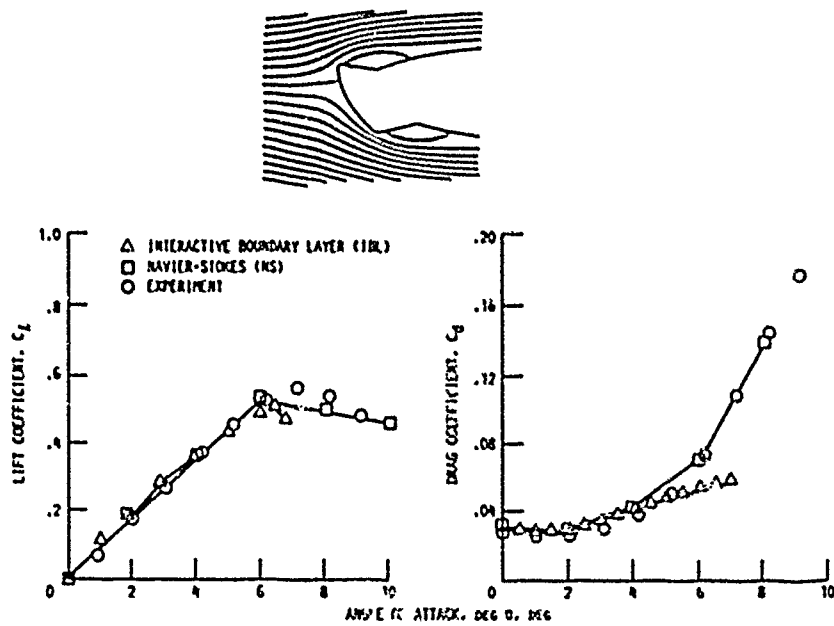


FIGURE 19. - COMPARISON OF CODE PREDICTIONS WITH EXPERIMENT FOR AN ICED AIRFOIL.

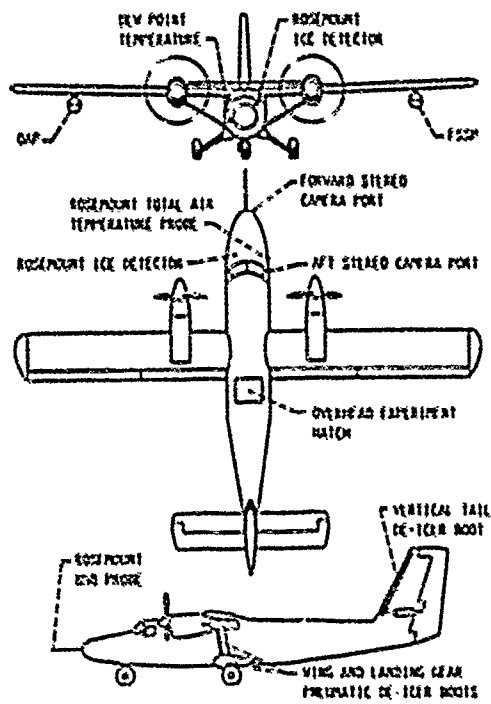


FIGURE 20. - NASA TWIN OTTER ICING RESEARCH AIRCRAFT.

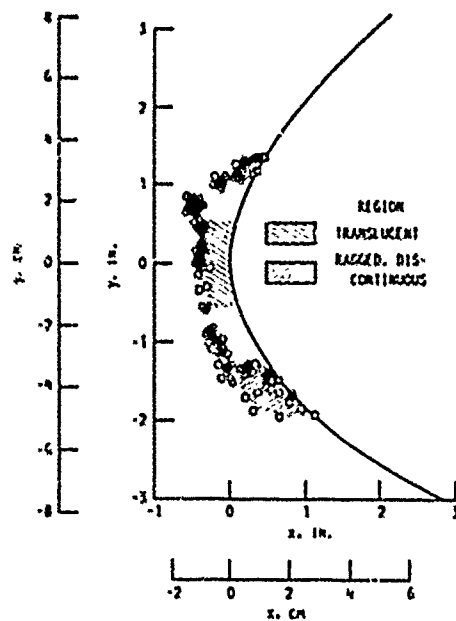


FIGURE 21. - ICE SHAPE PROFILE MEASURED BY STEREO PHOTOGRAPHY; FLIGHT 85-248.

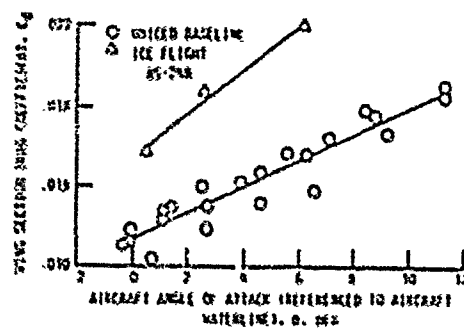
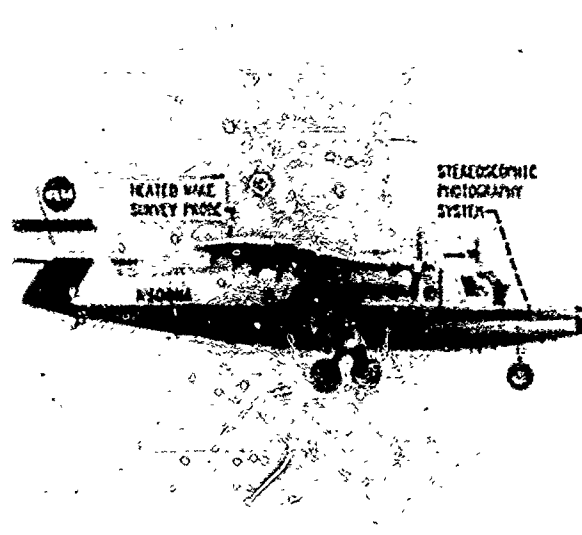


FIGURE 22. INCREASE IN WING SECTION DRAG DUE TO ICE ACCRETION; FLIGHT 85-248.

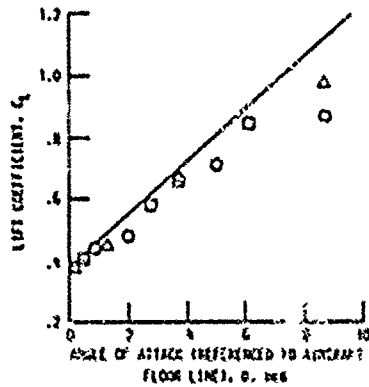
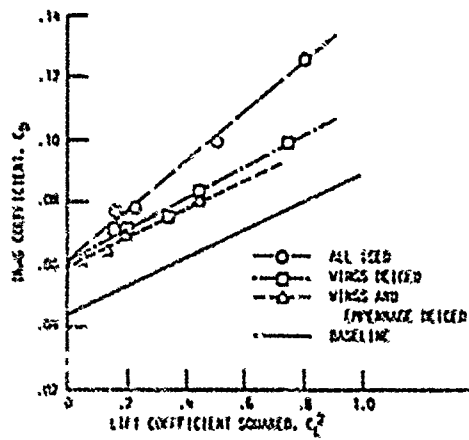


FULL SCALE WING SECTION
IN INT



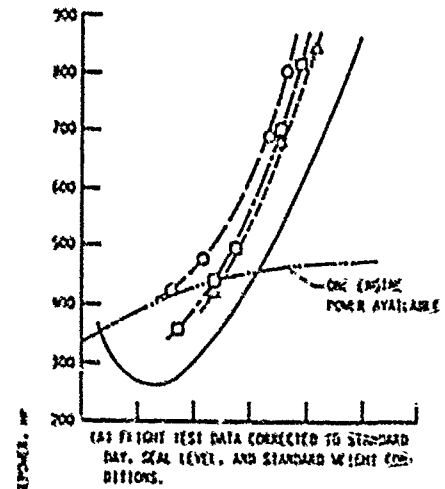
NASA ICING RESEARCH AIRCRAFT

FIGURE 23. - FLIGHT VERSUS TUNNEL COMPARISON OF AIRFOIL ICE ACCRETION AND DRAG INCREASE.

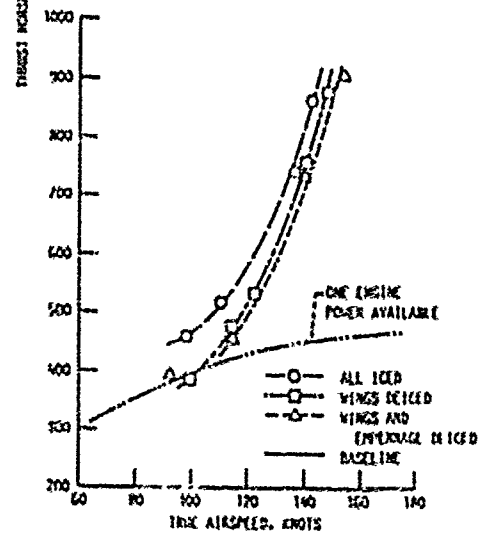
(a) VARIATION OF AIRCRAFT C_L VERSUS α .

(b) SHIFT IN AIRCRAFT DRAG POLAR.

FIGURE 24. - EFFECT OF GLAZE ICE ON AIRCRAFT LIFT CURVE AND DRAG POLAR; FLIGHT BS-10.



(a) FLIGHT TEST DATA CORRECTED TO STANDARD DAY, SEAL LEVEL, AND STANDARD WEIGHT CONDITIONS.



(b) TEST CONDITIONS AT 6000 FT FLIGHT TEST DATA CORRECTED TO STANDARD WEIGHT ONLY.

FIGURE 25. - EFFECT OF GLAZE ICE ON POWER REQUIRED COMPARED TO ONE ENGINE POWER AVAILABLE; FLIGHT BS-10.



FIGURE 26. - "STYROFOAM ICE" BONDED TO LEADING EDGE OF HORIZONTAL TAIL.

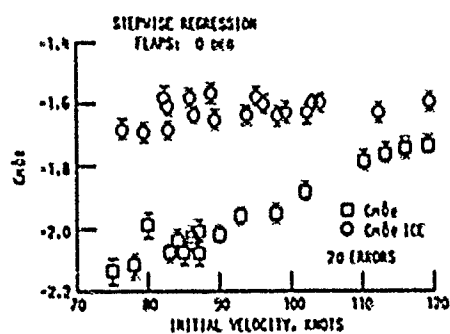


FIGURE 27. - DEGRADATION OF ELEVATOR CONTROL POWER AS MEASURED BY RCR ANALYSIS FOR "STYROFOAM ICE" ON HORIZONTAL TAIL.



ICED OH-58 TAIL ROTOR RIG IN IRT



END VIEW OF TYPICAL OH-58 ROTOR BLADE ICE SHAPE



OH-58 TAIL ROTOR RIG DRIVE SYSTEM



NEXT ROTOR TEST IN IRT: SIKORSKY POWERED FORCE MODEL WITH G-COMPONENT INTERNAL FORCE BALANCE

FIGURE 28. - ROTORCR/FT ICING TESTS IN NASA IRT.

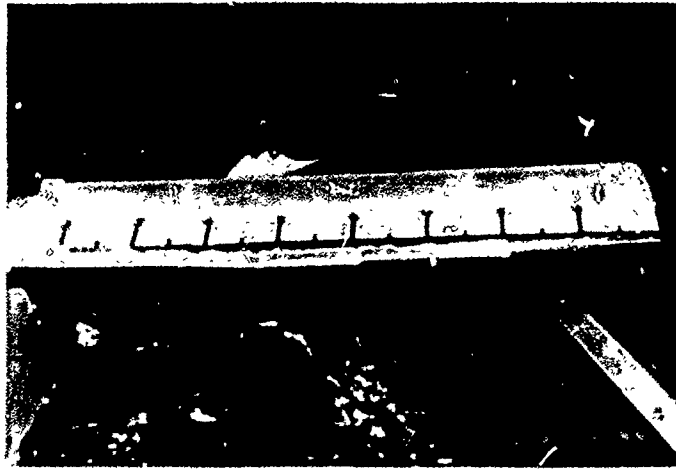


FIGURE 29. - ICE ACCRETION ALONG SPAN OF OH-58 TAIL ROTOR.

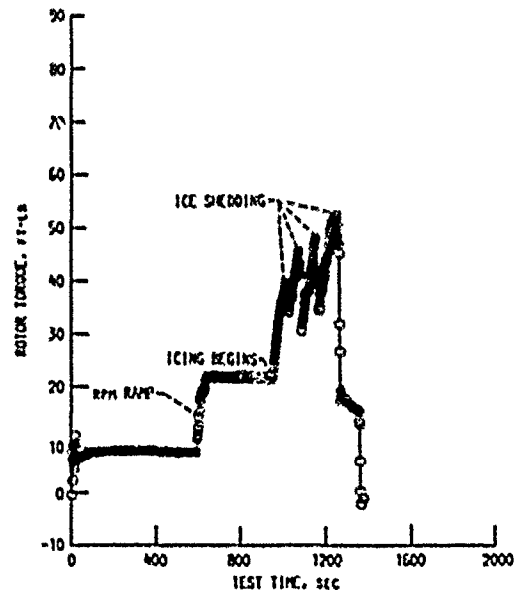


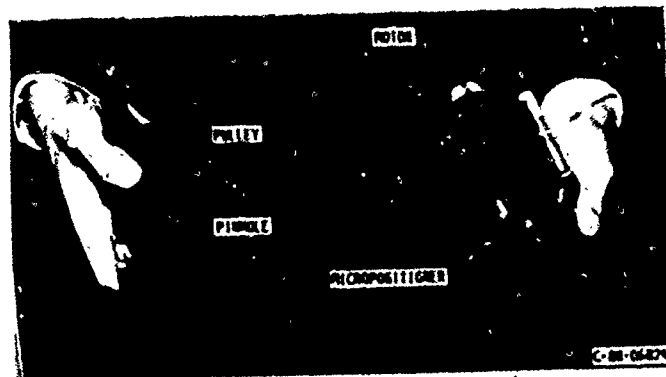
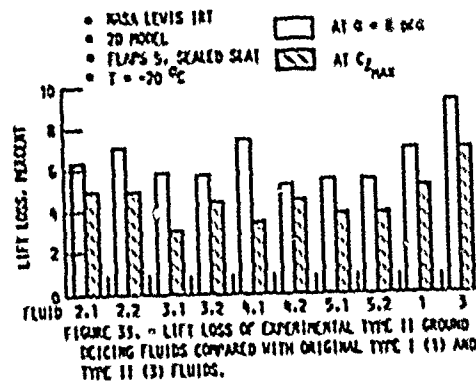
FIGURE 30. - OH-58 ROTOR TORQUE VARIATION WITH TIME DURING ICING TEST IN THE NASA INT.



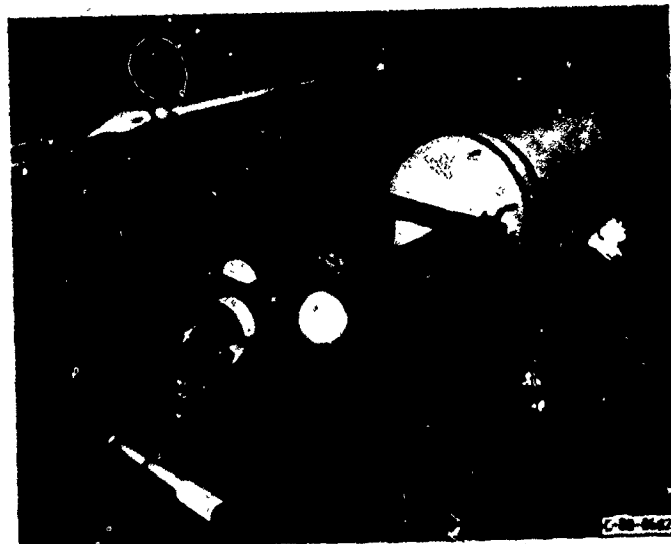
FIGURE 31. - BOEING 737-200 ADV HALF MODEL WITH GROUND PLANE, INSTALLED IN NASA IRT.



FIGURE 32. - FRONT VIEW OF 2D AIRFOIL MODEL (BOEING 737-200 ADV) INSTALLED BETWEEN SPLITTER WALLS IN NASA IRT.



(A) COMPONENTS OF THE CALIBRATOR.

(B) CALIBRATOR ATTACHED TO FSSP.
FIGURE 34. - ROTATING PINHOLE CALIBRATOR.

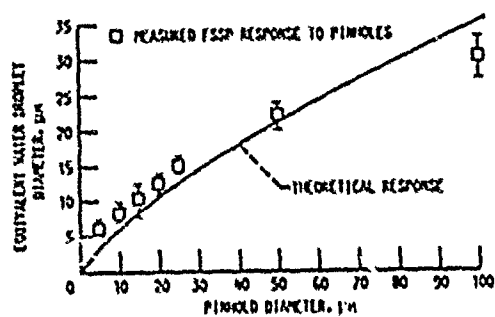


FIGURE 35. - CALIBRATION OF FSSP USING ROTATING PINHOLES.

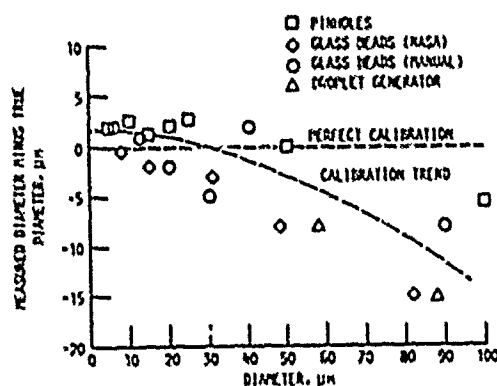


FIGURE 36. - CALIBRATION ACCURACY OF THE EXTENDED-RANGE FSSP.

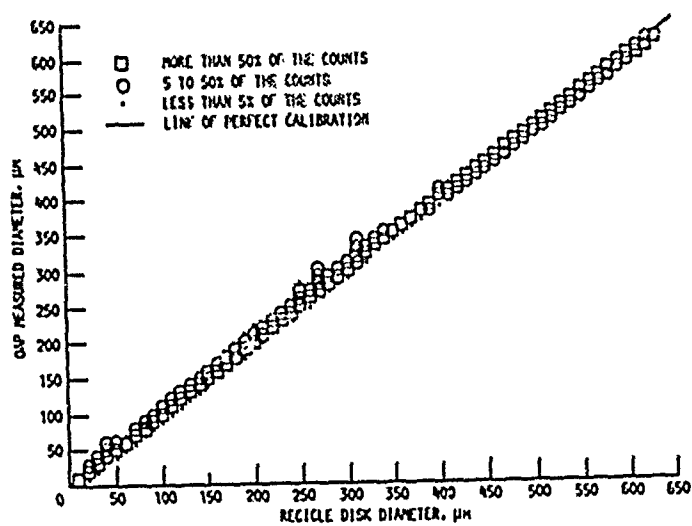


FIGURE 37. - CALIBRATION CURVE FOR THE OAP USING THE ROTATING RETICLE.

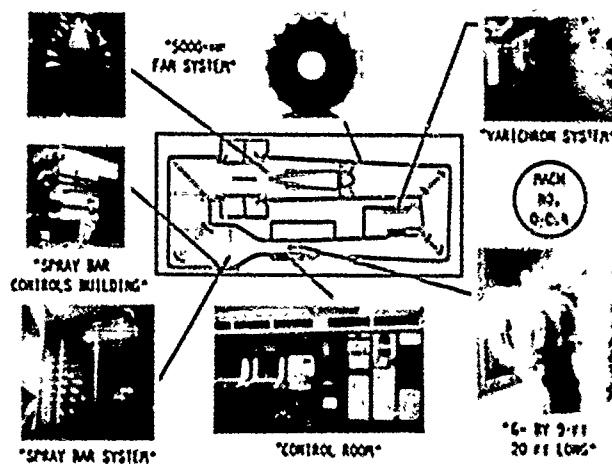


FIGURE 38. - SCHEMATIC OF NASA ICING RESEARCH TUNNEL FLOW CIRCUIT.

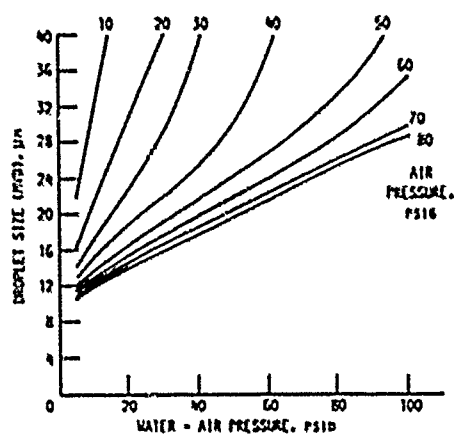


FIGURE 39. - DROPLET SIZE CALIBRATION FOR STANDARD NOZZLES IN NASA IRT.

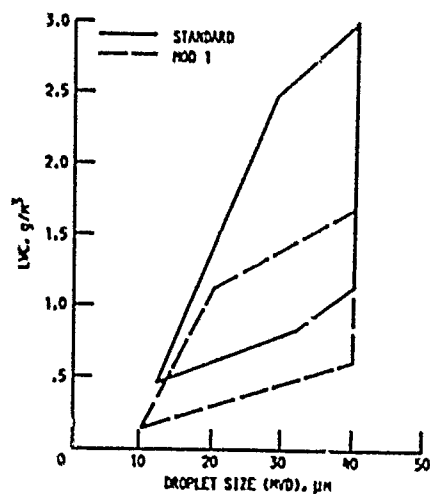


FIGURE 40. - OPERATING ENVELOPE FOR THE NASA IRT CLOUD AT 250 MPH.

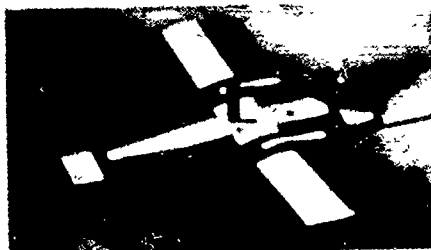


FIGURE 41. - AIRFOIL WITH HEAT TRANSFER CROSSES SHOWN
PAINTED ON THE TWIN OTTER.

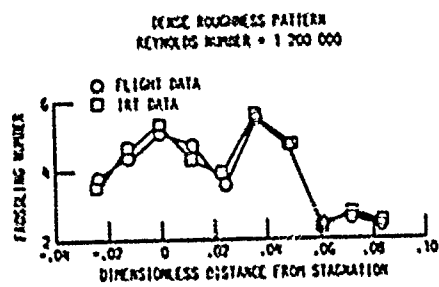


FIGURE 42. - COMPARISON OF HEAT TRANSFER BETWEEN
FLIGHT AND NASA IRT.

ICE INDUCED AERODYNAMIC PERFORMANCE DEGRADATION OF ROTORCRAFT - AN OVERVIEW

K.D. Korkan
Professor

R.W. Britton
Graduate Research Assistant

Aerospace Engineering Department
Texas A&M University
College Station, Texas 77843-3131
USA

ABSTRACT

The renewed interest in evaluating the performance degradation of helicopters due to icing has resulted in the development of methodologies to analytically predict the aerodynamic degradation increment. The progress in understanding the basic icing technology is reviewed citing major references. The analytical methodology is then summarized with respect to performance degradation of propellers, helicopter in hover, helicopter in forward flight, and the forerunner of the V-22 Osprey, the XV-15 propulsion mode(s). The experimental studies of the NACA 0012 airfoil with/without generic ice and the model helicopter main rotor experiments with/without generic ice are reviewed. Based upon these results, refinements are suggested to the current methodology with respect to near term/far term.

INTRODUCTION

The present emphasis on performance degradation of helicopters due to icing has resulted because of the desire to increase the overall utilization of the helicopter with a minimum of weather associated restrictions. Rotorcraft icing research requirements have been identified as early as 1981 by Peterson, et al.(1), where the required analytical prediction methods and test techniques necessary to define the ice accretion mechanism have been outlined. These areas are related to the discussion of the overview of helicopter ice protection system developments by Adams(2) covering such areas as meteorological design criteria, flight test objectives, microwave concept, electro-impulse concept, pneumatic concept, vibratory concept, and ice phobic coatings. That is, to address the areas of ice protection systems, prior knowledge of the basic mechanism of the ice accretion process must be known before identifying areas of needed research. The details of this approach have been further enhanced by short and long range icing research programs recommended by Koegeboehn(3) to NASA Lewis Research Center in 1981. These recommendations were a result of a survey of various industry and government agencies to obtain their views of needs for commercial aviation ice protection.

The generality of these plans for icing programs have distinct advantages in identifying areas of research, however, the solution must also be provided to a specific set of complicated problems dealing with performance degradation/ice protection on rotating systems. As pointed out by Sand(4), aircraft icing continues to be listed by the National Transportation Safety Board (NTSB) as a cause or factor in many aircraft accidents, e.g., 286 accidents in a recent seven year period. With regards to helicopter ice accretion and protection, Cansdale(5) has pointed out that the main effects of rotor icing are first an increase in rotor torque resulting in an increased horsepower to maintain a given flight condition, an increase in vibration levels and control loads, and a general decrease in the extent of the performance envelope. The rate at which this performance degradation due to icing takes place is obviously dependent on the atmospheric icing condition and the particular type of helicopter. In the most severe cases, both rotor torque and control limits can be reached in less than one minute after encountering an icing condition.

As noted, the interest in the ice accretion process on rotating systems is a result of attempting to widen the performance envelope and to assist in the definition of an ice protection system. Much effort has been expended in the

pursuit of understanding the ice accretion process both theoretically and experimentally. To this end, the analytical and experimental examination of the effect of icing circa 1960 has been covered in the classic document of Bowden, et al.(6), issued by the Federal Aviation Authority (FAA) in 1963 and referred to as the "Icing Bible". This publication covers the basic topics of icing data statistics, physics of ice collection, methods of protection, applications to aircraft and helicopters, ice detectors, ice protection systems, and controls. This document is currently being rewritten under contract to the FAA by Gates Learjet, Inc. reflecting the current state of the art and should be available to the public in 1989. FAA ADS-4, which is now one volume, will result in five volumes when revision reflecting the advances that have been made since the 1960's. Also, it is anticipated that updates by section will occur every two years, again to reflect the advances in icing technology.

Even though considerable progress has been made in the understanding of the ice accretion process, the complexity of the problem is indicated by the number of related disciplines. For example meteorology, cloud physics, ice fracture mechanics, and physics of ice collection to mention a few. Also to point out the present lack of understanding in terms of basics, it may be noted that the ice shapes found on fixed wing configurations have been classified into two categories, i.e., rime and glaze, and the type of ice encountered is dependent on the meteorological condition and geometry. The formation of rime ice is fairly well understood, however, the formation of glaze ice had been associated with "runback". Olean(?) in a movie made in 1984 and available from NASA, has indicated that this may not be the case and explains a process verified by freeze enlargements of experimental glaze ice accretion on an airfoil. Hansman and Turnock(?) in a later study, conducted a series of experimental investigations dealing with the primary factors that control the behavior of surface water during glaze ice accretion. In this investigation, distinct zones of surface water behavior were found consisting of a smooth wet zone in the stagnation region, a rough zone where surface tension effects produced coalescence of surface water into stationary beads, and a zone where surface water ran back as rivulets. These authors have suggested that existing ice accretion models could be improved by dividing the surface into two zones which reflects this surface water behavior. In the first region, the existing "Messinger-type models"(9) would be valid since it represents thin film runback. Further, as Hansman and Turnock emphasize, the remaining ice surface must be treated as a "rough" zone. However, when dealing with a rotating system, the ice accretion process is further complicated since as pointed out by Canadale and Gent(10), both rime and glaze ice accretion can take place on a helicopter main rotor blade under one performance/meteorological condition.

It is the purpose of this paper to review some of the major developments in the investigation of the icing area with regards to the aerodynamic degradation of airfoils hence performance degradation of rotating systems. This will be followed by a review of the current methodologies that have been developed under NASA sponsorship as applied to specific problems that are of interest. As a result of this review, the areas for further research can be defined in terms of suggested refinements to the current methodology.

REVIEW

Early attempts in evaluating performance degradation due to ice accretion on rotating systems dealt with not only natural icing encounters but also simulated ice. Corson and Haynard(11) in 1946 used simulated ice on propeller blades and measured average efficiency losses on the order of three percent, with maximum losses of fifteen percent. In 1948, Preston and Blackman(12) undertook a series of flight tests in which average decreases of roughly ten percent in propeller efficiency due to ice formation were noted. This study was of special significance since the authors made an attempt to examine the effects of ice accretion on all major components of the aircraft. Possibly the most complete and informative work relative to ice accretion on propellers was performed and documented by Neal and Bright(13) in 1950. In a series of flight tests in which efficiency loss was measured during natural icing encounters, observed values of approximately ten percent in most cases with maximum losses on the order of twenty percent were noted. Some early experimental work in dealing with de-icing on full scale counterrotating propellers was conducted by Haywood and Majly(14). The

purpose of these experiments was to run the A.S.N. D1. propeller system under artificial icing conditions to prove that the engine anti-icing and propeller deicing systems were adequate for the design power intensities down to -22°C . A series of experimental investigations of airfoil icing were also undertaken in the Icing Research Tunnel at NACA Lewis Research Center and documented by NACA personnel in the early to mid-1950's. Gray and von Glahn(15,16) looked at the effects of ice on the performance of NACA 65A004 and 651-212 airfoils, finding drag coefficient increases of up to 350% in the case of glaze ice formation. Lesser increases were noted for both airfoils with rime ice accretions. Brun, et al.(17-19) and Brun and Vege(20) dealt with experimental measurements of performance degradation of NACA 65A004, 651-208, and 651-212 airfoils, notably the impingement characteristics. Included in these investigations was a study of the effects of airfoil thickness and angle of attack on droplet impingement values. It was noted that airfoil thickness tends to increase the volume of water collected and decrease the rearward limit of droplet impingement. As expected, total impingement was found to increase with increasing angle of attack. Calder, Sayers, and von Glahn(21) in 1956 investigated droplet impingement properties on several airfoil sections of various thicknesses. The authors concluded in part that the total and maximum local collection efficiencies were strong functions of the modified inertia parameter. This parameter takes into account freestream velocity, droplet density and diameter, airfoil chord, absolute air viscosity and density, thickness/chord ratio, and angle of attack.

These early experimental programs served to provide valuable insight into the process and effects of ice accretion. In addition, a data base from which analytical ice growth and performance degradation predictions could be developed and/or verified.

One of the early theoretical efforts for rotating systems was done by Keel and Bright(13), who attempted to predict analytically the degree of propeller performance efficiency reduction as a result of ice accretion. Using blade element theory as the basis of analysis, and relating the change in airfoil drag to lift ratio to efficiency reduction, losses were predicted which agreed to the same order of magnitude with experimentally obtained values. Berggren(22) in 1951 offered a method for determining droplet impingement characteristics on an airfoil. Solving a set of simultaneous differential equations, Berggren described the particle dynamics of a water droplet moving in an air stream - a principle which forms the basis for present droplet trajectory codes. Along with Lewis in 1952(23), Berggren using probability analysis investigated the atmospheric factors responsible for ice formation and identified three parameters of primary importance in the ice accretion process, i.e., liquid water content, water droplet size, and ambient temperature. In 1958, Gray(24) conducted an icing study of the NACA 65A004 airfoil and attempted to develop a drag coefficient correlation for the glaze ice condition and connect droplet impingement rates to related aerodynamic penalties. Using experimental icing data, a dimensional correlation was found which was accurate for angles of attack \leq to four degrees. In 1964, Gray(25) examined aerodynamic icing data for other airfoils and modified the existing correlation for generality. Gray accomplished this result through the introduction of the airfoil leading edge radius of curvature in percent of chord. This modified correlation for the glaze ice condition represented the only available icing drag coefficient correlation at that time, and has been widely used. Only recently has the validity of the general glaze ice correlation been questioned, however it will most probably remain in use until a suitable replacement is found.

The formulation of the Gray drag coefficient correlation represented the last major development with respect to ice accretion effects for several years. The advent and use of the jet engine and turbofan de-emphasized the use of the propeller as a propulsive device, and subsequently drew attention away from the problem of ice accretion. However, with increased fuel costs and emphasis on commuter class aircraft and all-weather helicopters, interest in ice protection systems and a need to better understand the phenomenon of ice accretion has increased. For example, Bhaha and Evanich(26) as early as 1980 investigated pneumatic deicer boots for application to helicopters. The authors found in this experimental study of a non-rotating airfoil section, that the drag penalties of uninflated boots were small in comparison to the drag caused by one centimeter of ice. Also the aerodynamic effect of inflating the boot without ice was sizeable, however the drag penalty was not significantly different than that of fixed wing aircraft application. In this study, the pneumatic boot was shown to effectively

deice down to -14.4°C . Cansdale(5) has used a non-rotating airfoil section to test electrothermal deicing systems, and has shown to yield useful results comparable to those obtained in flight. Wilson(27) has also discussed the basic design philosophy for electrothermal deicing systems addressing such basic questions as anti-ice or deice in addition to power requirements. The author also discusses a number of deicing alternatives such as a vibratory method, pneumatic deice system, and silicone based organic compounds intended to enhance self shedding by reduction of surface adhesion of the ice formation and is referred to as ice-phobics. However, recent studies by Zumwalt(28) and Zumwalt, et al. (29) has shown that deicing by an electro-magnetic impulse has shown promise in deicing engine inlets, fixed aircraft wings, and helicopter blades. Electro-impulse deicing (EIDI) is attractive since the system requires very little energy and is nearly maintenance free. In this joint university/industry project funded by NASA Lewis Research Center, tunnel and flight tests have demonstrated reliable deicing at all flight and atmospheric conditions.

Researchers involved in the renewed study of ice accretion recognized the need to expand the limited experimental data base, especially to include tests of ice accretion on newer airfoils designed for use on current general aviation aircraft, propellers, and helicopter rotors. This work started as early as 1977 by the Swedish-Soviet Working Group on Scientific-Technical Co-Operation in the field of flight safety. The initial study resulted in a joint report by Ingelman-Sundberg (Sweden), Trunov and Ivaniko (USSR)(30), and involved the results from flight tests and an icing wind tunnel in addition to a conventional tunnel. Of particular interest in this work is the aerodynamic effects of numerous combinations of ice shapes and wing section configurations including advanced high-lift devices. This study was followed by another investigation by Ingelman-Sundberg and Trunov (31) in 1979 and involved a wind tunnel investigation of the sensitivity to ice of a number of geometrically different horizontal stabilizers. In another study by Trunov and Aaro(32), methods for preventing ground icing on aircraft are discussed and results from comparative testing of some anti-icing fluids are presented. Shav, Soton, and Solano(33) in 1982 discussed their findings of measured aerodynamic performance degradation data obtained for a NACA 63₂-A413 airfoil. Glaze and rime ice formations were studied in both cruise and climb configurations and significant performance degradation was noted. Also evaluated was the effect of aft frost growth on airfoil performance, which significantly increased the section drag coefficient. This study was of importance since new data was provided with which to test the Gray drag coefficient correlation. The authors found that the correlation was accurate in most cases as the original data set upon which the correlation was developed. However, the Gray correlation becomes questionable for higher liquid water content values. In 1982, Bragg and Gregorick(34) along with Bragg, et al. (35) used simulated ice shapes to investigate various aspects of the ice accretion problem. A simulated rime ice shape was applied, with and without surface roughness, to a NACA 63A413 airfoil. Surface roughness was determined to be an important factor in modelling ice shapes affecting drag coefficient and maximum lift coefficient. In this series of tests, the feasibility of using wood shapes to model ice accretions on a NACA 63₂A413 airfoil was demonstrated. Using this technique, surface pressure measurements could be made in the area of the ice accretion, thereby leading to a better understanding of the physics involved in the formation of ice on airfoils. Fleming and Lednicer in 1983(36) tested a series of helicopter airfoils to investigate the effects of natural ice accretion at high speeds. Aerodynamic performance degradation of the airfoils was noted, with the authors citing drag coefficient increases of up to approximately 300%. Also accomplished in this test were better definitions for ice growth and ice type boundaries as functions of static temperature, Mach number, and liquid water content. Other studies have been performed by Lee(37) and Abbott, et al.(38) concerning the actual ice shapes observed on the main rotor of a UH-1H helicopter in hover at the Canadian National Research Council spray rig in Ottawa, Canada. The ice formations accreted on the main rotor were documented after landing through utilization of molds, tracings, and stereophotographs(39). In a related study, Abbott, et al.(40) conducted level flight performance icing tests with a UH-1H helicopter in an artificial icing cloud created by the Helicopter Icing Spray System (HISS). Measurements of power required data were used to define rotor performance degradation due to icing, and the rotor blade ice shapes were documented with silicone molds after landing. The authors have concluded that simplistic one-dimensional ice shape descriptions are not adequate to predict

performance degradation of helicopter rotors, i.e., three dimensional ice shape representation as a function of rotor radius is required. Also, repeatability of the ice shapes is difficult since it was found by the authors that similar cloud conditions can produce widely different ice shapes on the main rotor. This conclusion has been verified by a theoretical study conducted by Foster and Bartlett(41) into the influence of droplet sizing uncertainty on icing test results. In this sensitivity analysis, these authors found that temperature and liquid water content was the critical parameters in dealing with thermal anti-icing. For ice accretion, i.e., shape and size, the volume median droplet diameter was the crucial factor. In another experimental study by Trunov and Fugelman-Sundberg(42), wind tunnel investigations have been made of the aerodynamic effects of ice on three different tailplane configurations. Here, flight test results of ice effects on the control characteristics for a number of transport aircraft are given and discussed. The authors have also studied a number of transport and light aircraft accidents and incidents with regards to tailplane separation due to icing. Balte(43) in a recent study utilized airfoil sections representing UH-1H and UH-60A helicopter rotor blades in both natural and artificial icing conditions (NIS6). The testbed aircraft was a JU-23A with a framework over the left wing to hold the airfoil sections. Analysis of the resulting ice shapes indicated a lower than expected thickness accretion rate for artificial icing conditions. Hansman, et al.(44) presented results of preliminary tests conducted to measure ice growth on an airfoil during flight icing conditions using ultrasonic pulse-echo measurements. These thickness measurements were then used to document the evolution of the ice shape as a function of time. The use of generic or artificial ice has obvious advantages because of the controlled environment. However, the validity of the ice shape on an airfoil is somewhat open to question. In an experimental program, Bragg and Khodadous(45) studied the effect of a simulated glaze ice accretion on the aerodynamic performance of a NACA 0012 airfoil. In this study, two ice shapes were tested, i.e., one from an accretion predicted using a computer model (LEWICE(46)) given the same meteorological/performance conditions. The authors had found that the aerodynamic performance of the two shapes compared well at positive, but not negative angles of attack. In another rather unique experimental program, Kunjan, et al.(47) conducted a flight and wind tunnel investigation of the effects of aircraft ground deicing/anti-icing fluids on the aerodynamic characteristics of a Boeing 737-200 ADV aircraft. Liquids tested included a newtonian and three nonnewtonian anti-icing commercially available fluids. Both the flight test and wind tunnel results showed that fluids remaining on the wing after liftoff caused a measurable lift loss and drag increase. As part of a program involving the four major helicopter manufacturers, NASA Lewis Research Center, and Texas A&M University, Miller and Bond(48) conducted an experimental program which consisted of a rotating OH-58 tail rotor in the NASA Lewis IRT during 1988. Values of torque rise/vibration levels as a function of time were measured for a variety of icing conditions in addition to strobe photography video of the ice accretion process. This study also provided valuable insight into the ice shedding process which is inherent in a rotating system, and is the forerunner for a series of tests that will be conducted during the fall of 1989 involving a Powered Force Model (PFM) to be placed into the NASA Lewis IRT. The performance data resulting from this series of tests will be used to validate existing helicopter performance codes that contains numerical analyses of the ice accretion process, e.g., as described by Canba(49) and Johnson, et al.(50).

Much has been learned in recent years as a result of these cited experimental programs. A major contribution of these tests has been in the expansion of the icing data base to provide current information with which to develop and evaluate analytical methods for icing related performance degradation predictions. As in the experimental area, many analytical advances have also been made. This progress has taken the form of improved methods of predicting drop impingement characteristics, use of numerical analysis, as well as accurate aerodynamic performance degradation correlations.

Bragg, et al.(51) and Bragg(52) developed a computer program in 1931 to calculate water droplet trajectories and thereby determine airfoil impingement efficiencies and theoretical ice shapes. Development of this code represented a major step toward the goal of analytical prediction of airfoil performance degradation due to ice accretion. It may also be noted that Carsdale(5) in 1980 also presented a series of calculations of droplet trajectories around airfoils in compressible flow. In this study, the effect on droplet impingement, droplet

diameter, and chord as related to the NACA 0012, NACA 9615, and RAE 9643 airfoils were theoretically studied. Cansdale, in this early work, has modeled the thermodynamic process of ice accretion in incompressible flow to predict the shape and position of helicopter rotor ice with acceptable comparison with experiment. Bragg and Gregorak(34) has also formulated a drag coefficient correlation for the rime ice condition. In this correlation, the change in drag due to ice is given as a function of several variables related to flight and atmospheric conditions, airfoil geometry, and duration of ice accretion. This correlation has seen widespread use since its development and has only recently been studied in detail to define the range of applicability. A study by Miller, et al.(53) has shown that the original correlation overpredicted the airfoil drag increment in several cases for icing data which appeared to be rime oriented. Recently, Bragg(54) revised the correlation resulting in a second function to cover a wider range of meteorological conditions. Cansdale and Gent in 1983(10) detailed the development of another two-dimensional droplet trajectory numerical analysis. Unlike the Bragg computer code, the effects of compressibility, kinetic heating, and water runback are taken into account thus making it applicable to both rime and glaze ice conditions. Designed to be applied to helicopter configurations, the analysis employs a heat balance to calculate the kinetic heating and runback effects. The authors have reported good agreement between predicted and experimentally obtained ice shapes, temperature distributions, and icing threshold conditions. Fleming and Lednicer(55) have used experimental icing data to formulate new rime and glaze ice drag coefficient correlations. In addition, this data has been used to formulate separate lift and moment coefficient correlations. These correlations have shown promise in preliminary evaluations(53). Miller, Korkan, and Shaw in 1983(56) attempted to develop a drag coefficient correlation for the glaze ice condition using statistical analysis of icing data as a basis of the correlation development. Although a resulting correlation was presented, it represented only the state of the study at that time, and indicated a need for much further modification and analysis. Feasibility of using such an analysis as the basis for correlation development was demonstrated. The results of such an analysis must be interpreted correctly and in tandem with physical observations of the associated phenomenon to make the method truly beneficial. Bragg(57) has also documented a study in which airfoil performance was predicted with both simulated rime and glaze ice shapes. Various computer codes were examined for possible use in calculating pressure distributions on an airfoil with glaze ice attached. The potential flow code of Bristow was determined to be suitable for this purpose after examination of several airfoil analysis codes, and provided good agreement between predicted and experimental pressure distributions. Bragg also investigated the effects of surface roughness in the laminar boundary layer on drag increment, and offered promising results for predicting drag increase by this method. However in 1986, a state of the art numerical analysis referred to as LEWICE(46) has been developed which predicts the general ice shape about the leading edge of an airfoil for rime, mixed, and glaze ice conditions. This numerical approach is valuable since it utilizes time stepping in the calculation of the ice shape, and a thermodynamic analysis of Messinger(9) and Tribus(58). As noted, Messinger advanced the work of Tribus to include surface temperature analysis in several important temperature regimes, and also developed the concept of the freezing fraction. The freezing fraction is defined as the ratio of liquid freezing within a control volume over the total amount of liquid entering the control volume. This work utilizes an inviscid flow field but does incorporate a surface roughness parameter which is a variable and specified as input data. LEWICE is currently under study, and will contain the work of Cebici(59) which includes viscosity. Cebici uses an approach which is based on interaction of inviscid flow solutions obtained by a panel method and improved upon by the use of a finite-difference boundary layer method. Korkan and Britton(60) have utilized LEWICE in a study where comparisons are made between the analysis of Bragg(52), Wilder(61), and actual ice shapes as found in flight tests of the NASA Lewis RC Twin Otter aircraft(62). Scott, et al.(63) taking a different approach, investigates the flow-field and resultant heat transfer rates over a series of ice accretion shapes through numerical solutions of the Navier-Stokes equations. These authors have achieved good agreement when compared to experimental data. Addressing variations in the surface texture of a fifteen minute glaze ice condition, Pais and Singh(64) have applied a two-dimensional Fourier analysis to experimentally determined surface profiles. In other related areas, Meijer(65) has developed a theoretical method to calculate rime ice accretion on airfoils.

of particular interest, this author is able to calculate the rime ice accretion for two-dimensional high lift wing devices consisting of a basic wing profile based on NACA 64-215, a leading edge slot, a trailing edge vane, and a trailing edge flap. In another important area, Bilanin(66) reviews past scaling analysis and suggests revisions based on recent experimental observations. The author also suggests that numerical analyses such as LEWICE when utilized in the glaze ice accretion regime, may need improvement to increase the accuracy of the estimate of ice build-up. As an example of how the present technology can be applied, Britton(67) has theoretically investigated elevator deflection effects on the icing process. The results indicate that the process is dependent on elevator deflection since the flowfield is affected by changing the camber of the horizontal stabilizer system. The results are presented in terms of total collection efficiency and impingement limits as functions of angle of attack and elevator deflection angle.

A brief review(68) of both theoretical and experimental work in regards to icing has been presented. Obviously, all references to this subject cannot be addressed in this paper since it is estimated that approximately 2500 exist dealing with all topics related to the general category of icing. However, there are several references that deal with an overview of the NASA program on icing research and technology such as that of Shau(69) and Reimann, et al.(70). These papers review the major program elements, e.g., new approaches to ice protection; numerical codes; measurement and prediction of ice accretion; special wind tunnel test techniques; improvements of research techniques; improvements of icing wind tunnels and research aircraft; ground deicing fluids; fundamental studies in icing; and droplet sizing instruments. There is also an excellent overview given at the recent NASA-FAA-ATAA-SAB International Aircraft Icing Technology Workshop at NASA Lewis RC in November 1987. The workshop also contained the FAA perspective on aircraft icing certification that has since been commented by Adams(71).

It has been the intent to give the reader some insight into the major published references and chronological order of the advances made in icing technology - both experimental and theoretical. To this end, the authors since 1980 have been involved in the subject of icing of rotating systems and have heavily relied on the results of the studies that have been reviewed. As a result, several theoretical and experimental studies were completed dealing with performance degradation of rotating systems due to ice accretion. These studies will be reviewed in the following Section to provide some detail to the reader as to the approach and results. In so doing, the limitations and need for further study of performance degradation of rotating systems due to icing can be defined.

PARENT METHODOLOGY

When the study of performance degradation of rotary systems due to icing was started in 1980, the decision was made to initially investigate the propeller. These results were then used to model the helicopter in hover, followed by a study of the helicopter in forward flight. The methodology was then applied collectively to the XV-15 tilt-rotor concept to find the mode of propulsion most sensitive to icing. In the process of attempting to theoretically model performance degradation of these rotary systems, experimental studies were also conducted using a NACA 0012 airfoil with generic ice and a model helicopter with generic ice on the main rotor. Each of these studies will be summarized here, and the reader is referred to the appropriate reference for additional detail.

Propeller system(72)

The study objectives of the present effort were to establish a theoretical methodology to predict the performance degradation of propeller in a natural icing encounter. Only the rime ice accretion case was considered to determine the effect on propeller thrust coefficient, power coefficient and efficiency as a function of icing time.

The first step in this study was the development of a two-dimensional theoretical icing model applicable to propellers. The propeller flowfield with rotating airfoil sections encounters not only the forward but also rotational and induced velocity components. These velocity components determine the resultant velocity, and hence angle of attack as seen by each airfoil section radially along the propeller blade.

The flowfield encountered by the rotating airfoil section in the disk plane, when considering only the resultant velocity vector does not differ to a great extent from that of a "fixed wing airfoil." However, since the local induced velocity is a function of the propeller radial location, each airfoil section must be treated separately as to the radial variation of the local Mach number and local angle of attack.

The airfoil icing analysis of Bragg, et al.(34,35) used in this study has been formulated to predict the fixed, i.e. nonrotation airfoil performance degradation due to ice accretion. A Theodoresen/Karman-Trefftz transformation method is used to calculate the inviscid flowfield around the airfoil. This flowfield is then used to compute by step integration, the trajectories of the water droplets and location of impingement of the water droplet on the airfoil surface. This information is utilized to predict the local impingement efficiency and accumulation parameter on the airfoil surface. Also note that this study, as does the method of Bragg, assumes the rime ice case, i.e., the entire mass of the water droplets freeze on contact at the point of impact, therefore no thermodynamic effects have been included. The analytical method then consists of the following steps:

- (1) An existing propeller performance method(73) is used to obtain the local Mach number and angle of attack as a function of radial location along the propeller at a preselected operating condition.
- (2) A volume median droplet diameter is selected. Through a previous study by Bragg and Gregorek(34), it has been shown that by appropriate selection of a volume median droplet diameter, the entire class of droplet diameters encountered need not be considered.
- (3) Select the liquid water content to be considered.
- (4) Using the Theodoresen/Karman-Trefftz transformation method, calculate and store the inviscid flowfield around each airfoil station at the given angle of attack for each radial location along the propeller for the operating condition of interest.
- (5) Calculate the water droplet trajectories using the volume median droplet diameter in Step 2 for each airfoil along the propeller.
- (6) Determine the impingement efficiency and accumulation parameter for each airfoil station along the propeller.
- (7) Calculate the drag increment for each airfoil station at the specified icing time and operating condition. The airfoil data bank for performance analysis is then modified by applying the $(1+\Delta C_D/C_D)$ factor.

The propeller performance analysis is again utilized to determine the performance degradation due to icing on the basis of η , C_T and C_P at the operating condition of interest.

In the calculation of the drag increment due to ice accretion, the empirical correlation of Bragg and Gregorek(34) was used directly, i.e.

$$\Delta C_D/C_D = 0.010[15.798 \ln(k/c) + 28.030 A_2 E + I]. \quad (1)$$

This empirical correlation includes the drag increment related to the distortion of the airfoil leading edge due to rime ice accretion and a step drag increase based on surface roughness data, i.e., frost. The constant I is dependent on airfoil type and ranges from 184 to 290.

The new drag of the airfoil in the icing condition which is used to modify the airfoil data bank may be obtained from the expression

$$C_{D_{ice}} = (1 + \Delta C_D/C_D) C_D \quad (2)$$

where the C_D value is for the no-ice condition and is contained in the airfoil data bank as used by the propeller performance analysis, or can be determined by existing airfoil analyses and/or experiment. The above drag correlation is only valid for the rime ice condition. It is emphasized that in all theoretical studies conducted, this approach has been used and has yielded acceptable results.

The analytical model just described was utilized to provide theoretical predictions of propeller performance degradation for comparison with experimental flight test results by Neel and Bright(13). Here, the authors conducted a series of flight tests with a C-46 twin-engine aircraft. The test propeller having a diameter of 13.5 ft, consisted of four blades with double-camber Clark-Y airfoil sections. Of the 12 encounters investigated by Neel and Bright, 5 were chosen for comparison with the analytical model of rime ice accretion based upon free-air temperature, liquid water content, and volume median droplet diameter.

The theoretical methodology described earlier, when applied to encounter 2 with a fixed J -value yields a trend in impingement efficiency variation as a function of airfoil surface length for each radial station along the propeller. Fig. 1 shows a typical variation for r/R of 0.975 and also indicated A_{max} . The total collection efficiency, maximum collection efficiency, and accumulation parameter(51) defined by:

$$A_c = U(LWC) \pi r / 100 C \quad (3)$$

are then determined for all radial locations along the propeller blade, as shown in Fig. 2. Next, these values are used in the drag coefficient correlation as given in equation (1) to determine the appropriate values of $(1 + C_D/C_D)$ for the basic two-dimensional airfoil sectional characteristics as used in the propeller performance method. Comparisons for encounter 2 between the experimental values and theoretical predictions are shown in Fig. 3. For the propeller efficiency, the agreement between theoretical prediction and experiment for both lead and clear conditions is acceptable as shown in Fig. 4 (encounter 4) and Fig. 5 (encounter 12).

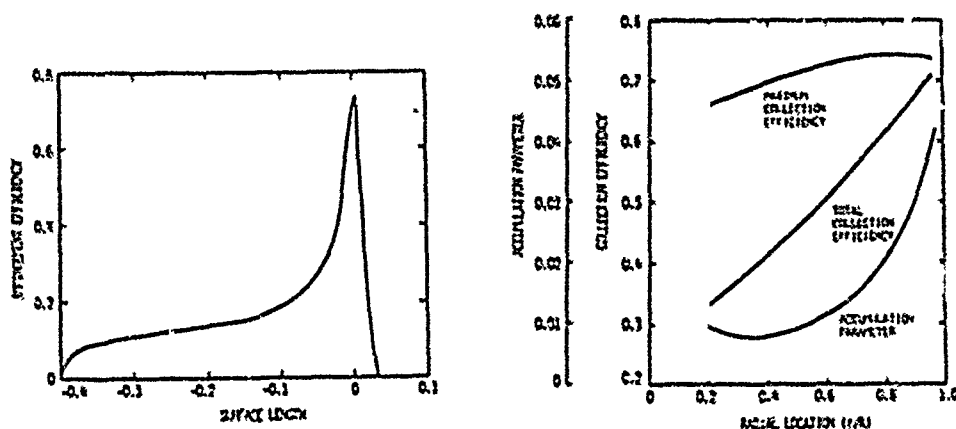


Figure 1. Example of impingement efficiency variation vs airfoil surface length - encounter 2, $r/R=0.975$, $J=1.2$, $\alpha=4.624$ deg.

Figure 2. Variation of accumulation parameter, total collection efficiency, and maximum collection efficiency as a function of radial location - encounter 2, $J=1.2$

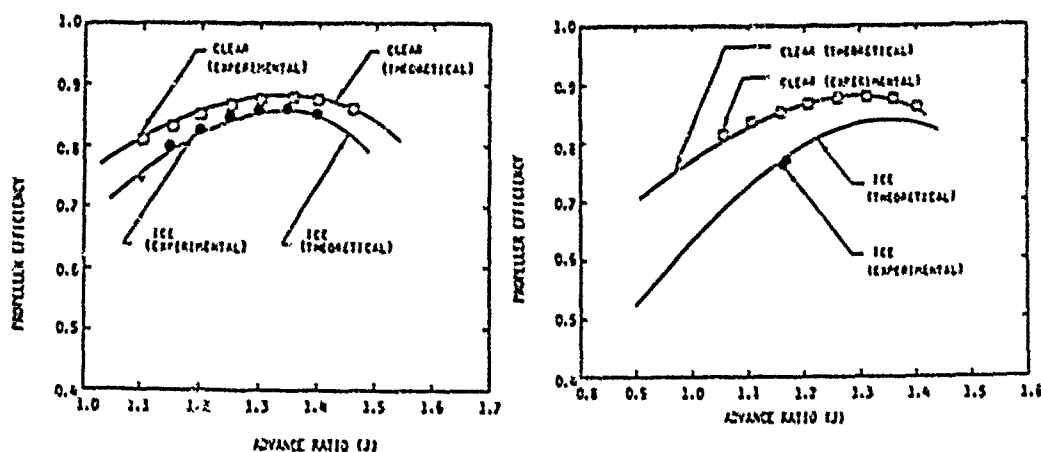


Figure 3. Comparison between theoretical/experimental η values - encounter 2.

Figure 4. Comparison between theoretical/experimental η values - encounter 4.

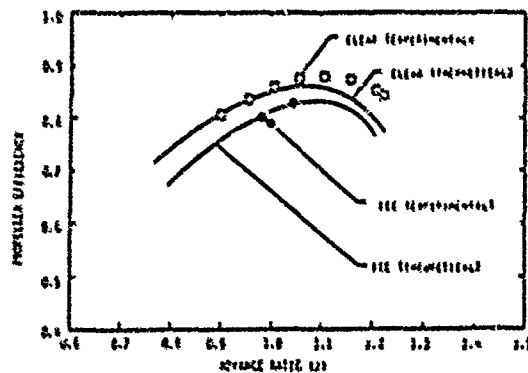


Figure 5. Comparison between theoretical/experimental η values - encounter 12.

Helicopter rotor-hover(74)

The analytical model as described by Korkan, et al. [72] as applied to the prediction performance degradation of propellers in a natural icing encounter, has been examined to determine the feasibility of prediction helicopter performance degradation in hover during natural icing. The front rotor of the CH47D helicopter was selected for analysis, where the rotor consists of three blades with a radius of 30 ft, a constant chord of 32 in, and rotates at 225 rpm. The rotor blade employed the VR-7 and VR-8 airfoils having a maximum thickness/chord ratio of 12 and 8%, respectively. The blade transitions linearly from VR-7 to the VR-8 airfoil at the rotor tip.

The flight condition selected for analysis was at an altitude of 3000 ft and a free-air temperature of 1°F . The Boeing Vertol B-92 helicopter performance analysis yielded the range of the thrust coefficient and horsepower for the CH47D rotor in the hover condition.

The rim ice condition selected for analysis consisted of a liquid water content of 0.44 g/m^3 , a volume median droplet diameter of $25 \mu\text{m}$ and a free-air temperature of 1°F . As in the propeller case, the total collection efficiency and the accumulation parameter have been determined for all radial locations along the rotor blade. These values have then been used in the rim ice drag coefficient correlation of Bragg and Gregorek [34] discussed earlier.

The factor $(1 + \Delta C_D / C_D)$, plotted as a function of radial location for selected times of 60, 180 and 300 s in Fig. 6, indicated the strong dependence of the performance degradation on actual icing time. Also, these data can be displayed as a function of time for selected radial locations, where the growth in drag is linear with time starting from the frost point which is noted as a step in the $(1 + \Delta C_D / C_D)$ variation at time 0 s.

When these drag increments are included in the airfoil data used for the hover analysis of the CH47D rotor, the resulting increase in required horsepower necessary to maintain a thrust level C_T of 0.004 as a function of icing time is shown in Fig. 7. The approximately 24% increase in required horsepower for a 5 min natural icing encounter for this C_T is evident. It should also be noted that if ice accretion is allowed to take place only up to the 83% radial location, the horsepower increment needed to maintain a C_T of 0.004 is reduced to approximately 12%. This illustrates the sensitivity of the rotor-tip region in the degradation of the helicopter performance in an icing encounter, and stresses the need to quantify the mechanism of both ice accretion and shedding.

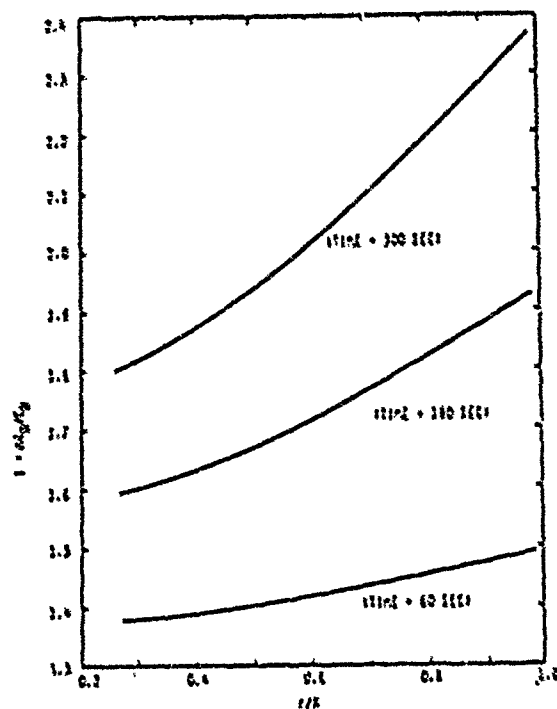


Figure 6. Variation of $(1 + ACN/CD)$ along a CH47D helicopter rotor blade for selected icing times of 60, 180, and 300 s. $C_T = 0.004$, hover condition.

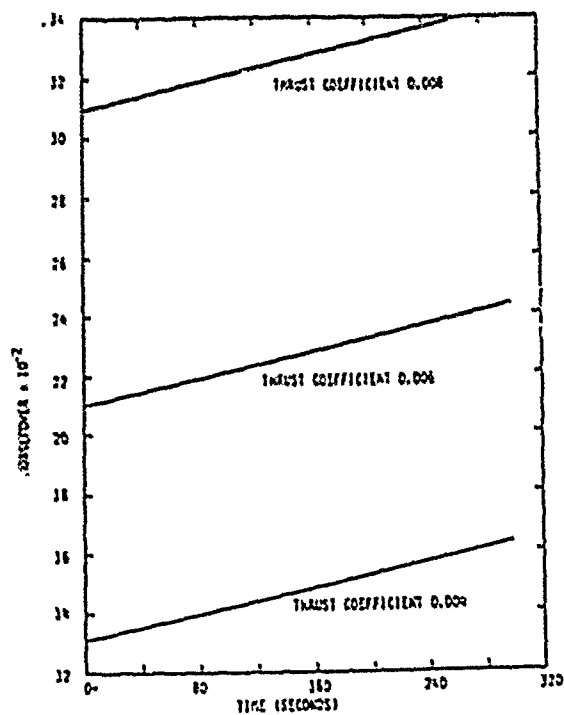


Figure 7. Horsepower required to maintain a C_T of 0.004 as a function of icing time. CH47D helicopter rotor blade, hover condition.

Helicopter rotor-forward flight(73)

The methodology established earlier to analyze and provide theoretical values of performance degradation of rotating systems, such as propellers and helicopter rotor blades in hover during natural icing conditions, yielded performance levels which were consistent with those experienced in actual flight. However, the methodology to theoretically analyze the performance of a helicopter in forward flight during icing remained to be fully established and demonstrated.

The method of helicopter forward-flight performance analysis used to determine the trends presented here is a state-of-the-art computer code (Boeing Vertol B-65) including all key aerodynamic and dynamic effects influencing the rotor flow environment, as well as the blade motions and elastic deflections. At present however, the most meaningful trends can be drawn by limiting the investigation to profile drag increase.

The analytical model described by Korkan et al.(72) and applied to the helicopter hover condition(74) can be meaningfully extended to the helicopter forward-flight condition. As noted in earlier studies, for a rotating system such as a propeller or helicopter rotor, the rotating airfoil sections encounter varying combinations of forward, rotational and induced velocity components resulting in local Mach number and angle-of-attack excursions which are repeated cyclically as a function of blade radial and azimuthal location. The method described earlier first calculates the impingement efficiency and accumulation parameter as a function of radial and azimuthal location and then the resulting drag increment ratio, $(1+\Delta C_D/C_D)$. The drag data used in the rotor performance analysis is then modified by the local drag factor and the performance is recalculated for a fixed icing time.

In the present study, the effect of rim ice accretion on the front rotor blades of the CH-7D was investigated to determine the horsepower required to maintain a given flight speed as a function of icing exposure time. Basic to the method are the assumptions that the fuselage was not reoriented during the icing period, that no ice was allowed to accumulate on the fuselage, and that only the cyclic pitch was adjusted to maintain the flight condition. The CH-7D front rotor consists of three blades with a radius of 30 ft having a constant chord of 32 in. and rotating at 221 rpm corresponding to a rotor tip speed of 695 ft/s. The rotor blades utilize the VK-7 and VK-8 airfoils as described by Korkan et al.(75).

The flight condition selected for analysis was at an altitude of 6800 ft and at a forward velocity of 133 kn with a required thrust of 20,775 lb and a propulsive force of 1460 lb (front rotor only). The rim ice condition selected for analysis consisted a liquid water content of 0.44 g/m^3 , volume median droplet diameter of 25 μm , and a free-air temperature of 4°F .

In applying the previously described methodology to a helicopter rotor blade in forward flight, it may be noted that the local Mach number and angle of attack are functions of both radial and azimuthal location on the rotor disk. The numerical procedure has been applied to 13 rotor spanwise stations for each of 24 azimuthal sectors which corresponded to 15° increments. The azimuthal variation of the total collection efficiency and accumulation parameter were determined as shown in Fig. 8 (a-d) and 9 (a-d) for each of the fixed spanwise radial locations. Values of the azimuthal variation of $(1+\Delta C_D/C_D)$ were calculated using equation (2) and are shown in Fig. 10 (a-d). These drag factors were applied directly to the rotor analysis to determine the performance degradation at each fixed icing time during the assumed natural icing encounter.

The approach used in the present study was to average the drag increment due to icing $(1+\Delta C_D/C_D)$ azimuthally at each radial location for each of the icing times. The results are shown in Fig. 11 as a function of radial extent of icing. As noted, the drag increment due to icing is linear with time spent during the icing encounter. Also, as the radial extent of icing increases, the drag increase due to icing rises significantly. These values were introduced into the Boeing Vertol B-65 helicopter performance analysis to determine the horsepower required to maintain a propulsive force of 1460 lb and a thrust of 20,750 lb. The results of these calculations are shown in Fig. 12 referenced to the clean front-rotor horsepower(hp) of 1990. The variation of the ratio of $\text{hp}(\text{ice})/\text{hp}(\text{ref})$ with icing time follows the same trend as the drag increments (Fig. 11), i.e. linearly with respect to time. The high sensitivity of the total performance to main-rotor tip accretion is also evident.

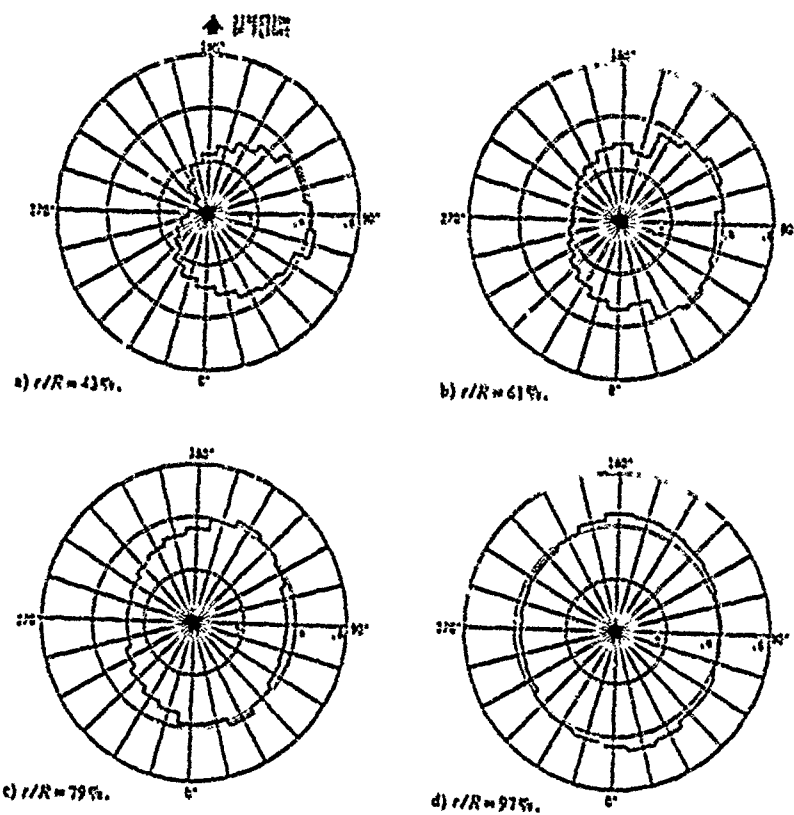


Figure 8(a). Azimuthal variation of total collection efficiency at $r/R = 43.00\%$ (counter-clockwise direction of rotation).

Figure 8(b). As for Fig. 8 (a) but at $r/R = 61.00\%$.

Figure 8(c). As for Fig. 8 (a) but at $r/R = 79.00\%$.

Figure 8(d). As for Fig. 8 (a) but at $r/R = 97.00\%$.

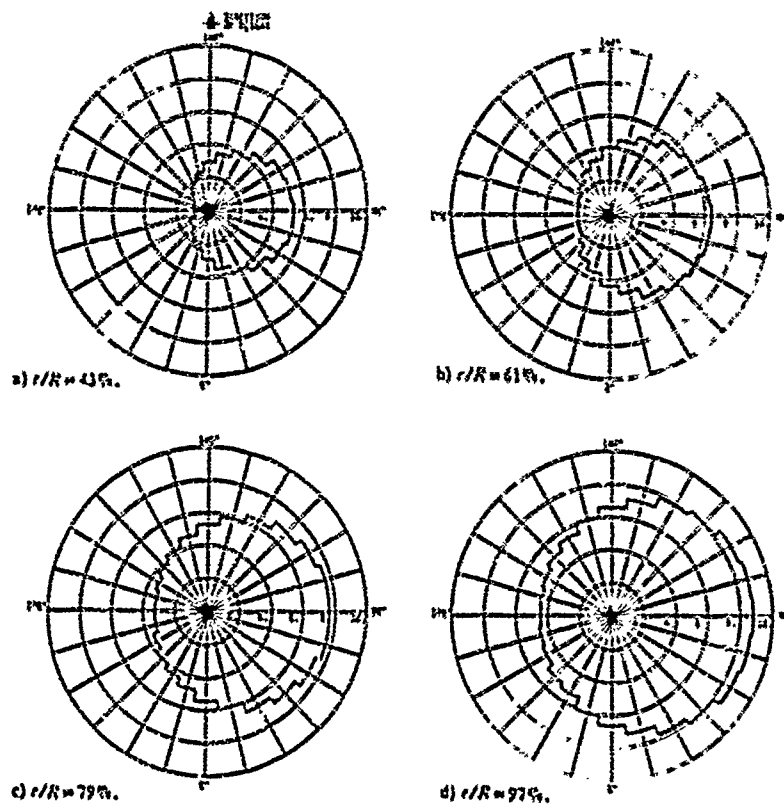


Figure 9(a). Azimuthal variation of accumulation parameter $AC \times 10^3$ at $r/R = 43.00\%$ (0-60 sec - counter-clockwise direction of rotation).

Figure 9(b). As for Fig. 9 (a) but at $r/R = 61.00\%$.

Figure 9(c). As for Fig 9 (a) but at $r/R = 79.00\%$.

Figure 9(d). As for Fig 9 (a) but at $r/R = 97.00\%$.

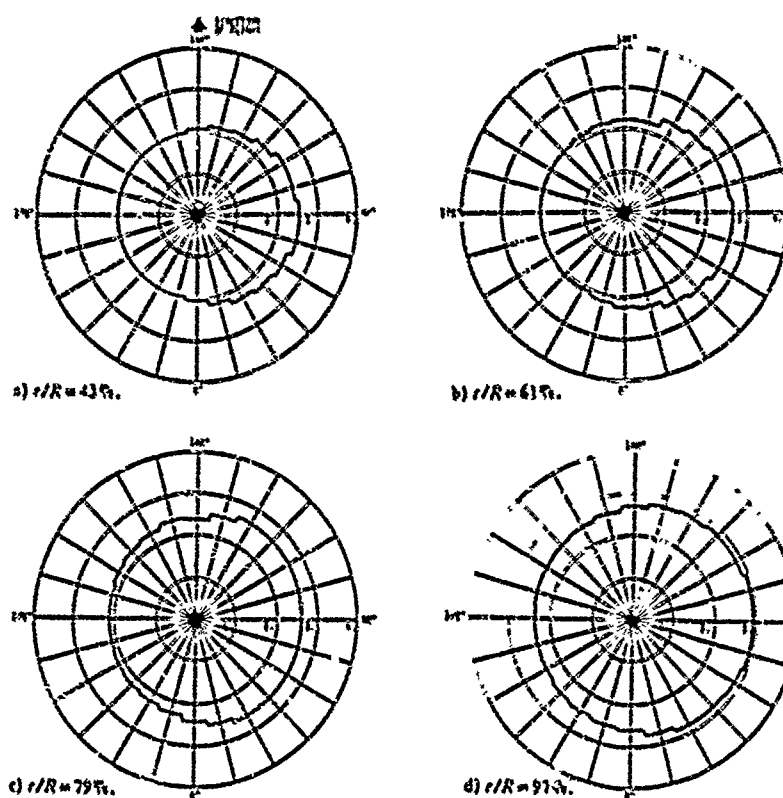


Figure 10(a). Azimuthal variation of $(1 + \Delta C_p/C_p)$ at $r/R = 43.00\%$ ($\Delta t = 60$ s. = counter-clockwise direction of rotation).

Figure 10(b). As for Fig. 10 (a), but at $r/R = 61.00\%$

Figure 10(c). As for Fig. 10 (a) but at $r/R = 79.00\%$

Figure 10(d). As for Fig. 10 (a) but at $r/R = 91.00\%$

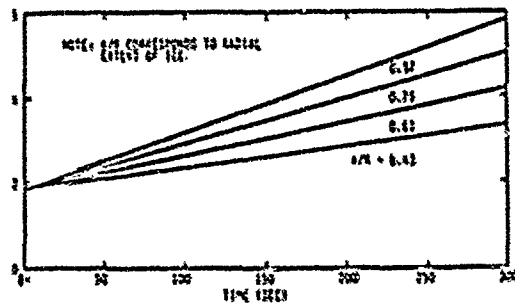


Figure 11. Variation of drag increment with icing time at fixed radial location (360° average - 15° segment).

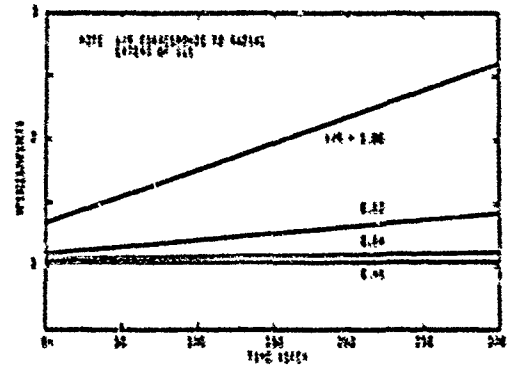


Figure 12. Horsepower required with time ice accretion to maintain a propulsive force of 1460 lbs and thrust of 20,750 lbs (hp_{req}-1990, front rotor - 360° average - 15° segment).

The numerical procedure previously described involves a matrix of 13 radial locations defined at 24 azimuthal sectors, and requires an intense computational task. Therefore, an averaging method was investigated to determine if a more expedient and still acceptable procedure could be established. This investigation was approached in three ways:

(1) Sum and average the values of $(1+\Delta C_D/C_D)$ calculated for each 15° azimuthal sector around the entire rotor disk for each radial location for a specified icing time.

(2) Sum and average the total collection efficiency (\bar{E}) and accumulation parameter (\bar{AC}) for each 15° azimuthal sector around the entire rotor disk. Values of \bar{E} and \bar{AC} can then be used to calculate an averaged value of $(1+\Delta C_D/C_D)$ for each radial location at a specified icing time.

(3) Sum and average the local Mach number and angle of attack values for each 15° azimuthal sector around the entire rotor disk for each radial location. Computation of the total collection efficiency and accumulation parameter is then performed from these averaged values of M and α . The corresponding values of \bar{E} and \bar{AC} are then used to calculate an azimuthally-averaged radial variation of $(1+\Delta C_D/C_D)$.

The three averaging methods have been applied to the case under investigation for an icing time of 60 s with ice accretion allowed to take place along the entire span of the rotor. The results are shown in Table 1 for four radial

locations along the rotor blade. Using the $(1+\Delta C_D/C_D)$ as a base, it can be seen that averaging \bar{E} and \bar{AC} and calculating $(1+\Delta C_D/C_D)$ results in a 0.26 to 2.58t variation from the values of $(1+\Delta C_D/C_D)$. However, if the α and M averaging procedure is employed, hence \bar{E} and \bar{AC} , the resulting values of $(1+\Delta C_D/C_D)$ differ only by -1.82 to 1.84t from the values of $(1+\Delta C_D/C_D)$ for an icing time of 60 s. This approach (Method 3) resulted in a required horsepower of 3190 to maintain a propulsive force of 1460 lb for the front-rotor thrust of 20,750 lb for ice accreting along the entire span of the blade. In contrast, when unaveraged values were used in the Boeing Vertol B-65 helicopter performance analysis, i.e. when 13 spanwise computational bays were assigned $(1+\Delta C_D/C_D)$ values for each of the 24 azimuthal sectors for the same icing time, 3364 hp was required to maintain the same flight condition. As can be seen for this flight condition, the horsepower when using values of the detailed 33x24 numerical scheme differs by approximately 5.2t from the most simplified method of averaging. Therefore based upon these results, the method of computing α and M and hence the performance, appears to be acceptable for the conditions under study.

Table 1. METHOD OF AVERAGING (15° - 15° SEGMENTS/60° ICING TIME)

X R			
	(1) E, AC	(1) α , H	(2) E, AC
	(2) $(1+\Delta C_D/C_D)$	(3) $(1+\Delta C_D/C_D)$	(3) $(1+\Delta C_D/C_D)$
	(1) $(1+\Delta C_D/C_D)$		
0.43	2.170	2.114 (2.38%)	2.130 (1.84%)
0.61	2.313	2.277 (1.56%)	2.339 (+1.13%)
0.79	2.424	2.447 (1.03%)	2.489 (+0.51%)
0.97	2.699	2.692 (0.26%)	2.749 (+1.82%)

* PERCENT DEVIATION FROM $(1+\Delta C_D/C_D)$

In summary, the results of the analytical prediction of performance degradation for a specified CH-7D helicopter forward-flight condition in the presence of rime ice has been evaluated. The analysis determined the horsepower required to maintain speed and trim as a function of time in an assumed natural icing encounter, and the predicted levels of performance degradation are qualitatively consistent with those experienced in actual flight. The calculations involved 13 rotor spanwise stations, where each computational bay was assigned a drag increment for a given icing time interval for each of 24 azimuthal sectors. The Boeing Vertol B-65 helicopter performance analysis was then used for the front rotor of the CH-7D helicopter configuration to assess the additional horsepower required to overcome the increased profile drag. The rotor cyclic controls were changed as necessary to maintain the flight condition. The method of averaging has also been investigated by comparing the $(1+\Delta C_D/C_D)$ for each 15° quadrant azimuthally at a fixed radial location to E and AC hence $(1+\Delta C_D/C_D)$, α and H resulting in E, AC and hence $(1+\Delta C_D/C_D)$. The procedure of averaging α and H at fixed radial locations to obtain E, AC and hence $(1+\Delta C_D/C_D)$ yielded acceptable results within $\pm 1.8\%$ of $(1+\Delta C_D/C_D)$ azimuthally for each 15° quadrant at a fixed radial location, thus greatly simplifying the calculation process. Also, the extent of the spanwise icing has been shown to have a significant effect on the horsepower required to maintain the specified flight condition.

XV-15 tilt rotor(76)

The objective of this study was to take the current methodology that has been previously established and apply these techniques to the XV-15 tilt-rotor system in a natural icing encounter. Since four modes of operation are experienced in this system, i.e., helicopter hover, helicopter forward flight, tilt rotor and propeller, the methodology did exist to determine the effect of rime ice accretion on horsepower required to maintain a specified flight condition as a function of icing time. In this approach, the conclusion can then be drawn as to which mode of operation experiences the greatest percentage of performance degradation in a natural icing encounter.

The basic assumptions used in this study consisted of the use of a single XV-15 propulsion unit, the fuselage was not reoriented during the icing period, no ice was allowed to accrete on the fuselage, and adjustment of cyclic was used to maintain the flight condition. The XV-15 prop/rotor has three blades with a radius of 12.5 ft, uses NACA 64 series airfoils with a constant chord of 14 in, and has a maximum thickness/chord ratio ranging from 8 to 27%. The meteorological condition chosen corresponded to rime ice at sea level with a free-air temperature of 3°F, liquid water content of 0.44 g/m³, and a volume median droplet diameter of 25µm.

The analysis condition chosen for each mode of propulsion is shown in Table 2. For each mode of propulsion, it can be conveniently classified into two types on azimuthal variation consisting of N sectors. Hence, the local Mach number and angle of attack is specified from the performance analysis of Boeing Vertol Co. as a function of rotor radius for each N sector. For the helicopter hover and propeller modes, $N=1$, whereas for the helicopter forward-flight and tilt-rotor modes, $N=24$, where each azimuthal sector consists of 15° . The method of averaging (Method 3) discussed earlier has been used for the $N=24$ case, and the theoretical analysis previously described has been applied.

TABLE 2. ANALYSIS CONDITION

HELICOPTER HOVER MODE	45° TILT ROTOR MODE
Rotor rpm 365.32	Forward Velocity - 120 kn
Rotor tip speed - 740 ft/s	Rotor rpm - 365.32
Thrust required - 6316 lb	Rotor tip speed - 1.0 ft/s
	Thrust required - 2341 lb
	Propulsive force - 1342 lb
HELICOPTER FORWARD FLIGHT MODE	PROPELLER MODE
Forward velocity - 80 kn	Forward velocity - 180 kn
Rotor rpm - 365.32	Rotor rpm - 438.37
Rotor tip speed - 740 ft/s	Rotor tip speed - 6.7 ft/s
Thrust required - 6316 lb	Thrust required - 761 lb
Propulsive force - 922 lb	Propulsive force - 772 lb

Typical results of this study are shown in Figs. 13 and 14 as a function of radial extent of ice vs the ratio of $hp(ice)/hp(ref.)$ necessary to maintain the flight condition for three icing times. It has been noted that for each mode of propulsion, if ice is allowed to accrete to the rotor tip, the required horsepower to maintain the flight condition for a 5 min encounter easily exceeds twice the horsepower for the no-ice condition.

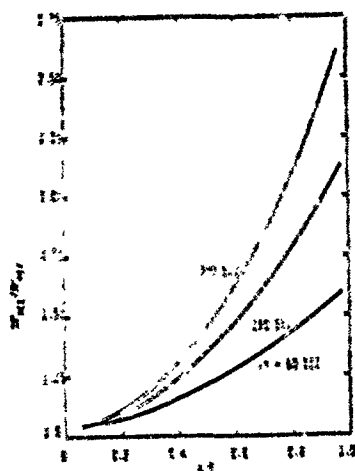


Figure 13. Horsepower required vs radial location for three fixed icing times - helicopter hover mode.

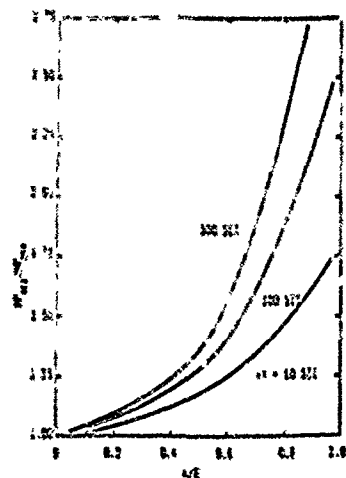


Figure 14. Horsepower required versus radial location for three fixed icing times - helicopter forward flight mode.

Based upon these numerical results, a performance degradation rating can now be established, and is shown in Table 3. The rating scheme has been utilized as a function of spanwise rim ice accretion. For example, if ice is allowed to accrete to the 100% radial location, the helicopter forward-flight mode requires the greatest amount of horsepower to maintain the flight condition over the clean or reference value of horsepower followed by the tilt-rotor mode, propeller mode and helicopter hover mode. If ice accretes only to the 80% radial location, the helicopter forward-flight mode still requires the greatest amount of horsepower, and propeller mode has moved to the second position followed by the helicopter hover mode and tilt-rotor mode. If ice accretes to the 60% radial location, it is interesting to note that the helicopter forward-flight mode is now replaced by the propeller mode followed by the helicopter hover mode. The helicopter forward-flight mode has now dropped to the number three location followed by the tilt-rotor mode.

TABLE 3. PERFORMANCE DEGRADATION RATING

(SPANWISE RIME ICE ACCRETION)		
100%	80%	60%
(1) Helicopter forward flight mode	(1) Helicopter forward flight mode	(1) Propeller mode
(2) Tilt-rotor mode	(2) Propeller mode	(2) Helicopter mode
(3) Propeller mode	(3) Helicopter hover mode	(3) Helicopter forward flight mode
(4) Helicopter hover mode	(4) Tilt rotor mode	(4) Tilt rotor mode

In summary, the performance degradation due to icing for the XV-15 tilt-rotor aircraft has been evaluated in terms of horsepower required to maintain a specified flight condition. This study has been conducted for the rim ice condition for the helicopter hover, helicopter forward-flight, tilt-rotor and propeller modes of operation. Based on the present results, the configuration mode most sensitive to rim ice accretion is dependent on the spanwise extent of ice accretion. This conclusion then gives rise to the need for studies of an adhesion force/centrifugal force model, aerodynamic heating model, and a further

NACA 0012 airfoil with generic ice(77,78)

Wind-tunnel tests were conducted with a two-dimensional NACA 0012 airfoil having a 21 in chord to investigate the effect of Reynolds number on the aerodynamic performance with and without a generic ice shape attached to the airfoil leading edge. The Reynolds number range investigated consisted of 0.36 to 3.36×10^6 which covers the operating regime of a model helicopter rotor tip(77,80). The airfoil experiment also served to generate a data bank for the generic ice shape addition including roughness in terms of C_D , C_L , C_{Lmax} , and $C_{ac}/4$.

The airfoil tests utilized the Texas A&M University 7x10 ft low-speed wind tunnel, which is a closed-circuit tunnel with a test section 7 ft high, 10 ft wide and 12 ft long. Any desired test-section Reynolds number up to $1.84 \times 10^6/\text{ft}$ may be obtained. Lift, drag, and moment measurements are taken via the six-component external balance. Resolution of forces and moments is accurate to within 0.1 lb and 0.1 ft-lb, respectively. Upon transmission of the measurements to the Perkin-Elmer 8/16 E data acquisition and analysis computer system, corrections are included for wind-tunnel interference and model support effects. The 21 in chord NACA 0012 airfoil section was mounted vertically in the test section, cantilevered to the external balance beneath the wind-tunnel floor and pivoted at the wind-tunnel ceiling.

The generic ice shape utilized during the present tests has been documented by Lee(37) and Abbott, et al.(38) on the main rotor of a UH-1H helicopter during an icing flight test program. The ice profile chosen for this study was based on the criteria that the shape could be reasonably scaled to the model helicopter main rotor including roughness (39,80). The 44% radial station of the UH-1H main rotor was selected corresponding to a flight-test condition corresponding of a 3 min icing encounter with a free-air temperature of -19°F and a liquid water content of 0.7 g/m^3 . Fig. 15 shows a projection of the ice shape as molded during the flight tests and that used on the tunnel airfoil model.

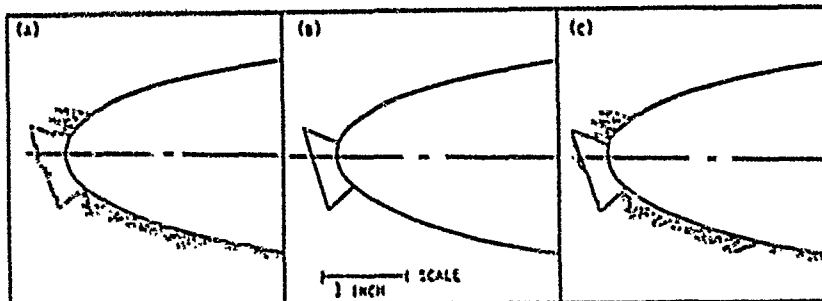


Figure 15. (a) Actual ice accretion as documented during flight tests of UH-1H helicopter. (b) Ice shape used on tunnel model (less roughness). (c) Comparison of (a) and (b).

The NACA 0012 airfoil section was initially tested with no generic ice addition to obtain baseline data and establish agreement with Abbott and Von Doenhoff(81) for the case of $Re=3.3 \times 10^6$. The generic ice shape was then attached to the leading edge of the airfoil and the test matrix repeated. Effects on the lift, drag, and pitching moment about the quarter-chord as a function of angle of attack and Reynolds number were then examined to determine aerodynamic increments due to addition of the generic ice shape.

In the study of lift with the addition of the asymmetric generic ice shape with roughness, early boundary-layer transition is expected in addition to leading-edge separation and reattachment. As shown in Fig. 16 for $Re=0.7 \times 10^6$, the addition of the generic ice shape does cause premature stall with a significant reduction in $C_{L_{max}}$ and stall angle of attack. Here it can also be seen that because of the asymmetric location of the generic ice shape on the airfoil leading edge, the maximum lift coefficient and corresponding angle of attack for both positive and negative values differ, unlike that of the symmetrical airfoil. Also due to the asymmetry of the ice addition, resulting in leading edge boundary layer separation and distortion of the airfoil pressure distribution, camber is introduced resulting in a zero lift angle of attack shift to approximately -0.5° . This appears to be consistent at all Reynolds numbers tested. Also, it was noted there was no change in the lift-curve slope which could be detected for the Reynolds number range of 0.7 to 3.4×10^6 . However, a slight dependence of the maximum lift coefficient on Reynolds number is indicated in comparison to the no-ice two-dimensional airfoil values.

The increase in the drag values for the airfoil with generic ice attached for $Re=2.1 \times 10^6$ is shown in Fig. 17. Here, upon comparison with the clean airfoil, it can be seen that an increase of approximately 120% is found for C_{D0} . The C_D values increase significantly as C_L increases, e.g. exceeding 200% at a C_L of 0.6. For negative angles of attack, due to the asymmetry of the generic ice shape, the C_D exceeds this value (Fig. 17). Reynolds number effects indicated a slight dependence for the range of 1.4 to 2.8×10^6 with an increase for $Re=3.4 \times 10^6$ for both positive and negative angles of attack. The magnitude of the C_D is of the same order as that predicted by Bragg and Gregorek(34) and Lee(37).

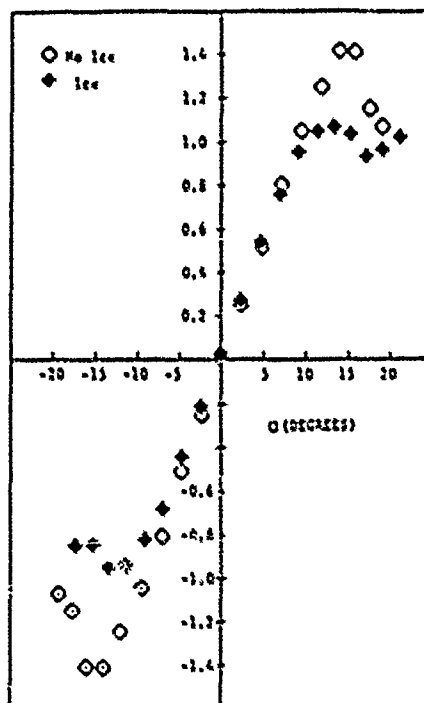


Figure 16. Experimental C_L - α data for an NACA 0012 airfoil clean and with simulated leading edge ice ($Re=1.4 \times 10^6$).

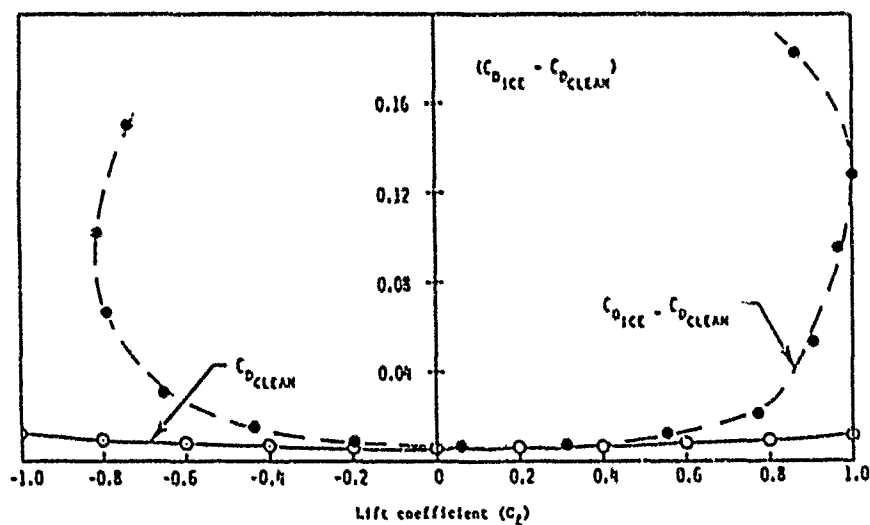


Figure 17. Wind-tunnel measurements of the increase in drag, ΔC_D , due to simulated ice on an NACA 0012 airfoil ($Re=2.1 \times 10^6$).

Moment coefficients about the airfoil quarter-chord were also measured, and a representative comparison of the clean and generic ice case is presented in Fig. 18 for $Re=2.1 \times 10^6$. The moment coefficient data for the clean configuration are characteristic of the symmetric airfoil and are agreeable within the resolution of the wind-tunnel balance. The addition of the generic ice shape results in two effects on the pitching moment variation as a function of C_L . A small nose-down pitching moment caused by the camber effect similar to the c_m shift was noted. Also, the influence of the simulated ice on dC_m/dC_L is large, where the slope of the curve becomes positive due to the region of incipient separation and its influence on the airfoil pressure distribution as a result of the artificial introduction of camber by the generic ice shape. This effect appeared to be relatively independent of Reynolds number for the range tested.

In summary, wind-tunnel tests were conducted with a two-dimensional NACA 0012 airfoil having a 21 in chord to investigate the effect of Reynolds number on the aerodynamic performance with and without a generic ice shape attached to the airfoil leading edge. The Reynolds number range investigated consisted of 0.36 to 3.36×10^6 which includes the operating regime of the model helicopter rotor tip (79,80). Values of C_D , C_L , C_{Lmax} and C_{ac4} were presented for the no-ice/generic ice airfoil configurations, and have shown that the addition of simulated ice to the leading edge of the airfoil creates premature stall with a considerable reduction in C_{Lmax} and stall angle of attack. An increase in the drag values of 120 to 200% compared to the clean airfoil values was measured in addition to a significant increase in the airfoil moment coefficient about the quarter-chord resulting in positive values of dC_m/dC_L . The aerodynamic coefficients of the airfoil with the leading-edge generic ice showed little dependence on the Reynolds number range tested.

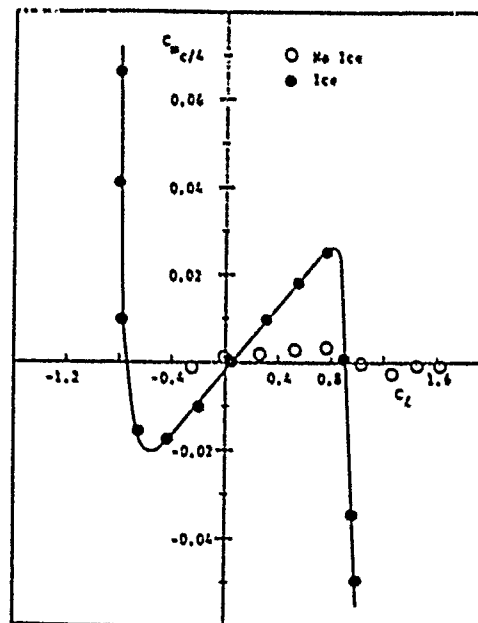


Figure 18. Measured pitching moment coefficient about the quarter-chord of an NACA 0012 airfoil clean and with simulated ice ($Re=2.1 \times 10^6$).

Model helicopter rotor with generic ice shape(79,80,82)

A radio-controlled model helicopter was tested in the 7 x 10 ft subsonic wind tunnel at Texas A&M University. Extensive testing of the helicopter was performed in both the clean and generic ice configurations of the main rotor for hover and forward flight. Data relative to helicopter performance were gathered as a function of freestream velocity, fuselage angle of incidence, main rotor rpm, rotor collective pitch angle, and radial extent of ice.

The generic ice geometry chosen for this test is representative of a shape that resulted from a 3 min natural icing exposure of a Bell UH-1H helicopter main rotor, as previously discussed in the NACA 0012 experimental study. Natural ice roughness, because of its relative importance to the aerodynamic characteristics (83), was simulated on the generic ice shape using an aluminium oxide grit. It has been previously noted(84) that an iced surface roughness k/c of 0.001 is typical. Therefore, a grit size of 0.028 in. was chosen to provide the proper roughness diameter for this test.

This test program makes use of a commercially available radio-controlled model helicopter. The model helicopter has a two blade main rotor that incorporates an untwisted NACA 0012 airfoil section with a 2.5 in constant chord and 53.375 in diameter. The main rotor is powered by an internal combustion engine of approximately 1 hp. Four servomechanisms were installed in the model to control the main rotor rpm, collective, and cyclic pitch. In this series of tests, the collective pitch and rotor rpm were controlled remotely with the cyclic pitch fixed at 0° .

The model helicopter was mounted on the TAMU subsonic 7 x 10 ft wind tunnel six-component balance, which is capable of measuring forces about the three principal axes and moments about the main rotor hub. The centerline of the model was aligned and fixed with the wind axis. Two mountings secured the model, which consisted of one directly beneath the fuselage aligned with the main rotor hub, and the second on the model tail boom. The tail rotor of the helicopter was removed to eliminate the effect on the main rotor torque measurements.

The model helicopter test consisted of three phases with the identical test submatrix repeated for each phase. Tare measurements were initially taken of the model with the rotor blades removed since it was desired to ultimately investigate the performance of the main rotor alone. Tare measurements were made at velocities of 0 to 40 mph in 10 mph increments. Phase 1 then involved testing the helicopter in the clean or no-ice configuration, obtaining thrust and torque measurements as functions of several variables for both the hover and forward-flight conditions. In Phase 2, the generic ice shape was applied to the main rotor blades to the 85% radial location, and thrust and torque measurements were again made for both hover and forward flight. Simulated ice was finally applied to the 100% radial location of the blades in Phase 3, and, once again, thrust and torque measurements were taken.

Thrust and torque measurements have been made for the model helicopter in the iced and no-ice configuration for both hover ($\alpha=0^\circ$) and forward flight ($\alpha=11^\circ$) conditions. Fig. 19 shows the effects of the spanwise simulated ice accretion in hover for a collective pitch setting of +50. An increase of approximately 150% in torque coefficient is noted for a given thrust coefficient when simulated ice is applied to the main rotor 85% radial location. An additional increase of nearly 150% in torque coefficient may be seen when the generic ice is applied out to the rotor 100% radial station. Using the results of Fig. 19, the large increase in torque coefficient that occurs when the outer 15% of the rotor is iced can be shown as in Fig. 20 for a constant thrust coefficient and illustrated the performance sensitivity of the rotor-tip region to ice accretion. The apparent exponential decay in thrust coefficient in the rotor-tip region for a given torque coefficient seen in Fig. 21, again illustrates the sensitivity of the outer radii of the main rotor to the ice accretion process.

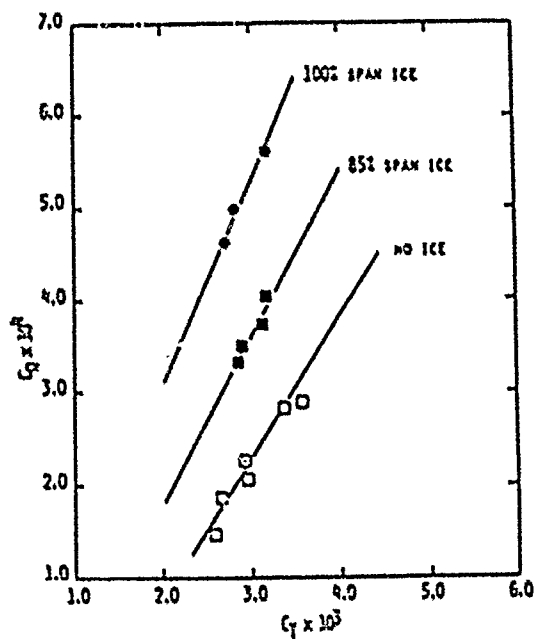


Figure 19. Variation of torque coefficient vs thrust coefficient for various spanwise additions of generic ice; hover condition ($\theta = 5^\circ$).

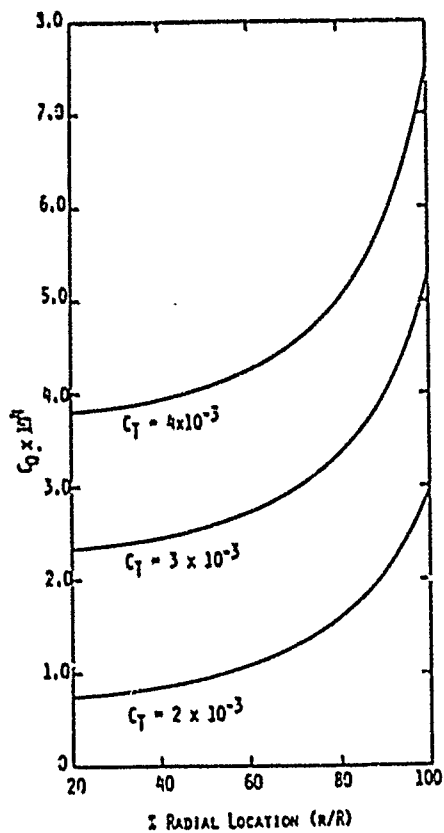


Figure 20. Increase in torque coefficient as a function of spanwise extent of ice accretion for a fixed thrust coefficient; hover condition ($\theta = 5^\circ$).

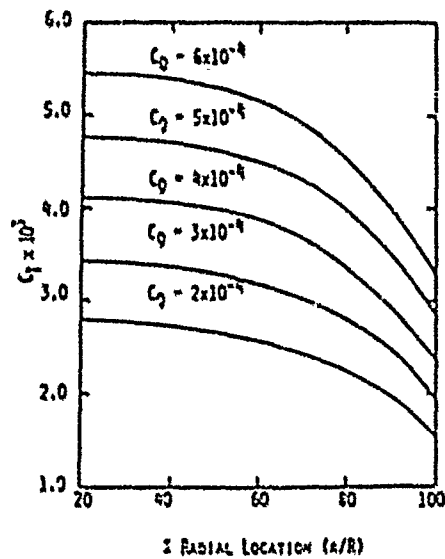


Figure 21. Decrease in thrust coefficient as a function of spanwise extent of ice accretion for a fixed torque coefficient; hover condition ($\delta = 5^\circ$).

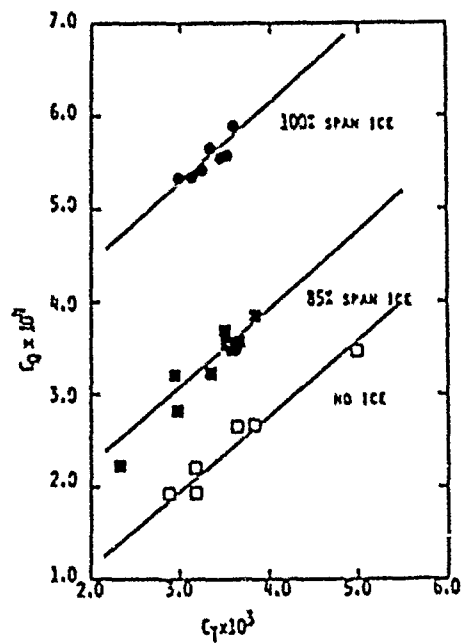


Figure 22. Variation of torque coefficient vs thrust coefficient for various spanwise additions of generic ice; forward flight condition ($\alpha = -11^\circ$, $\delta = 5^\circ$).

The forward-flight results also show considerable performance degradation due to the simulated ice accretion. Fig. 22 illustrates the increase in torque coefficient due to the spanwise ice addition for a given thrust coefficient at a collective pitch angle of $+5^\circ$. An increase of approximately 30% in torque coefficient is found going from the clean to the 85% simulated ice configuration, and a jump of approximately 175% occurs in the torque coefficient for the 100% ice condition over the clean configuration at a given thrust coefficient. This can be attributed to the extent of leading-edge separation and premature boundary-layer transition that is induced by the generic ice shape at the higher collective pitch angles.

For a given thrust coefficient, torque coefficient values are plotted as a function of spanwise icing extent as derived from the experimental data in Fig. 23 for a collective pitch of $+5^\circ$. Here again, as in the hover case, the increase in required torque coefficient is displayed. The sensitivity of the rotor-tip region is emphasized, e.g. for a given thrust coefficient of 3×10^{-3} , the required torque coefficient increases 150% when generic ice is applied to the 100% radial location. The sensitivity of the tip region appears to decrease as the thrust coefficient is increased. However, even at the highest thrust coefficient shown, an increase in torque coefficient of 100% results from the application of the ice shape to the 100% rotor radial location.

When a constant torque coefficient is maintained and thrust coefficient is plotted as a function of spanwise icing extent, Fig. 24 is obtained for a collective pitch of $+5^\circ$. The thrust coefficient is seen to decrease substantially as the generic ice is applied to the rotor 100% radial location. Once again, the severe performance degradation associated with icing to the rotor tip is emphasized. As in the previous Figure, tip sensitivity appears to decrease in terms of percentages with increasing torque coefficient, but considerable thrust degradation still exists for all torque coefficient values investigated. Similar results were obtained for pitch angles of $+1^\circ$ and 3° , with the decrease in thrust coefficient for a given torque coefficient becoming less severe with decreasing rotor collective pitch angle.

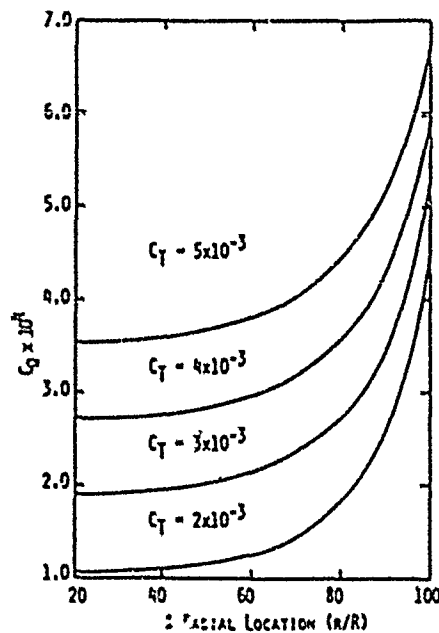


Figure 23. Increase in torque coefficient as a function of spanwise extent of ice accretion for a fixed thrust coefficient; forward flight ($\alpha = -11^\circ$, $\theta = 5^\circ$).

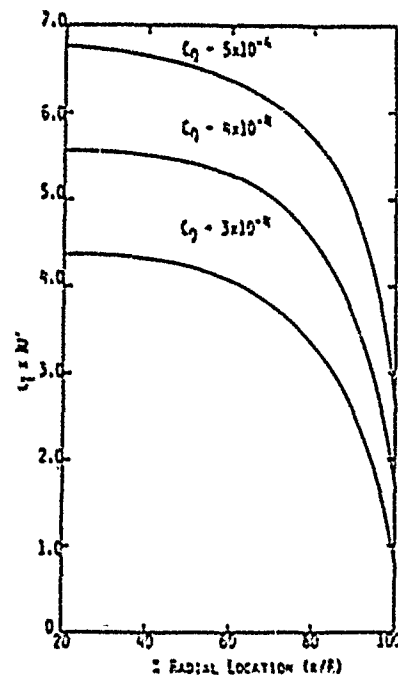


Figure 24. Decrease in thrust coefficient as a function of spanwise extent of ice accretion for a fixed torque coefficient; forward flight condition ($\alpha = -11^\circ$, $\theta = 5^\circ$).

In summary for this program, a model helicopter has been used to collect test data and provide an experimental means of studying helicopter performance in the 7 x 10 ft subsonic wind tunnel at Texas A&M University. The present study has demonstrated that use of a model helicopter is a viable means of procuring such test data. A simulated generic ice shape was attached to the rotor blades, first to the 85% rotor location and subsequently to the 100% radial location, and performance data were obtained for both hover and forward flight. These data illustrate significant degradation in helicopter performance with respect to torque and thrust coefficient when the simulated ice was applied to the rotor blades. The sensitivity of the rotor-tip region was also demonstrated by noting the considerable additional degradation that occurred when generic ice was applied to the rotor to the 100% radial location as compared with the 85% simulated ice performance values.

Recently, another study by Tinetti and Karkan(82) has been completed in which wind tunnel tests have also been conducted with the commercially available model helicopter described earlier to investigate the degradation in main rotor forward flight performance caused by generic ice adhesion. The effect of Reynolds number on the aerodynamic forces corresponding to conditions with and without generic ice formations attached to the leading edge were also investigated. This study utilized both primary and primary plus secondary generic ice shapes, which were tailored by radially according to the experimental data of Lee(37) and Abbott, et al. (38).

It was found in this study that in general, for high fuselage incidences, the presence of generic ice introduced a noticeable freestream and rotational velocity dependence (Fig. 25). It was also determined that the decrements in performance were caused by leading edge separation regions and increased surface roughness. For fully iced, i.e., primary plus secondary generic ice, the velocity influence upon lift to drag ratio, thrust coefficient, and torque coefficient apparently decreases with increments in blade pitch angle.

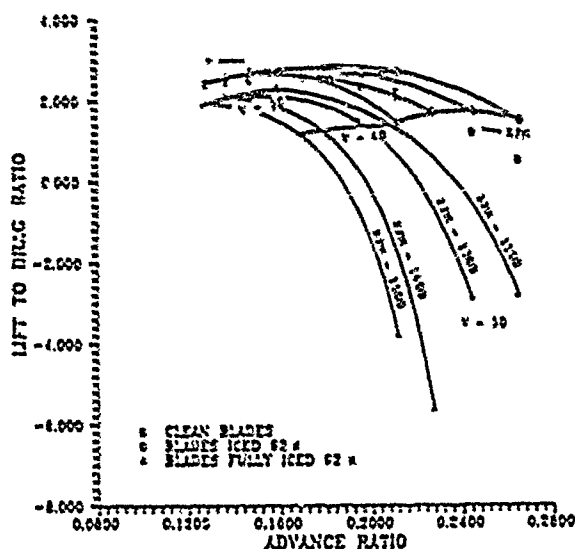


Figure 25. Lift to equivalent drag ratio. $\alpha = 11^\circ$, $0-5^\circ$

Aerodynamic characteristics are generally improved by decrements in fuselage angle of attack. For low collective settings, this improvement seems to reduce leading edge separation after the primary shape to the effect that performance is severely affected by increases in airfoil roughness. Incrementing blade collective angle yields better efficiency values, which are influenced by the presence of generic ice. However, this higher blade pitch introduces thrust and torque coefficient dependence upon velocity changes, as shown in Figs. 26, 27, and this dependence appears to be severe for clean conditions, i.e., no ice.

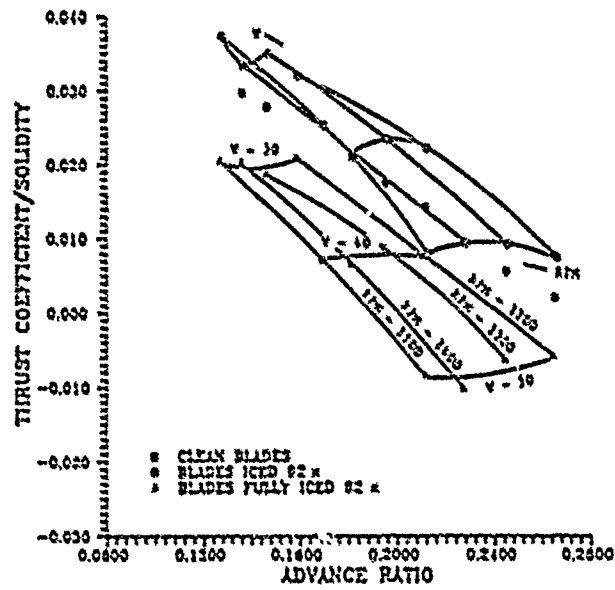


Figure 26. Thrust coefficient to solidity ratio. $\alpha=11^\circ$, $\theta=5^\circ$

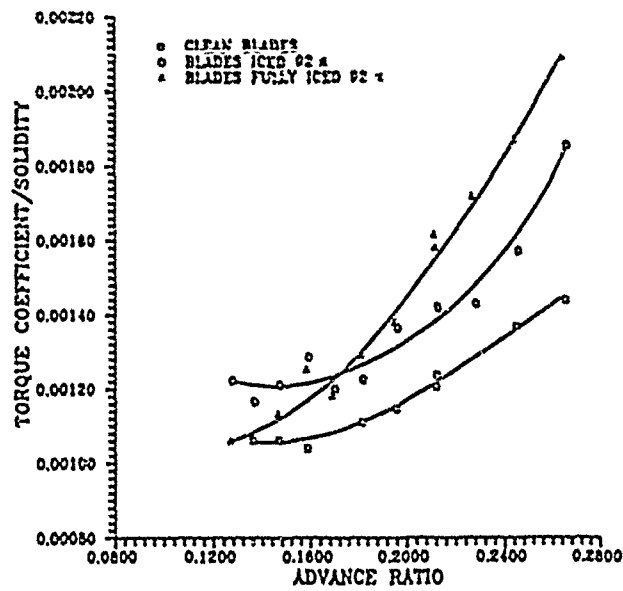


Figure 27. Torque coefficient to solidity ratio. $\alpha=11^\circ$, $\theta=5^\circ$

For all configurations tested, it was apparent that the presence of simulated secondary ice formations greatly affects the behavior of the parameters discussed in this investigation. Thus, the necessity of considering such formations in the overall performance degradation process is of paramount importance if generic ice testing is chosen over the more accurate, but more expensive methods of evaluating the effects of ice accretion on aircraft.

In addition to the expected changes in aerodynamic forces introduced by variations in test Reynolds number, forward flight data appear to be influenced by changes in freestream and rotational velocity (Fig. 28). The dependence of the data upon such velocity variations is apparently enhanced by increases in blade chord. Due to the possibility of atypical forces being exerted on the blades due to the high solidity ratio resulting from blade chord increments, any assessment of the effects upon performance introduced by intrinsically different Reynolds number may not be valid. However, it appears that the three parameters evaluated in the present investigation namely, lift to drag ratio, thrust coefficient to solidity ratio, and torque coefficient to solidity ratio are adversely affected by the increment in blade chord.

In this study(22), the authors have identified several areas for future investigation. To possibly avoid or reduce forward flight data dependence on freestream and rotational velocity, a rotor larger in diameter and blade chord could be tested. The proper increment in these two dimensions should be obtained from solidity ratios comparable to full scale values, and scaled to meet the requirements of the testing facilities. Flow similarity could also be achieved by matching the model helical tip Mach number to full scale values, a procedure commonly done. The test data obtained by testing such a configuration would be characterized by a more realistic behavior, and better suited for comparison.

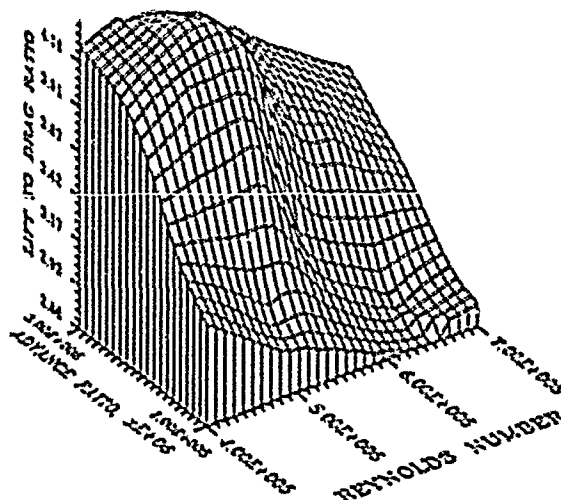


Figure 28. Reynolds number effects on lift to equivalent drag ratio. clean blades; $\alpha = 7^\circ$, $0-3^\circ$

NEAR-TERM/FAR-TERM REFINEMENTS OF CURRENT METHODOLOGY

Although the present analytical models does provide reasonable values of performance degradation for the complicated case of rotating systems such as propellers and helicopter rotor blades, the methodology requires refinement and further examination. This future work can be classified into near-term and far-term.

Near term

(a) Quantify cambering/decambering effects due to ice accretion at the leading edge of the airfoil with a resulting shift in the angle of attack for zero lift, and hence a change in the effective blade twist.

(b) Determine the effect of ice accretion on the moment coefficient as well as lift coefficient.

(c) Investigate an appropriate centrifugal/adhesion force model and its relation to the spanwise ice growth along the rotor blade.

(d) Assess the influence of kinetic heating on the spanwise ice growth along the rotor blade and its effect on the centrifugal/adhesion force model.

(e) Re-examine the drag coefficient correlation for rime, mixed, and glaze ice condition(s).

Far-term

(a) Establish a standardized helicopter rotor icing model to be used in conjunction with an existing performance rotor mechanical analysis.

(b) Investigate the degradation in the lift and moment stall boundaries due to the ice accretion process.

(c) Study the unsteady effects on airfoil performance under the influence of ice accretion.

(d) Determine the effect of ice accretion on the mode shapes, modal frequencies, and mass distributions of helicopter main rotor blades.

(e) Establish an airfoil design capability to minimize ice accretion penalties for both helicopter rotor and propeller systems.

Work has started and is continuing in several of these areas. As these new refinements become available, the current methodology will be enhanced and represent improved modelling of the ice accretion process for rotating systems.

SUMMARY

The methodology that has been developed to predict the performance degradation of rotating systems in natural icing conditions has been described and discussed. Theoretical studies of the performance degradation increments due to icing involving the propeller, helicopter in hover, helicopter in forward flight and XV-15 propulsion modes have been summarized. Experimental studies dealing with the NACA 0012 airfoil and model helicopter with/without generic ice shapes in support of these theoretical studies have also been summarized. In light of the results of these theoretical and experimental efforts, refinements to the current methodology have been suggested.

1. Petersen, A.A., Dadeka, L., and Olsen. "Rotorcraft Icing Research Requirements," AHS Preprint 81-39, 37th Annual Forum of the American Helicopter Society, May 1981.
2. Adams, R. "Aircraft Icing," NASA Conference Publication 2086, FAA-RD-76-109, July 1978.
3. Koenigsbach, L.P. "Commercial Aviation Icing Research Requirements," NASA CR-165336, April 1981.
4. Sand, W.R. "Aircraft Icing Conditions - Normal and Unusual," Paper presented at the Nineteenth JALC Air Law Symposium, 1983.
5. Canadale, J.T. "Helicopter Rotor Ice Accretion and Protection Research," Vertica, Vol. 5, pp. 357-368, 1981. Presented at the Sixth European Rotorcraft and Powered Lift Aircraft Forum, Bristol, England, 16-19 September 1980.
6. Bowden, D.Y., Consener, A.E., and Sheen, C.A. "Engineering Summary of Airframe Icing Technical Data," FAA ADS-4, December 1963.
7. Olsen, U. and Valkar, E. "Close Up Motion Pictures of the Icing Process," NASA Lewis Research Center, Photographic and Printing Branch, April 1983.
8. Hanaman, Jr., R.J. and Turnock, S.R. "Investigation of Surface Water Behavior During Glaze Ice Accretion," AIAA J. of Aircraft, Vol. 26, No. 2, February 1989, pp. 140-147.
9. Messinger, B.L. "Equilibrium Temperature of an Unheated Icing Surface as a Function of Airspeed," J. of the Aeronautical Sciences, Vol. 20, No. 1, January 1953, pp. 24-42.
10. Canadale, J.T. and Gent, R.W. "Ice Accretion on Aerofoils in Two-Dimensional Compressible Flow - A Theoretical Model," RAE TN 82128, January 1983.
11. Carson, H.W. and Haynard, J.D. "The Effect of Simulated Ice on Propeller Performance," NACA TN 1084, 1946.
12. Preston, C.M. and Blackman, C.D. "Effects of Ice Formations on Airplane Performance in Level Cruising Flight," NACA TN 1598, May 1948.
13. Neel, Jr., C.B. and Bright, G.L. "The Effect of Ice Formations on Propeller Performance," NACA TN 2212, October 1950.
14. Hayward, A.J., and Majj, A.G. "Deicing Tests on A.S.M. D8. Propeller at the National Research Council, Ottawa, Canada - Winter 1957-1958," Rotol Limited Development Dept. Report No. 073.1.103, 23 July 1958.
15. Gray, V.H. and von Glahn, U.H. "Effect of Ice and Frost Formations on Drag of NACA 65-212 Airfoil for Various Modes of Thermal Ice Protection," NACA TN 2762, June 1953.
16. Gray, V.H. and von Glahn, U.H. "Aerodynamic Effects Caused by Icing of an Unheated NACA 65A004 Airfoil," NACA TN 4155, February 1958.
17. Brun, R.J., Gallagher, H.M., and Vogt, D.E. "Impingement of Water Droplets on NACA 65-208 and 65-212 Airfoils at 4 Degree Angle of Attack," NACA TN 2932, May 1953.
18. Brun, R.J., Gallagher, H.M., and Vogt, D.E. "Impingement of Water Droplets on NACA 65A004 Airfoil and Effect of Change in Airfoil Thickness from 12 to 4 Percent at 4 Degree Angle of Attack," NACA TN 3047, November 1953.
19. Brun, R.J., Gallagher, H.M. and Vogt, D.E. "Impingement of Water Droplets on NACA 65A004 Airfoil at 8 Degree Angle of Attack," NACA TN 3155, July 1954.
20. Brun, R.J. and Vogt, D.E. "Impingement of Water Droplets on NACA 65A004 Airfoil at 0 Degree Angle of Attack," NACA TN 3386, November 1955.
21. Calder, T.F., Sayers, Jr., U.H., and von Glahn, U.H. "Experimental Droplet Impingement on Several Two-Dimensional Airfoils with Thickness Ratios of 6 to 16 Percent," NACA TN 3859, December 1956.
22. Bergrun, H.R. "An Empirical Method Permitting Rapid Determination of the Area, Rate, and Distribution of Water-Drop Impingement on an Airfoil of Arbitrary Section at Subsonic Speeds," NACA TN 2476, September 1951.
23. Lavis, V. and Bergrun, H.R. "A Probability Analysis of the Meteorological Factors Conducive to Aircraft Icing in the United States," NACA TN 2738, July 1952.

24. Gray, V.H., "Correlations Among Ice Measurements, Impingement Rates, Icing Conditions, and Drag Coefficients for Unheated NACA 63A004 Airfoil," NACA TN 4131, February 1958.
25. Gray, V.H., "Prediction of Aerodynamic Penalties Caused by Ice Formations on Various Airfoils," NACA TN-D 2166, February 1964.
26. Blaha, E.J., and Evanich, F.L., "Pneumatic Boot for Helicopter Rotor Deicing," Reprint from CP-2170, "1980 Aircraft Safety and Operating Problems," NASA Langley Research Center, Hampton, Virginia, 1-7 November 1980.
27. Wilson, G.U., "Helicopter Icing - Testing and Certification," J. of American Helicopter Society, Vol. 27, No. 2, pp. 66-72, 1962.
28. Dumval, G.U., "Electro-Impulse Deicing," Nineteenth JALC Air Law Symposium, 1985.
29. Dumval, G.U., Frischberg, R.A., and Schwartz, J.A., "Electro-Impulse De-Icing Research," DOT/TTA/CT-38/37, March 1989.
30. Ingelman-Sundberg, M., Trunov, O.K., and Ivaniko, A., "Methods for Prediction of the Influence of Ice on Aircraft Flying Characteristics," Swedish-Soviet Working Group on Flight Safety, Report No. JR-1, 1977.
31. Ingelman-Sundberg, M. and Trunov, O.K., "Wind Tunnel Investigation of the Hazardous Tail Stall Due to Icing," Swedish-Soviet Working Group on Flight Safety, Report No. JR-2, 1979.
32. Trunov, O.K. and Aaro, T., "A Study of Some Methods and Means for Protecting Aircraft Against Ground Icing," Swedish-Soviet Working Group on Flight Safety, Report No. JR-4, 1980.
33. Shaw, R.J., Sotes, R.G., and Salano, F.R., "An Experimental Study of Airfoil Icing Characteristics," NASA TM 82790, January 1982.
34. Bragg, M.B. and Gregorak, G.H., "Aerodynamic Characteristics of Airfoils with Ice Accretions," AIAA Paper No. 82-0282, January 1982.
35. Bragg, M.B., Zagull, R.J., and Gregorak, G.H., "Wind Tunnel Evaluation of Airfoil Performance Using Simulated Ice Shapes," NASA CR 167960, November 1982.
36. Fleming, R.J. and Ludwiger, D.A., "High Speed Ice Accretion on Rotorcraft Airfoils," AHS A-83-29-04-0000, May 1983.
37. Lee, J.D., "Aerodynamic Evaluation of a Helicopter Rotor Blade with Ice Accretion in Hover," AIAA Paper No. 84-0608, March 1984.
38. Abbott, W.Y., Belte, D., Williams, R.A., and Staller, F.U., "Evaluation of UH-1H Hover Performance Degradation Caused by Rotor Icing," USAAEFA Project No. 82-12, August 1983.
39. Falke, R.L., and Cassidy, P.L., "Photogrammetric Analysis of Ice Buildup on a U.S. Army UH-1H Helicopter Main Rotor in Hover Flight," AEDC-TR-83-43, October 1983.
40. Abbott, W.Y., Linchan, J.L., Lockwood, R.A., Todd, L.L., "Evaluation of UH-1H Level Flight Performance Degradation Caused by Rotor Icing," USAAEFA Project NO. 83-22, July 1984.
41. Foster, R.C. and Bartlett, C.S., "Influence of Droplet Sizing Uncertainty on Icing Test Results," Presented at the SAE AC-9C Meeting, April 1989.
42. Trunov, O.K. and Ingelman-Sundberg, M., "On the Problem of Horizontal Tail Stall Due to Ice," Swedish-Soviet Working Group on Flight Safety, Report No. JR-3, 1983.
43. Belte, D., "In-Flight Ice Accretion Characteristics of Rotor Blade Airfoil Sections," AIAA Paper No. 87-0176, January 1987.
44. Hansman, R.J., Kirby, M.S., McKnight, R.C., and Humes, R.L., "In-Flight Measurement of Ice Growth on an Airfoil Using an Array of Ultrasonic Transducers," AIAA Paper No. 87-0178, January 1987.
45. Bragg, M.B. and Khodadoust, A., "Experimental Measurements in a Large Separation Bubble Due to a Simulated Glaze Ice Accretion," AIAA Paper No. 88-0116, January 1988.
46. Ruff, G.A., "User's Manual for the NASA Lewis Ice Accretion Prediction Code (LEWICE)," Sverdrup Technology, Inc., September 1986.

47. Runyan, L.J., Zierlen, T.A., and Hill, E.C., "Flight and Wind Tunnel Investigation of Aerodynamic Effects of Aircraft Ground Deicing/Anti-icing Fluids," AICARD Symposium on "Flight in Adverse Environmental Conditions," Paper No. 24, Col, Norway, May 1989.
48. Miller, T.L. and Bird, T.M., "An icing Research Tunnel Test of a Model Helicopter Rotor," Paper presented to the American Helicopter Society 45th Annual Forum & Technology Display, May 1989.
49. Canba III, J., "Analytical Determination of Performance Degradation on a Helicopter Main Rotor Due to Ice Accretion," M. of Sc. Thesis, Texas A&M University, 1986.
50. Johnson, M.C., Britton, R.K., Petersen, A.A., and Korkan, K.D., "Analytical Determination and Experimental Comparison of Performance Degradation on a Helicopter Main Rotor Due to Ice Accretion," Paper presented to the American Helicopter Society 44th Annual Forum and Technology Display, June 1988.
51. Bragg, M.B., Gregorik, G.H., and Shaw, R.J., "An Analytical Approach to Airfoil Icing," AIAA Paper No. 81-0403, January 1981.
52. Bragg, M.B., "Rime Ice Accretion and Its Effect on Airfoil Performance," NASA CR 165599, March 1982.
53. Miller, T.L., Shaw, R.J., and Korkan, K.D., "Evaluation of Icing Drag Coefficient Correlations Applied to Iced Propeller Performance Prediction," SAE Paper No. 871033, April 1987.
54. Bragg, M.B., Private Communication, Aeronautical and Astronautical Research Laboratory, The Ohio State University, Columbus, Ohio, 1986.
55. Fleming, R.J., and Lednicer, D.A., "High Speed Ice Accretion on Rotocraft Airfoils," NASA CR 1910, August 1985.
56. Miller, T.L., Korkan, K.D., and Shaw, R.J., "Statistical Study of a Glaze Ice Drag Coefficient Correlation," SAE Paper No. 830753, April 1983.
57. Bragg, M.B., "Predicting Airfoil Performance with Rime and Glaze Ice Accretions," AIAA Paper No. 84-0106, January 1984.
58. Tribus, M.V., "Analysis of Heat Transfer Over a Small Cylinder in Icing Conditions," ASME Transactions, Vol. 70, 1949, pp. 871-876.
59. Gebeci, T., "The Calculation of Flow Over Iced Airfoils," AIAA Paper No. 88-0112, January 1988.
60. Korkan, K.D. and Britton, R.K., "On Ice Shape Prediction Methodologies and Comparison With Experimental Data," AIAA Paper No. 89-0732, 1989.
61. Wilder, R., "Techniques Used to Determine Artificial Ice Shapes and Ice Shedding Characteristics of Unprotected Airfoil Surfaces," Paper presented at the FAA Symposium on Aircraft Ice Protection, Washington, D.C., April 1969.
62. Mikkeleson, K., Juhasz, N., Manando, R., McKnight, R., Freedman, R., and Greising, J., "In-Flight Measurements of Wing Ice Shapes and Wing Section Drag Increases Caused by Natural Icing Conditions," NASA TM 87301, April 1986.
63. Scott, J.N., Glolda, T.F., and Hankey, N.L., "Navier-Stokes Solutions of Flow-field Characteristics Produced by Ice Accretion," AIAA Paper No. 88-0290, January 1988.
64. Pais, M.R. and Singh, S.N., "A Fourier Analysis Approach for Surface Definition and the Effect of Roughness on the Local Convective Heat-Transfer Coefficient as Related to Ice Accretion," AIAA Paper No. 88-0117, January 1988.
65. Heijer, S., "Computation of Rime Ice Accretion on Airfoils," The Aeronautical Research Institute of Sweden, FFA TN 1987-08, 1987.
66. Bilanin, A.J., "Proposed Modifications to Ice Accretion/Icing Scaling Theory," AIAA Paper No. 88-0203, January 1989.
67. Britton, R.K., "Elevator Deflection Effects on the Icing Process," AIAA Paper No. 89-0846, January 1989.

68. Korkan, K.D., Dadone, L., and Shaw, R.J., "Performance Degradation of Helicopters Due to Icing-A Review," *Vertica*, Vol. 10, No.1, pp. 1-23, 1986.
69. Shaw, R.J., "NASA's Aircraft Icing Analysis Program," NASA TM 88721, September 1986.
70. Weismann, J.J., Shaw, R.J., and Ramadori, R.J., "NASA's Program on Icing Research and Technology," NASA TM 101989, May 1989.
71. Adams, R.L., "Aircraft Icing Certification-In Perspective," AIAA 88-0204, January 1988.
72. Korkan, K.D., Dadone, L., and Shaw, R.J., "Performance Degradation of Propeller Systems Due to Rime Ice Accretion," AIAA J. of Aircraft, Vol. 21, No. 1, January 1984, pp. 44-49.
73. Cooper, J.F., "The Linearized Inflow Propeller Strip Analysis," WADC TR 56-615, March 1957.
74. Korkan, K.D., Dadone, L., and Shaw, R.J., "Helicopter Rotor Performance Degradation in Natural Icing Encounter," AIAA J. of Aircraft, Vol. 21, No. 1, January 1984, pp. 84-85.
75. Korkan, K.D., Dadone, L., and Shaw, R.J., "Performance Degradation of Helicopter Rotor Systems in Forward Flight Due to Rime Ice Accretion," AIAA Paper No. 83-0029, January 1983.
76. Korkan, K.D., Ramadori, J.C., Dadone, L., and Shaw, R.J., "Performance Evaluation of the XV-15 Tilt Rotor Aircraft in a Natural Icing Encounter," AIAA Paper No. 83-2534, October 1983.
77. Korkan, K.D., Cross, Jr., E.J., and Cornell, C.C., "Experimental Study of Performance Degradation of a Model Helicopter Main Rotor with Simulated Ice Shapes," AIAA Paper No. 84-0184, January 1984.
78. Korkan, K.D., Cross, Jr., E.J., and Cornell, C.C., "Experimental Aerodynamic Characteristics of a NACA 0012 Airfoil with Simulated Ice," AIAA J. of Aircraft, Vol. 22, No. 2, February 1985, pp. 130-134.
79. Korkan, K.D., Cross, Jr., E.J., and Miller, T.L., "Performance Degradation of a Model Helicopter Main Rotor in Hover and Forward Flight with a Generic Ice Shape," AIAA Paper No. 84-0609, March 1984.
80. Korkan, K.D., Cross, Jr., E.J., and Miller, T.L., "Performance Degradation of a Model Helicopter Rotor with a Generic Ice Shape," AIAA J. of Aircraft, Vol. 21, No. 10, October 1984, pp. 823-830.
81. Abbott, I.H., and Von Doenhoff, L.E., Theory of Wing Sections, Dover Publications, New York, 1959.
82. Tinetti, A.F. and Korkan, K.D., "Generic Icing Effects on Forward Flight Performance of a Model Helicopter Rotor," *Vertica*, Vol. 13, No. 1, pp. 63-85, 1989.
83. Brunby, R.E., "Wing Surface Roughness, Cause and Effect," DC Flight Approach, January 1979, pp. 2-7.

FLIGHT AND WIND TUNNEL INVESTIGATION OF AERODYNAMIC EFFECTS OF AIRCRAFT GROUND DEICING/ANTI-ICING FLUIDS

L. James Runyan*, Thomas A. Zienten**, and Eugene G. Hall†

*Senior Specialist Engineer

**Principal Engineer

†Manager

Boeing Commercial Airplanes
Configuration and Certification Group
Renton Division, Aerodynamics Staff
P.O. Box 3707
Seattle, Washington 98124
U.S.A.

SUMMARY

A flight and wind tunnel investigation of the effects of aircraft ground deicing/anti-icing fluids on the aerodynamic characteristics of a Boeing 737-200ADV airplane has been conducted. The flight test was performed in Kuopio, Finland, and the wind tunnel test was carried out in the NASA Lewis Research Center Icing Research Tunnel. Fluids tested in both flight and the wind tunnel include a newtonian deicing fluid and three nonnewtonian anti-icing fluids commercially available during or prior to 1988. Both the flight test results and the wind tunnel results show that fluids remain on the wing after liftoff and cause a measurable lift loss and drag increase. Eight newly developed nonnewtonian fluids, tested only in the wind tunnel, show significantly improved aerodynamic characteristics relative to the existing nonnewtonian fluids that were tested. Wind tunnel results also indicate that the fluid effects are configuration dependent. For a configuration with deflected leading edge high-lift devices, the fluid effect is largest at the maximum lift condition. For a configuration without leading edge high-lift devices, the fluid effect is very small at the maximum lift condition. It was also found that the fluid aerodynamic effects are related to the fluid surface roughness, particularly in the first 30% chord.

LIST OF SYMBOLS AND ABBREVIATIONS

ALPHAB	Angle of attack of body waterline
ALPHAW	Angle of attack of wing chord plane of 2D model
c	2D model chord length
\bar{c}	Mean aerodynamic chord of 3D half model
C_D	Airplane drag coefficient
C_{Df}	Skin friction coefficient
C_L	Airplane lift coefficient
$C_{L\alpha}$	Sectional lift coefficient
C_m	Sectional pitching moment coefficient
$C_{D\alpha}$	Drag coefficient in stability axes
$C_{L\alpha}$	Lift coefficient in stability axes
$C_{L\alpha\alpha}$	Sectional lift coefficient in stability axes
C_{PMQA25}	Pitching moment about quarter chord of MAC in stability axes
deg	Degrees
FWD	Forward
ft	Feet
h, H	Height
in	Inches
k	Average fluid wave height
keas	Equivalent airspeed in knots
kn	Knots
L	Length
m	Meters
mi/h	Miles per hour
min	Minutes
mm	Millimeters
P_t	Total pressure
sec	Seconds
T	Temperature
t	Time
V	Velocity
W	Width
X_{cp}	Center of pressure location
Y	Height above model surface
α	Angle of attack
2D	Two dimensional
3D	Three dimensional
Subscripts	
AERO	Indicates effects of thrust are not included
B	Body
c.g.	Center of gravity
MAX	Maximum
REF	Reference
SA	Stability axes
0	Initial value
1	Condition 1
2	Condition 2

1.0 INTRODUCTION

The aerodynamic effects of aircraft ground deicing/anti-icing fluids is a topic that has been receiving increasing attention in recent years as the use of these fluids becomes more widespread and sophisticated. Increased use of these fluids is a result of the need to maintain safety margins during adverse weather conditions. The presence of frost, ice, or snow on an airplane cannot be tolerated because of the resulting adverse aerodynamic effects. Use of newtonian deicing fluids ensures that none of these contaminants are on an aircraft at dispatch. These fluids offer protection from frost, ice, and snow for a relatively short time—typically about 15 min in steady snow. In many cases, however, exposure times prior to the beginning of the takeoff run can be much longer than this, particularly in adverse weather conditions. Nonnewtonian anti-icing fluids were designed by the fluid manufacturers, in cooperation with the airlines, to overcome this problem by providing protection for longer periods of time. These anti-icing fluids have been used extensively in Europe for many years, and their use is increasing in the United States. However, both the nonnewtonian anti-icing fluids and the newtonian deicing fluids can be highly viscous at low temperatures. As a result, there have been questions raised by airframe manufacturers and airlines about how completely the fluids flow off of the wing by liftoff and the magnitude of possible resulting adverse aerodynamic effects.

Boeing conducted a wind tunnel test on a small scale model in 1982 (Reference 1) to investigate the aerodynamic effects of anti-icing fluids. Since the test was conducted in an uncooled wind tunnel, the nonnewtonian anti-icing fluids were modified to have low-temperature viscosity characteristics at the warm tunnel temperatures. The results of that test indicated that the fluids may cause a measurable lift loss and drag increase. However, the modification of the fluids and the small model scale (0.24) decreased confidence in the validity of those results.

In 1984 the Association of European Airlines (AEA) undertook a followup to the Boeing investigation. Their objective was to test a larger scale model in a cold wind tunnel, which would allow the use of unmodified fluids. In a three-phase investigation that extended through 1987 (References 2, 3, and 4) they found that aircraft ground deicing/anti-icing fluids do cause measurable lift losses and drag increases. These tests were an important step forward in understanding the aerodynamic effects of fluids. However, they still did not overcome all of the drawbacks of the early Boeing tests. Although the model scale was much larger than in the Boeing test, it was still only 0.59, and it was a 2D model. This still left some question about scale effects and three-dimensional effects. Also, no data were obtained on the effect of the fluids on the maximum lift coefficient.

The objective of the present investigation was to overcome the drawbacks of these earlier tests. To minimize questions raised by scale effects, a flight test of fluid effects was conducted on a 737-200ADV airplane. In order to ensure that the test would be conducted in cold weather conditions and to allow the use of unmodified fluids, it was performed in Kuopio, Finland, during the month of January. The flight test results were then correlated with results subsequently obtained on a small-scale model in a cold wind tunnel. The wind tunnel program allowed a wider range of temperatures, configurations, data measurements, and fluid formulations than the flight test. It also allowed the effects of the fluids on the maximum lift coefficient to be determined. This paper presents the results of the flight test and the wind tunnel test. Included is a discussion of results from the wind tunnel that provide insight into the physical mechanisms behind the fluid aerodynamic effects.

2.0 FLIGHT TEST

The flight test was a joint effort of Boeing and the AEA, with assistance from three fluid manufacturers. The AEA provided the test airplane, gave technical assistance, and hosted the testing at the European test site. Boeing installed the instrumentation on the airplane, planned and conducted the flight test, and analyzed the data. The fluid manufacturers provided the fluids and transported them to the test site. The flight test was conducted from January 11 to January 20, 1988, at Kuopio, Finland.

2.1 TEST DESCRIPTION

The objective of the flight test was to determine the effects of ground deicing/anti-icing fluids on the aerodynamics of a large jet transport aircraft. In particular, data on the effects of the fluids on lift, drag, and handling characteristics were desired.

Two basic types of fluids were tested—newtonian deicing fluids and nonnewtonian anti-icing fluids. Newtonian deicing fluids have a high glycol content (minimum 80%) and a relatively low viscosity, except at very cold temperatures. The viscosity is a function of temperature only. These fluids provide limited protection against refreezing. Ethylene-glycol-based newtonian fluids are the principal type of fluid used in the United States. Nonnewtonian anti-icing fluids have a minimum glycol content of 50% with, typically, 45% to 50% water plus thickeners and inhibitors. They provide good protection against refreezing and are used extensively in Europe. Their use in the United States is increasing. They are highly viscous at low shear stress levels, and their viscosity decreases dramatically as shear stress increases.

The four specific fluids tested were provided by Hoechst AG, Kilfrost Ltd., and Union Carbide Corp. Fluid 1 was a nonethylene-glycol-based, AEA Type I, newtonian deicing fluid. Fluid 2 was a pre-1987 (obsolete) nonnewtonian anti-icing fluid. Fluids 3 and 4 were 1987 nonnewtonian anti-icing fluids. Fluid 3 was considered to be the "baseline" fluid for the test because, at the time of the test, it was representative of the most widely used nonnewtonian anti-icing fluids.

All fluids were dyed with a 0.005% concentration of Rhodamine 6G fluorescent dye by the fluid manufacturers. This improved fluid visibility and allowed the use of an ultraviolet photographic technique to measure fluid depth and roughness.

The fluids were applied to the wing and horizontal stabilizer upper surfaces using a two-step procedure, based on the AEA specification. The first step was to deice the surfaces using a hot 50/50 mixture of Fluid 1 and water. The second step was to apply the cold, undiluted fluid to be tested. Both steps were performed using the Finnair EFI 2000 deicing vehicle shown applying the fluid in Figure 1. The only exception to the two-step procedure was for the testing of Fluid 1, the deicing fluid. In that case, except for the first flight of the test series, for which it was necessary to deice the airplane, only a single application of cold 100% Fluid 1 was made.



Figure 1. Application of Anti-Icing Fluid

An onboard data system allowed all important airplane parameters to be recorded as a function of time, including gross weight, center of gravity, engine parameters (to compute thrust), velocity, and altitude. In addition, video and photographic records of fluid flow behavior were made, and fluid samples for defining rheological properties were taken. A new fluid film depth laser probe was developed specifically for this test to allow the fluid depth at specific locations on the wing to be determined as a function of time. However, a probe calibration problem limited the usefulness of these data. A complete description of the instrumentation is given in Reference 5.

The flight test airplane was a 737-200ADV. It was dry leased from Lufthansa Airlines, rental free on behalf of the AEA. Testing was performed using takeoff flap settings of Flaps 5, which has a sealed slot, and Flaps 15, which has a gapped slot. The thrust and weight of the airplane were varied in order to keep the time to liftoff and the liftoff velocity approximately constant for all takeoffs at a given flap setting. The exceptions to this were those flights in which the effect of these parameters was being studied.

A series of takeoffs was performed at each flap setting over a range of altitudes to establish lift curves in ground effect. Each takeoff defined a single point on the lift curve for a given fluid or for the dry baseline. This was done by rotating the airplane early to the desired altitude and then continuing to accelerate at that altitude through liftoff and initial climbout.

2.2 RESULTS

A typical set of lift curves is shown in Figure 2. The lift is clearly lower with the fluid on the wing than for the dry baseline, and the magnitude of the lift loss increases with increasing angle of attack. Note that the flagged symbols correspond to "normal" takeoffs (no early rotation).

Figure 3 summarizes the lift loss results for all of the fluids at a body altitude of 12 deg. This corresponds, approximately, to the one-engine-out takeoff safety speed condition. The airplane c.g. height for these data is 2.90m (9.5 ft), which corresponds to the condition when the tires have just cleared the runway. Due to abnormally warm weather conditions, no data were obtained at temperatures below about -10°C . The lift losses for the Flaps 5 configuration range from about 6% for Fluid 3 at $T = -10^{\circ}\text{C}$ to less than 2% for Fluid 4 at $T = -3^{\circ}\text{C}$. For the Flaps 15 configuration, the lift losses ran from about 7% for Fluid 2 at -10°C to about 2% for Fluid 4 at $T = -3^{\circ}\text{C}$. Based on the measurement uncertainty for gross weight, velocity, and angle of attack at liftoff, the estimated uncertainty in the effect of the fluid on lift is $\pm 1.5\%$.

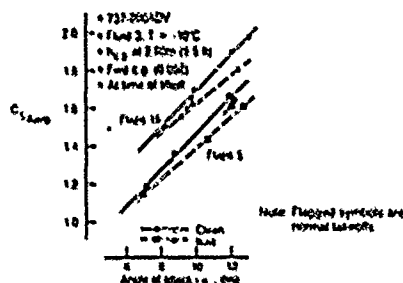


Figure 2. Typical Flight Test Lift Curves With and Without Fluid

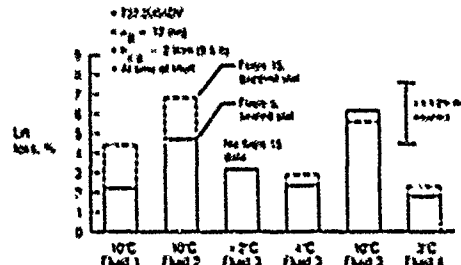


Figure 3. Flight Test Results for Effect of Fluids on Lift

A very limited assessment was made of the effect of variations in time to liftoff, speed at liftoff, and fluid exposure time. The results showed no measurable effect for any of these parameters. One flight was also made in which fluid was put on the left wing only. The pilot reported no noticeable effect of this fluid asymmetry on the handling characteristics of the airplane.

The effect of the fluids on the average takeoff acceleration drag during the ground run is shown in Figure 4 for the Flaps 5 configuration. The drag increase varies from about 24% for Fluid 2 at $T = -10^{\circ}\text{C}$ to about 4% for Fluid 1 at $T = -10^{\circ}\text{C}$.

An ultraviolet photographic technique was used in an attempt to obtain fluid depth and roughness data. The fluid was dyed with a 0.005% concentration of Rhodamine 6G, which is a fluorescent dye. A 60-mm Hasselblad camera was mounted on the vertical fin and focused on the 65% span region of the wing. Ultraviolet strobe lights located in cabin window cutouts at the wing root were synchronized with the camera to obtain photographs every 2 sec. In order to minimize ambient light interference, these flights were performed at night.

Figure 5 is a photograph of Fluid 3 at $T = -10^{\circ}\text{C}$ at 8 sec after brake release. Increased fluorescence corresponds to increased fluid depth. Fluid waves have just started moving aft and the fluid surface has become rough. Figure 6 is from the same flight, but just after liftoff. This photograph clearly shows a secondary wave moving aft from the wing leading edge. This secondary wave was observed on virtually all flights. It is hypothesized to be a result of the higher shearing stress that develops near the leading edge after rotation. This lowers the fluid viscosity and "scrubs" the remaining fluid from that area. The movement of the wing leading edge attachment line (the dividing line near the wing leading edge between flow over the upper surface and flow under the lower surface) toward the lower surface as the angle of attack increases is probably also a contributing factor to the secondary wave. Figure 6 also shows that the fluid is relatively thick in the locally low shearing stress region ahead of the flaps, and it is relatively thin in that portion of the forward region of the wing that has not yet been affected by the secondary wave.

2.3 FLIGHT TEST CONCLUSIONS

The primary conclusions that can be drawn from the 737-200ADV flight test results are as follows:

- 1) The fluids cause a measurable lift loss and drag increase.
- 2) In most cases, the lift loss is higher for the Flaps 15, gapped slot configuration than for the Flaps 5, sealed slot configuration.
- 3) The effect of the fluids on the handling qualities of the airplane is not noticeable to the pilots.
- 4) A secondary fluid wave flows back from the leading edge immediately after rotation.

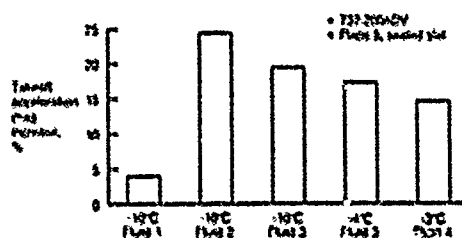


Figure 4. Flight Test Results for Effect Fluids on Average Takeoff Acceleration Drag

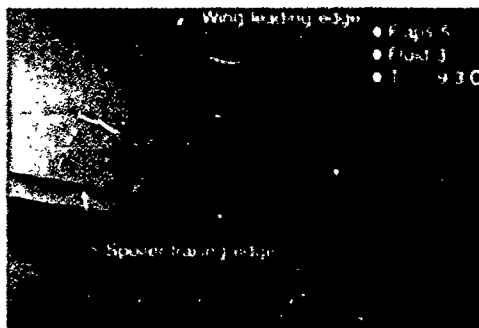


Figure 5. Photograph of Fluid 8 sec After Brake Release

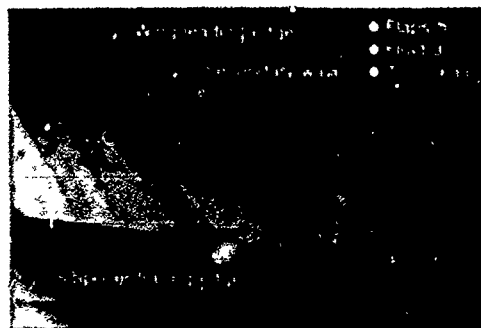


Figure 6. Photograph of Fluid 0.09 sec After Lift-off

3.0 WIND TUNNEL TEST

The wind tunnel test was conducted at the NASA Lewis Research Center Icing Research Tunnel (IRT) from April 4 through April 30, 1988. It was a joint Boeing/NASA/AEA effort, with assistance from four fluid manufacturers. Boeing planned and conducted the test, designed and built the models and installation hardware, analyzed the data, and documented the results. The NASA Lewis Research Center provided and operated the IRT, assisted in the tunnel modification and model installation, and monitored the test and data analysis. The AEA monitored the test to maintain continuity with the AEA deicing/anti-icing fluids study program. The fluids that were tested were provided by four fluid manufacturers—Hoechst AG, Kilfrost Ltd., SPCA, and Union Carbide Corp.

3.1 TEST DESCRIPTION

The wind tunnel test had five primary objectives:

- 1) Determination of the effect of the fluids on the maximum lift coefficient. This was one of the most important objectives. Maximum lift with fluids could not be investigated in flight because that would have required the airplane to be stalled near the ground.
- 2) Testing over a wider range of temperatures, high-lift configurations, and fluid formulations than was done in the flight test. This was made possible by controlled laboratory conditions and the lower cost of the wind tunnel test relative to the flight test.
- 3) Measurement of boundary layer data and fluid film roughness to achieve a better physical understanding of the lift loss mechanism.
- 4) Providing fluid manufacturers an opportunity to improve fluid technology through aerodynamic testing.
- 5) Contributing to a database for establishing aerodynamic acceptance standards for aircraft ground deicing/anti-icing fluids.

The NASA Lewis IRT layout is shown in Figure 7. It is a closed circuit, single return, continuous flow, closed throat tunnel with a test section size of 1.83m (6 ft) high by 2.74m (9 ft) wide by 6.10m (20 ft) long. The tunnel temperature can be varied from +27°C to -29°C. The test section turbulence level is approximately 0.5%. The maximum tunnel speed is 171 m/s (560 ft/s).

Both a 3D half model and a 2D model were tested. Figure 8 shows details of the 3D half model, which was a 0.091 scale model of the 737-200ADV. It was mounted on a splitter wall, which housed the turntable and force balance. Testing was conducted both with and without a ground plane.

Figure 9 shows details of the 2D model. The airfoil corresponded to that of the 65% span station of the 737-200ADV. The model scale was 0.18, and the chord was 0.457m (1.5 ft). Based on commonly accepted wind tunnel practices, the chord length was limited to one-quarter of the tunnel height. The model was mounted between two splitter walls, which housed the turntables and the force balances. Figure 10 shows the various 2D model configurations that were tested.

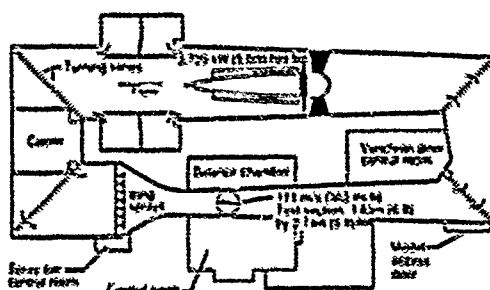


Figure 7. NASA Lewis Icing Research Tunnel

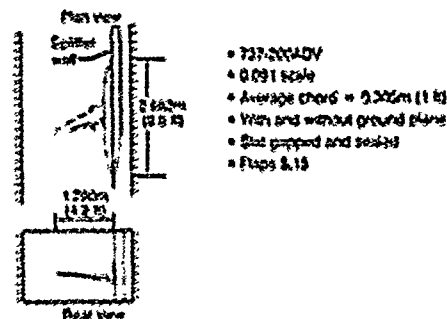


Figure 8. 3D Half Model

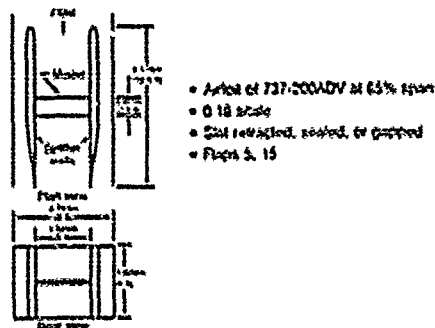


Figure 9. 2D Model

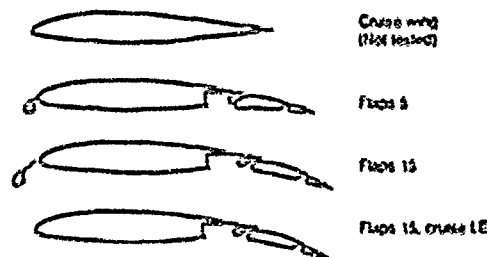


Figure 10. 2D Model Configurations

The four fluids tested in the flight test (Fluids 1, 2, 3, and 4) were also tested in the wind tunnel. Also included in the wind tunnel test were eight nonnewtonian "experimental" fluids developed by the four fluid manufacturers participating in the test. As was done in the flight test, all fluids were dyed with a 0.005% concentration of Rhodamine 6G fluorescent dye by the fluid manufacturers. This was done to improve fluid visibility and to allow the use of an ultraviolet photographic technique to measure fluid depth and roughness.

Data obtained in the test included the following:

- 1) Force data from internal balances
- 2) Fluid film depth (gap gauge measurement of initial depth and ultraviolet/fluorescent dye photography)
- 3) Video recordings of fluid flow characteristics
- 4) Boundary layer total pressure profiles (selected 2D model configurations only)
- 5) Wing surface static pressures (30 upper, 10 lower, 2D model only)

The data system provided online plots within about 10 min of the completion of the run. Final plots were available within an hour. The heart of the data acquisition system was an HP9845 computer, which sampled each of the 28 input channels four times per second. The output from the HP9845 was fed directly into a DEC MicroVAX minicomputer for immediate data analysis. Output was then plotted on a laser printer. A typical online data plot is shown in Figure 11.

The basic test procedures were as follows:

- 1) Wipe the wing clean with dry rags.
- 2) Wipe on a thin film of 50/50 water/Fluid 1 mixture.
- 3) Pour the fluid to be tested on the wing.
- 4) Use a fluid scraper to get the desired depth (usually 0.5 mm).
- 5) Operate the tunnel at idle speed of 6 m/s (12 kias) for 5 min.
- 6) Linearly increase the tunnel speed to 69 m/s (135 kias) in 30 sec.
- 7) At $t = 25$ sec, rotate the model from 0 degrees to the desired attitude at 3 deg/s.
- 8) Continue operating the tunnel for 30 sec past end of rotation.

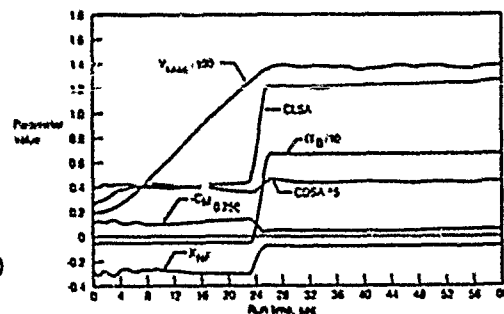


Figure 11. Typical Online Data Plot

Because of the characteristics of the tunnel motor control system, the tunnel speed first increased from the idle speed of about 6 m/s (12 kias) to a speed of about 12 m/s (24 kias), where it remained for several seconds. The subsequent tunnel flow acceleration to 60 m/s (135 kias) continued for approximately the next 25 seconds, as shown in Figure 11. This tunnel flow acceleration (neglecting the initial acceleration to 12 m/s (24 kias)) matched the airplane flight test ground roll acceleration very well.

3.2 3D HALF MODEL RESULTS

A typical set of three-component data for the 3D half model is shown in Figure 12. This figure shows lift coefficient versus 1) body angle of attack, 2) drag coefficient, and 3) pitching moment coefficient. There are four dry baseline runs and a single fluid run shown. The effects of the fluid are clearly evident.

Figure 12. Typical Three-Component Data for 3D Half Model

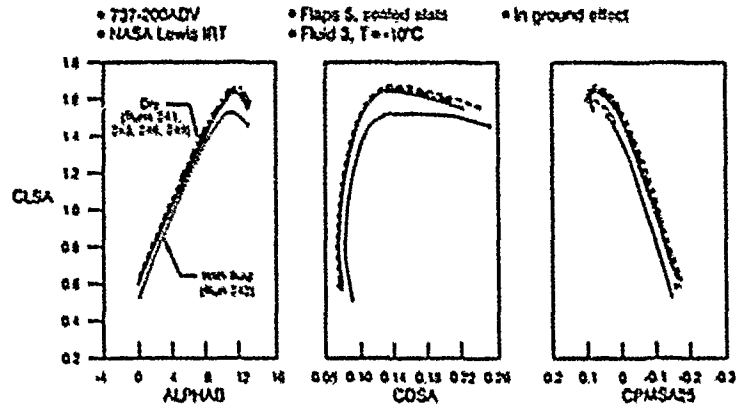


Figure 13 shows a summary of the lift losses due to the fluids. In most cases, the loss is higher at $C_{L_{max}}$ than at $\alpha = 7$ deg. This was one of the most important results of the wind tunnel test, since data at $C_{L_{max}}$ could not be obtained in the flight test. The lift loss, in most cases, increases as the temperature decreases. The losses are significantly higher for the Flaps 15, gapped slat configuration than for the Flaps 5, sealed slat configuration. This increased lift loss is believed to result, in part, from a larger secondary fluid wave that moves back from the leading edge after rotation than is present on the Flaps 5, sealed slat configuration. Data accuracy is estimated to be about $\pm 1\%$, based on the observed repeatability of the dry wing and the "with fluid" data.

A comparison of the lift losses for the Flaps 5 configuration with those from the flight test is shown in Figure 14. The flight test results are shown for a body attitude of 12 deg. This corresponds, approximately, to the one-engine inoperative takeoff safety speed condition and is about 75% of $C_{L_{max}}$. The wind tunnel results are shown for a body attitude of 7 deg, which results in a lift coefficient which is also about 75% of $C_{L_{max}}$. Because of the large Reynolds number difference between flight and wind tunnel, it is believed that this approach gives a better match of the boundary layer condition than a comparison at the same angle of attack. The agreement between wind tunnel and flight data is within the estimated accuracy of the data for all cases except Fluid 2 and is sufficient to lend credence to the direct use of the wind tunnel results, in spite of the small model scale. The agreement with the flight test data for the Flaps 15 configuration (not shown) is similar to that of the Flaps 5 configuration.

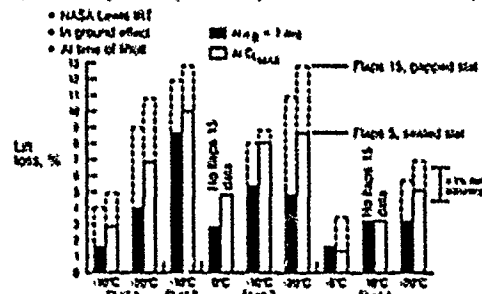


Figure 13. 3D Half Model, Lift Loss Due to Fluids

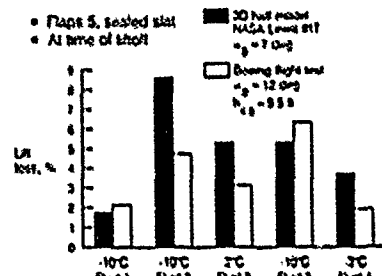


Figure 14. Comparison of 3D Half Model Lift Loss With Flight Test Results

The drag increase due to the fluids 15 sec after the start of tunnel acceleration is shown in Figure 15. This time corresponds, approximately, to the time during the airplane ground roll at which the average takeoff acceleration drag occurs. It is interesting to note that the fluids that have the lowest lift loss at the takeoff safety speed condition, as shown previously in Figure 13, do not necessarily have the lowest takeoff acceleration drag increase. In particular, for the Flaps 5 configuration, Fluid 4 results in a larger takeoff acceleration drag increase than Fluid 3 at $T = -20^\circ\text{C}$ even though it results in a much smaller lift loss at the takeoff safety speed condition. This is probably a result of the early rough surface developed by Fluid 4, which increases the shearing stress acting on the fluid. This makes the fluid flow off more quickly, resulting in a cleaner wing and a relatively low lift loss at the takeoff safety speed condition.

The drag increase due to the fluids at the takeoff safety speed condition is shown in Figure 16. For most cases, the drag increases are larger for the Flaps 15 configuration than for the Flaps 5 configuration.

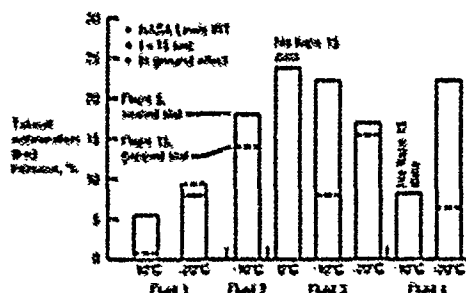


Figure 15. 3D Half Model Takeoff Drag Increase Due to Fluids

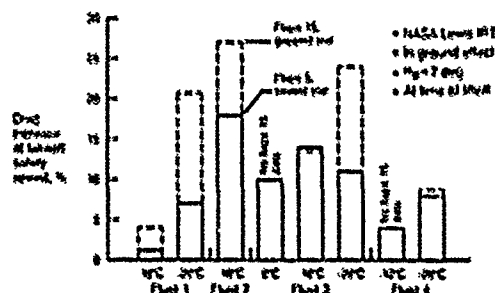


Figure 16. 3D Half Model Drag Increase at Takeoff Safety Speed Due to Fluids

Figure 17 shows the drag increase due to the fluids at the start of the second segment climb (gear up height), which occurs at about 10 sec after liftoff. A comparison with Figure 16 shows that the drag has already dropped significantly from that at the time of liftoff. This powerful effect of time after liftoff (time after the end of rotation) on the drag increase due to the fluid is shown in Figure 18. After one minute, the drag increase for both flap configurations has dropped to about 10% of its initial value after liftoff.

Although not shown, it was also found that the fluids decrease the magnitude of the pitching moment about the quarter-chord location of the mean aerodynamic chord relative to that of the dry wing. That is, if the dry wing pitching moment is negative, the fluid increment is positive; if the dry wing pitching moment is positive, the fluid increment is negative. This indicates that the pitching moment is being affected primarily by the loss in lift, rather than a change in the distribution of the lift.

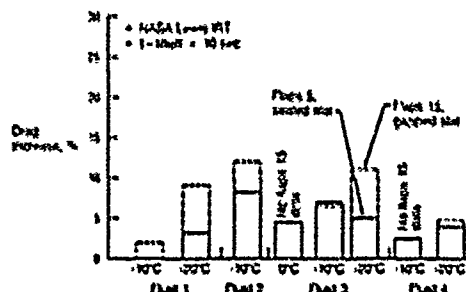


Figure 17. 3D Half Model Drag Increase Due to Fluids at Start of Second Segment

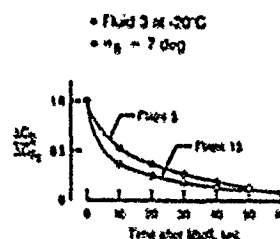
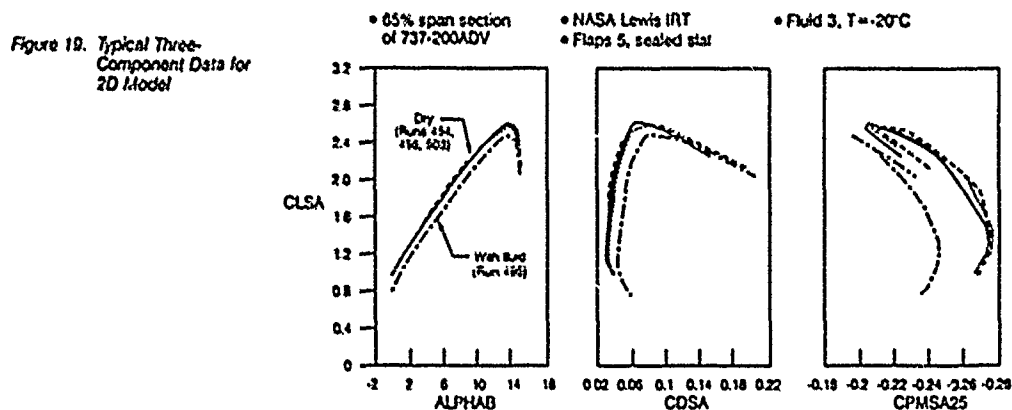


Figure 18. 3D Half Model Drag Increase Versus Time Due to Fluid

3.3 2D MODEL RESULTS

A typical set of three-component data for the 2D model is shown in Figure 19. There are three dry baseline runs and a single fluid run shown. Again, the effects of the fluid are clearly evident.



A summary of the lift losses due to the fluids for the Flaps 5, sealed slot configuration is shown in Figure 20. The accuracy of these data is estimated to be $\pm 1\%$, based on the observed repeatability of the dry wing and "with fluid" data. The data are shown at 8 deg and at $C_{L_{max}}$. An angle of attack of 8 deg represents the takeoff safety speed condition for the 2D model, corresponding to about 75% of $C_{L_{max}}$. Note that for the 2D model the angle of attack of the wing chord plane is used, while for the 3D model the angle of attack of a body water line is used. On the 737-200ADV, the wing chord plane incidence is 1 deg relative to a body water line.

The results shown in Figure 20 indicate that, in many cases, the lift loss at $C_{L_{max}}$ is lower than the lift loss at 8 deg. This indicates the importance of three-dimensional effects on $C_{L_{max}}$ since the 3D half model results had higher lift losses at $C_{L_{max}}$ than at 7 deg for almost all cases. It is also interesting to note that, at a temperature of -20°C , the lift loss for Fluid 1, which is a newtonian fluid, is about 13% at $C_{L_{max}}$. This is significantly higher than the corresponding 9% lift loss due to Fluid 3, which is a nonnewtonian fluid. At warmer temperatures, Fluid 1 has lower lift losses than Fluid 3.

There is no reason to expect agreement in the absolute level of lift losses on the two models, since the 2D model is representative of only the outboard portion of the 3D half model. However, in comparing the two sets of data, it was found that there is an empirical factor that can be applied to the 2D data at a given condition that gives agreement within 2% of the 3D half model lift loss values for all of the fluids. This is shown in Figure 21 at the maximum lift condition. Since the estimated data accuracy is $\pm 1\%$ for both models, these results indicate very good agreement between the two cases. This indicates that results on the 2D model can be used to estimate not only trends, but also absolute levels on the 3D half model, for this particular airplane. This good correlation is probably a result of the fact that the 2D model airfoil is based on the critical wing section for stall, which is the section that dominates wing behavior at $C_{L_{max}}$.

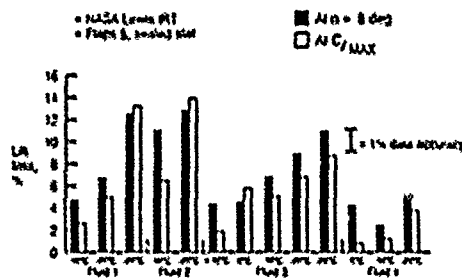


Figure 20. 2D Model Lift Loss Due to Fluids

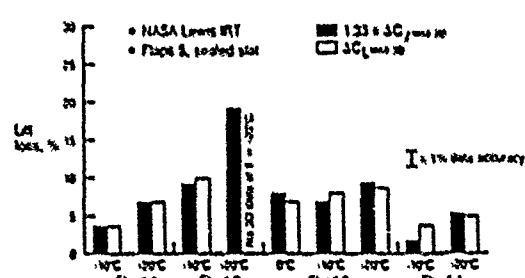


Figure 21. Comparison of 2D Model and 3D Model Lift Loss at Maximum Lift

One of the most important results of the test was the significant reduction in lift loss for the newly-developed "experimental" fluids, as compared to the baseline 1987 nonnewtonian fluid, Fluid 3. The experimental fluids were tested only on the 2D model, and only on the Flaps 5, sealed slot configuration. The lift loss results at a temperature of -20°C are shown in Figure 22. The lift losses for Fluid 1 and Fluid 3 are also shown for comparison. It is important to remember that these uncorrected 2D model results are only meaningful for relative (fluid-to-fluid and temperature-to-temperature), not absolute, lift losses. The results show that the lift loss varies from fluid to fluid. However, in most cases, the experimental fluids have lift losses that are about 40% lower than that of Fluid 3. This is true both at 0 deg and at $C_{L_{max}}$.

The effect of temperature on the lift losses of four of the experimental fluids at $C_{L_{max}}$ is shown in Figure 23. Note that at a temperature of 0°C the lift loss at $C_{L_{max}}$ for Fluids 3, 1, 4, 1, and 5, 1 is negligible; whereas, for Fluid 3 it is about 6%.

The average takeoff acceleration drag is shown for Flaps 5 in Figure 24 for all twelve of the fluids tested at $T = -20^{\circ}\text{C}$. It varies from a low of 26% for several of the experimental fluids to a high of over 60% for Fluid 2.

The drag increase for Flaps 5 at the takeoff safety speed condition for all twelve of the fluids tested is shown in Figure 25 at $T = -20^{\circ}\text{C}$. Note that at this condition, all of the experimental fluids show lower drag increases than Fluid 3.

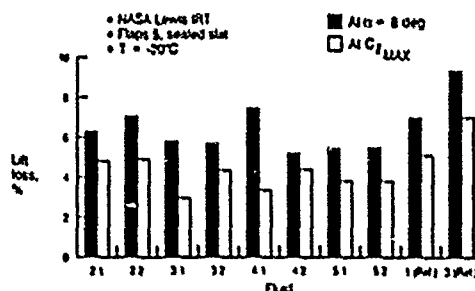


Figure 22. 2D Model Lift Loss Due to Experimental Fluids

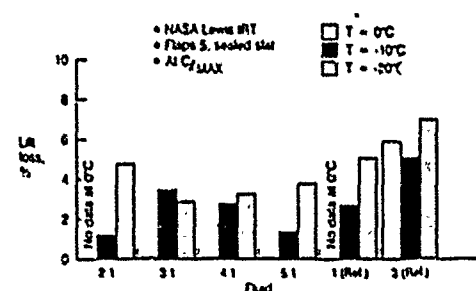


Figure 23. Effect of Temperature on Lift Loss Due to Experimental Fluids on 2D Model

A number of runs were made with Fluid 3 on a Flaps 15, cruise leading edge configuration to investigate the effect of the fluid on an aircraft not equipped with leading edge high-lift devices. For these runs, the tunnel flow velocity increased from 12 m/s (22 kts) to 46 m/s (80 kts) in about 22 sec, with rotation at 18 sec at a speed of about 41 m/s (80 kts). This modified procedure was used in order to be representative of commuter-type aircraft takeoff speeds. The lift loss results are shown in Figure 26. For this configuration, the takeoff safety speed condition (75% of $C_{L_{max}}$) corresponds to an angle of attack of 2 deg. The lift loss at this condition is much larger than that at $C_{L_{max}}$. The small effect on maximum lift may be due to the large velocities that occur at the wing leading edge without the slat. The resulting high shearing stresses and reduced viscosity of the nonnewtonian fluids result in a wing leading edge with less fluid residue than that for a configuration with a deflected slat, and there is no noticeable secondary wave.

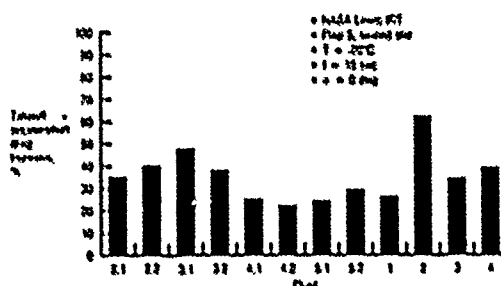


Figure 24. 2D Model Takeoff Acceleration Drag Increase Due to Fluids

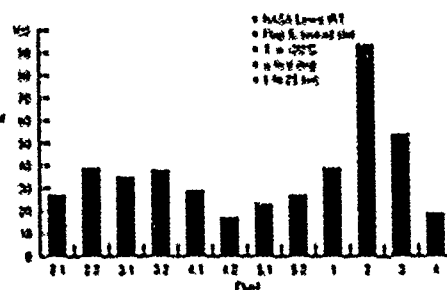


Figure 25. 2D Model Drag Increase at Takeoff Safety Speed Due to Fluids

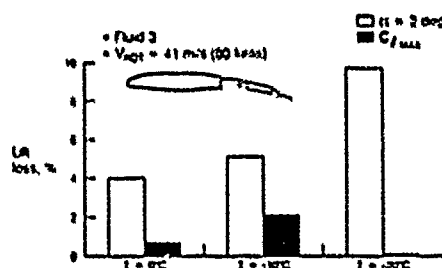


Figure 26. Lift Loss Due to Fluid for 2D Model With Cruise Leading Edge

3.4 PHYSICAL MECHANISMS OF FLUID AERODYNAMIC EFFECTS

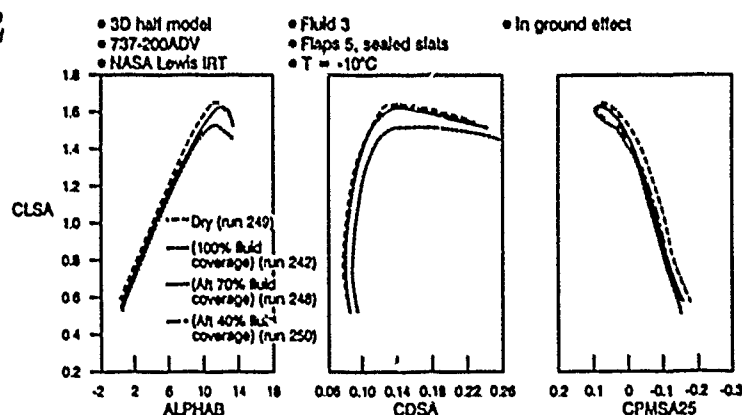
One of the objectives of the wind tunnel test was to investigate the physical mechanisms that cause the fluid aerodynamic effects. Boundary layer measurements were made and fluid surface roughness was determined to help achieve this objective.

3.4.1 Effect of Fluid Coverage

In order to investigate the relative importance of fluid chordwise location, two runs were made in which no fluid was applied forward of a specified chord location. The results, shown in Figure 27, indicate that fluid lift loss at C_{Lmax} is greatly reduced if fluid is applied only to the aft 70% of the chord. There is very little additional reduction in lift loss if only the aft 40% is covered. The effect on drag also depends strongly on whether or not fluid is present in the first 30% chord. The critical nature of the leading edge area may be due to the very thin boundary layer in that area and the resulting higher ratio of fluid wave height to boundary layer thickness.

Solid roughness of varying chordwise coverage was also investigated in this test. The results showed the same important effect of the roughness in the first 30% of the chord.

Figure 27. Effect of Chordwise Coverage on Fluid Aerodynamic Effects



3.4.2 Fluid Surface Waves and Roughness

The ultraviolet photographic technique used in the flight test was also used in the wind tunnel to record fluid depth and fluid surface wave height. Photographs were taken every 2 sec of the Rhodamine 6G-dyed fluid during each run. A calibration plate having grooves of various depths was filled with fluid and photographed prior to each run. After the test, a scanning microdensitometer was used to analyze the photograph negatives. This allowed fluid depth as a function of chordwise location to be determined. Figure 28 shows typical results for Fluid 3 on the 2D model at three times during the tunnel acceleration.

In order to be able to characterize the fluid roughness in each case by a single number, the mean height of the waves in the region from 50% to 55% chord was determined from the ultraviolet photo technique data. This location was chosen as being representative of a typical wave height. As discussed earlier, the first 30% of the chord appears to be the most important region in determining the fluid effects. However, the fluid wave heights in this region were very close to the noise level of the measurement technique, which was estimated to be about ± 0.1 mm. Thus, the more aft location was chosen for characterizing the roughness. This average roughness was normalized by the chord of the model and correlated with the drag increase at an angle of attack of 8 degrees. The results, shown in Figure 29, indicate a definite trend of increasing drag increment with increasing fluid roughness. The curve corresponds to the solid roughness skin friction drag increase, from an arbitrarily chosen base value corresponding to a k/s of 0.0001, for a fully rough surface (Reference 6). The reasonably good fit of the fluid data by this curve is an indication that fluid aerodynamic effects vary with fluid roughness height in a manner similar to the variation of aerodynamic effects with solid roughness size.

Figure 28. Fluid Depth Profiles and Wave Patterns

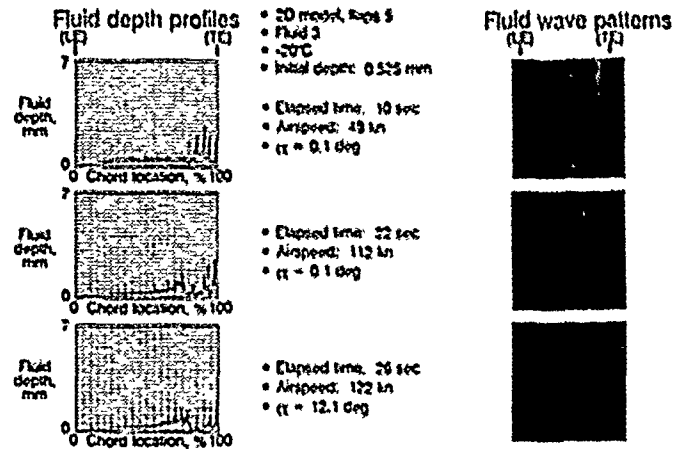
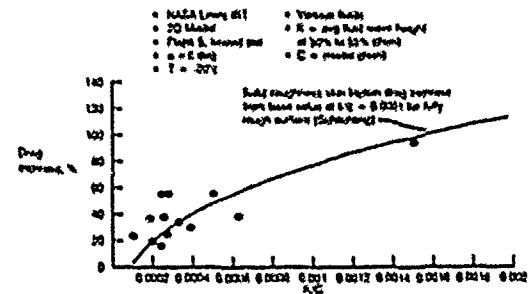


Figure 29. Correlation Between Drag Increase Due to Fluid and Fluid Roughness



3.4.3 Boundary Layer Data

A boundary layer rake was mounted on the 2D model just forward of the trailing edge flaps. The rake had 10 total pressure probes ranging from a height of 0.51 mm (0.02 in) to 40.64 mm (1.60 in) above the model surface. Total pressure profiles were measured for each of the four basic fluids and for the dry wing, as shown in Figure 30. The profiles measured with fluid on the wing do not extend below a height of 5.08 mm (0.2 in) above the model surface because fluid clogged the two probes below this height. The effect of the fluids on the profiles is very clear. This effect includes not only the effect of the fluid roughness on the boundary layer, but also the displacement effect of the fluid itself. As shown in Figure 31, there is fair correlation between the lift loss due to a given fluid and the height above the model surface at which the total pressure is 99% of the reference freestream value.

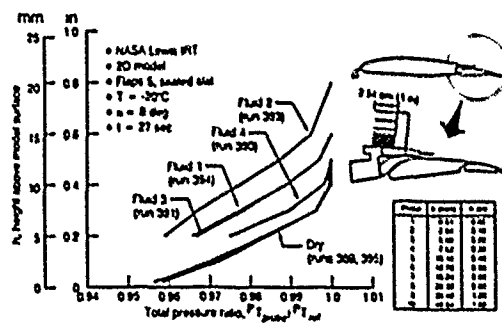


Figure 30. Boundary Layer Rake Data

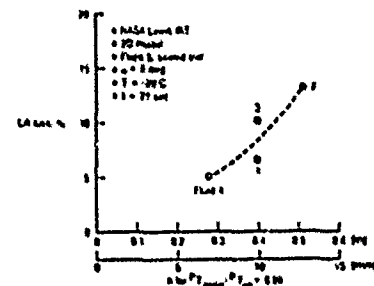


Figure 31. Correlation Between Lift Loss Due to Fluid and Height at Which $P_t/P_{t_\infty} = 0.99$

3.4.4 Physical Mechanism Hypothesis

Based on the fluid roughness data and the boundary layer measurements, the following physical mechanism for the fluid aerodynamic effects is hypothesized. The fluid surface roughness thickens the boundary layer in a manner similar to solid roughness. The fluid in the first 30% of the chord is the most important because the boundary layer is thinnest in this area. The thickened boundary layer (on the upper surface only), plus the effect of the fluid thickness itself, results in an effective decambering of the airfoil. This results in reduced lift at angles of attack below stall. At $C_{L_{max}}$, lift is further reduced because the energy loss suffered by the boundary layer (part of which is due to the energy required to move the fluid off of the wing) makes it less able to withstand adverse pressure gradients, resulting in earlier separation. The increased drag with fluid on the wing is a result of the increased extraction of energy from the flow caused by the rough fluid surface.

3.5 Wind Tunnel Test Conclusions

The most important conclusions that can be drawn from the results of the wind tunnel test are as follows:

- 1) The fluids cause a measurable lift loss and drag increase.
- 2) On the 3D half model, the lift loss at $C_{L_{max}}$ is larger than at the lower angle of attack conditions.
- 3) The lift loss on the 3D half model shows fair agreement with the flight test results.
- 4) The lift losses of the new experimental fluids are significantly lower than that of Fluid 3 and are comparable with that of the newtonian fluid, Fluid 1.
- 5) The lift loss is larger with a gapped slat than with a sealed slat.
- 6) At temperatures of -20°C , the lift losses due to the newtonian fluid, Fluid 1, are larger than those of Fluid 3.
- 7) Fluid lift loss at $C_{L_{max}}$ is greatly reduced for a configuration without a leading edge slat.
- 8) Fluid surface roughness appears to be a key factor in determining the magnitude of the fluid aerodynamic effects. In particular, the fluid roughness in the forward 30% of the chord has a large influence on the lift loss at $C_{L_{max}}$.
- 9) A secondary fluid wave flows aft from the leading edge region immediately after rotation. It appears to be caused by the scrubbing action of the increased shearing stress occurring in the leading edge region after rotation.
- 10) Fluid aerodynamic effects appear to scale with roughness height in a manner similar to that of solid roughness.

4.0 CONCLUDING REMARKS

Although additional work remains to be done, the present investigation has significantly improved our understanding of the aerodynamic effects of aircraft ground deicing and anti-icing fluids. The most significant finding is that the newly developed nonnewtonian anti-icing fluids have significantly smaller effects on aerodynamic characteristics than the previous generations of nonnewtonian anti-icing fluids. Four of these fluids are now commercially available. They provide airlines the benefit of the extended protection times offered by nonnewtonian anti-icing fluids without any larger aerodynamic effects than would result from a typical newtonian deicing fluid. This should result in increased use of these fluids and an attendant increase in airline safety. This investigation has also helped our understanding of the physical mechanism of the fluid effects by demonstrating the importance of the first 30% of the chord, the existence of the secondary fluid wave that replenishes the fluid in that region at rotation, and the important effect of fluid surface roughness. It is hoped that this improved understanding may ultimately be beneficial in the development of even better fluids.

REFERENCES

1. George S. Hendrickson and Eugene G. Hill, Effects of Aircraft De-/Anti-icing Fluids on Airfoil Characteristics, Paper presented at the von Karman Institute for Fluid Dynamics Lecture Series entitled "Influence of Environmental Factors on Aircraft Performance," February 16-19, 1987, Brussels, Belgium.
2. M. Carbonaro, Experimental Study of the Flow of a Film of Aircraft Deicing Fluid During A simulated Take Off at Subfreezing Temperature, von Karman Institute for Fluid Dynamics Report CR 1985-02, May 1985.
3. M. Carbonaro, Experimental Study of the Aerodynamic Characteristics of a Two-Dimensional Wing Model Covered with De-/Anti-icing Fluid During A simulated Take Off at Subfreezing Temperature, von Karman Institute for Fluid Dynamics Report CR 1986-22, August 1986.
4. M. Carbonaro, Further Study of the Aerodynamic Performance of a 2-D Wing Model Covered with Simulated Frost or with De-/Anti-icing Fluid During A simulated Take Off at Subfreezing Temperature, von Karman Institute for Fluid Dynamics Report CR 1987-29/AR, July 1987.
5. D. L. Cruise and T. A. Zierlein, Boeing/Association of European Airlines(AEA) Evaluation of the Aerodynamic Effects of Aircraft Ground De-/Anti-icing Fluids, Paper presented at the Society of Flight Test Engineers Nineteenth Annual Symposium, August 14-18, 1988, Arlington, Texas, U.S.A.
6. H. Schlichting, Boundary-Layer Theory, 4th Edition, 1960, McGraw-Hill, New York, p. 553.

ACKNOWLEDGMENTS

Valuable contributions to the work that made this paper possible were made by the following individuals: Philip V. Araujo, Michael J. Fong, Robert D. Freeland, David S. Mora, Timothy Siebersma, and Ronald P. Spoelhof.

EFFECTS OF LIGHTNING ON OPERATIONS OF AEROSPACE VEHICLES

by

Bruce D. Fisher
Senior Research Engineer
NASA Langley Research Center
Mail Stop 247
Hampton, VA 23665-5225
USA

SUMMARY

Traditionally, aircraft lightning strikes have not been a major aviation safety issue. However, the increasing use of composite materials and the use of digital avionics for flight critical systems will require that more specific lightning protection measures be incorporated in the design of such aircraft in order to maintain the excellent lightning safety record presently enjoyed by transport aircraft. In addition, several recent lightning mishaps, most notably the loss of the Atlas/Centaur-67 vehicle at Cape Canaveral Air Force Station, Florida in March 1987, have shown the susceptibility of aircraft and launch vehicles to the phenomenon of vehicle-triggered lightning. The purpose of this paper is to review the recent findings of the NASA Storm Hazards Program as they pertain to the atmospheric conditions conducive to aircraft lightning strikes. These data are then compared to recent summaries of lightning strikes to operational aircraft fleets. Finally, the new launch commit criteria for triggered lightning being used by NASA and the U.S. Defense Department are summarized. The NASA research data show that the greatest probability of a direct strike in a thunderstorm occurs at ambient temperatures of about -40°C. Relative precipitation and turbulence levels were characterized as negligible to light for these conditions. However, operational fleet data have shown that most aircraft lightning strikes in routine operations occur at temperatures near the freezing level in non-cumulonimbus clouds. The non-thunderstorm environment has not been the subject of dedicated airborne lightning research.

1. INTRODUCTION

Although commercial aircraft experience one direct strike approximately every 3000 flight hours (once per year per airframe) (1) and U.S. military aircraft experience one direct strike approximately every 35 000 flight hours (once per lifetime of each airframe) (1,2), aircraft lightning strikes have not been a major aviation safety issue. The damage usually is confined to burn marks on the skin and trailing edges (1-3). The minimal damage experienced on many aircraft can be attributed to the widespread use of aluminum (an excellent electrical conductor) for the skins and primary structure and the use of mechanical and hydraulic control systems, which are relatively immune from the adverse effects of lightning. However, even in aerospace vehicles utilizing these traditional, proven design techniques, lightning catastrophes involving loss of lives have occurred (3-6). Also, a NASA T-38 jet trainer recently suffered extensive fire damage from a fuel system fire ignited by an in-flight lightning strike (7).

Many new vehicle designs include the use of composite materials for primary structure and skins and the use of digital avionics for flight and engine controls and systems management. Although these new technologies promise improvements in vehicle performance and efficiency, their use will require that more specific lightning protection measures be incorporated in the design of new airframes and systems in order to maintain the excellent lightning safety record presently enjoyed by transport aircraft (1).

Two lightning mishaps involving NASA launch vehicles have shown the susceptibility of launch vehicles (and aircraft) to the phenomenon of vehicle triggered lightning. On November 14, 1969, the Apollo 12 space vehicle triggered two lightning flashes during ascent, causing minor damage (8). More recently, the Atlas/Centaur-67 unmanned launch vehicle was lost following a triggered cloud-to-ground flash in March 1987 (9). The latter mishap led to a new set of launch commit criteria for natural and triggered lightning (10) which are now applicable for all NASA and Defense Department launches.

The risks from lightning strikes to aircraft and launch vehicles can be managed by using the methods of vehicle hardening and in-flight avoidance (11). In the first method, the vehicle is designed so as to minimize the adverse effects of the lightning strike on the vehicle and its systems. The techniques of vehicle hardening are not the subject of this paper. Information on such techniques and the associated engineering waveform used for lightning certification of aerospace vehicles may be found in references 2 and 11-15. Research data on the electromagnetic properties of lightning and aircraft lightning strikes used to develop the engineering model are given in references 16-20.

In the second method, which is the subject of this paper, the aircraft or launch vehicle is operated in such a way as to avoid thunderstorms and other meteorological conditions conducive to aircraft lightning strikes. Unfortunately, lightning strikes occur under some conditions which are not predictable or readily identifiable using current instrumentation and techniques. These "non-thunderstorm" lightning strike conditions are not easily avoided by aircraft; and for launch vehicles, including the Shuttle, conservative launch commit criteria are required for lightning strike avoidance and prevention.

Significant insights into these lightning-related issues were made during the NASA Langley Research Center Storm Hazards Program (11, 16, 17, 21), which was conducted to improve the state of the art of severe storm hazards detection and avoidance, as well as protection of aircraft against those hazards which cannot be avoided reasonably. During this program, a specially-instrumented NASA F-106B research airplane was flown through thunderstorms to elicit in-flight lightning strikes in order to quantify the electromagnetic characteristics of in-flight lightning strikes and to identify atmospheric conditions most conducive to such strikes. The purpose of this paper is to review the findings of the Storm Hazards Program as they pertain to the atmospheric conditions conducive to aircraft lightning strikes. These

data are compared to recent summaries of lightning strikes to operational aircraft fleets. Finally, the new NASA/Defense Department launch commit criteria for natural and triggered lightning are summarized. This paper (and others in this session) will update the material presented in two AGARD Lecture Series on the interaction of atmospheric electricity and aircraft (22, 23).

2. SOURCES OF AIRCRAFT LIGHTNING STRIKE DATA

2.1 Operational Sources

Lightning strike data from civilian and military aircraft fleets collected during routine operations are available from several recent summaries (1, 3, 21-22). The principal sources are summarized chronologically in table 1, in which the country of origin, fleet source(s), and number of samples for each reference are shown along with selected flight conditions. In addition, earlier data from a number of sources have been compiled and summarized in previous reports (2, 28).

A further source of data is provided by the reports of the formal mishap boards which investigated each of the principal lightning accidents/incidents to aircraft and launch vehicles (4-9). The principal lightning accidents and incidents are listed chronologically in table 2, in which the type of vehicle, operator, geographical location of the mishap, and fate of the vehicle are summarized.

2.2 Thunderstorm Research Programs

Thunderstorm research programs which have collected or reported aircraft lightning strike data (11, 19, 20, 29-40) are summarized in table 3. In table 3, each program is listed chronologically by name, along with the principal participating agencies, probe aircraft, and number of strikes experienced. All the programs listed in table 3 were studies of active thunderstorms since this type of meteorological activity is the most prolific generator of natural lightning activity. No systematic, long-term research program on aircraft lightning strikes in non-thunderstorm meteorological conditions has been made to date, although there are Soviet data on airborne electric fields in such conditions (41).

One of the first investigations in thunderstorm research was the Thunderstorm Project, conducted at the end of World War II in Florida and Ohio (29, table 3). Although 21 lightning strikes were experienced by the fleet of USAF P-61C "Black Widows," the data were limited due to the limited operational ceiling of the P-61 and by the instrumentation.

The next major airborne lightning program was the multiagency (NOAA, USAF, FAA, Sandia), multiyear Rough Rider Program (30-33), in which a series of airplanes, including a USAF F-100F, was used to penetrate thunderstorms in the U.S. Midwest and Florida. Although the emphasis of the program was in-situ documentation of turbulence characteristics for comparison with ground-based radar data (33) considerable lightning strike data also were collected between 1964 and 1966 (30, 32).

During the Thunderstorm Research International Program-1976 (TRIP-76), a NASA Ames Research Center Lear 24B airplane instrumented by the Stanford Research Institute (SRI) experienced a single lightning strike which was analyzed extensively (34). TRIP-76 was conducted in the vicinity of the NASA Kennedy Space Center, Florida.

From 1978-1986, the NASA Langley Research Center conducted the Storm Hazards Program. Following a preliminary phase in 1978, in which a commercially-available airborne lightning locator was flown on the periphery of thunderstorms in Oklahoma and Virginia in a NASA DC-6 "Twin Otter" airplane (35), a specially instrumented and lightning-hardened NASA F-106B "Delta Dart" airplane, shown in Fig. 1, was flown through thunderstorms. The thunderstorm penetrations were made to elicit in-flight lightning strikes for documentation of the electromagnetic properties of these strikes and the associated meteorological conditions. The lightning hardening procedures (11) for the F-106B consisted of removing paint from most exterior surfaces of the airplane; installing surge protective devices and electromagnetic shielding of electrical power and avionics systems; and using flash-point certified JP-5 (or Jet A) fuel in lieu of the more volatile JP-4 (Jet B).

The instrumentation systems on the F-106B consisted of the following: Aircraft Instrumentation System (AIS) and Inertial Navigation System (INS) for measuring and recording airplane altitude, Mach number, attitudes, ambient temperature and position (42, 43); direct-strike lightning instrumentation system (16, 17) for recording the electromagnetic waveforms from direct lightning strikes and nearby flashes using electromagnetic sensors installed throughout the airplane and a shielded recording system in the weapons bay; several video, movie and still cameras (21, 44) for documenting the lightning attachment and the subsequent swept-stroke attachment patterns along the airplane's exterior; and, a commercially-available X-band color digital weather radar (45, 46) which also could display ground-based radar data uplinked to the airplane via a VHF radio. A summary of these and the other airborne experiments is given in reference 21.

During the 1979-1986 thunderstorm seasons, the NASA F-106B made 1496 thunderstorm penetrations during which 714 direct lightning strikes were experienced (see table 4). The research flights were made in conjunction with ground-based guidance and measurements by the NOAA National Severe Storms Laboratory (NSSL) and the NASA Wallops Flight Facility for flights in Oklahoma and Virginia, respectively. Starting in 1982, the ground-based VHF-band radar at NASA Wallops was used to direct the airplane to electrically-active regions of the thunderstorms and to provide data used to determine if the lightning strikes were random encounters with naturally-occurring lightning channels or if the strikes were triggered by the airplane itself (47, 48).

The thunderstorm penetration procedures used to guide the F-106B in Virginia were based on observations of storm structure and of lightning flash distribution with the NASA Wallops S-band and VHF-band radars, respectively (47, 48). In addition to the ground-based guidance from NASA Langley (where the mission control room was located (45, 46)) and NASA Wallops, the pilots used data from the onboard X-band digital weather radar to adjust the airplane's heading to avoid areas where hail might be expected (maximum precipitation reflectivity limit of 50 dBZ). These thunderstorm penetration procedures

were developed using the NOAA-NSSL guidelines used successfully in the Rough Rider Program and with the F-106B in 1980 and 1981.

During 1984 and 1985, the FAA and U.S. Air Force conducted the Low-Altitude Lightning Strike Characterization Program (19, 36) in which an FAA Convair 580 airplane was used to obtain direct lightning strikes at altitudes below 6 km (20 000 ft) while beneath thunderstorm cloud bases and during thunderstorm penetrations up to a maximum precipitation reflectivity limit of 35 dBZ. The onboard instrumentation, provided by the FAA, U.S. Air Force, Office of Naval Research, and France's ONERA, was similar to that installed on the NASA F-106B Storm Hazards research airplane but with a stronger emphasis on the measurement of static electric fields. The CV-580 airplane experienced 52 direct strikes during the two year campaign in Florida (table 3).

There have been three French government in-flight lightning strike programs utilizing a C.160 "Transall" airplane ((20), table 3). The French programs have emphasized the quantification of the electromagnetic properties of the aircraft lightning strikes, including the static electric fields, and the associated cloud microphysics. The operational procedures were very similar to those used by the FAA CV-580. In the 1978 campaign, the C.160 collected data from 13 strikes (37). The strike data from the Landes '84 and Transall '83 Programs are still being analyzed.

Finally, the armored T-28 tail research airplane (38, 39) operated by the South Dakota School of Mines and Technology (SDSMT), and the Special Purpose Test Vehicle for Atmospheric Research (SPTVAR - a modified Schweizer 845A) (40) operated by the New Mexico Institute of Mining and Technology (NMIMT) have been utilized in a number of atmospheric sciences programs, with each airplane experiencing occasional lightning strikes (table 3).

3. CONDITIONS CONDUCTIVE TO AIRCRAFT LIGHTNING STRIKES

3.1 Electrical Activity and Triggered Lightning

The lightning research community is especially interested in the manner in which lightning strikes occur to aircraft. One theory states that aircraft lightning strikes are the result of the aircraft simply being in the "wrong place at the right time," and being approached by a naturally-occurring lightning leader (2). If such a leader approaches within approximately 50 m (160 ft) of the aircraft, it is likely that the electric field presented to the aircraft will be of sufficient intensity to ionize air about the aircraft's extremities and induce a junction leader to propagate from the aircraft and join with the approaching lightning leader. The second theory states that the aircraft itself triggers the lightning flash (31).

When an aircraft flies through an electric field, the aircraft diverts and compresses adjacent equipotential lines as the aircraft flies between two charge centers. The highest electric fields about the aircraft will occur around extremities, where the equipotential lines are compressed closest together. Typically, these are the extremities of the nose, wing, and empennage, some engine nacelles, and also smaller protrusions, such as antennas or pitot probes. If an aircraft intercepts a naturally-occurring strike, the oncoming lightning leader will intensify the electric field and induce streamers from the aircraft extremities. One of these streamers will meet the nearest branch of the advancing lightning leader and form a continuous spark from the cloud charge center to the aircraft. Aircraft have very low capacitance, which means that comparatively little charge can accumulate on an aircraft. Therefore, the aircraft merely becomes an extension of the path being taken by the leader on its way to an ultimate destination at a reservoir of opposite polarity charge, which may be elsewhere in the cloud (an intracloud strike) or on the ground (a cloud-to-ground strike). Streamers may propagate onward from one or more extremities of the aircraft at the same time, with the branches continuing from the aircraft independently of each other until one or more of them reach their destination. Thus, the aircraft becomes part of the conducting path between charge centers. Heretofore, it generally had been believed that large aircraft (or launch vehicles) could cause a sufficient perturbation in the ambient electric field to initiate a lightning leader, but that such a leader would nevertheless originate from a nearby charge center and not from the aircraft. Such strikes were evident during natural icing tests of such wide-body aircraft as the Boeing 747 and the McDonnell-Douglas DC-10.

The research conducted in the NASA Storm Hazards Program has provided the first instrumental proof, using onboard camera systems and the ground-based UHF-band radar, of aircraft-triggered lightning flashes originating at the aircraft (47, 48). Approximately 90 percent of the airplane strikes observed by the UHF-band radar at altitudes above 6 km (20 000 ft) were triggered by the F-106B airplane (47). The UHF-band radar data also indicated that intercepted lightning strikes can occur, with most intercepted strikes in thunderstorms occurring at altitudes below 6 km (20 000 ft) (48). Analyses of simultaneous onboard and ground-based lightning electromagnetic data have shown that a high percentage of the strikes experienced by the FAA/USAF Convair 580 also were triggered by that airplane (19, 36). These findings confirmed the triggered lightning hypothesis developed during the Rough Rider Program (31, 32).

During the NASA Storm Hazards Program, the UHF-band radar data also were used to determine a Probability of Direct Strike (PDS), defined as the ratio of the number of direct strikes to the F-106B and the total number of flashes occurring in the radar resolution volume containing the airplane (47, 48). For all altitudes in thunderstorms, it was found that there was an inverse relationship between PDS and flash rate, with the higher PDS values occurring in regions of the storms with a flash rate of 0 to 10 flashes/min rather than in storm regions with flash rates greater than 10 flashes/min. This result implies that the greatest threat of triggered lightning may be located in storm regions with low natural lightning flash rates. Therefore, flight into an area with few indicated lightning discharges does not insure that the aircraft is in a region with low risk of triggered lightning.

The first firm indication that triggered lightning could be created by operational launch vehicles occurred with the Apollo 12 mission (see table 2 and (8)). On November 14, 1969, the Apollo 12 space vehicle was launched through clouds associated with a cold front. The vehicle experienced a cloud-to-ground strike at about 36.5 sec into the mission followed by an intercloud strike at 52 sec. As a

result, many temporary effects were noted along with loss of nine non-essential instrumentation sensors. Post-mishap analyses showed that lightning could be triggered by the presence of the long electrical length created by the space vehicle and its exhaust plume in an airborne electric field which would not otherwise have produced natural lightning. The possibility that the Apollo vehicle might trigger lightning had not been considered previously. Before the Apollo 12 flight, the only consideration of the effects of lightning on the space vehicle was for the period prior to flight.

On March 27, 1987, a triggered cloud-to-ground lightning flash caused the loss of the Atlas/Centaur-67 (A/C-67) unmanned launch vehicle (see table 2 and (9)). The A/C-67 vehicle was launched under weather conditions of heavy overcast and rain. The clouds originated in a squall line centered over the Gulf of Mexico which was moving eastward over the Florida panhandle. At approximately 49 sec into the mission, the A/C-67 vehicle triggered a cloud-to-ground flash with a minimum of 4 return strokes. The primary cause of the accident was an unplanned engine hardover command issued by the Centaur Digital Computer Unit (DCU), which resulted in out-of-limit dynamic loads and vehicle break up. The most credible mechanism for causing the booster engine hardover command was the DCU reacting to an externally-induced electrical transient caused by the triggered lightning strike on the flight vehicle. The triggered lightning analyses performed for the NASA Storm Hazards Program (49) were relied on extensively in developing the triggered lightning analyses for the A/C-67 mishap (50).

The current NASA theory on aircraft-triggered lightning strikes (49, 50) states that a sharp-edged metal object on an aircraft will concentrate the local electric field sufficiently to trigger a local breakdown in the presence of an ambient electric field of proper magnitude and orientation, with the streamers propagating from the aircraft outward to charge centers. The magnitude of the electric field in some triggering cases can be much less than that experienced in thunderstorms. Thunderstorm models (49) indicate that triggering should be far more prevalent at higher altitudes and colder temperatures (where field strengths are higher), as has been seen during the F-106B airplane flights. A comparison of the NASA data with that from commercial/military aircraft operations (1-3, 24, 27) indicates that some lightning strikes to these aircraft in "nonsunami" conditions near the freezing level also may be triggered lightning strikes. A common misconception is that bright flashes which are preceded or accompanied by St. Elmo's fire are "static discharges." As explained in references 2 and 11, a "static discharge" that produces a bright flash and/or an audible report is actually a lightning strike.

When an aircraft flies through dry precipitation in the form of sleet, hail, or snow, the impact of these particles on the aircraft will cause a charge to separate from the particle and join the aircraft, leaving the aircraft with a preponderance of positive or negative charge (depending on the form of precipitation), thereby changing the potential of the aircraft with respect to its surroundings. This phenomenon is known as triboelectric charging. It is commonly referred to as precipitation static, or P-static (51, 52). The P-static charging process is a different phenomenon from that of vehicle-triggered lightning, although they often occur in similar meteorological conditions. Recent reviews of natural and artificially-initiated lightning and electrification of thunderstorms are given in references 18 and 53, respectively.

As explained above, the ambient static electric field plays a key role in the two phenomena of vehicle triggered lightning and precipitation static. The strength of electric fields traditionally is measured by sensors called "field mills." Typical thunderstorm research aircraft are equipped with several field mills, located on the exterior of the airplane near crossing points of the lines of the airplane's electrical symmetry in order to make decoupled measurements of the three orthogonal components of the electric field and aircraft charge (19, 20, 29, 31, 32, 34, 36, 40, 41, 54). Usually, the field mill sensors are flush-mounted with the skin of the airplane, but have been mounted exterior to the airplane skin (40). Proper location and calibration of the field mills are critical for accurate measurements (55). A network of ground-based field mills is used at the NASA Kennedy Space Center and Cape Canaveral Air Force Station, Florida, in support of launch operations (9). Although the technology and data do not now exist for use of airborne field mills on operational aircraft for lightning avoidance, airborne field mills will be crucial for future research in vehicle triggered lightning.

The recent research data in aircraft-triggered lightning explain the lack of correlation between aircraft lightning strikes and other lightning activity or precipitation static (see table 1). For example, only 40 percent of reported strikes to U.S. commercial aircraft are associated with other lightning activity (1), and only 7 percent of the British military incidents report other lightning (24). Finally, only a "very small percentage" of U.S. Air Force reports mention other associated lightning (3).

In the case of precipitation static, roughly 50 percent of the strikes to U.S. commercial aircraft report this phenomenon (1); the corresponding value from the British data is 19 percent (24). There were no reported instances of precipitation static during the flights of the NASA F-106B airplane (11), but there were frequent instances during the operations of the FAA/USA Convair 580 airplane (19, 36). The differences in experiences of these two research airplanes may be attributed to the differences in the designs of the vehicles and in the installation details of the avionics systems in each airplane, and to the differences in flight conditions (51, 52).

3.2 Altitude and Ambient Temperature

A plot of lightning strike incidents as a function of altitude for commercial aircraft in routine operations is shown in Fig. 2 (from (2) with updated data from (1)). The corresponding strike incident data as a function of ambient temperature (1) are shown in Fig. 3. The flight conditions associated with the lightning strikes reported in (1, 3, 24-27) are summarized in table 1. (The Israeli Air Force data (25) do not contain information on meteorological conditions.) Comparing the data in Fig. 3 and table 1, it can be seen that the majority of lightning strikes to operational military and civilian aircraft fleets, regardless of geographical location, have occurred within $\pm 10^\circ\text{C}$ of the freezing level (0°C). However, there are significant differences in the altitude data from the different fleets and locations (Fig. 2 and table 1), with the commercial data from the 3 Japanese airlines showing a peak strike altitude of 0.5-2.0 km (1640-6562 ft) (27), which is much lower than that for the other data sets. It has been shown (1, 3, 24, 26) that the altitude data are operationally biased to the peculiarities of

each operator. In addition, atmospheric electricity studies (18, 53, 56) have shown that lightning and electric charge formation are a function of ambient temperature, not altitude. Therefore, altitude data cannot be used to determine the optimum height at which to maximize or minimize the probability of experiencing a lightning strike. The particularly low altitude for peak aircraft lightning strikes in Japan is caused by the low heights of the winter thunderclouds in Japan, with the height of the 0°C isotherm occurring at much lower altitudes than in storms in other parts of the world (57).

The number of missions, thunderstorm penetrations, direct strikes to the aircraft and nearby flashes (lightning channels close enough to the airplane to trigger the onboard lightning instrumentation without actually attaching to the airplane) for the NASA Storm Hazards 1980-1986 seasons are summarized by year in table 4. The data show that the 184 thunderstorm research missions resulted in 714 direct lightning strikes and 188 nearby flashes during 1496 penetrations.

Histograms showing the number and durations of penetrations, and the number of strikes and nearby flashes experienced from 1980-1986 are shown for altitude intervals of 610 m (2000 ft) in Fig. 4, and for ambient temperature intervals of 5°C in Fig. 5. Penetrations were made by the F-106B at pressure altitudes ranging from 0.7 km to 12 km (2400 ft to 40 000 ft) with a mean penetration altitude of 7 km (22 900 ft) (Fig. 4). Temperature data (mean value during the penetration) were available for 1368 penetrations, with values ranging from 20°C to -60°C, with an overall mean value of -19°C (Fig. 5). The distributions of penetration duration time with altitude and ambient temperature are very similar to the corresponding penetration distributions.

Based on data such as that shown in Figs. 2 and 3, most thunderstorm penetrations of the F-106B in the 1980 and 1981 seasons were made at altitudes corresponding to ambient temperatures between ±10°C in expectation of receiving a large number of strikes. However, very few strikes were experienced (see table 4). Starting in 1982, the NASA Wallops WLF-band radar was used to guide the F-106B through the upper electrically-active regions of thunderstorms (47, 56), resulting in hundreds of high altitude direct lightning strikes (table 4 and (47)). Starting in the 1984 season, the WLF-band radar was used to provide guidance to electrically-active regions in thunderstorms at altitudes below 6 km (20 000 ft) (48), the same range of altitudes studied previously in 1980 and 1981. The low altitude research efforts of 1980-81 and 1984-86 are shown in the low altitude/warm temperature peaks in the penetration and duration data in Figs. 4 and 5.

The NASA Storm Hazards Program strike statistics shown in Figs. 4 and 5 differ significantly from the published strike data for commercial and military aircraft fleets (Figs. 2 and 3 and table 1), in which most lightning strikes were found to occur between ambient temperatures of ±10°C. In the NASA Storm Hazards Program, direct strikes were experienced at pressure altitudes ranging from 4.3 km to 12 km (14 000 ft to 40 000 ft) with a mean value of 9 km (29 600 ft) (Fig. 4). The corresponding ambient temperature values ranged from 5°C to -65°C, with a mean value of -30°C (Fig. 5). The nearby flash data are very similar to the direct strike data.

Despite spending approximately 1559 min of penetration duration time at altitudes below 6 km (20 000 ft) (37 percent), only 98 direct strikes were experienced (14 percent) (see table 4). In fact, the peak strike rates in Fig. 4 of 7 strikes/penetration and 1.4 strikes/min occurred at pressure altitudes between 11.6 km and 12 km (38 000 ft and 40 000 ft) corresponding to ambient temperatures colder than -40°C. During one research flight through a thunderstorm anvil at 11.6 km (38 000 ft) altitude in 1984, the F-106B experienced 72 direct strikes in 45 min of penetration time, with the instantaneous strike rate twice reaching a value of 9 strikes/min. On the other hand, the peak strike rate near the freezing level (0°C) was only 0.1 strike/min (in the altitude interval between 5.5 km and 6 km (18 000 ft and 20 000 ft), corresponding to ambient temperatures of -5°C to -10°C).

The NASA Storm Hazards pressure and temperature lightning strike statistics differ from the commercial and military data for two reasons. First, the NASA data came solely from intentional thunderstorm penetrations, while the commercial and military data were derived from a variety of meteorological conditions, mostly in "nonstormy" clouds. For example, some of the commercial airline strikes were reported in snow storms or in winter time nimbostratus clouds (1). U.S. Air Force aircraft have reported lightning strikes in cirrus clouds downwind of previous thunderstorm activity, in cumulus clouds around the periphery of thunderstorms, and even in stratiform cloud, and light rain showers not associated with thunderstorms (57). In addition, the majority of lightning strikes to RAF aircraft have occurred in conditions which include cumulus or stratus type cloud (sometimes stratus with embedded cumulus) but no cumulonimbus observed either visually or on radar (24). (The NASA Storm Hazards Program did not study the non-thunderstorm lightning strike phenomenon.) Second, commercial and military aircraft will normally deviate from course to avoid thunderstorms which reach cruise altitudes, and only penetrate when required to do so in the terminal area, where typical assigned altitudes are near the freezing level. Therefore, the NASA distributions of lightning strikes with respect to pressure altitude and ambient temperature differ from the commercial/military data because of the higher percentage of time spent by the NASA F-106B research airplane in the upper flash density center of thunderstorms, compared with the low percentage of time spent in thunderstorms at those altitudes by aircraft in routine operations. However, lightning strikes have been encountered at nearly all temperatures and altitudes in the Storm Hazards Program, indicating that there is no altitude or ambient temperature at which aircraft are immune from the possibility of a lightning strike in a thunderstorm.

Although these Storm Hazards data differ from the commercial/military data, there is strong agreement with the results of the other thunderstorm flight test programs (table 3). The high altitude strike data are in good agreement with the results of the U.S. Air Force Rough Rider Program (32), in which the peak lightning activity was found to occur at an ambient temperature of -40°C. In addition, the Lear 24B airplane used in the TRIP-76 program experienced its lone lightning strike at an altitude of 11.2 km (37 000 ft) (34).

The low altitude strike data from the NASA program are very similar to the data from the USAF/FAA Convair 580 low altitude lightning measurement program (36), in which 31 percent of the 52 strikes experienced by that airplane in 1984 and 1985 occurred at an altitude of 5.5 km (18 000 ft).

(corresponding to ambient temperatures of -5°C to -10°C) although only 15 percent of the flying time was spent at that altitude. The data from the Convair 580, armored T-28 (39), and SPTVAR (40) research airplanes, and the results of the Thunderstorm Program (29) and of the C.160 flights in France in 1978 (32) show that virtually all lightning strikes occurred within $\pm 10^{\circ}\text{C}$ of the freezing level. However, these data are biased due to the low service ceiling of these aircraft or by the interest of the experimenters in flights in the vicinity of the freezing level.

3.3 Turbulence and Precipitation

The most successful plotting technique used during the NASA Storm Hazards Program in searching for lightning was to fly through the thunderstorm cells which were the best defined visually and on the airborne weather radar. Frequently, heavy turbulence and precipitation were encountered during these penetrations. However, the lightning strikes rarely occurred in the heaviest turbulence and precipitation, and occasionally, there was no lightning activity whatsoever. These findings are shown in Fig. 6, in which the percentage of direct strikes to the F-106 is plotted as a function of the flight crew's opinion of relative turbulence and precipitation intensity at the time of the strikes. The data are plotted for those strikes which occurred above and below 6 km (20 000 ft) altitude. In both altitude regimes, most lightning strikes (approximately 60 percent) occurred in thunderstorm regions in which the crew characterized the turbulence and precipitation as negligible to light. In addition, although a strong correlation between lightning strikes and vertical drafts (predominantly downdrafts) was found for a small data set in 1981 and 1982, most strong turbulence episodes encountered by the airplane were not associated with lightning (58, 59).

Although the Doppler radar data recorded in 1981 and 1982 using the NASA Wallops S-band radar (58) showed heavy turbulence within the high precipitation reflectivity cores of thunderstorms, heavy turbulence also was found between cells, near storm boundaries, and in innocuous-appearing low reflectivity factor regions. Similar results were found during the multi-year Rough Rider Program turbulence studies (33). Therefore, it was concluded that turbulence and precipitation are not necessarily correlated.

Unlike the temperature and altitude data discussed in Section 3.2 above, there are no appreciable discrepancies between the precipitation and turbulence data gathered in the NASA program and the data gathered during commercial (1, 2, 27) and military operations (3, 24). For the turbulence data, this can be seen by comparing the data in Fig. 6 with that in Fig. 7, in which the percentage of direct strikes to U.S. (1) and Japanese (27) commercial aircraft are plotted as a function of relative turbulence intensity. Although approximately 80 percent of U.S. and Japanese commercial strikes reported turbulence, 80 percent of these strikes were associated with negligible to light turbulence (Fig. 7 and table 1). Only 20 percent of U.S. Air Force strikes were associated with turbulence (table 3, (3)). Finally, for the USAF/FAA Convair 580 research flights, 85 percent of the strikes occurred in light to negligible turbulence (36).

Although virtually all reported lightning strikes have occurred in, or in the vicinity of clouds and in rain (table 1), very few strikes have occurred in heavy precipitation or hail. For example, 81 percent of all U.S. commercial strikes occurred in rain, but only 2 percent of the strikes were associated with rain and hail (1). For U.S. Air Force aircraft (3), 67 percent of the strikes occurred in rain, 5 percent occurred in hail or snow, and 10 percent occurred in "clear air." All the strikes to the FAA/USAF Convair 580 research airplane occurred in precipitation no more severe than rain with five strikes occurring with the airplane outside the clouds being studied (36). Finally, the strikes to the T-28 (39), SPTVAR (40) and Lear 248 (34) research airplanes occurred in the less severe portions of the storm cells under study, with the strike to the Lear 248 occurring when the airplane was flying between two cells. In summary, the thunderstorm research data and commercial/military operational data have shown that the number of direct strikes to aircraft do not show a positive correlation to turbulence and precipitation intensities.

4. LAUNCH COMMIT CRITERIA FOR NATURAL AND TRIGGERED LIGHTNING

Following the Atlas/Centaur-67 lightning mishap, NASA and the U.S. Air Force Space Division developed revised launch commit criteria for the avoidance of natural and triggered lightning. More recently, the NASA and U.S. Air Force have developed a common set of criteria for use during all NASA and U.S. Air Force launches, including those of the National Space Transportation System (Space Shuttle) (10). The constraints are based on the known cloud types which can produce lightning discharges and the distances to charge regions at which discharges are known to occur. There are similar criteria for the Space Shuttle Orbiter landing sites (60). These criteria were developed from data obtained from the broad spectrum of atmospheric electricity and lightning strike programs which have been conducted, including those referenced in this paper.

The revised launch commit criteria are (10):

The Launch Weather Officer must have clear and convincing evidence that the following constraints are not violated:

1. Do not launch if any type of lightning is detected within 10 n.mi. of the launch site or planned flight path within 30 minutes prior to launch, unless the meteorological condition that produced the lightning has moved more than 10 n.mi. away from the launch site or planned flight path.

(DEFINITION: The "planned flight path" is the trajectory of the flight vehicle from the launch pad through its flight profile until it reaches an altitude of 30.5 km (100 000 ft). The flight path may vary plus or minus 0.5 n.mi. horizontally up to an altitude of 7.6 km (25 000 ft).)

2. Do not launch if the planned flight path will carry the vehicle (see Figs. 8 and 9):
 - a. Through cumulus clouds with tops higher than the $+5^{\circ}\text{C}$ level; or,
 - b. Through or within 5 n.mi. of cumulus clouds with tops higher than the -10°C level; or,

c. Through or within 10 n.mi. of cumulus clouds with tops higher than the -20°C level; or,
 d. Through or within 10 n.mi. of the nearest edge of any cumulonimbus or thunderstorm cloud including its associated anvil. (See Fig. 10 for vertical separation of the flight path from these cloud types.)

(DEFINITION: A "cumulonimbus cloud" is any convective cloud which exceeds the -20°C temperature level.)

(DEFINITION: An "anvil" is a stratiform or fibrous cloud produced by the upper level outflow from thunderstorms or convective clouds. Anvil debris does not meet the definition if it is optically transparent.)

3. Do not launch if, for ranges equipped with a surface electric field mill network (9), at any time during the 15 minutes prior to launch time, the one minute average of absolute electric field intensity at the ground exceeds 1 kilovolt per meter (1 kV/m) within 5 n.mi. of the launch site unless:

- a. There are no clouds within 10 n.mi. of the launch site; and,
- b. Smoke or ground fog is clearly causing abnormal readings.

4. Do not launch if the planned flight path is through a vertically continuous layer of clouds with an overall depth of 1.4 km (4500 ft) or greater where any part of the clouds are located between the 0°C and the -20°C temperature levels (see Fig. 11).

(DEFINITION: A "cloud layer" is any broken or overcast layer or layers connected by cloud elements, e.g., turrets from one cloud layer to another.)

5. Do not launch if the planned flight path is through any cloud types that extend to altitudes at or above the 0°C level and that are associated with disturbed weather within 5 n.mi. of the flight path (see Fig. 12).

(DEFINITION: "Disturbed weather" is any meteorological phenomenon producing moderate or greater precipitation.)

6. Do not launch through thunderstorm debris clouds, or within 5 n.mi. of thunderstorm debris clouds not monitored by a field mill network or producing radar returns greater than or equal to 10 dBZ.

(DEFINITION: "Debris cloud" is any cloud layer other than a thin fibrous layer, that has become detached from the parent cumulonimbus within 3 hours before launch.)

GOOD SENSE RULE:

Even when constraints are not violated, if any other hazardous conditions exist, the Launch Weather Officer will report the threat to the Launch Director. The Launch Director may hold at any time based on the instability of the weather.

5. AIRBORNE FIELD MILL PROGRAM

In order to better quantify the atmospheric electrical threat to launch vehicles and to evaluate a state-of-the-art airborne field mill system, NASA and the U.S. Air Force have initiated a Joint Airborne Field Mill (ABFM) Program (61). During the feasibility phase in the summer of 1988, the NIMT SPTVAR airplane successfully demonstrated that ABFM data can be obtained with acceptable levels of accuracy and precision. In the upcoming operational test phase, the NASA Langley Research Center's Lear 28/29 airplane (Fig. 13) will be equipped with five field mills to be provided by the NASA Marshall Space Flight Center. The program objectives are:

- a) to build an ABFM data base which will be analyzed with concurrent weather data
- b) to build a data base for day of launch decisions to use as a basis to relax the current weather launch commit criteria (LCC)
- c) to characterize the electric field structure of clouds
- d) to determine electrical relaxation times of charged debris clouds
- e) to evaluate whether current weather LCC and Flight Rules for natural and triggered lightning should be changed
- f) to define situations when an ABFM-equipped aircraft is needed for day-of-launch support.

To accomplish these objectives, the NASA Langley Lear 28/29 airplane will be flown in Instrument Flight Rules (IFR) conditions in the vicinity of Cape Canaveral, Florida, in conjunction with ground-based data and guidance support from NASA Kennedy Space Center and the U.S. Air Force Eastern Space and Missile Center. These flights will occur in cloud types which produce the conditions described in the launch commit criteria: cumuli, thunderstorm debris clouds, disturbed weather (rain clouds), and layered clouds between the 0°C and -20°C isotherms. The aircraft is being prepared to safely operate in occasional moderate turbulence, conditions conducive to airframe icing, and maximum precipitation reflectivity values of 30 dBZ (moderate rain). Finally, the airplane will be inspected and modified, as necessary, to safely withstand lightning strikes, since occasional triggered lightning strikes can be expected.

The knowledge of the airborne electrical environments sufficient for vehicle triggered lightning which will be gathered in this program will be used to increase launch availability while maintaining the level of safety provided by the new launch commit criteria. These findings also may be used to avoid lightning strikes to aircraft flying through clouds of different types as well as to provide a reliable warning to pilots of impending lightning strikes.

6. CONCLUDING REMARKS

The experience and technical data produced by the NASA Langley Research Center Storm Hazards Program and by other recent research programs have resulted in a substantial increase in our knowledge regarding lightning interactions with aircraft. These data, in combination with data collected from commercial and military aircraft in routine operations, have provided insights into the effects of lightning on operations of aerospace vehicles.

The insights discussed in this paper are summarized as follows:

- o Aircraft lightning strikes occur in both thunderstorm and non-thunderstorm conditions.
- o The thunderstorm regions with the highest probability for an aircraft to experience a direct lightning strike were those areas where the ambient temperature was -40°C , where the relative turbulence and precipitation intensities were characterized as negligible to light, and where the lightning flash rate was less than 10 flashes/min. However, direct lightning strikes were encountered at nearly all temperatures and altitudes.
- o The non-thunderstorm regions with the highest probability for an aircraft to experience a direct lightning strike were those areas where the ambient temperature was between $\pm 10^{\circ}\text{C}$, in rain, where the relative turbulence intensity was characterized as negligible to light, and where there was little or no other lightning activity.
- o Most aircraft lightning strikes are triggered by the vehicle itself. Lightning strikes in which the aircraft intercepts a naturally-occurring lightning flash also occur, predominantly at lower altitudes.
- o The presence and location of lightning do not necessarily indicate the presence or location of hazardous precipitation and turbulence. In addition, hazardous precipitation and turbulence are not necessarily related to one another.
- o The NASA and U.S. Air Force have written new launch commit criteria for natural and triggered lightning to be used for launches of the Space Shuttle and expendable launch vehicles. These two agencies have begun an Airborne Field Mill Program which will provide data which can be used to safely revise the launch commit criteria so as to provide increased launch availability.

REFERENCES

1. Plumer, J. Anderson; Rasch, Nicholas O.; and Glynn, Michael S.: Recent Data from the Airlines Lightning Strike Reporting Project, J. Aircraft, vol. 22, no. 5, May 1985, pp. 429-433.
2. Fisher, Franklin A.; and Plumer, J. Anderson: General Electric Corp. for National Aeronautics and Space Administration: Lightning Protection of Aircraft, 1977, NASA Reference Pub. NASA RP-1008.
3. Corbin, John C.: Lightning Interaction with USAF Aircraft, Procs. of Eighth Inter. Aerospace and Gnd. Conf. on Lightning and Static Electricity, Ft. Worth, TX, 1983, Dept. of Transportation Rep. DOT/FAA/CT-83/25, pp. 66-1 - 66-6.
4. Civil Aeronautics Board: Aircraft Accident Report B-707-121, N709PA, Pan American World Airways, Inc., Near Elkton, MD, Dec. 8, 1963, 1965, CAB File No. 1-0015.
5. National Transportation Safety Board: Special Investigation Report - Wing Failure of Boeing 747-131, Near Madrid, Spain, May 9, 1976, 1978, NTSB Report No. NTSB-AAR-78-12.
6. Anon: Commercial Flight Safety, Flight International, vol. 134, no. 4122, July 16, 1988, p. 26.
7. Fisher, Bruce D.; Taeuber, Ralph J.; and Crouch, Keith E.: National Aeronautics and Space Administration: Implications of a Recent Lightning Strike to a NASA Jet Trainer, 1988, AIAA Paper 88-0394.
8. Godfrey, R.; Mathews, E. R.; and McDivett, J. A.: National Aeronautics and Space Administration: Analysis of Apollo 12 Lightning Incident, 1970, NASA Johnson Space Center Rep. MSC-01540.
9. Christian, Hugh J., Jr.; Crouch, Keith; Fisher, Bruce D.; Mazur, Vladislav; Perala, Rodney A.; and Ruhnke, Lothar: The Atlas Centaur 67 Incident, Procs. Addn. of 1988 Inter. Aerospace and Gnd. Conf. on Lightning and Static Elec., Oklahoma City, OK, 1988, MJAA Special Report No. PB88-197439, pp. 19-31.
10. National Aeronautics and Space Administration: Shuttle Launch Commit Criteria and Background, July 1988, NASA Johnson Space Center Doc. NTS 16007, Revision D, pp. 1.4-02 - 1.4-04.
11. Fisher, Bruce D.; and Plumer, J. Anderson: Managing Risks From Lightning Strikes to Aircraft, Procs. of Flight Safety Fndtn. 40th Inter. Air Safety Seminar, Tokyo, Japan, 1987, pp. 353-375.
12. Federal Aviation Administration: Protection of Airplane Fuel Systems Against Fuel Vapor Ignition Due to Lightning, 1985, FAA Advisory Circular AC 20-53A.
13. Society of Automotive Engineers Committee AE4L: Recommended Draft Advisory Circular: Protection of Aircraft Electrical/Electronic Systems Against the Indirect Effects of Lightning, 1987, SAE Comm. Rep. AE4L-87-3.

14. Society of Automotive Engineers Committee AE4L: Lightning Test Waveforms and Techniques for Aerospace Vehicles and Hardware, 1978, SAE Comm. Rep.
15. Plumer, J. Anderson: Lightning Protection of Advanced Avionics Systems, *Procs. of Flight Safety Fndtn. 40th Inter. Air Safety Seminar*, Tokyo, Japan, 1987, pp. 168-187.
16. Pitts, Felix L.; Fisher, Bruce D.; Mazur, Vladislav; and Perala, Rodney A.: Aircraft Jolts From Lightning Bolts, *IEEE Spectrum*, vol. 25, no. 7, 1988, pp. 34-38.
17. Pitts, Felix L.; Perala, Rodney A.; Rudolph, Terence H.; and Lee, Larry D.: New Results for Quantification of Lightning/Aircraft Electrodynamics, *J. Electromag.*, vol. 7, 1987, pp. 451-485.
18. Usan, Martin A.: Natural and Artificially-Initiated Lightning and Lightning Test Standards, *Procs. of IEEE*, vol. 76, no. 12, 1988, pp. 1548-1565.
19. Reazer, J. S.; Serrano, A. V.; Walko, L. C.; and Burket, H. D.: Analysis of Correlated Electromagnetic Fields and Current Pulses During Airborne Lightning Attachment, *Electromagnetics*, vol. 7, nos. 3-4, 1987, pp. 509-539.
20. Boulay, J.-L.: Main Characteristics of Lightning Strikes on Aircraft, *AGARD Symposium on Flight in Adverse Environmental Conditions*, Gol, Norway, 1989, in press.
21. Fisher, Bruce D.; Brown, Philip W.; Plumer, J. Anderson; and Wunschel, Alfred J., Jr.: Final Results of the NASA Storm Hazards Program, *Procs. Addn. of 1988 Inter. Aerospace and Gnd. Conf. on Lightning and Static Elec.*, Oklahoma City, OK, 1988, NOAA Special Report PB88-197439, pp. 113-130.
22. Advisory Group for Aerospace Research and Development: Atmospheric Electricity - Aircraft Interaction, *AGARD Lecture Series AGARD-LS-110*, 1980.
23. Advisory Group for Aerospace Research and Development: Interaction between EHP, Lightning and Static Electricity with Aircraft and Missile Avionics Systems, *AGARD Lecture Series AGARD-LS-144*, 1986.
24. Odum, G. A. M.: Highlights of RAE Lightning Strike Investigations, *Procs. Addn. of 1988 Inter. Aerospace and Gnd. Conf. on Lightning and Static Elec.*, Oklahoma City, OK, 1988, NOAA Special Report, pp. 1-10.
25. Joffe, Elya B.: Israel Air Force (IAF) In-Service Aircraft Lightning Strike and Damage Survey, *Procs. 1988 Inter. Aerospace and Gnd. Conf. on Lightning and Static Elec.*, Oklahoma City, OK, 1988, NOAA Special Rep. PB88-197439, pp. 8-12.
26. Ziegler, Wilfried: Lightning Strikes to Aircraft of the German Federal Armed Forces, *Procs. Inter. Aerospace and Gnd. Conf. on Lightning and Static Elec.*, Dayton, OH, 1986, U.S. Air Force Rep. AFWAL-TR-86-3098, pp. 10-1 - 10-6.
27. Goto, Yukihiko; and Murooka, Yoshihiro: Statistics of Lightning Interaction with Aircraft in Japan, *Procs. 1988 Inter. Aerospace and Gnd. Conf. on Lightning and Static Elec.*, Oklahoma City, OK, 1988, NOAA Special Rep. PB88-197439, pp. 1-11.
28. Clifford, Don W.: Aircraft Mishap Experience From Atmospheric Electricity Hazards, 1980, *AGARD Lecture Series AGARD-LS-110*, pp. 2-1 - 2-17.
29. Byers, Horace R.; and Braham, Roscoe R., Jr.: The Thunderstorm; Report of the Thunderstorm Project, Washington, DC, U.S. Govt. Printing Office, 1949, pp. 133-140.
30. Petterson, B. J.; and Wood, W. R.: Sandia Lab. for Federal Aviation Administration: Measurements of Lightning Strikes to Aircraft, 1968, FAA Rep. DS-68-1.
31. Fitzgerald, Donald R.: Probable "Triggering" of Lightning in Certain Thunderstorms, *Monthly Wea. Rev.*, vol. 95, Dec. 1967, pp. 835-842.
32. Fitzgerald, Donald R.: USAF Flight Lightning Research, *Lightning and Static Elec. Conf.*, 1968, Conf. Papers, 1969, U.S. Air Force Rep. AFAL-TR-68-290 - Part II, pp. 123-134. (Available from DTIC as AD 693 135.)
33. Lee, Jean T.; and Carpenter, D. H.: National Oceanic and Atmospheric Administration for Federal Aviation Administration: 1973-1977 Rough Rider Turbulence-Radar Intensity Study, 1979, FAA Rep. FAA-RD-78-115.
34. Hanevitz, J. E.; Adamo, R. C.; and Bly, R. T., Jr.: Stanford Res. Inst. for U.S. Air Force: Airborne Measurement of Electromagnetic Environment Near Thunderstorm Cells (TRIP-76), 1977, U.S. Air Force Tech. Rep. AFFDL-TR-77-62.
35. Fisher, Bruce D.; and Crabill, Norman L.: Summary of Flight Tests of an Airborne Lightning Locator System and Comparison with Ground-Based Measurements of Precipitation and Turbulence, 1980 Aircraft Safety and Operating Problems, Joseph W. Stickie, compiler, NASA Conference Publication NASA CP-2170, Part 1, 1981, pp. 251-277.
36. Burket, H. D.; Walko, L. C.; Reazer, J.; and Serrano, A.: Air Force Wright Aeronautical Laboratories: In-Flight Lightning Characterization Program on a CV-580 Aircraft, 1988, U.S. Air Force Tech. Rep. AFWAL-TR-88-3024.

37. Centre D'essais Aeronautique de Toulouse: Mesure des Caracteristique de la Foudre en Altitude, 1979, CEAT 76/650000 P.4.
38. Detweiler, Andrew G.; and Smith, Paul L.: Thunderstorm Observations with the Armored T-28 Aircraft, Third Interagency Airborne Geoscience Workshop, La Jolla, CA, 1989, pp. IV-111 - IV-114.
39. Musil, Dennis J.; and Prodan, John: Direct Effects of Lightning on an Aircraft During Intentional Penetrations of Thunderstorms, Lightning Technology, NASA Conf. Pub. NASA CP-2128, 1980, pp. 363-370.
40. Bullock, J. William; and Jones, J. J.: A Chronology of In-Cloud Electric Field and Lightning Strikes on an Instrumented Research Aircraft, Procs. of 1988 Inter. Aerospace and Gnd. Conf. on Lightning and Static Elec., Oklahoma City, OK, 1988, NOAA Special Rep. PB88-157439, pp. 175-180.
41. Imjanitov, I. M.; Chubarova, Ye. V.; and Shvarts, Ya. M.: Electricity of Clouds, trans. of Elektrichestvo Oblakov, Hydrometeor. Press, Leningrad, USSR, 1971, English trans., 1972, NASA Tech. Tran. NASA TT F-718.
42. Fisher, Bruce D.; and Plumer, J. Anderson: Lightning Attachment Patterns and Flight Conditions Experienced by the NASA F-106B Airplane, Procs. Adden., Eighth Inter. Aerospace and Gnd. Conf. on Lightning and Static Elec., Ft. Worth, TX, 1983, Dept. of Transportation Rep. DOT/FAA/CT-83/25(A), pp. 26-1 - 26-16.
43. Usry, Jimmy W.; Dunham, R. Earl, Jr.; and Lee, Jean T.: National Aeronautics and Space Administration: Comparison of Wind Velocity in Thunderstorms Determined From Measurements by a Ground-Based Doppler Radar and a F-106B Airplane, 1985, NASA Tech. Memo. NASA TM-86348.
44. Brown, Philip W.: National Aeronautics and Space Administration: Development of and Results From Camera Systems for Recording Daytime Lightning Strikes to an Airplane in Flight, 1986, AIAA Paper AIAA-86-0020.
45. Fisher, Bruce D.; Brown, Philip W.; Munschel, Maj. Alfred J., Jr.; Burket, 1Lt. Harold D.; and Terry, Jesse S.: Joint Thunderstorm Operations Using the NASA F-106B and FAATC/AFMIL Convair 580 Airplanes, Procs. of Inter. Conf. on Lightning and Static Elec., Dayton, OH, 1986, U.S. Air Force Tech. Rep. AFMIL-TR-86-3098, pp. 20-1 - 20-10.
46. Fisher, Bruce D.; Brown, Philip W.; Munschel, Alfred J., Jr.; and Stickle, Joseph W.: National Aeronautics and Space Administration: Cockpit Display of Ground-Based Weather Data During Thunderstorm Research Flights, 1989, AIAA Paper AIAA-89-0806.
47. Mazur, Vladislav; Fisher, Bruce D.; and Gerlach, John C.: Lightning Strikes to an Airplane in a Thunderstorm, J. Aircraft, vol. 21, no. 8, Aug. 1984, pp. 607-611.
48. Mazur, Vladislav; Fisher, Bruce D.; and Gerlach, John C.: Lightning Strikes to a NASA Airplane Penetrating Thunderstorms at Low Altitudes, J. Aircraft, vol. 23, no. 6, June 1986, pp. 499-505.
49. Rudolph, T. H.; Easterbrook, C. C.; Ng, P. H.; Haupt, R. W.; and Perala, R. A.: Electromagnetic Applications, Inc. for National Aeronautics and Space Administration: Experimental and Analytic Studies of the Triggered Lightning Environment of the F106B, 1987, NASA Contractor Rep. NASA CR-4104.
50. Perala, Rodney A.; and Rudolph, Terence H.: Triggering of Lightning by the Atlas Centaur Vehicle, Procs. of 1988 Inter. Aerospace and Ground Conf. on Lightning and Static Elec., Oklahoma City, OK, 1980, NOAA Special Rep. PB88-197439, pp. 47-57.
51. Manevitz, Joseph E.: Static Charging Effects on Avionic Systems, 1986, AGARD Lecture Series AGARD-LS-144, pp. 5-1 - 5-18.
52. Manevitz, Joseph E.: Alleviation/Testing Techniques for Aircraft Charging, 1986, AGARD Lecture Series AGARD-LS-144, pp. 6-1 - 6-16.
53. Williams, Earle R.: The Electrification of Thunderstorms, Scientific American, vol. 259, no. 5, Nov. 1988, pp. 88-92, 94, 96-99.
54. Zaepfel, Klaus P.: National Aeronautics and Space Administration: A Wide Bandwidth Electrostatic Field Sensor for Lightning Research, 1989, NASA Tech. Memo. NASA TM-101539.
55. Mazur, Vladislav; Ruhnke, Lothar H.; and Rudolph, Terence: Effect of E-Field Mill Location on Accuracy of Electric Field Measurements with Instrumented Airplane, J. Geophys. Res., vol. 92, no. D10, Oct. 1987, pp. 12013-12019.
56. Mazur, Vladislav; Rust, W. David; and Gerlach, John C.: Evolution of Lightning Flash Density and Reflectivity Structure in a Multicell Thunderstorm, J. Geophys. Res., vol. 91, no. D8, July 1986, pp. 8690-8700.
57. Zeller, Lt. Col. Earl F.: Avoid a Jolt From a Bolt, Flying Safety, Feb. 1987, pp. 2-7.
58. Bohne, Alan R.: Air Force Geophysics Laboratory: Joint Agency Turbulence Experiment Final Report, 1985, U.S. Air Force Tech. Rep. AFGL-TR-85-0012.
59. Bohne, Alan R.; and Chmela, Albert C.: Storm Structure During Aircraft Lightning Strike Events, J. Geophys. Res., vol. 91, 1986, pp. 13291-13298.

60. National Aeronautics and Space Administration: STS Operational Flight Rules, 1988, NASA Johnson Space Center Doc. JSC-12820, pp. 4-53 - 4-64.
61. Barnes, Arnold A., Jr.: Airborne Lightning Detection, Third Interagency Airborne Geoscience Workshop, La Jolla, CA, 1989, pp. IV-3 - IV-4.

ACKNOWLEDGEMENTS

Figures 8-12 of this paper, illustrating the launch commit criteria for triggered and natural lightning, are adapted from briefing charts prepared by the staff of Detachment 11, 2nd Weather Squadron, U.S. Air Force Air Weather Service. The author also is grateful to Col. William J. Bihner, Jr. of NASA Headquarters for his suggestions on this paper.

TABLE 1.- SUMMARY OF FLIGHT CONDITIONS ASSOCIATED WITH OPERATIONAL LIGHTNING STRIKES

Country of Origin	Source	No. of Samples	Years	Reference	Peak Strike Altitude	Peak Strike Temp.	Percent in Cloud	Percent in Turb.	Percent in Rain	Clas. Activ.
USA	5 airlines	~600	1971-1984	1	34% < 10kft 47% < 16kft	43% at $\pm 5^{\circ}\text{C}$	96	78 (78 none to light)	81	68%
Japan	JAL, ANA, and TDA	1091	1977-'87	27	33% at 0.5-2 km	44% at $\pm 10^{\circ}\text{C}$	93	82 (76.5 none to light)	54	NA
Israel	IAP	24	1973-'83	23	NA	NA	NA	NA	NA	NA
UK	MoD	270	1977-'83	24	77% < 8kft Peak at 2-4kft	49% at $\pm 9^{\circ}\text{C}$	61	NA	40	72
West Germany	Federal Armed Forces	~345	1977-'83	26	50% < 5kft 80% < 10kft	NA	NA	NA	NA	NA
USA	USAF	877	1977-'83	1	50% > 10kft 23% > 15kft	67% at $\pm 5^{\circ}\text{C}$	80	20 (NA)	67	Very small %

NOTE: NA = Not Available

TABLE 2.- PRINCIPAL LIGHTNING ACCIDENTS/INCIDENTS

B707-121 (PAN AM): 12/8/63

Elkton, MD
Fuel Ignition - Loss of aircraft - 82 fatalities

APOLLO 12 (NASA): 11/14/69

NASA Kennedy Space Center, FL
Minor Damage

B747-131 (IRAN AF): 5/9/76

Madrid, Spain
Fuel Ignition - Loss of aircraft - 17 fatalities

ATLAS/CENTAUR-67 (NASA): 3/26/87

Cape Canaveral AFS, FL
Memory upset in Digital Computer Unit (DCU) - Loss of vehicle

METRO III (NFD): 2/8/88

Mulheim, FRG
Loss of Electrical Power - Loss of aircraft - 21 fatalities

TABLE 3.- MAJOR AIRCRAFT LIGHTNING STRIKE RESEARCH PROGRAMS

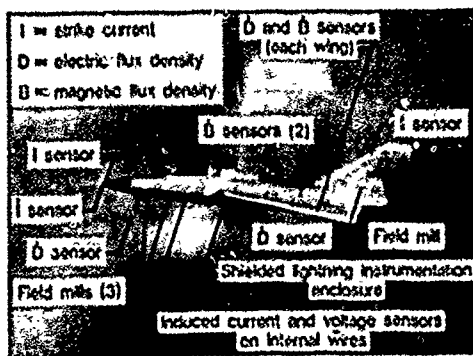
Program Name	Agencies	Airplane	No. Strikes	Years	References
Thunderstorm	USAF, USN, NASA, USMC	P-61C (A)	21	1946-'47	29
Rough Rider	USAF, FAA, NOAA, Sandia	F-100F (B,C)	55	1964-'66(C)	30-33
TRIP-76	USAF, NASA, SRI	Lear 24B	1	1976	34
Storm Hazards (D)	NASA	DHC-6 F-106D	0 714	1978 1979-1986	35 11, 15
Low-Altitude Direct Strike (E)	FAA, USAF, NRL, ONERA	CV-580	52	1984-'85	19, 36
CEAT (France)	CEAT	C.160	13	1978	20, 37
Landes '84	ONERA (France)	C.160	Unknown	1984	20
Transall '88	ONERA (France)	C.160	12 (est.)	1988	20
Misc.	SOSMUT(G)	T-28	4 (F)	1969-Present	38, 39
Misc.	MMINT(H)	SPIVAR	11	1975-Present	40

Notes:

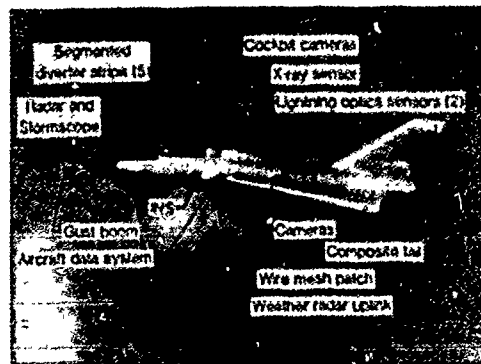
- (A) Up to 10 P-61C "Black Widow" aircraft were used in addition to several auxiliary aircraft.
 (B) A C-130 and U-2 also were used for non-penetration.
 (C) The overall Rough Rider Program commenced in 1960 and used a variety of aircraft (33).
 (D) See table 4 for details.
 (E) This program proceeded through several preliminary phases and aircraft (19).
 (F) Strikes with significant damage.
 (G) South Dakota School of Mines and Technology.
 (H) New Mexico Institute of Mining and Technology.

TABLE 4.- NASA STORM HAZARDS MISSION SUMMARY

Year	1980	1981	1982	1983	1984	1985	1986	Total
Missions	19	24	35	40	38	19	9	184
Penetrations: High	23	29	191	298	273	25	18	857
Low	46	82	50	26	136	197	100	639
Total	69	111	241	324	409	224	118	1496
Strikes: High	6	7	153	214	223	12	1	616
Low	4	3	3	0	24	41	23	98
Total	10	10	156	214	247	53	24	714
Nearbys: High	1	9	26	110	11	11	0	168
Low	5	13	0	2	0	0	0	20
Total	6	22	26	112	11	11	0	188



(a) Location of electromagnetic sensors.



(b) Location of additional research sensors.

Fig. 1.- NASA Langley Research Center F-106B Storm Hazards research airplane used from 1979-1986.

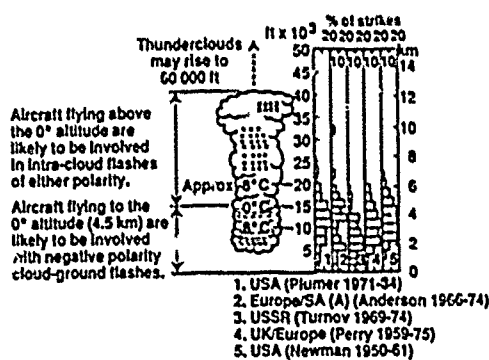


Fig. 2.- Aircraft lightning strike incidents as a function of altitude. From Fisher and Plumer (2) with updated data from Plumer, Rasch and Glynn (1).

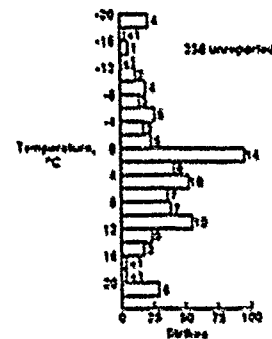


Fig. 3.- Aircraft lightning strike incidents as a function of outside air temperature. From Plumer, Rasch and Glynn (1).

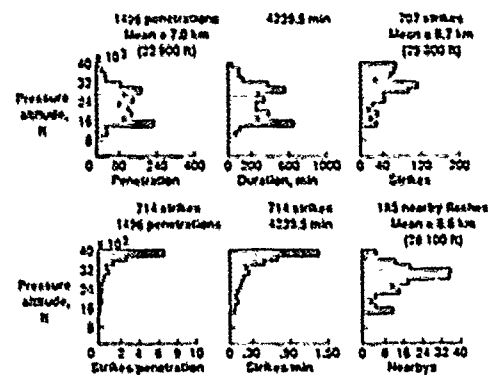


Fig. 4.- Thunderstorm penetrations and lightning statistics as a function of pressure altitude for NASA Storm Hazards '80-'86.

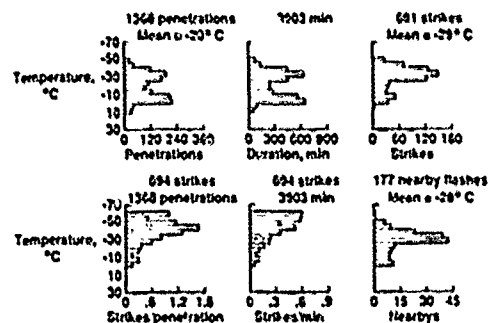


Fig. 5.- Thunderstorm penetrations and strike statistics as a function of ambient temperature for NASA Storm Hazards '80-'86.

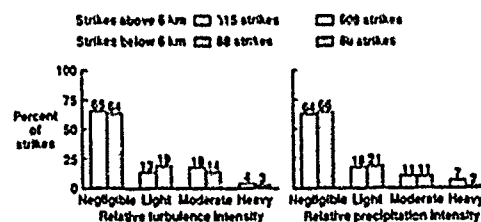


Fig. 6.- Relationship of lightning strikes to relative turbulence and precipitation intensities for NASA Storm Hazards '80-'86.

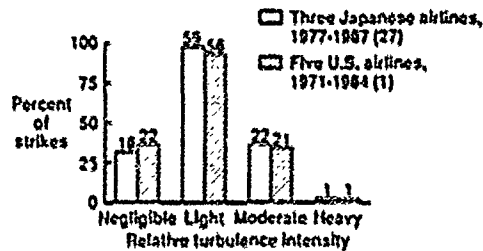


Fig. 7.- Relationship of lightning strikes to relative turbulence intensities for commercial aircraft in the U.S. and Japan. From Plumer, Rasch and Glynn (1) and Goto and Murooka (27).

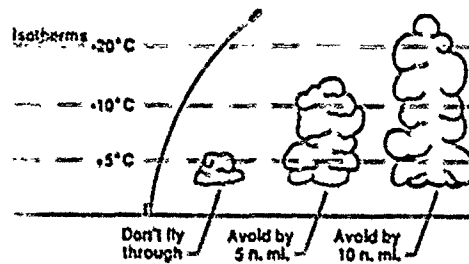


Fig. 8.- Shuttle launch commit criteria - cumulus avoidance.

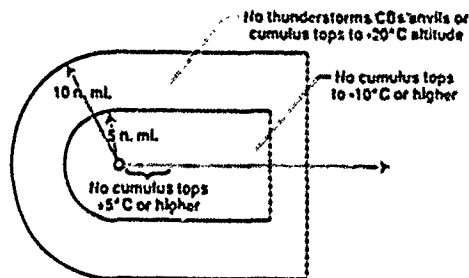


Fig. 9.- Shuttle launch commit criteria - horizontal avoidance from thunderstorms and building cumulus.

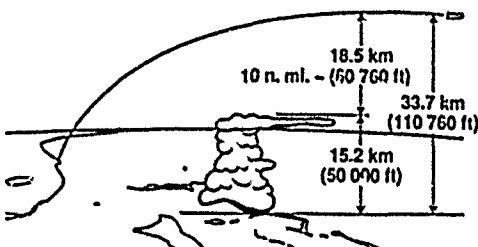


Fig. 10.- Shuttle launch commit criteria - down-range distance as a function of vertical separation.

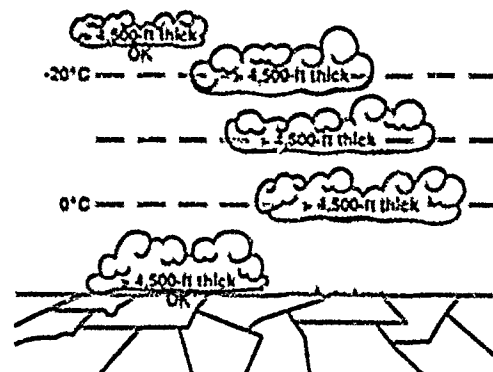


Fig. 11.- Shuttle launch commit criteria - layered cloud criteria. Cloud layers must be 1372 m (4500 ft) thick or thicker.

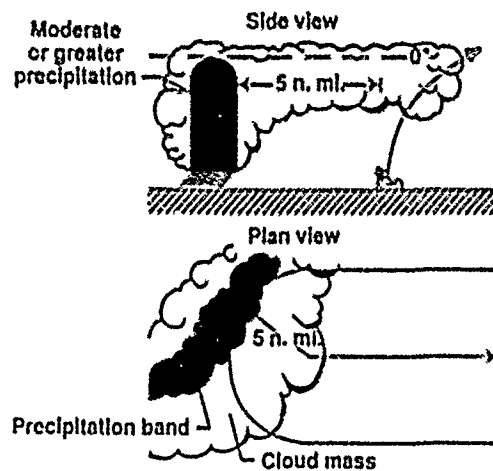


Fig. 12.- Shuttle launch commit criteria - disturbed weather.

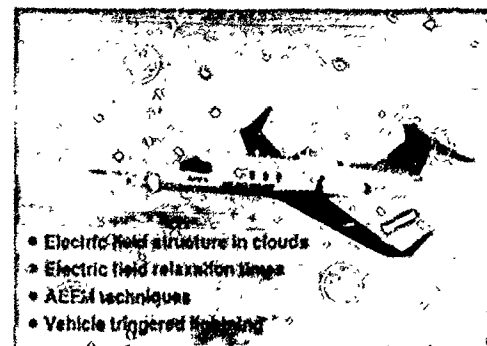


Fig. 13.- NASA Lear 28/29 airplane used in the Joint NASA/USAF Airborne Field MITI Program.

AIRCRAFT TESTING IN THE ELECTROMAGNETIC ENVIRONMENT

P M Newton, I Eng, MIEEE
 Electromagnetic Compatibility
 Engineering Systems
 Procurement Executive
 Ministry of Defence
 Aeroplane and Armament Experimental Establishment
 Boscombe Down
 Salisbury
 Wiltshire, UK
 SP4 GJF

Summary

Testing aircraft flight safety critical systems against the effects of electromagnetic interference (EMI) is normally carried out on the ground for reasons of safety, practicality and cost. This paper discusses the threat and the effects of EMI on aircraft systems, it reviews the current ground test methods used at the Aeroplane and Armament Experimental Establishment (AAEE), including the limitations, uncertainties of measurement and safety margins. A flight test method for assessing the effects on critical systems from both the on-board and external electromagnetic environment is described which should enable the ground test results to be factored thus providing a more precise clearance for service use without compromising safety.

1. Introduction

Electromagnetic compatibility (EMC) is considered to be established when no unacceptable effects occur to the aircraft systems from operation of the aircraft's equipment or from the external electromagnetic environment that it flies in. With the increasing dependence of flight safety critical (FSC) systems on electronics and the general rise in levels of the RF environment, the errors and resulting limitations imposed by the present EMC ground based test methods need to be examined in an attempt to provide a more accurate clearance without compromising safety. Over the past two years AAEE have been involved with some of the flight test aspects of EMC testing and have recently carried out a series of flight tests to quantify the errors.

On military aircraft EMC testing is required to cover Engineering, Armament and Mission systems, this paper is specifically concerned with engineering systems that are FSC, however the principles are applicable to other systems. A FSC system is defined as one where any failure to operate correctly could result in the loss of aircraft the aircraft or armaments which in turn could also threaten public safety. In most military aircraft this covers flight control, stability augmentation systems, engine control, gust alleviation, rotor de-icing and some flight instruments. The criticality of these systems may vary depending on the aircraft's role.

The susceptibility of installed FSC systems to radio frequency interference (RFI) can vary between aircraft of the same type. This variation results from the different coupling paths (to the system) due to aircraft wiring, the structure, and from the variation in the basic susceptibility of the equipment. Testing is normally carried out on one production aircraft and with a fleet of say 200 aircraft a margin of safety has to be applied to cover the spread. An additional safety margin is also required to cover the uncertainties of measurement.

The sources of RFI are from emissions within the aircraft (on-board) and from ground, ship or airborne (external) based transmitters. The frequency spectrum extends from several hundred kilohertz to tens of gigahertz, and can be continuous wave (CW) or pulsed. The electromagnetic behaviour of an aircraft when subjected to RF radiation in the high frequency (HF) band is similar to a combination of dipole antennae, currents flow in the aircraft skin which are then re-radiated within the aircraft structure. At higher frequencies external energy can penetrate through apertures in the aircraft's skin. The radiation can couple directly into circuit elements via gaps or holes in the equipment, or into the connecting cables. The dimensions of the structure and cables are important as coupling is more efficient when they are half of the energy's wavelength. The size of a strike aircraft enables frequencies in the HF band to couple more efficiently than other frequency bands thus causing higher currents to be induced into equipment cables. For example an aircraft with an overall length of 20 meters would have a half wavelength frequency of about 8 Mhz. The frequency where coupling is efficient is termed resonance. Transmitters both on-board and external at these frequencies are often high power and range from hundreds of watts to megawatts.

2. EMC Testing General

EMC testing of aircraft systems, requires the measurement of the magnitude and frequency of the interfering source, measurement of the coupled energy and observation of the effects, from both the on-board and external sources of RF interference. Energy couples either directly into the equipment via holes or slots typically above 500 Mhz, or indirectly by way of the aircraft skin and connecting cables at the lower frequencies. Once the energy has coupled into the equipments electronic circuits and if the level is high enough a disturbance or even damage can occur. The RF energy does not generally disturb the systems directly since the frequency is much higher than their operating bandwidth, which for example on an autopilot is only tens of hertz. However the non-linearity and high gain of the

electronic components within the circuit causes the process of demodulation and rectification to occur, similar to the basic process of a communications receiver. The result of this process is a low frequency component which is interpreted as a signal and if great enough will cause a system malfunction. RF energy can directly effect some systems if their operating bandwidths are high enough, an example being the clock in the CPU of a digital system which can operate up to 20 Mhz.

The normal practice in testing for EMC is to use the aircraft's own transmitters (on-board) and a remote transmitter (external) to assess equipment susceptibility. For the external environment the aircraft can be cleared to the field level at which the system malfunctions with a safety margin applied. For the on-board the aircraft is cleared if a margin of safety exists between the level of energy measured on the equipment cables and the level that causes an equipment malfunction.

If the level of the interfering source is insufficient to cause a malfunction and the malfunction threshold of the equipment needs to be related to a particular external field level or on-board transmitter, two parameters can be measured that together quantify any disturbance mechanism. These are the Coupling factor (often called the transfer function) which relates the interfering source to the equipment input and the Susceptibility factor of the equipment itself. To quantify the coupling factor measurements are made on the equipment cables of the induced RF current (Bulk Current Measurement) that results from the interfering source. If the source is external the field strength (expressed in volts per meter) is measured and the coupling factor, which is linear, is then defined as the magnitude of the current induced into the equipment cable per unit field strength expressed in milliamperes per volt per meter (mA/V/m). The susceptibility factor of the equipment is measured by either increasing the level of the interfering source until a disturbance occurs and recording the bulk current in the cable, or alternatively injecting current (Bulk Current Injection) into the cable bundle and raising the level until a disturbance occurs.

The bulk current measurement (BCM) technique has been in use in the UK and FRG for some time, and is really the only practical method of measuring the current in a cable bundle. To break each cable to facilitate measurement, or to measure individual wire currents, would be extremely time consuming and of course breaking the cable would modify the aircraft wiring and in some cases the results would be questionable. BCM was developed to overcome this and the technique uses a ferrite cored transformer (probe) which is clamped around the cable bundle close to the connector of the equipment under test (EUT). The RF current is coupled into the probe by transformer action, which in turn is connected to measuring equipment for example a spectrum analyser. The technique is also used in the test house during equipment qualification tests.

With the BCI technique RF energy is "injected" into the cable bundle using a transformer similar to a BCM probe but with greater power handling capacity (up to 100 watts). It is positioned on the cable close to the BCM probe and is driven from a frequency synthesizer with modulation applied via an RF power amplifier. The forward power to the probe is increased until malfunction occurs or until the test equipment limits are reached, the current at malfunction is measured using a BCM probe. This process is repeated on all cable bundles to or from the FSC equipments over the frequency spectrum 0.5 to 400 Mhz. The resulting malfunction currents can then be plotted against frequency thus producing the susceptibility factor for each cable bundle. As BCI uses local coupling the tests can be performed with the aircraft in a hanger using ground power supplies. The BCM probes are connected to the measuring equipment (spectrum analyser) via a commercial fibre optic link (FOL) as conductors attached to the aircraft could produce erroneous results. Fig 1 shows the general arrangement of the BCM/BCI technique.

A safety margin (SM) can be defined (Ref 1) as the ratio by which the level needed to upset the equipment exceeds the level of interference the aircraft fleet are cleared to operate in. The normal practice at ALAEE is to test one aircraft of a given type and provide a clearance for the whole fleet. Several surveys have been carried out in the UK to establish how the coupling factor can vary across a fleet of aircraft (Ref 2), and a survey is also planned to assess the variability of equipment susceptibility. The coupling factor surveys have shown that over samples of 10 and 21 aircraft worse case variations of 10/1 can exist, 4/1 is typical. MIL-6051D requires a safety margin of 2/1 for FSC equipment although no justification is given for this value. Equipment susceptibility tests are carried out during qualification as required by MIL-461 and DEF P14N 59/41, these consist of radiated and conducted susceptibility tests and are essentially for assessing the equipment withstand capability in a defined test house environment. The electromagnetic environment within the aircraft structure cannot be simulated in the test house as the field conditions are practically impossible to measure inside a strike aircraft using conventional antennas and measuring receivers. One point to consider is that a fleet of aircraft with a coupling factor variation of 4/1 would also have equipments which vary in susceptibility. In most military applications equipments are moved from aircraft to aircraft, therefore the probability exists that the aircraft with the highest coupling factor could have equipment fitted with the highest susceptibility. Therefore with a single aircraft test a SM is essential.

EMC testing on the ground can not simulate precisely the RF environment that an aircraft is subjected to in flight. However, safety, cost and time dictate that ground testing will continue to be the primary test method. However there is some evidence, from UK experience, that the energy induced into systems and the disturbance effects could vary between the ground and flight condition. Therefore there is a need to carry out limited flight tests with a view to establishing a factor for future ground testing. This paper will now describe the present ground test methods used at ALAEE and the limitations, uncertainties and safety margins associated with each method, followed by the flight test methods and the initial results of a flight trial on a rotorcraft. The problems of EMC flight test instrumentation will also be described.

3. Ground Test Methods

On-Board

The purpose of this test is to assess the susceptibility of FSC systems to the RF environment produced by the aircraft's own transmitters. Prior to starting this test system performance checks are carried out. The transmitters are removed from the aircraft and checked for minimum output power. Very few transmitters have a maximum output power specified. BCM probes are clipped on the cables to be tested and the transmitters operated over their frequency spectrum. At each test frequency modulation is employed and the maximum current recorded and the FSC systems operated and assessed for malfunction. If the operation of the transmitters does not cause a malfunction a BCM test is then performed on the same cables and the levels raised at each frequency until malfunction or a (planned) maximum disturbance occurs or test equipment limits are reached. The equipment susceptibility is then compared with induced currents (Fig 2) and a SM established.

Because of resonance the coupling can be significantly higher at some frequencies and a SM criteria may not be met, or even worse no SM exists and FSC systems may be disturbed by the transmitters. If this occurs there are four possible options: 1. Restrict the operation of the transmitters at these frequencies, 2. Reduce the power of the transmitters, 3. Harden the FSC equipment 4. Modify the coupling. However before these steps are taken flight testing should be carried out as the effect of the ground plane can influence the results. Option 2 has been used successfully particularly at HF frequencies, but it does mean that the airborne performance of the communication system has to be re-tested at reduced power before this solution can be employed.

On-Board Enhanced Level

This method has the same purpose as the previous test but does not use the BCM technique to determine malfunction and SM. This method is required when the available space to fit BCM & BCM probes is limited and if the additional SM required for BCM/BCM is unacceptable. With this method the transmitter output power is increased to obtain the required SM by inserting a linear power amplifier between the transmitter and aircraft aerial and radiating across the frequency band at this "enhanced" level. BCM probes are fitted where possible to monitor the increase in coupled current and if no malfunctions occur a true SM is demonstrated. This seems an ideal method, however it suffers from a major drawback as some HF systems particularly the aerial tuning unit cannot cope with the increase in power. For most VHF/UHF systems the method works well and the same options apply as with the previous on-board method. Flight testing is difficult and is only practical with large aircraft.

High Level Testing (External Environment)

This is a test method that has been in use at AAEE for many years and has been continually developed to its present state. The whole aircraft is illuminated by high level RF fields in the frequency range 250 KHz to 9 GHz at selected frequencies. These tests are performed in an open site facility called the Radio Frequency Environmental Generator. The testing is semi-automated under computer control and can be performed on a variety of fixed and rotary wing aircraft with engines running and rotors engaged. The main advantage of this test is that the whole aircraft and systems are illuminated simultaneously in a relatively high field strength and system interaction can be studied, which is not the case with the BCM technique.

Before the aircraft is positioned in the test site, the area is calibrated using a free field probe which measures the electric and magnetic components of the horizontal and vertical fields at specified heights. Calibration would be meaningless with the aircraft in position as the field would be severely disturbed, it is the magnitude of free space field conditions that are specified when defining the electromagnetic limits in which the aircraft can operate.

BCM probes are positioned on the cables and connected via the fibre optic link to the test facility. The aircraft is operated in a simulated flight condition however, for flight control systems (FCS) this is not possible to achieve as the controls and surfaces are in an open loop condition with no aerodynamic feedback. Engines that have electronic control need to be operated at maximum thrust to exercise the limiters, or changes to software to artificially limit temperature and RPM. With all systems operational the field strength is raised at each spot frequency until malfunction or the maximum field is reached, modulation is also applied at each frequency. On some engine control systems certain malfunctions can cause the engine to accelerate to destruction and mechanical limiters have to be fitted to avoid this situation. The currents on the cable looms are recorded at each frequency and the records of any system disturbance. A 2:1 SM can be achieved by halving the field level that caused a disturbance, or the maximum field that could be generated if no disturbance occurs.

The major shortcomings of high level testing are, that only spot frequencies are available, the effects of the ground reflected wave, the proximity of the aircraft to the transmitter and the non representative condition of testing a flight control system stationary on the ground. The latter two cases can be overcome with flight testing. Spot frequencies can miss important resonance points and some method is required to sweep the frequency band. This cannot be done at high power levels for any length of time because of the risk of interference, also there are technical difficulties in designing a high power swept frequency source. To overcome this problem a low level test method has been developed.

Low Level Sweep (LLS)

To eliminate some of the disadvantages of high level testing the LLS method was developed by AAEE and the Royal Aerospace Establishment (RAE). The aircraft is illuminated by a swept low level source

over the frequency range 1 to 300 MHz at field levels of typically 1 V/M from different aspects (both sides, nose and tail), the resulting induced currents on selected cables are measured using ECM probes. The test site is first calibrated (without the aircraft) at a distance of 20m from the source at various heights for both horizontal and vertical fields across the frequency range. The aircraft is then positioned in the test site and the currents measured on cables during the frequency sweep. The aircraft systems are normally unpowered during this test as research has shown that the coupling factor to control and signal lines is not significantly changed when systems are powered, however the coupling to power supply lines can be affected. The coupling factor can then be calculated in terms of induced current per unit field in a similar manner to that used in the high level test. Any sharp resonances will not be missed because of its swept nature.

The results of the LIS derived coupling factor can then be combined with the BCI susceptibility results and, with the appropriate SM, provides an RF operating clearance for the aircraft which is independent of any other test method. From AAIK's experience LIS testing generally produces reasonable results when compared with high level testing.

The LIS test method can also be used to compare the coupling factor, both before and after the installation of a modification, to establish whether the EMC state of the aircraft has changed. This is a very cost effective solution for determining the effects of modifications when the aircraft is in service and can significantly reduce the re-certification test time.

If high level testing is going to be performed, LIS results allow the spot frequencies to be optimised on the identified resonances and in some cases reduces the need to cover all the available frequencies.

4. Ground Testing Limitations

All of the test methods described so far are influenced by the proximity of the ground plane. The aircraft is subjected to both the incident wave and the ground reflected wave and depending on distance and wavelength these can add or subtract which is not the case in flight other than at very long wavelengths. Also, in the high level test it is not always possible in the HF band to operate the aircraft in true far field conditions as close proximity to the transmitting source is required in order to obtain high field strength levels.

Flight control systems modify pilot demand inputs depending on the magnitude and sense of a number of parameters eg air data, G, attitude etc. With the aircraft on the ground and stationary, some of these parameters are static, therefore the FCS is in an open loop configuration so that the susceptibility of circuits could be different from the dynamic (closed loop) condition in flight. Some parameters like airspeed and altitude can be changed by using ground equipment, but the proximity of bulky equipment near the aircraft could affect the coupling factor.

Flight testing to date has shown that ground testing is usually worse-case, however very little work has been carried out to establish if a factor could be used to modify ground test results. The following describes two flight test methods and the initial results of a trial to identify any differences between the magnitude of currents induced in FCS cables during ground and hover flight when exposed to similar electromagnetic fields.

5. Flight Testing On-Board

The main reasons for carrying out flight tests on the on-board emitters is if unwanted effects or unusually high susceptibilities are seen during the ground tests, or if the aircraft type has a history of EMI related problems in flight. In general the on-board flight assessment is usually subjective, however cable currents can be measured during flight although on strike aircraft this may be impractical. A method for measuring cable currents during flight will be described later.

As one of the criteria for flight testing is to assess any unwanted effects the flight safety and planning (Ref 3) has to be carefully considered, particularly if ordnance is being carried. The loss of the aircraft or armaments is always a possibility, therefore testing should take place in a safe area. It may be necessary to carry armaments, including external fuel tanks, which are operated by electro explosive devices. If they cannot be made safe for flight extreme care has to be taken. For some aircraft there may be a need to provide a chase aircraft to monitor the behaviour of external stores, as cockpit indications of their status can be unreliable if they are fired by the effects of electromagnetic interference.

The ground tests would have revealed the frequencies at which unwanted effects occurred and if the frequencies and power output of the transmitter cannot be restricted flight testing should be carried out. This will establish if the effects remain or are modified in flight. With military strike aircraft the configuration of external stores and wing geometry significantly changes the coupling, therefore the flight test should include the worse case configuration, however the aircraft should first be tested without any stores if the unwanted effects are on FSC systems.

The flight testing is normally carried out by the crew making voice modulated transmissions across the frequency band and observing the effects on the systems. The test frequencies to be covered are mainly dependent on the ground test results, however 0.2 MHz steps across the HF band are typical. Transmissions between 5 and 10 seconds are usually long enough to enable the crew to assess systems behaviour. If cable currents have been measured in flight, they can be compared to the ground test results and using the BCI test and SM a fleet clearance can be provided. Quite often there is an unacceptable malfunction in flight over a narrow band of frequencies, the only solution if system hardening is unacceptable is to limit the use of these frequencies in flight.

6. Flight Testing External Environment.

Flight testing against an external RF environment is usually only considered if the level of RF environment that the aircraft is cleared to fly in is not acceptable. One option would be to fly the aircraft over a calibrated RF environment and assess system behaviour. This is likely to be prohibitively expensive and technically difficult. However some limited flight tests have been carried out against specific transmitters where a special requirement exists. A simple option is to base the clearance on the ground tests with suitable SM's and limit the environment the aircraft can fly in, or for example, switch off ships transmitters when aircraft are in close proximity. This approach to the problem has been in use for a number of years but is becoming increasingly difficult to administer as transmitter operation becomes automated and frequency agile, also the loss of vital communications may be unacceptable. An ideal solution would be to factor the ground test results to provide a more accurate flight clearance. The following describes a flight test method that has recently been used by ALAEE.

Before considering the aircraft requirements, the problem of producing a calibrated field in free space must be addressed. To date ALAEE have only considered the HF frequency spectrum and used the HF facility in the Radio Environmental Generator for flight trials. The requirement is to produce a plane wave over a reasonable altitude, 100 to 300m a.g.l. at a minimum distance from the transmitter of 50m. The field is calibrated by suspending a purpose built probe from a rotorcraft which measures the magnitude of the electric and magnetic fields in three axes. The field data is transmitted from the probe to the aircraft via a telemetry link. Markers are placed on the ground at regular intervals corresponding to the E field magnitude at the chosen height of operation. If the aircraft used for the field calibration is to be the test aircraft or is shown to be susceptible to EMI then sensitive systems should be inhibited or increasing fields should be approached progressively. A safety assessment is always required before the field calibration.

Fig 3 shows the aircraft instrumentation used to measure the induced currents in two cables for both a ground and flight test in a rotorcraft which had sufficient cockpit space for a flight observer. The bulk current probes were developed for ground use; they are heavy and need to be supported on the cable lugs for operation in flight. The power supply arrangements for the spectrum analyser need to be considered carefully. Ideally it should be powered from a battery, via an inverter, as the quality of the aircraft supply may be inadequate for reliable operation. This would be the case on some rotorcraft where the generators are tied to rotor speed.

Measuring the system disturbance could be achieved by using conventional instrumentation on control surfaces. However although this would provide a comparison between the ground and flight cases care should be taken when using this method for clearance purposes as the instrumentation wiring could significantly alter the coupling. Full use should be made of any suitable parameters if an accident data recorder is a permanent feature of the aircraft. An alternative is to use an aircraft instrument. One example on the test aircraft being the flight control system position and demand indicator, sometimes referred to as a Hall indicator. This instrument is quite suitable for comparison purposes, particularly if there is a video available for time fixing events. In addition the pilot will probably be making reference to this instrument during the flight test.

The object of the flight test is to measure the magnitude of current induced in a given cable when the aircraft is subjected to the same field strength level as on the ground, also to compare any effects on a flight control system in both a closed and open loop condition. Before any high level testing is carried out the aircraft is subjected to LLS/BCI test to establish the main resonant frequencies and equipment susceptibility thresholds. Following this a full ground high level test is completed initially on-ground power and finally on aircraft internal power with engines and rotors turning. Tests can be carried out at various field levels to establish system behaviour with the final test matching the levels chosen from the flight calibration. All four aspects are checked, to establish the worse case coupling profile. The currents and any system disturbances are recorded at each frequency and field level. A one hertz modulation was found to produce the worse disturbances on the ground on the test aircraft and this was achieved simply by keying the transmitter.

Before the flight test the ground test results should be analysed to determine a safe maximum field in which the aircraft can operate and the procedures to be adopted in the event of a flight control system or engine runaway. With a rotorcraft the flight test procedure would be to hover above the weakest field ground marker, at a safe altitude with the correct aspect to the transmitter and record the currents and system disturbances at each frequency, then proceed to a higher field strength. Three frequencies at the main resonances should be the minimum requirement. Reliable communications with the ground transmitter is essential, the aircraft system is usually adequate if operated at a different frequency to the RFI source.

Fig 4 and 5 show the induced currents in a FCS cable bundle for the ground and flight case, when the aircraft is subjected to an external field of 14 volts per meter. Both the nose and side aspects are shown. These initial results have been shown to illustrate that the test method does produce the required data. In this particular test it can be seen that the induced currents are similar for the port aspect when comparing ground and hover. However there is some difference near the resonance for the nose aspect. Further testing on this aircraft is required before a factor for clearance can be derived. Two areas will need to be addressed: one, to determine how the current varies due to the angle of illumination and two, the effects of operating the aircraft in a far field plane wave condition (flight) compared to the more complex field on the ground. If the illumination angle is the dominant factor then additional flight testing is required to define the angle and aircraft aspect that produces the highest current. The system susceptibility on this test was similar for ground and hover flight at these three frequencies but it could vary considerably if the control loop gain varies with airspeed.

On this aircraft the control laws are scheduled to change and additional sensors are introduced at 60 knots therefore further tests over the speed range are required.

The test method detailed above is ideally suited to a rotorcraft however a fixed wing aircraft does present additional problems. There is no room in a single seat strike aircraft for the general purpose test equipment, therefore, special to type instrumentation is required to record the cable currents and system disturbances if an accident data recorder is not fitted. It was mentioned earlier that instrumentation can change the coupling, therefore coupling tests with and without the instrumentation is necessary if the results are required for clearance. Several alternative methods are presently being considered to measure cable currents. One is to record the cable currents on a digital recording system. The flight test method will be different without the capability to hover; tangential slices are flown over the speed range at each field strength value. However this method only covers a side aspect, testing nose and tail aspects would be difficult and potentially dangerous and no work has been carried out by AIAA in this area to date.

7. CONCLUSIONS

The ground test methods presently used for aircraft EMC clearance testing are limited by the proximity of the ground plane and interference source, also some flight safety critical systems are being tested in a condition which is not representative of flight.

This paper has discussed the flight test methods that are being developed to compare flight and ground test results to enable a more precise clearance to be given and to provide a factor to be used with future ground tests without compromising safety. The initial work with rotorcraft has shown encouraging results, however some problems need to be resolved with instrumentation and the flight test technique on fixed wing strike aircraft before clearance testing using this method can be undertaken.

Reference

1. The determination of safety for critical systems. G M SMITH, AGARD Conference (No 229) Subsystem Testing and Flight Test Instrumentation, 1980.
 2. The variation of induced currents on aircraft wiring. P M NEWTON, IERE conference on EMC - Southampton 1980.
 3. Electromagnetic Compatibility and the Flight Test Engineer. M B REDMAN, SFTE 16th Annual Symposium Amsterdam 1987.
- 'C' Controller, Her Majesty's Stationery Office London 1989.

BULK CURRENT INJECTION AND MEASUREMENT.

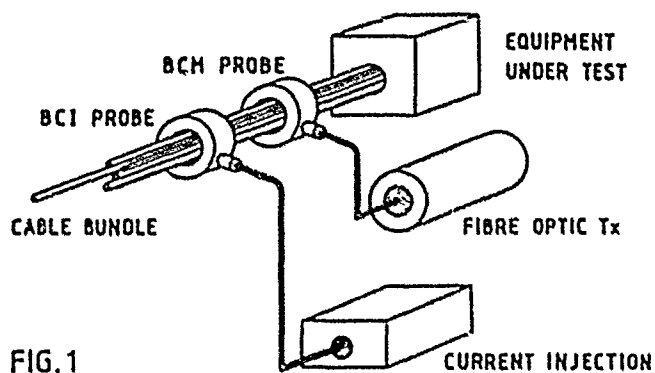


FIG. 1

INDUCED CURRENT AND BCM SUSCEPTIBILITY

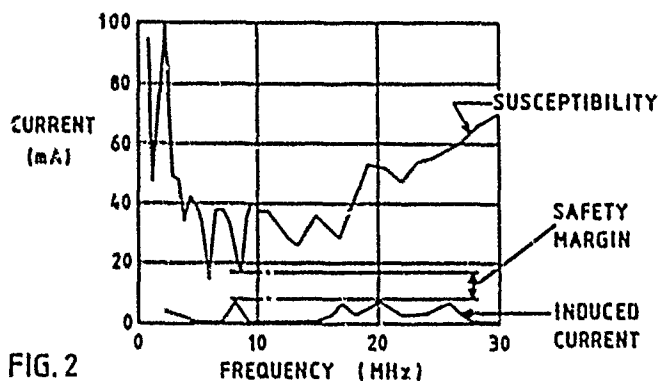


FIG. 2

FLIGHT TEST CURRENT MEASUREMENT EQUIPMENT

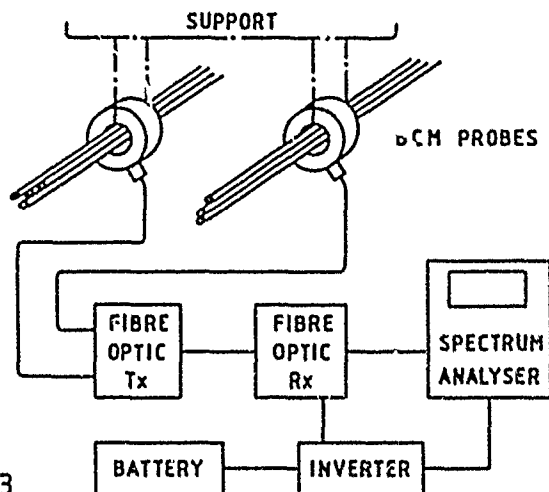


FIG. 3

GROUND AND FLIGHT INDUCED CURRENTS ON
PLUG No.1 FOR 14 V/m EXTERNAL FIELD STRENGTH.

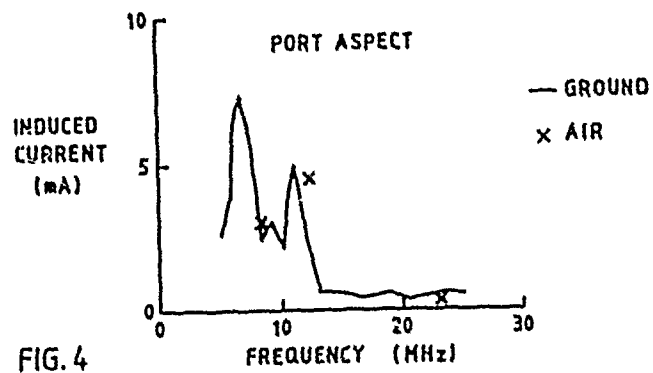


FIG. 4

GROUND AND FLIGHT INDUCED CURRENTS ON
PLUG No.1 FOR 14 V/m EXTERNAL FIELD STRENGTH.

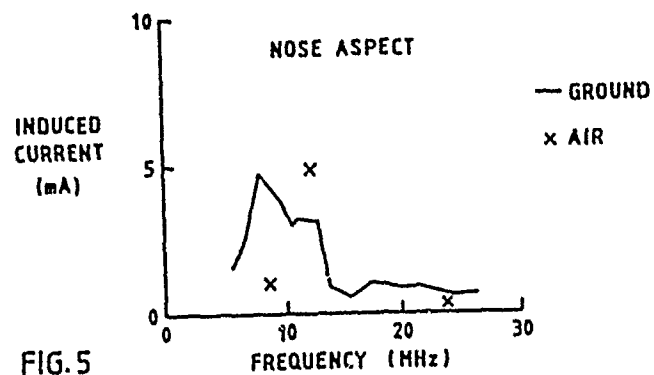


FIG. 5

PRINCIPALES CARACTERISTIQUES DES FOUOROIENTS SUR AVIONS

par J.L. Boulay

Office National d'Etudes et de Recherches Aéronautiques
 BP 72, 92322 Châtillon Cedex
 France

RESUME

La première partie de l'exposé est consacrée à l'examen des paramètres de simulation de l'environnement foudre qui sont actuellement appliqués dans le domaine aéronautique ; on indique ensuite les raisons qui entraînent un approfondissement et une extension de ces techniques d'essais. On analyse les principaux résultats qui viennent d'être obtenus lors de campagnes d'essais en vol sur des avions directement impactés par des décharges de foudre ; enfin, on aborde les conséquences de ces nouvelles données au plan des essais d'environnement à la foudre à mener dans un proche avenir.

1. PARAMETRES DE SIMULATION ACTUELLEMENT UTILISES

Jusqu'à ce jour, les équipements aéronautiques ainsi que les structures d'aéronefs sont testés ou qualifiés à un environnement foudre suivant des procédures d'essais directement adaptées de mesures effectuées en présence de foudroiements au sol.

Ces mesures ont été réalisées depuis de nombreuses années par certains laboratoires spécialisés en Europe et aux Etats-Unis [1,2] et pour la plupart, elles consistent en des relevés de courant de décharge sur des points d'impact de foudre appropriés. Depuis 1970, des expériences sont réalisées en France [3,4], aux Etats-Unis [5] et au Japon [6], grâce à des techniques de déclenchement artificiel de la foudre : ces techniques basées sur le lancement de petites fusées munies d'un fil conducteur connecté au sol sont très efficaces et surtout permettent de s'affranchir du caractère aléatoire de la foudre naturelle à la fois dans le temps et dans l'espace.

La communauté aéronautique dispose ainsi d'un grand nombre de données sur le courant de décharge de foudre et c'est l'enveloppe de ces données qui a permis de définir et de réaliser les moyens de simulation utilisés aujourd'hui.

Rappelons brièvement les différents mécanismes mis en jeu dans la décharge de foudre qui s'établit entre nuage et sol. Au départ, on considère qu'il existe une différence de potentiel de l'ordre de 10^6 V entre le sol et le nuage électrisé ; cette différence de potentiel conduit à une distribution de champ électrique dont la valeur peut atteindre 10^6 V.m⁻¹ au sol et quelques 10^5 V.m⁻¹ à l'intérieur du nuage. C'est précisément lorsque ce champ atteint en un endroit donné du milieu nuageux une valeur critique qu'une décharge est initiée puis peut se propager vers le sol.

Comme l'indique le schéma de la figure 1, cette décharge "précurseur" progresse par bonds, typiquement de l'ordre de 50 m, à une vitesse maximale de 10^8 m.s⁻¹ ; lorsque cette décharge parvient au voisinage du sol elle induit une autre décharge de polarité inverse en provenance du sol ; les deux décharges vont se connecter et ainsi établir un court-circuit entre le nuage et le sol ; c'est à cet instant qu'apparaît dans le canal préalablement formé une décharge extrêmement violente que l'on appelle "onde de retour" et qui correspond à la première impulsion majeure du courant de foudre.

Après un temps d'attente qui peut durer plusieurs dizaines de ms, une seconde décharge "précurseur" s'établit (en général cette seconde décharge et les suivantes ont une progression continue et très rapide) conduisant à une seconde "onde de retour" et par conséquent à une seconde impulsion de courant. Tant que le nuage n'est pas complètement déchargé, de tels processus se répètent, sachant qu'entre deux impulsions de courant, peut s'établir un régime de courant permanent dont l'amplitude atteint 10^3 A.

Les différentes "ondes de retour" sont visibles sur la photographie de la figure 2 représentant un foudroiement déclenché artificiellement sur une structure d'étude au sol ; la zone blanche et diffuse correspond au passage d'un courant permanent.

A titre d'exemple on donne sur la figure 3 l'onde de courant obtenue lors d'un foudroiement déclenché réalisé aux Etats-Unis en 1981 ; l'échelle du haut permet de suivre l'évolution du courant permanent qui dans le cas présent dure plus de 700 ms et dont l'amplitude atteint 300 A ; l'échelle du bas indique les impulsions d'"onde de retour" qui peuvent parfois se superposer à la composante continue ; on note que la première impulsion atteint ici pratiquement 40000 A.

C'est à partir de ces données que la communauté aéronautique a défini une "agression normalisée" devant être appliquée en essais d'environnement.

S'agissant jusqu'à maintenant d'avions à structure essentiellement métallique et disposant d'équipements électroniques jugés peu vulnérables aux effets électromagnétiques, l'"agression normalisée" a eu pour objectif principal de représenter correctement les ondes de retour et les composantes persistantes de la décharge, c'est-à-dire les processus énergétiques du phénomène ; il s'agit en effet de vérifier, entre autres, la tenue mécanique des éléments de structure, le comportement des réservoirs de carburant, et la vulnérabilité des équipements externes [7].

Afin d'établir des conditions d'essais donnant des marges de garantie suffisantes, l'agression simulée, correspond à un cas de foudroiement majorant relevé dans 1 % des cas (99 % des cas de foudroiement recensés sont donc couverts par les essais). Une forme d'onde approchée est celle donnée sur la figure 4 ; elle se compose :

- d'une première impulsion définie par les points ABCDE, dont la valeur crête est de 2.10^4 A et dont l'intégrale d'action $\int i^2 dt = 2.10^4 A^2.s$ est surtout fournie par la phase CD ;
- d'une composante persistante EG de valeur moyenne 470 A et correspondant à environ 200 C ;
- d'une seconde impulsion définie par les points FHIJK dont la valeur crête est de 5.10^3 A.

Plusieurs laboratoires dans le monde sont équipés de générateurs de puissance qui permettent d'assurer l'agression de la figure 4.

Cependant, depuis peu, apparaissent de nouveaux projets d'avions ou d'hélicoptères où les caractéristiques de base qui ont été signalées plus haut ne sont plus vraies, à savoir :

- les structures des aéronefs de la prochaine génération seront de plus en plus fabriquées à partir de matériaux composites de type kevlar, composite carbone, etc... et ceci dans le but de gagner en masse et en performance à tenue mécanique équivalente ;
- l'électronique de bord devient non seulement plus sophistiquée mais devient également vitale sur le plan de la sécurité des vols ; l'exemple le plus significatif est celui des commandes de vol électriques. Par ailleurs, en raison de l'évolution des composants utilisés, les électroniques de bord s'avèrent beaucoup plus vulnérables aux interactions électromagnétiques parasites.

Les moyens de protection à mettre en oeuvre sur les aéronefs modernes et les moyens d'essais d'environnement à la foudre pour les qualifier nécessitent l'approfondissement de la connaissance de la menace et surtout la prise en compte de tous les aspects de cette menace et pas seulement celui du courant direct de la décharge.

2. L'INTERACTION Foudre AERONEF

Il est clair que le but final à atteindre dans un programme de qualification est de s'assurer du bon fonctionnement des équipements embarqués et ceci avec une marge de sécurité suffisante. Pour arriver à cette analyse de vulnérabilité, plusieurs étapes sont à franchir ; de manière très sommaire, essayons de définir ces étapes successives :

a) Il s'agit tout d'abord de caractériser l'agression foudre celle-ci devant être exprimée non seulement en terme de courant de décharge, mais également en terme de champs électromagnétiques ; comme l'indique le schéma de la figure 5, l'aéronef peut en effet être soumis :

- soit à un foudroiement direct, le courant traverse alors la structure entre un point d'entrée et un (ou plusieurs) point(s) de sortie,
- soit à un foudroiement de proximité, l'avion est alors uniquement affecté par le champ électromagnétique de la décharge.

Depuis quelques années, plusieurs programmes importants de recherches sur la foudre sont menés dans le monde ; ils ont apporté de nouvelles connaissances de base et en particulier dans le domaine du rayonnement électromagnétique des décharges [8,9,10].

b) La seconde étape consiste à déterminer (figure 5) le "problème externe" de l'avion qui correspond à la distribution des composantes électrique et magnétique (E_e , H_e) du champ sur sa structure ; dans le cas d'un foudroiement de proximité, E_e et H_e sont les champs induits par le rayonnement dû à $i(t)$; dans le cas d'un foudroiement direct, H_e sera dû essentiellement au courant de décharge et E_e aux variations de potentiel de l'aéronef. En effet, l'avion étant situé entre des sources dont la différence de potentiel atteint 10^6 V, on peut logiquement admettre de grandes variations des termes E_e ou H_e sur la structure pendant la phase de connexion de l'arc électrique. Si l'on connaît les principales propriétés d'une décharge de foudre, l'application de codes numériques tridimensionnels permet en théorie de résoudre le "problème externe" sur des structures complexes d'aéronefs [11-13]. Par ailleurs, l'objectif principal des programmes de mesures sur avions qui seront présentés au paragraphe 3 a porté sur la détermination expérimentale de ce "problème externe" de façon à pouvoir corréler concrètement, en présence de foudroiements réels, le courant de décharge et les champs électromagnétiques sur la structure.

c) La troisième étape vise à analyser le "problème interne", c'est-à-dire à déterminer la distribution des composantes E_i et H_i du champ électromagnétique à l'intérieur du fuselage de l'aéronef ; cette distribution peut être obtenue par l'application de diverses fonctions de transfert T telles que :

$$(H_i, E_i) = T \otimes (H_e, E_e)$$

Ces fonctions de transfert correspondent à des mécanismes de pénétration du champ électromagnétique soit par diffusion, soit par les ouvertures électromagnétiques créées par différents éléments de la structure. Les propriétés de ces différents éléments de structure sont évidemment essentielles pour l'analyse du couplage.

A titre d'illustration, on a indiqué sur la figure 6, les effets de ces mécanismes de couplage électromagnétique sur une structure ; il s'agit de résultats obtenus grâce à une expérience très simple de

laboratoire : une maquette cylindrique en aluminium possède une ouverture carrée de 20 mm de côté qui peut être, soit laissée ouverte, soit fermée par un capotage métallique vissé ; un câble-test est disposé axialement à l'intérieur de la maquette et est connecté, électriquement aux deux flasques extrêmes de la maquette cylindrique. On mesure globalement les perturbations induites par l'enregistrement du courant de court-circuit affectant un câble-test. L'excitation de la maquette est créée par la décharge d'un condensateur donnant un courant $I(t)$ de type bi-exponentiel avec un temps de montée de 30 ns et une valeur crête de quelques 10^4 A. Ouverture fermée, le courant parasite sur le câble est d'une part de faible amplitude mais également de temps de montée assez long : il s'agit ici d'un mécanisme de couplage par diffusion agissant comme un filtre passe-bas dont la constante de temps est la constante de diffusion du matériau (10 μ s pour 1 mm d'aluminium). Ouverture libre, on enregistre une perturbation beaucoup plus importante (l'amplitude atteint ici 150 mA), avec un temps de montée identique à celui de l'agression (pas de filtrage) ; on note aussi l'apparition d'un signal oscillatoire parasite qui correspond à la résonance de la structure. En changeant la position du câble test, à l'intérieur du cylindre et en l'approchant de l'ouverture, on peut atteindre des modulations oscillatoires du courant dépassant 5 à crête à crête.

Toujours à titre d'exemple, on donne sur la figure 7 un résultat de mesures de couplage électromagnétique par ouverture, obtenu sur avion en vol pendant un foudroiement. Il s'agit, pour cet exemple, d'une ouverture circulaire de 38 cm de diamètre ; deux capteurs mesurent respectivement le champ magnétique externe H_e et le champ magnétique interne H_i dans l'axe de l'ouverture à 50 cm de celle-ci.

On remarque, comme pour l'expérience de laboratoire, d'une part que H_e et H_i ont la même forme d'onde, d'autre part que superposées à l'impulsion globale, on voit apparaître des oscillations caractéristiques de la résonance du fuselage de l'avion. Dans le cas précis de la figure 7, la fonction de transfert T du couplage est égale à $1/20$.

d) Enfin, la dernière étape vise, connaissant les distributions internes H_i et E_i , à déterminer les perturbations susceptibles d'affecter les équipements de bord. Ces déterminations sont recherchées à partir des équations de ligne, l'agression finale étant représentée par le courant de court-circuit I_{cc} ou la tension de circuit ouvert V_{cc} affectant l'équipement. A titre d'exemple, on examine maintenant un cas réel observé en vol en présence de foudroiement ; la configuration utilisée correspond à un câble court-circuité placé dans le fuselage de l'avion à 50 cm de l'ouverture déjà signalée précédemment. On dispose ici des mesures des deux composantes E_e et H_e du champ électromagnétique externe à proximité de l'ouverture ainsi que de celle du courant I_{cc} traversant le câble. Les résultats obtenus lors d'un foudroiement direct de l'avion sont présentés sur la figure 8. Les courbes (a) et (b) correspondent aux variations des paramètres E_e et H_e enregistrés sur une période de 100 μ s ; la courbe (c) qui fournit le courant de court-circuit sur la ligne montre que celui-ci a une forme d'onde très voisine de H_e .

Cette similitude peut être démontrée théoriquement ; en effet, on sait qu'en présence d'ouvertures de petites dimensions, la valeur de I_{cc} est calculable à partir de la théorie des dipôles équivalents. Cette théorie donne la source de tension équivalente V_{eq} et la source de courant équivalente I_{eq} , ainsi que les inductances et capacités équivalentes L_{eq} et C_{eq} liées à la configuration ouverture-ligne. On a [14] :

$$\begin{cases} V_{eq} = \mu_0 \frac{d}{\pi R^2} \alpha_e p H_e \\ I_{eq} = \epsilon_0 \frac{d}{\pi R^2} \frac{Z_0}{Z_c} \alpha_m p E_e \\ L_{eq} = \mu_0 \alpha_e \left(\frac{d}{\pi R^2} \right)^2 \\ C_{eq} = \epsilon_0 \frac{\alpha_m}{Z_c^2} \alpha \left(\frac{d}{\pi R^2} \right)^2 \end{cases}$$

α_e et α_m sont respectivement les polarisabilités électrique et magnétique de l'ouverture de rayon R ; d est la distance entre la ligne et la paroi, R est la plus petite distance entre la ligne et l'ouverture, Z_0 et Z_c sont respectivement l'impédance d'onde et l'impédance caractéristique de la ligne. Pour une ligne en court-circuit I_{eq} peut être négligé devant V_{eq} et on a par conséquent :

$$I_{cc} = \mu_0 \frac{d}{\pi R^2} \frac{\alpha_m}{L_{eq} + L_l} H_e$$

L_l est l'inductance de la ligne ; on remarque que I_{cc} est bien proportionnel à la composante magnétique H_e .

Avec $\alpha_m = \frac{4 R^2}{3}$, on calcule ainsi : $\frac{I_{cc}}{H_e} = 1,4 \cdot 10^{-3}$

Pour les impulsions (2) et (3) de la figure 8, on obtient les résultats suivants :

Impulsions	$He (A.m^{-1})$	Icc (A) calculé	Icc (A) mesuré
2	4,2	5,9	6,5
3	10,5	14,7	17,1

La comparaison des valeurs de Icc mesurées et calculées permet ainsi de valider l'application du modèle des dipôles équivalents pour une ouverture de petite dimension. Signalons également qu'en règle générale I_e ne peut pas être négligé, l'exemple cité n'étant qu'un cas particulier où la ligne-test est en court-circuit.

L'examen de l'interaction foudre-avion qui vient d'être sommairement abordé, montre à l'évidence que l'un des tous premiers aspects à examiner est celui du "problème externe" : ce "problème externe" ne peut être que partiellement abordé si l'on s'en tient aux caractéristiques des foudroiements, détectés au sol, ceux-ci ne donnant qu'une information liée aux ondes de retour.

La connaissance complète des formes d'ondes liées à He et à I_e pour un avion en vol suppose successivement l'analyse des phénomènes liés à la connexion de la décharge avec la structure, celle des phénomènes associés aux décharges dites intra-nuage donc ne prenant pas en compte l'influence du sol et enfin celle, bien entendu, des phénomènes associés aux décharges nuage-sol. Jusqu'en 1980, aucune donnée sur avion n'était disponible ; depuis, trois programmes importants sur les interactions foudre-avion ont été entrepris en France [15-17] et aux Etats-Unis [17-20].

L'objet du prochain paragraphe est de donner un aperçu des principaux résultats obtenus au cours de ces programmes de recherches et de montrer l'orientation que devrait prendre les nouveaux moyens d'essais d'environnement à la foudre à partir de 1990 que ce soit pour les aéronefs de la nouvelle génération ou que ce soit pour les lanceurs ou avions spatiaux.

3. CARACTERISTIQUES DES FOUDROIEMENTS OBSERVÉS EN VOL

En France, plusieurs campagnes d'essais ont été effectuées sur un avion Transall avec comme objectifs essentiels les mesures des composantes He et I_e ainsi que celles des courants de décharge [16,17].

Aux Etats-Unis, deux programmes ont été mis en place :

- le premier par la NASA à partir de 1981 avec un avion de type F106 ; pour des détails sur l'instrumentation de l'avion et sur les objectifs de l'étude, le lecteur pourra se reporter au document [18].
- le second par l'USAF et la FAA à partir de 1984 avec un avion de type CONVAIR CV 580 ; l'ONERA a été associé à ce programme en 1985 dans le but de procéder, avec ses propres moyens de mesure, à la détermination des champs externes [19,20].

Tous ces programmes ont, de fait, suivi la même démarche :

- a) tenter de confirmer les paramètres associés aux ondes de retour qui peuvent toujours être considérés comme majeurs pour la sécurité des avions,
- b) approcher les effets spécifiques correspondant à la phase d'attachement de l'arc sur la structure,
- c) examiner les conditions critiques du champ électrique atmosphérique qui conduisent à l'établissement de la décharge de foudre sur l'aéronef.

3.1. Mesures obtenues sur l'avion TRANSALL

Le système de mesure utilisé sur l'avion Transall est représenté sur le schéma de la figure 9. On y distingue cinq capteurs de champ électrostatique destinés à connaître les conditions critiques de déclenchement ainsi que la valeur du potentiel électrique de l'avion au moment de l'impact de la foudre, deux capteurs de courant de décharge l'un étant placé sur une première perche située à l'avant de l'appareil, le second sur la seconde perche placée à l'arrière, enfin 2 capteurs placés à l'avant, sur le fuselage de l'avion, permettant de mesurer les composantes électrique et magnétique externes du champ. Cette installation a été considérablement complétée lors de la campagne 1988.

Le Transall a effectué ces vols d'essais à des altitudes typiquement comprises entre 0°C et - 10°C. On dispose actuellement d'informations sur une cinquantaine de déclenchements de foudre dont 10 en 1988.

Un résultat typique obtenu avec un capteur de champ He externe est donné sur la figure 10. Cet événement a été observé le 7 juin 1984, l'altitude de l'avion était de 3500 m et la température extérieure de - 10°C.

On observe sur la courbe (a) que le signal He est essentiellement composé d'impulsions pendant une période de quelques centaines de ms. Pour pratiquement toutes les mesures, la forme d'onde du paramètre He

comprend un premier train d'impulsions (1) pendant un temps compris entre 2 et 1 ms dont l'amplitude crête à crête augmente de quelques A.m² jusqu'à 700 A.m² ; ce premier train est généralement suivi d'impulsions isolées (2), (3) avec des intervalles de temps compris entre 10 et 100 ns.

La courbe (b) indique, avec plus de détails, les caractéristiques des impulsions. Ne pendant les deux premières ms. Les intervalles de temps entre impulsions ne sont pas toujours constants et ils restent néanmoins du même ordre grandeur, à savoir entre 100 et 100 ns ; après cette phase, on observe généralement une décroissance de cet intervalle qui peut atteindre une valeur minimale d'environ 20 ns. Bien que non représentées sur cette figure, on observe des impulsions de champ électrique E_e identiques aux impulsions E_c (les deux étant parfaitement synchronisées). Les valeurs crête à crête de la composante E_c restent sensiblement constantes pendant toute la durée du train, avec une valeur moyenne de 100 kV/m.

La courbe (c) montre une impulsion E_c isolée pendant une période de l'ordre de 1.6 ns ; le temps de montée de l'impulsion est d'environ 10⁻⁹s et on observe une oscillation superposée pendant la phase de relaxation de l'impulsion ; la demi-période de ces oscillations est ici voisine de 1.60.10⁻⁹s valeur correspondant à la première résonance du fuselage du Transall.

La valeur maximale de l'impulsion E_c est de 750 A/m ; si nous considérons, dans ces conditions, une densité de courant uniforme autour du fuselage dans la zone d'implantation du capteur l'amplitude correspondante du courant serait de 3.5 kA. Bien que les paramètres E_c et E_e soient essentiels pour l'analyse du couplage électromagnétique sur avion, on sait qu'il est important d'obtenir des informations aussi précises que possible sur les formes d'onde du courant de décharge.

On rappelle que dans sa configuration d'essai, l'avion Transall est équipé de 2 perches de 4 m de longueur fixées sur le radome et sur la partie arrière de l'appareil. Un shunt résistif est placé entre chaque perche et la structure. Cette configuration correspond à la situation la plus favorable pour l'étude des courants de décharge puisque les extrémités de ces perches sont, la plupart du temps, les zones d'attachement de l'arc électrique. Nous nous limitons à la présentation d'une seule forme d'onde obtenue au cours du vol du 21 juin 1986 : cette forme est typique de toutes celles qui ont été observées durant les essais. Sur la figure 11, les courbes (a) et (b) donnent, pendant le même intervalle de temps, l'évolution des courants enregistrés sur la perche avant (I_a) et sur la perche arrière (I_r). Les polarités de ces deux courants indiquent un point d'entrée à l'arrière de l'appareil et un point de sortie sur le radome.

Pendant une première période de 120 ns, on observe des évolutions identiques pour les deux courants : au départ, un accroissement très rapide de l'amplitude du courant I_a est suivi par une phase de courant permanent comportant des impulsions isolées C ; on constate une impulsion importante D détectée par les 2 capteurs. L'arrêt du courant I_a en E est attribué à un phénomène d'arc balayant entre l'extrémité de la perche et le fuselage sans modification du signal I_r . Les valeurs crêtes pour I_a et I_r sont supérieures à 2.10³A et la valeur de la composante continue est d'environ 300 A.

Par intégrations successives de I_a et I_r , on obtient :

$$\text{Pour } I_a : Q = 19 \text{ C et } \int i^2 dt = 6.6 \cdot 10^3 \text{ A}^2 \cdot \text{s}$$

$$\text{Pour } I_r : Q = 20 \text{ C et } \int i^2 dt = 4.8 \cdot 10^3 \text{ A}^2 \cdot \text{s}$$

La courbe (c) donne le détail de la zone A ; on voit clairement apparaître un train d'impulsions pendant environ 3 ms ; après cette zone, le courant devient essentiellement constant avec des impulsions isolées de faible amplitude.

Le démarrage du train d'impulsions est correctement visualisé, sur les deux courbes (d) et (e) pendant une période de temps de 4 ms ; les impulsions correspondantes de I_a et I_r sont quasi-identiques. Deux phases caractéristiques peuvent ainsi être mises en évidence :

- une première phase 1, où les impulsions sont séparées par des intervalles de temps non réguliers et où aucune composante permanente n'est mise en évidence,
- une seconde phase 2 correspondant au démarrage de la composante permanente qui croît régulièrement avec le temps ; les impulsions successives sont séparées par des intervalles de temps à peu près égaux.

Nous allons montrer que ces caractéristiques sont également observées sur le CV 580 de l'USAF.

1.2. Mesures observées sur l'avion CV 580

L'instrumentation de l'avion CV 580 [19] est schématiquement représentée sur la figure 12 ; on dispose de 4 capteurs de courant installés en extrémités d'ailes, sur le haut de dérive et sur la partie arrière, de plusieurs capteurs E_c et E_e et de capteurs de type antenne VHF et MF, cette dernière permettant de suivre le potentiel instantané de l'avion.

Les expériences effectuées sur le CV 580 ont donné de nombreux résultats ; nous allons limiter notre présentation à quelques données spécifiques concernant essentiellement la phase d'attachement de l'arc électrique sur la structure de l'avion.

Mesures de champ électromagnétique et de courant

Les mesures obtenues avec le CY 380 permettent d'identifier sans ambiguïté la stricte corrélation entre les impulsions H_e et I observées sur l'avion Transall. Cette corrélation apparaît clairement sur la figure 13. Cette figure correspond à un foudroiement sur l'avion à une altitude de 14000 pieds pour une température extérieure de 0°C. L'attachement du canal de décharge s'établit sur la voilure droite et la forme d'onde complète de ce courant I_m est donnée par la courbe (a) ; on constate que la durée du phénomène est d'environ 300 ns et que cette forme d'onde est constituée d'une composante permanente à laquelle se superposent des impulsions. L'intégration de ce signal permet de calculer une charge neutralisée de 300 C.

Les courbes (c) et (b) montrent en détail les formes d'ondes I_m et H_m correspondant aux 5 premières ns de la séquence. Le train d'impulsions du champ électromagnétique est tout à fait stable à celui détecté sur le Transall, de même que pour le courant. Nous associons donc sans ambiguïté les impulsions successives du champ et du courant pendant cette phase de l'éclair.

Mesures spécifiques liées à l'attachement

Au point de vue de l'ingénieur, il est évident que les caractéristiques de courant et de champ décrites conduisent à de nouveaux concepts pour les méthodes de simulation d'un environnement foudre. D'un point de vue plus fondamental et pour une meilleure compréhension des besoins de simulation, d'autres informations sont nécessaires pour caractériser le comportement de l'avion pendant la phase d'attachement.

Sachant que l'avion, juste avant l'impact de l'arc est dans une configuration à potentiel flottant, il est évident que des déplacements de charges électriques sur la structure vont intervenir avant toute détection de courant ou de champ magnétique ; ces déplacements peuvent être observés par des antennes soit de type BF, soit de type VHF. Ces phénomènes sont illustrés sur la figure 14 qui correspond à un foudroiement déclenché, l'avion est à une altitude de 14000 pieds, sa vitesse est de 80 m/s et la température extérieure de +1°C.

La courbe (a) représente l'évolution du courant de décharge, sa forme d'onde est tout à fait identique à celles qui viennent d'être décrites. Les courbes (b) et (c) représentent les signaux détectés par les antennes BF et VHF ; elles conduisent aux commentaires suivants :

- on observe un processus de pré-attachement au point 0 qui se caractérise par une grande variation du champ BF (100 kV/m) et par une augmentation importante du signal détecté par l'antenne VHF (tout ceci sans détection notable de courant),
- après une phase d'attente de 400 ns, le déclenchement réel du foudroiement apparaît au point A ; cette phase d'attachement est caractérisée par des impulsions simultanées du champ BF et du courant ainsi que par une augmentation notable du champ VHF,
- cette phase d'attachement est suivie par une période correspondant à une composante permanente du courant à laquelle se superposent des impulsions isolées que l'on retrouve à la fois sur les capteurs de courant, de champ BF et de champ VHF.

4. CONSÉQUENCES AU PLAN DE LA SIMULATION

A/ Bien qu'aucun des essais sur avion n'ait mis en évidence de façon certaine des phénomènes de foudroiement entre avion et sol (environ 700 événements répertoriés pour les trois programmes connus à ce jour), il est clair que les méthodes de simulation au sol visant à reproduire l'"onde de retour" doivent être maintenues. Au plan énergétique et particulièrement dans le domaine des essais de qualification des réservoirs de carburant en composite carbone, l'application de cette onde de courant majorante (figure 4) restera le test de sécurité nécessaire.

Rappelons que toutes les mesures récentes effectuées sur les "ondes de retour" ne conduisent pas à des modifications importantes des équipements d'essai utilisés jusqu'à maintenant ; on peut seulement admettre que des modifications seront probablement nécessaires et appliquées dans le futur au niveau des spécifications du temps de montée de la première impulsion (zone AB de la figure 4).

B/ Les essais menés sur avion ont mis en évidence une phase très spécifique liée à la connexion de l'arc électrique sur la structure du véhicule. Cette phase correspond à une série d'impulsions de champ électromagnétique définies par les paramètres suivants :

- valeur crête de H_e : 2 à 3.10^3 A.m⁻¹,
- valeur crête de E_e : 1 à 2.10^3 V.m⁻¹,
- fréquence de répétition : entre 100 et 300 μ s pendant 4 ns,
- durée totale de la phase d'attachement : 10 à 15 ns.

Ces impulsions peuvent avoir des répercussions très importantes sur les équipements électroniques de bord ; il faut par conséquent que cette phase de foudroiement soit prise en compte dans le futur.

Les instances de normalisation américaines et européennes discutent déjà de l'appropriation des effets de H_e sur les équipements et des accords internationaux devraient être trouvés assez rapidement.

Reste le problème de E_e qui doit être analysé en détail de façon à être persuadé de son intérêt pratique ; l'application de spécifications relatives au paramètre E_e entraînerait la définition puis la réalisation de nouveaux générateurs d'essais qui n'existent pas pour le moment.

REFERENCES

- [1] - R.A. Uman, "Lightning", Mc Graw Hill Book Company, New York, 1969.
- [2] - R.W. Golde, "Lightning", Vol. 1, Academic Press, 1977.
- [3] - St Privat d'Allier Research Group, "Eight years of lightning experiments at St Privat d'Allier", R.G.E., n° 9, septembre 1982.
- [4] - P. Laroche, A. Delannoy, F. Metzger, "Neutralized electrical charges location during triggered lightning flashes", ICOLSE, Oxford, 23-25 mars 1982.
- [5] - F. Hubert et al., "Triggered lightning in New Mexico", J.G.S., Vol. 89, n° D2, p. 2511-2521, 1984.
- [6] - E. Morii and M. Sakurao, "Observation on final jump of discharge in the experiment of artificially triggered lightning", IRE Trans. PAS-104, pp. 29.10-29.17, 1985.
- [7] - J.A. Fisher, J.A. Flunar, "Lightning protection of aircraft", NASA reference publication 1008, octobre 1977.
- [8] - E.P. Krider, C.D. Veidman, "The submicrosecond structure of lightning radiation fields", ICOLSE, Fort Worth, Texas, juin 1983.
- [9] - A. Bondiou, G. Labaune, J.P. Marque, "Electromagnetic radiation associated with the formation of an electric breakdown in air", J.A.P., 61 (2), janvier 1987.
- [10] - P. Richard et al., "UMF interferometric imaging of lightning", ICOLSE, Fort Worth, Texas, juin 1983.
- [11] - K. Holland, "Threde, a free field coupling and scattering code", IEEE Nuclear Science, Décembre 1977.
- [12] - K. Holland, L. Simpson, "Finite difference analysis of EMP coupling of thin struts and wires", IEE EMC, mai 1981.
- [13] - J. Grando, G. Labaune, "Using finite difference analysis in the calculation of current flow over structures", 7th Int. Symp. on Electromagnetic Compatibility, Zurich, 3-5 mars 1987.
- [14] - K.S.M. Lee, "EMP interactions: principles, techniques and reference data", AFVL TR 80-M02, décembre 1980.
- [15] - P. Laroche et al., "In flight thunderstorm environment measurements during the Landes 84 campaign", 10th ICOLSE, Paris, juin 1985.
- [16] - J.P. Moreau, J.C. Alliot, "E and H fields measurements on the Transall C160 aircraft during lightning flashes", 10th ICOLSE, Paris, juin 1985.
- [17] - P. Laroche, "Airborne measurements of electrical atmospheric field produced by convective clouds", 10th ICOLSE, Paris, juin 1985.
- [18] - F.L. Pitts, "Electromagnetic measurements on lightning strikes to aircraft", AIAA 19th Aerospace Sci. Meeting, 1981.
- [19] - F.L. Rustan et al., "Airborne measurements of the rise-time in lightning return stroke fields", ICOLSE, Fort Worth, Texas, juin 1983.
- [20] - F.L. Rustan, J.P. Moreau, "Aircraft lightning attachment at low altitudes", 10th ICOLSE, Paris, juin 1985.

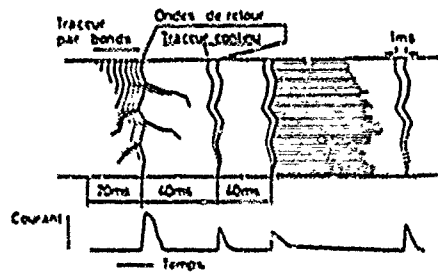


Fig. 1 - Schéma de principe d'une décharge de foudre entre nuage et sol.

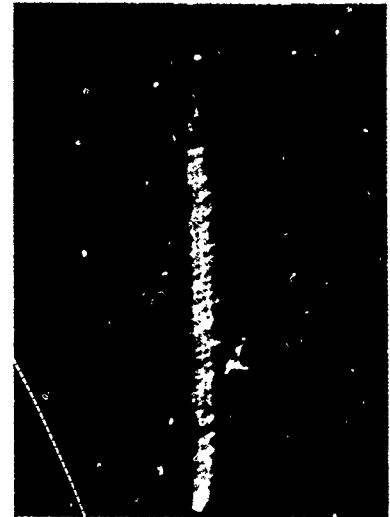


Fig. 2 - Illustration d'un foudroiement déclenché.



Fig. 3 - Onde de courant associée à un foudroiement au sol.

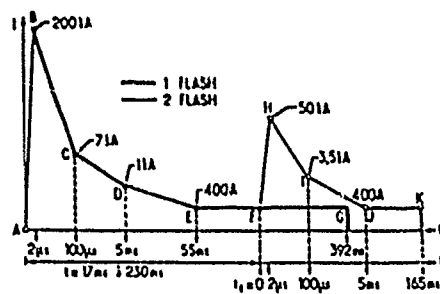


Fig. 4 - Formes d'onde de courant utilisées en essais d'environnement dans le domaine aéronautique.

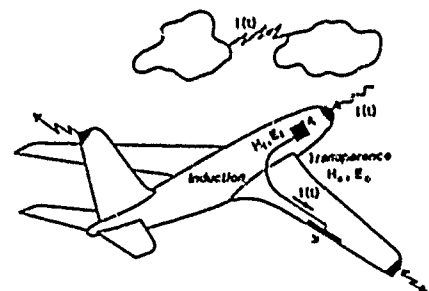


Fig. 5 - Interaction foudre-aéronef. Décharges directe et de proximité.

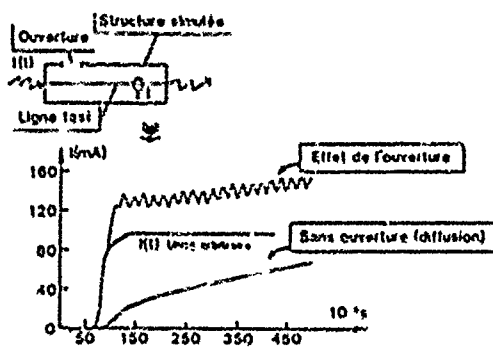


Fig. 6 - Mécanismes de couplage électromagnétique sur une structure.

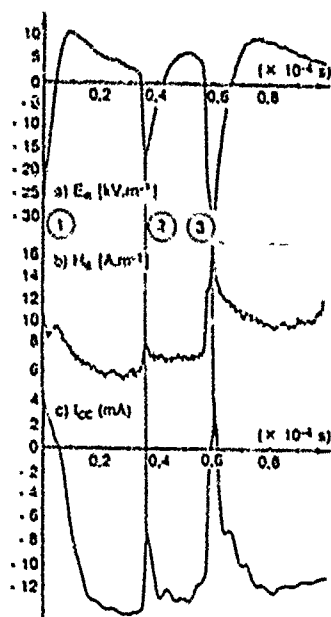
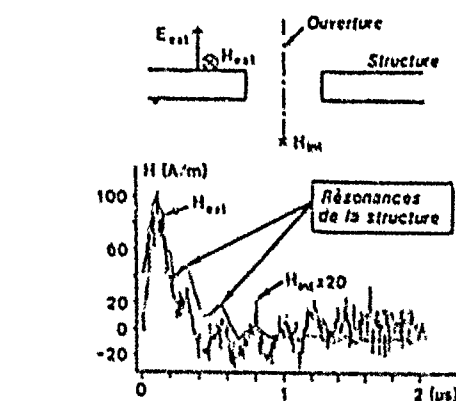
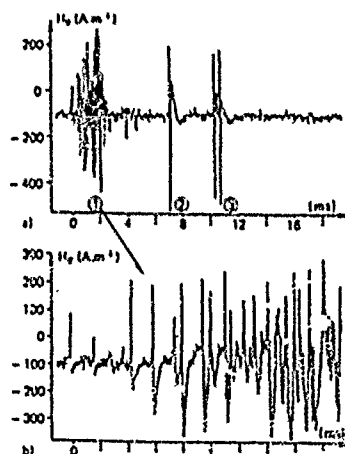


Fig. 8 - Perturbations électromagnétiques observées en vol pendant un orage.

a) Champ E_a ; b) Champ H_a ; c) Courant I_{cc} .



$$\text{Théorie dipole} \quad \frac{H_{01}}{H_{02}} = \dots \pm 10\%$$

Fig. 7 - Fonction de transfert mesurée sur aile en présence de foudroiement.

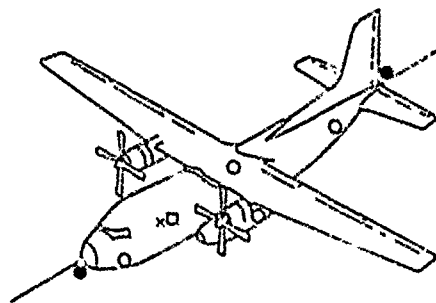
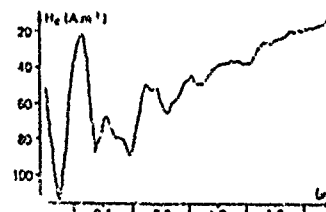


Fig. 9 - Instrumentation utilisée sur l'avion Transat.

Fig. 10 - Champ électromagnétique H_a en vol.



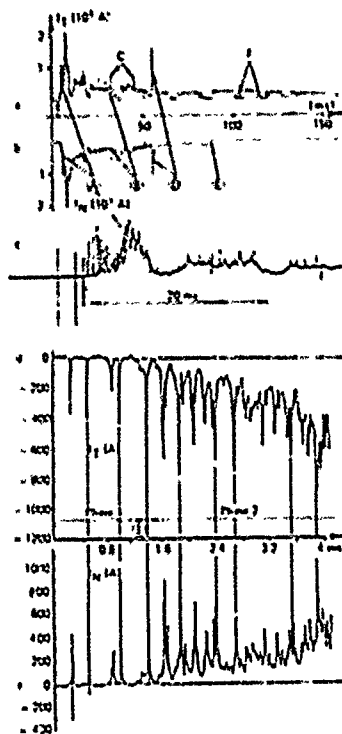


Fig. 11 - Courants de décharge en vol.

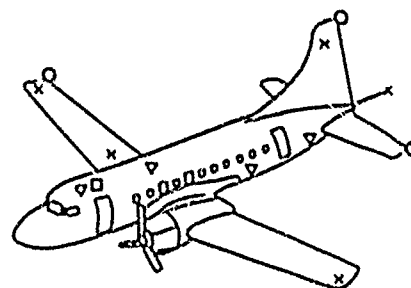


Fig. 12 - Instrumentation de l'avion CV 580.

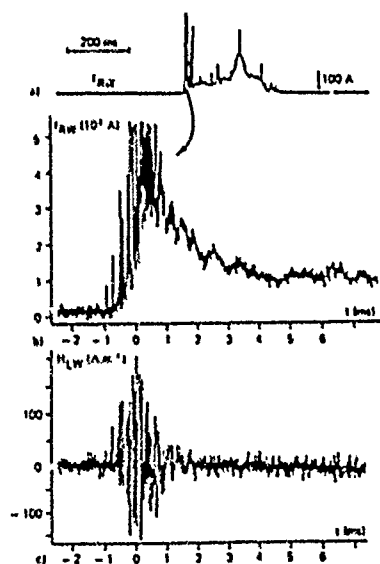
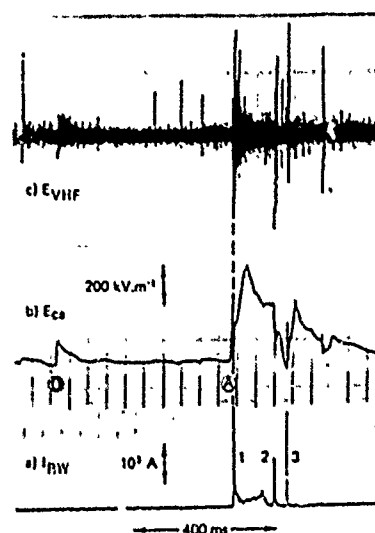
Fig. 13 - Courant et champ H_e associés à un foudroiement sur l'avion CV 580.

Fig. 14 - Phénomènes d'attachement sur l'avion CV 580.

DISCUSSION SESSION WITH REPRESENTATIVES
OF THE ROYAL NORWEGIAN AIR FORCE

Summary prepared by

J. F. RENAUDIE

Service Technique des Programmes Aeronautiques
France

General Introduction

The attendees at this Symposium included about twelve pilots from various squadrons of the Royal Norwegian Air Force who could be expected to have very relevant experience of operating in adverse environmental conditions. These pilots were therefore invited to take part in a specially organised discussion period in order to share their experiences in these areas with the rest of the Symposium attendees, and try to answer their questions.

INTRODUCTION

By Captain SKOGSTROM - Norwegian Air Force (Flight Safety Staff) :

On behalf of the participants at this Symposium, I would like to point out that we appreciate all the efforts made during the Symposium to present the background of the job of flying.

A few of the papers were a bit too theoretical for us, but most papers were very interesting, in particular those addressing wind shear, microburst, the Canadian Storm Campaign, icing research, electromagnetic interference. The Norwegian observers in the audience are members of the Royal Norwegian Air Force : Pilots of the P-3 ORION, SEA-KING rescue helicopter, and LYNX helicopters operating from coast-guard ships. These three types of aircraft are flying mostly over the BARENTS Sea, between NORWAY and SPITZ-BERGEN. We also have pilots of THIN OTTER and BELL 412 Helicopters, operating mostly in the Northern part of Norway, LOCKHEED C-130 HERCULES which operate mostly in Norway, but also in the USA, CANADA, EUROPE, THE MIDDLE EAST and AFRICA. Unfortunately, there are no F-16 pilots present. We will try to answer all your questions.

1 - Question (P. NEWTON, UK, BOSCOMBE DOWN): could you comment on whether you had operational problems when operating the LYNX on-board ships, in regard to electromagnetic interference. What are your major operating problems?

Answer (Lt. MIKKELSEN): We don't have any electromagnetic interference problem operating the LYNX. The major problems are found during winter weather: heavy winds, snow, icing.

2 - Question (G. F. LANGDON, UK, BOSCOMBE DOWN): How do you manage to keep operating when you have such a lot of darkness during winter in Norway? What are the implications for using your present equipment?

Answer (Lt. J. SALVESEN): Even in winter time there is some light; additionally the Northern part of Norway is well equipped for IFR flight, which is practiced by helicopters, in darkness; the ORION which flies over the sea does not have this problem.

3 - Question (R. C. A'HARRAH, USA): From your world-wide experience of the C-130, what was the most adverse flight environment encountered?

Answer (Capt. A. SKOGSTROM): According to my experience, the worst cases are met in the USA with the heavy cumulo-nimbus activities, and associated turbulence.

4 - Comment (Dr. J. A. MULDER, The Netherlands): We have spoken a lot these past days about wind shear, down drafts, microburst, etc. ... but, according to my own experience of flying over Europe, you find heavy winds, turbulence, crosswinds, rain, of course, more than wind shear such as found in the DALLAS accident, illustrated by a video-film. In thousands of flying hours I have never seen such an event!

Answer (Capt. A. SKOGSTROM): In Norway we try to teach our pilots to keep away from microbursts and other similar events; we have seen microbursts, in summer-time, as heavy as you could experience in the Mediterranean or in the USA. In addition, we encounter what we may call orographic wind shear, in the mountains.

Comment (Lt. J. SALVESEN): We have many problems with turbulence and associated windshear, but we seldom see downbursts due to cumulo-nimbus activities because there are only a few days when we encounter them, and in addition we are trained to avoid them.

- 5 - Question (Capt. I. PAYZIC - Turkey): Have you any experience with problems of fuel and hydraulic systems due to adverse weather?

Answer (Capt. A. SKOGSTROM): We have fuel leakage problems in turbulence, but no hydraulic problems.

Answer (Lt. HALVORSEN): I fly OELL A12 in the North of Norway. Our first A12 crashed in Norway on a day when the temperature was -27°C . We believe that it may have been a problem with the hydraulics system in cold weather that caused the crash, but this is still under investigation.

Comment (Mr. H.F. HOISETH) Material Command of the Norwegian Air Force): This last statement needs to be commented on. We have an on-going case with OELL helicopter, and nobody knows today the reason of the investigation, which is going on. Definitely temperature has something to do with that crash, since it has an effect on hydraulic fluids. In general, however I don't think that cold weather has any adverse effect to the extent that it has an impact on safety of flight. In Norway we are carrying out trials on the F16, to come to a decision on the use of the new hydraulic fluid MIL H 83292 on all aircraft in Norway. Unfortunately, the last winters in Norway were not cold enough to reach the expected -35°C (the lowest temperature recorded was -21° , and there is no significant difference down to that figure). So far we have not noticed any severe problem with hydraulics fluid, and therefore we have not changed to the new fluid used for instance in the US Air Force.

- 6 - Comment (Mr. H. F. HOISETH): I would like to comment on vision. We do have a problem with operating helicopters, and there is a programme going on to study some types of night vision goggles, which will most probably be used in the Royal Norwegian Air Force. We have not yet decided on the type to use.
- 7 - Question (J.H. DUC - France): Do you encounter operational problems at take-off and landing, such as slush ingestion at take-off or slipping on icy surfaces on landing? Also have you any evidence of the effects of the Aurora Borealis on aircraft avionics/electronic equipment?

Answer (Capt. A. SKOGSTROM): Operating on icy surfaces may be difficult in strong cross-wind conditions. Regarding the Aurora Borealis, there are only very minor effects on radio equipment.

- 8 - Question (J. RUNYAN - Boeing, USA): What type of de-icing or anti-icing fluid do you use. What has been your experience with these fluids.

Answer 1 (Capt. A. SKOGSTROM): We use "type 2" de-icing fluid called "KILL-FROST". I have no bad experience with it, if you use the right mixture for the temperature.

Answer 2 (Lt. H. VESTIGREN): Flying the TWIN OTTER in North Norway, we may encounter snow that no de-icing fluid or mixture can take away, and therefore we can't take off with a lot of snow on the wings.

Answer 3 (Lt. J. SALVESEN): On the P-3/ORION when there is heavy snow we keep the aircraft inside the hangar for as long as possible before expected take-off. We take it out of the hangar in order to have time to anti ice it, and we take off as soon as possible afterwards, especially when the temperature is close to 0°C . But it is true that we have many difficulties when heavy snow falls are present.

- 9 - Question (D. KEY, USA). I wonder what your experience is, in the Royal Norwegian Air Force, of aircraft lightning strikes, and in particular at what outside air temperature they are occurring?

Answer 1 (Capt. A. SKOGSTROM): In the Northern Part of Norway, in winter-time we experienced a lot of lightning strikes, some years ago, but we learnt to keep away from the clouds which generate strikes.

Answer 2 (Lt. J. SALVESEN): I have been in the Royal Norwegian Air Force for five years now; I have experienced one lightning strike: thanks to the new procedure we have had no lightning strikes for three years; when we had lightning strikes earlier there was some damage to the structure, especially the magnetic detector, which is a plastic boom, banana shaped; we also had some problems with the antennas, but nothing serious.

Answer 3 (Capt. A. SKOGSTROM): During the ten years that I have been flying the C-130, I just have had 3 to 4 lightning strikes with that aircraft, but as I said we learnt to keep out of this special environment.

10 - Comment (Mr. H.F. HOISETH): Speaking on behalf of the fighter pilots, since none of them were able to attend this meeting, I want to mention the bad experience we had with an F16: it was a build up of static electricity on the transparent part of the canopy, and a very strong discharge inside the cockpit like lightning, between the canopy and the helmet of the pilot. In fact this has been experienced by several pilots flying the F16 in Europe. Therefore, all F16 are now grounded for the time to improve the design and grounding of the transparent surface of the canopy.

11 - Question (C. YOHKINS, AFFIC, Edwards AFB, USA): Have you any corrosion problems flying aircraft so close to salt water?

Answer (Mr. H.F. HOISETH): Not really; corrosion in Norway is far less severe than, for instance, in central Europe, and operating close to the ocean does not seem to raise a problem. This is probably due to low temperature, which is more important than closeness to the sea. But of course, I must point out that we take great care to keep our aircraft in good shape.

12 - Question (Capt. I. PAYZC, Turkey): Could you tell us about operating your rescue helicopters with respect to wind, temperature and visibility. When do you have to cancel operations in Norway?

Answer (Lt. H. ANDERSEN, from Ode Air Station): It all depends on the mission. Is it a narrow fjord, or far from the sea? There are flying limitations depending on the pilot, and the mission.

13 - Comment (Lt. J. HALVORSEN/DELL 4126): I want to address darkness and icing.

Let's take icing first:

In the North of Norway you may encounter a special kind of icing, due to the warm sea current on the western coast, which produces moisture of the air. Even in clear sky, without clouds, with temperatures from -10 to -15 you can encounter icing because this moist air freezes on the rotorblades.

Let's take flying in darkness:

The problem is that you cannot see the showers and the clouds producing them. This is the biggest problem; but when the sky is clear, the snow reflects a lot of light, and it is not difficult to fly at moderate altitudes, of the order of 5000ft above the terrain.

CLOSING REMARKS

At the end of this discussion period, Professor SCHAEZLER, for the Technical Programme Committee, said that in his view this had been a worthwhile and informative discussion period. It was particularly appropriate to have had the positive involvement of attendees from the 'host' country and he greatly thanked the Norwegian pilots for this contribution to the Symposium.

REPORT DOCUMENTATION PAGE			
1. Recipient's Reference	2. Originator's Reference AGARD-CP-470	3. Further Reference ISBN 92-835-0527-1	4. Security Classification of Document UNCLASSIFIED
5. Originator	Advisory Group for Aerospace Research and Development North Atlantic Treaty Organization 7 rue Ancelle, 92200 Neuilly sur Seine, France		
6. Title	FLIGHT IN ADVERSE ENVIRONMENTAL CONDITIONS		
7. Presented at	the Flight Mechanics Panel Symposium held at Gol, Norway from 8 to 11 May 1989.		
8. Author(s)/Editor(s) Various	9. Date September 1989		
10. Author's/Editor's Address Various	11. Pages 390		
12. Distribution Statement	This document is distributed in accordance with AGARD policies and regulations, which are outlined on the Outside Back Covers of all AGARD publications.		
13. Keywords/Descriptors <div style="display: flex; justify-content: space-between;"> <div> All weather aviation Atmospheric disturbances Visibility </div> <div> Ice formation Electromagnetic pulses </div> </div>			
14. Abstract <p>These proceedings contain the papers presented at the AGARD Flight Mechanics Panel Symposium on Flight in Adverse Environmental Conditions held in Gol, Norway from 8 to 11 May 1989.</p> <p>Although AGARD has continued to be active in the various fields of flight in adverse environmental conditions it was considered to be important and timely to review the subject in a wider forum such as a Symposium.</p> <p>Four aspects of adverse environmental conditions of interest to the flight mechanics specialist were addressed by this Symposium; atmospheric disturbances, reduced visibility, icing, and electromagnetic disturbances. All four of these can seriously affect flight safety, comfort, and operational capability.</p> <p>The topic was considered to be particularly relevant to the needs of the military community which is putting increased emphasis on the ability of today's and tomorrow's aircraft to fly safely and effectively in the types of adverse conditions dealt with in this symposium.</p>			

<p>AGARD Conference Proceedings No.470 Advisory Group for Aerospace Research and Development, NATO FLIGHT IN ADVERSE ENVIRONMENTAL CONDITIONS Published September 1989 390 pages</p> <p>These proceedings contain the papers presented at the AGARD Flight Mechanics Panel Symposium on Flight in Adverse Environmental Conditions held in Gd, Norway from 8 to 11 May 1989.</p> <p>Although AGARD has continued to be active in the various fields of flight in adverse environmental conditions it was considered to be important and timely to review the subject in a wider forum such as a Symposium.</p> <p>P.T.O.</p>	<p>AGARD-CP-470</p> <p>All weather aviation Atmospheric disturbances Visibility Ice formation Electromagnetic pulses</p>	<p>AGARD Conference Proceedings No.470 Advisory Group for Aerospace Research and Development, NATO FLIGHT IN ADVERSE ENVIRONMENTAL CONDITIONS Published September 1989 390 pages</p> <p>These proceedings contain the papers presented at the AGARD Flight Mechanics Panel Symposium on Flight in Adverse Environmental Conditions held in Gd, Norway from 8 to 11 May 1989.</p> <p>Although AGARD has continued to be active in the various fields of flight in adverse environmental conditions it was considered to be important and timely to review the subject in a wider forum such as a Symposium.</p> <p>P.T.O.</p>	<p>AGARD-CP-470</p> <p>All weather aviation Atmospheric disturbances Visibility Ice formation Electromagnetic pulses</p>
<p>AGARD Conference Proceedings No.470 Advisory Group for Aerospace Research and Development, NATO FLIGHT IN ADVERSE ENVIRONMENTAL CONDITIONS Published September 1989 390 pages</p> <p>These proceedings contain the papers presented at the AGARD Flight Mechanics Panel Symposium on Flight in Adverse Environmental Conditions held in Gd, Norway from 8 to 11 May 1989.</p> <p>Although AGARD has continued to be active in the various fields of flight in adverse environmental conditions it was considered to be important and timely to review the subject in a wider forum such as a Symposium.</p> <p>P.T.O.</p>	<p>AGARD-CP-470</p> <p>All weather aviation Atmospheric disturbances Visibility Ice formation Electromagnetic pulses</p>	<p>AGARD Conference Proceedings No.470 Advisory Group for Aerospace Research and Development, NATO FLIGHT IN ADVERSE ENVIRONMENTAL CONDITIONS Published September 1989 390 pages</p> <p>These proceedings contain the papers presented at the AGARD Flight Mechanics Panel Symposium on Flight in Adverse Environmental Conditions held in Gd, Norway from 8 to 11 May 1989.</p> <p>Although AGARD has continued to be active in the various fields of flight in adverse environmental conditions it was considered to be important and timely to review the subject in a wider forum such as a Symposium.</p> <p>P.T.O.</p>	<p>AGARD-CP-470</p> <p>All weather aviation Atmospheric disturbances Visibility Ice formation Electromagnetic pulses</p>

<p>Four aspects of adverse environmental conditions of interest to the flight mechanics specialist were addressed by this Symposium: atmospheric disturbances, reduced visibility, icing, and electromagnetic disturbances. All four of these can seriously affect flight safety, comfort, and operational capability.</p> <p>The topic was considered to be particularly relevant to the needs of the military community which is putting increased emphasis on the ability of today's and tomorrow's aircraft to fly safely and effectively in the types of adverse conditions dealt with in this symposium.</p> <p>ISBN 92-835-0527-1</p>	<p>Four aspects of adverse environmental conditions of interest to the flight mechanics specialist were addressed by this Symposium: atmospheric disturbances, reduced visibility, icing, and electromagnetic disturbances. All four of these can seriously affect flight safety, comfort, and operational capability.</p> <p>The topic was considered to be particularly relevant to the needs of the military community which is putting increased emphasis on the ability of today's and tomorrow's aircraft to fly safely and effectively in the types of adverse conditions dealt with in this symposium.</p> <p>ISBN 92-835-0527-1</p>
<p>Four aspects of adverse environmental conditions of interest to the flight mechanics specialist were addressed by this Symposium: atmospheric disturbances, reduced visibility, icing, and electromagnetic disturbances. All four of these can seriously affect flight safety, comfort, and operational capability.</p> <p>The topic was considered to be particularly relevant to the needs of the military community which is putting increased emphasis on the ability of today's and tomorrow's aircraft to fly safely and effectively in the types of adverse conditions dealt with in this symposium.</p> <p>ISBN 92-835-0527-1</p>	<p>Four aspects of adverse environmental conditions of interest to the flight mechanics specialist were addressed by this Symposium: atmospheric disturbances, reduced visibility, icing, and electromagnetic disturbances. All four of these can seriously affect flight safety, comfort, and operational capability.</p> <p>The topic was considered to be particularly relevant to the needs of the military community which is putting increased emphasis on the ability of today's and tomorrow's aircraft to fly safely and effectively in the types of adverse conditions dealt with in this symposium.</p> <p>ISBN 92-835-0527-1</p>